CARDIAC OPTOGENETICS: USING LIGHT TO OBSERVE AND EXCITE THE HEART

EDITED BY: Tobias Bruegmann, Stephan E. Lehnart and Godfrey Smith
PUBLISHED IN: Frontiers in Physiology

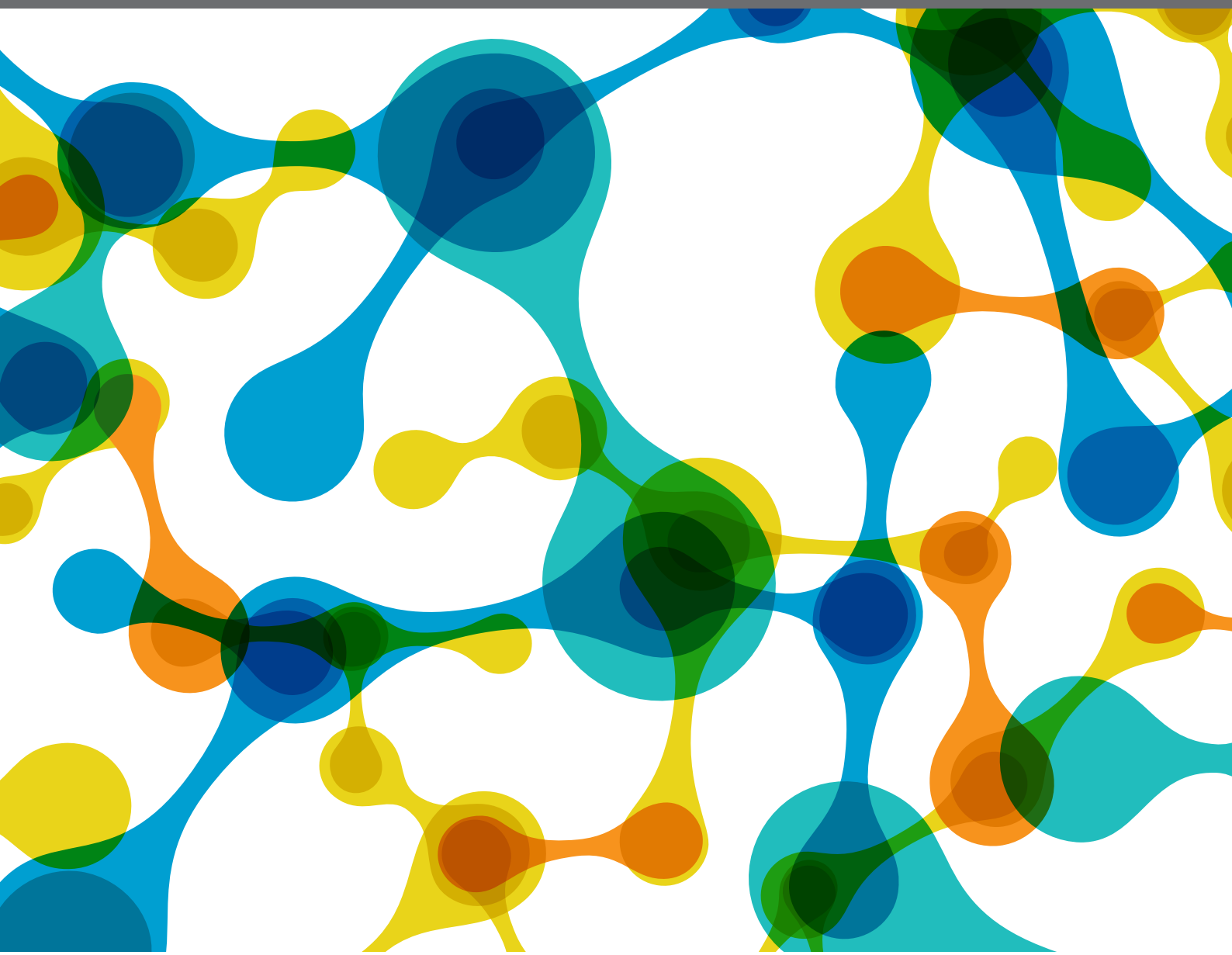

frontiers Research Topics

ISSN 1664-8714
ISBN 978-2-83250-582-3
DOI 10.3389/978-2-83250-582-3

About Frontiers

Frontiers is more than just an open-access publisher of scholarly articles: it is a pioneering approach to the world of academia, radically improving the way scholarly research is managed. The grand vision of Frontiers is a world where all people have an equal opportunity to seek, share and generate knowledge. Frontiers provides immediate and permanent online open access to all its publications, but this alone is not enough to realize our grand goals.

Frontiers Journal Series

The Frontiers Journal Series is a multi-tier and interdisciplinary set of open-access, online journals, promising a paradigm shift from the current review, selection and dissemination processes in academic publishing. All Frontiers journals are driven by researchers for researchers; therefore, they constitute a service to the scholarly community. At the same time, the Frontiers Journal Series operates on a revolutionary invention, the tiered publishing system, initially addressing specific communities of scholars, and gradually climbing up to broader public understanding, thus serving the interests of the lay society, too.

Dedication to Quality

Each Frontiers article is a landmark of the highest quality, thanks to genuinely collaborative interactions between authors and review editors, who include some of the world's best academicians. Research must be certified by peers before entering a stream of knowledge that may eventually reach the public - and shape society; therefore, Frontiers only applies the most rigorous and unbiased reviews.
Frontiers revolutionizes research publishing by freely delivering the most outstanding research, evaluated with no bias from both the academic and social point of view. By applying the most advanced information technologies, Frontiers is catapulting scholarly publishing into a new generation.

What are Frontiers Research Topics?

Frontiers Research Topics are very popular trademarks of the Frontiers Journals Series: they are collections of at least ten articles, all centered on a particular subject. With their unique mix of varied contributions from Original Research to Review Articles, Frontiers Research Topics unify the most influential researchers, the latest key findings and historical advances in a hot research area! Find out more on how to host your own Frontiers Research Topic or contribute to one as an author by contacting the Frontiers Editorial Office: frontiersin.org/about/contact

CARDIAC OPTOGENETICS: USING LIGHT TO OBSERVE AND EXCITE THE HEART

Topic Editors:
Tobias Bruegmann, University Medical Center Göttingen, Germany
Stephan E. Lehnart, University Medical Center Göttingen, Germany
Godfrey Smith, University of Glasgow, United Kingdom

Topic Editor Godfrey Smith is the founder, director and honorary Chief Scientific Officer of Clyde Biosciences Ltd (UK). The other Topic Editors declare no competing interests with regard to the Research Topic subject.

Citation: Bruegmann, T., Lehnart, S. E., Smith, G., eds. (2022). Cardiac Optogenetics: Using Light to Observe and Excite the Heart. Lausanne: Frontiers Media SA. doi: 10.3389/978-2-83250-582-3

Table of Contents

frontiers | Frontiers in Physiology

TYPE Editorial
PUBLISHED 11 October 2022
DOI 10.3389/fphys.2022.1031062

OPEN ACCESS

EDITED AND REVIEWED BY
Ruben Coronel,
University of Amsterdam, Netherlands

*CORRESPONDENCE
Tobias Bruegmann,
tobias.bruegmann@med.uni-goettingen.de

SPECIALTY SECTION
This article was submitted to Cardiac Electrophysiology, a section of the journal Frontiers in Physiology

RECEIVED 29 August 2022
ACCEPTED 05 September 2022
PUBLISHED 11 October 2022

CITATION
Bruegmann T, Smith GL and Lehnart SE (2022), Editorial: Cardiac optogenetics: Using light to observe and excite the heart.
Front. Physiol. 13:1031062.
doi: 10.3389/fphys.2022.1031062

Editorial: Cardiac optogenetics: Using light to observe and excite the heart

Tobias Bruegmann[1,2,3]*, Godfrey L. Smith[4] and Stephan E. Lehnart[2,3,5,6]

[1]Institute for Cardiovascular Physiology, University Medical Center Goettingen, Goettingen, Germany, [2]Cluster of Excellence "Multiscale Bioimaging: From Molecular Machines to Networks of Excitable Cells" (MBExC), University of Goettingen, Goettingen, Germany, [3]DZHK (German Centre for Cardiovascular Research), Partner Site Goettingen, Goettingen, Germany, [4]School of Cardiovascular and Metabolic Health, University of Glasgow, Glasgow, United Kingdom, [5]Department of Cardiology and Pulmonology, Heart Research Center Göttingen, University Medical Center Göttingen, Georg August University of Göttingen, Göttingen, Germany, [6]Collaborative Research Center SFB1190 "Compartmental Gates and Contact Sites in Cells", University of Goettingen, Goettingen, Germany

KEYWORDS

optogenetics, channelrhodopsins, cardiac arrhythmia, imaging, heart

Editorial on the Research Topic
Cardiac optogenetics: Using light to observe and excite the heart

This is the editorial to the special edition "Cardiac optogenetics: using light to observe and excite the heart.

The application of fluorescent voltage sensitive dyes to study excitable cells was established 50 years ago (Tasaki et al., 1969) but only recently has chemical and imaging technology developed sufficiently for its mainstream use. In contrast, the field of cardiac optogenetics was established only a decade ago by publications demonstrating light-mediated excitation of the heart in mice (Bruegmann et al., 2010), zebrafish (Arrenberg et al., 2010) and cardiomyocytes *in vitro* (Abilez et al., 2011; Jia et al., 2011). Ever since, the subject of optogenetics has expanded to encompass a number of different applications. Early translational approaches considered light-mediated cardiac resynchronization therapy (Nussinovitch and Gepstein 2015), defibrillation (Bruegmann et al., 2016; Crocini et al., 2016; Nyns et al., 2017) and cardioversion (Bruegmann et al., 2018; Nyns et al., 2019). In this regard, Diaz-Maue et al. developed a mesh of electrodes and LEDs to correlate electrical rotor activity during arrhythmias with defibrillation efficacy of optogenetic stimulation and Patrick Boyle's group explored in simulations the use and application of anion conducting channelrhodopsins (Ochs et al.). While leading also to depolarization in cardiomyocytes (Kopton et al., 2018), the much larger ion conductance improved the efficiency of optogenetic defibrillation, which is an intriguing result directly demanding experimental verification. State-of-the-art solutions for one of the biggest hurdles of translation, the development of implantable light devices has been expertly summarized and thoughtfully discussed by Igor Efimov's group in this issue (Madrid et al.).

One big advantage of optogenetic stimulation is the cell type-specific expression providing not only the chance for pain-free stimulation but also to characterize the specific role of different cell types by cell type-specific (e.g. ventricular cardiomyocytes versus Purkinje fibers) stimulation (Zaglia et al., 2015; Hulsmans et al., 2017; Wang et al., 2017) as well as imaging (Quinn et al., 2016) within the heart. In this context, Zaglia and Mongilo have expertly summarized new developments of optogenetic stimulation to assess the function and role of the intracardiac nervous system (Scalco et al.), emphasizing the heterocellular, increasingly complex composition and functions of specific cardiac tissues, and further raising the importance of optogenetic strategies to explore these.

Moreover, the range of applications of voltage-sensitive dyes combined with optogenetic stimulation in basic cardiovascular research have been critically reviewed by a group of scientists from the European Society of Cardiology Working Group for Cardiac Cellular Electrophysiology (Mullenbroich et al.). The review examines many of the novel techniques that optical physics have provided to extend the use of optical probes and actuators while also posing the next set of challenges to be addressed to extend further the applicability of these techniques. In this content, Jan Lebert and Jan Christoph present new algorithms for the analysis of voltage imaging with motion tracking stabilization to avoid the alterations of cardiac electrophysiology by contraction inhibitors with significant side effects (Lebert et al., 2022). Furthermore, Wegener and colleagues took advantage of transgenic biosensor mouse models to analyze the cytosolic and mitochondrial glutathione redox potential in single cardiomyocytes and the intact heart. Thereby they were able to show that Ca^{2+} leak caused by a ryanodine receptor missense mutation increases mitochondrial energy demand and ROS production under conditions of catecholaminergic stress (Wegener et al.). Finally, Philipp Sasse's group expanded the optogenetic toolbox for cardiac research demonstrating that the human coneopsin allows to control G_i signaling in embryonic stem cell derived cardiomyocytes (Cokic et al.). Thus, the three canonical G-protein pathways of the heart (Makowka et al., 2019; Wagdi et al., 2022) can now be investigated and their underlying kinetics precisely determined.

Daniel Pijnappel's group characterized potential long term effects of optogenetic stimulation via channelrhodopsins (Ordog et al.) and the groups of Christina Schüler and Leonardo Sacconi developed new methods and platforms for cardiac toxicity screening (Credi et al.; Engel et al.) which is one of the evolving cardiac research fields in which the use of optogenetic stimulation is becoming more and more standard (Klimas et al., 2016; Lapp et al., 2017; Rehnelt et al., 2017). Notably, the optical transparency of zebrafish and their rather easy handling as animal model as well as fast generation and genetic manipulation of transgenic animals, has led to their increasing use to study heart function using optogenetics (Baillie et al.), whereas intact hearts from mice and even bigger animals have to be cleared for imaging of the cell composition and structure (Olianti et al., 2022; Ren et al.).

In conclusion, this special issue is covering the broad range of dye-based imaging and optogenetic applications in the heart and the advances made in each branch of the subject by new technical improvements and comprehensive reviews. We hope that we and all contributors are able to trigger further interest in and advance the use of optogenetic stimulation and imaging within the field of cardiac research.

Author contributions

All authors listed have made a substantial, direct, and intellectual contribution to the work and approved it for publication.

Funding

This editorial was supported by funding from Deutsche Forschungsgemeinschaft SFB1190-P03 (number 264061860) to SEL; SFB1002 (number 193793266), SPP1926 (number 315212873) and Germany's Excellence Strategy EXC 2067/1 (number 390729940) each to TB and SEL. SEL is an investigator of the DZHK (German Centre for Cardiovascular Research). GS was funded by the British Heart Foundation project grant (number PG/14/66/30927).

Acknowledgments

We thank all contributors and reviewers for their work and impact on this special issue.

Conflict of interest

The authors declare that the writing of this editorial was conducted in the absence of any commercial or financial relationships that could be construed as a potential conflict of interest.

Publisher's note

References

Abilez, O. J., Wong, J., Prakash, R., Deisseroth, K., Zarins, C. K., and Kuhl, E. (2011). Multiscale computational models for optogenetic control of cardiac function. *Biophys. J.* 101, 1326–1334. doi:10.1016/j.bpj.2011.08.004

Arrenberg, A. B., Stainier, D. Y., Baier, H., and Huisken, J. (2010). Optogenetic control of cardiac function. *Science* 330, 971–974. doi:10.1126/science.1195929

Bruegmann, T., Beiert, T., Vogt, C. C., Schrickel, J. W., and Sasse, P. (2018). Optogenetic termination of atrial fibrillation in mice. *Cardiovasc. Res.* 114, 713–723. doi:10.1093/cvr/cvx250

Bruegmann, T., Boyle, P. M., Vogt, C. C., Karathanos, T. V., Arevalo, H. J., Fleischmann, B. K., et al. (2016). Optogenetic defibrillation terminates ventricular arrhythmia in mouse hearts and human simulations. *J. Clin. Invest.* 126, 3894–3904. doi:10.1172/JCI88950

Bruegmann, T., Malan, D., Hesse, M., Beiert, T., Fuegemann, C. J., Fleischmann, B. K., et al. (2010). Optogenetic control of heart muscle *in vitro* and *in vivo*. *Nat. Methods* 7, 897–900. doi:10.1038/nmeth.1512

Crocini, C., Ferrantini, C., Coppini, R., Scardigli, M., Yan, P., Loew, L. M., et al. (2016). Optogenetics design of mechanistically-based stimulation patterns for cardiac defibrillation. *Sci. Rep.* 6, 35628. doi:10.1038/srep35628

Hulsmans, M., Clauss, S., Xiao, L., Aguirre, A. D., King, K. R., Hanley, A., et al. (2017). Macrophages facilitate electrical conduction in the heart. *Cell.* 169, 510–522. doi:10.1016/j.cell.2017.03.050

Jia, Z., Valiunas, V., Lu, Z., Bien, H., Liu, H., Wang, H. Z., et al. (2011). Stimulating cardiac muscle by light: Cardiac optogenetics by cell delivery. *Circ. Arrhythm. Electrophysiol.* 4, 753–760. doi:10.1161/CIRCEP.111.964247

Klimas, A., Ambrosi, C. M., Yu, J., Williams, J. C., Bien, H., and Entcheva, E. (2016). OptoDyCE as an automated system for high-throughput all-optical dynamic cardiac electrophysiology. *Nat. Commun.* 7, 11542. doi:10.1038/ncomms11542

Kopton, R. A., Baillie, J. S., Rafferty, S. A., Moss, R., Zgierski-Johnston, C. M., Prykhozhij, S. V., et al. (2018). Cardiac electrophysiological effects of light-activated chloride channels. *Front. Physiol.* 9, 1806. doi:10.3389/fphys.2018.01806

Lapp, H., Bruegmann, T., Malan, D., Friedrichs, S., Kilgus, C., Heidsieck, A., et al. (2017). Frequency-dependent drug screening using optogenetic stimulation of human iPSC-derived cardiomyocytes. *Sci. Rep.* 7, 9629. doi:10.1038/s41598-017-09760-7

Lebert, J., Ravi, N., Kensah, G., and Christoph, J. (2022). Real-time optical mapping of contracting cardiac tissues with GPU-accelerated numerical motion tracking. *Front. Cardiovasc. Med.* 9, 787627. doi:10.3389/fcvm.2022.787627

Makowka, P., Bruegmann, T., Dusend, V., Malan, D., Beiert, T., Hesse, M., et al. (2019). Optogenetic stimulation of Gs-signaling in the heart with high spatio-temporal precision. *Nat. Commun.* 10, 1281. doi:10.1038/s41467-019-09322-7

Nussinovitch, U., and Gepstein, L. (2015). Optogenetics for *in vivo* cardiac pacing and resynchronization therapies. *Nat. Biotechnol.* 33, 750–754. doi:10.1038/nbt.3268

Nyns, E. C. A., Kip, A., Bart, C. I., Plomp, J. J., Zeppenfeld, K., Schalij, M. J., et al. (2017). Optogenetic termination of ventricular arrhythmias in the whole heart: Towards biological cardiac rhythm management. *Eur. Heart J.* 38, 2132–2136. doi:10.1093/eurheartj/ehw574

Nyns, E. C. A., Poelma, R. H., Volkers, L., Plomp, J. J., Bart, C. I., Kip, A. M., et al. (2019). An automated hybrid bioelectronic system for autogenous restoration of sinus rhythm in atrial fibrillation. *Sci. Transl. Med.* 11, eaau6447. doi:10.1126/scitranslmed.aau6447

Olianti, C., Giardini, F., Lazzeri, E., Costantini, I., Silvestri, L., Coppini, R., et al. (2022). Optical clearing in cardiac imaging: A comparative study. *Prog. Biophys. Mol. Biol.* 168, 10–17. doi:10.1016/j.pbiomolbio.2021.07.012

Quinn, T. A., Camelliti, P., Rog-Zielinska, E. A., Siedlecka, U., Poggioli, T., O'Toole, E. T., et al. (2016). Electrotonic coupling of excitable and nonexcitable cells in the heart revealed by optogenetics. *Proc. Natl. Acad. Sci. U. S. A.* 113, 14852–14857. doi:10.1073/pnas.1611184114

Rehnelt, S., Malan, D., Juhasz, K., Wolters, B., Doerr, L., Beckler, M., et al. (2017). Frequency-Dependent multi-well cardiotoxicity screening enabled by optogenetic stimulation. *Int. J. Mol. Sci.* 18, E2634. doi:10.3390/ijms18122634

Tasaki, I., Carnay, L., Sandlin, R., and Watanabe, A. (1969). Fluorescence changes during conduction in nerves stained with Acridine Orange. *Science* 163, 683–685. doi:10.1126/science.163.3868.683

Wagdi, A., Malan, D., Sathyanarayanan, U., Beauchamp, J. S., Vogt, M., Zipf, D., et al. (2022). Selective optogenetic control of Gq signaling using human Neuropsin. *Nat. Commun.* 13, 1765. doi:10.1038/s41467-022-29265-w

Wang, Y., Lin, W. K., Crawford, W., Ni, H., Bolton, E. L., Khan, H., et al. (2017). Optogenetic control of heart rhythm by selective stimulation of cardiomyocytes derived from Pnmt(+) cells in murine heart. *Sci. Rep.* 7, 40687. doi:10.1038/srep40687

Zaglia, T., Pianca, N., Borile, G., Da Broi, F., Richter, C., Campione, M., et al. (2015). Optogenetic determination of the myocardial requirements for extrasystoles by cell type-specific targeting of ChannelRhodopsin-2. *Proc. Natl. Acad. Sci. U. S. A.* 112, E4495–E4504. doi:10.1073/pnas.1509380112

frontiers in Physiology

ORIGINAL RESEARCH
published: 23 August 2021
doi: 10.3389/fphys.2021.710020

The Effects of Repetitive Use and Pathological Remodeling on Channelrhodopsin Function in Cardiomyocytes

Balázs Ördög, Alexander Teplenin, Tim De Coster, Cindy I. Bart, Sven O. Dekker, Juan Zhang, Dirk L. Ypey, Antoine A. F. de Vries† and Daniël A. Pijnappels†*

Laboratory of Experimental Cardiology, Department of Cardiology, Leiden University Medical Center, Leiden, Netherlands

OPEN ACCESS

Edited by:
Godfrey Smith, University of Glasgow, United Kingdom

Reviewed by:
Claudia Richter, Deutsches Primatenzentrum, Germany
Robert Kass, Columbia University, United States

***Correspondence:**
Balázs Ördög
B.Ordog@lumc.nl

†These authors share senior authorship

Specialty section:
This article was submitted to Cardiac Electrophysiology, a section of the journal Frontiers in Physiology

Received: *14 May 2021*
Accepted: *23 July 2021*
Published: *23 August 2021*

Citation:
Ördög B, Teplenin A, De Coster T, Bart CI, Dekker SO, Zhang J, Ypey DL, de Vries AAF and Pijnappels DA (2021) The Effects of Repetitive Use and Pathological Remodeling on Channelrhodopsin Function in Cardiomyocytes. Front. Physiol. 12:710020. doi: 10.3389/fphys.2021.710020

Aim: Channelrhodopsins (ChRs) are a large family of light-gated ion channels with distinct properties, which is of great importance in the selection of a ChR variant for a given application. However, data to guide such selection for cardiac optogenetic applications are lacking. Therefore, we investigated the functioning of different ChR variants in normal and pathological hypertrophic cardiomyocytes subjected to various illumination protocols.

Methods and Results: Isolated neonatal rat ventricular cardiomyocytes (NRVMs) were transduced with lentiviral vectors to express one of the following ChR variants: H134R, CatCh, ReaChR, or GtACR1. NRVMs were treated with phenylephrine (PE) to induce pathological hypertrophy (PE group) or left untreated [control (CTL) group]. In these groups, ChR currents displayed unique and significantly different properties for each ChR variant on activation by a single 1-s light pulse (1 mW/mm^2: 470, 565, or 617 nm). The concomitant membrane potential (V_m) responses also showed a ChR variant-specific profile, with GtACR1 causing a slight increase in average V_m during illumination ($V_{plateau}$: −38 mV) as compared with a $V_{plateau} > -20$ mV for the other ChR variants. On repetitive activation at increasing frequencies (10-ms pulses at 1–10 Hz for 30 s), peak currents, which are important for cardiac pacing, decreased with increasing activation frequencies by 17–78% ($p < 0.05$), while plateau currents, which are critical for arrhythmia termination, decreased by 10–75% ($p < 0.05$), both in a variant-specific manner. In contrast, the corresponding $V_{plateau}$ remained largely stable. Importantly, current properties and V_m responses were not statistically different between the PE and CTL groups, irrespective of the variant used ($p > 0.05$).

Conclusion: Our data show that ChR variants function equally well in cell culture models of healthy and pathologically hypertrophic myocardium but show strong, variant-specific use-dependence. This use-dependent nature of ChR function should be taken into account during the design of cardiac optogenetic studies and the interpretation of the experimental findings thereof.

Keywords: optogenetics, *in vitro*, cellular electrophysiology, action potential, ionic currents

INTRODUCTION

Optogenetics uses the light-sensitive proteins as actuators to take control over cellular function (Fenno et al., 2011; Ferenczi et al., 2019). In cardiology, optogenetics has become an important experimental approach during the past decade in the context of both basic and translational research, mostly owing to its unique capacity to precisely and reversibly modulate the membrane potential of cardiomyocytes by the use of microbial rhodopsins. This method has been successfully applied to achieve a wide range of research goals, including cardiac pacing (Arrenberg et al., 2010; Bruegmann et al., 2010), shaping of action potential (AP) waveforms (Park et al., 2014; Govorunova et al., 2016), sympathetic (Yu et al., 2017) and parasympathetic (Moreno et al., 2019; Machhada et al., 2020) neuromodulations of the heart, termination (Bingen et al., 2014), and spatiotemporal control (Majumder et al., 2018) of spiral waves *in vitro*, as well as the termination of ventricular (Bruegmann et al., 2016; Nyns et al., 2017; Li et al., 2021) and atrial fibrillation (Bruegmann et al., 2018; Nyns et al., 2019) *in vivo*. Such great diversity of possible applications has been fueled by the continuous expansion of the optogenetic toolbox with newly identified native microbial rhodopsins and engineered variants of previously identified microbial rhodopsins. Due to these efforts, a greatly diversified set of microbial rhodopsins is now available with distinctly different biophysical properties, such as ion selectivity, gating kinetics, or light absorption spectrum, allowing selection of the optimal variant for a particular application.

Channelrhodopsins (ChRs) are a group of microbial rhodopsins that function as light-gated ion channels. Channelrhodopsin-2 (ChR2) is a blue light-gated cation channel first described in the green alga *Chlamydomonas reinhardtii* (Nagel et al., 2003). ChR2 and its engineered variant carrying the gain-of-function mutation H134R (H134R) (Nagel et al., 2005) are the most frequently used microbial rhodopsin in optogenetic studies (Arrenberg et al., 2010; Bruegmann et al., 2010, 2016, 2018; Park et al., 2014; Moreno et al., 2019). The Ca^{2+}-translocating ChR (CatCh) was generated by introducing the L132C mutation into ChR2 (Kleinlogel et al., 2011). Since CatCh possesses increased activation kinetics and light sensitivity compared with ChR2, it has been the microbial rhodopsin of choice in several previous studies in cardiac optogenetics (Bingen et al., 2014; Feola et al., 2017; Watanabe et al., 2017; Majumder et al., 2018). Since the longer wavelengths of visible light penetrate the biological tissues better than the shorter wavelengths, the red-activatable ChR (ReaChR) (Lin et al., 2013), which is excited with orange to red light (590–630 nm), has been the ChR of choice in many *in vivo* studies (Nyns et al., 2017, 2019; Men et al., 2020). In contrast to cation ChRs, anion ChRs, such as the one first isolated in the cryptophyte *Guillardia theta* (GtACR1) (Govorunova et al., 2015), mainly conduct Cl^- ions. Given the distinctly different charge carriers, anion ChRs provide an alternative mechanism for controlling the membrane potential (V_m) in cardiomyocytes (Govorunova et al., 2016; Kopton et al., 2018). Considering their prevalence in the literature on cardiac optogenetics and their unique features, these four ChR variants have been included in this study.

To date, microbial rhodopsin variants have been characterized mainly in permanent (non-cardiac) cell lines (e.g., human embryonic kidney 293), *Xenopus laevis* oocytes, or primary neuronal cells to guide the selection of the best-suited variant for a particular application. Comparative data on the performance of different ChRs in cardiomyocytes have not yet been published, leaving the cardiac research community without proper selection guides. Furthermore, in the translational context, one aims to apply optogenetics in the pathological setting, while the ChR of choice should continue to perform well even after extensive and repetitive use. Dedicated and detailed studies into this matter are also lacking. Therefore, in this study, the functional properties of the aforementioned four ChR variants are investigated side-by-side in cardiomyocytes, under normal and pathological conditions while being subjected to illumination protocols of varying duration and intensiveness.

MATERIALS AND METHODS

Additional experimental procedures are described in the **Supplementary Material**.

Neonatal Rat Ventricular Cardiomyocytes

Neonatal rat ventricular cardiomyocytes (NRVMs) were isolated as described in detail in previous studies (Askar et al., 2013; Bingen et al., 2013). Two-day-old Wistar rats were anesthetized by 5% of isoflurane inhalation, and adequate anesthesia was confirmed by the absence of reflexes. The use of these animals for this particular purpose was approved by the Animal Experiments Committee of the Leiden University Medical Center (AVD116002017818) and conformed to the Guide for the Care and Use of Laboratory Animals as stated by the US National Institutes of Health.

Molecular Cloning and Lentiviral Vector Production

The lentiviral vector (LV) shuttle constructs encoding influenza A virus hemagglutinin (HA) epitope- and fluorescent protein-tagged ChR variants were constructed by standard cloning procedures using plasmids pAAV-hSyn-hChR2(H134R)-EYFP (RRID:Addgene_26973), pLenti-CaMKIIa-hChR2(L132C)-EYFP-WPRE (Feola et al., 2017), pLenti-ReaChR-citrine (RRID:Addgene_50956) (Lin et al., 2013), and pFUG-hGtACR1-EYFP (RRID:Addgene_67795) as starting materials (**Figure 1A**). Self-inactivating LV particles were produced in 293T cells and were purified as previously described (Feola et al., 2016). The functional titer of each LV batch was determined by limiting dilution assays in NRVM monolayers and was taken into consideration during transductions to ensure equal LV dose in each experimental group. A single batch of each LV vector was used for the entire study to eliminate any possible experimental variability arising from the use of vector batches of different titer purity and/or quality.

Cell Culture and Transduction

Neonatal rat ventricular cardiomyocytes were seeded on bovine fibronectin (Sigma-Aldrich)-coated culture plates or round

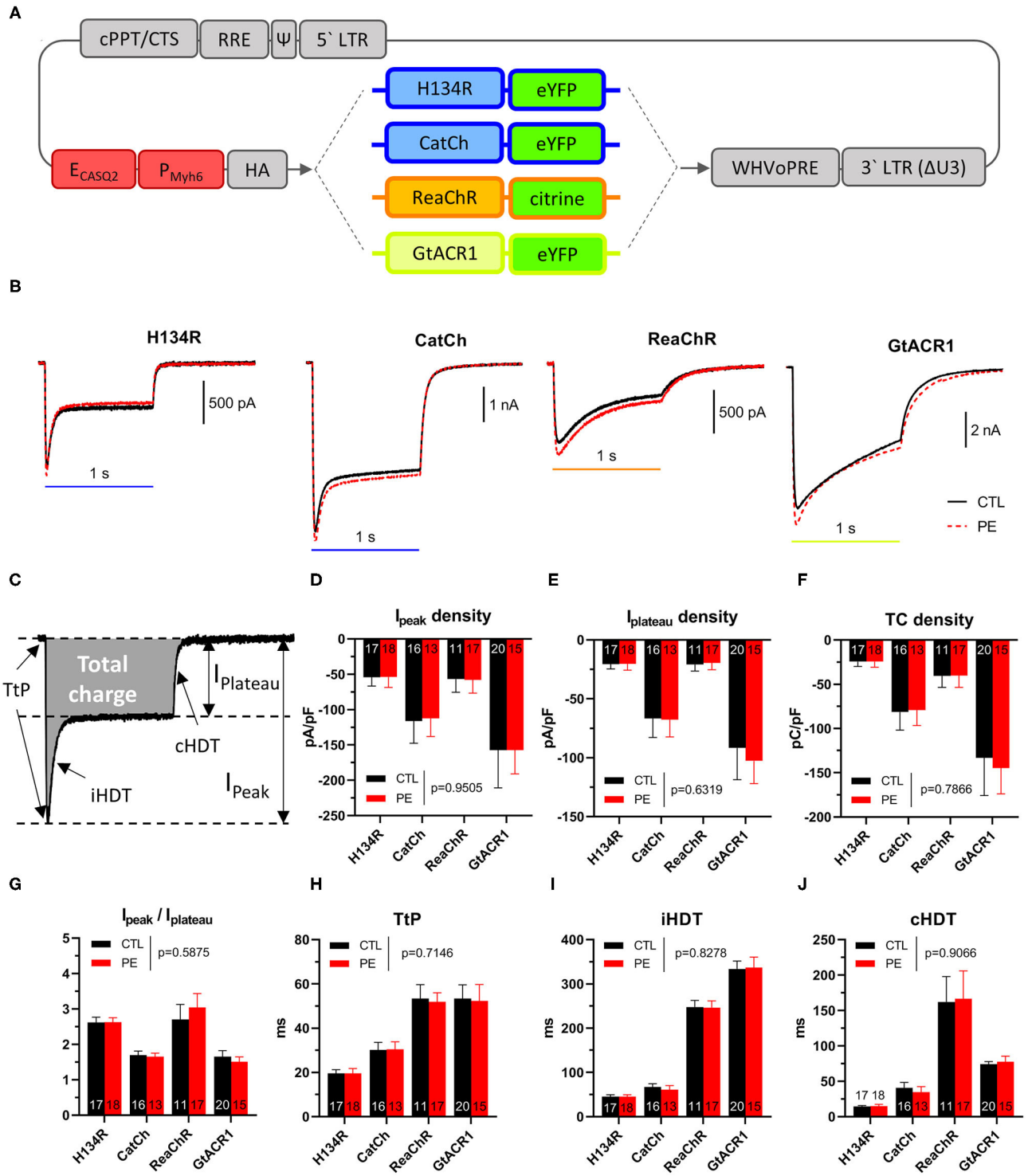

FIGURE 1 | (A) Schematic map of lentiviral vector shuttle constructs used in this study. Gray indicates viral vector elements, including the human immunodeficiency virus type 1, 5′ and 3′ long terminal repeats [5′ LTR, 3′ LTR (ΔU3)], packaging signal (Ψ), Rev-response element, central termination site and polypurine tract (cPPT/CTS), the woodchuck hepatitis virus posttranscriptional regulatory element (WHVoPRE), a chimeric cardiomyocyte-specific promoter (dark red) consisting of the enhancer of the human calsequestrin 2 gene (E_{CASQ2}) and the promoter of the mouse myosin heavy chain 6 gene (P_{Myh6}), the coding sequence of influenza A virus hemagglutinin (HA; N-terminal), and fluorescent protein-tagged (eYFP or citrine, C-terminal) ChR variants (H134R, CatCh, ReaChR, and GtACR1). **(B–J)** Characterization of photocurrents produced by dark-adapted ChR variants after activation by blue (470 nm, for H134R and CatCh), amber (565 nm, for GtACR1) or red (617 nm, for ReaChR) light (1 s, 1 mW/mm^2) in control (CTL) and in phenylephrine (PE)-treated neonatal rat ventricular cardiomyocytes (NRVMs).

(Continued)

FIGURE 1 | (B) Representative photocurrent recordings from CTL (black) and PE-treated (red) cells expressing ChR variants. **(C)** Schematic representation of the quantified parameters. **(D)** Peak current (I_{peak}) densities. **(E)** Plateau current densities ($I_{plateau}$). **(F)** Total charge densities. **(G)** I_{peak}–$I_{plateau}$ ratios. **(H)** Time to peak current (TtP). **(I)** Inactivation half-decay time (iHDT). **(J)** Closing half-decay time (cHDT). Data are presented as mean ± 95% CI for the number of cells indicated in the bar graphs. The *p*-values corresponding to the effects of PE treatment vs. CTL conditions were calculated by using two-way ANOVA.

coverslips and were kept in Advanced Dulbecco's Modified Eagle Medium supplemented with 2% of heat-inactivated horse serum, GlutaMAX Supplement (2 mM), and Penicillin-Streptomycin (50 U and 50 μg/ml, respectively, all from Thermo Fisher Scientific). Fibroblast growth was suppressed by mitomycin-C treatment (Askar et al., 2011) on Day 2. On the same day, NRVMs were transduced with equal doses of each LV at a multiplicity of infection of 1.5, which resulted in ∼80% yellowish-green fluorescent cells as assessed by fluorescence microscopy. Hypertrophy was induced by exposing the NRVMs for 24 h to 100 μM of phenylephrine (PE) on Day 3. PE-treated NRVMs showed hallmarks of pathological hypertrophy, including significantly ($p < 0.05$) increased cell surface area, atrial natriuretic peptide level, total protein content, and AP duration (APD) compared with control (CTL) cells as early as on Day 5 (**Supplementary Figure 1**).

Patch Clamp and Light Delivery

Patch clamp experiments were carried out at room temperature (23–25°C) on single, well-separated NRVMs cultured on round coverslips in 24-well plates at a density of 10^4 cells/well. The measurements took place in yellowish-green fluorescent NRVMs on Days 5 and 6, using the perforated and ruptured patch clamp configurations for the recording of V_m and transmembrane currents, respectively, as described in detail in the **Supplementary Material**.

To activate ChRs, NRVMs were illuminated by using commercially available 470-, 565- or 617-nm collimated light-emitting diodes (LEDs) (Thorlabs, Newton, NJ, United States) mounted on three independent camera ports of a Zeiss Axiovert 35 inverted microscope *via* a 40× magnification objective lens. LEDs were controlled by using Clampex software (Molecular Devices, San Jose, CA, United States) using independent analog outports of the Digidata 1440 D/A interface (v10, Molecular Devices, San Jose, CA, United States). The same illumination intensity (1 mW/mm^2) was used in all experiments and for all wavelengths.

Data Analysis and Statistical Methods

Numeric data were extracted from Axon Binary Format files by using the pyABF module[1] and were analyzed using custom software written in house dedicated to each experimental type, as described in detail in the **Supplementary Material**. Statistical analyses were carried out by using GraphPad Prism software (version 8.4.2, Graphpad Software, LLC, San Diego, CA, United States). In most of the analyses, group means were compared by using the two-way ANOVA, considering "treatment" (i.e., PE and CTL) and "ChR variant" (i.e., H134R, CatCh, ReaChR, and GtACR1) or "treatment" and "preconditioning frequency" (1, 2, 3, 4, 5, 7.5, and 10 Hz) as independent discrete variables and using Tukey's *post-hoc* analysis to correct for multiple comparisons. Preconditioned current parameters were normalized to the corresponding dark-adapted values obtained from the same cell, yielding relative preconditioned parameters. The one-sample Student's *t*-test was used to test whether relative 1-Hz preconditioned values differed from the corresponding dark-adapted values represented by the hypothetical value of 1. To assess the "ChR variant" effect on relative 1-Hz preconditioned current parameters, 2–10-Hz preconditioning data were omitted, and the two-way ANOVA was carried out on 1-Hz preconditioned values using "ChR variant" and "treatment" as independent variables. Linear regression was used to detect preconditioning frequency-dependent changes by testing whether non-zero slopes were present. A possible effect of "treatment" or "ChR variant" on slopes was assessed in follow-up tests using two-way ANOVA. A $p < 0.05$ was considered statistically significant. Numerical data are presented as mean and the 95% CI in the form of [lower boundary, upper boundary], and *n* represents the number of experiments from independent cells.

[1]Harden, S.W. (2020). pyABF 2.2.3. https://pypi.org/project/pyabf/

RESULTS

Dark-Adapted Photocurrent Properties

Channelrhodopsin currents are known to undergo inactivation (also known as desensitization) due to use-dependent transitions between dark- and light-adapted states and to recover from inactivation on the seconds time scale (Nagel et al., 2003; Schneider et al., 2015). When ChRs are activated repetitively, partial recovery from inactivation results in decreased photocurrent amplitudes. In order to prevent such bias, in the first set of experiments, ChRs were allowed to undergo complete dark adaptation. To this end, NRVMs expressing ChR variants were kept in the dark for 3 min before the application of each light pulse. Cells were then illuminated by a single, 1-s light pulse of 1 mW/mm^2. H134R and CatCh were activated by blue (470 nm) light, while GtACR1 and ReaChR were opened with amber (565 nm) and red (617 nm) light, respectively.

Whole-cell photocurrents showed distinct characteristics for each of the four ChR variants, with similar dynamics observed in CTL and in PE-treated NRVMs (**Figure 1B**). For each ChR variant, the maximal current (I_{peak}) density was reached shortly after light onset with the time to I_{peak} (TtP, **Figure 1C**) being indicative for the opening speed of a particular ChR variant. After reaching I_{peak}, photocurrent amplitudes decayed to the so-called plateau current ($I_{plateau}$), which was defined as the current amplitude at the end of the light pulse. The rate of current decay from I_{peak} to $I_{plateau}$ was characterized by the inactivation half-decay time (iHDT). Following light offset, currents returned to

baseline with kinetics distinctly different for each ChR variant, characterized as closing half-decay time (cHDT).

Quantitative properties of dark-adapted photocurrents are shown in **Table 1** and **Figures 1D–J**. I_{peak} did not differ between CTL and PE-treated NRVMs ($p = 0.9505$, **Figure 1D**). GtACR1 produced the largest I_{peak}, followed by CatCh ($p = 0.0298$). I_{peak} of ReaChR and H134R was similar but smaller than that of CatCh ($p = 0.034$ and $p = 0.0007$ compared with CatCh, respectively). Similar to I_{peak}, $I_{plateau}$ did not significantly differ between PE-treated and CTL cells ($p = 0.6319$, **Figure 1E**). NRVMs expressing GtACR1 exhibited the largest $I_{plateau}$, followed by CatCh ($p = 0.0007$), ReaChR ($p < 0.0001$), and H134R ($p < 0.0001$). ReaChR and H134R $I_{plateau}$ densities were not different ($p > 0.9999$). GtACR1 and CatCh conduct the largest and second largest amount of cell size-normalized total charge (TC), respectively ($p < 0.0001$) (**Figure 1F**). TC densities were not different ($p = 0.5191$) between ReaChR and H134R but much smaller than those of GtACR1 and CatCh ($p < 0.05$, **Figure 1F**). PE administration did not affect TC densities ($p = 0.7866$, **Figure 1F**). Interestingly, I_{peak}–$I_{plateau}$ ratios were similar for CatCh and GtACR1 ($p > 0.05$) but were lower compared with those of H134R and ReaChR ($p < 0.05$) (**Figure 1G**), which can be explained by the relatively low level of CatCh and GtACR1 inactivation (**Figure 1B**).

Then, the kinetic properties (i.e., TtP, iHDT, and cHDT) of dark-adapted ChR currents were determined for each ChR variant both in CTL and in PE-treated NRVMs (**Table 1** and **Figures 1H–J**). Pathological hypertrophy of NRVMs, as induced by PE, had no significant effect on TtP, iHDT, or cHDT ($p = 0.7654$, $p = 0.8278$, and $p = 0.9066$, compared with CTL, respectively). However, each variant exhibited distinctive kinetic properties. For example, H134R exhibited the smallest average TtP, iHDT, and cHDT and was therefore the fastest ChR variant ($p < 0.05$, **Figures 1H–J**). CatCh was slower compared with H134R ($p < 0.05$), but faster than ReaChR and GtACR1 ($p < 0.05$) with respect to all three kinetic parameters. ReaChR and GtACR1 showed similar TtP values ($p = 0.9999$) and required a prolonged period to reach I_{peak} following the activation by light (**Figure 1H**). However, ReaChR was inactivating faster compared with GtACR1 ($p < 0.0001$, **Figure 1I**), whereas GtACR1 was closing much faster than ReaChR ($p < 0.0001$, **Figure 1J**).

TABLE 1 | Dark-adapted photocurrent properties in control (CTL) and phenylephrine (PE)-treated NRVMs expressing H134R, CatCh, ReaChR, or GtACR1.

	CTL	PE
	I_{peak} (pA/pF)	
H134R	−54.4 [−66.8, −41.9], $n = 17$	−54.2 [−68.8, −39.5], $n = 18$
CatCh	−116.2 [−147.7, −84.7], $n = 16$	−112.5 [−138.2, −86.9], $n = 13$
ReaChR	−57 [−75.5, −38.4], $n = 11$	−58.2 [−76.7, −39.7], $n = 17$
GtACR1	−157.5 [−210.6, −104.3], $n = 20$	−157.4 [−191, −123.9], $n = 15$
	$I_{plateau}$ (pA/pF)	
H134R	−20.5 [−24.7, −26.3], $n = 17$	−20.4 [−25.7, −15.1], $n = 18$
CatCh	−66.8 [−82.8, −50.7, $n = 16$]	−67.8 [−82.3, −53.2, $n = 13$]
ReaChR	−20.9 [−26.5, −15.2], $n = 11$	−19.5 [−25.3, −13.5], $n = 17$
GtACR1	−91.8 [−118.6, −64.9, $n = 20$]	−102.7 [−122, −83.4], $n = 15$
	Total charge (pC/pF)	
H134R	−24.5 [−29.9, −19.1], $n = 17$	−24.4 [−30.8, −18.1], $n = 18$
CatCh	−81.3 [−101.9, −60.7], $n = 16$	−79.4 [−96.6, −62.2], $n = 13$
ReaChR	−40.8 [−53.6, −28], $n = 11$	−40.2 [−53.6, −26.8], $n = 17$
GtACR1	−133.2 [−175.7, −90.8], $n = 20$	−144.7 [−173.8, −115.6], $n = 15$
	I_{peak}/$I_{plateau}$	
H134R	2.6 [2.5, 2.8], $n = 17$	2.6 [2.5, 2.6], $n = 18$
CatCh	1.7 [1.6, 1.8], $n = 16$	1.6 [1.5, 1.8], $n = 13$
ReaChR	2.7 [2.3, 3.1], $n = 11$	3 [2.6, 3.4], $n = 17$
GtACR1	1.6 [1.5, 1.8], $n = 20$	1.5 [1.4, 1.6], $n = 15$
	Time to peak (ms)	
H134R	19.6 [17.9, 21.2], $n = 17$	19.5 [17.3, 21.8], $n = 18$
CatCh	30.1 [26.7, 33.6], $n = 16$	30.5 [27.1, 33.9], $n = 13$
ReaChR	53.4 [47.2, 59.7], $n = 11$	51.9 [47.7, 56], $n = 17$
GtACR1	53.3 [47.1, 59.6], $n = 20$	52.3 [44.9, 59.7], $n = 15$
	Inactivation half-decay time (ms)	
H134R	45.7 [41.7, 49.7], $n = 17$	45.7 [41.8, 49.6], $n = 18$
CatCh	67 [59.6, 74.4], $n = 16$	60.8 [51.4, 70.1], $n = 13$
ReaChR	247.6 [232.7, 262.6], $n = 11$	246.4 [231.3, 261.5], $n = 17$
GtACR1	333.7 [315.5, 351.8], $n = 20$	337 [313.4, 360.6], $n = 15$
	Closing half-decay time (ms)	
H134R	14.4 [13, 15.9], $n = 17$	14.7 [11.9, 17.5], $n = 18$
CatCh	40.5 [32.7, 48.3], $n = 16$	34.6 [26.7, 42.4], $n = 13$
ReaChR	161.9 [126.1, 197.8], $n = 11$	166.8 [127.7, 205.8], $n = 17$
GtACR1	74.1 [70.3, 77.8], $n = 20$	77.7 [70, 85.3], $n = 15$

Data are presented as mean and 95% CI, n represents the number of cells.

Membrane Potential (V_m) Response to Dark-Adapted ChR Activation

The V_m response to dark-adapted ChR activation was studied by the perforated patch clamp technique under the previously used illumination regime, using a single, 1-s light pulse of 1 mW/mm^2, following a dark period of 3 min to allow complete ChR recovery from inactivation. For the cation ChRs (i.e., H134R, CatCh, and ReaChR) and the anion ChR (i.e., GtACR1), illumination resulted in pronounced membrane depolarization (**Figure 2A**). During the dark period, electrically triggered APs were recorded, showing PE-induced prolongation of APD at 80% repolarization (APD_{80}) as a sign of electrical remodeling ($p < 0.0001$, **Figure 2B**). The effect of ChR activation on the membrane potential was characterized by measuring V_m at the time of light offset, yielding a parameter that is often referred to as the plateau potential ($V_{plateau}$). Despite the marked electric remodeling of PE-treated NRVMs (**Figure 2B**), average $V_{plateau}$ values were not statistically different in CTL compared with PE-treated cells ($p = 0.5147$, **Figure 2C**). GtACR1 activation resulted in the most negative average $V_{plateau}$ (−38 mV, 95% CI [−42.6, −33.4] in CTL and −37.8 mV, 95% CI [−44.3, −31.3] in PE-treated cells). Significantly, more positive $V_{plateau}$ values were achieved with H134R and ReaChR ($p < 0.0001$), as H134R activity resulted in −18.8 mV (95% CI [−22.0, −15.7]) and −16.7 mV (95% CI [−19.7, −13.6]) $V_{plateau}$ values on average, whereas ReaChR activation depolarized the cell membrane to

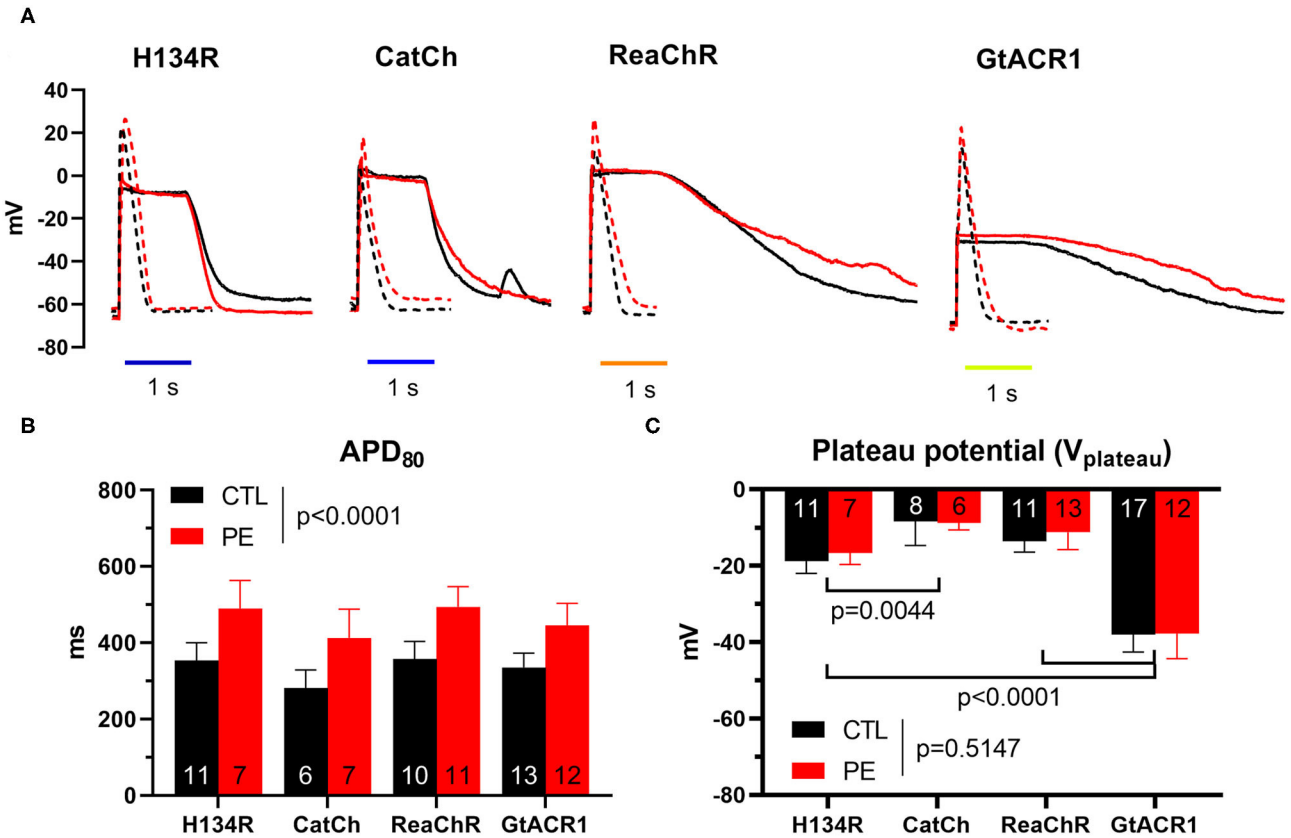

FIGURE 2 | Membrane potential (V_m) responses of CTL and PE-treated NRVMs expressing one of the dark-adapted ChR variants, elicited by electrical pacing at 1 Hz or illumination by blue (470 nm, for H134R and CatCh), amber (565 nm, for GtACR1), or red (617 nm, for ReaChR) light (1 s, 1 mW/mm^2). **(A)** APs (dashed) and light-induced V_m response (solid) in CTL (black) and in PE-treated (red) cells. **(B)** Action potential durations (APDs), represented by APD_{80} values. **(C)** Plateau potential ($V_{plateau}$) values, defined as V_m at the end of the illumination. Data are presented as mean ± 95% CI for the number of cells indicated in the bar graphs. The *p*-values corresponding to the effects of PE treatment vs. CTL conditions were calculated by using two-way ANOVA.

−13.5 mV (95% CI [−16.4, −10.7]) and −11.3 mV (95% CI [−15.8, −6.7]) in CTL vs. PE-treated NRVMs, respectively (**Figure 2C**). Illumination gave rise to the most robust membrane depolarization in the presence of CatCh ($p = 0.0044$ vs. H134R), resulting in −8.3 mV (95% CI [−14.7, −2.0]) and −8.9 mV (95% CI [−10.6, −6.9]) average $V_{plateau}$ values in CTL and PE-treated NRVMs, respectively (**Figure 2C**). Despite the varying degree of light-induced membrane depolarization, each ChR variant prevented the initiation of APs by electrical stimulation during illumination (**Supplementary Figure 2**).

Photocurrent Properties During Preconditioning by Light

The effects of light adaptation on ChR currents were determined, both in PE-treated and in CTL NRVMs. To this end, ChRs were subjected to a preconditioning illumination protocol consisting of trains of 10-ms light pulses (1 mW/mm^2), delivered at increasing frequencies ranging from 1 to 10 Hz and lasting for 30 s at each frequency (**Figure 3A** and **Supplementary Figure 3**). The first preconditioning light pulse train (1 Hz) was preceded by a 3-min dark period allowing complete ChR relaxation and was followed without interruption by the higher-frequency preconditioning illumination protocols. To gain insight into the effects of light adaptation on ChR function, NRVMs were illuminated after each preconditioning pulse train by a light pulse of the same duration, intensity and wavelengths as used to characterize the dark-adapted ChRs. This allowed us to directly compare dark-adapted and light-adapted ChR function and to study the effects of recurrent activation by light in a quantitative manner both in PE-treated and CTL cells.

The data obtained by this programmed illumination regime are presented as follows. ChR current behavior and the concomitant V_m response during the preconditioning pulse train are presented further in the "Membrane potential (V_m) response to preconditioning illumination protocol" section and in **Figures 3**, **4**, whereas ChR current properties and changes in V_m elicited by the prolonged illumination following each preconditioning pulse train are analyzed in the "Effects of preconditioning by light on photocurrents," "Membrane potential (V_m) response to preconditioned photocurrents" sections and in **Figures 5**, **6**, respectively.

First, ChR current behavior under preconditioning illumination protocols was assessed. Peak currents were

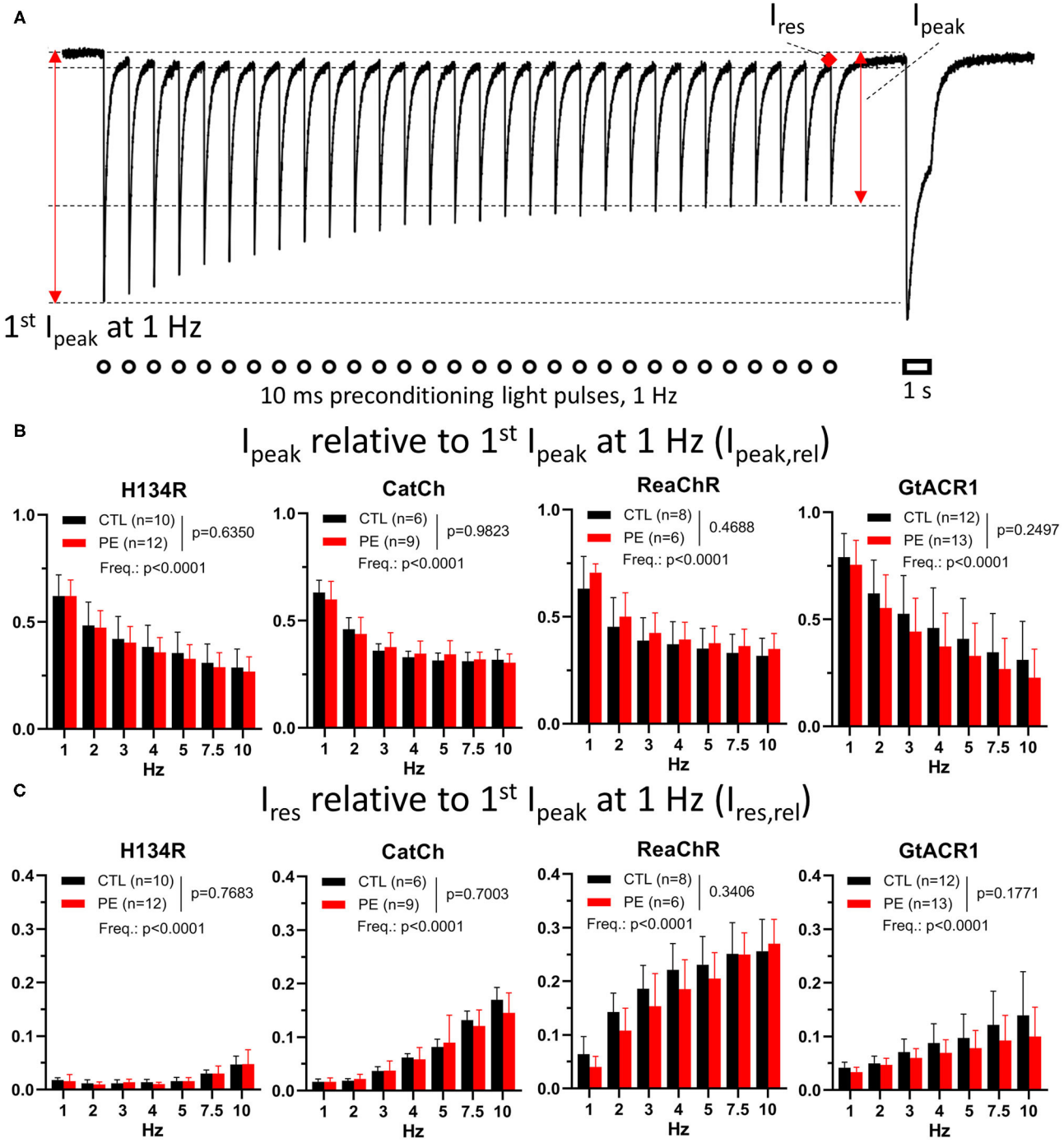

FIGURE 3 | Photocurrent amplitudes during preconditioning by light in CTL and in PE-treated ChR-expressing NRVMs. **(A)** Schematic representation of the quantified parameters and the experimental protocol, overlaid with a single current trace from a ReaChR-expressing CTL NRVM subjected to a 1-Hz preconditioning light pulse train. The preconditioning illumination protocol consisted of brief (i.e., 10-ms) blue (470 nm, for H134R and CatCh), amber (565 nm, for GtACR1), or red (617 nm, for ReaChR) light (1 mW/mm^2) pulses delivered at a range of frequencies between 1 and 10 Hz for a duration of 30 s. Each preconditioning pulse train was followed by a 1-s light pulse of the corresponding wavelength and identical intensity. The 1-Hz pulse train was applied after a 3-min dark period and was followed without interruption by higher-frequency pulse trains. The quantified current properties included peak current amplitude elicited by the first light pulse of the 1-Hz pulse train (first I_{peak} at 1 Hz), peak current (I_{peak}), as defined by the maximal current amplitude measured at the end of the light pulse train at each frequency and the residual current (I_{res}), which was measured at the end of the dark period before the last light pulse at each frequency. Open circles and the open bar indicate illumination times. **(B)** Average $I_{peak,rel}$ values calculated as I_{peak} at the end of the pulse train normalized to the first I_{peak} at 1 Hz for each frequency. **(C)** Average $I_{res,rel}$ values calculated as I_{res} at the end of the pulse train normalized to the first I_{peak} at 1 Hz for each cell. Data are presented as mean ± 95% CI for the number of cells (n) indicated in each panel. The p-values corresponding to the effects of PE treatment vs. CTL conditions and the effect of preconditioning light pulse frequency (Freq.) were calculated by using two-way ANOVA.

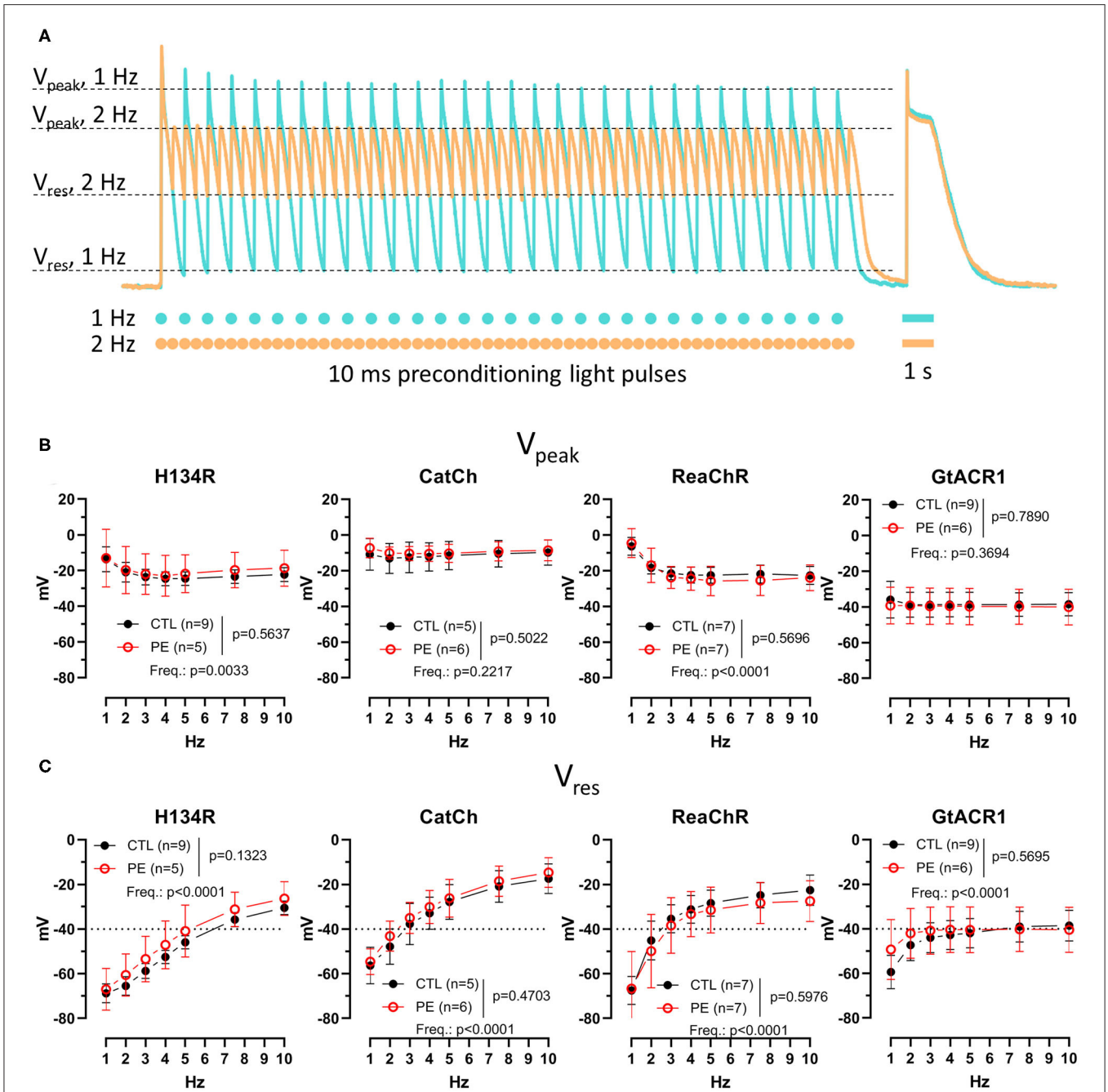

FIGURE 4 | Membrane potential (V_m) response during preconditioning by light in CTL and in PE-treated ChR-expressing NRVMs. **(A)** Schematic representation of the quantified parameters and the experimental protocol, overlaid with representative V_m recordings for 1-Hz (turquoise) and 2-Hz (apricot) preconditioning pulse trains obtained from an NRVM expressing ReaChR. Dots and bars below the V_m recording indicate the timing of the 10-ms and 1-s light pulses, respectively. **(B)** Peak V_m (V_{peak}) measured at the end of the pulse train. **(C)** Residual V_m (V_{res}) measured at the end of the pulse train. Data are presented as mean ± 95% CI for the number of cells (n) indicated in each panel. The p-values corresponding to the effects of PE treatment vs. CTL conditions and the effect of preconditioning light pulse frequency (Freq.) were calculated by using two-way ANOVA.

measured at the end of the pulse train of each frequency and were normalized to the peak current triggered by the first light pulse of the 1-Hz pulse train representing the dark-adapted state, yielding relative peak currents ($I_{peak,rel}$, **Figure 3A**). In general, average $I_{peak,rel}$ values decreased with an increase in the frequency of the preconditioning light pulse train (**Figure 3B**). At the end of the first train of light pulses (1 Hz train), I_{peak} was ∼35% lower for H134R, CatCh, and ReaChR than at its

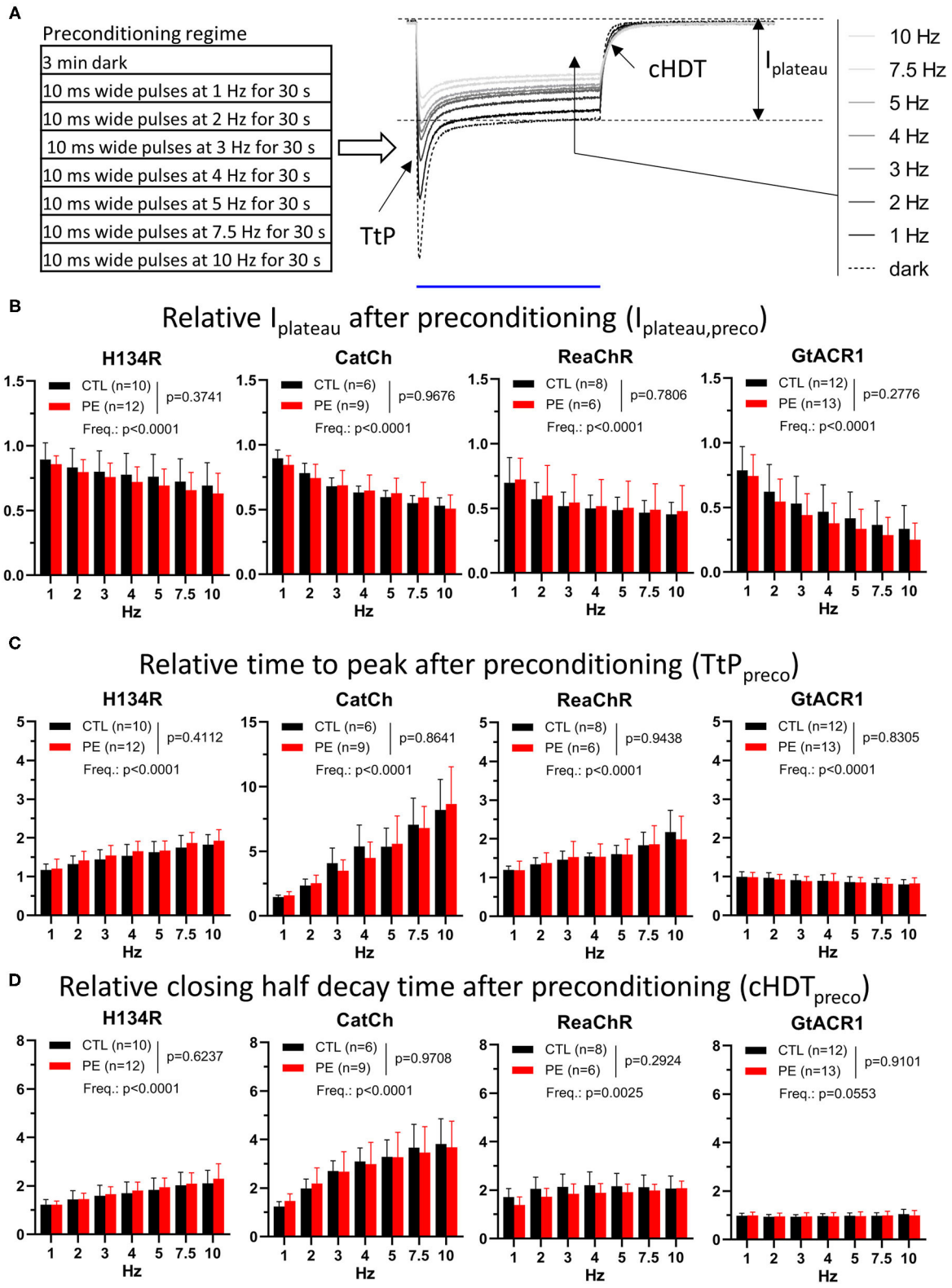

FIGURE 5 | Properties of photocurrents elicited by blue (470 nm, for H134R and CatCh), amber (565 nm, for GtACR1), or red (617 nm, for ReaChR) light pulses of 1 s (1 mW/mm^2) following preconditioning in CTL and in PE-treated ChR-expressing NRVMs. **(A)** Schematic representation of the experimental protocol (left) and the quantified current parameters together with a representative recording of a series of preconditioned photocurrents from an NRVM expressing the H134R ChR variant

(Continued)

FIGURE 5 | (right). The blue line below the current traces represents the 1-s illumination period. **(B)** Preconditioned plateau current amplitudes ($I_{plateau,preco}$) relative to $I_{plateau}$ observed in the dark-adapted state. **(C)** Preconditioned time to peak (TtP_{preco}) relative to TtP observed in the dark-adapted state. **(D)** Preconditioned closing half-decay time ($cHDT_{preco}$) relative to cHDT measured in the dark-adapted state. Each measured value was normalized by the corresponding data point obtained from the experiment carried out in the same cell under dark-adapted conditions (dark) as shown in **Figure 1**. Data are presented as mean ± 95% CI for the number of cells (*n*) indicated in each panel. The *p*-values corresponding to the effects of PE treatment vs. CTL conditions and the effect of preconditioning light pulse frequency (Freq.) were calculated by using two-way ANOVA.

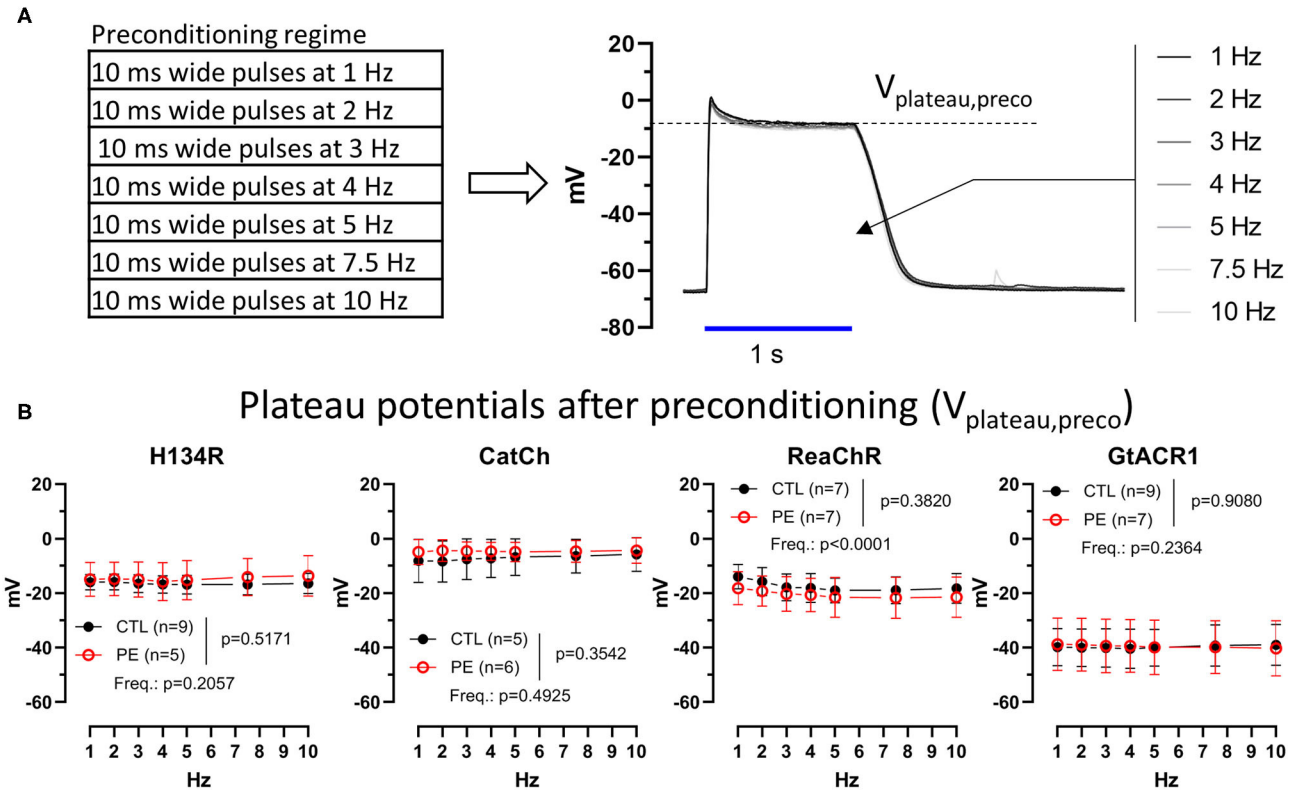

FIGURE 6 | Membrane potential (V_m) response to a 1-s blue (470 nm, for H134R and CatCh), amber (565 nm, for GtACR1), or red (617 nm, for ReaChR) light pulse (1 mW/mm^2) following preconditioning in CTL and PE-treated ChR-expressing NRVMs. **(A)** Schematic representation of the experimental protocol (left) and a representative example of a series of V_m traces recorded from an NRVM expressing H134R following preconditioning by different optical pacing frequencies (right). **(B)** Plateau potentials as the function of preconditioning pulse train frequency. Data are presented as mean ± 95% CI for the number of cells (*n*) indicated in each panel. The *p*-values corresponding to the effect of PE treatment vs. CTL conditions and the effect of preconditioning light pulse frequency (Freq.) were calculated by using two-way ANOVA.

beginning. Of all ChR variants, I_{peak} was most stable ($p < 0.05$) under the 1-Hz preconditioning illumination protocol for GtACR1, showing only ∼25% decrease compared with the dark-adapted state (**Figure 3B**). Pathological hypertrophy, as induced by PE treatment, had no effect on average $I_{peak,rel}$ values, whereas the effect of pulse train rate was highly significant for each ChR variant (**Figure 3B**). Linear regression of the data presented in **Figure 3B** confirmed the existence of a negative correlation between $I_{peak,rel}$ and preconditioning frequency by yielding significantly non-zero negative slopes ($p < 0.0001$) for all ChR variants, with the steepest negative slope being calculated for GtACR1 ($p < 0.0001$), indicating a stronger use-dependence of the GtACR1 I_{peak} compared with other variants (**Supplementary Figure 7A**).

Residual currents (I_{res}) were measured 1 ms before the application of the last light pulse of each train and were normalized to the first peak current of the 1-Hz pulse train, yielding $I_{res,rel}$ (**Figure 3C**). Average $I_{res,rel}$ values were not different in PE-treated compared with CTL cells ($p > 0.05$), while the effect of pulse train frequency was highly significant ($p < 0.0001$, **Figure 3C**). $I_{res,rel}$ observed at the end of the 1-Hz pulse train was smallest for H134R ($p < 0.05$) and largest for ReaChR ($p < 0.05$). Linear regression revealed that $I_{res,rel}$ increased with increasing frequency of the preconditioning pulse train, i.e., for each ChR variant, a significantly non-zero positive slope ($p < 0.0001$) was obtained. Slopes of trend lines were smallest for H134R ($p < 0.05$), significantly larger for GtACR1 ($p < 0.05$), and largest for CatCh and ReaChR ($p < 0.05$, **Figure 3C** and

Supplementary Figure 7B). Notably, the variants displaying the highest frequency-dependence of I_{res} (i.e., CatCh and ReaChR) also showed the slowest closing kinetics in the dark-adapted state (cHDT, **Figure 1J**), indicating the existence of a correlation between these two functional parameters.

Membrane Potential (V_m) Response to Preconditioning Illumination Protocol

The V_m response during the preconditioning illumination protocol was characterized by two distinct indicative V_m values for each pulse train. V_{peak} was defined as the most positive V_m value observed during the last duty cycle of each pulse train, whereas V_{res}, to the analogy of I_{res}, was measured as the V_m value within 1 ms preceding the onset of the last light pulse of each pulse train (**Figure 4A** and **Supplementary Figure 4**). Neither V_{peak} nor V_{res} values were different in PE-treated NRVMs compared with CTL cells ($p > 0.05$, **Figures 4B,C**). Pulse train frequency had a significant effect on V_{peak} for H134R and ReaChR ($p < 0.05$), but not for CatCh and GtACR1 (**Figure 4B**). In cells expressing H134R or ReaChR, V_{peak} values decreased with increasing preconditioning pulse train frequency until 3 Hz, but stabilized between −20 and −25 mV at higher frequencies of the light pulses. Average V_{peak} values were within the range of -10 ± 2 mV for CatCh and -38 ± 2 mV for GtACR1, irrespective to the preconditioning pulse train frequency (**Figure 4B**). Similar to V_{peak}, average V_{res} values remained unaffected by PE treatment, but were highly dependent on pulse train frequency ($p < 0.0001$, **Figure 4C**). V_{res} increased with increasing preconditioning pulse rate for all ChR variants. In cells expressing the H134R variant, V_{res} remained < -40 mV at preconditioning pulse train frequencies of up to 5 Hz. However, for CatCh and ReaChR, V_{res} values already became > -40 mV at an optical pacing frequency of 3 Hz. V_{res} for GtACR1 approached −40 mV when the pulse train frequency was increased from 1 to 3 Hz and remained relatively stable later (**Figure 4C**).

Effects of Preconditioning by Light on Photocurrents

As mentioned above, in order to elicit (partially) light-adapted photocurrents in a standardized way, each preconditioning light pulse train was followed by an additional illumination period of 1 s (**Figure 5A** and **Supplementary Figure 5**). The preconditioned photocurrents captured in this way were used to assess the effects of light adaptation on ChR function both in PE-treated and in CTL NRVMs. Properties of the preconditioned photocurrents were determined and normalized to the same parameters obtained for the dark-adapted ChR state (**Figures 1**, **2**) for each cell, yielding relative parameters, herein labeled with the "preco" suffix.

Strikingly, preconditioning induced a decrease in I_{peak}, $I_{plateau}$, and TC. However, each current property responded differently to preconditioning with relative changes characteristic for each ChR variant. I_{peak} decreased significantly ($p < 0.05$) for all four ChR variants after 1-Hz preconditioning, with GtACR1 showing the smallest ($p < 0.05$) decrease (CTL: 17%, PE: 24%) (**Supplementary Figure 6A** and **Supplementary Table 1**). Delivery of preconditioning pulse trains of higher frequencies resulted in a further reduction of mean $I_{peak,preco}$. As a consequence, plotting $I_{peak,preco}$ values against preconditioning pulse frequency yielded lines with non-zero ($p < 0.0001$) negative slopes for all four ChR variants, indicating strong use-dependence of $I_{peak,preco}$ (**Supplementary Figure 7C** and **Supplementary Table 1**). Similar to peak currents, plateau currents were also affected by light adaptation. $I_{plateau}$ showed a significant ($p < 0.05$) decrease of >10% in response to 1-Hz preconditioning relative to dark-adapted state for all four ChR variants and decreased further with increasing preconditioning intensity ($p < 0.0001$) (**Figure 5B**, **Supplementary Figure 7D** and **Supplementary Table 1**). Interestingly, the plateau current generated by ReaChR appeared to be the least resistant to repetitive use among the cation ChR variants, since it showed the smallest average $I_{plateau,preco}$ values (CTL: 30%, PE: 28%) ($p < 0.05$) after 1-Hz preconditioning. In accord with the use-dependent decrease in $I_{peak,preco}$ and $I_{plateau,preco}$ amplitudes, all ChR currents carried a lower amount of charge during 1-s illumination following 1-Hz preconditioning compared with dark-adapted currents ($p < 0.05$) with ReaChR, showing the largest average decrease (CTL: 33%, PE: 35%) compared with any other cation ChR variant ($p < 0.05$) (**Supplementary Figures 6B, 7E** and **Supplementary Table 1**). It is also noteworthy that $I_{peak}-I_{plateau}$ ratios of the cation ChRs decreased ($p < 0.05$) following 1-Hz preconditioning and decreased further with increased preconditioning frequencies (**Supplementary Figures 6C, 7F** and **Supplementary Table 1**). 1-Hz preconditioning had no significant effect on GtACR1 $I_{peak}-I_{plateau}$ ratios ($p > 0.05$), but higher pulse rates caused increasing trends with non-zero ($p < 0.0001$) positive slopes (**Supplementary Figures 6C, 7F** and **Supplementary Table 1**). Therefore, our data show that ChRs generate lower current amplitudes, thus conducting less charge in the light-adapted state than in the dark-adapted state. The preconditioning-induced changes in any of the assessed quantitative current properties, however, were not different between CTL and PE-treated cells ($p > 0.05$) (**Figure 5B**, **Supplementary Figures 6A–C**, and **Supplementary Table 1**).

Channelrhodopsin current amplitudes are not the sole determinants of the efficacy of optogenetic maneuvers. The kinetic properties of ChRs, such as activation and deactivation times, may critically limit the temporal resolution of optogenetic interventions, yet their stability under conditions of repetitive use and in the setting of cardiac disease is unknown. Therefore, we compared the kinetic properties of preconditioned ChR currents with those measured in the dark-adapted state (**Figure 5A** and **Supplementary Figure 5**). Activation kinetics of all cation ChR variants, represented by TtP_{preco}, decelerated ($p < 0.05$) following preconditioning, as indicated by average TtP_{preco} values >1 (**Figure 5C** and **Supplementary Table 2**). CatCh decelerated the most, showing a >45% increase of average TtP following 1-Hz preconditioning (CTL: 46%, PE: 59%). These changes were exaggerated following more intense preconditioning for all cation ChRs, as all average TtP_{preco} values showed trends having non-zero ($p < 0.0001$) positive slopes, with the highest ($p < 0.05$) slope for CatCh (**Figure 5C**,

Supplementary Figure 7G and **Supplementary Table 2**). Surprisingly, the kinetics of GtACR1 current activation did not change following 1-Hz preconditioning ($p > 0.05$), but GtACR1 TtP_{preco} decreased slightly with higher preconditioning pulse train rates showing a trend with a significantly non-zero ($p < 0.0001$) negative slope (**Figure 5C**, **Supplementary Figure 7G** and **Supplementary Table 2**). Use-dependent deceleration of channel activation was accompanied by slowing of channel closure in case of the cation ChR variants (**Figure 5D** and **Supplementary Table 2**). cHDT values following 1-Hz preconditioning were increased by >20% for all cation ChRs relative to dark-adapted cHDT values. Higher preconditioning pulse rates induced further deceleration of ion channel closure, as indicated by non-zero ($p < 0.05$), positive average $cHDT_{preco}$ trends with steeper slopes for H134R compared with ReaChR ($p < 0.05$) and for CatCh compared with H134R ($p < 0.05$) (**Figure 5D** and **Supplementary Figure 7H**). Interestingly, GtACR1 cHDT was affected neither by 1-Hz preconditioning (CTL: 2%, PE: 1%, $p > 0.05$) nor by higher optical pacing frequencies ($p = 0.0553$, **Figure 5D**, **Supplementary Figure 7H** and **Supplementary Table 2**). Inactivation kinetics, as characterized by iHDT, decelerated >10% for H134R and >2-fold for CatCh following 1-Hz preconditioning pulses compared with dark-adapted iHDT values and slowed even more with more intense preconditioning (**Supplementary Figure 6D** and **Supplementary Table 2**). In this comparison, CatCh showed the highest ($p < 0.05$) positive slope of average $iHDT_{preco}$ values among all ChR variants. The inactivation kinetics of ReaChR and GtACR1 were not affected by 1-Hz preconditioning, but while the former showed a trend of deceleration, the latter showed acceleration with higher pulse rates (**Supplementary Figures 6D, 7I** and **Supplementary Table 2**). Importantly, the effects of light adaptation on ChR kinetics did not differ ($p > 0.05$) between CTL and PE-treated NRVMs (**Figures 5C,D** and **Supplementary Figures 6C,D, 7G–I**).

In summary, these data show strong use-dependence of important characteristics of ChR currents, including nearly all quantitative and kinetic properties of the photocurrents produced by the four ChR variants, while these parameters remained unchanged under conditions of cellular hypertrophy. Such use-dependence may result in decreased current amplitudes reducing ChR performance, as well as altered temporal responses to repetitive light activation and thus has to be taken into account during the development of any optogenetic application seeking to employ ChR variants. These findings predict that the efficacy of optogenetic applications might become limited when repeated ChR activation is required.

Membrane Potential (V_m) Response to Preconditioned Photocurrents

The V_m response to light-adapted ChR activation was assessed by quantifying plateau potentials following ChR preconditioning by light ($V_{plateau,preco}$) both in CTL and in PE-treated NRVMs under the same illumination regime that was used to compare dark-adapted and (partially) light-adapted ChR current properties (**Figure 6** and **Supplementary Figure 8**). We found that average $V_{plateau}$ values did not differ significantly ($p > 0.05$) following preconditioning with a 1-Hz pulse train compared with dark-adapted $V_{plateau}$ values for any of the ChR variants (**Figure 6B**). Preconditioning pulse rate had no effect on average V_{plateu} in case of H134R, CatCh, and GtACR1 ($p > 0.05$). ReaChR $V_{plateau}$ decreased slightly with increasing preconditioning pulse frequency; however, linear regression failed to detect a significantly non-zero slope ($p > 0.05$). PE stimulation had no effect on average $V_{plateau}$ values ($p > 0.05$) (**Figure 6B**).

DISCUSSION

In this study, we compared the functioning of different ChR variants in cardiomyocytes under normal and pathological conditions when challenged by various illumination protocols. The results reveal that ChR function remains largely unaltered in a cellular model of pathological hypertrophy but shows strong, variant-specific use-dependence. This use-dependent nature of ChR function should not only be considered in the selection of a certain ChR variant for a given purpose but also in the interpretation of the experimental findings.

The rationale for this study was 3-fold. First, ChR variants are the most frequently used optogenetic tools in cardiac research. There is a rich and diverse repertoire of ChR-based tools with unique biophysical properties, including ion selectivity, conductivity, kinetic properties, and light absorption spectra. The combination of these properties is crucial for the successful application of ChRs for both basic and translational research purposes. Nevertheless, studies carried out under rigorously standardized conditions are scarce and have thus far been conducted in permanent (non-cardiac) cell lines, *Xenopus laevis* oocytes, and neurons (Nagel et al., 2003; Lin, 2011; Mattis et al., 2011). Considering that the time course and changes in the magnitude of V_m caused by ChR currents critically depend on the properties of the host cell membrane, the characterization of ChR behavior in cardiomyocytes is vital for optimal application of optogenetics in cardiac research. Therefore, we used standardized experimental conditions to perform a reliable, side-by-side comparison of important ChR variant properties that cardiac applications crucially rely on, such as I_{peak} and TtP for cardiac pacing and $I_{plateau}$ and $V_{plateau}$ for cardiac arrhythmia termination.

Second, considering that both basic research and translational studies often target the diseased heart, testing ChR function in the setting of cardiac disease is pivotal. Pathological cardiac hypertrophy is a maladaptive response to increased hemodynamic stress and is associated with a large variety of inherited and acquired cardiac diseases (Frey and Olson, 2003; Bernardo et al., 2010; Nakamura and Sadoshima, 2018). Such hypertrophy involves structural and electrical remodeling at the cellular level, thereby potentially limiting ChR performance. NRVM cultures are the most used and one of the best characterized cellular cardiac electrophysiological models (Askar et al., 2011; Bingen et al., 2013, 2014; Feola et al., 2016; Majumder et al., 2016, 2018). In response to chronic adrenergic stimulus, NRVMs undergo marked structural and electrical remodeling and show characteristic features of pathological cardiac hypertrophy, such as cell enlargement, APD prolongation, an increase in total protein content, and

reactivation of "fetal" genes including the ANP-encoding *NPPA* gene (Eble et al., 1998; Gaughan et al., 1998; Bernardo et al., 2010; Askar et al., 2013; Neshati et al., 2020). These features make NRVM cultures a very suitable and relevant cardiomyocyte-based model for the functional characterization of optogenetic tools both under physiological conditions and in the setting of pathological hypertrophy.

Third, the use of optogenetic tools to control the V_m of cardiomyocytes often involves repeated activation of ChRs by using the application of multiple consecutive light pulses (Bingen et al., 2014; Park et al., 2014; Govorunova et al., 2016; Feola et al., 2017; Majumder et al., 2018). Such repetitive use is intrinsic to the application of ChRs for optogenetic pacing, but also ChR-based termination of arrhythmias might rely on more than one light pulse. In fact, termination of cardiac arrhythmias by light might fail at the first attempt, in which a second light flash or more light pulses are required (Bruegmann et al., 2018; Nyns et al., 2019). Importantly, if cardiac optogenetics would enter the phase of clinical exploration, reaching optimal efficacy and safety would be of paramount importance. This makes the requirement for optimal ChR performance during repeated illumination even more pivotal, especially considering other challenges, like those concerning effective and safe delivery of both the transgene (like ChR) and light (e.g., *via* a biocompatible LED device). Previous optogenetic studies in the field of neurology revealed that ChR currents are prone to inactivation, which means that I_{peak} decreases during consecutive illumination pulses and that a dark period lasting for several seconds is required to regain its original amplitude (Boyden et al., 2005; Lin et al., 2009; Schneider et al., 2015), the insight that we have currently extended to the field of cardiology. This aspect of photocurrent inactivation, combined with the potentially challenging features of transgene expression and light delivery, might compromise the efficacy of optogenetic applications in the translational and clinical setting. Therefore, in this study, we investigated and compared photocurrent properties under conditions that allowed the complete dark adaptation of ChRs and graded light adaptation afterwards by exposing ChRs to illumination regimens of increasing intensity.

In terms of how our results could help the selection of the best-suited ChR variant for a given application, the dark-adapted current properties provide an initial selection guide. For example, the H134R variant produces the lowest current amplitudes, while it is also the fastest to activate. The H134R variant, therefore, might be an ideal choice for applications requiring fast activation, provided that sufficiently high ChR gene expression and irradiation levels can be achieved. Our data show that CatCh generates the largest current amplitudes among the cation ChR variants investigated in this study. However, it is worth noting that CatCh activates slower than H134R, potentially limiting its applicability when fast activation is required. Since visible light of longer wavelengths penetrates biological tissues better than visible light of shorter wavelengths, the use of red-shifted variants such as ReaChR is considered to be beneficial in *in vivo* experiments. Although ReaChR delivers photocurrents with similar amplitudes as H134R, the remarkably slower activation and closing kinetics of ReaChR potentially resulting in end-diastolic depolarization may limit its usefulness for experiments requiring high optical pacing rates. Finally, GtACR1 seems more suited for optical pacing than for arrhythmia termination because of its relatively modest depolarizing effect on NRVMs.

In contrast, the properties of dark-adapted ChR currents may not be the only aspect of ChR function one should consider in search of the ideal ChR variant. Our data show that all ChR variants included in this study generated reduced current amplitudes and displayed characteristically different kinetic properties in the light-adapted state compared with the dark-adapted state and some of these changes translated into differential cell membrane responses as well. Most importantly, in accord with the well-known phenomenon of ChR current inactivation (Lin, 2011; Schneider et al., 2015), preconditioning decreased average I_{peak} for all four ChR variants. The use-dependent I_{peak} decrease was accompanied by a reduction of $I_{plateau}$. $I_{plateau}$ is an important parameter of ChR function when employed for arrhythmia termination since sustained membrane depolarization and the resulting conduction block critically depend on the amount of current that remains relatively stable during long-lasting (i.e., 100-ms to 1-s) illumination. Under optimal conditions, where ChR expression levels are not limited, the use-dependent $I_{plateau}$ reduction may not translate into a diminished ability to maintain membrane depolarization. This scenario is exemplified by the experimental settings employed in this study, as average $V_{plateau}$ values remained independent of the amount of preconditioning in most experimental groups. However, one may speculate that under limiting conditions, where the ChR expression levels are suboptimal, the use-dependent reduction of $I_{plateau}$ might lead to less depolarized $V_{plateau}$ values.

The use-dependent reduction of $I_{plateau}$ amplitudes has not been documented earlier but may well be in line with the most recent ChR photocycle model (Kuhne et al., 2019). According to this model, ChRs can occupy two parallel photocycles, the "anti-cycle," which involves an early and a late open state ($O_{1-early}$ and O_{1-late}, respectively) with higher and lower conductivity, respectively, and the "syn-cycle," which enrolls a third open O_2 state with even lower conductivity (Kuhne et al., 2019). Branching between the anti- and syn-cycles takes place in the dark-adapted, closed state (C_1) under illumination, while relaxation from the syn- to the anti-cycle is possible *via* two routes. Light-induced branching is characterized by a fast time constant (<1 ns), whereas relaxation from the syn- to the anti-cycle *via* any of the two possible routes is slower by several orders of magnitude (250 ms and 40 s). Therefore, it is possible that ChRs activated by a single light pulse following sufficiently long dark adaptation will reside in the anti-cycle predominantly. However, the relative occupancy of the two photocycles may shift toward the syn-cycle during recurrent use, thereby favoring occupancy of the less conductive O_2 state.

In this study, we showed that repetitive activation causes use-dependent reduction of ChR current amplitudes and altered ChR kinetics. Such use-dependence might limit the efficacy of optogenetic interventions under suboptimal conditions and hence requires careful evaluation depending on the specific application. In addition, efforts directed at the engineering of new ChR variants with tailored properties for particular purposes should take this ChR use-dependency into

consideration to maximize experimental outcomes (Bedbrook et al., 2019).

Activation of ChRs leads to robust depolarization of the cell membrane, which under ideal conditions, can be maintained for a virtually unlimited time. During this time, large amounts of sodium and calcium ions enter the cell quickly exceeding physiological intracellular ion concentrations when the illumination is maintained. These conditions may represent stress to which cardiomyocytes have never been exposed and will likely result in as yet unexplored cellular responses. Future translational studies thus should be focused not only on the efficacy of optogenetic interventions but also on the possible adverse side effects.

Importantly, despite the characteristic structural and electrical remodeling present in PE-treated NRVMs, V_m changes induced by ChR activation and the properties of the underlying ChR currents did not differ between CTL and PE-treated cells. These findings support the use of cardiac optogenetics to modulate the electrical activity of cardiomyocytes both under normal conditions and in the setting of cardiac disease for fundamental and translational research purposes and also eventually for clinical applications.

DATA AVAILABILITY STATEMENT

The original contributions presented in the study are included in the article/**Supplementary Material**, further inquiries can be directed to the corresponding author/s.

ETHICS STATEMENT

The animal study was reviewed and approved by the Animal Experiments Committee of the Leiden University Medical Center.

AUTHOR CONTRIBUTIONS

BÖ conceptualized the research, designed and carried out experiments, analyzed and interpreted the data, and wrote the manuscript. AT interpreted the data and reviewed the manuscript. TDC contributed to software development and reviewed the manuscript. CIB, SOD, and JZ helped with molecular cloning, cell culture and immunocytochemical staining, and reviewed the manuscript. DLY interpreted the data and critically evaluated and reviewed the manuscript. AAFdV and DAP conceptualized the research, designed experiments, reviewed and edited the manuscript. All authors approved the submitted version.

FUNDING

This work was supported by the European Research Council (Starting grant 716509 to DAP).

SUPPLEMENTARY MATERIAL

The Supplementary Material for this article can be found online at: https://www.frontiersin.org/articles/10.3389/fphys.2021.710020/full#supplementary-material

REFERENCES

Arrenberg, A. B., Stainier, D. Y., Baier, H., and Huisken, J. (2010). Optogenetic control of cardiac function. *Science* 330, 971–974. doi: 10.1126/science.1195929

Askar, S. F., Bingen, B. O., Schalij, M. J., Swildens, J., Atsma, D. E., Schutte, C. I., et al. (2013). Similar arrhythmicity in hypertrophic and fibrotic cardiac cultures caused by distinct substrate-specific mechanisms. *Cardiovasc. Res.* 97, 171–181. doi: 10.1093/cvr/cvs290

Askar, S. F., Ramkisoensing, A. A., Schalij, M. J., Bingen, B. O., Swildens, J., Van Der Laarse, A., et al. (2011). Antiproliferative treatment of myofibroblasts prevents arrhythmias *in vitro* by limiting myofibroblast-induced depolarization. *Cardiovasc. Res.* 90, 295–304. doi: 10.1093/cvr/cvr011

Bedbrook, C. N., Yang, K. K., Robinson, J. E., Mackey, E. D., Gradinaru, V., and Arnold, F. H. (2019). Machine learning-guided channelrhodopsin engineering enables minimally invasive optogenetics. *Nat. Methods* 16, 1176–1184. doi: 10.1038/s41592-019-0583-8

Bernardo, B. C., Weeks, K. L., Pretorius, L., and McMullen, J. R. (2010). Molecular distinction between physiological and pathological cardiac hypertrophy: experimental findings and therapeutic strategies. *Pharmacol. Ther.* 128, 191–227. doi: 10.1016/j.pharmthera.2010.04.005

Bingen, B. O., Askar, S. F., Schalij, M. J., Kazbanov, I. V., Ypey, D. L., Panfilov, A. V., et al. (2013). Prolongation of minimal action potential duration in sustained fibrillation decreases complexity by transient destabilization. *Cardiovasc. Res.* 97, 161–170. doi: 10.1093/cvr/cvs288

Bingen, B. O., Engels, M. C., Schalij, M. J., Jangsangthong, W., Neshati, Z., Feola, I., et al. (2014). Light-induced termination of spiral wave arrhythmias by optogenetic engineering of atrial cardiomyocytes. *Cardiovasc. Res.* 104, 194–205. doi: 10.1093/cvr/cvu179

Boyden, E. S., Zhang, F., Bamberg, E., Nagel, G., and Deisseroth, K. (2005). Millisecond-timescale, genetically targeted optical control of neural activity. *Nat. Neurosci.* 8, 1263–1268. doi: 10.1038/nn1525

Bruegmann, T., Beiert, T., Vogt, C. C., Schrickel, J. W., and Sasse, P. (2018). Optogenetic termination of atrial fibrillation in mice. *Cardiovasc. Res.* 114, 713–723. doi: 10.1093/cvr/cvx250

Bruegmann, T., Boyle, P. M., Vogt, C. C., Karathanos, T. V., Arevalo, H. J., Fleischmann, B. K., et al. (2016). Optogenetic defibrillation terminates ventricular arrhythmia in mouse hearts and human simulations. *J. Clin. Invest.* 126, 3894–3904. doi: 10.1172/JCI88950

Bruegmann, T., Malan, D., Hesse, M., Beiert, T., Fuegemann, C. J., Fleischmann, B. K., et al. (2010). Optogenetic control of heart muscle *in vitro* and *in vivo*. *Nat. Methods* 7, 897–900. doi: 10.1038/nmeth.1512

Eble, D. M., Qi, M., Waldschmidt, S., Lucchesi, P. A., Byron, K. L., and Samarel, A. M. (1998). Contractile activity is required for sarcomeric assembly in phenylephrine-induced cardiac myocyte hypertrophy. *Am. J. Physiol.* 274, C1226–C1237. doi: 10.1152/ajpcell.1998.274.5.C1226

Fenno, L., Yizhar, O., and Deisseroth, K. (2011). The development and application of optogenetics. *Annu. Rev. Neurosci.* 34, 389–412. doi: 10.1146/annurev-neuro-061010-113817

Feola, I., Teplenin, A., De Vries, A. A., and Pijnappels, D. A. (2016). Optogenetic engineering of atrial cardiomyocytes. *Methods Mol. Biol.* 1408, 319–331. doi: 10.1007/978-1-4939-3512-3_22

Feola, I., Volkers, L., Majumder, R., Teplenin, A., Schalij, M. J., Panfilov, A. V., et al. (2017). Localized optogenetic targeting of rotors in atrial cardiomyocyte monolayers. *Circ. Arrhythm. Electrophysiol.* 10:e005591. doi: 10.1161/CIRCEP.117.005591

Ferenczi, E. A., Tan, X., and Huang, C. L. (2019). Principles of optogenetic methods and their application to cardiac experimental systems. *Front Physiol* 10:1096. doi: 10.3389/fphys.2019.01096

Frey, N., and Olson, E. N. (2003). Cardiac hypertrophy: the good, the bad, and the ugly. *Annu. Rev. Physiol.* 65, 45–79. doi: 10.1146/annurev.physiol.65.092101.142243

Gaughan, J. P., Hefner, C. A., and Houser, S. R. (1998). Electrophysiological properties of neonatal rat ventricular myocytes with alpha1-adrenergic-induced hypertrophy. *Am. J. Physiol.* 275, H577–H590. doi: 10.1152/ajpheart.1998.275.2.H577

Govorunova, E. G., Cunha, S. R., Sineshchekov, O. A., and Spudich, J. L. (2016). Anion channelrhodopsins for inhibitory cardiac optogenetics. *Sci. Rep.* 6:33530. doi: 10.1038/srep33530

Govorunova, E. G., Sineshchekov, O. A., Janz, R., Liu, X., and Spudich, J. L. (2015). Natural light-gated anion channels: a family of microbial rhodopsins for advanced optogenetics. *Science* 349, 647–650. doi: 10.1126/science.aaa7484

Kleinlogel, S., Feldbauer, K., Dempski, R. E., Fotis, H., Wood, P. G., Bamann, C., et al. (2011). Ultra light-sensitive and fast neuronal activation with the Ca(2)+-permeable channelrhodopsin CatCh. *Nat. Neurosci.* 14, 513–518. doi: 10.1038/nn.2776

Kopton, R. A., Baillie, J. S., Rafferty, S. A., Moss, R., Zgierski-Johnston, C. M., Prykhozhij, S. V., et al. (2018). Cardiac electrophysiological effects of light-activated chloride channels. *Front. Physiol.* 9:1806. doi: 10.3389/fphys.2018.01806

Kuhne, J., Vierock, J., Tennigkeit, S. A., Dreier, M. A., Wietek, J., Petersen, D., et al. (2019). Unifying photocycle model for light adaptation and temporal evolution of cation conductance in channelrhodopsin-2. *Proc. Natl. Acad. Sci. U.S.A.* 116, 9380–9389. doi: 10.1073/pnas.1818707116

Li, J., Wang, L., Luo, J., Li, H., Rao, P., Cheng, Y., et al. (2021). Optical capture and defibrillation in rats with monocrotaline-induced myocardial fibrosis 1 year after a single intravenous injection of adeno-associated virus channelrhodopsin-2. *Heart Rhythm* 18, 109–117. doi: 10.1016/j.hrthm.2020.08.002

Lin, J. Y. (2011). A user's guide to channelrhodopsin variants: features, limitations and future developments. *Exp. Physiol.* 96, 19–25. doi: 10.1113/expphysiol.2009.051961

Lin, J. Y., Knutsen, P. M., Muller, A., Kleinfeld, D., and Tsien, R. Y. (2013). ReaChR: a red-shifted variant of channel rhodopsin enables deep transcranial optogenetic excitation. *Nat. Neurosci.* 16, 1499–1508. doi: 10.1038/nn.3502

Lin, J. Y., Lin, M. Z., Steinbach, P., and Tsien, R. Y. (2009). Characterization of engineered channelrhodopsin variants with improved properties and kinetics. *Biophys. J.* 96, 1803–1814. doi: 10.1016/j.bpj.2008.11.034

Machhada, A., Hosford, P. S., Dyson, A., Ackland, G. L., Mastitskaya, S., and Gourine, A. V. (2020). Optogenetic stimulation of vagal efferent activity preserves left ventricular function in experimental heart failure. *JACC Basic Transl. Sci.* 5, 799–810. doi: 10.1016/j.jacbts.2020.06.002

Majumder, R., Feola, I., Teplenin, A. S., De Vries, A. A., Panfilov, A. V., and Pijnappels, D. A. (2018). Optogenetics enables real-time spatiotemporal control over spiral wave dynamics in an excitable cardiac system. *eLife* 7:e41076. doi: 10.7554/eLife.41076.018

Majumder, R., Jangsangthong, W., Feola, I., Ypey, D. L., Pijnappels, D. A., and Panfilov, A. V. (2016). A mathematical model of neonatal rat atrial monolayers with constitutively active acetylcholine-mediated K+ current. *PLoS Comput. Biol.* 12:e1004946. doi: 10.1371/journal.pcbi.1004946

Mattis, J., Tye, K. M., Ferenczi, E. A., Ramakrishnan, C., O'shea, D. J., Prakash, R., et al. (2011). Principles for applying optogenetic tools derived from direct comparative analysis of microbial opsins. *Nat. Methods* 9, 159–172. doi: 10.1038/nmeth.1808

Men, J., Li, A., Jerwick, J., Li, Z., Tanzi, R. E., and Zhou, C. (2020). Non-invasive red-light optogenetic control of Drosophila cardiac function. *Commun. Biol.* 3:336. doi: 10.1038/s42003-020-1065-3

Moreno, A., Endicott, K., Skancke, M., Dwyer, M. K., Brennan, J., Efimov, I. R., et al. (2019). Sudden heart rate reduction upon optogenetic release of acetylcholine from cardiac parasympathetic neurons in perfused hearts. *Front. Physiol.* 10:16. doi: 10.3389/fphys.2019.00016

Nagel, G., Brauner, M., Liewald, J. F., Adeishvili, N., Bamberg, E., and Gottschalk, A. (2005). Light activation of channelrhodopsin-2 in excitable cells of Caenorhabditis elegans triggers rapid behavioral responses. *Curr. Biol.* 15, 2279–2284. doi: 10.1016/j.cub.2005.11.032

Nagel, G., Szellas, T., Huhn, W., Kateriya, S., Adeishvili, N., Berthold, P., et al. (2003). Channelrhodopsin-2, a directly light-gated cation-selective membrane channel. *Proc. Natl. Acad. Sci. U.S.A.* 100, 13940–13945. doi: 10.1073/pnas.1936192100

Nakamura, M., and Sadoshima, J. (2018). Mechanisms of physiological and pathological cardiac hypertrophy. *Nat. Rev. Cardiol.* 15, 387–407. doi: 10.1038/s41569-018-0007-y

Neshati, Z., Schalij, M. J., and De Vries, A. F. (2020). The proarrhythmic features of pathological cardiac hypertrophy in neonatal rat ventricular cardiomyocyte cultures. *J. Appl. Physiol.* 128, 545–553. doi: 10.1152/japplphysiol.00420.2019

Nyns, E. C. A., Kip, A., Bart, C. I., Plomp, J. J., Zeppenfeld, K., Schalij, M. J., et al. (2017). Optogenetic termination of ventricular arrhythmias in the whole heart: towards biological cardiac rhythm management. *Eur. Heart J.* 38, 2132–2136. doi: 10.1093/eurheartj/ehw574

Nyns, E. C. A., Poelma, R. H., Volkers, L., Plomp, J. J., Bart, C. I., Kip, A. M., et al. (2019). An automated hybrid bioelectronic system for autogenous restoration of sinus rhythm in atrial fibrillation. *Sci. Transl. Med.* 11:eaau6447. doi: 10.1126/scitranslmed.aau6447

Park, S. A., Lee, S. R., Tung, L., and Yue, D. T. (2014). Optical mapping of optogenetically shaped cardiac action potentials. *Sci. Rep.* 4:6125. doi: 10.1038/srep06125

Schneider, F., Grimm, C., and Hegemann, P. (2015). Biophysics of channelrhodopsin. *Annu. Rev. Biophys.* 44, 167–186. doi: 10.1146/annurev-biophys-060414-034014

Watanabe, M., Feola, I., Majumder, R., Jangsangthong, W., Teplenin, A. S., Ypey, D. L., et al. (2017). Optogenetic manipulation of anatomical re-entry by light-guided generation of a reversible local conduction block. *Cardiovasc. Res.* 113, 354–366. doi: 10.1093/cvr/cvx003

Yu, L., Zhou, L., Cao, G., Po, S. S., Huang, B., Zhou, X., et al. (2017). Optogenetic modulation of cardiac sympathetic nerve activity to prevent ventricular arrhythmias. *J. Am. Coll. Cardiol.* 70, 2778–2790. doi: 10.1016/j.jacc.2017.09.1107

Conflict of Interest: The authors declare that the research was conducted in the absence of any commercial or financial relationships that could be construed as a potential conflict of interest.

Publisher's Note: All claims expressed in this article are solely those of the authors and do not necessarily represent those of their affiliated organizations, or those of the publisher, the editors and the reviewers. Any product that may be evaluated in this article, or claim that may be made by its manufacturer, is not guaranteed or endorsed by the publisher.

frontiers in Physiology

ORIGINAL RESEARCH
published: 30 August 2021
doi: 10.3389/fphys.2021.718622

Optogenetic Stimulation Using Anion Channelrhodopsin (GtACR1) Facilitates Termination of Reentrant Arrhythmias With Low Light Energy Requirements: A Computational Study

Alexander R. Ochs[1†], Thomas V. Karathanos[2†], Natalia A. Trayanova[2,3] and Patrick M. Boyle[1,4,5]*

[1] Department of Bioengineering, University of Washington, Seattle, WA, United States, [2] Department of Biomedical Engineering, Johns Hopkins University, Baltimore, MD, United States, [3] Alliance for Cardiovascular Diagnostic and Treatment Innovation, Johns Hopkins University, Baltimore, MD, United States, [4] Institute for Stem Cell and Regenerative Medicine, University of Washington, Seattle, WA, United States, [5] Center for Cardiovascular Biology, University of Washington, Seattle, WA, United States

OPEN ACCESS

Edited by:
Stephan E. Lehnart, University Medical Center Göttingen, Germany

Reviewed by:
Anthony Varghese, University of Wisconsin–River Falls, United States
Trine Krogh-Madsen, Cornell University, United States

***Correspondence:**
Patrick M. Boyle
pmjboyle@uw.edu

[†] These authors have contributed equally to this work

Specialty section:
This article was submitted to Computational Physiology and Medicine, a section of the journal Frontiers in Physiology

Received: 01 June 2021
Accepted: 23 July 2021
Published: 30 August 2021

Citation:
Ochs AR, Karathanos TV, Trayanova NA and Boyle PM (2021) Optogenetic Stimulation Using Anion Channelrhodopsin (GtACR1) Facilitates Termination of Reentrant Arrhythmias With Low Light Energy Requirements: A Computational Study. Front. Physiol. 12:718622. doi: 10.3389/fphys.2021.718622

Optogenetic defibrillation of hearts expressing light-sensitive cation channels (e.g., ChR2) has been proposed as an alternative to conventional electrotherapy. Past modeling work has shown that ChR2 stimulation can depolarize enough myocardium to interrupt arrhythmia, but its efficacy is limited by light attenuation and high energy needs. These shortcomings may be mitigated by using new optogenetic proteins like *Guillardia theta* Anion Channelrhodopsin (GtACR1), which produces a repolarizing outward current upon illumination. Accordingly, we designed a study to assess the feasibility of GtACR1-based optogenetic arrhythmia termination in human hearts. We conducted electrophysiological simulations in MRI-based atrial or ventricular models (n = 3 each), with pathological remodeling from atrial fibrillation or ischemic cardiomyopathy, respectively. We simulated light sensitization via viral gene delivery of three different opsins (ChR2, red-shifted ChR2, GtACR1) and uniform endocardial illumination at the appropriate wavelengths (blue, red, or green light, respectively). To analyze consistency of arrhythmia termination, we varied pulse timing (three evenly spaced intervals spanning the reentrant cycle) and intensity (atrial: 0.001–1 mW/mm^2; ventricular: 0.001–10 mW/mm^2). In atrial models, GtACR1 stimulation with 0.005 mW/mm^2 green light consistently terminated reentry; this was 10–100x weaker than the threshold levels for ChR2-mediated defibrillation. In ventricular models, defibrillation was observed in 2/3 models for GtACR1 stimulation at 0.005 mW/mm^2 (100–200x weaker than ChR2 cases). In the third ventricular model, defibrillation failed in nearly all cases, suggesting that attenuation issues and patient-specific organ/scar geometry may thwart termination in some cases. Across all models, the mechanism of GtACR1-mediated defibrillation

was voltage forcing of illuminated tissue toward the modeled channel reversal potential of −40 mV, which made propagation through affected regions impossible. Thus, our findings suggest GtACR1-based optogenetic defibrillation of the human heart may be feasible with ≈2–3 orders of magnitude less energy than ChR2.

Keywords: defibrillation, optogenetics, GtACR1, arrhythmia (any), computational simulation and analysis

INTRODUCTION

Cardiac optogenetics is an emerging field that stems from work involving genetic transduction of light-sensitive ion channels into mammalian neurons (Boyden et al., 2005; Arrenberg et al., 2010). The use of light for current induction in cardiac tissue with precise spatial and temporal precision has led to *in vivo* studies describing selective excitation of specific cell populations (Jia et al., 2011; Addis et al., 2013), control of spiral waves (Burton et al., 2015; Hussaini et al., 2021), and cardiac pace-making (Bruegmann et al., 2010; Ambrosi and Entcheva, 2014; Nussinovitch and Gepstein, 2015a; Vogt et al., 2015) or arrhythmia termination in animal models (Bruegmann et al., 2016; Nyns et al., 2017, 2019; Cheng et al., 2020). *In vitro* applications of optogenetics have yielded all-optical methods for contactless, high-throughput measurement of electrophysiological properties like action potential duration and inter-cellular electric coupling at different spatial scales (Klimas et al., 2016; Boyle et al., 2021). Lastly, *in silico* tools have been created to elucidate mechanisms and test feasibility of optogenetic approaches in larger hearts without the use of preclinical animal models (Nussinovitch et al., 2014; Zaglia et al., 2015; Crocini et al., 2016; Gepstein and Gruber, 2017; Boyle et al., 2018b).

An appealing, long-term translational application of cardiac optogenetics is selectively exciting the heart to terminate arrhythmia. Current standard-of-care treatments for individuals at risk of sudden cardiac death include implantable cardioverter defibrillators (ICDs) and anti-arrhythmic drugs (Siebels and Kuck, 1994; Moss et al., 2002; Poole et al., 2008). While ICDs reduce mortality by eliciting high-energy electrical shocks to defibrillate lethal arrhythmias such as ventricular fibrillation, electrotherapy is also associated with increased mortality, chronic anxiety, and post-traumatic stress disorder (Poole et al., 2008; Pedersen et al., 2011). For individuals with atrial arrhythmias, cardioversion treatments are effective but limited by the in-patient nature of the procedure and the need for anesthesia (Sulke et al., 2007). Optogenetic defibrillation has the potential to circumvent these drawbacks, but prior modeling studies (Bruegmann et al., 2016, 2018; Karathanos et al., 2016; Boyle et al., 2018b) suggest that it would be very difficult to accomplish with current tools, like the channelrhodopsin-2 (ChR2) H134R variant, due to light-attenuating properties of myocardium and high energy requirements.

A potential avenue for moving beyond these limitations is a recently discovered family of opsins called anion channelrhodopsins (ACRs), such as *Guillardia theta* anion channelrhodopsin-1 (GtACR1) (Govorunova et al., 2015). Originally derived from archaea, GtACR1 has desirable cardiac optogenetic characteristics including high single channel conductance, fast response kinetics, specificity in narrow wavelength ranges, and more negative reversal potential values than ChR2 (Govorunova et al., 2015, 2016, 2017). When excited by green illumination, GtACR1 conducts a flow of anions (e.g., Cl^-), eliciting outward current that accelerates repolarization (Govorunova et al., 2015, 2016, 2017). As such, a new ACR-based paradigm for arrhythmia termination would be distinct from approaches used in past optogenetic defibrillation studies, which have used light-based depolarization to disrupt arrhythmia reentry (Karathanos et al., 2016; Boyle et al., 2018b).

Here, we conduct simulations in patient-derived, biophysically realistic computational models of the diseased atria and ventricles, reconstructed from human late gadolinium enhanced magnetic resonance imaging (LGE-MRI) scans, to investigate the feasibility of GtACR1-based optogenetic defibrillation. Specifically, we aim to determine if uniform endocardial illumination with green light can terminate reentrant arrhythmias in these models with suitable modifications to represent viral GtACR1 expression. Our analysis is designed to reveal (1) the illumination intensity sufficient for GtACR1 to terminate arrhythmia, (2) the mechanisms of defibrillation, and (3) the differences in efficacy between atrial and ventricular models. Simulations with different permutations are used to explore the robustness of light stimulus timing and magnitude. As a basis for comparison, we conduct parallel simulations in the same models expressing blue and red light-sensitive ChR2-H134R variants.

MATERIALS AND METHODS

Computational Modeling of Diseased Atrial and Ventricles

We conducted computational simulations using six patient-specific finite element models (three atrial, three ventricular) reconstructed from LGE-MRI scans (**Figure 1**). Atrial models were sourced from a cohort of patients with persistent atrial fibrillation (AFib) reconstructed for a prior modeling study (Zahid et al., 2016a); ventricular models came from a different simulation-based study of ischemic cardiomyopathy patients (Arevalo et al., 2016). The approach for simulation of cardiac electrophysiology in such models has been previously validated for their respective applications (Maguire et al., 2003; Ashikaga et al., 2013; Deng et al., 2015); detailed descriptions of atrial (Zahid et al., 2016a,b) and ventricular (Arevalo et al., 2016) simulation methodologies can be found elsewhere (Bruegmann et al., 2016; Karathanos et al., 2016). Briefly, patient-specific geometry and spatial distribution of diseased tissue [fibrotic

and non-fibrotic tissue in atrial models (Krummen et al., 2012); normal, scar, and peri-infarct border zone (BZ) tissue in ventricular models (Vadakkumpadan et al., 2010)] were extracted from each patient's clinical MRI scan (**Figure 1**). Realistic fiber orientations were introduced in each model. For atrial models, large deformation diffeomorphic metric mapping (LDDMM) was used to transform fiber orientations from an atrial atlas geometry into each patient-specific model. This methodology has been described extensively in prior work (McDowell et al., 2012, 2013, 2015; Zahid et al., 2016a). For ventricular models, we used a rules-based approach that involved solving several Laplacian equations with boundary conditions set on different surfaces of the heart; this has been described and extensively validated by our lab in prior work (Bayer et al., 2012). Human atrial and ventricular myocyte membrane kinetics were represented using the formulations derived by Courtemanche et al. (1998) and ten Tusscher and Panfilov (2006), respectively. As in our earlier studies (Arevalo et al., 2016; Zahid et al., 2016a), average finite element edge length was ∼400 μm in ventricular models and ∼450 μm in atrial models; the temporal discretization was 25 μs in ventricular simulations and 50 μs in atrial simulations. Electrical propagation in cardiac tissue was governed by the monodomain formulation (Vigmond et al., 2003; Plank et al., 2008). As in prior studies using the same cardiac models (Arevalo et al., 2016; Zahid et al., 2016a), ordinary differential equations associated with simulation of action potentials were solved using the Rush-Larsen scheme for ion channel gating variables and forward Euler integration for all other variables; the parabolic partial differential equation was solved with the full (non-lumped) mass matrix using a Crank-Nicholson scheme to improve model stability. All simulations were conducted using the Cardiac Arrhythmia Research Package (CARP) software (Vigmond et al., 2003, 2008; Plank et al., 2008). Patient-specific data used in this study cannot be made publicly available due to data privacy concerns. In the interest of replicability and reproducibility, source files for a complete example of optogenetic stimulation of a publicly available ventricular model (with ChR2, ChR2-RED, or GtACR1) using software tools that are publicly available and free for non-commercial reuse can be found at this link: https://doi.org/10.6084/m9.figshare.14945412. Documentation for this example includes instructions on the use of the openCARP electrophysiology simulator and the meshalyzer visualization software (available via https://opencarp.org/) to run all simulations.

Mathematical Representation of Light-Induced Current Mediated by GtACR1

We formulated a model of GtACR1 photocurrent kinetics using patch clamp data from GtACR1-expressing neonatal rat ventricular cardiomyocytes as published by Govorunova et al. (2016). Since previous works have suggested structural differences between ACRs and chloride-conducting channelrhodopsins (Govorunova et al., 2017), along with an absence of any reported dark- and light-adapted photocurrent branches in ACRs, we developed a two-state Markov chain model with a conducting [$P(O)$; light-activated/open] and non-conducting [$P(C)$; dark/closed] states:

$$P(O) + P(C) = 1 \tag{1}$$

$$\frac{dP(O)}{dt} = k_{OC} \tag{2}$$

$$\frac{dP(C)}{dt} = k_{CO} \tag{3}$$

$$k_{OC} = \frac{1}{\tau_{off}} \tag{4}$$

$$k_{CO} = \frac{1}{\tau_{on}} * \frac{5.878134701+\ln(E_e+0.0028)}{0.369864-0.1072 * \ln(E_e+0.0028)} \tag{5}$$

where $P(O)$ is the open-state probability, $P(C)$ is the closed-state probability, k_{OC} is the open-to-closed transition rate, k_{CO} is the closed-to-open transition rate, τ_{off} is the inactivation time constant (119 ms), τ_{on} is the activation time constant (1110 ms), and E_e is the applied irradiance.

The open-to-closed transition rate (k_{OC}) was calibrated based on inactivation constant of GtACR1, and was fitted via the logarithmic relation of the opening rate to irradiance to ensure that the steady-state currents under illumination matched reported data (Govorunova et al., 2016). The closed-to-open transition rate (k_{CO}) equation varies as a function of irradiance (E_e); k_{CO} was derived by assuming equilibrium during the photocurrent plateau generated by steady state illumination, then fitting to the open probability $P(O)$ derived from experimental current traces. To derive maximal GtACR1 channel conductance (g_{GtACR1}), we assumed a membrane capacitance of 100 pF, which is within the physiological range of previously reported NRVM single cell experiments (Guo et al., 1996). The GtACR1 photocurrent model was then characterized at different irradiances under voltage forcing conditions (**Figures 2A,B**). When a holding potential of –80 mV was used, illumination elicited inward currents, with higher irradiance values leading to larger magnitudes (**Figure 2A**). With a holding potential of 0 mV, the polarity of the induced photocurrents was reversed (**Figure 2B**). Using a bisection approach, we found that the best value reconciling current values observed for these clamp levels with experimental data was g_{GtACR1} = 1.4 mS/cm^2. We also characterized the ChR2 photocurrent model for comparison to GtACR1 at holding potentials of –80 mV and 0 mV (**Figure 2C**); GtACR1 currents were several-fold stronger than ChR2 at all irradiances when using –80 mV holding potential (**Figure 2D**).

Finally, the current density of the channel (I_{GtACR1}) was calculated using Ohm's law, adjusted for the channel open probability:

$$I_{GtACR1} = P(O) * g_{GtACR1} * (V - E_{GtACR1}) \tag{6}$$

where E_{GtACR1} is the GtACR1 reversal potential (–40 mV), which we based on prior reports for the reversal potential of chloride ions in cardiac cells under physiologic conditions (Govorunova et al., 2016; Kopton et al., 2018). Notably, the reported reversal potential for GtACR1 in experimental

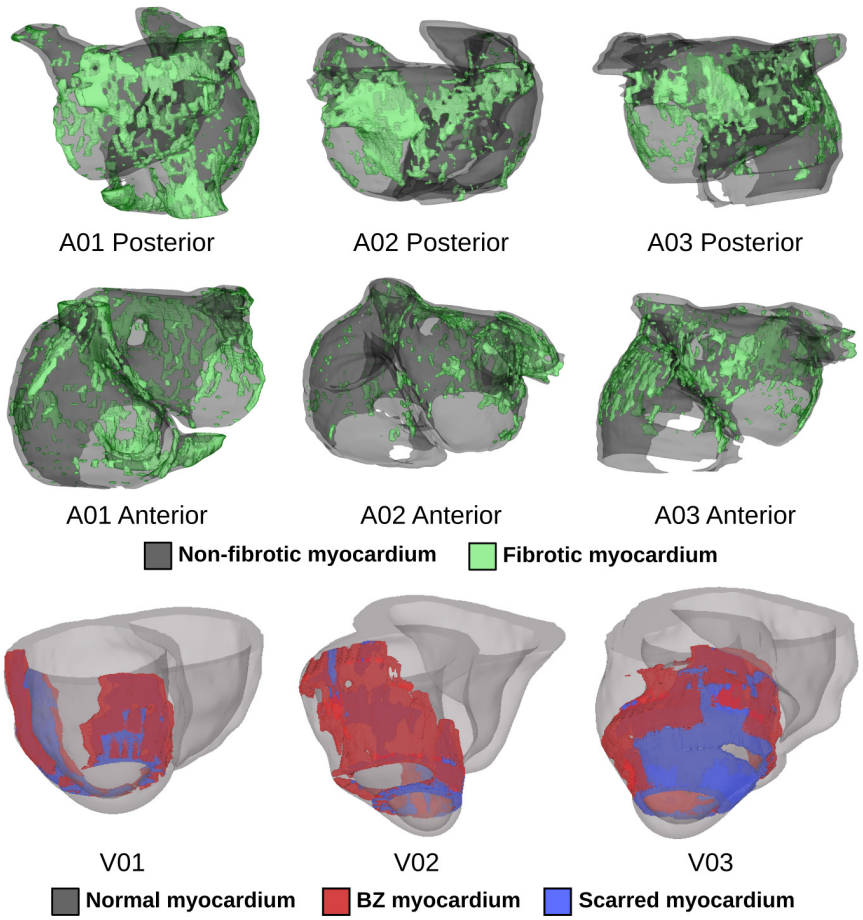

FIGURE 1 | Patient-specific atrial (top two rows) and ventricular (bottom row) models reconstructed from LGE-MRI scans. Spatial distribution of diseased tissue is shown for all cases.

cardiomyocyte preparations was –90 mV (Govorunova et al., 2016); this discrepancy was likely a consequence of bath solution composition.

An implementation of our GtACR1 model compatible with the openCARP framework for cardiac electrophysiology simulations (https://opencarp.org), which is made freely available for non-commercial applications, is provided as supplementary material (see **Supplementary Material** or https://doi.org/10.6084/m9.figshare.14945412).

ChR2 Model Variants

The ChR2 photocycles were simulated using an model for ChR2-H134R (Williams et al., 2013), as in previous works (Karathanos et al., 2014, 2016; Bruegmann et al., 2016; Boyle et al., 2018b; Hussaini et al., 2021). Briefly, the ChR2 was modeled as a 4-state Markov chain model with light-gated transitions between two closed (non-conducting) and two open states (permeable to cation flow). The ChR2 model conductance (g_{ChR2}) was originally calculated to be 0.4 mS/cm^2 based on experiments in HEK-293 cells (Williams et al., 2013), but photocurrents measured from patch clamped cells following viral gene delivery of ChR2 to mouse hearts suggest a lower value (Vogt et al., 2015). Thus, we adjusted our model to fit ∼2.2 pA/pF steady-state currents at 5 mW/mm^2 illumination (Vogt et al., 2015), which resulted in a conductance of g_{ChR2} = 0.11 mS/cm^2. As in prior studies (Bruegmann et al., 2016; Karathanos et al., 2016; Boyle et al., 2018b), we assumed ChR2 stimulation with 488 nm blue light. Since prior modeling studies showed higher defibrillation success rates with red light stimulation (Bruegmann et al., 2016; Karathanos et al., 2016), we also used a theoretical ChR2 model variant with red-shifted absorption (ChR2-RED). This model had the same properties as ChR2 (no modifications to light sensitivity or g_{ChR2}) but peak energy absorption wavelength was adjusted to 669 nm.

Simulation of Opsin Expression and Light Attenuation

To simulate optogenetic transduction of either the human atria or ventricles via viral gene delivery, we used our previously validated computational modeling framework (Ambrosi et al., 2014; Boyle et al., 2013, 2015a; Bruegmann et al., 2016). Based on mouse experiments studying the effects of gene delivery and expression

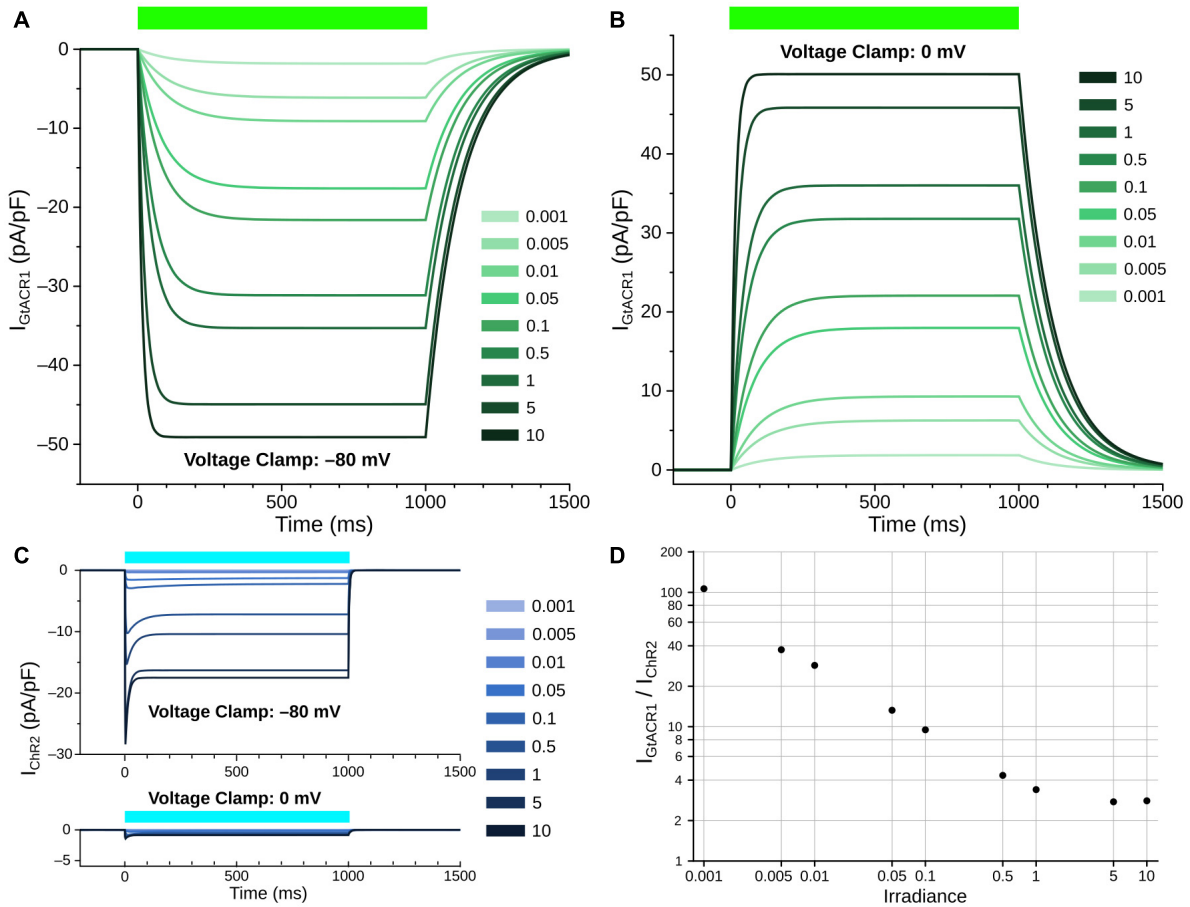

FIGURE 2 | Simulated GtACR1 and ChR2 currents in illumination voltage forcing experiments. **(A,B)** Photocurrent conducted by GtACR1 generated in response to illumination with holding potentials of −80 **(A)** and 0 mV **(B)**. **(C)** Same as A/B but for ChR2. **(D)** Comparison of steady-state I_{GtACR1} and I_{ChR2} values (plateau currents at t = 500 ms) for different irradiances under voltage clamp condition. In all panels, units of irradiance are mW/mm^2. Colored bars: intervals of illumination with green (515 nm; 1000 ms) or blue light (488 nm, 1000 ms).

in cardiomyocytes (Vogt et al., 2015; Bruegmann et al., 2016; Karathanos et al., 2016), opsin expression (ChR2, ChR2-RED, or GtACR1) was incorporated into 58.2% of mesh nodes in a diffuse pattern (i.e., random selection with a uniform distribution), as described previously (Boyle et al., 2013). To facilitate comparison of results across different experimental configurations, we only generated one 58.2% distribution per atrial/ventricular model (i.e., spatial patterns of opsin expression for different opsins were identical).

Light attenuation due to scattering and energy absorption in myocardial tissue was approximated using the steady-state photon diffusion equation (Ripoll et al., 2005; Jacques and Pogue, 2008), as in previous modeling studies (Bishop et al., 2006, 2007; Boyle et al., 2013, 2018a; Ambrosi et al., 2015; Bruegmann et al., 2016; Karathanos et al., 2016). We defined the a parameter (values between 0 and 1) using the coefficient for light scattering μ_s', coefficient for light absorption μ_a, and the anisotropy factor g:

$$a = 1 - \frac{4}{5} \cdot \frac{\mu_s' + \mu_a}{\mu_s' \cdot (1+g) + \mu_a} \quad (7)$$

We then defined the diffusion coefficient D using the formula (Ripoll et al., 2005):

$$D = \frac{1}{3\left(\mu_s' + \mu_a * a\right)} \quad (8)$$

We used experimentally derived values found in the literature (Bishop et al., 2006) for blue (μ_a = 0.52, D = 0.183) and red light (μ_a = 0.1, D = 0.34). For green light in cardiac tissue [μ_a = 0.7, μ_s' = 1.42 and g = 0.9 (Swartling et al., 2003)] a was calculated to be 0.5, leading to a diffusion coefficient of D = 0.189. In effect, this means the penetration depth for green light is the shallowest of all the wavelengths used in the study ($\delta = \sqrt{D/\mu_a}$ = 519.6 μm vs. 593.2 μm and 1.844 mm for blue and red light, respectively).

We simulated uniform illumination of the left atrial (LA) endocardium in atrial models, and the left ventricular (LV) endocardium in ventricular models. Illumination was represented by defining a constant E_e value on the target surface, then modifying that value by an attenuation factor (derived by solving the photon diffusion equation)

(Bishop et al., 2006, 2007; Karathanos et al., 2016; Boyle et al., 2018b) in the myocardial bulk. **Figure 3** shows the effects of light attenuation in atrial and ventricular models using the associated wavelengths of each opsin: blue light for ChR2 (488 nm), red light for ChR2-RED (669 nm), and green light for GtACR1 (515 nm).

Simulation Protocol for Arrhythmia Induction and Optogenetic Defibrillation

Arrhythmias were induced by simulated rapid pacing in both atrial (Zahid et al., 2016a) and ventricular (Arevalo et al., 2016) models, as in prior studies (Karathanos et al., 2016; Bruegmann et al., 2016; Zahid et al., 2016a,b; Boyle et al., 2018b). In atrial models, six electrical pulses of 5 ms duration were paced at coupling interval (CI) = 300 ms, decreasing in 20 ms decrements until CI = 200 ms (6 pulses), followed by six pulses at CI = 200 ms to induce AFib (12 pulses total). In ventricular models, eight pulses of 5 ms duration at CI = 600 ms were initially paced, followed by two pulses at reduced CIs of variable length to induce ventricular tachycardia (VT).

In atrial models, we simulated optogenetic defibrillation attempts with 1000 ms-long LA endocardial illumination pulses at E_e values varying from 0.001 to 1 mW/mm^2; these values are consistent with those used in prior experimental studies (Bruegmann et al., 2018; Boyle et al., 2018b; Nyns et al., 2019). In each model, we carried out separate simulation sets assuming expression of ChR2, ChR2-RED, and GtACR1. To span the re-entrant cycle, three light pulse onset times (+0, +70, +140 ms) were used for each E_e/opsin condition. A similar, experimentally consistent (Bruegmann et al., 2010, 2016; Karathanos et al., 2016) protocol was used in ventricular models, with the primary differences being E_e values (varying from 0.001 to 10 mW/mm^2), and light onset times (+0, +100, +200 ms) due to longer VT cycle length. In all cases, defibrillation was deemed successful if reentry terminated within 800 ms after the 1000 ms illumination pulse ended; this gave us an adequate timeframe to monitor for resumption of stable reentry (following failed attempts) or indirect successes [as described elsewhere (Boyle et al., 2018b)], wherein spontaneous termination occurs after the end of illumination due to light-induced destabilization.

RESULTS

GtACR1 Photocurrent Model Characterization

The GtACR1 photocurrent model and its response to light were evaluated in atrial (Courtemanche et al., 1998) (**Figure 4A**) and ventricular (ten Tusscher and Panfilov, 2006) (**Figure 4B**) myocyte models. In both cell types, following an initial action potential evoked by electrical stimulation (first red star), subsequent light stimulation (green bar) resulted in an abrupt transient depolarization, after which the membrane voltage (V_m) was forced to the GtACR1 reversal potential (−40 mV). This light-induced forcing effect prevented the triggering of subsequent action potentials by electrical stimuli (second red star). After illumination ended, simulated cells repolarized to their resting potentials.

Optogenetic Defibrillation in Atrial Models

Here, we simulated optogenetic defibrillation attempts in three patient-specific atrial models using LA endocardial illumination at irradiances varying from 0.001 to 1 mW/mm^2. As summarized in **Table 1**, GtACR1-based termination was reliable (i.e., reentry activity terminated for all three light onset times tested) for light stimuli as weak as 0.005 mW/mm^2. Notably, this was 2–3 orders of magnitude lower than the weakest stimuli that reliably defibrillated models expressing ChR2-RED or ChR2 (0.1 and 0.5 mW/mm^2, respectively).

The effects of very weak (0.05 mW/mm^2) light stimuli in atrial models with expression of different opsins are illustrated in **Figure 5** and **Supplementary Movie 1**. In the absence of light stimulation (i.e., control case), reentry persisted; action potential timing and morphology were similar between epicardial and endocardial surfaces (**Figure 5A**, right-most column). Attempted optogenetic defibrillation in the ChR2-expressing model did not disrupt reentrant activity transmurally (**Figure 5B**); endocardial action potentials were blunted, but remained temporally synchronized with epicardial excitations, which were largely unaffected by optogenetic stimulation. Stimulation of ChR2-RED had a more prominent effect on the transmural spatiotemporal excitation sequence due to deeper penetration of red light (∼3x exponential decay constant of blue light; **Figure 5C**); some isolated instances of conduction block were observed (e.g., double lines in 600 ms panel), but arrhythmia did not terminate. In contrast, illumination in the GtACR1-expressing atrial models imposed a voltage forcing effect throughout the LA (**Figure 5D**, 600 ms), leading to rapid extinguishing of reentrant drivers. Notably, this light-induced forcing effect was non-uniform, with less depolarized plateau voltage at the epicardial surface (spatial gradient: 2.8 mV/mm) due to transmural light attenuation.

At extremely weak irradiances (i.e., 0.005 mW/mm^2) in GtACR1-expressing atria, light that reached the epicardium was too weak to induce optogenetic voltage forcing. Despite this, defibrillation succeeded in all cases (9/9). To illustrate how this was possible, **Figure 6** presents side-by-side activation maps for a GtACR1 defibrillation attempt (E_e = 0.005 mW/mm^2) and its corresponding control case (**Supplementary Movie 2**). In the absence of light stimulus, a reentrant driver in the inferolateral LA propagates unabated (**Figure 6A**); in contrast, GtACR1 activity elicited by weak illumination of the endocardium disrupted reentry and ultimately terminated the arrhythmia (**Figure 6B**). Examination of transmural voltage traces in the latter case (**Figure 6C**) showed that propagating wavefronts in sub-epicardial LA tissue created transient depolarizations from the forced level in the sub-endocardium, but arrhythmia extinguished ∼100 ms after the end of illumination due to

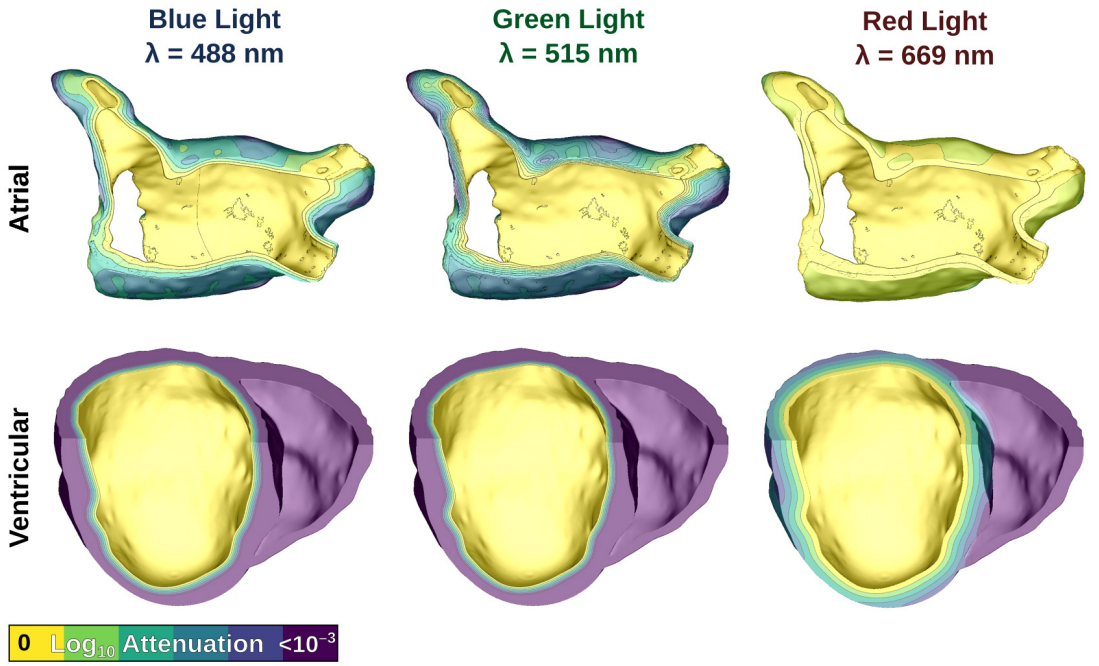

FIGURE 3 | Modeling illumination of atrial (top) and ventricular (bottom) models with light of different wavelengths. Attenuation color scale is shown on a log10 scale. Please note that despite the similarity of the first two panels in the bottom row, these are in fact distinct attenuation patterns for blue and green light.

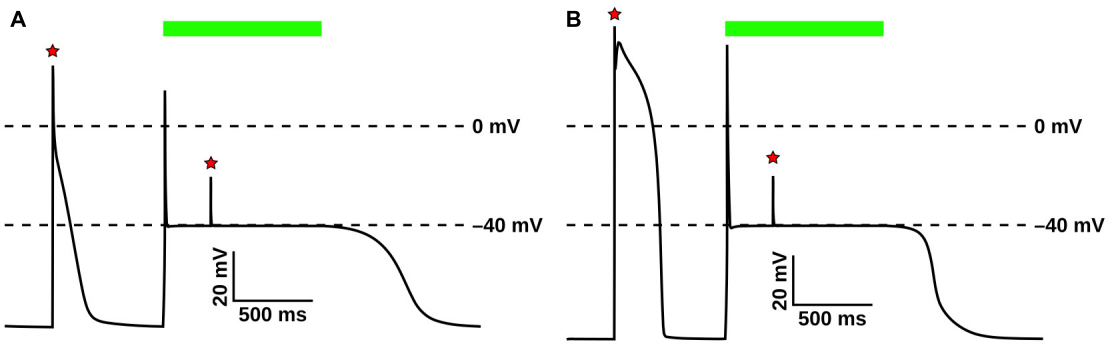

FIGURE 4 | Evaluation of GtACR1 currents upon illumination in single cell simulations. Light-elicited GtACR1 currents suppressed action potential formation in simulated atrial **(A)** or ventricular **(B)** myocyte models. Red stars show timing of electrical stimuli (30 pA/pF) and green bars represent the interval of illumination with green light (515 nm; 1.00 mW/mm^2; 1000 ms).

light-induced perturbation of excitation patterns near the arrhythmia driver.

Optogenetic Defibrillation in Ventricular Models

Next, we simulated optogenetic defibrillation attempts in three patient-specific ventricular models using LV endocardial illumination at irradiances varying from 0.001 to 10 mW/mm^2. As summarized in **Table 2**, GtACR1-based defibrillation was effective with light stimuli as weak as 0.005 mW/mm^2, which was 2–3 orders of magnitude weaker than for ChR2-RED or ChR2 (0.5 and 1 mW/mm^2, respectively). A representative example of VT termination (E_e = 0.5 mW/mm^2 in GtACR1-expressing model V01) is presented in **Figure 7**. Without light stimulus, the arrhythmia is sustained (**Figure 7A**) whereas illumination prevents conduction at the endocardial surface (**Figure 7B**), resulting in successful GtACR1-mediated defibrillation via light-induced voltage forcing (**Figure 7C**), like atrial models discussed in the prior section (**Supplementary Movie 3**).

One notable example of inconsistent defibrillation behavior between ventricular models was that defibrillation failed in V02 for nearly all stimuli, regardless of opsin, with success observed in only 2/27 simulations with ChR2-RED. The non-responsiveness of model V02 to optogenetic defibrillation is scrutinized in **Figure 8**. In a representative GtACR1-expressing defibrillation

TABLE 1 | Defibrillation success rates for ChR2, ChR2-RED, or GtACR1-expressing atrial models for different irradiance values.

		Irradiance (mW/mm^2)						
		0.001	**0.005**	**0.01**	**0.05**	**0.1**	**0.5**	**1**
ChR2 (blue)	A01	0/3	0/3	0/3	0/3	0/3	3/3	3/3
	A02	0/3	0/3	0/3	0/3	0/3	3/3	3/3
	A03	0/3	0/3	0/3	0/3	2/3	3/3	3/3
ChR2-RED (red)	A01	0/3	0/3	0/3	2/3	3/3	3/3	2/3
	A02	0/3	0/3	0/3	0/3	3/3	3/3	3/3
	A03	0/3	0/3	0/3	2/3	3/3	3/3	3/3
GtACR1 (green)	A01	0/3	3/3	3/3	3/3	3/3	3/3	3/3
	A02	0/3	3/3	3/3	3/3	3/3	3/3	3/3
	A03	0/3	3/3	3/3	3/3	3/3	3/3	3/3

"n/3" denotes that defibrillation was successful for n of the 3 light onset times tested (i.e., arrhythmia terminated within 800 ms of illumination ending).

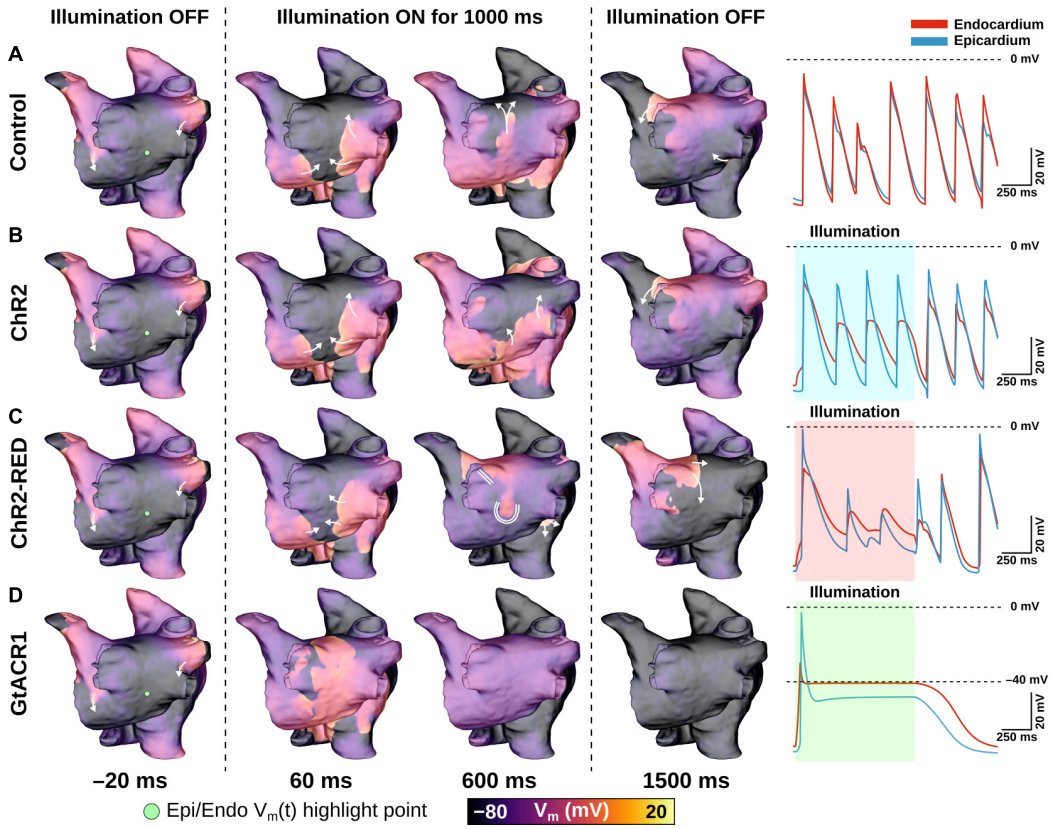

FIGURE 5 | LA defibrillation attempts with E_e = 0.05 mW/mm^2 in model A01 for all three opsins. The control case **(A)** is compared to endocardial illumination of ChR2- **(B)**, ChR2-RED- **(C)**, or GtACR1- **(D)** expressing models. Arrows indicate wavefront propagation directions. Double lines show sites of conduction block. Representative V_m(t) traces are shown from endocardial (red line) and epicardial (blue line) nodes at the same point on the LA posterior wall (green dot); shaded regions in rows **(B–D)** indicate illumination intervals. All illumination begins at t = 0 ms and lasts 1000 ms.

failure (**Figures 8A,B**, E_e = 1 mW/mm^2), endocardial excitation was suppressed by the optogenetic stimulus (endocardial trace) while the epicardium was unaffected (**Figure 8A**). Due to light attenuation in the ventricular walls, the proportion of tissue directly depolarized by GtACR1 stimulation was smaller compared to atrial models, so reentrant wavefront conduction continued along a thin layer of epicardium (**Figure 8B**, inset; **Supplementary Movie 4**). This was made possible by the presence of a dense ring of scar and BZ near the LV apex (**Figure 8C**), which created a protected region that was too far from the illuminated endocardium to be affected by the light stimulus and insulated from indirect (electrotonic) effects in areas that *were* optogenetically depolarized. In cases where the reentrant wavefront was dislodged from that area, the arrhythmia

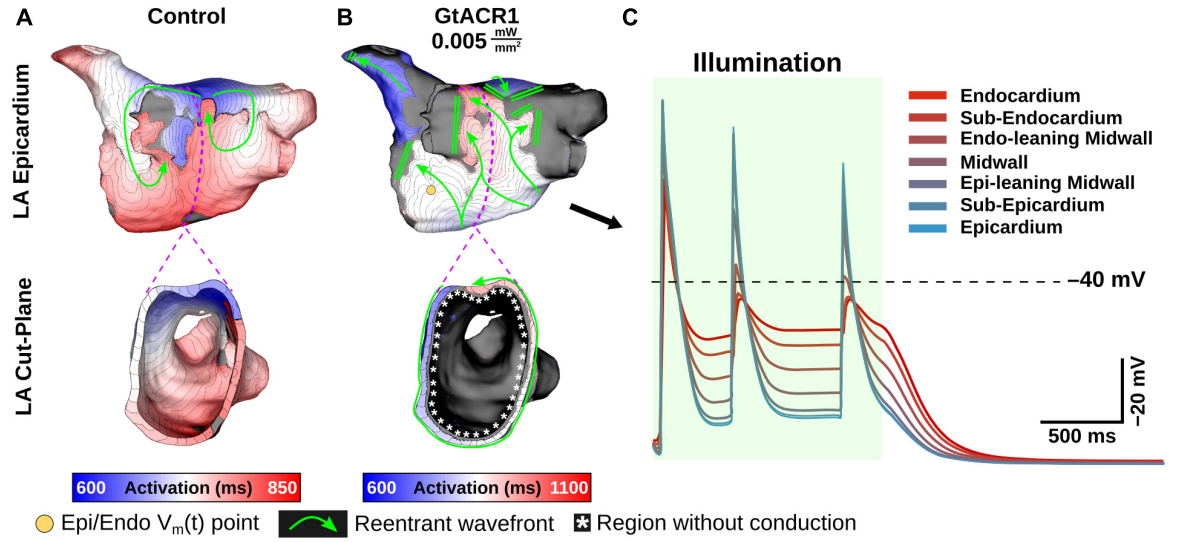

FIGURE 6 | Defibrillation with very weak light stimuli succeeds in GtACR1-expressing models despite persistent sub-epicardial conduction. **(A,B)** Activation maps for no light control **(A)**, and E_e = 0.005 mW/mm^2 stimulus applied to GtACR1-expressing model **(B)**. Dashed lines (top) show cut plane locations for cross-sections (bottom). Arrows indicate wavefront propagation directions. Double lines show sites of conduction block. Asterisks highlight conduction block region on endocardium. **(C)** V_m(t) traces for nodes spanning from LA endocardium to epicardium (golden dot) in the GtACR1 condition are provided. Illumination (green shaded region) begins at t = 0 ms and lasts 1000 ms.

TABLE 2 | Defibrillation success rates for ChR2, ChR2-RED, or GtACR1-expressing ventricular models for different irradiance values.

		Irradiance (mW/mm^2)								
		0.001	**0.005**	**0.01**	**0.05**	**0.1**	**0.5**	**1**	**5**	**10**
ChR2 (blue)	V01	0/3	0/3	0/3	0/3	0/3	1/3	3/3	3/3	3/3
	V02	0/3	0/3	0/3	0/3	0/3	0/3	0/3	0/3	0/3
	V03	0/3	0/3	0/3	0/3	0/3	0/3	2/3	2/3	2/3
ChR2-RED (red)	V01	0/3	0/3	0/3	0/3	0/3	3/3	3/3	2/3	3/3
	V02	0/3	0/3	0/3	0/3	0/3	0/3	0/3	1/3	1/3
	V03	0/3	0/3	0/3	0/3	0/3	3/3	3/3	2/3	2/3
GtACR1 (green)	V01	0/3	1/3	3/3	3/3	3/3	3/3	3/3	3/3	3/3
	V02	0/3	0/3	0/3	0/3	0/3	0/3	0/3	0/3	0/3
	V03	0/3	3/3	3/3	3/3	3/3	3/3	3/3	2/3	3/3

"n/3" denotes that defibrillation was successful for n of the 3 light onset times tested (i.e., arrhythmia terminated within 800 ms of illumination ending).

driver then relocated to one of many other sites that could sustain a new spiral wave (**Figure 8D**; GtACR1 expression, examples shown for E_e = 5 and 10 mW/mm^2). In the small handful of V02 cases where light-based defibrillation did succeed, termination always occurred several hundred milliseconds after the end of illumination. The apparent mechanism (e.g., **Figures 8E,F**) was that the dislodged reentrant wavefront serendipitously encountered tissue excited by propagation from another part of the ventricles, resulting in conduction block and subsequent termination.

DISCUSSION

In this study, we used computational models reconstructed from LGE-MRI scans of diseased human atrial and ventricles to assess the feasibility of reentrant arrhythmia termination via GtACR1-mediated optogenetic stimulation. To achieve this, we developed a 2-state photocurrent model for GtACR1 and evaluated it under realistic organ-scale conditions. In doing so, we showed that GtACR1-mediated optogenetic defibrillation of the atria or ventricles is feasible and more efficacious than a ChR2-based approach, the limitations of which are well known from prior work. Our main findings are: (1) GtACR1-mediated voltage forcing to near the channel Cl^- reversal potential of –40 mV consistently terminated arrhythmia in most atrial and ventricular models (3/3 and 2/3, respectively); (2) the threshold irradiance for GtACR1-based atrial defibrillation was extremely low (E_e = 0.005 mW/mm^2) in all three cases, corresponding to a ∼10–100x lower energy requirement than ChR2-based optogenetic therapy; and (3) the same very low E_e threshold was observed in two of three ventricular models.

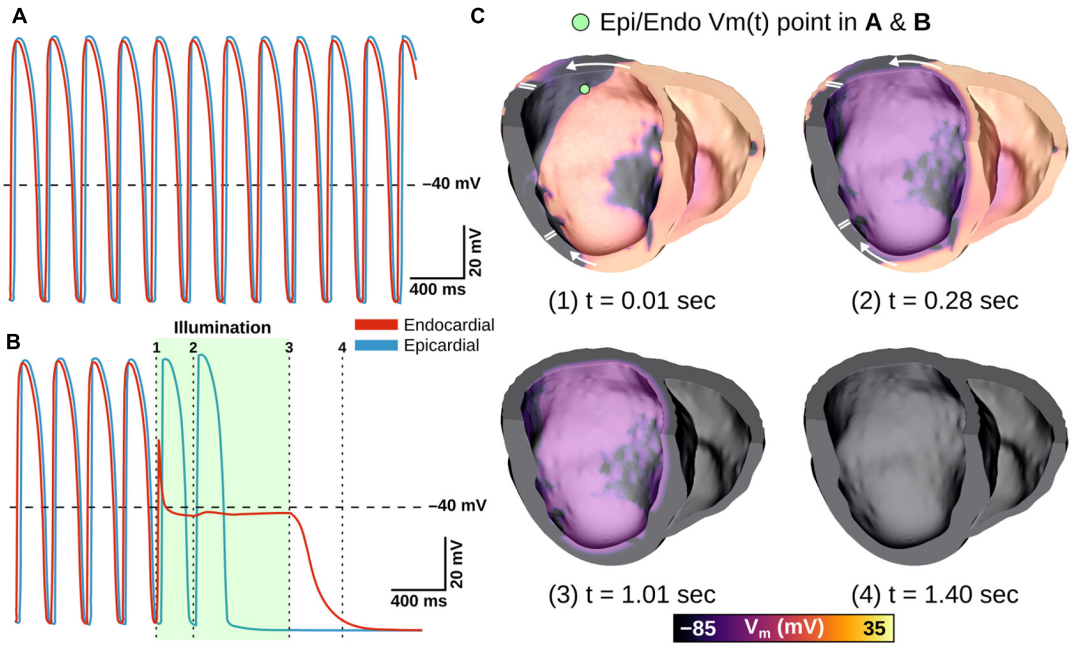

FIGURE 7 | Representative example of LV defibrillation attempt in GtACR1-expressing model V01 with E_e = 0.5 mW/mm^2. V_m(t) traces from the LV endocardial surface are provided for the control case **(A)** and GtACR1-expressing model **(B)**. Green shaded region in **(B)** shows illumination interval. Cut plane V_m(t) snapshots of the GtACR1 case **(C)** show conduction block affecting wavefront propagating circumferentially in LV free wall, followed by eventual arrhythmia termination. Arrows indicate wavefront propagation directions. Double lines show sites of conduction block.

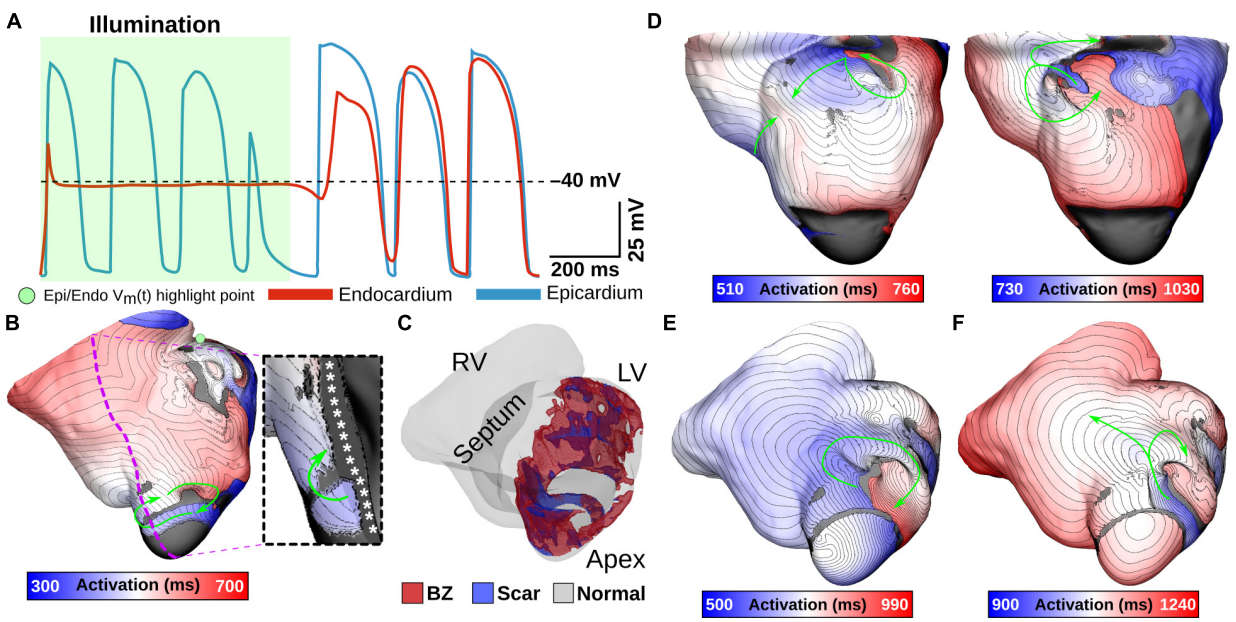

FIGURE 8 | Examining low optogenetic defibrillation success rates in V02. V_m(t) traces **(A)** and an activation map **(B)** showing an example of GtACR1-based defibrillation failure (E_e = 1 mW/mm^2). Green shaded region in **(A)** shows illumination interval. Excitation is silenced at the endocardium, but arrhythmia persists at the epicardium (inset) due to a protected VT circuit created by a particular geometry of BZ and scar **(C)**. **(D)** Representative examples to illustrate differences between destabilized reentrant circuits in GtACR1-expressing defibrillation failures (E_e = 5 mW/mm^2 and E_e = 10 mW/mm^2). **(E,F)** Example of defibrillation success (ChR2-RED, E_e = 5 mW/mm^2) showing a normal cycle **(E)** and cycle with conduction block near LV apex **(F)** that leads to termination. Arrows indicate wavefront propagation.

Optogenetic stimulation is an appealing alternative to electric shocks for defibrillation or cardioversion due to its ability to affect V_m in the light-sensitized heart alone without triggering excitation and contraction of surrounding skeletal muscle (Ambrosi and Entcheva, 2014; Boyle et al., 2014, 2015b; Karathanos et al., 2016; Crocini et al., 2017). Nearly all past experimental and modeling studies exploring optogenetic defibrillation have used depolarizing opsins such as ChR2-H134R (Entcheva, 2013; Williams et al., 2013; Nussinovitch and Gepstein, 2015a; Karathanos et al., 2016; Boyle et al., 2018a,b), CatCh (Bingen et al., 2014), and ReaChR (Nyns et al., 2017). Opsins that hasten repolarization such as halorhodopsin Cl^- pumps (Arrenberg et al., 2010) and bacteriorhodopsin proton pumps (e.g., Arch-3 and ArchT) (Nussinovitch et al., 2014; Nussinovitch and Gepstein, 2015b) have been used previously to silence action potentials in cardiomyocyte monolayers. However, these opsins can only transport a single ion per absorbed photon, resulting in relatively weak photocurrents (Govorunova et al., 2016). Consequently, when ventricular defibrillation via ArchT stimulation was attempted in Langendorff-perfused mouse hearts, termination success was much lower and more variable (∼55%) (Funken et al., 2019) than a comparable study that used ChR2 instead (∼97%) (Bruegmann et al., 2016). Engineered ACRs (Berndt et al., 2014; Wietek et al., 2014) also have limited photocurrent due to the intrinsic pore size of the channels (Guru et al., 2015). In contrast, natural-occurring ACRs (including GtACR1) from cryptophyte algae have higher photocurrents than previous alternatives by an order of magnitude (Govorunova et al., 2015, 2016). As noted elsewhere (Kopton et al., 2018), GtACR1 current depends on the chloride reversal potential (≈–40 mV in cardiomyocytes) and thus *depolarizes* cells at rest while *hastening early repolarization* in cells already undergoing excitation. This differs from the outright silencing of action potentials seen in experimental preparations where the GtACR1 reversal potential was ≈–90 mV due to low $[Cl^-]$ in the pipette (Govorunova et al., 2016). Nevertheless, our analysis shows that GtACR1-mediated optogenetic defibrillation in large mammalian hearts is theoretically feasible, with suppression of reentrant activity facilitated by forcing large tissue regions toward the reversal potential.

This GtACR1-mediated "optogenetic voltage forcing" mechanism is distinct from depolarization-based routes to termination, as described in prior studies. In the context of constant epicardial illumination of a ChR2-expressing model of infarcted ventricles, Bruegmann et al. (2016) showed the defibrillation mechanism was steady state inactivation of fast Na^+ channels, resulting in reduced tissue excitability and conduction block; however, in contrast to the present work, the level of sustained depolarization observed in that study (≈–50 mV) was well below the effective ChR2 reversal potential (≈+10 mV) (Williams et al., 2013) due to offsetting effects from other ionic currents. In a different computational study (Karathanos et al., 2016), simulated punctate illumination of the cardiac surfaces by multi-optrode grids in the fibrillating human ventricles under heart failure conditions. In that case, arrhythmia termination was facilitated by creation of new wavefronts via ChR2 stimulation, which eliminated excitable gaps.

Prior studies have identified poor transmural light penetration as a key limiting factor for optogenetic defibrillation of larger hearts, with deeper penetrating red light being highlighted as the most promising potential workaround (Bruegmann et al., 2016; Karathanos et al., 2016). Thus, it is notable that the present study predicts high success rates for optogenetic stimulation based on stimulation of GtACR1-expressing hearts with green light, which has inferior penetration depth compared to both blue and red light. This is a direct result of the lower irradiance threshold for evoking photocurrents in GtACR1 that are large enough to markedly change cardiomyocyte electrophysiology. For example, as shown in **Figure 2C** using cells clamped to –80 mV, the same current (≈2 pA/pF) elicited by illumination of ChR2 at 0.5 mW/mm^2 can be achieved by stimulating GtACR1 at 0.001 mW/mm^2. Thus, for equally bright light stimuli, even though the penetration of green light across the myocardial wall is weaker, the dim illumination of distant regions with attenuated stimuli can produce photocurrents large enough to create a more pronounced electrophysiological effect compared to blue or red light. The recent discovery of red-shifted ACRs from non-algae sources (Govorunova et al., 2020) is also noteworthy in this context, although very slow on/off kinetics (>1 s time constants) make these unsuitable for cardiac applications. Nevertheless, the implication is that opsins even more promising than GtACR1 for optogenetic defibrillation may soon become available. Notably, the modeled virus transfection assumed random dispersion of opsins. This is consistent with prior experimental studies exploring the consequences of long-term ChR2 expression via systemic injection of a viral vector in rodents (Vogt et al., 2015), but it is impossible to know for certain that it would be safe and feasible to achieve this type of distribution in human hearts.

Our computational findings complement a growing body of evidence from experimental work in animal models that light-based cardiac rhythm control is both feasible and efficacious. Initial proof-of-concept work involving optogenetic pacing of Langendorff-perfused transgenic mouse hearts (Bruegmann et al., 2010) and optogenetic modulation of zebrafish heart rate *in vivo* (Arrenberg et al., 2010) prompted speculation that light-based cardioversion and defibrillation might also be feasible (Entcheva, 2013). Subsequent studies demonstrated highly reliable approaches for optogenetic termination of ventricular arrhythmias in explanted mouse hearts expressing ChR2 (Bruegmann et al., 2016) or ReaChR (Nyns et al., 2017), or *in vivo* in open-chest preparations of rats following myocardial infarction (Cheng et al., 2020). Proof of concept has also been shown for light-based defibrillation of atrial arrhythmias in open chest preparations *ex vivo* or *in vivo* (Bruegmann et al., 2018), as well as closed-chest rat models involving automatic detection and termination (Nyns et al., 2019). Prior computational modeling work has suggested that scaling these experiments in larger pre-clinical animal models with contemporary optogenetic tools would be difficult to justify due to constraints imposed by light attenuation in hearts with thicker walls (Bruegmann et al., 2016; Karathanos et al., 2016); the present work suggests that those studies can now be contemplated, thanks to the addition of GtACR1 to the optogenetic armamentarium. However, additional studies may

still be needed to verify GtACR1 channel conductance values *in vivo*.

Should delivery of light to beating human hearts prove unfeasible, an interesting potential alternative to the use of GtACR1 could be over-expression of the inward rectifier potassium current I_{K1}. This would work by a similar mechanism described in this paper, since it would result in depolarization of the resting potential. Moderate upregulation via the I_{K1} channel agonist zacopride has previously been shown to reduce triggered arrhythmias in animal models of acute ischemia (Liu et al., 2012; Elnakish et al., 2017; Zhai et al., 2017; Lin et al., 2020). AAV-mediated upregulation of I_{K1} ion channels could thus create a similar effect to GtACR1 excitation, although the effects would be at least semi-permanent and extensive safety studies would be needed.

Translation of the cardiac optogenetics for clinical applications remains an attractive goal due to the possibility of pain-free light-based defibrillation replacing electric shock therapy. The present study shows the most convincing evidence to date that arrhythmia in human atria or ventricles could, in theory, be terminated with extremely low-energy light stimuli. Nevertheless, two major hurdles to translation remain, and these parallel two major caveats that must be taken into consideration when interpreting our findings. First, long-term studies are needed to evaluate the safety and durability of opsin expression induced by viral gene delivery to light-sensitize the heart, which has not yet been studied in larger animals. In our study, we simulated distribution of opsin-expressing cells based on reported expression levels in mice one year after AAV9-ChR2 injection (58.2% in a diffuse spatial pattern) (Vogt et al., 2015); a more recent study in rats with hearts light-sensitized by AAV-ChR2 showed defibrillation efficacy one year post-transfection (Li et al., 2021). Although there are no known safety concerns for AAV-based transfection in humans (Wasala et al., 2011; Greenberg et al., 2016), it is not yet known if safe, long-term light-sensitization via ChR2, GtACR1, or any opsin is possible.

Second, even in the context of reduced light energy requirements facilitated by GtACR1, the delivery of sufficient optical energy to the intracardiac milieu in large mammalian hearts remains an unsolved problem. Here, we opted to simulate uniform endocardial illumination, rather than light stimuli focused on specific areas (Boyle et al., 2018b) or delivered by a grid of point sources (Karathanos et al., 2016). We made this choice to facilitate comparison with prior experimental work in animal models, which has used uniform illumination of some kind (Bruegmann et al., 2010, 2016, 2018; Nyns et al., 2017, 2019; Cheng et al., 2020); moreover, whole surface stimulation has been shown to result in lower energy requirements (Quiñonez Uribe et al., 2018). Nevertheless, it would be challenging to use endocardial illumination *in vivo* due to concerns regarding hemodynamic stability. Although it might be possible to implant flexible and biocompatible LED strips (Kim et al., 2010, 2013) along the endocardial surface, it remains unknown whether this type of device would be feasible in practice. An exciting possible alternative is the use of up-converting nanoparticles to facilitate local light release triggered by deeper-penetrating energy like near-infrared light, ultra-sound, and X-rays (Berry et al., 2015; Huang et al., 2016; Boyle et al., 2018a; Entcheva and Kay, 2021). The first proof of concept for optogenetic pacing of rat hearts with this type of technology was recently shown (Rao et al., 2020), but more work will be needed to validate the approach and to determine the most suitable way of representing the relevant physics in our computational models. Finally, our approach to modeling illumination does not account for any inhomogeneities that might arise from uneven light delivery by an LED field or a flexible biocompatible fluorescent membrane (Xu et al., 2014); this simplification was deemed an acceptable tradeoff, since it allowed us to assay feasibility of optogenetic defibrillation in various atrial and ventricular models with distinct organ geometry and functional heterogeneity from disease-related remodeling in a straightforward way.

CONCLUSION

We have demonstrated the first computational proof-of-concept for optogenetic defibrillation via stimulation of GtACR1 in biophysically detailed models of diseased human hearts. In all atrial cases and two of three ventricular cases, arrhythmia termination via endocardial light delivery was effective using irradiances as low as 5 $\mu W/mm^2$. The defibrillation mechanism was identified as transmural optogenetic voltage forcing, which was possible because very dim light stimuli can produce large photocurrents in GtACR1-expressing myocytes, thereby mitigating the limitation imposed by light attenuation in cardiac tissue.

DATA AVAILABILITY STATEMENT

The original contributions presented in the study are included in the article/**Supplementary Material**, further inquiries can be directed to the corresponding author.

AUTHOR CONTRIBUTIONS

TK, NT, and PB conceived and designed the study. AO and TK constructed the computational models, ran the simulations, and analyzed the results. AO, TK, and PB wrote the manuscript. All authors contributed to manuscript revision, read, and approved the submitted version.

FUNDING

This project has received funding from the Fondation Leducq (Research Grant No. 16 CVD 02).

SUPPLEMENTARY MATERIAL

The Supplementary Material for this article can be found online at: https://www.frontiersin.org/articles/10.3389/fphys.2021.718622/full#supplementary-material

REFERENCES

Addis, R. C., Ifkovits, J. L., Pinto, F., Kellam, L. D., Esteso, P., Rentschler, S., et al. (2013). Optimization of direct fibroblast reprogramming to cardiomyocytes using calcium activity as a functional measure of success. *J. Mol. Cell. Cardiol.* 60, 97–106. doi: 10.1016/j.yjmcc.2013.04.004

Ambrosi, C. M., Boyle, P. M., Chen, K., Trayanova, N. A., and Entcheva, E. (2015). Optogenetics-enabled assessment of viral gene and cell therapy for restoration of cardiac excitability. *Sci. Rep.* 5:17350.

Ambrosi, C. M., and Entcheva, E. (2014). Optogenetics' promise: pacing and cardioversion by light? *Future Cardiol.* 10, 1–4. doi: 10.2217/fca.13.89

Ambrosi, C. M., Klimas, A., Yu, J., and Entcheva, E. (2014). Cardiac applications of optogenetics. *Prog. Biophys. Mol. Biol.* 115, 294–304. doi: 10.1016/j.pbiomolbio.2014.07.001

Arevalo, H. J., Vadakkumpadan, F., Guallar, E., Jebb, A., Malamas, P., Wu, K. C., et al. (2016). Arrhythmia risk stratification of patients after myocardial infarction using personalized heart models. *Nat. Commun.* 7:11437.

Arrenberg, A. B., Stainier, D. Y., Baier, H., and Huisken, J. (2010). Optogenetic control of cardiac function. *Science* 330, 971–974. doi: 10.1126/science.1195929

Ashikaga, H., Arevalo, H., Vadakkumpadan, F., Blake, R. C. III, Bayer, J. D., Nazarian, S., et al. (2013). Feasibility of image-based simulation to estimate ablation target in human ventricular arrhythmia. *Heart Rhythm* 10, 1109–1116. doi: 10.1016/j.hrthm.2013.04.015

Bayer, J. D., Blake, R. C., Plank, G., and Trayanova, N. A. (2012). A novel rule-based algorithm for assigning myocardial fiber orientation to computational heart models. *Ann. Biomed. Eng.* 40, 2243–2254.

Berndt, A., Lee, S. Y., Ramakrishnan, C., and Deisseroth, K. (2014). Structure-guided transformation of channelrhodopsin into a light-activated chloride channel. *Science* 344, 420–424. doi: 10.1126/science.1252367

Berry, R., Matthew, G., Gjesteby, L., and Wang, G. (2015). X-optogenetics and U-optogenetics: feasibility and possibilities. *Photonics* 2, 23–39. doi: 10.3390/photonics2010023

Bingen, B. O., Engels, M. C., Schalij, M. J., Jangsangthong, W., Neshati, Z., Feola, I., et al. (2014). Light-induced termination of spiral wave arrhythmias by optogenetic engineering of atrial cardiomyocytes. *Cardiovasc. Res.* 104, 194–205. doi: 10.1093/cvr/cvu179

Bishop, M. J., Rodriguez, B., Eason, J., Whiteley, J. P., Trayanova, N., and Gavaghan, D. J. (2006). Synthesis of voltage-sensitive optical signals: application to panoramic optical mapping. *Biophys. J.* 90, 2938–2945. doi: 10.1529/biophysj.105.076505

Bishop, M. J., Rodriguez, B., Qu, F., Efimov, I. R., Gavaghan, D. J., and Trayanova, N. A. (2007). The role of photon scattering in optical signal distortion during arrhythmia and defibrillation. *Biophys. J.* 93, 3714–3726. doi: 10.1529/biophysj.107.110981

Boyden, E. S., Zhang, F., Bamberg, E., Nagel, G., and Deisseroth, K. (2005). Millisecond-timescale, genetically targeted optical control of neural activity. *Nat. Neurosci.* 8, 1263–1268. doi: 10.1038/nn1525

Boyle, P. M., Entcheva, E., and Trayanova, N. A. (2014). See the light: can optogenetics restore healthy heartbeats? And, if it can, is it really worth the effort? *Expert Rev. Cardiovasc. Ther.* 12, 17–20. doi: 10.1586/14779072.2014.864951

Boyle, P. M., Karathanos, T. V., Entcheva, E., and Trayanova, N. A. (2015a). Computational modeling of cardiac optogenetics: methodology overview & review of findings from simulations. *Comput. Biol. Med.* 65, 200–208. doi: 10.1016/j.compbiomed.2015.04.036

Boyle, P. M., Karathanos, T. V., and Trayanova, N. A. (2015b). "Beauty is a light in the heart": the transformative potential of optogenetics for clinical applications in cardiovascular medicine. *Trends Cardiovasc. Med.* 25, 73–81. doi: 10.1016/j.tcm.2014.10.004

Boyle, P. M., Karathanos, T. V., and Trayanova, N. A. (2018a). Cardiac optogenetics: 2018. *JACC Clin. Electrophysiol.* 4, 155–167. doi: 10.1016/j.jacep.2017.12.006

Boyle, P. M., Murphy, M. J., Karathanos, T. V., Zahid, S., Blake, R. C. III, and Trayanova, N. A. (2018b). Termination of re-entrant atrial tachycardia via optogenetic stimulation with optimized spatial targeting: insights from computational models. *J. Physiol.* 596, 181–196. doi: 10.1113/jp275264

Boyle, P. M., Williams, J. C., Ambrosi, C. M., Entcheva, E., and Trayanova, N. A. (2013). A comprehensive multiscale framework for simulating optogenetics in the heart. *Nat. Commun.* 4:2370.

Boyle, P. M., Yu, J., Klimas, A., Williams, J. C., Trayanova, N. A., and Entcheva, E. (2021). OptoGap is an optogenetics-enabled assay for quantification of cell-cell coupling in multicellular cardiac tissue. *Sci. Rep.* 11:9310.

Bruegmann, T., Beiert, T., Vogt, C. C., Schrickel, J. W., and Sasse, P. (2018). Optogenetic termination of atrial fibrillation in mice. *Cardiovasc. Res.* 114, 713–723. doi: 10.1093/cvr/cvx250

Bruegmann, T., Boyle, P. M., Vogt, C. C., Karathanos, T. V., Arevalo, H. J., Fleischmann, B. K., et al. (2016). Optogenetic defibrillation terminates ventricular arrhythmia in mouse hearts and human simulations. *J. Clin. Invest.* 126, 3894–3904. doi: 10.1172/jci88950

Bruegmann, T., Malan, D., Hesse, M., Beiert, T., Fuegemann, C. J., Fleischmann, B. K., et al. (2010). Optogenetic control of heart muscle in vitro and in vivo. *Nat. Methods* 7, 897–900. doi: 10.1038/nmeth.1512

Burton, R. A., Klimas, A., Ambrosi, C. M., Tomek, J., Corbett, A., Entcheva, E., et al. (2015). Optical control of excitation waves in cardiac tissue. *Nat. Photonics* 9, 813–816. doi: 10.1038/nphoton.2015.196

Cheng, Y., Li, H., Wang, L., Li, J., Kang, W., Rao, P., et al. (2020). Optogenetic approaches for termination of ventricular tachyarrhythmias after myocardial infarction in rats in vivo. *J. Biophotonics* 13:e202000003.

Courtemanche, M., Ramirez, R. J., and Nattel, S. (1998). Ionic mechanisms underlying human atrial action potential properties: insights from a mathematical model. *Am. J. Physiol.* 275, H301–H321.

Crocini, C., Ferrantini, C., Coppini, R., Scardigli, M., Yan, P., Loew, L. M., et al. (2016). Optogenetics design of mechanistically-based stimulation patterns for cardiac defibrillation. *Sci. Rep.* 6:35628.

Crocini, C., Ferrantini, C., Pavone, F. S., and Sacconi, L. (2017). Optogenetics gets to the heart: a guiding light beyond defibrillation. *Prog. Biophys. Mol. Biol.* 130(Pt B), 132–139. doi: 10.1016/j.pbiomolbio.2017.05.002

Deng, D., Arevalo, H., Pashakhanloo, F., Prakosa, A., Ashikaga, H., McVeigh, E., et al. (2015). Accuracy of prediction of infarct-related arrhythmic circuits from image-based models reconstructed from low and high resolution MRI. *Front. Physiol.* 6:282. doi: 10.3389/fphys.2015.00282

Elnakish, M. T., Canan, B. D., Kilic, A., Mohler, P. J., and Janssen, P. M. (2017). Effects of zacopride, a moderate IK1 channel agonist, on triggered arrhythmia and contractility in human ventricular myocardium. *Pharmacol. Res.* 115, 309–318. doi: 10.1016/j.phrs.2016.11.033

Entcheva, E. (2013). Cardiac optogenetics. *Am. J. Physiol. Heart Circ. Physiol.* 304, H1179–H1191.

Entcheva, E., and Kay, M. W. (2021). Cardiac optogenetics: a decade of enlightenment. *Nat. Rev. Cardiol.* 18, 349–367. doi: 10.1038/s41569-020-00478-0

Funken, M., Malan, D., Sasse, P., and Bruegmann, T. (2019). Optogenetic hyperpolarization of cardiomyocytes terminates ventricular arrhythmia. *Front Physiol.* 10:498. doi: 10.3389/fphys.2019.00498

Gepstein, L., and Gruber, A. (2017). Optogenetic neuromodulation of the heart. *J. Am. Coll. Cardiol.* 70, 2791–2794. doi: 10.1016/j.jacc.2017.10.003

Govorunova, E. G., Cunha, S. R., Sineshchekov, O. A., and Spudich, J. L. (2016). Anion channelrhodopsins for inhibitory cardiac optogenetics. *Sci. Rep.* 6:33530.

Govorunova, E. G., Sineshchekov, O. A., Janz, R., Liu, X., and Spudich, J. L. (2015). Natural light-gated anion channels: a family of microbial rhodopsins for advanced optogenetics. *Science* 349, 647–650. doi: 10.1126/science.aaa7484

Govorunova, E. G., Sineshchekov, O. A., Li, H., Wang, Y., Brown, L. S., and Spudich, J. L. (2020). RubyACRs, nonalgal anion channelrhodopsins with highly red-shifted absorption. *Proc. Natl. Acad. Sci. U.S.A.* 117, 22833–22840. doi: 10.1073/pnas.2005981117

Govorunova, E. G., Sineshchekov, O. A., Rodarte, E. M., Janz, R., Morelle, O., Melkonian, M., et al. (2017). The expanding family of natural anion channelrhodopsins reveals large variations in kinetics, conductance, and spectral sensitivity. *Sci. Rep.* 7:43358.

Greenberg, B., Butler, J., Felker, G. M., Ponikowski, P., Voors, A. A., Desai, A. S., et al. (2016). Calcium upregulation by percutaneous administration of gene therapy in patients with cardiac disease (CUPID 2): a randomised, multinational, double-blind, placebo-controlled, phase 2b trial. *Lancet* 387, 1178–1186. doi: 10.1016/s0140-6736(16)00082-9

Guo, W., Kamiya, K., Cheng, J., and Toyama, J. (1996). Changes in action potentials and ion currents in long-term cultured neonatal rat ventricular cells. *Am. J. Physiol.* 271(1 Pt 1), C93–C102.

Guru, A., Post, R. J., Ho, Y. Y., and Warden, M. R. (2015). Making sense of optogenetics. *Int. J. Neuropsychopharmacol.* 18:pyv079. doi: 10.1093/ijnp/pyv079

Huang, K., Dou, Q., and Loh, X. J. (2016). Nanomaterial mediated optogenetics: opportunities and challenges. *RSC Adv.* 6, 60896–60906. doi: 10.1039/c6ra11289g

Hussaini, S., Venkatesan, V., Biasci, V., Romero Sepúlveda, J. M., Quiñonez Uribe, R. A., Sacconi, L., et al. (2021). Drift and termination of spiral waves in optogenetically modified cardiac tissue at sub-threshold illumination. *Elife* 10:e59954.

Jacques, S. L., and Pogue, B. W. (2008). Tutorial on diffuse light transport. *J. Biomed. Opt.* 13:041302. doi: 10.1117/1.2967535

Jia, Z., Valiunas, V., Lu, Z., Bien, H., Liu, H., Wang, H. Z., et al. (2011). Stimulating cardiac muscle by light: cardiac optogenetics by cell delivery. *Circ. Arrhythm. Electrophysiol.* 4, 753–760. doi: 10.1161/circep.111.964247

Karathanos, T. V., Bayer, J. D., Wang, D., Boyle, P. M., and Trayanova, N. A. (2016). Opsin spectral sensitivity determines the effectiveness of optogenetic termination of ventricular fibrillation in the human heart: a simulation study. *J. Physiol.* 594, 6879–6891. doi: 10.1113/jp271739

Karathanos, T. V., Boyle, P. M., and Trayanova, N. A. (2014). Optogenetics-enabled dynamic modulation of action potential duration in atrial tissue: feasibility of a novel therapeutic approach. *Europace* 16(Suppl. 4), iv69–iv76.

Kim, R. H., Kim, D. H., Xiao, J., Kim, B. H., Park, S. I., Panilaitis, B., et al. (2010). Waterproof AlInGaP optoelectronics on stretchable substrates with applications in biomedicine and robotics. *Nat. Mater.* 9, 929–937. doi: 10.1038/nmat2879

Kim, T. I., McCall, J. G., Jung, Y. H., Huang, X., Siuda, E. R., Li, Y., et al. (2013). Injectable, cellular-scale optoelectronics with applications for wireless optogenetics. *Science* 340, 211–216. doi: 10.1126/science.1232437

Klimas, A., Ambrosi, C. M., Yu, J., Williams, J. C., Bien, H., and Entcheva, E. (2016). OptoDyCE as an automated system for high-throughput all-optical dynamic cardiac electrophysiology. *Nat. Commun.* 7:11542.

Kopton, R. A., Baillie, J. S., Rafferty, S. A., Moss, R., Zgierski-Johnston, C. M., Prykhozhij, S. V., et al. (2018). Cardiac electrophysiological effects of light-activated chloride channels. *Front. Physiol.* 9:1806. doi: 10.3389/fphys.2018.01806

Krummen, D. E., Bayer, J. D., Ho, J., Ho, G., Smetak, M. R., Clopton, P., et al. (2012). Mechanisms of human atrial fibrillation initiation: clinical and computational studies of repolarization restitution and activation latency. *Circ. Arrhythm. Electrophysiol.* 5, 1149–1159. doi: 10.1161/circep.111.969022

Li, J., Wang, L., Luo, J., Li, H., Rao, P., Cheng, Y., et al. (2021). Optical capture and defibrillation in rats with monocrotaline-induced myocardial fibrosis 1 year after a single intravenous injection of adeno-associated virus channelrhodopsin-2. *Heart Rhythm* 18, 109–117. doi: 10.1016/j.hrthm.2020.08.002

Lin, Y., Li, J., Zhu, B., Liu, Q., Bai, X., Chang, B., et al. (2020). Zacopride exerts an antiarrhythmic effect by specifically stimulating the cardiac inward rectifier potassium current in rabbits: exploration of a new antiarrhythmic strategy. *Curr. Pharm. Des.* 26, 5746–5754. doi: 10.2174/1381612826666200701135508

Liu, Q. H., Li, X. L., Xu, Y. W., Lin, Y. Y., Cao, J. M., and Wu, B. W. (2012). A novel discovery of IK1 channel agonist: zacopride selectively enhances IK1 current and suppresses triggered arrhythmias in the rat. *J. Cardiovasc. Pharmacol.* 59, 37–48. doi: 10.1097/fjc.0b013e3182350bcc

Maguire, C. T., Wakimoto, H., Patel, V. V., Hammer, P. E., Gauvreau, K., and Berul, C. I. (2003). Implications of ventricular arrhythmia vulnerability during murine electrophysiology studies. *Physiol. Genomics* 15, 84–91. doi: 10.1152/physiolgenomics.00034.2003

McDowell, K. S., Vadakkumpadan, F., Blake, R., Blauer, J., Plank, G., MacLeod, R. S., et al. (2012). Methodology for patient-specific modeling of atrial fibrosis as a substrate for atrial fibrillation. *J. Electrocardiol.* 45, 640–645. doi: 10.1016/j.jelectrocard.2012.08.005

McDowell, K. S., Vadakkumpadan, F., Blake, R., Blauer, J., Plank, G., Macleod, R. S., et al. (2013). Mechanistic inquiry into the role of tissue remodeling in fibrotic lesions in human atrial fibrillation. *Biophys. J.* 104, 2764–2773. doi: 10.1016/j.bpj.2013.05.025

McDowell, K. S., Zahid, S., Vadakkumpadan, F., Blauer, J., MacLeod, R. S., and Trayanova, N. A. (2015). Virtual electrophysiological study of atrial fibrillation in fibrotic remodeling. *PLoS One* 10:e0117110. doi: 10.1371/journal.pone.0117110

Moss, A. J., Zareba, W., Hall, W. J., Klein, H., Wilber, D. J., Cannom, D. S., et al. (2002). Prophylactic implantation of a defibrillator in patients with myocardial infarction and reduced ejection fraction. *N. Engl. J. Med.* 346, 877–883. doi: 10.1056/nejmoa013474

Nussinovitch, U., and Gepstein, L. (2015a). Optogenetics for in vivo cardiac pacing and resynchronization therapies. *Nat. Biotechnol.* 33, 750–754. doi: 10.1038/nbt.3268

Nussinovitch, U., and Gepstein, L. (2015b). Optogenetics for suppression of cardiac electrical activity in human and rat cardiomyocyte cultures. *Neurophotonics* 2:031204.

Nussinovitch, U., Shinnawi, R., and Gepstein, L. (2014). Modulation of cardiac tissue electrophysiological properties with light-sensitive proteins. *Cardiovasc. Res.* 102, 176–187. doi: 10.1093/cvr/cvu037

Nyns, E. C. A., Kip, A., Bart, C. I., Plomp, J. J., Zeppenfeld, K., Schalij, M. J., et al. (2017). Optogenetic termination of ventricular arrhythmias in the whole heart: towards biological cardiac rhythm management. *Eur. Heart J.* 38, 2132–2136.

Nyns, E. C. A., Poelma, R. H., Volkers, L., Plomp, J. J., Bart, C. I., Kip, A. M., et al. (2019). An automated hybrid bioelectronic system for autogenous restoration of sinus rhythm in atrial fibrillation. *Sci. Transl. Med.* 11:eaau6447. doi: 10.1126/scitranslmed.aau6447

Pedersen, S. S., den Broek, K. C., Theuns, D. A., Erdman, R. A., Alings, M., Meijer, A., et al. (2011). Risk of chronic anxiety in implantable defibrillator patients: a multi-center study. *Int. J. Cardiol.* 147, 420–423. doi: 10.1016/j.ijcard.2009.09.549

Plank, G., Zhou, L., Greenstein, J. L., Cortassa, S., Winslow, R. L., O'Rourke, B., et al. (2008). From mitochondrial ion channels to arrhythmias in the heart: computational techniques to bridge the spatio-temporal scales. *Philos. Trans. A Math. Phys. Eng. Sci.* 366, 3381–3409. doi: 10.1098/rsta.2008.0112

Poole, J. E., Johnson, G. W., Hellkamp, A. S., Anderson, J., Callans, D. J., Raitt, M. H., et al. (2008). Prognostic importance of defibrillator shocks in patients with heart failure. *N. Engl. J. Med.* 359, 1009–1017.

Quiñonez Uribe, R. A., Luther, S., Diaz-Maue, L., and Richter, C. (2018). Energy-reduced arrhythmia termination using global photostimulation in optogenetic murine hearts. *Front. Physiol.* 9:1651. doi: 10.3389/fphys.2018.01651

Rao, P., Wang, L., Cheng, Y., Wang, X., Li, H., Zheng, G., et al. (2020). Near-infrared light driven tissue-penetrating cardiac optogenetics via upconversion nanoparticles in vivo. *Biomed. Opt. Express* 11, 1401–1416. doi: 10.1364/boe.381480

Ripoll, J., Yessayan, D., Zacharakis, G., and Ntziachristos, V. (2005). Experimental determination of photon propagation in highly absorbing and scattering media. *J. Opt. Soc. Am. A Opt. Image Sci. Vis.* 22, 546–551. doi: 10.1364/josaa.22.000546

Siebels, J., and Kuck, K. H. (1994). Implantable cardioverter defibrillator compared with antiarrhythmic drug treatment in cardiac arrest survivors (the Cardiac Arrest Study Hamburg). *Am. Heart J.* 127(4 Pt 2), 1139–1144. doi: 10.1016/0002-8703(94)90101-5

Sulke, N., Sayers, F., Lip, G. Y., and Guideline Development Group for the NCGFTMOAF (2007). Rhythm control and cardioversion. *Heart* 93, 29–34. doi: 10.1136/hrt.2006.099879

Swartling, J., Palsson, S., Platonov, P., Olsson, S. B., and Andersson-Engels, S. (2003). Changes in tissue optical properties due to radio-frequency ablation of myocardium. *Med. Biol. Eng. Comput.* 41, 403–409. doi: 10.1007/bf02348082

ten Tusscher, K. H., and Panfilov, A. V. (2006). Alternans and spiral breakup in a human ventricular tissue model. *Am. J. Physiol. Heart Circ. Physiol.* 291, H1088–H1100.

Vadakkumpadan, F., Arevalo, H., Prassl, A. J., Chen, J., Kickinger, F., Kohl, P., et al. (2010). Image-based models of cardiac structure in health and disease. *Wiley Interdiscip. Rev. Syst. Biol. Med.* 2, 489–506. doi: 10.1002/wsbm.76

Vigmond, E. J., Hughes, M., Plank, G., and Leon, L. J. (2003). Computational tools for modeling electrical activity in cardiac tissue. *J. Electrocardiol.* 36(Suppl. 1), 69–74. doi: 10.1016/j.jelectrocard.2003.09.017

Vigmond, E. J., Weber dos Santos, R., Prassl, A. J., Deo, M., and Plank, G. (2008). Solvers for the cardiac bidomain equations. *Prog. Biophys. Mol. Biol.* 96, 3–18. doi: 10.1016/j.pbiomolbio.2007.07.012

Vogt, C. C., Bruegmann, T., Malan, D., Ottersbach, A., Roell, W., Fleischmann, B. K., et al. (2015). Systemic gene transfer enables optogenetic pacing of mouse hearts. *Cardiovasc. Res.* 106, 338–343. doi: 10.1093/cvr/cvv004

Wasala, N. B., Shin, J. H., and Duan, D. (2011). The evolution of heart gene delivery vectors. *J. Gene Med.* 13, 557–565. doi: 10.1002/jgm.1600

Wietek, J., Wiegert, J. S., Adeishvili, N., Schneider, F., Watanabe, H., Tsunoda, S. P., et al. (2014). Conversion of channelrhodopsin into a light-gated chloride channel. *Science* 344, 409–412. doi: 10.1126/science.1249375

Williams, J. C., Xu, J., Lu, Z., Klimas, A., Chen, X., Ambrosi, C. M., et al. (2013). Computational optogenetics: empirically-derived voltage- and light-sensitive channelrhodopsin-2 model. *PLoS Comput. Biol.* 9:e1003220. doi: 10.1371/journal.pcbi.1003220

Xu, L., Gutbrod, S. R., Bonifas, A. P., Su, Y., Sulkin, M. S., Lu, N., et al. (2014). 3D multifunctional integumentary membranes for spatiotemporal cardiac measurements and stimulation across the entire epicardium. *Nat. Commun.* 5:3329.

Zaglia, T., Pianca, N., Borile, G., Da Broi, F., Richter, C., Campione, M., et al. (2015). Optogenetic determination of the myocardial requirements for extrasystoles by cell type-specific targeting of ChannelRhodopsin-2. *Proc. Natl. Acad. Sci. U.S.A.* 112, E4495–E4504.

Zahid, S., Cochet, H., Boyle, P. M., Schwarz, E. L., Whyte, K. N., Vigmond, E. J., et al. (2016a). Patient-derived models link re-entrant driver localization in atrial fibrillation to fibrosis spatial pattern. *Cardiovasc. Res.* 110, 443–454. doi: 10.1093/cvr/cvw073

Zahid, S., Whyte, K. N., Schwarz, E. L., Blake, R. C. III, Boyle, P. M., Chrispin, J., et al. (2016b). Feasibility of using patient-specific models and the "minimum cut" algorithm to predict optimal ablation targets for left atrial flutter. *Heart Rhythm* 13, 1687–1698. doi: 10.1016/j.hrthm.2016.04.009

Zhai, X. W., Zhang, L., Guo, Y. F., Yang, Y., Wang, D. M., Zhang, Y., et al. (2017). The IK1/Kir2.1 channel agonist zacopride prevents and cures acute ischemic arrhythmias in the rat. *PLoS One* 12:e0177600. doi: 10.1371/journal.pone.0177600

Conflict of Interest: The authors declare that the research was conducted in the absence of any commercial or financial relationships that could be construed as a potential conflict of interest.

Publisher's Note: All claims expressed in this article are solely those of the authors and do not necessarily represent those of their affiliated organizations, or those of the publisher, the editors and the reviewers. Any product that may be evaluated in this article, or claim that may be made by its manufacturer, is not guaranteed or endorsed by the publisher.

frontiers in Physiology

REVIEW
published: 31 August 2021
doi: 10.3389/fphys.2021.726895

Neurohumoral Cardiac Regulation: Optogenetics Gets Into the Groove

Arianna Scalco[1,2†], *Nicola Moro*[1,2†], *Marco Mongillo*[2,3*] *and Tania Zaglia*[2,3*]

[1] Department of Cardiac, Thoracic, Vascular Sciences and Public Health, University of Padova, Padova, Italy, [2] Veneto Institute of Molecular Medicine, Padova, Italy, [3] Department of Biomedical Sciences, University of Padova, Padova, Italy

The cardiac autonomic nervous system (ANS) is the main modulator of heart function, adapting contraction force, and rate to the continuous variations of intrinsic and extrinsic environmental conditions. While the parasympathetic branch dominates during rest-and-digest sympathetic neuron (SN) activation ensures the rapid, efficient, and repeatable increase of heart performance, e.g., during the "fight-or-flight response." Although the key role of the nervous system in cardiac homeostasis was evident to the eyes of physiologists and cardiologists, the degree of cardiac innervation, and the complexity of its circuits has remained underestimated for too long. In addition, the mechanisms allowing elevated efficiency and precision of neurogenic control of heart function have somehow lingered in the dark. This can be ascribed to the absence of methods adequate to study complex cardiac electric circuits in the unceasingly moving heart. An increasing number of studies adds to the scenario the evidence of an intracardiac neuron system, which, together with the autonomic components, define a little brain inside the heart, in fervent dialogue with the central nervous system (CNS). The advent of optogenetics, allowing control the activity of excitable cells with cell specificity, spatial selectivity, and temporal resolution, has allowed to shed light on basic neuro-cardiology. This review describes how optogenetics, which has extensively been used to interrogate the circuits of the CNS, has been applied to untangle the knots of heart innervation, unveiling the cellular mechanisms of neurogenic control of heart function, in physiology and pathology, as well as those participating to brain–heart communication, back and forth. We discuss existing literature, providing a comprehensive view of the advancement in the understanding of the mechanisms of neurogenic heart control. In addition, we weigh the limits and potential of optogenetics in basic and applied research in neuro-cardiology.

Keywords: optogenetics, autonomic neurons, heart innervation, brain–heart axis, neurogenic heart control

OPEN ACCESS

Edited by:
Tobias Brügmann, University Medical Center Göttingen, Germany

Reviewed by:
Beth A. Habecker, Oregon Health and Science University, United States
Matthew W. Kay, George Washington University, United States

***Correspondence:**
Marco Mongillo
marco.mongillo@unipd.it
Tania Zaglia
tania.zaglia@unipd.it

[†] *These authors have contributed equally to this work*

Specialty section:
This article was submitted to Cardiac Electrophysiology, a section of the journal Frontiers in Physiology

Received: *17 June 2021*
Accepted: *27 July 2021*
Published: *31 August 2021*

Citation:
Scalco A, Moro N, Mongillo M and Zaglia T (2021) Neurohumoral Cardiac Regulation: Optogenetics Gets Into the Groove. Front. Physiol. 12:726895. doi: 10.3389/fphys.2021.726895

PREFACE

From a simplistic point of view, the heart is a muscular pump which powers blood in the circulation, supplying oxygen, nutrients, hormones, and other tissue-derived mediators to all cells in the body (Braunwald et al., 1967). The initial observation that automaticity of heart contractions was independent from neuronal inputs, dates back to the second century, when Galen noted that "the fact that the heart, removed from the thorax, can be seen to move for a considerable time, is a definite indication that it does not need the nerves to perform its own function" (Charles, 1956). Throughout the more recent history of physiology, the concept of the heart as a strictly "muscular

self-operating organ" was sometimes disputed, but did finally consolidate into a rock-solid notion with the cellular and molecular characterization of cardiac pacemaker and conduction system cells, still unanimously agreed (Keith and Flack, 1906; Tawara, 1906; Wybauw, 1910; Lewis, 1911; James and Sherf, 1971; Monfredi et al., 2010; Padala et al., 2021). It is undoubted that the explanted heart, if perfused with an appropriate solution, continues pumping while harvested from the organism (Ringer, 1883), and transplant of a heart disconnected from higher nervous components is a common life-saving procedure for patients with e.g., cardiac failure (McCartney et al., 2017).

It is, however, well-understood that the activity of the cardiac pump is finely tuned to match blood supply with the varied perfusional demand of the organism, e.g., increase of cardiac output during exercise to fuel skeletal muscle requirements (Higginbotham et al., 1986). Such extrinsic modulation of heart contraction is primarily operated by the sympathetic and parasympathetic branches of the autonomic nervous system (ANS), which innervate the atrial (both branches) and ventricular [mainly sympathetic neurons (SNs)] myocardium, exerting grossly opposite effects on the frequency and force of contraction (Zaglia and Mongillo, 2017). While the full-blown activation of SNs, easily detectable, suggests the dominant effect of the sympathetic branch of the ANS on heart control, preclinical and clinical evidence underscores the regulatory power of the parasympathetic nervous system (PNS) on heart function. While the remainder parts of this review will mainly focus on SNs, the reader is referred to Li et al. (2004) Lee et al. (2016), and Zasadny et al. (2020) for reference.

A reductionist example of neurogenic heart regulation by SNs is shown by the effect of a decrease in blood pressure, which is immediately perceived by peripheral baroceptors, and reflects centrally on the activation of sympathetic nervous system (SNS), increasing heart rate (HR), contraction force, and peripheral vasoconstriction, to restore the physiologic pressure values (Heesch, 1999; Fadel, 2008). Beyond such rather unsophisticated, single lane neuro-cardiac connection, however, the activity of cardiac autonomic neurons is orchestrated by a complex network of neural circuits established in the central nervous system (CNS) [i.e., the central autonomic network (CAN)], which includes various regions in the cortex, amygdala, hypothalamus, in the midbrain and pons, and in several nuclei in the medulla (Silvani et al., 2016). These stations receive information from other parts of the brain (e.g., emotional inputs), peripheral body sensors (i.e., homeostatic inputs), as well as from the external environment (i.e., sensory inputs), all of which are integrated to come up with an appropriate response, acutely dictated to the heart through preganglionic efferents converging on the sympathetic and parasympathetic ganglia (Ardell and Armour, 2016; Silvani et al., 2016). Post-ganglionic "motor" neurons, in turn, divaricate from the ganglia toward appropriate sections of the heart and blood vessels, delivering the operative information to the cardiovascular system (Franzoso et al., 2016; Di Bona et al., 2020) (**Figure 1**).

In addition to a "loud" brain–heart communication in the "fight-or-flight" reaction, however, a whispered and perpetual neurocardiac dialogue, finalized to preserve the heart, and organism's homeostasis, has been demonstrated by a large number of studies, including ours (Ogawa et al., 1992; Kanevskij et al., 2002; O'Connell et al., 2003; Zaglia et al., 2012; Kreipke and Birren, 2015; Pianca et al., 2019). Constitutive activity of the ANS (both from the sympathetic and parasympathetic branches) regulates HR on a beat-to-beat basis (Ahmed et al., 1994; Lombardi et al., 1996; Poletto et al., 2011; Vanderlaan et al., 2012; Moreno et al., 2019) and controls, in parallel, signaling pathways impinging on cardiomyocyte (CM) proteostasis, size, electrophysiology, and division (Ogawa et al., 1992; Kanevskij et al., 2002; O'Connell et al., 2003; Zaglia et al., 2012; Kreipke and Birren, 2015; Pianca et al., 2019). Beyond cardiac physiology, the role of the "brain–heart axis" is increasingly being recognized in cardiac pathology, as highlighted by the widespread use of sympatholytic therapies (e.g., β-blockers) (Ponikowski et al., 2016; Ibanez et al., 2018; Neumann et al., 2020). Chronic sympathetic disturbances have a role in myocardial hypertrophy (Zimmer et al., 1995; Kimura et al., 2007; Fukuda et al., 2015) and heart failure (HF) (Kishi, 2012; Fukuda et al., 2015), and acute sympathetic hyperactivity, during acute physical exercise or following intense emotional stresses, is responsible for arrhythmias and sudden cardiac death (SCD) in several genetic cardiac disorders (e.g., Arrhythmogenic Cardiomyopathy, ACM; Catecholaminergic Polymorphic Ventricular Tachycardia, CPVT; Long QT Syndrome) (Leenhardt et al., 1995; Schwartz et al., 2001; Wehrmacher et al., 2005; Lehnart et al., 2008; Basso et al., 2009; Fukuda et al., 2015; Taggart et al., 2016; Corrado et al., 2017; Agrimi et al., 2020; Winbo and Paterson, 2020; Wleklinski et al., 2020), as well as in Takotsubo syndrome (Sharkey et al., 2011). In addition, it is now well-accepted that brain damage, by modifying autonomic control of heart function, reflects negatively on cardiac health [e.g., patients suffering a stroke have higher probability to develop secondary adverse cardiac events (Touzé et al., 2005; Kim et al., 2017)]. Along the same lines, cerebrovascular diseases may cause cardiac arrhythmias, potentially evolving in SCD (Mikolich and Jacobs, 1981; Kallmünzer et al., 2012; Ruthirago et al., 2016), and depression has been shown to increase the incidence of coronary artery disease (Bunker et al., 2003; Van der Kooy et al., 2007; Carney and Freedland, 2017) and heart attacks (Van der Kooy et al., 2007).

Abbreviations: ACM, arrhythmogenic cardiomyopathy; ANS, autonomic nervous system; α-MHC, α-myosin heavy chain; AP, action potential; AVN, atrio-ventricular node; β-ARs, β-adrenoceptors; ChR, channelrhodopsin; CAN, central autonomic network; CNS, central nervous system; CPVT, catecholaminergic polymorphic ventricular tachycardia; CM, cardiomyocyte; DBH, dopamine-β-hydroxylase; DRG, Dorsal Root Ganglion; ECG, electrocardiography; ENDO, subendocardium; EPI, subepicardium; GFP, green fluorescent protein; HF, heart failure; HR, heart rate; HRV, heart rate variability; INS, intrinsic nervous system; LSG, left stellate ganglion; LV, left ventricle; ms, milliseconds; NA, noradrenaline; NIR, near-infrared radiation; NG, Nodose Ganglion; NPY, neuropeptide Y; OLED, organic light-emitting diode; PF, Purkinje fibers; PKA, PNS, parasympathetic nervous system; protein kinase A; preBötC, preBötzinger Complex; PSN, parasympathetic neuron; RA, right atrium; RV, right ventricle; SAN, sino-atrial node; SCD, sudden cardiac death; SCG, Sympathetic Cardiac Ganglia; SN, sympathetic neuron; SNS, sympathetic nervous system; TH, tyrosine hydroxylase; 3-D, three-dimension; UCNP, upconversion nanoparticles; VIP, vasoactive intestinal polypeptide; VT, ventricular tachycardia; VF, ventricular fibrillation.

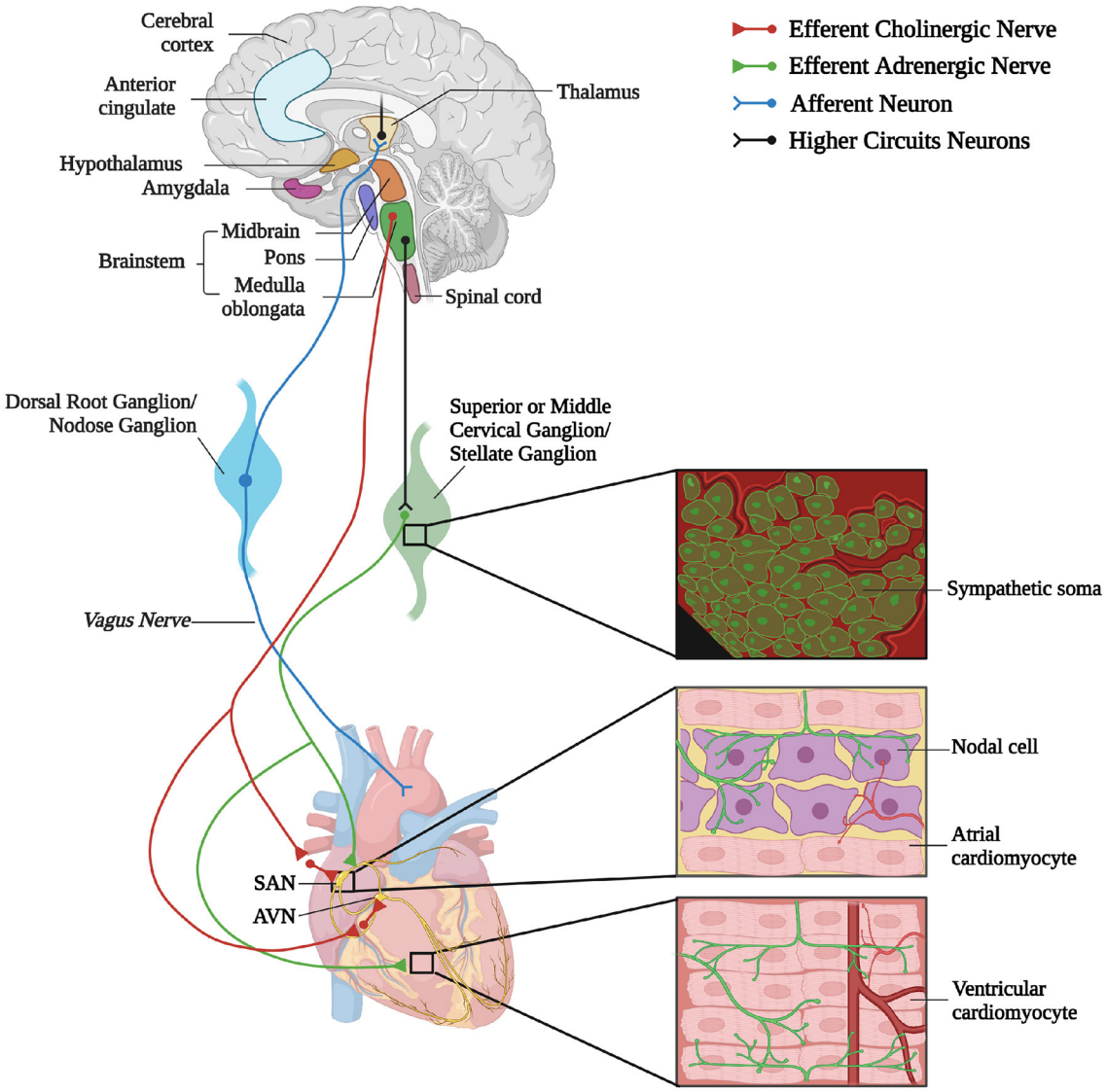

FIGURE 1 | The complex neuronal circuitries underlying bidirectional "brain–heart" connection. Schematic representation of the "brain–heart axis." Different regions of the brain, belonging to the CAN process precise orders which are transmitted, through efferent preganglionic fibers, to both sympathetic (adrenergic) and parasympathetic (cholinergic) cardiac ganglia. While PSN processes mainly innervate the SAN and the AVN, SNs invade the conduction system and the working myocardium. The cardiac muscle is also innervated by intrinsic neurons (INS) and cardiac sensory neurons, whose cell bodies organize into the dorsal root ganglion and nodose ganglion, and their afferent fibers project to different areas of the brain (created with BioRender.com).

In parallel with the increased interest in the "brain-to-heart" communication, a number of studies unveiled that, besides a highly intricated network of post-ganglionic autonomic neurons (Janes et al., 1986; Kawashima, 2005; Zaglia and Mongillo, 2017; Wink et al., 2020), the myocardium homes an intrinsic nervous system (INS) (Armour et al., 1997; Fedele and Brand, 2020). In addition, afferent neurons may mediate the reverse "heart-to-brain" communication, by continuously sending information to the CNS, which impacts on neuronal circuits involved in perception, cognition, and emotional processing (Schievink et al., 2017; Dal Lin et al., 2018) (**Figure 1**).

When considering such complexity of the brain–heart neural wiring, the awareness emerges that brain-to-heart communication should not be simplified to the interaction between a brainy regulator and a heartly executor. The "little brain of the heart," promoting this self-excitable muscle from mere hydraulic pump to sophisticated "neuro-muscular" organ (Armour, 2007, 2008), calls for its bright spot in the theater of physiology.

Traditional methodologies of neuroanatomy, neurophysiology, and pharmacology, which have commonly been used in neuro-cardiology, are inadequate to untangle the complex neuronal circuits linking the brain and the heart

in an intimate bidirectional interaction. On the contrary, optogenetics represents the novel biotechnological tool which, by allowing spatially- and cell type-selective neuromodulation, has the potential to functionally dissect the components of the entire "brain–heart" circuitry, and resolve open questions on physiologic mechanisms which have remained obscure for a long time. This review will provide a description of the brain–heart connection and discuss how optogenetics has started to contribute shedding light on the unexpectedly intricated "neuro-cardiac liaison."

THE LIGHT TOUCH OF OPTOGENETICS

Optogenetics is a recently developed technology, which combines physics, molecular biology, and electrophysiology (Boyden et al., 2005; Deng et al., 2014) to enable contactless control of ion flux across the plasma membrane of cells exogenously expressing photoactivatable channel proteins consistently named "opsins." The method, singled out as Nature's "*Method of the Year 2010,*" relies on the discovery that a microbial-derived class of proteins, with structural features resembling the well-known rhodopsins, form ion channels with variable selectivity, while retaining light sensitivity, two properties that allow to either depolarize or hyperpolarize the membrane potential of excitable cells with light irradiation at appropriate (i.e., depending on the opsin type) wavelength. The algal light-sensitive cation-conducting channelrhodopsins (ChRs) were among the first opsins to be characterized and expressed in a specific cell population, within a multicellular tissue of the experimental animal (Nagel et al., 2002, 2003; Zhang et al., 2008), to interrogate the role of specific neuronal circuits of the CNS. Two ChR variants have initially been used in neuroscience: ChR2 from *Chlamydomonas reinhardtii* (Boyden et al., 2005; Li et al., 2005; Nagel et al., 2005; Bi et al., 2006; Ishizuka et al., 2006; Zhang et al., 2006) and VChR1 from *Volvox carteri* (Zhang et al., 2008), endowed with sufficiently fast kinetics to achieve action potential (AP) triggered with brief light pulses (1–5 ms), delivered at a frequency suited to neuronal activation. For more detailed description on the history and development of optogenetics, the readers are referred to several topical reviews, some included in this same Special Issue (Hegemann and Nagel, 2013; ref to be included by editors).

The unique aspect which signed success of the technique, compared with conventional electrophysiological methods, based on electrical perturbation, are its non-invasiveness, spatial-temporal accuracy, and cellular specificity (Pianca et al., 2017; Sasse, 2018). The latter allowed to "interrogate" the function of a selected cell type while enclosed in a complex tissue, and intermingled with numerous different cells, giving neuroscientists the tools to selectively study a given brain region or even a single neural circuit (Rajasethupathy et al., 2016; Pianca et al., 2017). Moreover, the non-invasiveness of the technique allows to stimulate cells multiple times or for long periods, with no damage, an incredible advancement in experimental neuroscience, where such technology was firstly tested, and rapidly became a reference method (Pianca et al., 2017; Deubner et al., 2019).

The rocketing potential of optogenetics drove molecular biologists to expand the opsin variants toolkit, including newly identified (i.e., from other microbial species) and molecularly engineered opsins (for reference see: www.optogenetics.org). This led to the generation of a large number of opsin variants, endowed with specific ionic selectivity (e.g., for cations or anions) enabling either cell hyperpolarization [i.e., PAK-K (Bernal Sierra et al., 2018), BLINK-1 (Cosentino et al., 2015), GtACR1 (Govorunova et al., 2016), ArchT (Han et al., 2011), Halorhodopsin (Gradinaru et al., 2008), Jaws (Chuong et al., 2014)] or depolarization [i.e., ChR2 (Nagel et al., 2003), CheRiff (Hochbaum et al., 2014), ReaChR (Lin et al., 2013), Crimson (Klapoetke et al., 2014)], different photocurrent kinetics and sensitivity to differently-colored activation light, covering almost the entire visible spectrum, from blue- to red-shifted variants.

Some years after its initial application to neurosciences, the pioneering studies of Arrenberg (Arrenberg et al., 2010), Bruegmann (Bruegmann et al., 2010), and Jia (Jia et al., 2011) demonstrated that optogenetics can be applied also for the study of heart electrophysiology. In particular, Bruegmann and colleagues developed transgenic mice expressing ChR2 in CMs and were able to pace heart contractions by shining light on the epicardium, thus inducing ectopic heart beats *in vivo* (Bruegmann et al., 2010). Simultaneously, Arrenberg and colleagues combined the expression of Halorhodopsin and ChR2 in zebrafish CMs, with the use of light sheet microscopy, and achieved bidirectional control of HR *in vivo*, remotely inducing tachycardia, bradycardia and cardiac arrest (Arrenberg et al., 2010). In parallel, Jia et al. demonstrated "the utility of optogenetics to cardiac muscle by a tandem cell unit (TCU)," which "can serve not only as an elegant tool in arrhythmia research but may form the basis for a new generation of light-driven cardiac pacemakers and muscle actuators" (Jia et al., 2011).

These proof-of concept experiments signed the beginning of "cardiac optogenetics," which was subsequently applied to investigate biophysical aspects of cardiac physiology and pathology [i.e., minimal cell mass required to activate ectopic beats; role of Purkinje fibers (PFs) in arrhythmias (Zaglia et al., 2015; Pianca et al., 2017)]. Undoubtedly, these studies opened fascinating perspectives, but the inherent potential of cardiac optogenetics (i.e., cell type specificity and non-invasiveness) was uncovered by approaching the heart as a complex network of different structurally and functionally interconnected cell populations, including excitable (i.e., working CMs, conduction system cells, efferent, intrinsic, and afferent neurons), conducting (i.e., fibroblasts, resident, and recruited inflammatory cells), and non-excitable (i.e., vascular cells) cells (Pianca et al., 2017) (**Figure 2**). As heart homeostasis relies on the activity of many multicellular "circuitries," fine dissection of the individual role of each cell type, with respect to localization and myocardial interactions, has benefitted, alike neurobiology, from optogenetic studies. Here, we will focus on heart-innervating autonomic neurons, and present examples of existing literature which describes how optogenetics

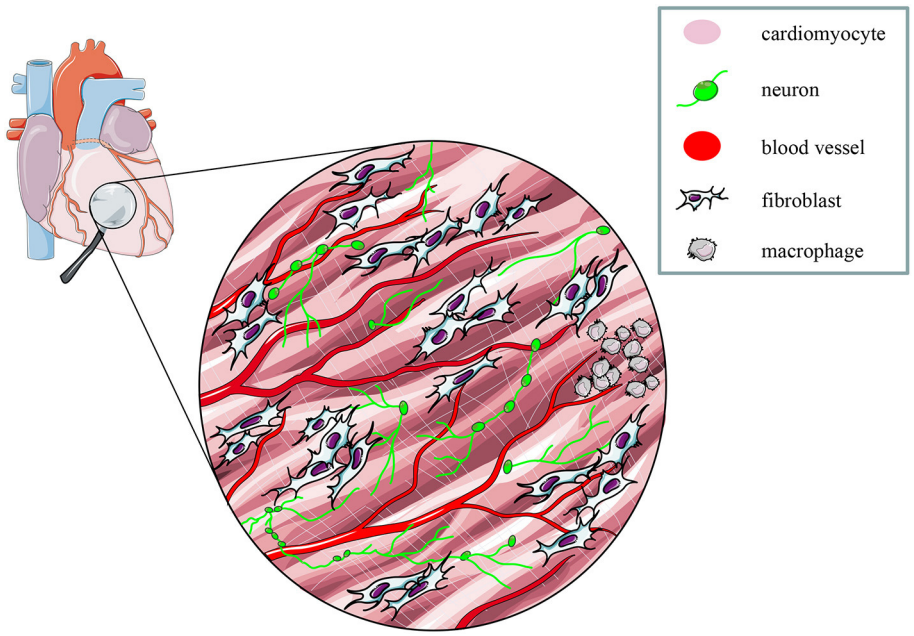

FIGURE 2 | The multicellular nature of the myocardium. The myocardium is a complex network of different structural and functional interconnected cell types, including intrinsic and extrinsic excitable, as well as non-excitable cells. Modified with permission from Zaglia et al. (2019).

allowed to: (i) improve the knowledge on the mechanisms underlying physiologic neurogenic control of heart function; (ii) investigate and lay new therapeutic concepts in arrhythmology, and (iii) add new tiles to the understanding of the bidirectional "brain–heart" interaction. In addition, we will comment on the opportunities that optogenetic-based neuromodulation of the heart could offer in the inspection of the multiplexed connections between brain and heart, from the central to the peripheral and heart intrinsic neuronal networks, impinging on heart function, in physiological and pathological contexts (**Figure 3**).

OPTOGENETICS ALLOWS UNTANGLE CARDIAC NEURONAL CIRCUITRIES

In June 2021, the simple query of "optogenetics" and "neuron" retrieves 5,700 hits in Pubmed, highlighting the aptness of the method in neuroscience research, and as such its use to interrogate the function of the cardiac neural network would thus appear a trivial task. Non-invasive optical actuation of heart neurons is a tremendously powerful technique, but it has to be considered that the spectrum of cardiac effects of acute neuro-cardiac modulation is rather limited. Granted, HR and contractile function can be monitored with standard methodologies (ECG, echocardiography), but study of e.g., heart electrophysiology at cellular level requires state-of-the-art methods to allow investigation *in vivo*. Thus, combination with equally advanced readouts of heart function is necessary, as discussed in more detail in **Chapter 6**.

The Unexpected Extent of Cardiac Sympathetic Innervation

As discussed in **Chapter 1**, the parasympathetic and sympathetic branches of the ANS are both present in the myocardium, with parasympathetic neurons (PSNs) detectable in SAN, atrioventricular node (AVN), atria and cardiac blood vessels, and SNs innervating both the conduction system and the working myocardium of atria and ventricles (Franzoso et al., 2016) (**Figures 4A,B**). Heart innervation by the ANS has long been recognized in both physiology and diseases, as exemplified by the common use of β-adrenoceptor (β-AR) antagonists, inhibiting the main sympathetic neurotransmitter receptor, in several cardiovascular diseases (Zaglia and Mongillo, 2017). However, the precise anatomy, the extent and intercellular contacts of cardiac innervation have remained, quite surprisingly, understudied and elusive for a long time, partly due to technical limitations and methodologic difficulties. Here, we will mainly focus on SNs, whose processes display a "pearl necklace" morphology, characterized by regularly distributed varicosities, which are the neurotransmitter [i.e., mainly noradrenaline (NA) and neuropeptide Y (NPY)] releasing sites, contacting myocardial target cells (Zaglia and Mongillo, 2017) (**Figures 4A,B**). Characterization of SN topology was initially obtained by the analysis of thin rodent heart sections, stained with antibodies to enzymes involved in NA biosynthesis, which allowed to demonstrate that SNs heterogeneously distribute among the four heart chambers, with the highest density of nerve fibers in the atria, followed by the right (RV) and left (LV) ventricle (Di Bona et al., 2020). Moreover, across the ventricular walls a transmural gradient of SN density, from the epicardium to

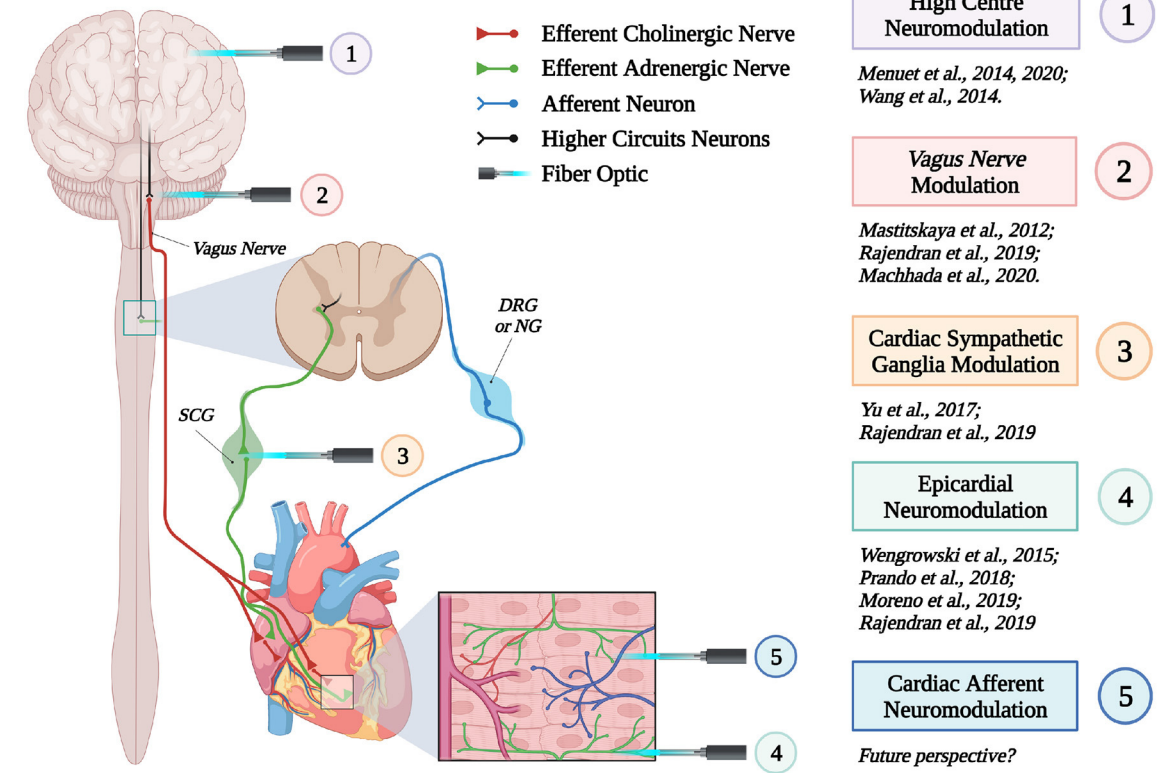

FIGURE 3 | Optogenetic interrogation of the brain–heart axis at multiple sites. Schematic representation of the different brain–heart connecting circuitries which have been or could be interrogated by optogenetics (created with BioRender.com).

the endocardium can be detected in a specie-specific distribution in different mammalian hearts (Randall et al., 1968; Glebova and Ginty, 2004). Consistently, we recently estimated, in the mouse heart, one SN process every two CMs in the sub-epicardium (EPI), while the density appeared decreased in the sub-endocardial region (ENDO) (Pianca et al., 2019). Interestingly, such innervation pattern is different, in rat hearts, in which SN density is similar in the EPI and ENDO regions, while in rabbit, pig, and human, SNs are highly represented in the ENDO region (Pianca et al., 2019). Although the results presented above advanced the anatomical details in the study of heart innervation, they were not designed to define the three-dimensional (3-D) topology of the cardiac sympathetic network. To achieve this goal (and aligned with the broader definition of "optogenetics" i.e., the use of genetically-developed and cell-targeted optical sensors in biology), Freeman et al. used two-photon fluorescence microscopy, combined with computer-assisted image analyses, to generate, in small cardiac volumes from mice with SN-specific expression of Green Fluorescent Protein (GFP), the first 3-D reconstruction of the cardiac SN network (Freeman et al., 2014) (**Figure 4C**). While the inspection of thin heart sections suggested the coexistence of innervated and denervated CMs, the 3-D reconstruction of the neuronal tree revealed that SNs are represented in the heart with a density much higher than expected and suggested that each CM may be simultaneously contacted by several neuronal processes, all of which establish multiple neuro-muscular contacts at the regularly displaced neuronal varicosities. In keeping with the inclusive definition of opto-genetics, we took advantage from the co-expression of fluorescent *td-Tomato* in CMs of the α-MHC/ChR2-*td-Tomato* transgenic mice, to define in higher detail, in the intact 3-D tissue, the topology of interactions between SNs and CMs. To this aim, we applied a modified version of "CLARITY" tissue transformation (Chung and Deisseroth, 2013; Chung et al., 2013) and imaged with multiphoton microscopy both the red-native fluorescence of CM sarcolemma and SNs stained with anti-Tyrosine Hydroxylase (TH) antibody. This allowed demonstrate that, in the mouse heart, each CM is contacted by at least one SN and that, most frequently, a single CM receives multiple neuronal inputs from different processes (**Figure 5**). Notably, the 3-D reconstruction of the SN network in autoptic human heart blocks confirmed both such extent and the complexity of cardiac sympathetic innervation at microscopic level (**Figure 6**) (Pianca et al., 2019), although a fine characterization of the topology of autonomic innervation, throughout the whole myocardium, is still unavailable.

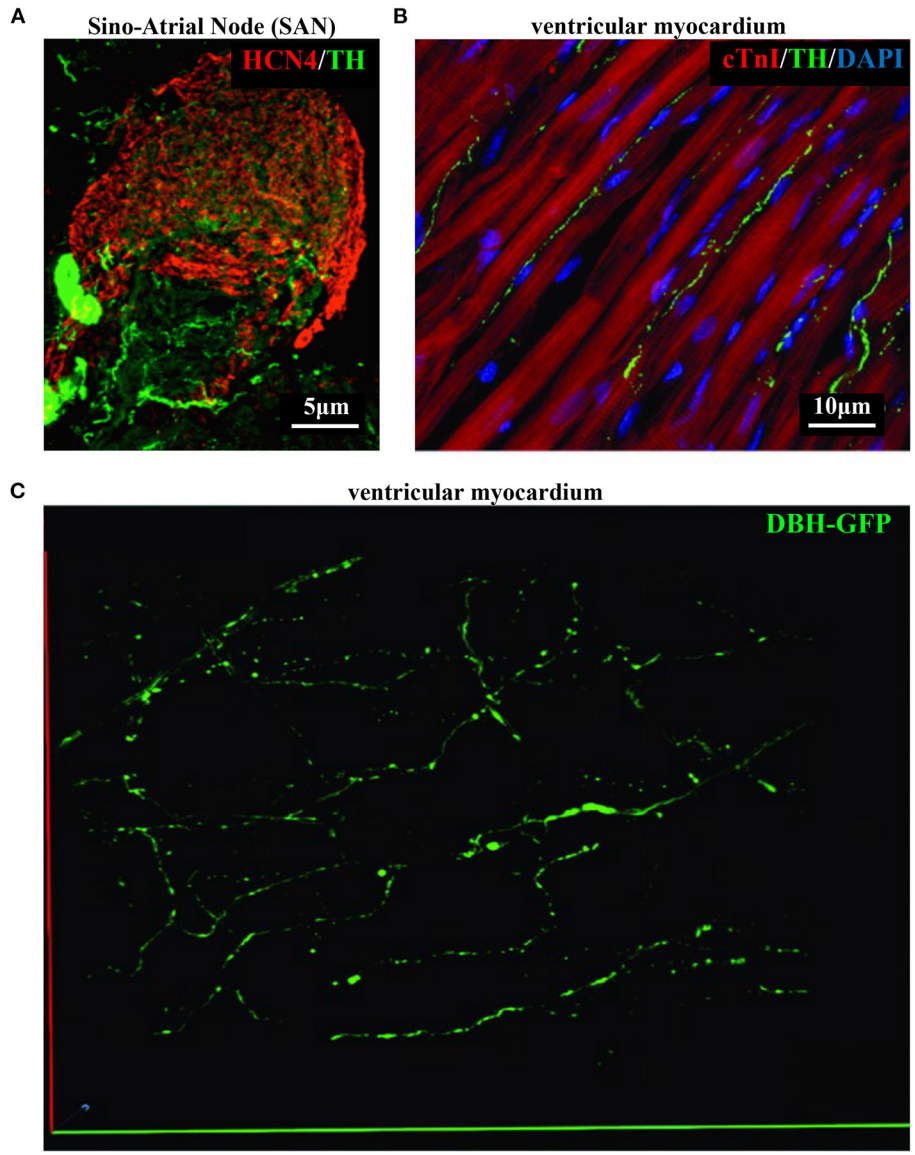

FIGURE 4 | Bi- and three-dimensional topology of cardiac sympathetic innervation. **(A)** Confocal immunofluorescence of the SAN of a normal adult mouse, co-stained with antibodies to tyrosine hydroxylase (TH) and HCN4, to identify SN processes and pacemaker cells, respectively. **(B)** Confocal immunofluorescence imaging of ventricular myocardial section from normal adult mice, stained with antibodies to TH and cardiac troponin I (cTnI). Nuclei are counterstained with DAPI. The image is a detail from the LV subepicardial region. **(C)** 3-D reconstruction, at the multi-photon microscope of the sympathetic network within a portion of the LV subepicardium in an adult, Langendorff-perfused DBH-GFP heart. A segment of 230 µm by 28 µm by 50 µm was imaged. **(A–C)** Modified with permission from Prando et al. (2018) **(A)**, Zaglia and Mongillo (2017) **(B)**, and Freeman et al. (2014) **(C)**.

A Lightly Inspection of Neurogenic Control of Heart Activity

Sympathetic neurons modulate the rhythm and force of heart contraction through the effects of NA activation of CM β-ARs (mainly β1-ARs), increasing intracellular [cAMP] which, in the SAN, directly enhances I_f, increasing the rate of spontaneous automaticity, and, in ventricular CMs, enhances, mainly through PKA activity, the extent of Ca^{2+} turnover at each cardiac cycle (Zaccolo and Pozzan, 2002; Stieber et al., 2003; Rochais et al., 2004; Bers, 2008; Difrancesco, 2010). While these effects allow short-term adaptation of cardiac function to increased perfusional demand (e.g., exercise or emotional stress, intrinsic homeostatic mechanisms), we recently demonstrated that, in parallel, constitutive SN inputs are required to maintain physiologic size of the adult heart, acting on the equilibrium between protein synthesis and degradation, *via* the β2-AR/Akt/Foxo/ubiquitin ligase signaling pathway (Zaglia et al., 2012). That the SNS affects heart structure and signaling, in basal conditions, has been demonstrated by several studies (Ogawa et al., 1992; Kanevskij et al., 2002; O'Connell et al.,

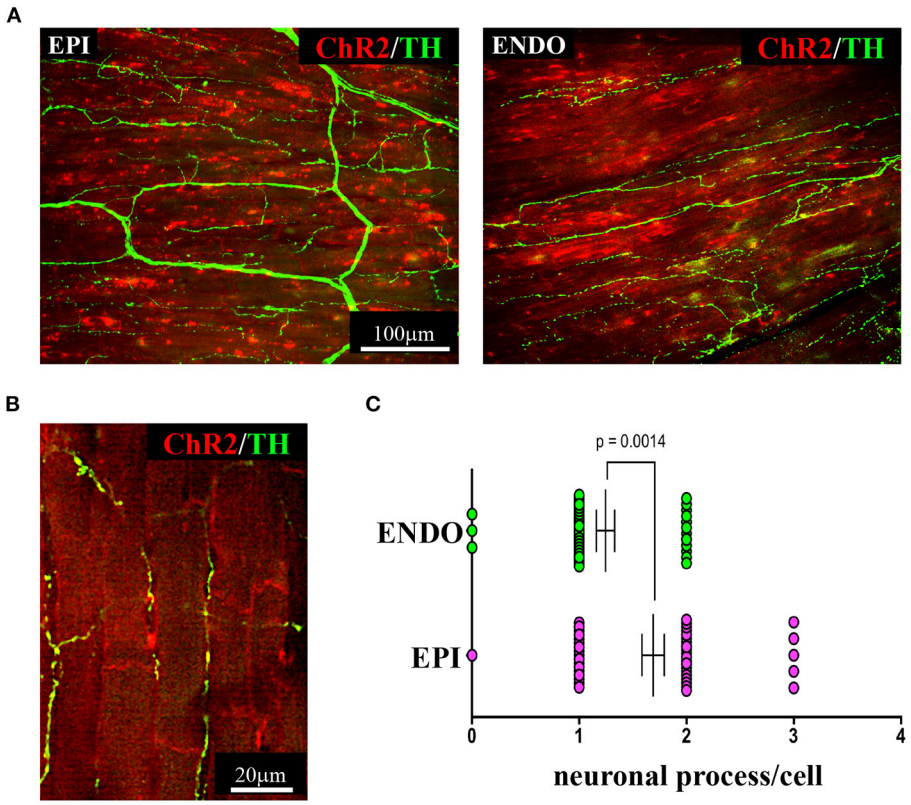

FIGURE 5 | Three-dimensional imaging of the neuronal network in the murine myocardium. **(A)** Maximum intensity projection of multiphoton image stacks acquired along 400 μm in tissue clarified LV blocks from the EPI and ENDO regions of a α-MHC/ChR2-*td-Tomato* mouse heart, stained with an antibody to TH. Red emission of *td-Tomato* was used to identify CM membrane. **(B)** Representative single optical section of a sample processed as in **(A)**, resolving the neuro-cardiac interactions, and used for quantification of neuronal processes/cell in EPI and ENDO regions **(C)**. **(A–C)** Modified with permission from Pianca et al. (2019).

2003; Zaglia et al., 2012; Kreipke and Birren, 2015; Pianca et al., 2019). Taken altogether the results described above support the concept whereby the ANS controls cardiac function across a wide effect range covering both the subtle physiological variation in inter-beat interval (known as heart rate variability, HRV) and constitutive control of CM trophism, in basal conditions, to the urgent chronotropic and inotropic responses of the "fight-or-flight" reaction (Zaglia and Mongillo, 2017). In view of this evidence, one naturally wonders what mechanisms allow such flexible, yet accurate, control of heart homeostasis, and the unique potential of optogenetics was thus exploited to delve into neuroeffector mechanisms underlying cardiac SN function. With this scope, the Kay group generated in 2015, transgenic mice expressing ChR2 under control of the SN promoter, TH, which were used, in a proof-of-principle study, to optogenetically activate SNs and address the dynamics of the events linking β-AR activation to changes in cardiac function, in isolated Langendorff perfused hearts. In support of the method feasibility, photo-stimulation of cardiac neurons on the epicardial surface of isolated hearts caused positive chronotropic and inotropic responses, accompanied to reduced AP duration, and fast pacing elicited sustained arrhythmias, thus demonstrating the usefulness of the technique to address the effects of SNs in cardiac physiologic and pathologic mechanisms (Wengrowski et al., 2015). The neural influence on HR was also studied using optogenetics in *Drosophila melanogaster*, which, although phylogenetically far from mammals, represents an experimental model suited for genetic manipulation and allows easy molecular investigation of signaling mechanisms in both heart physiology and pathology (Malloy et al., 2017). Optogenetic actuation was, additionally, exploited in *in vitro* studies, both in primary and human Pluripotent Stem Cells (hPSC)-derived SNs, establishing "physical and functional connections and controlling the beating rate of cultured CMs" which, in turn, impacted on neuronal maturation, thus supporting that bi-directional crosstalk takes place between SNs and CMs (Oh et al., 2016). The retrograde transfer of molecules from heart to cardiac autonomic neurons was exploited for organ-targeted expression of opsins, by heart injection of adeno-associated virus, which allowed vagal neuromodulation of HR (Fontaine et al., 2021).

Altogether, these studies support the potential of optogenetics in the study of fundamental questions in neuro-cardiology, including the signaling dynamics underlying neuro-cardiac communication.

Although the rapid and efficient control of heart contraction, operated by SNs, exemplifies neurogenic regulation of organ

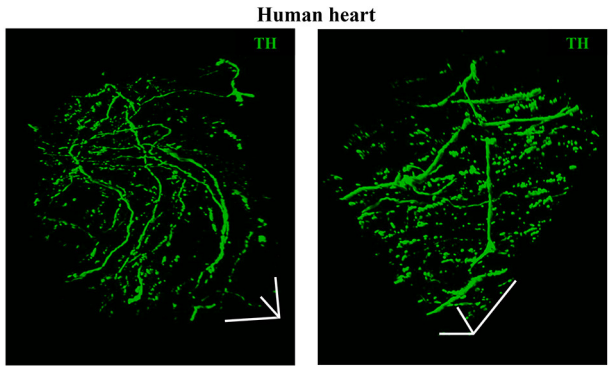

FIGURE 6 | Three-dimensional imaging of the neuronal network in the human myocardium. Topology of the SN network, reconstructed with 3-D rendering of 600 images acquired with a multiphoton microscope along 200 μm, upon whole-mount immunofluorescence in 1 mm^3 LV blocks from the EPI region, stained with anti-TH antibody. Images were acquired with an 18× objective, 1.1 NA, allowing a large field of view (850 × 850 μm) at high resolution. A segment of (850 × 850 × 200) μm was imaged. mage series were acquired along the Z-axis, with a step size of 1.5 μm and processed and analyzed with a software for 3-D rendering (Imaris). Images modified with permission from Pianca et al. (2019).

function, the preferred view on sympatho-cardiac coupling in mainstream physiology aligns it more to a neuro-endocrine process than to a mechanism underlain by direct intercellular signaling. Activated SN processes, flanking CMs with no structured contacts, would simply discharge NA in the myocardial interstitium, at a concentration sufficient to activate β-ARs (Mann et al., 2014). However, such "reductionist" model does not explain convincingly the very fast (i.e., immediate) kinetics of heart response to SN activation, its efficiency and repeatability. With the aim to resolve these discrepancies, we used a combination of static (i.e., confocal immunofluorescence, electron microscopy) and dynamic (i.e., neuronal optogenetics combined to live imaging of cAMP or pharmacologic assays) optical methods to comprehensively address the neuro-cardiac interaction *in vitro* and *in vivo*. Co-cultures of SNs and CMs showed that neuronal varicosities establish structured intercellular contacts with CM membrane which define a diffusion-restricted, small volume intercellular signaling domain, allowing few molecules of NA to activate target cells at high concentration. These results indicated that direct synaptic communication occurred between SNs and CMs. To test whether this concept held true in the intact innervated heart, we reckoned optogenetics was the election method, and exploited the same set up, previously developed for cardiac optogenetics (Zaglia et al., 2015), to photo-stimulate the sympathetic efferents innervating the right atrium (RA), in living TH/ChR2-*td-Tomato* transgenic mice, while monitoring HR (**Figures 7A,B**). By combining photoactivation of sub-millimetric regions of the RA surface with pharmacologic inhibition assays using β-blockers, we demonstrated that SNs communicate with target CMs at directly interacting neurocardiac junctional sites, with fast kinetics and high [NA], favoring a "synaptic" rather than endocrine coupling model (Prando et al., 2018) (**Figures 7C–E**). Following a similar approach, Burton and colleagues applied optogenetics to interrogate the effects of SNs on "macroscopic" dynamics of a CM network *in vitro*, with the aim to identify arrhythmia mechanism in a cell-based system (Burton et al., 2020). In line with the results described in Prando et al., and those corroborated by the same group in 2019 (Pianca et al., 2019), this research promoted the concept that innervated CMs "can potentially receive NA simultaneously from multiple point sources, and integrate downstream the cumulative neuronal input at signaling level," which support our speculation that direct neurocardiac coupling may explain how heart responses "can be graded across the wide physiological range of action of the cardiac SNS" (Zaglia and Mongillo, 2017) (**Figure 8**).

By taking advantage from the cell-type specificity of optogenetics, Kay's group progressed with the cognate of their previous work on SNs (Wengrowski et al., 2015), by targeting ChR2 to cholinergic neurons, and showed that PSN photoactivation, by inducing acetylcholine release, resulted in very rapid HR decrease (Moreno et al., 2019). In the same year, Rajendran et al. combined optogenetics to tissue clearing and physiological measurements, achieving higher anatomical details of vagal afferent and efferent fibers innervating the heart, thus further confirming the high complexity of heart neuronal circuitry, and advanced the understanding of the mechanisms involved in neurogenic control of HR (Rajendran et al., 2019).

Overall, these studies undoubtedly indicate that optogenetics is a tool suited "to provide new scientific insights into the structure and function of peripheral neural circuits" although "to disentangle neural control of autonomic physiology and enable a new era of targeted neuromodulation approaches" a combination of functional, imaging and physiologic approaches needs to be employed (Rajendran et al., 2019).

Optogenetic Interruption of The Cardiac Arrhythmic Chaos

In normal hearts, the origin, sequence, and timing of cardiac activation repeat with identical characteristics at every heartbeat. The term arrhythmia, which means "out of rhythm," indicates the alteration of any of the physiologic features of heart activation, including both faster and slower HRs, the abnormal origin of the cardiac activation wave, its faulty propagation throughout the different heart regions or, in its extreme manifestation, the erratic depolarization of heart cells. Due to the dramatic consequences which arrhythmias may have (i.e., SCD), the heart possesses a series of protective mechanisms to avoid uncontrolled cardiac activation, which include both cellular factors (i.e., refractoriness) and tissue properties, including the functional anatomy of the conduction system, and the electrotonic coupling of the CM network, which protects from initiation of cardiac contraction following stochastic activation of few cells (Hoyt et al., 1989; Rohr et al., 1997; Xie et al., 2010; Myles et al., 2012; Zaglia et al., 2015). As arrhythmias may develop when such protective properties are overcome, deeper understanding of these mechanisms is necessary to identify the cause and possible treatment of specific rhythm disturbances. In this context, the cell specificity, the

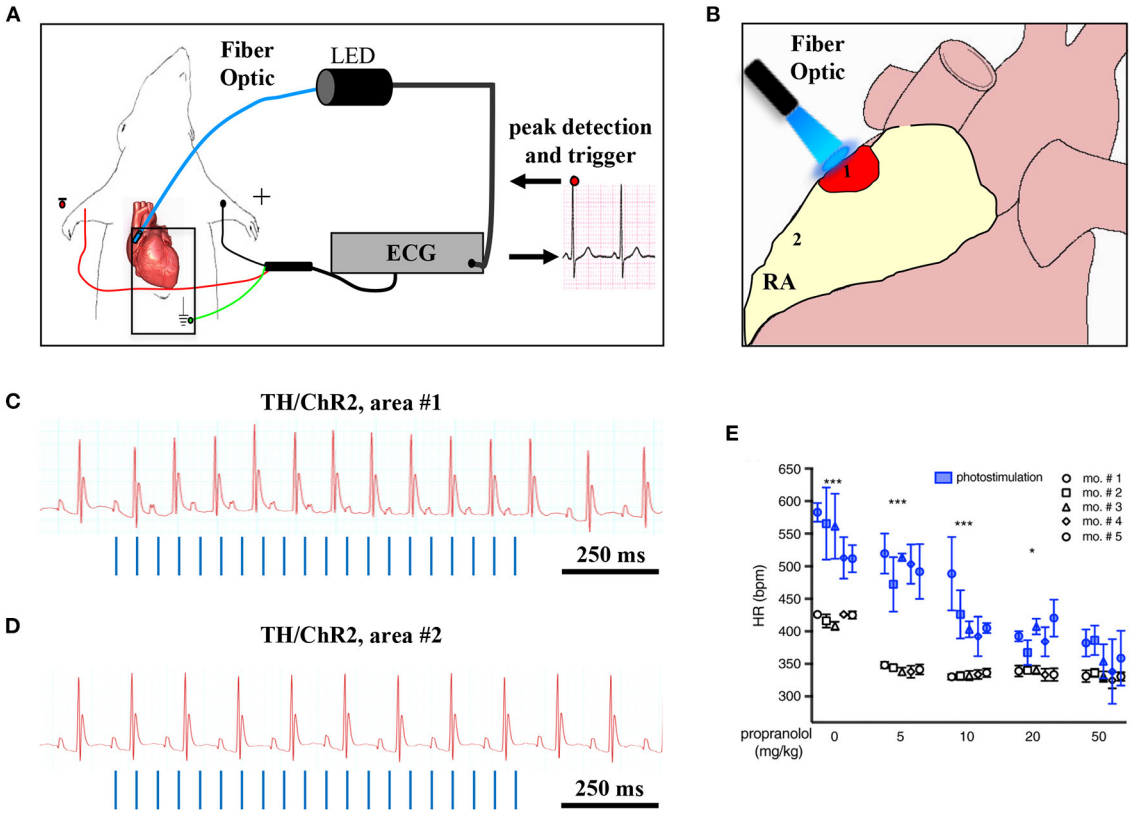

FIGURE 7 | Optogenetic assessment of neuro-cardiac coupling *in vivo*. **(A)** Schematic illustration of the neuronal optogenetic set up used for right atrium (RA) illumination in open chest anesthetized mice. **(B)** Representation of the different photostimulated atrial regions (areas#1–2). **(C)** Representative ECG trace of the optogenetic experiment, showing positive chronotropic response upon photoactivation (blue lines) of the RA area#1 in TH/ChR2 mice. **(D)** Representative ECG trace showing unchanged HR upon illumination of RA area#2. **(E)** Dose-effect analysis of the treatment with the β-AR antagonist, propranolol, on the chronotropic response to neuronal photostimulation. Blue symbols identify responses to photostimulation, while the white ones show the effects of systemically delivered NA (***$P < 0.001$; *$P < 0.05$). Images modified with permission from Prando et al. (2018).

elevated spatial and temporal precision of optogenetics have been exploited to determine the respective role of aberrant activation of either PFs or common CMs in the generation of ectopic cardiac activation foci and subsequent initiation of sustained arrhythmias (Zaglia et al., 2015). In addition, based on the advantages which optogenetics may offer, compared to conventional defibrillation (for a review see Entcheva and Kay, 2021), this technology allowed to successfully achieve cardioversion of atrial fibrillation in living mice (Bruegmann et al., 2018) and optogenetic cardioversion or defibrillation have been described, up to now, in a number of studies (Bruegmann et al., 2016; Scardigli et al., 2018; Uribe et al., 2018; Cheng et al., 2020; to name a few).

It is well-appreciated that the activity of SNs may increase arrhythmic vulnerability both through direct effects on single cell physiology and by reducing the "protective" myocardial properties at tissue level. In stress-dependent arrhythmogenic syndromes (e.g., CPVT, ACM), the link between SN activation and arrhythmia triggering has been shown both in single cells and experimental animals (Cerrone et al., 2005; Lehnart et al., 2008), and extensively supported by clinical evidence (Corrado et al., 1990, 2015; Amar et al., 2003; Collura et al., 2009; Shen and Zipes, 2014). In addition to the cellular effects of adrenergic stimulation, the concept that unbalanced NA discharge, by cardiac SNs, has arrhythmogenic potential has been suggested a few decades ago, and demonstrated since then in both structurally normal hearts of arrhythmic patients and ischemic hearts (Fukuda et al., 2015; Zipes, 2015; Gardner et al., 2016). The mechanism whereby regional heterogeneity of sympathetic inputs causes arrhythmia is indeed associated with AP dispersion, an electrophysiological state favoring ventricular arrhythmias. In support that regional differences in cardiac adrenergic stimulation promote arrhythmias, local injection of NA, in isolated perfused hearts, caused the onset of ectopic beats, which were not elicited by global perfusion with the same concentration of the catecholamine (Myles et al., 2012). It is foreseeable that optogenetics, allowing to deliver, with flashes of differently colored lights, the "go" (neuronal depolarization) or "stop" (neuronal hyperpolarization) signs to selected neuronal populations, appears ideally tailored to experimentally address the mechanisms correlating arrhythmias with SN function. The strong link between autonomic neuron input and cardiac

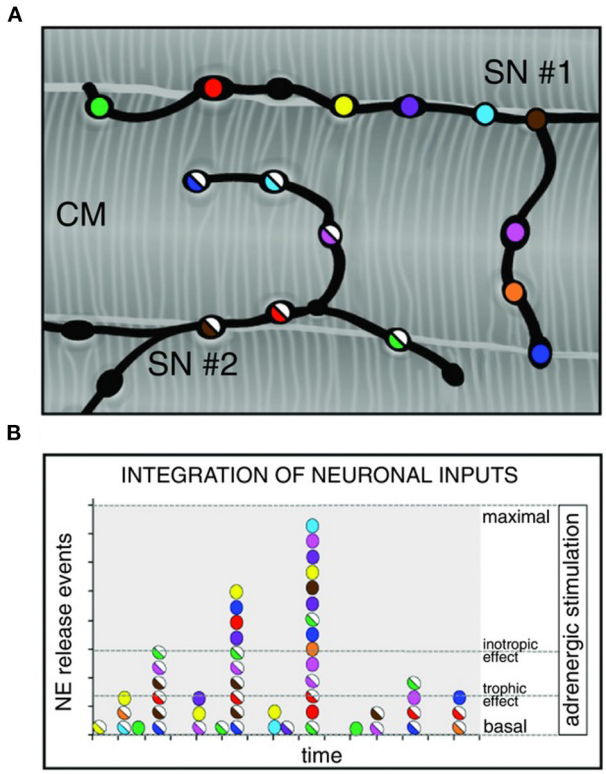

FIGURE 8 | Integration of multiple neuronal inputs by the innervated cardiomyocyte. **(A)** Recent advancements in imaging cardiac sympathetic innervation demonstrate that each CM interacts with multiple contacts from the same neuronal process (each varicosity is highlighted by one color) and may simultaneously be innervated by different neurons (two neurons in the picture are represented by filled or half-filled circles, respectively). **(B)** We thus made the hypothesis that activation of increasing number of varicosities, and recruitment of more neuronal processes, may allow grading of the responses of target cells from basal to maximal activation, across a wide range of intermediate effects. Modified with permission from Zaglia and Mongillo (2017).

arrhythmias, and the success of heart sympathetic denervation in reducing ventricular arrhythmias in sufferers from familial stress-dependent arrhythmogenic syndromes, have already fueled trust in the potential of autonomic neuromodulation of interrupting the electrical chaos of fibrillating arrhythmias, preserving the consonance of regular heart activation. This concept has been tested in the study by Yu and colleagues, showing that reversible optogenetic inhibition of the left stellate ganglion (LSG) activity increased electrophysiological stability and protected against post-ischemic ventricular arrhythmias. The authors expressed, by AAV9 infection, the photoactivated hyperpolarizing protein ArchT in the LSG of dogs and induced myocardial ischemia with left descending coronary artery ligation. Notably, photoinhibition of the transduced neurons significantly reduced the incidence of post-ischemic ventricular tachycardia (VT) and ventricular fibrillation (VF), providing "*proof-of-concept results of optogenetic arrhythmia therapy in a large-animal model*" (Yu et al., 2017; Entcheva and Kay, 2021) (**Figure 9**). The results of this study are in line with those obtained in 2012 by Mastitskaya et al. who demonstrated that photoactivation of vagal preganglionic neurons exerted protective anti-arrhythmic effect in a rat model of myocardial ischemia/reperfusion injury (Mastitskaya et al., 2012). Thus, the distinctive properties of optogenetics, and the flexibility of opsin expression in either selective intrinsic heart cells (i.e., CMs, PFs) or extrinsic modulators (i.e., SNs, PSNs) have opened the road to better understanding and novel treatment of arrhythmia mechanisms. Excitement and curiosity are in the air while expecting to see, as in the words of the poet Apollinaire, the *voice of light* tune cardiac rhythm.

CAN OPTOGENETICS UNCOIL THE INTERTWINED BRAIN-TO-HEART CONNECTIONS?

The functional connection between the brain and the heart has been surmised several centuries ago, based on the appreciation that intense emotions and/or stresses reflected on the perceivable increase of HR and contraction force, frequently occurring in physiologic contexts, but could, at times, cause sudden heart arrest and death (Coote, 2007; Samuels, 2007). The neurogenic modulation of heart function, enacted by heart-innervating autonomic neurons, is in fact the integrated end-effect of numerous higher-order neuronal circuits which, from cortical, subcortical, and brainstem sites, converge on and regulate the activity of "motor" post-ganglionic autonomic neurons. Such hierarchical and multiplexed neuronal network allows the simultaneously active inputs of the somato-sensory system, sense organs, brain areas processing emotions, memory, and fear, to be marshaled into the system and reflect, with varied intensity and dynamics, on the degree of regulation of heart function.

The anatomical basis of the "brain-to-heart" communication are, accordingly, grounded on complex neuronal circuitries, which lay the physical connection between the two organs (**Figure 10**). In its schematized representation, this neuronal network includes cortical and subcortical forebrain structures (i.e., cortex, insula, amygdala, and hippocampus, and their interconnecting systems), as well as the hypothalamus, the gray matter around the cerebral aqueduct (i.e., periaqueductal gray), and the nuclei of the parabrachial complex at the junction between the pons and brainstem (Augustine, 1996; Verberne and Owens, 1998). To further increase the complexity of this scenario, the central portion of the amygdala "receives inhibitory projections from the prefrontal and orbitofrontal area and is connected with the hypothalamus and the brain stem nuclei involved in control of the cardiac function and, thereby, seems to modulate the effects of emotional stimuli (especially negative emotions) on the heart" (see Tahsili-Fahadan and Geocadin, 2017 for a compendium). Furthermore, the hypothalamus is a transit point of information from the brain cortex and, in preclinical models, "the cardiac effects of stimulation of the lateral and anterior hypothalamus are preventable by sympathectomy and vagotomy, respectively" (see Tahsili-Fahadan and Geocadin, 2017 for a compendium). Although the detailed anatomy and function of each of these brain regions, and the modalities whereby they

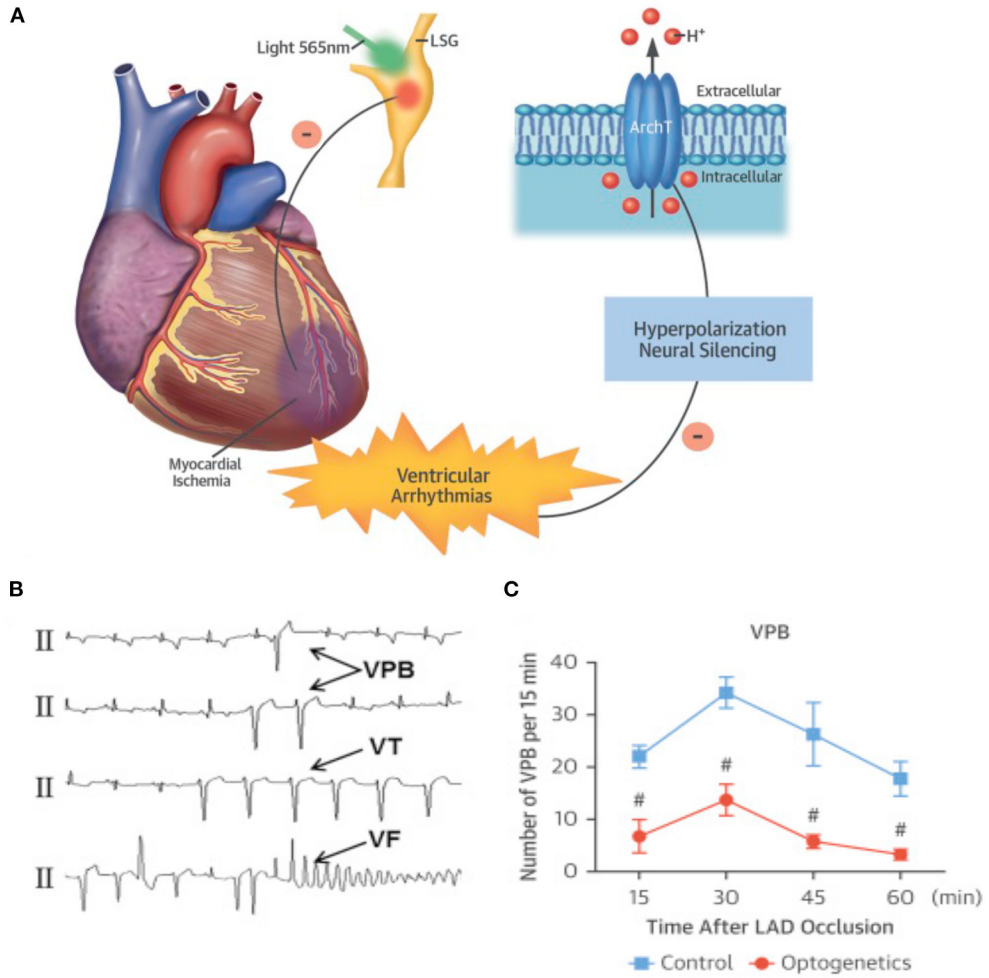

FIGURE 9 | Optogenetic-based interruption of cardiac arrhythmias. **(A)** Schematic representation of the potential role of neuronal optogenetics in stopping ventricular arrhythmias. Photostimulation of ArchT with 565 nm light inhibits SNs, leading to significant decrease in arrhythmic events after myocardial ischemia. **(B)** Representative examples of ischemia-induced ventricular arrhythmias (Vas). **(C)** Quantitative analysis of the incidence of ischemia-induced VAs showed that optogenetic modulation significantly decreased the number of ventricular premature beats (VPBs). **(A–C)** Modified with permission from Yu et al. (2017) .

are connected to the gray matter of the spinal cord, where cell bodies of sympathetic ganglia neurons reside, is beyond the scopes of this review, this outlook serves to show the complexity of the extended brain–heart axis.

Understanding of the effects of brain areas described above on the heart, has mostly been obtained in animal models, and has conventionally used either electrophysiologic stimulation as trigger, and assessment of cardiac function as readout, or the destructive approach based on the analysis of functional effects of removal/lesion of specific brain regions. As an example, stimulation of the caudal and rostral posterior insular cortex in rats has been shown to decrease or increase HR, respectively, the latter effect elicited by activation of sympathetic outflow, as shown by its ablation with the β-blocker, atenolol (Oppenheimer and Cechetto, 1990). Combination of electrophysiological studies with surgical procedures (i.e., occlusion of cerebral arteries) has been employed to increase the depth of investigation. As example, monolateral occlusion of cerebral arteries supplying the insular cortex, in rats, prompted the "laterality hypothesis" whereby the right and left insula mediate increased sympathetic and parasympathetic tone, respectively, a phenomenon attributed to "the lateralized distribution of the baroreceptor units and processing of the emotions" (Oppenheimer et al., 1992; Zhang et al., 1998; Hilz et al., 2001) (see Tahsili-Fahadan and Geocadin, 2017 for a compendium).

Although these studies have undoubtedly advanced the understanding of neuro-cardiac anatomy and physiology, further progress requires higher precision and better definition of the function of cardiac wiring. Optogenetics is suited to be the "Rosetta Stone" enabling to decode the "brain–heart" talk, by systematically interrogating the effect of the different neuronal circuits impinging on heart function, in the living organism. Although such studies are still relatively scarce, we here present some relevant examples. Paul

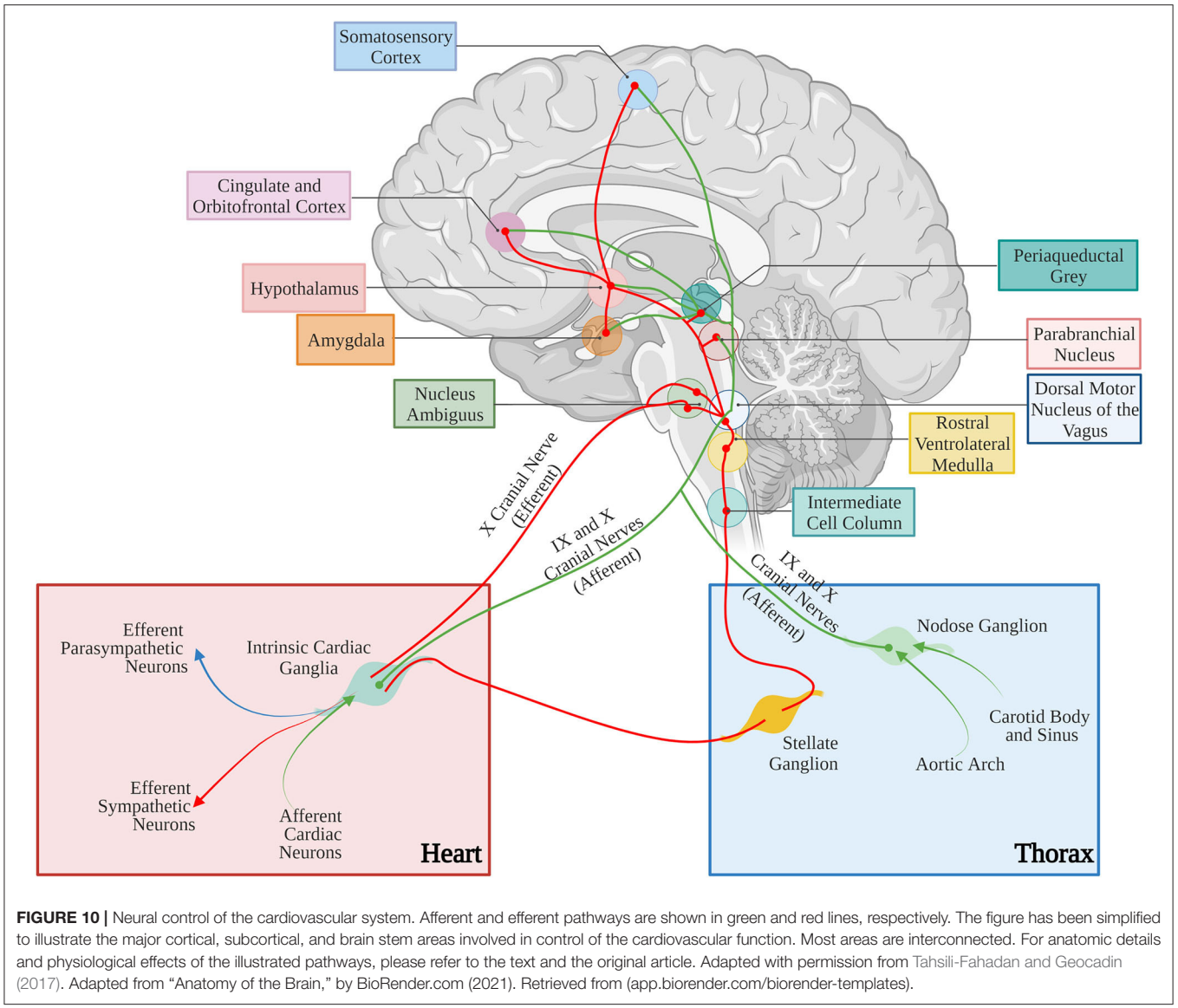

FIGURE 10 | Neural control of the cardiovascular system. Afferent and efferent pathways are shown in green and red lines, respectively. The figure has been simplified to illustrate the major cortical, subcortical, and brain stem areas involved in control of the cardiovascular function. Most areas are interconnected. For anatomic details and physiological effects of the illustrated pathways, please refer to the text and the original article. Adapted with permission from Tahsili-Fahadan and Geocadin (2017). Adapted from "Anatomy of the Brain," by BioRender.com (2021). Retrieved from (app.biorender.com/biorender-templates).

and colleagues, by combining multielectrode recording with optogenetic manipulations, showed that vasoactive intestinal polypeptide (VIP)-releasing neurons elicit diurnal waves of GABAergic input to cells of the paraventricular hypothalamus and ventral thalamus, while suppressing their activity during the mid to late hours of the day. Such circuit is involved in the circadian modulation of several physiologic functions, including HR (Paul et al., 2020). In addition, optogenetics elucidated how coordination between respiratory and cardiovascular functions is achieved. The combination of excitatory and inhibitory optogenetics with experiments of neuronal tracing, in rats, demonstrated that "preBötzinger Complex" (preBötC) neurons modulate cardiac PSN activity whilst excitatory preBötC neurons modulate sympathetic vasomotor neuron activity, resulting in HR and blood pressure oscillations in phase with respiration (Menuet et al., 2020). A similar approach, in rodents, was able to discern the mechanisms involved in arousal, wake-sleep cycle, and their impact on cardiovascular and respiratory control (Guyenet, 2006; Guyenet and Abbott, 2013; Smith et al., 2013; Dampney, 2016; Luppi et al., 2017; Saper and Fuller, 2017; Scammell et al., 2017; Del Negro et al., 2018; Benarroch, 2019).

In parallel to studies aimed to untangle central neuronal circuitries impacting on heart activity in physiology, optogenetics was also applied to complex neuro-cardiac pathologies, including e.g., the study of the bidirectional link between psychiatric disorders and heart diseases (Cheng et al., 2012).

Thus, the message emerging from this frugal overview of some examples on the theme, is that optogenetics may be a valuable tool to uncover the mysterious and multifaced "brain-to-heart" relationship. However, because of the incredible anatomical and functional complexity of the neuronal circuitries, which tie reason to feeling, optogenetics needs to be assisted in the task by other methodologies, including neuronal imaging, tissue clarification, behavioral, and functional studies.

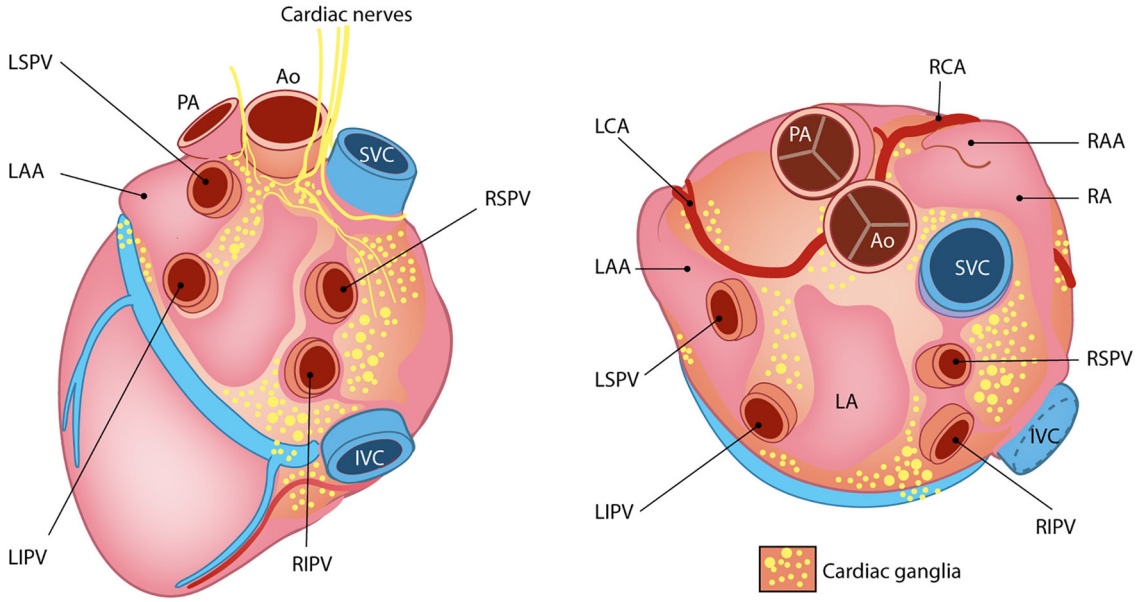

FIGURE 11 | The little heart brain. Schematic representation of cardiac intrinsic ganglia. Ao, aorta; PA, pulmonary artery; LAA, left atrial appendage; LCA, left coronary artery; LIPV, left inferior pulmonary vein; LSPV, left superior pulmonary vein; RAA, right atrial appendage; RCA, right coronary artery; RIPV, right inferior pulmonary vein; RSPV, right superior pulmonary vein. Modified with permission from Wink et al. (2020).

MAY OPTOGENETICS SHED LIGHT ON THE UNEXPECTED "HEART-TO-BRAIN" CORRESPONDENCE?

The long consolidated understanding on the basic principles of heart physiology has somewhat concealed, or obscured, the increasing number of studies showing the extent of its nervous component.

The heart homes indeed a large series of different neuron types orderly networked in subsystems and circuits, receiving (as described above), integrating and sending neuronal impulses from and to the brain, justifying the proposed concept of "the little brain" of the heart (Armour, 2007, 2008). In addition to the efferent fibers of the two main branches of the ANS, the myocardium is densely innervated by sensory neurons, and the two systems are peripherally regulated by the interacting neurons residing in the INS. Cardiac sensory afferent neurons project to the CNS, transferring information of the chemo-, pain, and mechano-sensors which monitor the biochemical and mechanical state of the heart, mainly *via* release of substance P and calcitonin gene-related peptide (Hoover et al., 2008). The cell bodies of sensory neurons are found in spinal dorsal root ganglia, extracardiac intrathoracic, and intrinsic cardiac ganglia (Tahsili-Fahadan and Geocadin, 2017), and their ascending fibers take part to the IX and X cranial nerve and interact with the autonomic nuclei of brainstem, hypothalamus, amygdala, thalamus, and cerebral cortex (Tahsili-Fahadan and Geocadin, 2017) (**Figure 10**).

The cardiac INS consists of a network of interconnected neuronal plexi which are located within specific heart regions, mainly the epicardial fat pads, and innervate the SAN (by the right atrial ganglionated plexi) and AVN (by the inferior vena cava–inferior atrial ganglionated plexi), as well as the pulmonary vein–left atrial junction (Armour et al., 1997; Tan et al., 2006; Tahsili-Fahadan and Geocadin, 2017) (**Figure 11**). Most cardiac intrinsic neurons are interneurons, mediating transmission of information within the resident ganglia. Such neuronal population is functionally connected to the efferent fibers of autonomic neurons in a two-way communication, which leads to a mutual influence on the nervous activity (Beaumont et al., 2013). Such complexity of cardiac neuronal circuitries and the notion that the heart sends collectively more signals to the brain than it receives, supports the recent findings attributing to the heart the capacity to perceive pain, independently from specialized brain centers (e.g., the thalamus), and may explain the involvement of the heart in regulation of central neurons of those regions (Alshami, 2019).

Interestingly, like the autonomic extrinsic efferents, remodeling of the cardiac afferents, and the INS may also occur in cardiac diseases, and have an impact on central neuronal circuitries (Armour, 2004). That a primary heart dysfunction negatively impacts on the correct function of higher neuronal centers is now supported by a large number of researches. As an example, it is a well-accepted notion that patients suffering from HF have increased incidence of stroke (mainly attributed to reduction in brain perfusion caused by cardiac contractile dysfunction), but also show cognitive decline, anxiety (Scherbakov and Doehner, 2018) and depression (Moradi et al., 2021). These may in turn, reflect on the activity of cardiac autonomic efferents, in a vicious cycle whereby

cardiac pathology alters "heart-to-brain" communication, affecting "brain-to-heart" response, further compromising heart structure and function. In support of this concept, Koba and colleagues, have recently used optogenetics to show that sympatho-excitatory input from hypothalamic neurons, which project to the rostral ventrolateral medulla (RVLM), is enhanced after myocardial infarction (Koba et al., 2020). In addition, photostimulation of ChR2-expressing astrocytes in the RVLM of rats increased HR, through ATP-dependent enhancement of sympathetic activity. Notably, "facilitated breakdown of ATP in the RVLM attenuates the progression of LV remodeling and HF secondary to myocardial infarction" (Marina et al., 2013). The studies described above are based on the identification of central circuitries which, by receiving erroneous information from damaged myocardium, give wrong orders to the heart, thus further worsening its dysfunction. On the contrary, the use of neuronal optogenetics to decode the communication among the different cardiac neuronal circuitries and define their effects on heart function and homeostasis, although fascinating, has never been tested thus far, likely because of several technical limitations, discussed below in **Chapter 6**. Similarly, the use of cardiac optogenetics to dissect the mechanisms linking changes in myocardial contractile activity to alteration in CNS, which holds a high translational potential, has not been attempted. These represent rather unexplored territories to take a look at with neurocardiac optogenetics.

OPTOGENETICS IN NEURO-CARDIOLOGY: ONLY A DELUSION?

The studies described so far support that optogenetics is a very promising technique potentially very useful for decoding nerve circuits which bind, in a mutual dependence, the brain and the heart. However, peripheral neuron optogenetics (including that applied to neuro-cardiology) has a number of specific limitations with respect to its more common application in the field of neuroscience. Firstly, the popularity of the method in the study of central neuronal circuits has prompted the parallel development of technical means to deliver light (e.g., through lightweight fiber optics stably implanted in the skull), while similar devices usable for peripheral neuronal optogenetics are still in the early phase. This allowed to perform experiments in freely moving mice, often with immediate and easily quantifiable readouts (i.e., movement, behavior). On the contrary, interrogation of cardiac autonomic neurons has been performed, due to obvious anatomical constraints, in mice under anesthesia, which is well-known to interfere with neuronal activity (Yu et al., 2017; Prando et al., 2018; Moreno et al., 2019; Rajendran et al., 2019; to cite a few). In addition, when conscious animals are experimented, peripheral nerves in soft, moving tissues are easily injured during fiber-optic implantation, which may cause persistent irritation at the biotic/abiotic interface and constraint natural movements, thereby affecting or preventing free motions and increasing e.g., stress and anxiety (Zhang et al., 2019). This is particularly important when addressing the study of intra-organ (SN-CM) and inter-organ (brain–heart) neuronal communication. The scenario is further complicated by the technical difficulty of simultaneously operating optogenetic neuronal actuation, while monitoring cardiac readouts (e.g., ECG), in freely moving animals.

With these considerations in mind, understanding in full whether the potential of neuro-cardiac optogenetics is confined to science glamor, or if it is a guiding light in understanding neuro-cardiac pathophysiology, some additional steps should be overcome. Firstly, as the time of proofs-of-principle is now surpassed, optogenetics should be used when it represents the adequate solution to a scientific problem, and the research question is not based on the technique itself. Secondly, a broader consideration concerns how neurocardiac optogenetics can be translated to human research and therapy, which is inherently limited by the method specifics.

When the road to optogenetics for a specific application has been undertaken, questions which guide the experimental design concern:

- **The choice of the most suited opsin:** from the first use of ChR2 in neuroscience (Boyden et al., 2005) to the time being, a large number of optogenetic actuators are now available, showing varied spectral and biophysical properties, which meet most of the experimental needs (www.optogenetics.org). The choice of the most appropriate opsin variant has to carefully be taken, and possibly confirmed in *in vitro* systems prior to investing in *in vivo* research.
- Due to its structure, **the myocardium is a dense highly diffractive tissue**, and as such, light in the visible spectrum has poor penetration capacity, thereby hindering minimally invasive translation of cardiac optogenetics to externally applied optical stimuli (Boyle et al., 2018). This has represented a crucial limitation for both cardiac and neurocardiac optogenetics, which has, so far, mostly been applied to surgically exposed organs (thus "canceling" the benefits of non-invasiveness). Solutions to overcome this hindrance are in the air, however. It is well-appreciated that near-infrared radiation (NIR) (780–1,100 nm) has deeper penetration capacity in tissues and minimal damaging effects, and as such, it is commonly used in deep tissue imaging (e.g., multiphoton microscopy) in both basic and clinical research, in different tissues (Gussakovsky and Kupriyanov, 2008; Nagarajan and Zhang, 2011; Wang et al., 2013). Although NIR is, at the time being, not suited for cardiac optogenetics, recent promising research has developed "upconversion nanoparticles (UCNPs)," absorbing tissue-penetrating NIR and emitting wavelength-specific visible light. Using this strategy, Chen et al. in 2018 demonstrated that UCNPs can serve as optogenetic actuators of transcranial NIR, and assist the photostimulation of deep brain neurons (Chen et al., 2018) (**Figure 12**). The combination of NIR laser with UCNPs methodology, after being successfully tested in neuroscience (Wang et al., 2017; Chen et al., 2018; Lin et al., 2018), has been applied to cardiac optogenetics, demonstrating the reliable and repeatable tissue-penetrating cardiac optical pacing *in vivo*, which demonstrated a convenient and less invasive way to use

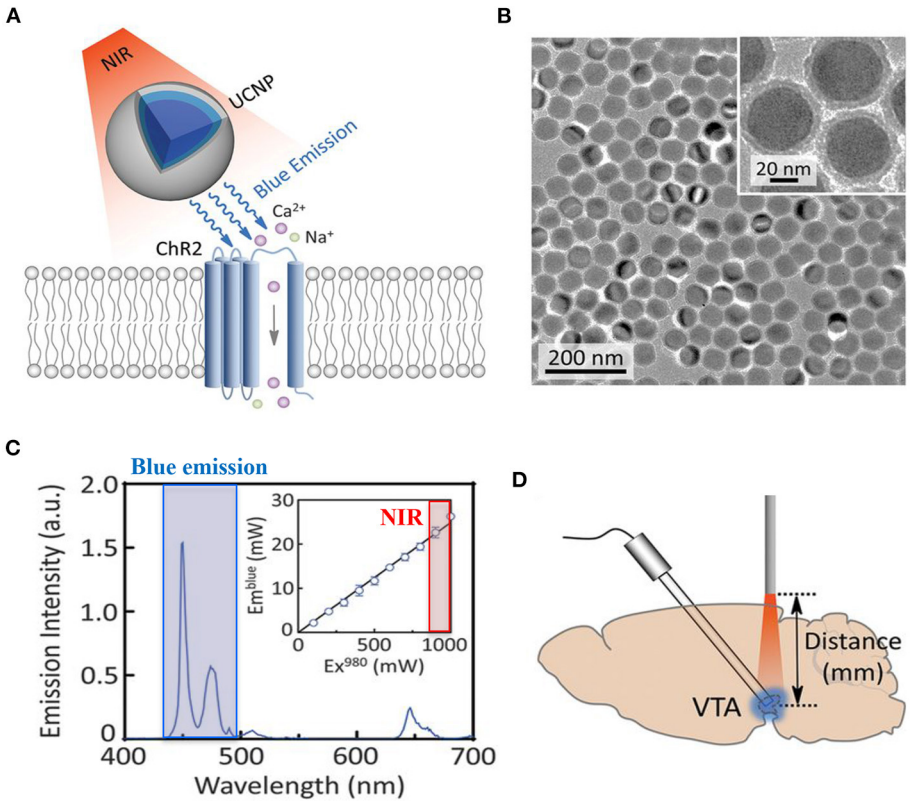

FIGURE 12 | UCNP-mediated NIR upconversion optogenetics for deep brain stimulation. **(A)** Schematic principle of UCNP-mediated NIR upconversion optogenetics. **(B)** Transmission electron microscopy images of the silica-coated UCNPs. **(C)** Emission spectrum of the nanoparticles upon excitation at 980 nm. (Inset) Upconversion emission intensity of UCNPs as a function of excitation intensity at 980 nm. **(D)** Scheme of *in vivo* fiber photometry for measuring UCNP-mediated NIR upconversion in deep brain tissue. The tip of an optic fiber, transmitting NIR excitation light, was positioned at various distances from the ventral tegmental area (VTA) where UCNPs were injected. Modified with permission from Chen et al. (2018).

external radiation in optogenetic stimulation of cardiac tissue (Rao et al., 2020).

- In approaching a preclinical study focused on peripheral nerves, an inevitable task is **how to lightly control peripheral neurons within the tortuous nerve route.** Due to the infeasibility of implanting light delivery interface in peripheral nerves, in 2013 Towne et al. demonstrated the possibility to optically stimulate ChR2-expressing motor neurons, eliciting muscle contraction, in freely moving rats, thanks to the use of an implanted optical nerve-cuff around the sciatic nerve (Towne et al., 2013). From this first study, modern engineering has developed "optocuffs," as optical peripheral nerve interfaces to achieve optogenetic control of peripheral nerves in freely moving mice (Michoud et al., 2018). Similarly, Song et al. invented a novel optical nerve cuff electrode allowing to simultaneously actuate and monitor neural signals, whose efficacy was tested in the sciatic nerve of Thy1:ChR2 mice (Song et al., 2018) (**Figure 13**). Since optogenetics study are often associated to pharmacological tests, recent interesting technological developments include the design of wireless, battery-free, fully implantable devices, capable of programmed delivery of localized optical, and/or pharmacological stimuli, using miniaturized electrochemical micropumps (Zhang et al., 2019). Organic light-emitting diode (OLED) able to adapt to curve surface and soft neuronal tissues have also been generated, which allow register the effect of optogenetics-based neuronal stimulation by magnetic resonance imaging (Kim et al., 2020). Here, we presented only some of the numerous examples of recently developed optical stimulation and recording devices (Samineni et al., 2017; Maimon et al., 2018) for a review see which, at the time being, have been successfully applied for optogenetic manipulation of motor and spinal nerves. Such devices are well-suited to instrument brain–heart connecting nerves and assess the effects of optically modulated neurons in freely moving animals, while recording heart rhythm or blood pressure changes (in telemetry implanted animals), or animal behavior. The development of similar tools apt to photoactivate heart-residing neurons in conscious animals, while monitoring central neuronal functions, would likely represent the tools of choice to investigate the reverse heart-to-brain axis.
- In preclinical studies, another fundamental aspect is **the choice of the most suited animal model.** At the time being the majority of optogenetics studies have been performed in

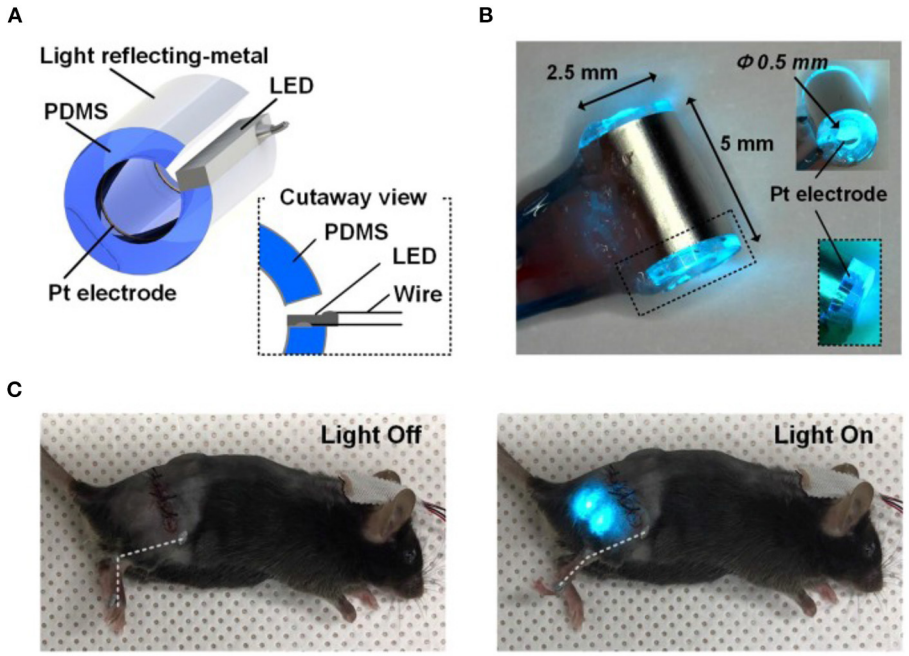

FIGURE 13 | Optical nerve-cuff electrode for optogenetic stimulation of peripheral neurons in freely moving animals. **(A)** Overall schematic illustration of the optical nerve cuff electrode. **(B)** Picture of an active photo-stimulating device. **(C)** Pictures of a mouse implanted with the opto-cuff electrode in **(A,B)**. Examples of light off and light on states are shown. Modified with permission from Song et al. (2018).

mice, due to the availability of transgenic models. However, the use of larger animals (i.e., rats, minipigs, pigs, ovines), in which opsin expression may be achieved by viral infection (Yu et al., 2017; Booth et al., 2021), may increase the feasibility of *in vivo* analyses and the translability of the results to the human context.

Taken altogether, data described above indicates that all the ingredients are available to make of optogenetics a keystone to finally uncover, in depth and un-intrusively, the physiologic mechanisms underlying neurogenic control of heart function, as well as the brain–heart cross-regulation, thus bringing to the light novel targets for therapeutic intervention. Thus, optogenetics, although not directly used as a therapeutic strategy, may be potentiated to discover novel targetable players underlying neuro-cardiac disorders.

A different issue concerns the widely advertised therapeutic potential of optogenetics in neurocardiac diseases in humans. In general terms, the clinical applicability requires resolving two main obstacles: (**a**) optogenetics requires expression of an exogenous gene in neurons; (**b**) photo-actuation requires implantation of a light emitting source. For point (**a**), it has to be kept in mind that viral vectors suited to the use in humans, encoding ChR2, have been approved by FDA (NCT04278131; NCT03326336; NCT02556736; for details see www.clinicaltrials.gov), and their use for neuronal expression may thus be foreseen. As for (**b**), medical bioengineering may easily develop implantable and remotely powered devices similar to the ones already in use (e.g., pacemakers, ICD). For critical reading on the perspective applications of cardiac optogenetics in clinical settings (see Boyle et al., 2015; Entcheva and Kay, 2021).

CONCLUSIONS

This review was conceived and written with the brain and the heart to enhance the concept of brain–heart connection, which, even if supported by a gradually wider literature, is struggling to be an integral part of cardiovascular physiology and research. Here, we present an overview of current literature regarding the heart as a neuro-muscular organ, which not only is responding to hierarchically higher orders, but is capable of interpretation and decision-making, and reply back in the same language. Looking at the heart from this angle, we presented the contribution of optogenetics, treating the heart with light but not lightly, in untangling the "neuronal cardiac circuitries," by unveiling the complexity of heart innervation, defining the mechanisms underlying neurogenic control of the heart in physiology and pathology, and perceiving the brain-to-heart communication. In assessing whether optogenetics is a truly revolutionary tool in cardiology, or only a mirage, we believe that, even if its applicability in the clinic may be limited to some pathologies, in basic research optogenetics can still give a lot, especially in a field as little explored, such as that of neuro-cardiology (**Figure 14**). However, as the constant synergy

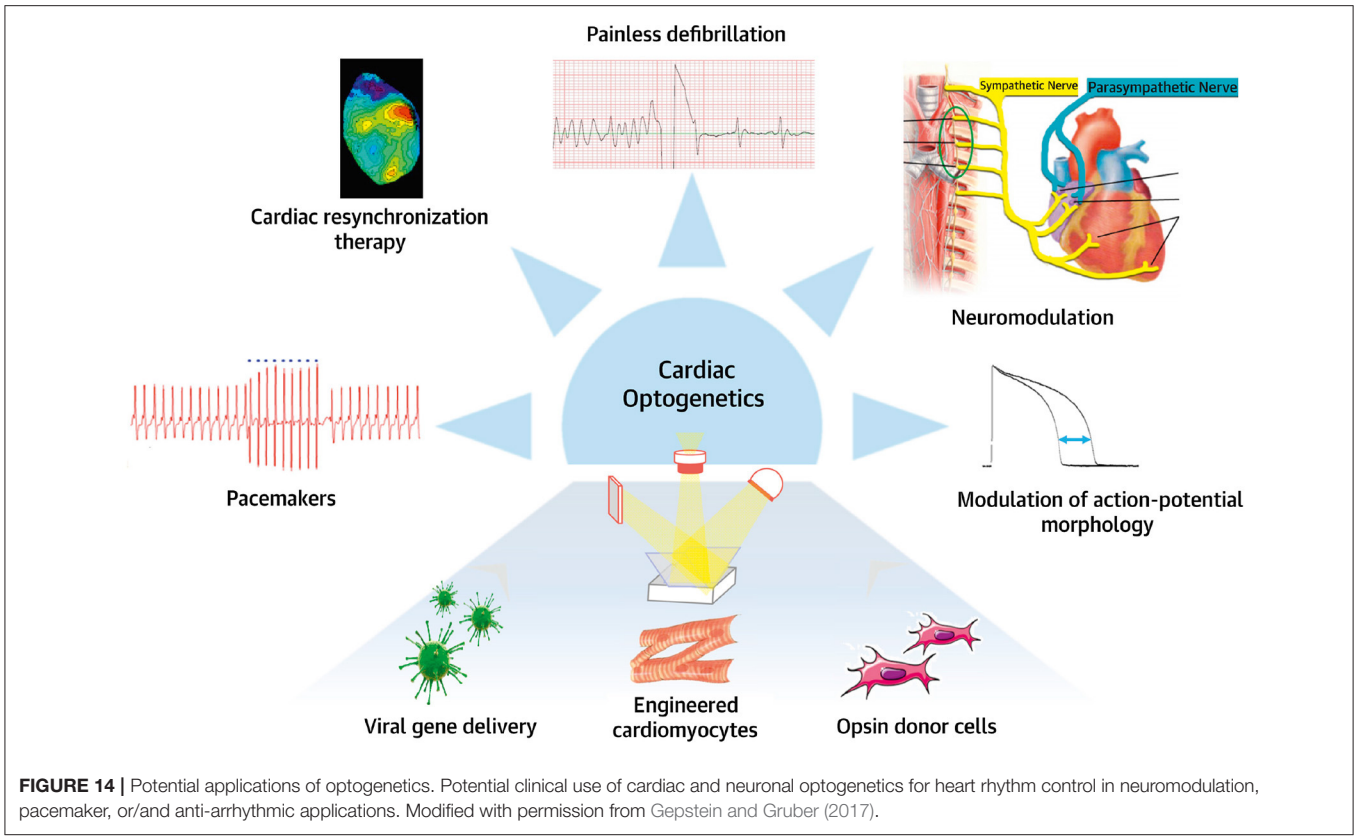

FIGURE 14 | Potential applications of optogenetics. Potential clinical use of cardiac and neuronal optogenetics for heart rhythm control in neuromodulation, pacemaker, or/and anti-arrhythmic applications. Modified with permission from Gepstein and Gruber (2017).

of the dialogue between the brain and the heart teaches us, to illuminate the dark sides of brain–heart connection, as well as of the intrinsic "cardiac little brain," optogenetics must work synergistically with other methodologies, some traditional, others more innovative. Finally, we want to underly that this summary is by no means comprehensive, and we apologize to the many colleagues who contributed to the field, but have not been cited.

AUTHOR CONTRIBUTIONS

AS and NM contributed to manuscript and figure preparation. MM and TZ designed the review layout, drafted, and wrote the manuscript. All authors approved the final version of the manuscript and agree to be accountable for all aspects of the work, in ensuring that questions related to the accuracy or integrity of any part of the work are appropriately investigated and resolved, and that all persons designated as authors qualify for authorship and have been listed.

FUNDING

This work was supported by STARS-miniheartwork (UNIPD) to MM and STARS-SKoOP (UNIPD) to TZ.

ACKNOWLEDGMENTS

We thank the collaborators who have, in time, contributed to set up the described method, especially Drs. Nicola Pianca, Giulia Borile, Valentina Prando, Francesca Da Broi, and Anna Pia Plazzo. We are also grateful to Gilberto Benetton and Corvallis for supporting MM and TZ laboratories, respectively.

REFERENCES

Agrimi, J., Scalco, A., Agafonova, J., Williams, III, L., Pansari, N., et al. (2020). Psychosocial stress hastens disease progression and sudden death in mice with arrhythmogenic cardiomyopathy. *J. Clin. Med.* 9:3804. doi: 10.3390/jcm9123804

Ahmed, M. W., Kadish, A. H., Parker, M. A., and Goldberger, J. J. (1994). Effect of physiologic and pharmacologic adrenergic stimulation on heart rate variability. *J. Am. Coll. Cardiol.* 24, 1082–1090. doi: 10.1016/0735-1097(94)90874-5

Alshami, A. M. (2019). Pain: is it all in the brain or the heart? *Curr. Pain Headache Rep.* 23:88. doi: 10.1007/s11916-019-0827-4

Amar, D., Zhang, H., Miodownik, S., and Kadish, A. H. (2003). Competing autonomic mechanisms precede the onset of postoperative atrial fibrillation. *J. Am. Coll. Cardiol.* 42, 1262–1268. doi: 10.1016/S0735-1097(03)00955-0

Ardell, J. L., and Armour, J. A. (2016). Neurocardiology: structure-Based function. *Compr. Physiol.* 6, 1635–1653. doi: 10.1002/cphy.c150046

Armour, J. A. (2004). Cardiac neuronal hierarchy in health and disease. *Am. J. Physiol. Regul. Integr. Comp. Physiol.* 287:R262–R271. doi: 10.1152/ajpregu.00183.2004

Armour, J. A. (2007). The little brain on the heart. *Cleve. Clin. J. Med.* 74, 48–51. doi: 10.3949/ccjm.74.Suppl_1.S48

Armour, J. A. (2008). Potential clinical relevance of the "little brain" on the mammalian heart. *Exp. Physiol.* 93, 165–176. doi: 10.1113/expphysiol.2007.041178

Armour, J. A., Murphy, D. A., Yuan, B. X., Macdonald, S., and Hopkins, D. A. (1997). Gross and microscopic anatomy of the human intrinsic cardiac nervous system. *Anat. Rec.* 247, 289–298. doi: 10.1002/(SICI)1097-0185(199702)247:2<289::AID-AR15>3.0.CO;2-L

Arrenberg, A. B., Stainier, D. Y. R., Baier, H., and Huisken, J. (2010). Optogenetic control of cardiac function. *Science* 330, 971–974. doi: 10.1126/science.1195929

Augustine, J. R. (1996). Circuitry and functional aspects of the insular lobe in primates including humans. *Brain Res. Rev.* 22, 229–244. doi: 10.1016/S0165-0173(96)00011-2

Basso, C., Corrado, D., Marcus, F. I., Nava, A., and Thiene, G. (2009). Arrhythmogenic right ventricular cardiomyopathy. *Lancet* 373, 1289–1300. doi: 10.1016/S0140-6736(09)60256-7

Beaumont, E., Salavatian, S., Southerland, E. M., Vinet, A., Jacquemet, V., Armour, J. A., et al. (2013). Network interactions within the canine intrinsic cardiac nervous system: implications for reflex control of regional cardiac function. *J. Physiol.* 591, 4515–4533. doi: 10.1113/jphysiol.2013.259382

Benarroch, E. E. (2019). Control of the cardiovascular and respiratory systems during sleep. *Auton. Neurosci. Basic Clin.* 218, 54–63. doi: 10.1016/j.autneu.2019.01.007

Bernal Sierra, Y. A., Rost, B. R., Pofahl, M., Fernandes, A. M., Kopton, R. A., Moser, S., et al. (2018). Potassium channel-based optogenetic silencing. *Nat. Commun.* 9:4611. doi: 10.1038/s41467-018-07038-8

Bers, D. M. (2008). Calcium cycling and signaling in cardiac myocytes. *Annu. Rev. Physiol.* 70, 23–49. doi: 10.1146/annurev.physiol.70.113006.100455

Bi, A., Cui, J., Ma, Y.-P., Olshevskaya, E., Pu, M., Dizhoor, A. M., et al. (2006). Ectopic expression of a microbial-type rhodopsin restores visual responses in mice with photoreceptor degeneration. *Neuron* 50, 23–33. doi: 10.1016/J.NEURON.2006.02.026

Booth, L. C., Yao, S. T., Korsak, A., Farmer, D. G. S., Hood, S. G., McCormick, D., et al. (2021). Selective optogenetic stimulation of efferent fibers in the vagus nerve of a large mammal. *Brain Stimul.* 14, 88–96. doi: 10.1016/j.brs.2020.11.010

Boyden, E. S., Zhang, F., Bamberg, E., Nagel, G., and Deisseroth, K. (2005). Millisecond-timescale, genetically targeted optical control of neural activity. *Nat. Neurosci.* 8, 1263–1268. doi: 10.1038/nn1525

Boyle, P. M., Karathanos, T. V., and Trayanova, N. A. (2015). "Beauty is a light in the heart": the transformative potential of optogenetics for clinical applications in cardiovascular medicine. *Trends Cardiovasc. Med.* 25, 73–81. doi: 10.1016/J.TCM.2014.10.004

Boyle, P. M., Karathanos, T. V., and Trayanova, N. A. (2018). Cardiac optogenetics 2018. *JACC Clin. Electrophysiol.* 4, 155–167. doi: 10.1016/j.jacep.2017.12.006

Braunwald, E., Ross, J., and Sonnenblick, E. H. (1967). Mechanisms of contraction of the normal and failing heart. *N. Engl. J. Med.* 277, 910–920. doi: 10.1056/NEJM196710262771706

Bruegmann, T., Beiert, T., Vogt, C. C., Schrickel, J. W., and Sasse, P. (2018). Optogenetic termination of atrial fibrillation in mice. *Cardiovasc. Res.* 114, 713–723. doi: 10.1093/cvr/cvx250

Bruegmann, T., Boyle, P. M., Vogt, C. C., Karathanos, T. V., Arevalo, H. J., Fleischmann, B. K., et al. (2016). Optogenetic defibrillation terminates ventricular arrhythmia in mouse hearts and human simulations. *J. Clin. Invest.* 126, 3894–3904. doi: 10.1172/JCI88950

Bruegmann, T., Malan, D., Hesse, M., Beiert, T., Fuegemann, C. J., Fleischmann, B. K., et al. (2010). Optogenetic control of heart muscle *in vitro* and *in vivo*. *Nat. Methods* 7, 897–900. doi: 10.1038/nmeth.1512

Bunker, S. J., Colquhoun, D. M., Esler, M. D., Hickie, I. B., Hunt, D., Jelinek, V. M., et al. (2003). "Stress" and coronary heart disease: psychosocial risk factors: national heart foundation of australia position statement update. *Med. J. Aust.* 178, 272–276. doi: 10.5694/j.1326-5377.2003.tb05193.x

Burton, R. A. B., Tomek, J., Ambrosi, C. M., Larsen, H. E., Sharkey, A. R., Capel, R. A., et al. (2020). Optical interrogation of sympathetic neuronal effects on macroscopic cardiomyocyte network dynamics. *iScience* 23:101334. doi: 10.1016/j.isci.2020.101334

Carney, R. M., and Freedland, K. E. (2017). Depression and coronary heart disease. *Nat. Rev. Cardiol.* 14, 145–155. doi: 10.1038/nrcardio.2016.181

Cerrone, M., Colombi, B., Santoro, M., di Barletta, M. R., Scelsi, M., Villani, L., et al. (2005). Bidirectional ventricular tachycardia and fibrillation elicited in a knock-in mouse model carrier of a mutation in the cardiac ryanodine receptor. *Circ. Res.* 96, e77–e82. doi: 10.1161/01.res.0000169067.51055.72

Charles, S. (1956). *Galen - On Anatomical Procedures: Translation of the Surviving Books with Introduction and Notes*. New York, NY: Oxford University Press.

Chen, S., Weitemier, A. Z., Zeng, X., He, L., Wang, X., Tao, Y., et al. (2018). Near-infrared deep brain stimulation via upconversion nanoparticle–mediated optogenetics. *Science* 359, 679–684. doi: 10.1126/science.aaq1144

Cheng, J., Zhang, J., Lu, C., and Wang, L. (2012). Using optogenetics to translate the "inflammatory dialogue" between heart and brain in the context of stress. *Neurosci. Bull.* 28, 435–448. doi: 10.1007/s12264-012-1246-2

Cheng, Y., Li, H., Wang, L., Li, J., Kang, W., Rao, P., et al. (2020). Optogenetic approaches for termination of ventricular tachyarrhythmias after myocardial infarction in rats *in vivo*. *J. Biophotonics* 13:e202000003. doi: 10.1002/jbio.202000003

Chung, K., and Deisseroth, K. (2013). CLARITY for mapping the nervous system. *Nat. Methods* 10, 508–513. doi: 10.1038/nmeth.2481

Chung, K., Wallace, J., Kim, S. Y., Kalyanasundaram, S., Andalman, A. S., Davidson, T. J., et al. (2013). Structural and molecular interrogation of intact biological systems. *Nature* 497, 332–337. doi: 10.1038/nature12107

Chuong, A. S., Miri, M. L., Busskamp, V., Matthews, G. A. C., Acker, L. C., Sørensen, A. T., et al. (2014). Noninvasive optical inhibition with a red-shifted microbial rhodopsin. *Nat. Neurosci.* 17, 1123–1129. doi: 10.1038/nn.3752

Collura, C. A., Johnson, J. N., Moir, C., and Ackerman, M. J. (2009). Left cardiac sympathetic denervation for the treatment of long QT syndrome and catecholaminergic polymorphic ventricular tachycardia using video-assisted thoracic surgery. *Heart Rhythm* 6, 752–759. doi: 10.1016/j.hrthm.2009.03.024

Coote, J. H. (2007). Landmarks in understanding the central nervous control of the cardiovascular system. *Exp. Physiol.* 92, 3–18. doi: 10.1113/expphysiol.2006.035378

Corrado, D., Basso, C., and Judge, D. P. (2017). Arrhythmogenic cardiomyopathy. *Circ. Res.* 121, 785–802. doi: 10.1161/CIRCRESAHA.117.309345

Corrado, D., Thiene, G., Nava, A., Rossi, L., and Pennelli, N. (1990). Sudden death in young competitive athletes: clinicopathologic correlations in 22 cases. *Am. J. Med.* 89, 588–596. doi: 10.1016/0002-9343(90)90176-E

Corrado, D., Wichter, T., Link, M. S., Hauer, R. N. W., Marchlinski, F. E., Anastasakis, A., et al. (2015). Treatment of arrhythmogenic right ventricular cardiomyopathy/dysplasia: an international task force consensus statement. *Circulation* 132, 441–453. doi: 10.1161/CIRCULATIONAHA.115.017944

Cosentino, C., Alberio, L., Gazzarrini, S., Aquila, M., Romano, E., Cermenati, S., et al. (2015). Engineering of a light-gated potassium channel. *Science* 348, 707–710. doi: 10.1126/science.aaa2787

Dal Lin, C., Tona, F., and Osto, E. (2018). "The heart as a psychoneuroendocrine and immunoregulatory organ," in *Advances in Experimental Medicine and Biology* (New York, NY: Springer) 225–239. doi: 10.1007/978-3-319-77932-4_15

Dampney, R. A. L. (2016). Central neural control of the cardiovascular system: current perspectives. *Adv. Physiol. Educ.* 40, 283–296. doi: 10.1152/advan.00027.2016

Del Negro, C. A., Funk, G. D., and Feldman, J. L. (2018). Breathing matters. *Nat. Rev. Neurosci.* 19, 351–367. doi: 10.1038/s41583-018-0003-6

Deng, W., Goldys, E. M., Farnham, M. M. J., and Pilowsky, P. M. (2014). Optogenetics, the intersection between physics and neuroscience: light stimulation of neurons in physiological conditions. *Am. J. Physiol. Regul. Integr. Comp. Physiol.* 307, R1292–R1302. doi: 10.1152/ajpregu.00072.2014

Deubner, J., Coulon, P., and Diester, I. (2019). Optogenetic approaches to study the mammalian brain. *Curr. Opin. Struct. Biol.* 57, 157–163. doi: 10.1016/j.sbi.2019.04.003

Di Bona, A., Vita, V., Costantini, I., and Zaglia, T. (2020). Towards a clearer view of sympathetic innervation of cardiac and skeletal muscles. *Prog. Biophys. Mol. Biol.* 154, 80–93. doi: 10.1016/j.pbiomolbio.2019.07.003

Difrancesco, D. (2010). The role of the funny current in pacemaker activity. *Circ. Res.* 106, 434–446. doi: 10.1161/CIRCRESAHA.109.208041

Entcheva, E., and Kay, M. W. (2021). Cardiac optogenetics: a decade of enlightenment. *Nat. Rev. Cardiol.* 18, 349–367. doi: 10.1038/s41569-020-00478-0

Fadel, P. J. (2008). Arterial baroreflex control of the peripheral vasculature in humans: rest and exercise. *Med. Sci. Sports Exerc.* 40, 2055–2062. doi: 10.1249/MSS.0b013e318180bc80

Fedele, L., and Brand, T. (2020). The intrinsic cardiac nervous system and its role in cardiac pacemaking and conduction. *J. Cardiovasc. Dev. Dis.* 7, 1–33. doi: 10.3390/jcdd7040054

Fontaine, A. K., Futia, G. L., Rajendran, P. S., Littich, S. F., Mizoguchi, N., Shivkumar, K., et al. (2021). Optical vagus nerve modulation of heart and respiration via heart-injected retrograde AAV. *Sci. Rep.* 11:3664. doi: 10.1038/s41598-021-83280-3

Franzoso, M., Zaglia, T., and Mongillo, M. (2016). Putting together the clues of the everlasting neuro-cardiac liaison. *Biochim. Biophys. Acta Mol. Cell Res.* 1863, 1904–1915. doi: 10.1016/j.bbamcr.2016.01.009

Freeman, K., Tao, W., Sun, H., Soonpaa, M. H., and Rubart, M. (2014). *In situ* three-dimensional reconstruction of mouse heart sympathetic innervation by two-photon excitation fluorescence imaging. *J. Neurosci. Methods* 221, 48–61. doi: 10.1016/j.jneumeth.2013.09.005

Fukuda, K., Kanazawa, H., Aizawa, Y., Ardell, J. L., and Shivkumar, K. (2015). Cardiac innervation and sudden cardiac death. *Circ. Res.* 116, 2005–2019. doi: 10.1161/CIRCRESAHA.116.304679

Gardner, R. T., Ripplinger, C. M., Myles, R. C., and Habecker, B. A. (2016). Molecular mechanisms of sympathetic remodeling and arrhythmias. *Circ. Arrhythmia Electrophysiol.* 9:e001359. doi: 10.1161/CIRCEP.115.001359

Gepstein, L., and Gruber, A. (2017). Optogenetic neuromodulation of the heart. *J. Am. Coll. Cardiol.* 70, 2791–2794. doi: 10.1016/j.jacc.2017.10.003

Glebova, N. O., and Ginty, D. D. (2004). Heterogeneous requirement of NGF for sympathetic target innervation *in vivo*. *J. Neurosci.* 24, 743–751. doi: 10.1523/JNEUROSCI.4523-03.2004

Govorunova, E. G., Cunha, S. R., Sineshchekov, O. A., and Spudich, J. L. (2016). Anion channelrhodopsins for inhibitory cardiac optogenetics. *Sci. Rep.* 6:33530. doi: 10.1038/srep33530

Gradinaru, V., Thompson, K. R., and Deisseroth, K. (2008). eNpHR: a natronomonas halorhodopsin enhanced for optogenetic applications. *Brain Cell Biol.* 36, 129–139. doi: 10.1007/s11068-008-9027-6

Gussakovsky, E., and Kupriyanov, V. (2008). Assessment of near-infrared path length in fibrous phantom and muscle tissue. *Appl. Spectrosc.* 62, 671–676. doi: 10.1366/000370208784658174

Guyenet, P. G. (2006). The sympathetic control of blood pressure. *Nat. Rev. Neurosci.* 7, 335–346. doi: 10.1038/nrn1902

Guyenet, P. G., and Abbott, S. B. G. (2013). Chemoreception and asphyxia-induced arousal. *Respir. Physiol. Neurobiol.* 188, 333–343. doi: 10.1016/j.resp.2013.04.011

Han, X., Chow, B. Y., Zhou, H., Klapoetke, N. C., Chuong, A., Rajimehr, R., et al. (2011). A high-light sensitivity optical neural silencer: development and application to optogenetic control of non-human primate cortex. *Front. Syst. Neurosci.* 5:18. doi: 10.3389/fnsys.2011.00018

Heesch, C. M. (1999). Reflexes that control cardiovascular function. *Am. J. Physiol.* 277, 234–243. doi: 10.1152/advances.1999.277.6.s234

Hegemann, P., and Nagel, G. (2013). From channelrhodopsins to optogenetics. *EMBO Mol. Med.* 5, 173–176. doi: 10.1002/EMMM.201202387

Higginbotham, M. B., Morris, K. G., Williams, S., McHale, P. A., Coleman, R. E., and Cobb, F. R. (1986). Regulation of stroke volume during submaximal and maximal upright exercise in normal man. *Circ. Res.* 58, 281–291. doi: 10.1161/01.RES.58.2.281

Hilz, M. J., Dütsch, M., Perrine, K., Nelson, P. K., Rauhut, U., and Devinsky, O. (2001). Hemispheric influence on autonomic modulation and baroreflex sensitivity. *Ann. Neurol.* 49, 575–584. doi: 10.1002/ana.1006

Hochbaum, D. R., Zhao, Y., Farhi, S. L., Klapoetke, N., Werley, C. A., Kapoor, V., et al. (2014). All-optical electrophysiology in mammalian neurons using engineered microbial rhodopsins. *Nat. Methods* 11, 825–833. doi: 10.1038/NMETH.3000

Hoover, D. B., Shepherd, A. V., Southerland, E. M., Armour, J. A., and Ardell, J. L. (2008). Neurochemical diversity of afferent neurons that transduce sensory signals from dog ventricular myocardium. *Auton. Neurosci. Basic Clin.* 141, 38–45. doi: 10.1016/j.autneu.2008.04.010

Hoyt, R. H., Cohen, M. L., and Saffitz, J. E. (1989). Distribution and three-dimensional structure of intercellular junctions in canine myocardium. *Circ. Res.* 64, 563–574. doi: 10.1161/01.RES.64.3.563

Ibanez, B., James, S., Agewall, S., Antunes, M. J., Bucciarelli-Ducci, C., Bueno, H., et al. (2018). 2017 ESC Guidelines for the management of acute myocardial infarction in patients presenting with ST-segment elevation. *Eur. Heart J.* 39, 119–177. doi: 10.1093/eurheartj/ehx393

Ishizuka, T., Kakuda, M., Araki, R., and Yawo, H. (2006). Kinetic evaluation of photosensitivity in genetically engineered neurons expressing green algae light-gated channels. *Neurosci. Res.* 54, 85–94. doi: 10.1016/J.NEURES.2005.10.009

James, T. N., and Sherf, L. (1971). Fine structure of the his bundle. *Circulation* 44, 9–28. doi: 10.1161/01.CIR.44.1.9

Janes, R. D., Christopher Brandys, J., Hopkins, D. A., Johnstone, D. E., Murphy, D. A., and Armour, J. A. (1986). Anatomy of human extrinsic cardiac nerves and ganglia. *Am. J. Cardiol.* 57, 299–309. doi: 10.1016/0002-9149(86)90908-2

Jia, Z., Valiunas, V., Lu, Z., Bien, H., Liu, H., Wang, H.-Z., et al. (2011). Stimulating Cardiac Muscle by Light. *Circ. Arrhythmia Electrophysiol.* 4, 753–760. doi: 10.1161/CIRCEP.111.964247

Kallmünzer, B., Breuer, L., Kahl, N., Bobinger, T., Raaz-Schrauder, D., Huttner, H. B., et al. (2012). Serious cardiac arrhythmias after stroke: incidence, time course, and predictors-a systematic, prospective analysis. *Stroke* 43, 2892–2897. doi: 10.1161/STROKEAHA.112.664318

Kanevskij, M., Taimor, G., Schäfer, M., Piper, H. M., and Schlüter, K. D. (2002). Neuropeptide Y modifies the hypertrophic response of adult ventricular cardiomyocytes to norepinephrine. *Cardiovasc. Res.* 53, 879–887. doi: 10.1016/S0008-6363(01)00517-X

Kawashima, T. (2005). The autonomic nervous system of the human heart with special reference to its origin, course, and peripheral distribution. *Anat. Embryol. (Berl).* 209, 425–438. doi: 10.1007/s00429-005-0462-1

Keith, A., and Flack, M. W. (1906). The auriculo-ventricular bundle of the human heart. *Lancet* 168, 359–364. doi: 10.1016/S0140-6736(01)32375-9

Kim, D., Yokota, T., Suzuki, T., Lee, S., Woo, T., Yukita, W., et al. (2020). Ultraflexible organic light-emitting diodes for optogenetic nerve stimulation. *Proc. Natl. Acad. Sci. U.S.A.* 117, 21138–21146. doi: 10.1073/pnas.2007395117

Kim, Y. D., Song, D., Nam, H. S., Choi, D., Kim, J. S., Kim, B. K., et al. (2017). Increased risk of cardiovascular events in stroke patients who had not undergone evaluation for coronary artery disease. *Yonsei Med. J.* 58, 114–122. doi: 10.3349/ymj.2017.58.1.114

Kimura, K., Ieda, M., Kanazawa, H., Yagi, T., Tsunoda, M., Ninomiya, S. I., et al. (2007). Cardiac sympathetic rejuvenation: a link between nerve function and cardiac hypertrophy. *Circ. Res.* 100, 1755–1764. doi: 10.1161/01.RES.0000269828.62250.ab

Kishi, T. (2012). Heart failure as an autonomic nervous system dysfunction. *J. Cardiol.* 59, 117–122. doi: 10.1016/j.jjcc.2011.12.006

Klapoetke, N. C., Murata, Y., Kim, S. S., Pulver, S. R., Birdsey-Benson, A., Cho, Y. K., et al. (2014). Independent optical excitation of distinct neural populations. *Nat. Methods* 11, 338–346. doi: 10.1038/nmeth.2836

Koba, S., Hanai, E., Kumada, N., and Watanabe, T. (2020). Sympathoexcitatory input from hypothalamic paraventricular nucleus neurons projecting to rostral ventrolateral medulla is enhanced after myocardial infarction. *Am. J. Physiol. Hear. Circ. Physiol.* 319, H1197–H1207. doi: 10.1152/AJPHEART.00273.2020

Kreipke, R. E., and Birren, S. J. (2015). Innervating sympathetic neurons regulate heart size and the timing of cardiomyocyte cell cycle withdrawal. *J. Physiol.* 593, 5057–5073. doi: 10.1113/JP270917

Lee, S. W., Li, Q., Libbus, I., Xie, X., KenKnight, B. H., Garry, M. G., et al. (2016). Chronic cyclic vagus nerve stimulation has beneficial electrophysiological effects on healthy hearts in the absence of autonomic imbalance. *Physiol. Rep.* 4:e12786. doi: 10.14814/PHY2.12786

Leenhardt, A., Lucet, V., Denjoy, I., Grau, F., Dien Do, N.goc, and Coumel, P. (1995). Catecholaminergic polymorphic ventricular tachycardia in children: a 7- year follow-up of 21 patients. *Circulation* 91, 1512–1519. doi: 10.1161/01.CIR.91.5.1512

Lehnart, S. E., Mongillo, M., Bellinger, A., Lindegger, N., Chen, B. X., Hsueh, W., et al. (2008). Leaky Ca^{2+} release channel/ryanodine receptor 2 causes seizures and sudden cardiac death in mice. *J. Clin. Invest.* 118, 2230–2245. doi: 10.1172/JCI35346

Lewis, T. (1911). Galvanometric curves yielded by cardiac beats generated in various areas of the auricular musculature. The pacemaker of the heart. *Heart* 2:23.

Li, M., Zheng, C., Sato, T., Kawada, T., Sugimachi, M., and Sunagawa, K. (2004). Vagal nerve stimulation markedly improves long-term survival after chronic heart failure in rats. *Circulation* 109, 120–124. doi: 10.1161/01.CIR.0000105721.71640.DA

Li, X., Gutierrez, D. V., Hanson, M. G., Han, J., Mark, M. D., Chiel, H., et al. (2005). Fast noninvasive activation and inhibition of neural and network activity by vertebrate rhodopsin and green algae channelrhodopsin. *Proc. Natl. Acad. Sci. U.S.A.* 102, 17816–17821. doi: 10.1073/PNAS.0509030102

Lin, J. Y., Knutsen, P. M., Muller, A., Kleinfeld, D., and Tsien, R. Y. (2013). ReaChR: a red-shifted variant of channelrhodopsin enables deep transcranial optogenetic excitation. *Nat. Neurosci.* 16, 1499–1508. doi: 10.1038/nn.3502

Lin, X., Chen, X., Zhang, W., Sun, T., Fang, P., Liao, Q., et al. (2018). Core-shell-shell upconversion nanoparticles with enhanced emission for wireless optogenetic inhibition. *Nano Lett.* 18, 948–956. doi: 10.1021/acs.nanolett.7b04339

Lombardi, F., Malliani, A., Pagani, M., and Cerutti, S. (1996). Heart rate variability and its sympatho-vagal modulation. *Cardiovasc. Res.* 32, 208–216. doi: 10.1016/0008-6363(96)00116-2

Luppi, P. H., Peyron, C., and Fort, P. (2017). Not a single but multiple populations of GABAergic neurons control sleep. *Sleep Med. Rev.* 32, 85–94. doi: 10.1016/j.smrv.2016.03.002

Maimon, B. E., Sparks, K., Srinivasan, S., Zorzos, A. N., and Herr, H. M. (2018). Spectrally distinct channelrhodopsins for two-colour optogenetic peripheral nerve stimulation. *Nat. Biomed. Eng.* 2, 485–496. doi: 10.1038/s41551-018-0255-5

Malloy, C., Sifers, J., Mikos, A., Samadi, A., Omar, A., Hermanns, C., et al. (2017). Using optogenetics to assess neuroendocrine modulation of heart rate in *Drosophila melanogaster* larvae. *J. Comp. Physiol. A Neuroethol. Sensory, Neural, Behav. Physiol.* 203, 791–806. doi: 10.1007/s00359-017-1191-7

Mann, D., Zipes, D., Libby, P., and Bonow, R. (2014). *Braunwald's Heart Disease: A Textbook of Cardiovascular Medicine*. Amsterdam: Elsevier Health Sciences.

Marina, N., Tang, F., Figueiredo, M., Mastitskaya, S., Kasimov, V., Mohamed-Ali, V., et al. (2013). Purinergic signalling in the rostral ventro-lateral medulla controls sympathetic drive and contributes to the progression of heart failure following myocardial infarction in rats. *Basic Res. Cardiol.* 108:317. doi: 10.1007/s00395-012-0317-x

Mastitskaya, S., Marina, N., Gourine, A., Gilbey, M. P., Spyer, K. M., Teschemacher, A. G., et al. (2012). Cardioprotection evoked by remote ischaemic preconditioning is critically dependent on the activity of vagal pre-ganglionic neurones. *Cardiovasc. Res.* 95, 487–494. doi: 10.1093/cvr/cvs212

McCartney, S. L., Patel, C., and Del Rio, J. M. (2017). Long-term outcomes and management of the heart transplant recipient. *Best Pract. Res. Clin. Anaesthesiol.* 31, 237–248. doi: 10.1016/j.bpa.2017.06.003

Menuet, C., Connelly, A. A., Bassi, J. K., Melo, M. R., Le, S., Kamar, J., et al. (2020). Prebötzinger complex neurons drive respiratory modulation of blood pressure and heart rate. *Elife* 9, 1–30. doi: 10.7554/eLife.57288

Michoud, F., Sottas, L., Browne, L. E., Asboth, L., Latremoliere, A., Sakuma, M., et al. (2018). Optical cuff for optogenetic control of the peripheral nervous system. *J. Neural Eng.* 15:015002. doi: 10.1088/1741-2552/aa9126

Mikolich, J. R., and Jacobs, W. C. (1981). Cardiac arrhythmias in patients with acute cerebrovascular accidents. *J. Am. Med. Assoc.* 246, 1314–1317. doi: 10.1001/jama.1981.03320120018018

Monfredi, O., Dobrzynski, H., Mondal, T., Boyett, M. R., and Morris, G. M. (2010). The anatomy and physiology of the sinoatrial node-a contemporary review. *Pacing Clin. Electrophysiol.* 33, 1392–1406. doi: 10.1111/j.1540-8159.2010.02838.x

Moradi, M., Doostkami, M., Behnamfar, N., Rafiemanesh, H., and Behzadmehr, R. (2021). Global prevalence of depression among heart failure patients: a systematic review and meta-analysis. *Curr. Probl. Cardiol.* 2021:100848. doi: 10.1016/j.cpcardiol.2021.100848

Moreno, A., Endicott, K., Skancke, M., Dwyer, M. K., Brennan, J., Efimov, I. R., et al. (2019). Sudden heart rate reduction upon optogenetic release of acetylcholine from cardiac parasympathetic neurons in perfused hearts. *Front. Physiol.* 10:16. doi: 10.3389/fphys.2019.00016

Myles, R. C., Wang, L., Kang, C., Bers, D. M., and Ripplinger, C. M. (2012). Local β-adrenergic stimulation overcomes source-sink mismatch to generate focal arrhythmia. *Circ. Res.* 110, 1454–1464. doi: 10.1161/CIRCRESAHA.111.262345

Nagarajan, S., and Zhang, Y. (2011). Upconversion fluorescent nanoparticles as a potential tool for in-depth imaging. *Nanotechnology* 22:395101. doi: 10.1088/0957-4484/22/39/395101

Nagel, G., Brauner, M., Liewald, J. F., Adeishvili, N., Bamberg, E., and Gottschalk, A. (2005). Light activation of channelrhodopsin-2 in excitable cells of *Caenorhabditis elegans* triggers rapid behavioral responses. *Curr. Biol.* 15, 2279–2284. doi: 10.1016/J.CUB.2005.11.032

Nagel, G., Ollig, D., Fuhrmann, M., Kateriya, S., Musti, A. M., Bamberg, E., et al. (2002). Channelrhodopsin-1: a light-gated proton channel in green algae. *Science* 296, 2395–2398. doi: 10.1126/science.1072068

Nagel, G., Szellas, T., Huhn, W., Kateriya, S., Adeishvili, N., Berthold, P., et al. (2003). Channelrhodopsin-2, a directly light-gated cation-selective membrane channel. *Proc. Natl. Acad. Sci. U. S. A.* 100, 13940–13945. doi: 10.1073/pnas.1936192100

Neumann, F. J., Sechtem, U., Banning, A. P., Bonaros, N., Bueno, H., Bugiardini, R., et al. (2020). 2019 ESC Guidelines for the diagnosis and management of chronic coronary syndromes. *Eur. Heart J.* 41, 407–477. doi: 10.1093/eurheartj/ehz425

O'Connell, T. D., Ishizaka, S., Nakamura, A., Swigart, P. M., Rodrigo, M. C., Simpson, G. L., et al. (2003). The α1A/C- and α1B-adrenergic receptors are required for physiological cardiac hypertrophy in the double-knockout mouse. *J. Clin. Invest.* 111, 1783–1791. doi: 10.1172/jci16100

Ogawa, S., Barnett, J. V., Sen, L., Galper, J. B., Smith, T. W., and Marsh, J. O. (1992). Direct contact between sympathetic neurons and rat cardiac myocytes *in vitro* increases expression of functional calcium channels. *J. Clin. Invest.* 89, 1085–1093. doi: 10.1172/JCI115688

Oh, Y., Cho, G.-S., Li, Z., Hong, I., Zhu, R., Kim, M.-J., et al. (2016). Functional coupling with cardiac muscle promotes maturation of hPSC-derived sympathetic neurons. *Cell Stem Cell* 19, 95–106. doi: 10.1016/j.stem.2016.05.002

Oppenheimer, S. M., and Cechetto, D. F. (1990). Cardiac chronotropic organization of the rat insular cortex. *Brain Res.* 533, 66–72. doi: 10.1016/0006-8993(90)91796-J

Oppenheimer, S. M., Gelb, A., Girvin, J. P., and Hachinski, V. C. (1992). Cardiovascular effects of human insular cortex stimulation. *Neurology* 42, 1727–1732. doi: 10.1212/wnl.42.9.1727

Padala, S. K., Cabrera, J. A., and Ellenbogen, K. A. (2021). Anatomy of the cardiac conduction system. *Pacing Clin. Electrophysiol.* 44, 15–25. doi: 10.1111/pace.14107

Paul, S., Hanna, L., Harding, C., Hayter, E. A., Walmsley, L., Bechtold, D. A., et al. (2020). Output from VIP cells of the mammalian central clock regulates daily physiological rhythms. *Nat. Commun.* 11, 1–14. doi: 10.1038/s41467-020-15277-x

Pianca, N., Di Bona, A., Lazzeri, E., Costantini, I., Franzoso, M., Prando, V., et al. (2019). Cardiac sympathetic innervation network shapes the myocardium by locally controlling cardiomyocyte size through the cellular proteolytic machinery. *J. Physiol.* 597, 3639–3656. doi: 10.1113/JP276200

Pianca, N., Zaglia, T., and Mongillo, M. (2017). Will cardiac optogenetics find the way through the obscure angles of heart physiology? *Biochem. Biophys. Res. Commun.* 482, 515–523. doi: 10.1016/j.bbrc.2016.11.104

Poletto, R., Janczak, A. M., Marchant-Forde, R. M., Marchant-Forde, J. N., Matthews, D. L., Dowell, C. A., et al. (2011). Identification of low and high frequency ranges for heart rate variability and blood pressure variability analyses using pharmacological autonomic blockade with atropine and propranolol in swine. *Physiol. Behav.* 103, 188–196. doi: 10.1016/j.physbeh.2011.01.019

Ponikowski, P., Voors, A. A., Anker, S. D., Bueno, H., Cleland, J. G. F., Coats, A. J. S., et al. (2016). 2016 ESC Guidelines for the diagnosis and treatment of acute and chronic heart failure: The Task Force for the diagnosis and treatment of acute and chronic heart failure of the European Society of Cardiology (ESC). Developed with the special contribution of the Heart Failure Association (HFA) of the ESC. *Eur. J. Heart Fail.* 18, 891–975. doi: 10.1002/ejhf.592

Prando, V., Da Broi, F., Franzoso, M., Plazzo, A. P., Pianca, N., Francolini, M., et al. (2018). Dynamics of neuroeffector coupling at cardiac sympathetic synapses. *J. Physiol.* 596, 2055–2075. doi: 10.1113/JP275693

Rajasethupathy, P., Ferenczi, E., and Deisseroth, K. (2016). Targeting neural circuits. *Cell* 165, 524–534. doi: 10.1016/j.cell.2016.03.047

Rajendran, P. S., Challis, R. C., Fowlkes, C. C., Hanna, P., Tompkins, J. D., Jordan, M. C., et al. (2019). Identification of peripheral neural circuits that regulate heart rate using optogenetic and viral vector strategies. *Nat. Commun.* 10:1944. doi: 10.1038/s41467-019-09770-1

Randall, W. C., Szentivanyi, M., Pace, J. B., Wechsler, J. S., and Kaye, M. P. (1968). Patterns of sympathetic nerve projections onto the canine heart. *Circ. Res.* 22, 315–323. doi: 10.1161/01.RES.22.3.315

Rao, P., Wang, L., Cheng, Y., Wang, X., Li, H., Zheng, G., et al. (2020). Near-infrared light driven tissue-penetrating cardiac optogenetics via upconversion nanoparticles *in vivo*. *Biomed. Opt. Express* 11:1401. doi: 10.1364/boe.381480

Ringer, S. (1883). A third contribution regarding the influence of the inorganic constituents of the blood on the ventricular contraction. *J. Physiol.* 4, 222–225. doi: 10.1113/jphysiol.1883.sp000127

Rochais, F., Vandecasteele, G., Lefebvre, F., Lugnier, C., Lum, H., Mazet, J. L., et al. (2004). Negative feedback exerted by cAMP-dependent protein kinase and cAMP phosphodiesterase on subsarcolemmal cAMP signals in intact cardiac myocytes: an *in vivo* study using adenovirus-mediated expression of CNG channels. *J. Biol. Chem.* 279, 52095–52105. doi: 10.1074/jbc.M405697200

Rohr, S., Kucera, J. P., Fast, V. G., and Kléber, A. G. (1997). Paradoxical improvement of impulse conduction in cardiac tissue by partial cellular uncoupling. *Science* 275, 841–844. doi: 10.1126/science.275.5301.841

Ruthirago, D., Julayanont, P., Tantrachoti, P., Kim, J., and Nugent, K. (2016). Cardiac arrhythmias and abnormal electrocardiograms after acute stroke. *Am. J. Med. Sci.* 351, 112–118. doi: 10.1016/j.amjms.2015.10.020

Samineni, V. K., Yoon, J., Crawford, K. E., Jeong, Y. R., McKenzie, K. C., Shin, G., et al. (2017). Fully implantable, battery-free wireless optoelectronic devices for spinal optogenetics. *Pain* 158, 2108–2116. doi: 10.1097/j.pain.0000000000000968

Samuels, M. A. (2007). The brain-heart connection. *Circulation* 116, 77–84. doi: 10.1161/CIRCULATIONAHA.106.678995

Saper, C. B., and Fuller, P. M. (2017). Wake–sleep circuitry: an overview. *Curr. Opin. Neurobiol.* 44, 186–192. doi: 10.1016/j.conb.2017.03.021

Sasse, P. (2018). Sympathetic control of cardiac output by noradrenaline: quasi-synaptic quantal release or interstitial diffusion and spillover? *J. Physiol.* 596, 2031–2032. doi: 10.1113/JP276109

Scammell, T. E., Arrigoni, E., and Lipton, J. O. (2017). Neural circuitry of wakefulness and sleep. *Neuron* 93, 747–765. doi: 10.1016/j.neuron.2017.01.014

Scardigli, M., Müllenbroich, C., Margoni, E., Cannazzaro, S., Crocini, C., Ferrantini, C., et al. (2018). Real-time optical manipulation of cardiac conduction in intact hearts. *J. Physiol.* 596, 3841–3858. doi: 10.1113/JP276283

Scherbakov, N., and Doehner, W. (2018). Heart–brain interactions in heart failure. *Card. Fail. Rev.* 4, 87–91. doi: 10.15420/cfr.2018.14.2

Schievink, S. H. J., van Boxtel, M. P. J., Deckers, K., van Oostenbrugge, R. J., Verhey, F. R. J., and Köhler, S. (2017). Cognitive changes in prevalent and incident cardiovascular disease: a 12-year follow-up in the Maastricht Aging Study (MAAS). *Eur. Heart J.* doi: 10.1093/eurheartj/ehx365. [Epub ahead of print].

Schwartz, P. J., Priori, S. G., Spazzolini, C., Moss, A. J., Vincent, G. M., Napolitano, C., et al. (2001). Genotype-phenotype correlation in the long-QT syndrome. *Circulation* 103, 89–95. doi: 10.1161/01.CIR.103.1.89

Sharkey, S. W., Lesser, J. R., and Maron, B. J. (2011). Takotsubo (stress) cardiomyopathy. *Circulation* 124, e460–e462. doi: 10.1161/CIRCULATIONAHA.111.052662

Shen, M. J., and Zipes, D. P. (2014). Role of the autonomic nervous system in modulating cardiac arrhythmias. *Circ. Res.* 114, 1004–1021. doi: 10.1161/CIRCRESAHA.113.302549

Silvani, A., Calandra-Buonaura, G., Dampney, R. A. L., and Cortelli, P. (2016). Brain-heart interactions: physiology and clinical implications. *Philos. Trans. R. Soc. A Math. Phys. Eng. Sci.* 374:20150181. doi: 10.1098/rsta.2015.0181

Smith, J. C., Abdala, A. P. L., Borgmann, A., Rybak, I. A., and Paton, J. F. R. (2013). Brainstem respiratory networks: building blocks and microcircuits. *Trends Neurosci.* 36, 152–162. doi: 10.1016/j.tins.2012.11.004

Song, K. I., Park, S. E., Lee, S., Kim, H., Lee, S. H., and Youn, I. (2018). Compact optical nerve cuff electrode for simultaneous neural activity monitoring and optogenetic stimulation of peripheral nerves. *Sci. Rep.* 8:15630. doi: 10.1038/s41598-018-33695-2

Stieber, J., Herrmann, S., Feil, S., Löster, J., Feil, R., Biel, M., et al. (2003). The hyperpolarization-activated channel HCN4 is required for the generation of pacemaker action potentials in the embryonic heart. *Proc. Natl. Acad. Sci. U. S. A.* 100, 15235–15240. doi: 10.1073/pnas.2434235100

Taggart, P., Critchley, H., van Duijvendoden, S., and Lambiase, P. D. (2016). Significance of neuro-cardiac control mechanisms governed by higher regions of the brain. *Auton. Neurosci. Basic Clin.* 199, 54–65. doi: 10.1016/j.autneu.2016.08.013

Tahsili-Fahadan, P., and Geocadin, R. G. (2017). Heart-brain axis: effects of neurologic injury on cardiovascular function. *Circ. Res.* 120, 559–572. doi: 10.1161/CIRCRESAHA.116.308446

Tan, A. Y., Li, H., Wachsmann-Hogiu, S., Chen, L. S., Chen, P. S., and Fishbein, M. C. (2006). Autonomic innervation and segmental muscular disconnections at the human pulmonary vein-atrial junction. Implications for catheter ablation of atrial-pulmonary vein junction. *J. Am. Coll. Cardiol.* 48, 132–143. doi: 10.1016/j.jacc.2006.02.054

Tawara, S. (1906). *Eine Anatomisch-Histologische Studie Über das Atrio-Ventrikularbündel und die Purkinjeschen Fäden*. Jena Verlag von Gustav Fischer 200.

Touzé, E., Varenne, O., Chatellier, G., Peyrard, S., Rothwell, P. M., and Mas, J. L. (2005). Risk of myocardial infarction and vascular death after transient ischemic attack and ischemic stroke: a systematic review and meta-analysis. *Stroke* 36, 2748–2755. doi: 10.1161/01.STR.0000190118.02275.33

Towne, C., Montgomery, K. L., Iyer, S. M., Deisseroth, K., and Delp, S. L. (2013). Optogenetic control of targeted peripheral axons in freely moving animals. *PLoS ONE* 8:e0072691. doi: 10.1371/journal.pone.0072691

Uribe, R. A. Q., Luther, S., Diaz-Maue, L., and Richter, C. (2018). Energy-reduced arrhythmia termination using global photostimulation in optogenetic murine hearts. *Front. Physiol.* 9:1651. doi: 10.3389/fphys.2018.01651

Van der Kooy, K., van Hout, H., Marwijk, H., Marten, H., Stehouwer, C., and Beekman, A. (2007). Depression and the risk for cardiovascular diseases: systematic review and meta analysis. *Int. J. Geriatr. Psychiatry* 22, 613–626. doi: 10.1002/gps.1723

Vanderlaan, R. D., Conway, J., Manlhiot, C., McCrindle, B. W., and Dipchand, A. I. (2012). Enhanced exercise performance and survival associated with evidence of autonomic reinnervation in pediatric heart transplant recipients. *Am. J. Transplant.* 12, 2157–2163. doi: 10.1111/j.1600-6143.2012.04046.x

Verberne, A. J. M., and Owens, N. C. (1998). Cortical modulation of the cardiovascular system. *Prog. Neurobiol.* 54, 149–168. doi: 10.1016/S0301-0082(97)00056-7

Wang, Y., Lin, X., Chen, X., Chen, X., Xu, Z., Zhang, W., et al. (2017). Tetherless near-infrared control of brain activity in behaving animals using fully implantable upconversion microdevices. *Biomaterials* 142, 136–148. doi: 10.1016/j.biomaterials.2017.07.017

Wang, Y. F., Liu, G. Y., Sun, L. D., Xiao, J. W., Zhou, J. C., and Yan, C. H. (2013). Nd3+-sensitized upconversion nanophosphors: efficient *in vivo* bioimaging probes with minimized heating effect. *ACS Nano* 7, 7200–7206. doi: 10.1021/nn402601d

Wehrmacher, W. H., Puglisi, J. L., Bers, D. M., and Messmore, H. (2005). Sudden unexpected death. *Compr. Ther.* 31, 176–180. doi: 10.1385/COMP:31:3:176

Wengrowski, A. M., Wang, X., Tapa, S., Posnack, N. G., Mendelowitz, D., and Kay, M. W. (2015). Optogenetic release of norepinephrine from cardiac sympathetic neurons alters mechanical and electrical function. *Cardiovasc. Res.* 105, 143–150. doi: 10.1093/cvr/cvu258

Winbo, A., and Paterson, D. J. (2020). The brain-heart connection in sympathetically triggered inherited arrhythmia syndromes. *Hear. Lung Circ.* 29, 529–537. doi: 10.1016/j.hlc.2019.11.002

Wink, J., van Delft, R., Notenboom, R. G. E., Wouters, P. F., DeRuiter, M. C., Plevier, J. W. M., et al. (2020). Human adult cardiac autonomic innervation: controversies in anatomical knowledge and relevance for cardiac neuromodulation. *Auton. Neurosci. Basic Clin.* 227:102674. doi: 10.1016/j.autneu.2020.102674

Wleklinski, M. J., Kannankeril, P. J., and Knollmann, B. C. (2020). Molecular and tissue mechanisms of catecholaminergic polymorphic ventricular tachycardia. *J. Physiol.* 598, 2817–2834. doi: 10.1113/JP276757

Wybauw, R. (1910). Sur le point d'origine de la systole cardiaque dans l'oreillette droite. *Arch. Int. Physiol.* 10, 78–90.

Xie, Y., Sato, D., Garfinkel, A., Qu, Z., and Weiss, J. N. (2010). So little source, so much sink: requirements for afterdepolarizations to propagate in tissue. *Biophys. J.* 99, 1408–1415. doi: 10.1016/j.bpj.2010.06.042

Yu, L., Zhou, L., Cao, G., Po, S. S., Huang, B., Zhou, X., et al. (2017). Optogenetic modulation of cardiac sympathetic nerve activity to prevent ventricular arrhythmias. *J. Am. Coll. Cardiol.* 70, 2778–2790. doi: 10.1016/j.jacc.2017.09.1107

Zaccolo, M., and Pozzan, T. (2002). Discrete microdomains with high concentration of cAMP in stimulated rat neonatal cardiac myocytes. *Science* 295, 1711–1715. doi: 10.1126/science.1069982

Zaglia, T., Di Bona, A., and Mongillo, M. (2019). A light wand to untangle the myocardial cell network. *Methods Protoc.* 2:34. doi: 10.3390/mps2020034

Zaglia, T., Milan, G., Franzoso, M., Bertaggia, E., Pianca, N., Piasentini, E., et al. (2012). Cardiac sympathetic neurons provide trophic signal to the heart via β2-adrenoceptor-dependent regulation of proteolysis. *Cardiovasc. Res.* 97, 240–250. doi: 10.1093/cvr/cvs320

Zaglia, T., and Mongillo, M. (2017). Cardiac sympathetic innervation, from a different point of (re)view. *J. Physiol.* 595, 3919–3930. doi: 10.1113/JP273120

Zaglia, T., Pianca, N., Borile, G., Da Broi, F., Richter, C., Campione, M., et al. (2015). Optogenetic determination of the myocardial requirements for extrasystoles by cell type-specific targeting of ChannelRhodopsin-2. *Proc. Natl. Acad. Sci. U.S.A.* 112, E4495–E4504. doi: 10.1073/pnas.1509380112

Zasadny, F. M., Dyavanapalli, J., Dowling, N. M., Mendelowitz, D., and Kay, M. W. (2020). Cholinergic stimulation improves electrophysiological rate adaptation during pressure overload-induced heart failure in rats. *Am. J. Physiol. Heart. Circ. Physiol.* 319, H1358–H1368. doi: 10.1152/AJPHEART.00293.2020

Zhang, F., Prigge, M., Beyrière, F., Tsunoda, S. P., Mattis, J., Yizhar, O., et al. (2008). Red-shifted optogenetic excitation: a tool for fast neural control derived from *Volvox carteri*. *Nat. Neurosci.* 11, 631–633. doi: 10.1038/nn.2120

Zhang, F., Wang, L. P., Boyden, E. S., and Deisseroth, K. (2006). Channelrhodopsin-2 and optical control of excitable cells. *Nat. Methods* 3, 785–792. doi: 10.1038/nmeth936

Zhang, Y., Mickle, A. D., Gutruf, P., McIlvried, L. A., Guo, H., Wu, Y., et al. (2019). Battery-free, fully implantable optofluidic cuff system for wireless optogenetic and pharmacological neuromodulation of peripheral nerves. *Sci. Adv.* 5:eaaw5296. doi: 10.1126/sciadv.aaw5296

Zhang, Z. H., Dougherty, P. M., and Oppenheimer, S. M. (1998). Characterization of baroreceptor-related neurons in the monkey insular cortex. *Brain Res.* 796, 303–306. doi: 10.1016/S0006-8993(98)00268-6

Zimmer, H. G., Kolbeck-Ruhmkorff, C., and Zierhut, W. (1995). Cardiac hypertrophy induced by α- and β-adrenergic receptor stimulation. *Cardioscience* 6, 47–57.

Zipes, D. P. (2015). Antiarrhythmic therapy in 2014: contemporary approaches to treating arrhythmias. *Nat. Rev. Cardiol.* 12, 68–69. doi: 10.1038/nrcardio.2014.211

Conflict of Interest: The authors declare that the research was conducted in the absence of any commercial or financial relationships that could be construed as a potential conflict of interest.

Publisher's Note: All claims expressed in this article are solely those of the authors and do not necessarily represent those of their affiliated organizations, or those of the publisher, the editors and the reviewers. Any product that may be evaluated in this article, or claim that may be made by its manufacturer, is not guaranteed or endorsed by the publisher.

frontiers in Physiology

ORIGINAL RESEARCH
published: 03 September 2021
doi: 10.3389/fphys.2021.692496

Fast Optical Investigation of Cardiac Electrophysiology by Parallel Detection in Multiwell Plates

*Caterina Credi[1,2†], Valentina Balducci[3†], U. Munagala[3,4], C. Cianca[1], S. Bigiarini[1], Antoine A. F. de Vries[5], Leslie M. Loew[6], Francesco S. Pavone[1,2,7], Elisabetta Cerbai[1,3], Laura Sartiani[3] and Leonardo Sacconi[1,2]**

[1] European Laboratory for Non-linear Spectroscopy, Sesto Fiorentino, Italy, [2] National Institute of Optics, National Research Council, Florence, Italy, [3] Department of Neurosciences, Psychology, Drugs and Child Health, University of Florence, Florence, Italy, [4] Core Research Laboratory, ISPRO, Florence, Italy, [5] Laboratory of Experimental Cardiology, Department of Cardiology, Leiden University Medical Center, Leiden, Netherlands, [6] R. D. Berlin Center for Cell Analysis and Modeling, University of Connecticut School of Medicine, Farmington, CT, United States, [7] Department of Physics and Astronomy, University of Florence, Sesto Fiorentino, Italy

OPEN ACCESS

Edited by:
Godfrey Smith,
University of Glasgow,
United Kingdom

Reviewed by:
Arkady M. Pertsov,
Upstate Medical University,
United States
Wayne Rodney Giles,
University of Calgary, Canada

***Correspondence:**
Leonardo Sacconi
sacconi@lens.unifi.it

[†] These authors have contributed equally to this work

Specialty section:
This article was submitted to Cardiac Electrophysiology, a section of the journal Frontiers in Physiology

Received: 08 April 2021
Accepted: 11 August 2021
Published: 03 September 2021

Citation:
Credi C, Balducci V, Munagala U, Cianca C, Bigiarini S, de Vries AAF, Loew LM, Pavone FS, Cerbai E, Sartiani L and Sacconi L (2021) Fast Optical Investigation of Cardiac Electrophysiology by Parallel Detection in Multiwell Plates. Front. Physiol. 12:692496. doi: 10.3389/fphys.2021.692496

Current techniques for fast characterization of cardiac electrophysiology employ optical technologies to control and monitor action potential features of single cells or cellular monolayers placed in multiwell plates. High-speed investigation capacities are commonly achieved by serially analyzing well after well employing fully automated fluorescence microscopes. Here, we describe an alternative cost-effective optical approach (MULTIPLE) that exploits high-power LED arrays to globally illuminate a culture plate and an sCMOS sensor for parallel detection of the fluorescence coming from multiple wells. MULTIPLE combines optical detection of action potentials using a red-shifted voltage-sensitive fluorescent dye (di-4-ANBDQPQ) with optical stimulation, employing optogenetic actuators, to ensure excitation of cardiomyocytes at constant rates. MULTIPLE was first characterized in terms of interwell uniformity of the illumination intensity and optical detection performance. Then, it was applied for probing action potential features in HL-1 cells (i.e., mouse atrial myocyte-like cells) stably expressing the blue light-activatable cation channel CheRiff. Under proper stimulation conditions, we were able to accurately measure action potential dynamics across a 24-well plate with variability across the whole plate of the order of 10%. The capability of MULTIPLE to detect action potential changes across a 24-well plate was demonstrated employing the selective $K_V11.1$ channel blocker (E-4031), in a dose titration experiment. Finally, action potential recordings were performed in spontaneous beating human induced pluripotent stem cell derived cardiomyocytes following pharmacological manipulation of their beating frequency. We believe that the simplicity of the presented optical scheme represents a valid complement to sophisticated and expensive state-of-the-art optical systems for high-throughput cardiac electrophysiological investigations.

Keywords: optogenetics, voltage imaging, action potential, multiwell plate, microscopy

INTRODUCTION

Fast investigation of cardiac electrophysiology is found convenient for the assessment of cardiac ion channel activity of new chemical entities (Dunlop et al., 2008). In this respect, optical techniques for actuating and sensing cardiac action potentials (APs) represent a reference method for preclinical drug screening and cardiotoxicity testing, especially in combination with human induced pluripotent stem cell-derived cardiomyocytes (hiPSC-CMs) (Klimas et al., 2016). Conventional methods for multisite optical interrogation generally require movement of the sample (McGlynn et al., 2018) or of the imaging system (Hansen et al., 2010). These approaches intrinsically limit the acquisition time and require complex and expensive fully automated microscope platforms. Recently, Ashraf et al. (2021) proposed an innovative optical scheme (Random Access Parallel; RAP) that enables near-simultaneous imaging of multiple sites without moving parts or robotics. Although the system was successfully applied for imaging the contraction waves of multiple cardiac monolayers, the possibility of performing high-speed voltage imaging using a fluorescent voltage-sensitive dye (VSD) is precluded due to the requirement of coherent light in the RAP image formation mechanism.

Here, we describe a simple and cost-effective optical approach (MULTIPLE) that exploits high-power light-emitting diode (LED) arrays to globally illuminate a multiwell plate and an sCMOS sensor coupled with a camera lens for parallel detection of the fluorescence coming from multiple sites. The platform has been tested and characterized using VSD-loaded HL-1 cells (i.e., mouse atrial myocyte-like cells) stably expressing the blue light-activatable ion channel CheRiff (Hochbaum et al., 2014) and spontaneously beating hiPSC-CMs. MULTIPLE optically stimulates channelrhodopsin-expressing HL-1 cells across the multiwell plate with blue light pulses assuring constant pacing rates (Bruegmann et al., 2010) while global plate illumination with red light allows recording of APs using the near-infrared VSD di-4-ANBDQPQ (Matiukas et al., 2007). Notably, the use of a red-shifted VSD avoids ChR2/CheRiff excitation allowing optical recording without introducing any variation of resting membrane potential (Scardigli et al., 2018). The capability of MULTIPLE to detect electrophysiological changes was demonstrated in drug dose titration experiments in HL-1 cells and in hiPSC-CMs.

MATERIALS AND METHODS

HL-1 Cell Culture and Staining

HL-1 cells were obtained from Sigma-Aldrich (LOT: 2955183) and were seeded on gelatin-fibronectin (Sigma-Aldrich, Schnelldorf, Germany)-coated 25-cm^2 culture flasks, as previously described (Claycomb et al., 1998; Sartiani et al., 2002a). Briefly, cells were maintained in 'Claycomb Medium' (JRH Biosciences, Lenexa, KS), supplemented with 10% fetal bovine serum (Life Technologies, Cergy Pontoise, France), 4 mM L-glutamine (Life Technologies), 10 μM noradrenaline (norepinephrine; Sigma-Aldrich), and 1× penicillin-streptomycin (Life Technologies). Cultures were maintained at 37°C, in an atmosphere of 5% CO_2 and 95% air at a relative humidity of ≈ 95%; medium was changed every 24 h. HL-1 cells were split at 100% confluency, using a 5-min enzymatic dissociation with trypsin-EDTA (Life Technologies). The enzymatic reaction was stopped by adding medium and the sedimented cells were either replated at a split ratio of 1:3 to maintain cell culture or 1:4 for transduction and staining. Before recordings, total live cell counts were determined after enzymatic dissociation by Trypan blue exclusion assay using a LUNA-II automated cell counter (Logos Biosystems, Anyang, South Korea). Voltage imaging was performed in Tyrode's solution (mM): D-(++)-glucose 10, NaCl 140, KCl 5.4, $CaCl_2$ 1.8, $MgCl_2$ 1.2, HEPES 5.0, adjusted to pH 7.3 with NaOH and supplemented with 4 μg/mL of di-4-ANBDQPQ (Matiukas et al., 2007). E-4031 (Sigma-Aldrich) stock solution (10 mM) was prepared in H_2O and diluted in Tyrode's solution to 10 μM.

Transduction With Viral Vectors

In order to generate a channelrhodopsin-expressing cell line, HL-1 cells were plated on precoated 6-well plates. At 70–80% confluency, cells were incubated for 24 h at 37°C in 5% CO_2-95% air with channelrhodopsin-encoding adeno-associated virus vector (AAVV) or lentiviral vector (LV) particles. The AAVV particles were prepared from shuttle plasmid pAAV.CAG.hChR2(H134R)-mCherry.WPRE.SV40 (Addgene, 100054-AAV9), which codes for the *Chlamydomonas reinhardtii* channelrhodopsin2 (ChR2) gain-of-function mutant H134R extended at its C-terminus with the fluorescent protein tag mCherry. The LV particles were custom-made using shuttle plasmid LV.GgTnnt2.CheRiff∼eGFP.WHVPRE, which codes for a C-terminally enhanced green fluorescent protein (eGFP)-tagged version of the *Scherffelia dubia* channelrhodopsin. To improve transduction efficiency, the inocula contained 8 μg/mL of the cationic polymer polybrene (Sigma-Aldrich) in order to neutralize repulsion between virions and the cell surface.

Flow Cytometry

Flow cytometry was performed using a 13-color, 4-laser CytoFLEX S N-V-B-R flow cytometer, equipped with 405-, 488-, 561-, and 638-nm lasers (B78557, Beckman Coulter, Brea, CA, United States) and operated by CytExpert Software v1.2 (Beckman Coulter, Brea, CA, United States). 48 h after infection, dissociated HL-1 cells were resuspended in phosphate-buffered saline (PBS)-2 mM EDTA (Sigma-Aldrich). eGFP and mCherry expression were detected by excitation at 488 and 561 nm and detection at 525/40 and 610/20 nm, respectively.

Confocal Imaging

A total of 24 h after seeding on glass coverslips, HL-1 cells were washed with PBS and fixed with 4% paraformaldehyde in PBS by incubation for 10 min at room temperature. Next, cells were treated for 10 min with 0.1% Tween 20 (Sigma-Aldrich) and 4',6-diamidin-2 phenylindole (DAPI; Sigma-Aldrich; 1 μg/mL) to stain nuclei. Fluorescence images were taken using a confocal microscope (Nikon Eclipse TE300 equipped with Nikon C2 scanning head) using the Nikon CFI Plan Fluor 20× objective

(Minato-ku, Tokyo, Japan). Excitation wavelengths of 355, 488 and 561 nm were used for DAPI, eGFP, and mCherry, respectively. Band-pass emission filters of 457/50, 528/38, and 620/15 nm were used for DAPI, eGFP, and mCherry, respectively. The confocal images consisted of 1024 × 1024 pixels.

Patch-Clamp Recordings of APs on HL-1 Cells

Patch-clamp recordings were performed using the whole-cell configuration of the patch-clamp technique. The patch-clamp set-up has been described elsewhere (Sartiani et al., 2002a,b). Briefly, isolated cells were placed in an experimental bath on the platform of an inverted microscope (Nikon Diaphot TMD). Recordings were performed using a patch amplifier (Axopatch-200B, Axon Instruments, CA, United States) interfaced to a personal computer by means of a DAC/ADC interface (Labmaster Tekmar, Scientific Solutions, Hamilton, OH, United States). Data were viewed on-line on a computer screen. Experimental control, data acquisition and preliminary analysis were performed by means of the integrated software package pClamp (Axon Instruments). For action potential (AP) recordings, cells were superfused with normal Tyrode's solution at room temperature. Patch-clamp pipettes, prepared from glass capillary tubes (Garner Glass, CA, United States) by means of a two-stage vertical puller (Hans Otchoski, Homburg, Germany), had a resistance of 3-4 MΩ when filled with the internal solution (composition (mM): K-Aspartate 130, Na_2ATP 5, $MgCl_2$ 2, $CaCl_2$ 5, EGTA 11, HEPES–KOH 10, pH 7.2). The patch-clamped cell was superfused by means of a micro-superfusor, which allowed rapid changes of the solution bathing the cell. APs were elicited at 0.2 Hz in the current-clamp mode and sampled at 2 kHz.

hiPSC Culture and Cardiac Differentiation

hiPSCs (WTC11) were differentiated by a monolayer-based protocol, using the cardiac PSC Cardiomyocyte Differentiation Kit (Life Technologies, Thermo Fisher Scientific, Carlsbad, CA, United States) and following the manufacturer's instructions (Dell'Era et al., 2015; Pioner et al., 2019). Briefly, hiPSCs were maintained under feeder-free conditions in mTeSR Plus medium (Stem Cell Technologies, Vancouver) on a Matrigel hESC-Qualified Matrix (Corning, New York, NY, United States) and passaged every 4–5 days. For cardiac differentiation, 70–80% confluent hiPSC colonies were chemically dissociated using 1 × Tryple (Life Technologies). After suspension into mTeSR supplemented with 5μM ROCK inhibitor Y27632 (Stem Cell Technologies, 72302), cells were seeded as single cells onto Matrigel-coated 24 well plates at a density of 6x10^4 cells/well. At 70% confluency, which was reached after 2–3 days, the culture medium was changed to Cardiomyocyte Differentiation Medium A (referred as day 0) to start cardiomyogenic differentiation. After 2 days, medium A was replaced with Medium B, followed by Medium C after two additional days to promote final differentiation. Thereafter, cells were fed every other day with Medium C until the appearance of spontaneously beating monolayers, which occurred at day 8–10. At day 12, to complete hiPSC–CM maturation, Medium C was replaced with RPMI plus B27 supplement (Life Technologies, which was refreshed every 2 days. For AP recordings, hiPSC-CMs were used on day 30 of differentiation.

MULTIPLE Optomechanical Design

As shown in **Figure 1**, illumination for optical actuation and sensing is provided by high-power LEDs controlled by a LED driver (DC20, Thorlabs, Newton, NJ, United States). Optical actuation of ChR2 (H134R) and CheRiff is provided by a LED operating at a wavelength centered at 470 nm (SOLIS-470C, Thorlabs) while illumination for sensing is provided by a red LED centered at 623 nm (SOLIS-623C, Thorlabs), followed by a band-pass filter (625PB50, Omega Optical, Brattleboro, VT, United States). The light paths for optical sensing and actuation are combined by a large-area dichroic mirror (550 DCLP, Omega Optical) mounted on a kinematic fluorescence cube (DFM2/M, Thorlabs) holding also a plane-concave lens (f = –75 mm LC1315-A-ML, Thorlabs) and an optical diffuser (DG20-1500, Thorlabs). The diverging lens and the diffuser are exploited to achieve global and homogeneous illumination of the multiwell plate which is placed at ≈ 12 mm distance onto a customized 3D printed holder. The bottom part of the holder is designed to selectively deliver light to the wells thus avoiding spurious signals originating from the autofluorescence of the plastic culture plate. Emitted fluorescence is passed through a long-pass filter (LP700, Omega Optical) and collected in the forward direction by a camera lens (f = 12 mm, MVL12M43, Thorlabs) placed in front of an sCMOS camera (ORCA-Flash 4.0 V3, Hamamatsu Photonics, Hamamatsu City, Japan) operating at a frame rate of 100 Hz. The illumination, detection and sample holder blocks are vertically aligned on a construction rail (XT95-750, Thorlabs) through drop on rail carriages (XT95RC2/M, Thorlabs) for proper relative positioning between the blocks. Aluminum spacers produced by a traditional milling process were used to attach the illumination and detection blocks to the rail carriages at the optimal relative distance with respect to the vertical rail (**Supplementary Figures 2**, **3**). All the commercial optomechanical components implemented in the MULTIPLE platform are listed in **Table 1**. The final overall dimensions of the MULTIPLE system are 450 × 450 × 900 mm. The SolidWorks file of the system is available upon request.

Image and Data Analysis

The main experiments were carried out using a 24-well plate at the LEDs' maximum irradiance. A custom-developed script in LabVIEW (National Instruments, Austin, TX, United States) was used to control the optical pacing blue LED in terms of pulse duration (10–50 ms) and frequency (1 Hz), to maintain the optical sensing LED switched on and to trigger the camera which was programmed to record from 5 to 10 s with 10-ms integration times through HC Image Live dedicated software (Hamamatsu Corporation, Sewickley, PA, United States).

After images recording, a second LabVIEW script was used to select a region of interest (ROI) for each well and to extract associated traces reported in terms of percent change of fluorescence from baseline ($\Delta F/F_0$). Raw traces

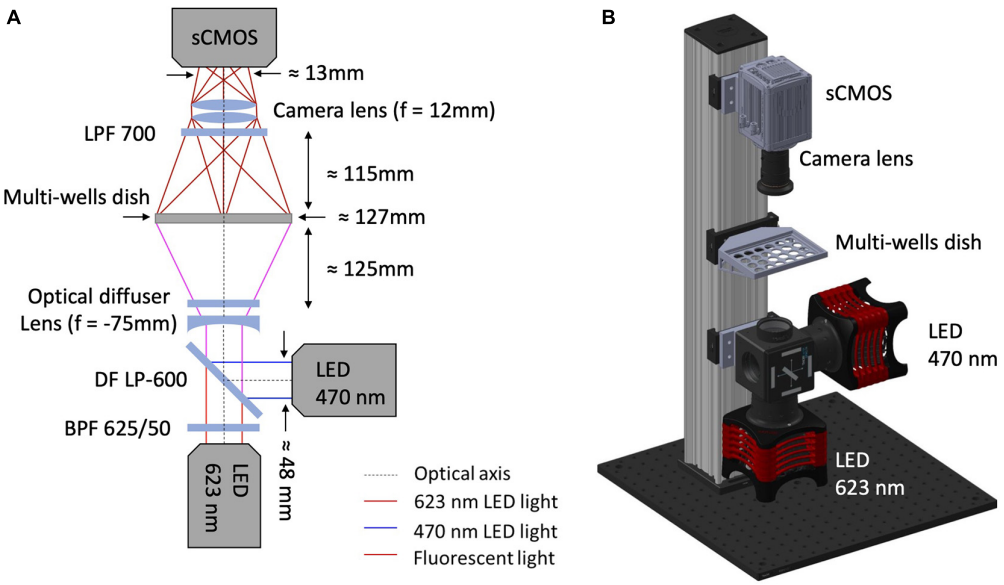

FIGURE 1 | MULTIPLE optomechanical system design. **(A)** Optical scheme of MULTIPLE platform. The excitation system combines a red LED followed by a band-pass filter (625/50 nm) with a blue LED using a large-area dichroic beam mounted on a kinematic fluorescence cube (DFM2/M, Thorlabs). A divergent lens combined with an optical diffuser is used to homogenize the light intensity irradiating the multiwell plate. The fluorescence signal is filtered with a long-pass filter and focused into a sCMOS camera sensor through a camera lens. **(B)** 3D mechanical scheme of MULTIPLE characterized by a final footprint of 450 × 450 × 900 mm. The illumination, detection and sample holder blocks are vertically aligned on a construction rail through drop on rail carriages.

were processed by photobleaching correction and normalization using Fiji-ImageJ (National Institutes of Health, Bethesda, MD) and OriginLab (Northampton, MA, United States) software. AO amplitude (APA) and duration (i.e., APD_{50} and APD_{90}) were automatically extracted from normalized traces averaged over 9 beats.

TABLE 1 | MULTIPLE Optomechanical components list.

Description	Code	Company
Aluminum breadboard	MB4545/M	Thorlabs
900 mm long construction rail	XE25L900/M	Thorlabs
450 mm long construction rail	XE25L450/M	Thorlabs
95 mm construction rail	XT95-750	Thorlabs
Drop-on-rail carriage	XT95RC2/M	Thorlabs
12 mm fixed focal lengths	MVL12M43	Thorlabs
Kinematic fluorescence filter cube	DFM2/M	Thorlabs
High-power LED for microscopy	SOLIS-470C	Thorlabs
High-power LED for microscopy	SOLIS-623C	Thorlabs
Ø2" N-BK7 piano-concave lens	LC1315-A-ML	Thorlabs
High-power driver for solis LEDs	DC20	Thorlabs
Ø2" unmounted N-BK7 ground glass diffuser	DG20-1500	Thorlabs
sCMOS ORCA-Flash 4.0 V3	C13440-20CU	Hamamatsu Photonics
550 dichroic longpass	550DCLP	Omega Optical
625 nm bandpass 50 nm	625BP50	Omega Optical
700 nm longpass	700LP	Omega Optical
Base plate for 95 mm rails	XT95P3	Thorlabs
End plate for 95 mm construction Rails	XT95EC1	Thorlabs
Quick corner cube for 25 mm rails	XE25W3	Thorlabs

RESULTS

Illumination and Detection Performance of MULTIPLE

MULTIPLE allows global illumination of multiwell plates by diverging a collimated beam produced by high-intensity LED matrices. The system combines two LED matrices emitting blue (for optogenetic actuation) and red (for AP sensing) light using a large-area dichroic beam splitter. The red LED matrix is filtered by a 2" band-pass filter to select the optimal spectral range for VSD excitation. Finally, an optical diffuser is placed in front of the divergent lens to homogenize the light intensity across the multiwell plate. This configuration allows a maximum light intensity on the multiwell plane along the optical axis of the order of 30 and 60 mW/cm^2 for the blue and red light, respectively. As a consequence of this basic illumination scheme, the intensity radially decreases away from the optical axis causing non-uniform illumination across the multiwell plates (see **Figures 2A,B**). With the exception of the peripheral wells, we found an intensity reduction below 50% across the 24-well plate for both light sources. While the spatial heterogeneity of the red light intensity is not expected to be a critical issue (considering that potentiometric optical recordings imply normalized fluorescent signals), the heterogeneity of the blue light intensity could introduce interwell differences in the electrical response upon optical stimulation.

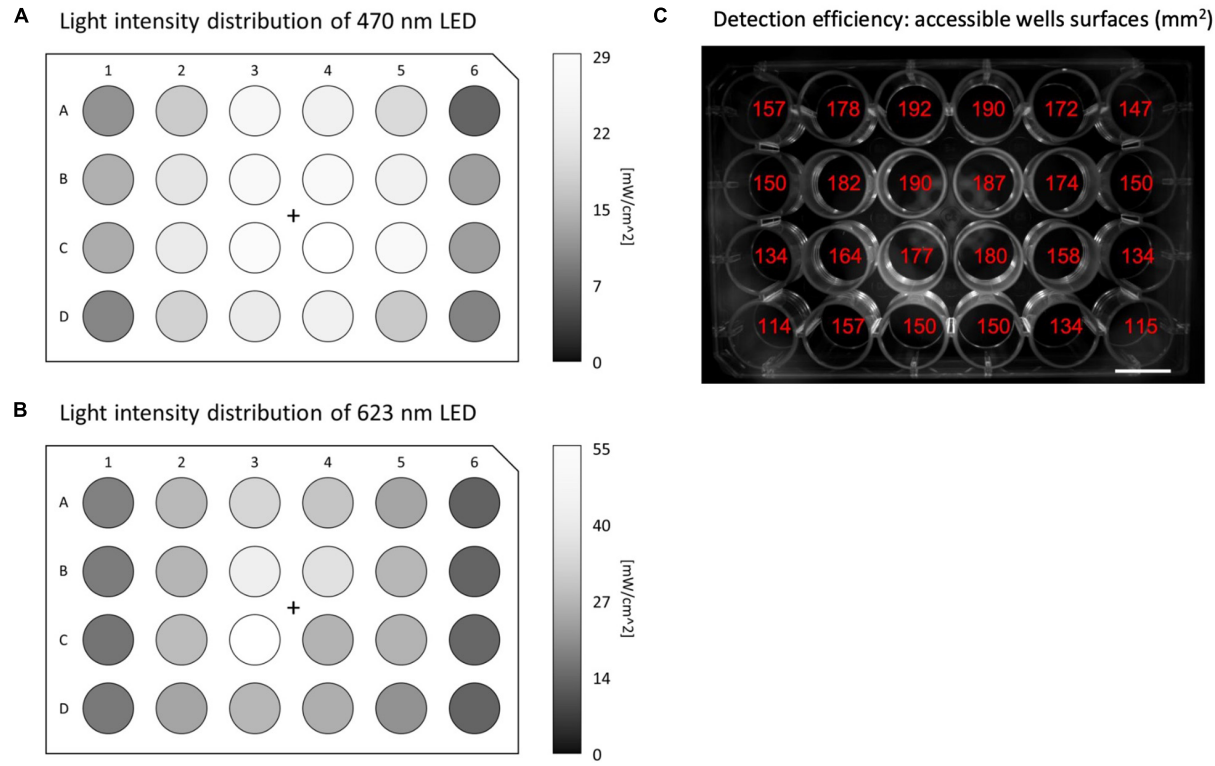

FIGURE 2 | Illumination and detection performances of MULTIPLE. Light intensity distribution across the whole 24-well plate for **(A)** blue and **(B)** red LED light, respectively, using maximum LED power. The intensity of both LEDs radially decreases moving away from the optical axis causing a more than 50% reduction for the outermost wells. **(C)** Image of the 24-well plate reporting for each well the accessible area exploitable for ROI measurements. Detection losses registered at the peripheral wells are introduced by the non-telecentric camera adopted in the optical scheme.

The fluorescence signal coming from the multiwell plate is collected in the forward direction using a camera lens place in front of a 4-megapixel sCMOS camera operating at a frame rate of 100 Hz. The fluorescence signal is filtered by a large-area long-pass filter placed in front of the camera lens. The non-telecentric camera lens adopted in this cost-effective optical scheme intrinsically introduces detection loss in the peripheral wells due to the perspective view of the multiwell plate (**Figure 2C**). However, by choosing a camera lens with an appropriate working distance this unwanted effect can be contained, and even in the outermost wells, signals can be collected from more than 100 mm^2.

Optical Recording of Optogenetically Induced APs in Channelrhodopsin-Expressing HL-1 Cells

MULTIPLE has been tested on mouse atrial myocyte-like cells (i.e., HL-1 cells) expressing blue light-activatable cation channels. To this end, HL-1 cells were either transduced with an AAVV encoding mCherry-tagged ChR2(H134R) or with an LV coding for eGFP-tagged CheRiff. The transduced cell populations were analyzed by flow cytometry, which resulted in the detection of, respectively, 51.74% $mCherry^+$ cells and 97.52% $eGFP^+$ cells (**Supplementary Figure 1**). Confocal imaging of the transduced HL-1 cell populations confirmed the results of the flow cytometric analysis by showing transduction of nearly all cells with the LV, but only a subpopulation of the cells using the AAVV (**Figure 3A**). By loading cell cultures with a near-infrared VSD (i.e., di-4-ANBDQPQ), we assessed the capability of MULTIPLE in combination with optogenetically induced APs. Cells were used at 100% confluency corresponding to $(5.53 \pm 0.06).10^5$ cells/cm^2 in each well. This initial investigation was performed on wells placed close to the optical axis of the MULTIPLE system for achieving maximum light intensities. During channelrhodopsin activation using 30-ms blue light pulses (stimulation frequency of 1 Hz), the cells were constantly illuminated with red light for optical detection of APs. As shown in **Figure 3B**, under these conditions, we were able to detect optically induced APs only in cells transduced with the LV. This result shows that under proper illumination conditions, MULTIPLE allows to optically induce and record APs in HL-1 cells stably expressing CheRiff. This investigation was performed integrating the signal derived from entire wells (190 mm^2). However, MULTIPLE sensitivity allows to detect APs also in a significantly smaller area (**Figure 4**). Setting a signal-to-noise ratio 2 as limit of detection, we were able to detect APs in areas as small as of 0.17 mm^2, which corresponds of 10^3 cells.

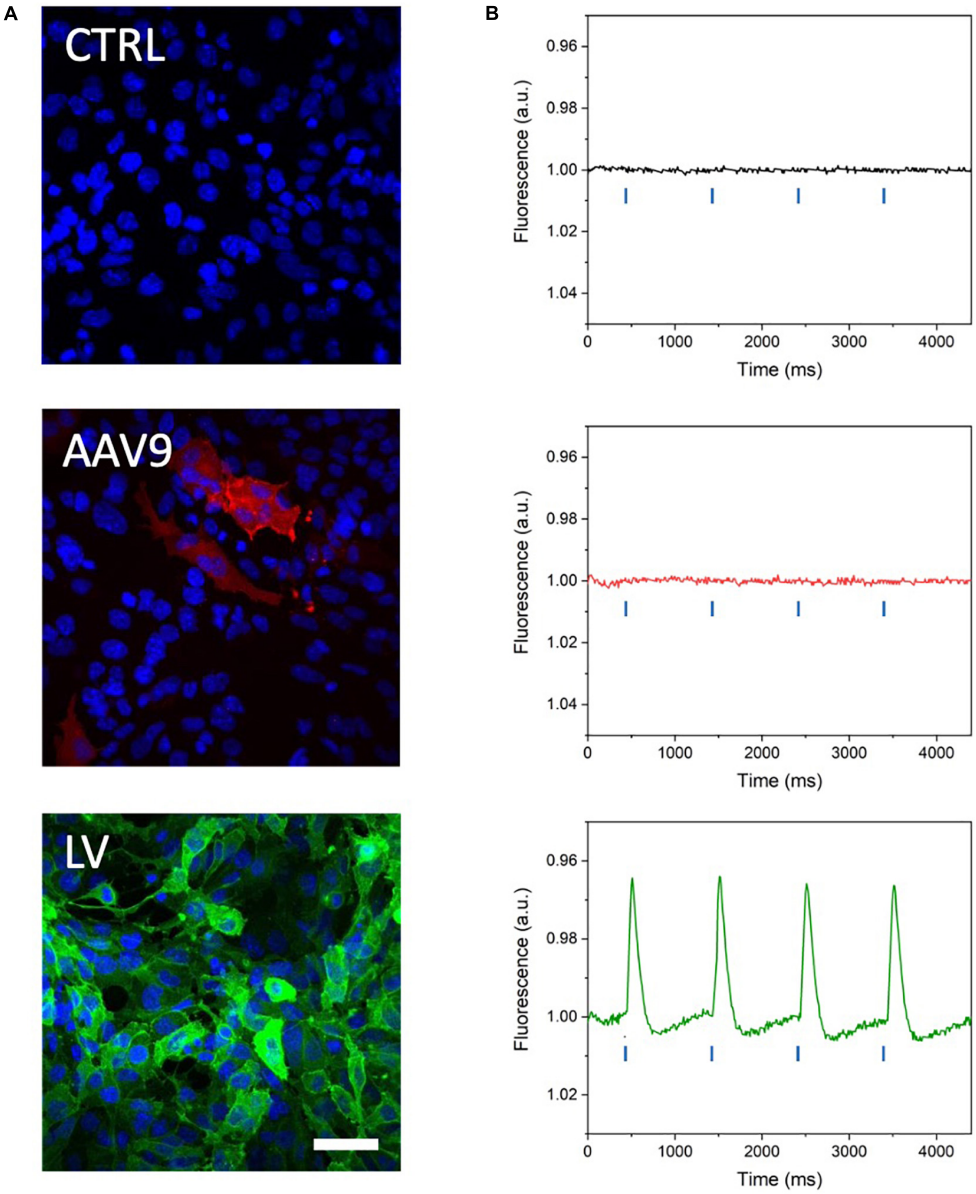

FIGURE 3 | Optical recording of optogenetically induced APs in channelrhodopsin-expressing HL-1 cells. **(A)** Representative confocal microscope images of HL-1 cells expressing blue light-activable ion channels after transduction with a commercial AAV serotype capsid 9-pseudotyped AAVV encoding mCherry-tagged ChR2(H134R) (red channel) and a custom-made vesicular stomatitis G protein-pseudotyped LV encoding eGFP-tagged CheRiff expression (green channel). Cell nuclei were stained with DAPI (blue channel). The higher eGFP signal attests to the more efficient transduction of the HL-1 cells with the LV than with the AAVV. Scale bar = 25 μm. **(B)** Representative traces of optically induced APs registered in AAVV- and LV-transduced HL-1 cell layers after loading of the cells with VSD and stimulating with blue light pulses at 1 Hz (blue lines in the graph). Consistent with the higher transduction efficiency of the HL-1 cells, APs were registered only in the LV-transduced HL-1 cells. CTRL, untransduced HL-1 cells.

AP Kinetics vs. Optogenetic Pulse Duration

In order to investigate if the non-uniform blue light intensity distribution affects the interwell AP kinetics, CheRiff-expressing HL-1 cells were irradiated at maximum light intensities while being stimulated with light pulses of increasing duration from 10 to 50 ms (at 1 Hz stimulation frequency; **Figure 5**). As expected, significant interwell differences in APA, APD_{50}, and APD_{90} were found, especially for pulse duration lower than 30 ms. This heterogeneity is probably related to the fact that CheRiff depolarizing current is not sufficient to activate the whole cell population producing an overall reduction of APA as well as an increment of APD probably ascribable to currents propagation across the electrically coupled confluent cells. It is worth reminding that the main repolarizing current in these cells is I_{Kr}, which undergoes rapid C-type inactivation upon

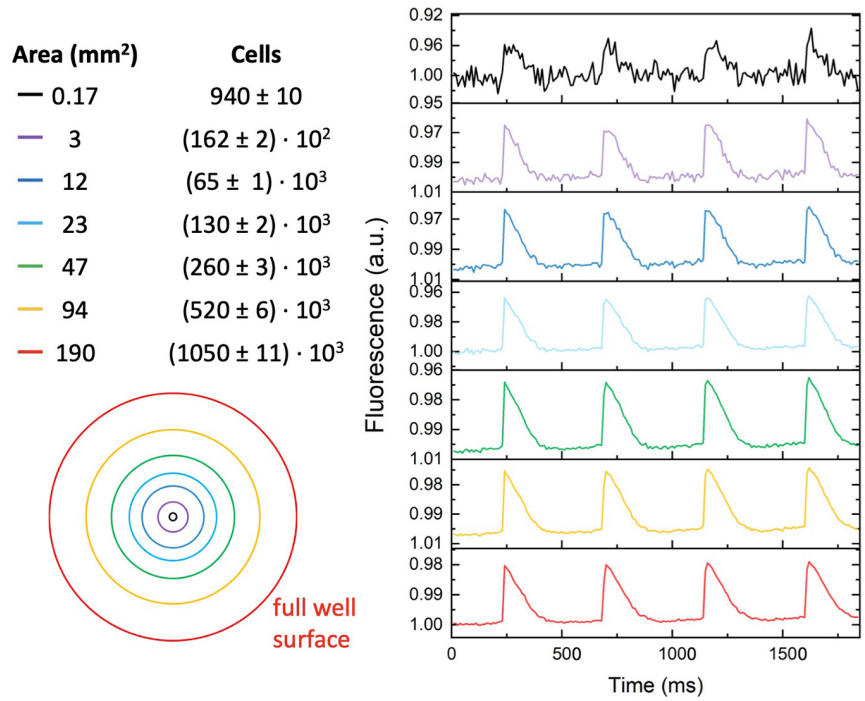

FIGURE 4 | Signal-to-noise ratio *versus* detection area. Representative optical recording of optogenetically induced APs collected from different-sized surface areas (2 Hz stimulation frequency with blue light pulses duration of 30 ms). Reduction of the detection area from the whole well area (≈190 mm^2) to 0.17 mm^2, reduced the signal-to-noise ratio from ≈ 600 to ≈ 2. The estimated number of cells present in the different-sized detected area is indicated in the right column.

depolarization thus reducing the net outward current and delaying repolarization. For pulse duration higher than 30 ms, lower interwell variability of AP kinetics was observed as evinced by smaller standard deviations for APA, APD_{50}, and APD_{90} across wells. The coefficient of variation (CV) calculated for the three AP dynamic parameters, corroborated the trend of decreasing interwell variability in AP kinetics with increasing optical pulse duration (**Figure 6**). This identifies 30 ms as the pulse duration threshold needed in MULTIPLE for proper optogenetic induction of APs across the whole plate. The need to apply relatively long stimulation pulses to elicit APs relates to the low blue light intensity achievable with our optical scheme considering, which is one order of magnitude lower than the blue light intensity typically used for optogenetic stimulation of cardiomyocytes (∼ mW/mm^2) (Crocini et al., 2016; Scardigli et al., 2018). This is nicely illustrated by an experiment in which we raised the blue light intensity by removing the divergence lens to concentrate the blue LED only on the central portion of the multi-well plate. As expected, increasing the light intensity allowed us to optogenetically induce APs using stimulation pulses much shorter than 30 ms (**Supplementary Figure 4**). Finally, to check whether long optogenetic stimulation pulses may affect repolarization, optical recording of optogenetically induced APs (pulses duration: 30, 40, and 50 ms at 0.2 Hz stimulation frequency) were directly compared with single cell patch-clamp recording where APs were induced by inward current injection (2 ms current square pulses, 500–1000 pA, at 0.2 Hz frequency; **Figure 7**). Notably, no differences were found in ADP_{50} and APD_{90} recorded by means of the two approaches, thus demonstrating MULTIPLE's suitability in assessing AP dynamics. Based on these findings, all subsequent measurements were performed at maximum light intensities and by using 40-ms blue light pulses.

MULTIPLE Detection of AP Duration With E-4031

To further validate the high-throughput capability of MULTIPLE as well as to illustrate the range of dynamic information that can be acquired simultaneously, a dose response experiment was performed using the selective $K_v11.1$ channel blocker E-4031. The drug was applied in 7 doses (0 – 10 μM) to CheRiff-expressing HL-1 layers across the entire 24-well plate according to the scheme shown in **Figure 8A**. This specific drug loading configuration was selected to further demonstrate that, by using optimal acquisition parameters in terms of light intensity and pulse duration, undesired effects of optical pacing due to non-uniform illumination can be overcome. Indeed, as clearly depicted in **Figures 8B–D** very similar APD90 values were obtained for wells exposed to the same concentration of E-4031, irrespective of their position in the culture plate. However, randomization in assigning wells with same drug concentration could be beneficial to improve the solidness of data acquired during a parallel investigation. As expected, prolongation of AP duration was observed especially at drug concentrations above 0.5 μM due to E-4031 inhibiting the rapidly activating delayed

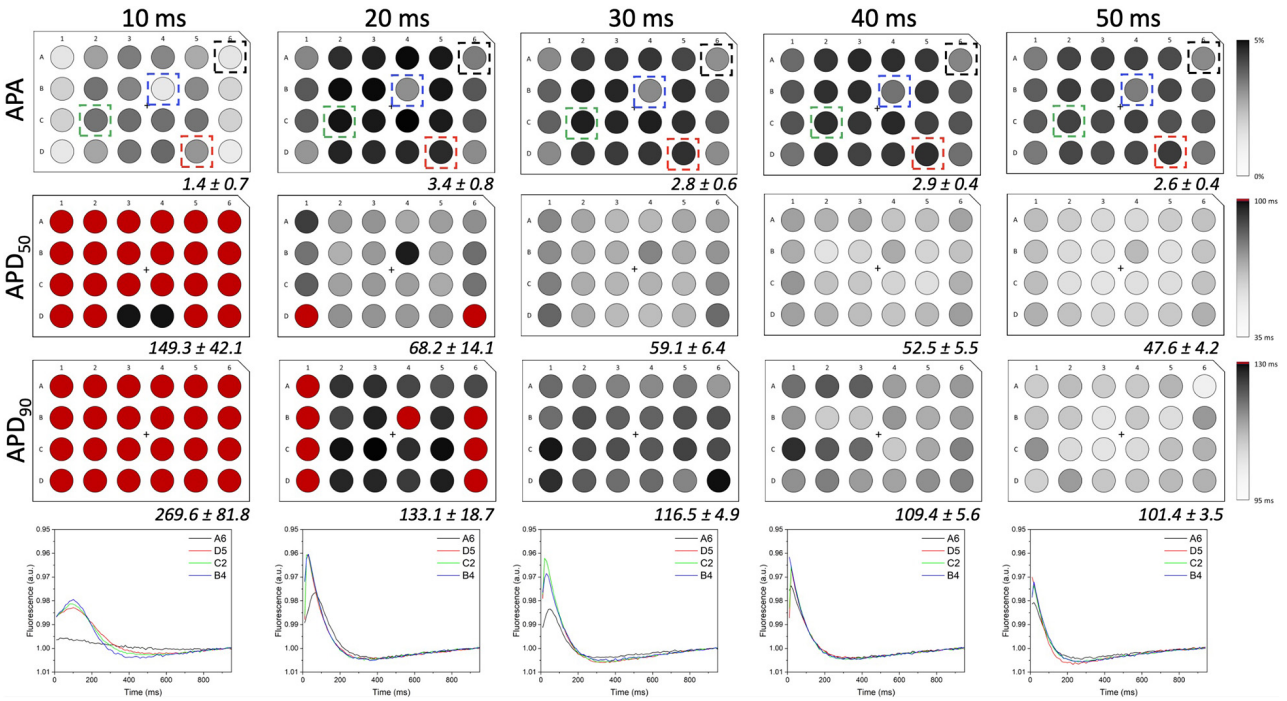

FIGURE 5 | AP kinetics *versus* optogenetic pulse duration. APA and AP duration (i.e., APD_{50} and APD_{90}) values registered from LV-transduced HL-1 cells seeded in 24-well plates and irradiated at maximum light intensities and for the pulse durations indicated at the top of the figure (1 Hz stimulation frequency). Average ± standard deviation of APAs and AP durations were calculated for all 24 wells in the plate and for each experimental condition. Representative traces taken from wells placed at different distances from the optical axis are shown for each stimulation time. By increasing pulses duration from 10 to 50 ms, interwell differences decreased for all the AP parameters considered, thus overcoming the spatial heterogeneity induced by the simplicity of the implemented optical scheme.

rectifier K^+ current (I_{Kr}) (**Figures 8C,D**). Thus, MULTIPLE was able to successfully track the dose-dependent effects of E-4031 in terms of AP duration even at lower concentrations of this class III antiarrhythmic drug (**Figure 9**). The effect of E4031 on AP duration is in line with that observed previously in Hl-1 cells (Wondergem et al., 2012) and in mouse native atrial cardiomyocytes (Nakamura et al., 2010). Interestingly, the decrease of AP amplitude induced by E-4031 has already been reported in HL-1 cells (Wondergem et al., 2012) and likely attributable to depolarization of membrane potential with consequent reduction of inward currents, I_{Na} and $I_{Ca,T}$. Further investigation is necessary to fully clarify this point.

Detection and Modulation of Spontaneous APs on hiPSC-CMs

As a final experiment, we tested MULTIPLE's ability to detect APs in monolayer of hiPSC-CMs at day 30 of differentiation. In this developmental stage, hiPSC-CMs display spontaneous firing activity that retains major functional properties of human native pacemaker centers and respond to heart rate-limiting drugs (Blazeski et al., 2012; Mandel et al., 2012; Karakikes et al., 2015). hiPSC-CMs were loaded with di-4-ANBDQPQ and excited with red LED light in order to detect variations of membrane potential arising from spontaneous electrical activity. This allowed detection of repetitive membrane voltage variations that typically originated from clustered cells and propagated throughout the monolayer (**Figure 10A**). Next, in order to validate MULTIPLE ability to detect pharmacological responses in the hiPSC-CM model, we challenged the system

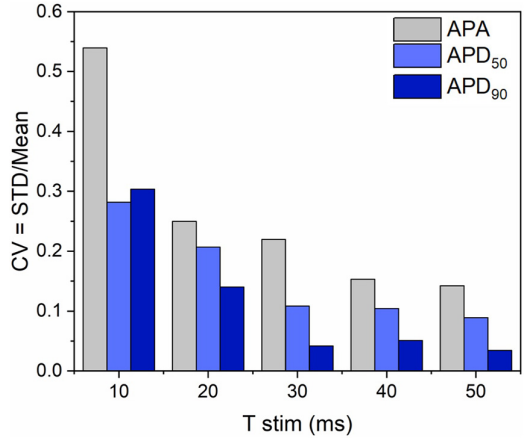

FIGURE 6 | Interwell variability of optogenetically induced APs. Interwell variability of APA and AP duration as a function of the light pulse duration. Upon increasing the optical stimulus from 10 to 50 ms, decreasing trends in the interwell variability of APA and AP duration (i.e., APD_{50} and APD_{90}) were observed, confirming that differences in AP triggering due to non-uniform illumination can be overcome by stimulating with pulses ≥ 30 ms.

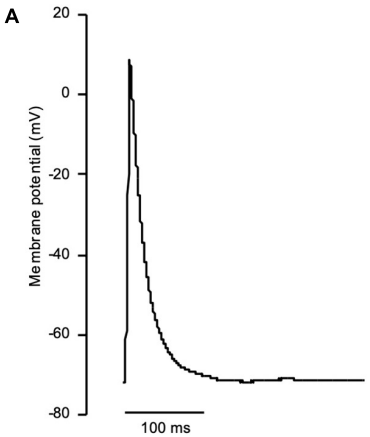

B

	Patch – clamp Stim: 0.2 Hz	MULTIPLE (30 ms) Stim: 0.2 Hz	MULTIPLE (40 ms) Stim: 0.2 Hz	MULTIPLE (50 ms) Stim: 0.2 Hz
MDP (mV)	-69.8 ± 1.5			
APA (mV / %)	89.5 ± 4.5	2.2 ± 0.4	2.2 ± 0.4	2.0 ± 0.3
APD_{50} (ms)	51.2 ± 6.0	47.4 ± 6.7	43.1. ± 5.1	39.7. ± 4.1
APD_{90} (ms)	85.1 ± 8.2	97.4 ± 7.1	91.4 ± 5.9	83.4 ± 6.3

FIGURE 7 | Patch-clamp recording of AP in HL-1 cells. **(A)** Representative AP recording on a HL-1 cells using single cell patch-clamp (whole-cell configuration). APs were elicited at 0.2 Hz in current-clamp mode. **(B)** Table reporting average ± standard error of maximal diastolic potential (MDP), APA, APD_{50}, and APD_{90} measured in patch-clamp cells (number of cells = 15). APA, APD_{50}, and APD_{90} measured with MULTIPLE (pulses duration of 30, 40, and 50 ms) at the same stimulation frequency (0.2 Hz) are reported for direct comparison.

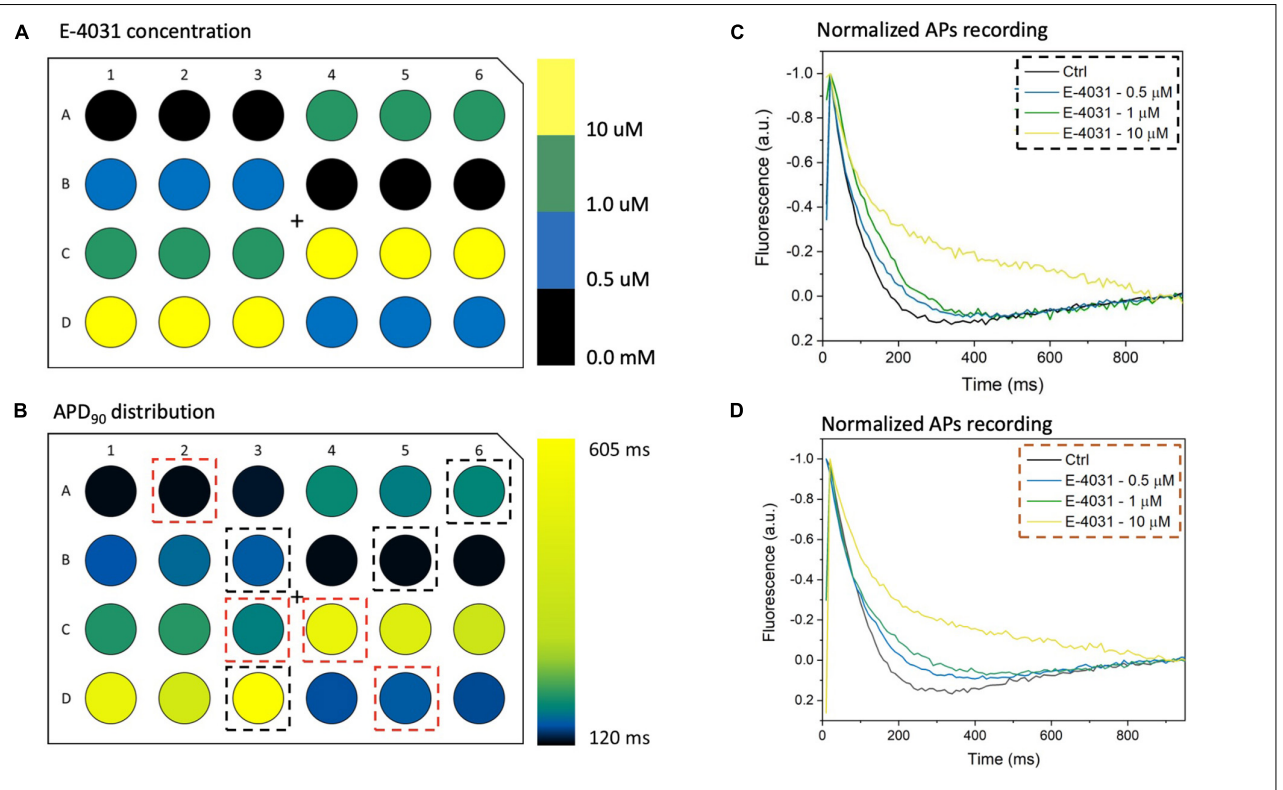

FIGURE 8 | MULTIPLE detection of AP duration with E-4031. **(A)** E-4031, a selective Kv11.1 channel blocker, was applied at 7 different concentrations ranging from 0 to 10 μM to CheRiff-expressing HL-1 cells in a 24-well plate with each dose given to six wells distributed across the whole plate. **(B)** Resulting APD_{90} values were quantified, which attested that interwell variability was not a critical issue since similar values were registered from wells with cells exposed to the same E-4031 concentration. **(C,D)** Average AP traces of CheRiff-expressing HL-1 cells from 10 optical recordings (1 Hz stimulation frequency). For comparison datasets (two for each concentration) were taken from wells randomly positioned. AP duration increased in a drug dose-dependent manner, with clear APD prolongation at E-4031 concentrations higher than 1 μM.

with two different agents, namely ivabradine and carbachol, which are able to negatively modulate native human pacemaker activity by targeting hyperpolarization-activated cyclic nucleotide gated (HCN) channels and muscarinic receptors, respectively. **Figure 10B** shows representative traces of APs detected from hiPSC-CMs before and after application of ivabradine (10μM,

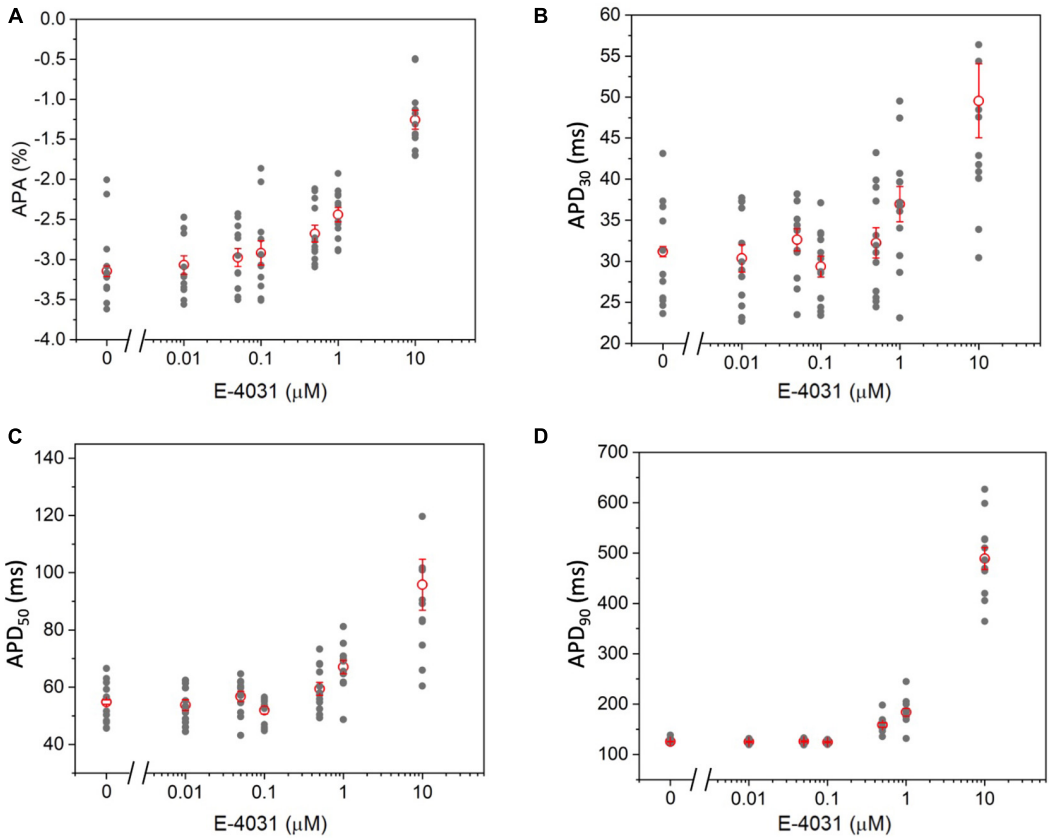

FIGURE 9 | Dose–dependent effects of E-4031 on AP kinetics. **(A)** APA, **(B)** APD_{30}, **(C)** APD_{50}, and **(D)** APD_{90} as a function of E-4031 dose.

Figure 10B) or carbachol (20 nM, **Figure 10C**), which in both cases decreased spontaneous AP firing rate, as expected.

DISCUSSION

Advantages, Limitations, and Optical Implementations

MULTIPLE represents a simple and cost-effective optical platform engineered to enable fast characterization of cardiac electrophysiology. To this end, standard optical technologies to simultaneously control and monitor AP features of cells in multiwell plates are integrated in a compact platform. The main advantage of MULTIPLE is its high-speed investigation capacity achieved by coupling a scientific CMOS sensor with a camera lens. The large field of view enables parallel detection of the optical signal coming from the entire plate thus overcoming limitations of state-of-the-art optical systems, which commonly rely on well-by-well serial analysis. The simplicity of the optical scheme, as well as the cost-effectiveness of MULTIPLE, are further reflected in the illumination path where two high-power LED arrays are used to globally illuminate the multiwell plate enabling simultaneous voltage imaging and optogenetic stimulation. The practical applicability of MULTIPLE was demonstrated by probing the AP-modulating effects of a $K_v11.1$ channel blocker at different concentrations during a single imaging session and by investigating the responses of hiPSC-AMs to chronotropic agents.

Despite its advantages, MULTIPLE has some limitations. The biggest limitation of MULTIPLE is the low and spatially heterogeneous light intensity especially with respect to the blue light. As shown in the Result section, the non-uniform illumination affects the efficiency of optical stimulation, especially for the peripheral wells. In the present work, we show that application of blue light-pulse durations longer than 30 ms activates all the wells with AP kinetics similar to those observed by electrical recordings. However, we cannot rule out the possibility that long-lasting and/or high-frequency optogenetic stimulation of the cells with long blue light pulses alters their electrophysiological responses. Considering that this effect could significantly depend on the cellular type, an *ad hoc* investigation is recommended based on the specific MULTIPLE employment. Another limitation of the proposed platform is that it is not telecentric. Although we showed that this aspect does not represent a true limiting factor in a 24-well plate, this may become problematic using plates with a higher number of wells.

Initially designed as an inexpensive and easy to assemble platform, the performance of MULTIPLE could be improved by adopting specialized optics, more powerful light sources and faster detectors. For example, a more sophisticated illumination

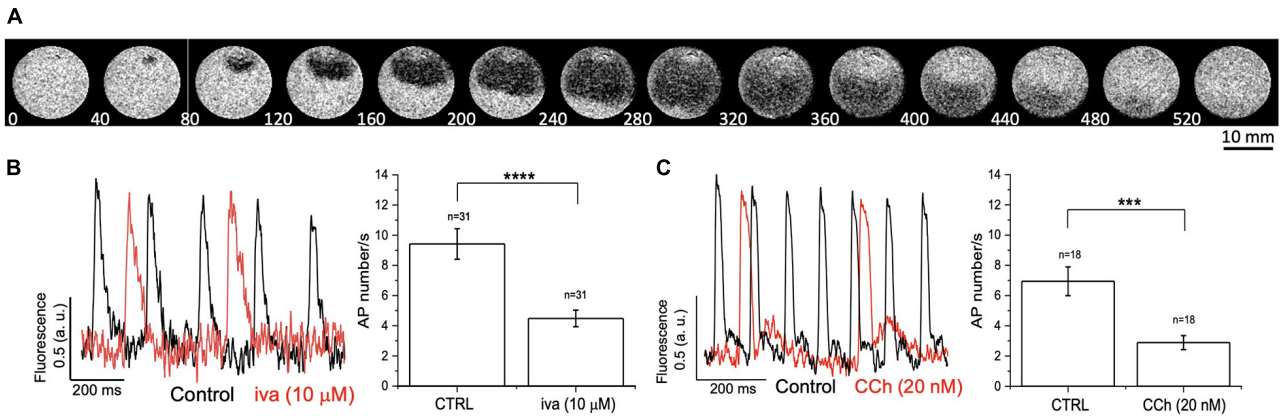

FIGURE 10 | Effect of ivabradine and carbachol on spontaneously beating hiPSC-CMs. **(A)** Representative fluorescence imaging of spontaneous AP propagation in a hiPSC-CM monolayer during a 520 ms recording. **(B,C)** Spontaneous AP traces recorded in hiPSC-CM monolayer in the absence (black lines, CTR) and presence (red lines) of ivabradine (Iva, 10 μM) or carbachol (CCh, 20 nM). Histograms represent AP number/s, expressed as mean ± standard error of the mean, before and after Iva or CCh treatment. ****$p < 0.0001$ CTRL vs. Iva (10 μM); ***$p < 0.001$ CTRL vs. CCh (20 nM).

scheme based on high-power LEDs and projection lens could be employed to maximize and homogenize the light intensity across the multiwell. Moreover, orthographic collection of the fluorescent signal using a high-resolution telecentric lens would be very beneficial in increasing the detection efficiency from all wells. Finally, the system could be equipped with a next-generation CMOS sensor capable of reaching kHz frame rates in a full-frame configuration, which would be advantageous for recording the fast up-stroke phase of cardiac APs.

Applicability

Screening compound libraries of drug candidates is expensive, time-consuming and usually involves extensive use of animal models. To ameliorate cost effectiveness ratio, predictive *in vitro* models of cell monolayers in multiwell plates are increasingly being utilized for drug screenings because of their simplicity and the low consumption of candidate compounds and target cells. In the field of excitable cells, such as cardiomyocytes or neurons, fast and reliable *in vitro* approaches to study drugs modulating ion channel activity in multicellular preparations are particularly appealing but are still poorly available among current experimental sources. MULTIPLE fills at least part of this gap, providing a screening tool able to detect cardiac AP profiles of cell monolayers in 24-well plates. Importantly, using MULTIPLE, the assessment of the acute effects of a drug on the cardiac AP was rapid and accurate, which provides a great advantage compared to classical single cell-recordings by the patch-clamp technique. Indeed, MULTIPLE allowed fast investigation of drugs effect in HL-1 cells as demonstrated employing the selective $K_v11.1$ channel blocker (E-4031), in a dose titration experiment. Furthermore, being designed for use in combination with multiwell plates, MULTIPLE allows parallel testing of various compounds and/or of a single compound at different concentrations, reducing the variability due to use of different cell batches or other experimental variables usually present in subsequent experimental sessions. As proof of principle MULTIPLE has been also used to assess electrical dynamic in spontaneously beating hiPSC-CM. The sensitivity of the platform allows to monitor wave propagation within a single well thus opening the possibility to test the effects of drug on conduction velocity. Finally, we validated MULTIPLE's ability to detect pharmacological responses in the hiPSC-CM model using ivabradine and carbachol, which both gave expected effect on spontaneous electrical activity. This finding further extends and corroborates MULTIPLE potential as valuable experimental approach to study the effect of drugs on cardiomyocyte electrical properties.

Based on the studies described above, future applications will explore the potential of MULTIPLE to detect mid- and long-term effects of biologically relevant compounds in the hiPSC-CM model. To this end, MULTIPLE will be equipped with a heating system and O_2/CO_2 regulation, which are crucial to preserve the excitability of living cells in long-term experiments. Furthermore, future investigations will explore whether MULTIPLE can be used in combination with other cell types, including c smooth muscle cells and neurons differentiated from hiPSCs. All these cell models are readily amenable to genetic modification and at present represent appealing platforms of relevant translation value for preclinical screening and safety studies of novel drug candidates.

DATA AVAILABILITY STATEMENT

The original contributions presented in the study are included in the article/**Supplementary Material**, further inquiries can be directed to the corresponding author.

AUTHOR CONTRIBUTIONS

LSac, CCr, LSar, and EC contributed to the conception and design of the study. CCi, LSac, and CCr developed and characterized

the optical system. LSac and SB developed the software. AV produced the lentivirus. LL syntetized the VSD. FP contributed with equipment. SB, VB, and UM performed the transfection. SB, VB, LSac, and CCr performed the optical measurements. CCr and LSac performed the analysis. LSac, VB, and CCr wrote the first draft of the manuscript. All authors contributed to manuscript revision, read, and approved the submitted version.

FUNDING

This work was supported by Telethon–Italy (GUP19012).

ACKNOWLEDGMENTS

Annemarie Kip and Cindy I. Bart (Laboratory of Experimental Cardiology, Leiden University Medical Center, Leiden, Netherlands) are gratefully acknowledged for LV production.

SUPPLEMENTARY MATERIAL

The Supplementary Material for this article can be found online at: https://www.frontiersin.org/articles/10.3389/fphys.2021.692496/full#supplementary-material

REFERENCES

Ashraf, M., Mohanan, S., Sim, B. R., Tam, A., Rahemipour, K., Brousseau, D., et al. (2021). Random access parallel microscopy. *Elife* 10:e56426. doi: 10.7554/eLife.56426

Blazeski, A., Zhu, R., Hunter, D. W., Weinberg, S. H., Zambidis, E. T., and Tung, L. (2012). Cardiomyocytes derived from human induced pluripotent stem cells as models for normal and diseased cardiac electrophysiology and contractility. *Prog. Biophys. Mol. Biol.* 110, 166–177. doi: 10.1016/j.pbiomolbio.2012.07.013

Bruegmann, T., Malan, D., Hesse, M., Beiert, T., Fuegemann, C. J., Fleischmann, B. K., et al. (2010). Optogenetic control of heart muscle in vitro and in vivo. *Nat. Methods* 7, 897–900. doi: 10.1038/nmeth.1512

Claycomb, W. C., Lanson, N. A. Jr., Stallworth, B. S., Egeland, D. B., Delcarpio, J. B., Bahinski, A., et al. (1998). HL-1 cells: a cardiac muscle cell line that contracts and retains phenotypic characteristics of the adult cardiomyocyte. *Proc. Natl. Acad. Sci. U.S.A.* 95, 2979–2984. doi: 10.1073/pnas.95.6.2979

Crocini, C., Ferrantini, C., Coppini, R., Scardigli, M., Yan, P., Loew, L. M., et al. (2016). Optogenetics design of mechanistically-based stimulation patterns for cardiac defibrillation. *Sci. Rep.* 17:35628. doi: 10.1038/srep35628

Dell'Era, P., Benzoni, P., Crescini, E., Valle, M., Xia, E., Consiglio, A., et al. (2015). Cardiac disease modeling using induced pluripotent stem cell-derived human cardiomyocytes. *World J. Stem Cells* 7, 329–342. doi: 10.4252/wjsc.v7.i2.329

Dunlop, J., Bowlby, M., Peri, R., Vasilyev, D., and Arias, R. (2008). High-throughput electrophysiology: an emerging paradigm for ion-channel screening and physiology. *Nat. Rev. Drug Discov.* 7, 358–368. doi: 10.1038/nrd2552

Hansen, A., Eder, A., Bönstrup, M., Flato, M., Mewe, M., Schaaf, S., et al. (2010). Development of a drug screening platform based on engineered heart tissue. *Circ. Res.* 107:35. doi: 10.1161/CIRCRESAHA.109.211458

Hochbaum, D., Zhao, Y., Farhi, S., Klapoetke, N., Werley, C. A., Kapoor, V., et al. (2014). All-optical electrophysiology in mammalian neurons using engineered microbial rhodopsins. *Nat. Methods* 11, 825–833. doi: 10.1038/nmeth.3000

Karakikes, I., Ameen, M., Termglinchan, V., and Wu, J. C. (2015). Human induced pluripotent stem cell-derived cardiomyocytes: insights into molecular, cellular, and functional phenotypes. *Circ. Res.* 117, 80–88. doi: 10.1161/circresaha.117.305365

Klimas, A., Ambrosi, C., Yu, J., Williams, J. C., Bien, H., and Entcheva, E. (2016). OptoDyCE as an automated system for high-throughput all-optical dynamic cardiac electrophysiology. *Nat. Commun.* 7:11542. doi: 10.1038/ncomms11542

Mandel, Y., Weissman, A., Schick, R., Barad, L., Novak, A., Meiry, G., et al. (2012). Human embryonic and induced pluripotent stem cell-derived cardiomyocytes exhibit beat rate variability and power-law behavior. *Circulation* 125, 883–893. doi: 10.1161/circulationaha.111.045146

Matiukas, A., Mitrea, B. G., Qin, M., Pertsov, A. M., Shvedko, A. G., Warren, M. D., et al. (2007). Near-infrared voltage-sensitive fluorescent dyes optimized for optical mapping in blood-perfused myocardium. *Heart Rhythm.* 4:1441. doi: 10.1016/j.hrthm.2007.07.012

McGlynn, K. P., LaChaud, Q., Burton, F. L., and Smith, G. L. (2018). Measurements of action potentials, intracellular Ca2+ and contraction in stimulated isolated adult cardiomyocytes using CellOPTIQ® platform for lead development screening. *J. Pharmacol. Toxicol. Methods* 93:119. doi: 10.1016/j.vascn.2018.01.406

Nakamura, H., Ding, W., Sanada, M., Maeda, K., Kawai, H., Maegawa, H., et al. (2010). Presence and functional role of the rapidly activating delayed rectifier K(+) current in left and right atria of adult mice. *Eur. J. Pharmacol.* 649, 14–22. doi: 10.1016/j.ejphar.2010.08.025

Pioner, J. M., Santini, L., Palandri, C., Martella, D., Lupi, F., Langione, M., et al. (2019). Optical investigation of action potential and calcium handling maturation of hiPSC-cardiomyocytes on biomimetic substrates. *Int. J. Mol. Sci.* 20:3799. doi: 10.3390/ijms20153799

Sartiani, L., Bochet, P., Cerbai, E., Mugelli, A., and Fischmeister, R. (2002a). Functional expression of the hyperpolarization-activated, non-selective cation current I(f) in immortalized HL-1 cardiomyocytes. *J. Physiol.* 545, 81–92. doi: 10.1113/jphysiol.2002.021535

Sartiani, L., Cerbai, E., Lonardo, G., DePaoli, P., Tattoli, M., Cagiano, R., et al. (2002b). Prenatal exposure to carbon monoxide affects postnatal cellular electrophysiological maturation of the rat heart: a potential substrate for arrhythmogenesis in infancy. *Circulation* 109, 419–423. doi: 10.1161/01.CIR.0000109497.73223.4D

Scardigli, M., Müllenbroich, C., Margoni, E., Cannazzaro, S., Crocini, C., Ferrantini, C., et al. (2018). Real-time optical manipulation of cardiac conduction in intact hearts. *J. Physiol.* 596, 3841–3858. doi: 10.1113/JP276283

Wondergem, R., Graves, B. M., Li, C., and Williams, D. L. (2012). Lipopolysaccharide prolongs action potential duration in HL-1 mouse cardiomyocytes. *Am. J. Physiol. Cell Physiol.* 303, C825–C833. doi: 10.1152/ajpcell.00173.2012

Conflict of Interest: The authors declare that the research was conducted in the absence of any commercial or financial relationships that could be construed as a potential conflict of interest.

Publisher's Note: All claims expressed in this article are solely those of the authors and do not necessarily represent those of their affiliated organizations, or those of the publisher, the editors and the reviewers. Any product that may be evaluated in this article, or claim that may be made by its manufacturer, is not guaranteed or endorsed by the publisher.

frontiers in Physiology

REVIEW
published: 05 October 2021
doi: 10.3389/fphys.2021.720190

Advances in Implantable Optogenetic Technology for Cardiovascular Research and Medicine

*Micah K. Madrid, Jaclyn A. Brennan, Rose T. Yin, Helen S. Knight and Igor R. Efimov**

Department of Biomedical Engineering, The George Washington University, Washington, DC, United States

Optogenetic technology provides researchers with spatiotemporally precise tools for stimulation, sensing, and analysis of function in cells, tissues, and organs. These tools can offer low-energy and localized approaches due to the use of the transgenically expressed light gated cation channel Channelrhodopsin-2 (ChR2). While the field began with many neurobiological accomplishments it has also evolved exceptionally well in animal cardiac research, both *in vitro* and *in vivo*. Implantable optical devices are being extensively developed to study particular electrophysiological phenomena with the precise control that optogenetics provides. In this review, we highlight recent advances in novel implantable optogenetic devices and their feasibility in cardiac research. Furthermore, we also emphasize the difficulties in translating this technology toward clinical applications and discuss potential solutions for successful clinical translation.

Keywords: optogenetic, implantable, arrhythmia, wireless, heart

OPEN ACCESS

Edited by:
Godfrey Smith,
University of Glasgow,
United Kingdom

Reviewed by:
Teun P. de Boer,
Utrecht University, Netherlands
Thomas Beiert,
Universität Bonn, Germany

***Correspondence:**
Igor R. Efimov
efimov@gwu.edu

Specialty section:
This article was submitted to Cardiac Electrophysiology, a section of the journal Frontiers in Physiology

Received: *03 June 2021*
Accepted: *31 August 2021*
Published: *05 October 2021*

Citation:
Madrid MK, Brennan JA, Yin RT, Knight HS and Efimov IR (2021) Advances in Implantable Optogenetic Technology for Cardiovascular Research and Medicine. Front. Physiol. 12:720190. doi: 10.3389/fphys.2021.720190

INTRODUCTION

Optogenetics is a technological approach that utilizes light to control and sense genetically modified neurons or proteins. Though the roots of this technology extend back decades prior, the utility of this concept first broke ground in the field of neuroscience in 2002 when Zemelman et al. developed a method for optically stimulating groups of rhodopsin-sensitized neurons (Zemelman et al., 2002). This light-based methodology gained widespread traction in the field after the seminal publication by Boyden et al. in 2005 (Boyden et al., 2005). Here, cultured rat neurons transfected with the light-gated proton channel Channelrhodopsin-2 (ChR2) uncovered an effective and simple-to-use method for driving neuronal depolarization with blue light. This feat addressed the longstanding need in neuroscience to selectively control and decipher anatomically dispersed groups of neurons, tasks not previously attainable by pharmacological or electrical means (Zemelman et al., 2002; Entcheva, 2013; Joshi et al., 2020). The fast kinetics and cell-type specificity of this new technology led to exponential growth in the field of neuroscience, and in 2010, it was named Nature Methods' "Method of the Year" (Adamantidis et al., 2015; Boyle et al., 2018). To-date, nearly 8,000 papers have been published on optogenetics. Now, almost 20 years since its original proof-of-concept, optogenetics is making significant headway into cardiovascular research and other areas of medicine.

In cardiovascular research and development, there are three main areas of study in which optogenetics holds unique promise: basic scientific research, optogenetic pacing, and optogenetic

termination of arrhythmias. First, in the realm of basic scientific research, the use of light has been a longstanding tool in understanding healthy and abnormal cardiac electrical functioning. In 1976, optical mapping was developed as a means to temporally and spatially measure cardiac action potentials (Salama and Morad, 1976). Optical mapping is now a widely used fluorescent-imaging technique that allows for the visualization of both cardiac action potentials and calcium transients through the use of potentiometric dyes. In optical mapping, light is used as a sensor. On the other hand, in optogenetics, light can be used as a sensor or an actuator. Light as an optogenetic actuator creates myriad opportunities for unprecedented characterizations of electrophysiological properties. For instance, opsins can perturb selective cations within a cell (e.g., H^+, Na^+, K^+, and Ca^{2+}) to exclusively stimulate selective inward currents for the examination of individual channel effects in selective areas of the heart (e.g., cardiomyocytes, purkinje cells, or neurons) under a variety of healthy or unhealthy conditions. Furthermore, optogenetics can be combined with optical mapping to allow for "all-optical" cardiac investigations. All-optical approaches provide high spatio-temporal resolution for both sensing and actuating in a purely contactless manner (O'Shea et al., 2019). The excitation wavelength of ChR2 (∼470 nm) works well with properly selected voltage and calcium sensitive dyes; for instance, the voltage-sensitive dye (di-4-ANBDQBS) and calcium sensitive-dye (Rhod-4) have Ex/Em wavelengths at 640/722 and 540/590, respectively, and since the absorption spectra of these dyes do not interfere with one another, or the opsin, the system works. Klimas et al. successfully demonstrated the capacity of such an all-optical system for electrophysiology studies in human stem-cell derived cardiomyocytes (Klimas et al., 2020). Of course, all-optical approaches only provide relative measurements of physiology (e.g., Vm, Ca^{2+}), making it difficult to determine absolute values of membrane potentials.

Second, in addition to basic scientific interrogations in the laboratory setting, cardiac optogenetics also has the potential for translational biological control (Entcheva, 2013). Light-based pacing offers the ability to induce cardiac excitability in a clinically relevant manner (Nussinovitch and Gepstein, 2015). Currently, only external pacemakers are available to electrically correct irregular heart rhythms and treat debilitating conditions such as heart failure. These devices restore normal rhythm in the whole heart through brief depolarization of small groups of cardiomyocytes. Though nascent in its clinical translation, optogenetic pacing is a beneficial alternative to traditional electronic pacemakers. Conceptually, the optical stimulus strength needed to trigger a response is lower than that of external electrical stimuli, as it only needs to act on a focused group of opsin-expressing cardiomyocytes rather than a large extracellular space for cellular excitation. Furthermore, the technology itself is more physiologic in nature, as selective stimulation of action potentials via ion channels closely mimics that of native excitable cell activation (Zgierski-Johnston et al., 2020). Additionally, unlike electrical devices, optogenetic stimulation only requires targeted light access, so it does not require invasive surgical procedures or bulky delivery hardware (Joshi et al., 2020).

Finally, optogenetics has the potential to be used as a therapy for the termination of arrhythmias. Electrophysiological function disorders such as ischemic heart diseases, cardiomyopathies, channelopathies, myocarditis, genetic abnormalities, and congenital defects, can result in arrhythmias that have the capacity to lead to sudden cardiac arrest (Joshi et al., 2020). Electronic defibrillators are commonly adopted clinical tools for terminating life-threatening ventricular arrhythmias, but they require depolarization of large areas of cells with high energies. They also can result in non-selective excitation of nerves, muscle damage, discomfort, and even pain from irreversible electrochemical reactions (Joshi et al., 2020). Optogenetic termination of arrhythmias is a particularly appealing alternative technology to cardiac defibrillators because light-based defibrillation negates the need for high energy shocks. Overall, the high spatial and temporal resolution of optogenetics hold great promise for the rapid, precise, and controlled termination of ventricular arrhythmias (Joshi et al., 2020).

The field of cardiac optogenetics has already come a long way, with successes evident in isolated cardiomyocytes, cellular monolayers, Purkinje fibers, neural cells, and whole hearts (Pianca et al., 2017). A number of proteins, cells, or tissues of interest can now be rendered optically sensitive through the delivery of viral-vectors (typically adenoviruses or adeno-associated viruses), enabling either light-based depolarization or light-based hyperpolarization (O'Shea et al., 2019). Since its initial isolation and cloning, ChR2 has also undergone several alterations with application-based modifications (e.g., ReaChR for deeper tissue penetration, CatCh for calcium permeability or ChR2-H134R for enhanced conductance) (O'Shea et al., 2019). Such developments now allow for enhanced selectivity with options for diverse spectral and kinetic properties. However, in order for optogenetic technologies to feasibly make their way into the clinic, there is need for both the efficient delivery of opsins into the area of interest as well as the efficient non-invasive access of light stimulation.

For the excitation of opsins, implantable optogenetic devices hold much promise. In this review, we discuss recent advances in optogenetic technology for implantable studies. Specifically, we highlight papers with unique design elements that can fortify subsequent implantable optogenetic studies, focusing on those that are conformal, transparent, and wireless. We conclude with a discussion of the clinical limitations of these technologies, and we provide insights into future alternatives.

OVERVIEW OF IMPLANTABLE OPTOGENETIC DEVICES

The use of optical interfaces for investigating cardiac diseases has evolved as a crucial technology for both diagnostics and therapeutics. Implantable systems can measure a broad range of biophysical, chemical, and environmental signals over time for long-term disease screening and treatments. Conventional medical devices succeeded in their targeted therapy but often lacked biocompatibility in the components of their design. The first cardiac pacemaker was designed with a cadmium battery in

1960. Though the initial design never commercially succeeded, it was later improved with different energy sources (Mond and Freitag, 2014). At this time, in order to create ideal therapeutic results, it was difficult to circumvent incompatible design components from cardiac devices. Until limiting components such as the battery, transistors, and overall configuration could be completely controlled, other design elements (e.g., conformal, transparent, and stretchable) could never be developed.

Flexible and Stretchable Conformal Optoelectronics

Conformal electronics are flexible, stretchable devices that can conform to the diverse topology of specific organ systems to sense and influence physiology. The implementation of this technology in biomedical applications offers important advantages in research, diagnosis, and treatment of disease. However, traditional electronics have been housed on rigid, bittle, and flat substrates. These characteristics are highly incompatible with soft, dynamic organs – such as the heart – and restrict the scenarios in which these devices can be deployed in the body. Conformal electronics solves these limitations by mounting electronic components on deformable substrates in ways that do not disrupt the electronics. In both basic science research and clinical applications, it is ideal that the disruption of native physiology is minimized. These flexible and stretchable electronics are highly suitable for biomedical applications because they allow for soft mechanical coupling to organs to enable physiological sensing and stimulation.

A challenge for conformal devices as a chronic implant is how sufficient power can be supplied to the device. The advent of optogenetics enables optical control of cells and tissue, which is beneficial for conformal electronics because optical stimulation can influence cells with significantly lower power consumption compared to electrical stimulation. Low power consumption means that battery size for powering can be decreased to achieve more miniaturized devices and that wireless devices are increasingly feasible, both of which contribute to implantability. Thus, the optoelectronic configuration is an advantageous next step for conformal electronics.

Conformal optoelectronics can be implemented into already-existing clinical technologies as well as in novel configurations of devices. Kim et al. mounted an array of light-emitting diodes (LEDs) and photodetectors (Kim et al., 2010) onto a balloon catheter (Kim et al., 2011), which is a device commonly employed in non-invasive surgeries. Light-emitting diodes and photodetectors mounted in an array on the balloon retain robust operation despite random bending, folding, and wrinkling during multiple cycles of balloon inflation and deflation. The performance of the electronics does not degrade in the moist dynamic biological environment. The stretchable inflatable nature of the balloon enables soft conformal contact that can be adjusted to accommodate the complex surfaces without disrupting the tissue. Inspired by the native pericardium, Xu et al. developed a novel three-dimensional integumentary membrane that can achieve optical stimulation, pH sensing, mechanical measurements, ECG recording, and temperature sensing across the entire epicardium (**Figure 1**) (Xu et al., 2014). This elastic membrane was custom-formed to match the geometries of the heart onto which it was deployed. This configuration enables consistent reliable yet non-invasive interfacing to all points on the heart throughout dynamic cycles of the heart. The membrane is outfitted with a variety of sensors and actuators, such as LEDs, electrogram electrodes, pH probes, strain gauges, and temperature sensors. This membrane enables electrophysiological mapping under normal beating conditions where LEDs can provide optical stimulation while sensing electrodes monitor electrical activity. In addition, this membrane can be useful when paired with genetically encoded optical reporters where photodetector arrays can sense intrinsic activity as reported by the genetically encoded indicators to monitor native physiology with minimal disruption. This type of multi-sensing platform presents the future possibility of combined use of μ-LED stimulation and optical sensing by photodetectors for colocalized optical control and recording.

Transparent Interconnects and Electrodes

Transparent interfaces for cardiac research have been developed as a promising tool in optical electrophysiology research (Chen et al., 2020). One-dimensional silver nanowires (Ag NWs) and gold (Au) nanomesh can be tuned in devices to be variably transparent with outstanding electrical conductivity and mechanical flexibility (**Figure 2**) (Lee et al., 2015 and Seo et al., 2017). Although these tools are highlighted for their transparent properties, Ag NWs and Au nanomesh are also highly flexible and biocompatible components. Other transparent interfaces that have been developed include indium tin oxide, graphene, and carbon nanotubes.

Transparency is directly controlled by the network density of the material in Ag Nanowires. Decreasing the density will in return create open regions of NWs resulting in transparency. This does, however, reduce conductivity of the electrical pathways and effective interfacial regions, reducing electrochemical performance. During the spin coating, the concentration of Ag NWs can be changed to create different levels of transparency. Chen et al. (2020) reports that the average transmittance from concentrations ranging from 20 to 10, 8.5, and 5.0 mg/mLs were: 57.7% to 76.1%, 81.3%, and 90.0% (**Figure 2b**). Their fabrication strategy can reach high resolutions of approximately 15 μm through photolithography, which is of the highest reported for Ag NWs. **Figure 2c** shows an image of the grid structure with a transmittance of 95.2%. The fabrication strategy presented in this article was also designed to be able to be upscaled for larger interfaces.

Nanosphere lithography and microfabrication techniques have been used to create Au nanomesh interfaces. With nanosphere lithography, the nanomesh properties can be tuned to control transmittance and sheet resistance by altering properties such as sphere size, metal deposition, and reactive ion etching. Seo et al. (2017) demonstrates electrodes with over 70% transmittance at 550 nm with 8.14 $\Omega \cdot cm^2$. In this study, *in vitro* functionality was validated through cellular testing.

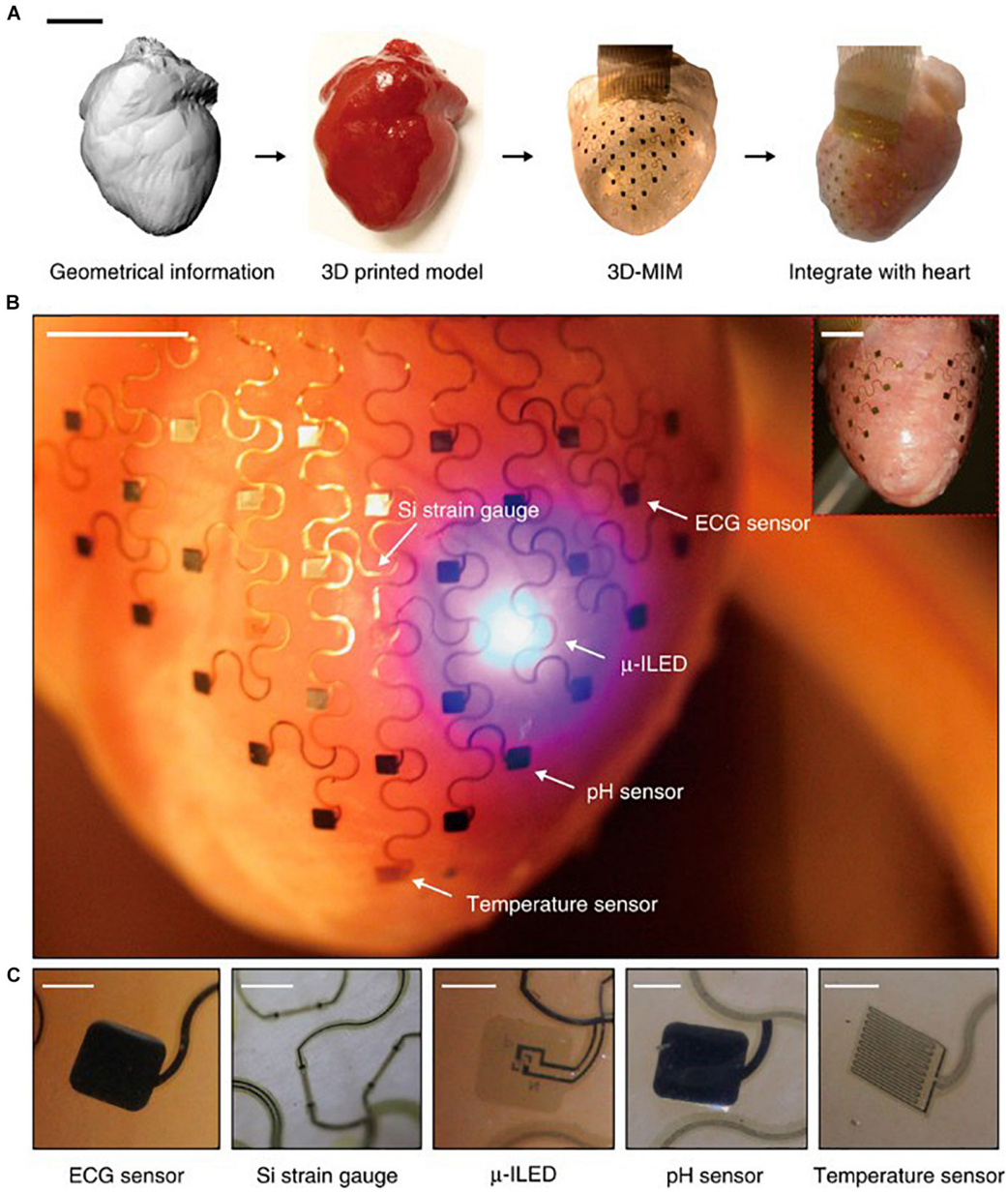

FIGURE 1 | Pericardium-inspired conformal three-dimensional multifunctional integumentary membrane (3D-MIM) for optical stimulation. **(A)** The 3D-MIM substrate is created by capturing the 3D geometry of the heart, rendering a solid model, and casting and curing a thin silicone elastomer. Scale bar, 2 cm. **(B)** A representative image of the 3D-MIM deployed on a Langendorff-perfused rabbit heart with u-ILEDs, pH sensors, and temperature sensors that cover both the anterior and posterior sides of the heart. Scale bar, 6 mm. **(C)** Detailed view of each type of sensor that is integrated into the 3D-MIM. Scale bars, 500 um. Reproduced from Xu et al. (2014).

Au nanogrid electrodes can also be colocalized with microscale inorganic light-emitting diodes (μ-ILEDs) for simultaneous electrophysiological recordings and optical actuation (**Figure 3**). The parameters of this multifunctional system can be easily adjusted to a variety of applications in optogenetics. Obaid et al. (2020) additionally designed this device to be mechanically flexible, highly biocompatible, and to minimize light artifacts during measurement. *Ex vivo* testing showed that they can record abnormal heart rhythms and restore sinus rhythm through optical pacing. Transparent colocalized interfaces are a versatile approach to improving optogenetic research in order to minimize disruption during sensing and stimulation.

Wireless Devices

Wireless optogenetic devices provide a sophisticated, state-of-the-art means for chronic optogenetic stimulation. Conventional means of long-term or sustained light delivery in genetically

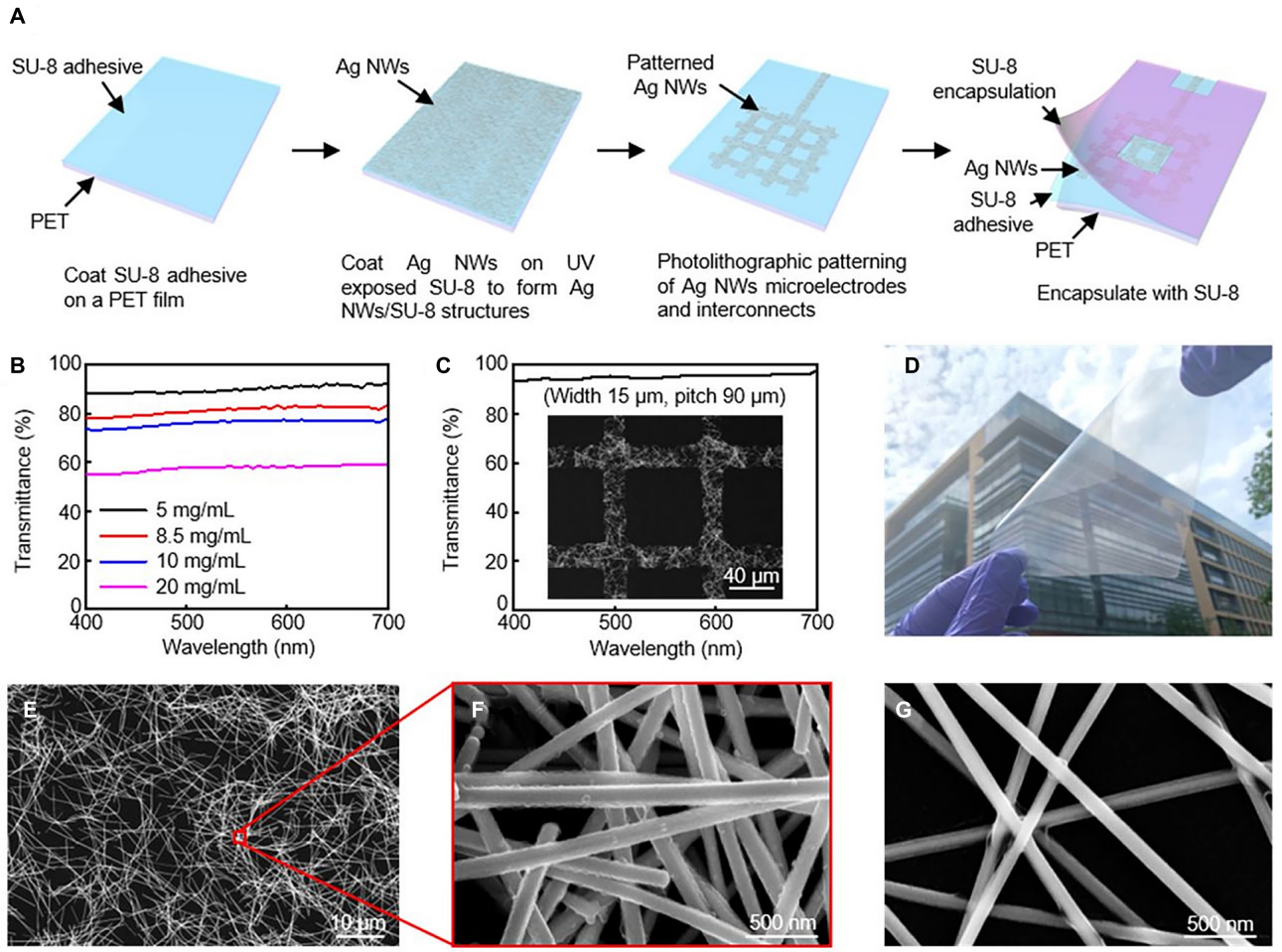

FIGURE 2 | Silver nanowires microelectrodes and interconnects. **(A)** Schematic illustration of fabrication procedure for AgNW microelectrodes and interconnects. **(B)** Transmission spectra for varying concentrations of AgNWs. **(C)** High transmittance AgNW grid from SEM image. **(D)** Optical image of 10 × 10 cm^2 Ag NW/SU-8/PET film. SEM images of AgNW at **(E,F)** 8.5 mg/mL, and **(G)** 5 mg/mL. Reproduced from Chen et al. (2020).

engineered animals have relied on lasers or rigid optical fibers held in place with glues, cements, sutures, and external fixtures (Gutruf and Rogers, 2018). However, these physical tethers impose strict limitations on animal movements and lack controlled scalability for *in vivo* studies (Kim et al., 2021). For cardiac optogenetic applications such as chronic pacing or programmed termination of arrhythmias, wireless devices offer unprecedented flexibility as a minimally invasive therapeutic option.

Current wireless technologies are largely either battery-powered or battery-free (Kim et al., 2021). Both technologies offer stable, stand-alone power supplies, but those that are able to function without batteries (such as near-field inductive power transfer or far-field radio-frequency circuits) obviate the need for intermittent battery replacements. Battery-free wireless devices can be fully implanted inside the body, and the control of light delivery for optogenetic control can occur outside the body. Still, there is ongoing work aimed at improving the capabilities of such devices for optogenetics, as present-day wireless technologies require specialized cages with RF power transfers, particular angular orientations, and separate animal studies (as crosstalk can be a concern).

An ideal wireless optogenetic system for *in vivo* cardiac pacing is one that is fully implantable, mechanically soft, wirelessly rechargeable, and easily controlled with readily available technologies. Since optogenetics originated for neuroscience, much work to-date has been done with applications focused on the brain or spinal cord (Zhang et al., 2019; Wang et al., 2020). For a thorough review of wireless optogenetic devices with a range of applications, we refer the readers to articles published by Gutruf and Rogers (2018) and Han and Shin (2020). However, it should be noted that many of these technological advancements can similarly be applied to the heart. The first study which created and deployed a battery-free, fully implantable multimodal and multisite pacemaker for applications in small animal heart models was just recently published by Gutruf et al. (2019). Here, a highly miniaturized wireless energy-harvesting device weighing only 110 mg displayed capabilities for subdermal implantation

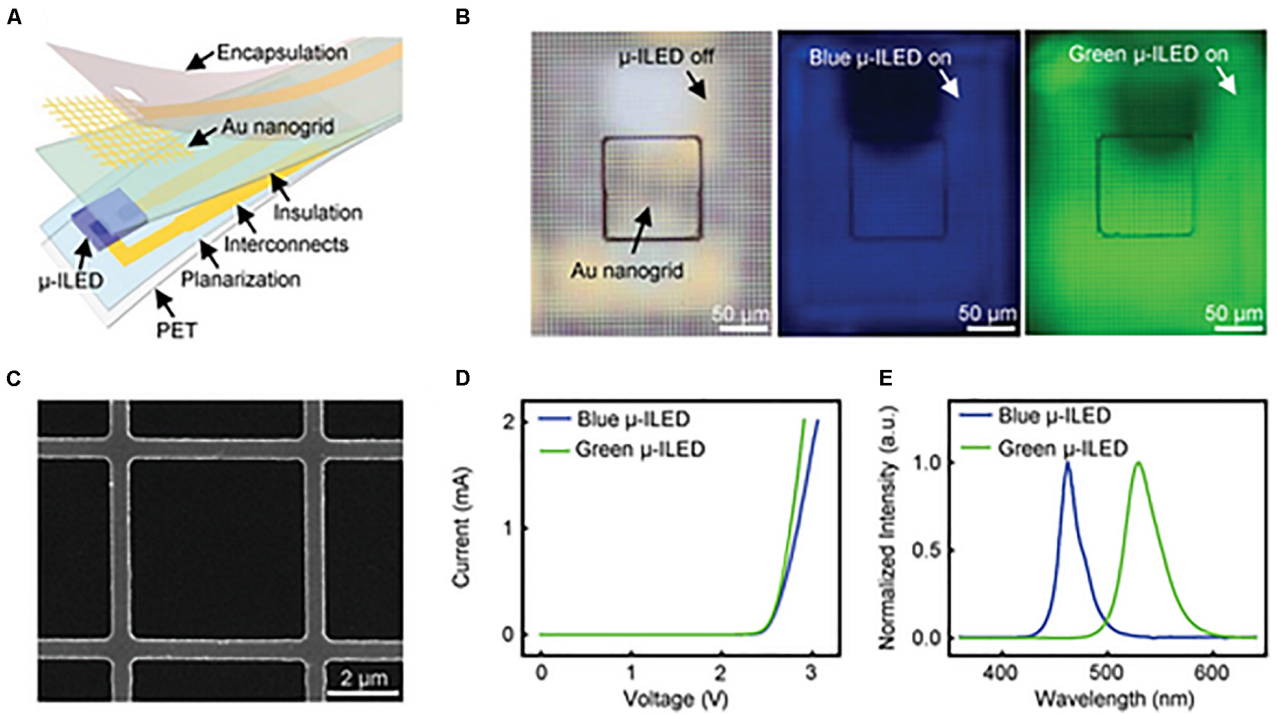

FIGURE 3 | Gold optoelectronic devices for simultaneous optical modulation and electrophysiology possess superior properties including low electrical impedance, high transparency, good cell viability, and superb flexibility. **(A)** Exploded illustration of a multifunctional optoelectronic device containing a transparent gold nanogrid electrode directly on top of a μ-ILED. **(B)** Optical images of a device with μ-ILED turned off (left) and a blue (middle) and green (right) μ-ILED turned on. **(C)** SEM image of a representative Au nanogrid electrode with a width at 500 nm and a line spacing at 5 μm. **(D)** Current and voltage characteristics of the blue and green μ-ILEDs. **(E)** Normalized emission spectra of the blue and green μ-ILEDs. Reproduced from Obaid et al. (2020).

and tolerance to over 200,000 multiaxial cycles of strain without degradation in electrical or optical performance in freely moving ChR2 + rats (**Figure 4**) (Gutruf et al., 2019).

CLINICAL TRANSLATION

Cardiac optogenetics could have some benefits over certain pacemaker or defibrillator devices. Ventricular tachycardia for example, can often be treated with pharmaceuticals or regional ablation. However, patients who suffer from ventricular arrhythmias are susceptible to having them recur as well as even sudden cardiac death. These patients often receive implantable defibrillators (ICDs) which deliver strong electrical shocks or antitachycardic pacing to terminate arrhythmias. In order to successfully terminate the arrhythmia, the ICDs need to fill the excitable gap between the trailing edge of the bypassed and leading edge of the reentrant wave (Adgey et al., 2005). Filling the excitable gap with light in optogenetics could be a solution to treating this condition without further pain or damage to the heart. Common methods utilize combined cell and gene approaches to shorten activation times via multisite pacing and resynchronize areas with conduction blocks (Nussinovitch and Gepstein, 2015). Nussinovich also characterizes the use of ChR2 to suppress certain activities of the heart by inducing hyperpolarization. However, the dependability of implantable optogenetic cardiac devices for arrhythmia treatment is limited. Successful device therapy would depend on both stable, safe optogenetic gene delivery and expression as well as a reliable device. In contrast, a totally electrical cardiac arrhythmia therapy would depend only on the functionality of the device. Optogenetic arrhythmia treatment necessitates a "double jeopardy" scenario where the failure modality of the therapy could be either the gene expression or the device itself.

The benefits of optogenetic control are demonstrated in many studies, but the challenge remains to effectively generate opsin expression *in vivo* in a cell-type specific manner. There are a large number of cell specific promoters known that can permit spatially controlled expression to different parts of the heart (e.g., sinus node, atria, ventricle). There are even genetic motifs that could potentially control the expression at a subcellular level to different domains (Koopman et al., 2017). A number of groups have turned to using viral vectors as a means to introduce optogenes into the heart. Adeno-associated viruses (AAV) are recognized to be safe and potentially a target for potential applications in humans (Ferenczi et al., 2019). Adeno-associated viruses vectors have caused a resurgence in gene therapy efforts and there are many ongoing clinical trials. This method has the ability to introduce new genetic material without leaving behind any viral information (Naso et al., 2017). One successful optogenetic study treating ventricular arrhythmias in a large animal model using AAV

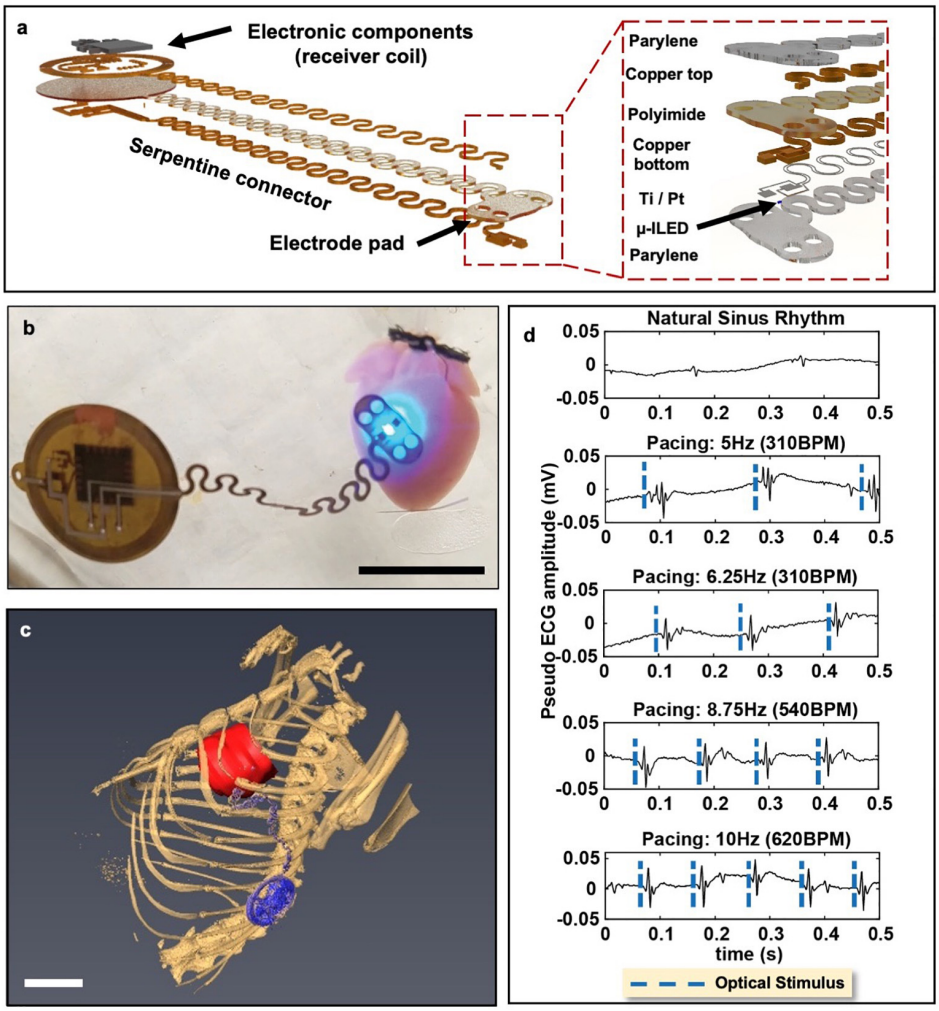

FIGURE 4 | Wireless, battery-free, full implantable optical pacemaker. **(a)** Rendered images of the layered composition of the miniature wireless optical pacemaker. The receiver coil receives energy to power the pacemaker. The electrode pad is placed onto the epicardium for pacing. **(b)** A representative image of the pacemaker performing optical pacing on a ChR2-expressing mouse heart. Scale bar, 1 cm. **(c)** 3D segmentation of anatomical positioning of the pacemaker (blue) with respect to the rat heart (red). Scale bar, 1 cm. **(d)** *Ex vivo* ChR2-expressing mouse hearts were paced at 280 BPM, 310 BPM, 540 BPM, and 600 BPM. Adapted from Gutruf et al. (2019).

vectors was performed by Yu et al. (2017). Here, optogenetic modulation of the sympathetic nerves could reversibly inhibit their neural activity to protect against myocardial ischemia-induced ventricular arrhythmias.

Adeno-associated viruses (AAV) gene therapy strategies need to be potent and have high efficacy to achieve long term stable expression for therapeutic intervention. Clinical studies have shown that AAV methods can achieve therapeutic levels in a dose-dependent manner with expression for over a year. Manufacturing AAV vectors is complex and resource-intensive, however, and the optimization of production is an important goal for therapy (Colella et al., 2018). Achieving this would provide a technology that is: (1) capable of efficient transduction, (2) minimally immunogenic, and (3) could trigger persistent expression over time, even without genomic integration (Katz et al., 2017).

Therapeutic optogenetics has received scrutiny for its immunogenic potential with AAV vectors, but there have been numerous methodologies presented to subside many concerns. Such methodologies include removing surface proteins from the virus that cause the immune response and increasing the efficiency and sensitivity of optogenetic proteins in order to reduce the needed strength of expression (Shen et al., 2020). Although currently the technology is immature, by the time therapeutic approaches are ready, these concerns should be addressed.

The effective therapeutic period of optogenetic defibrillation is limited to the length of optogene expression, which is currently approximately one year. On the other hand, ICDs that provide high energy electrical defibrillation can reliably function for five to ten years. Clearly ICDs have a stronger advantage in longer device functional lifetimes, but the high energy shocks

that ICDs deliver are physically damaging and psychologically taxing (Mark et al., 2008). The appeal of pain-free optogenetic defibrillation is attractive for improving patient experiences with defibrillation therapy.

ALTERNATIVES TO OPTOGENETICS

Due to difficulties in translating optogenetic control into patients, methods for non-invasive optical control are being developed. Graphene has attracted substantial interest due to its unique optoelectronic properties, like high carrier mobility, zero bandgap, and electron hole symmetry. In 2020, Savtcenko et al. present a novel graphene biointerface that does not require the genetic modification of cells but rather capitalizes on the unique optoelectrical properties of reduced graphene oxide (rGO). It is shown that while rGO flakes dispersed at 0.02 to 0.1 mg/ml are in contact with cardiomyocytes, you can optically stimulate the cells at different wavelengths of light. rGO interfaces work through a capacitive energy transfer through electron clouds made at the surface of the polymer (Freitag et al., 2013). This adjacent charge can potentially depolarize whole hearts at the interface between LED devices made for optogenetic tissue. Although this does not currently have the cellular precision that gene therapy can provide, it is a start to a new form of opto-electrical stimulation.

Other facets of control are being developed in transient potential (TRP) channels. TRP channels are a superfamily of cation channels with gates that respond to physical and chemical stimuli (Zheng and Wen, 2019). Thermogenetic tools could be used to drive cardiac activity by increases or decreases in temperature. These tools have been primarily driven through basic science research in the investigation of processes like nutrient uptake, receptor mediated endocytosis and other signaling pathways (Bernstein et al., 2012). X-ray crystallography and Molecular Docking simulations have elucidated critical structural and functional characteristics of these channels (Zheng and Wen, 2019). Although this technology is still very early in its development, there's potential for integration with cardiac biointerfaces.

FUTURE DIRECTIONS

Optoelectronic devices serve as a critical tool to realize the full advantages of optogenetics in monitoring and affecting tissue activity. When paired with genetically encoded fluorescent indicators, photosensors optically monitor physiological activity. Together with transgenically expressed rhodopsin photoreceptors, optical stimulators can modulate biological activity. Implanted optoelectronic devices allow for *in vivo* optogenetic studies in fully conscious freely roaming animals. This configuration enables biological studies in the most physiologically natural environment with minimal hindrance from research instrumentation.

Device-enabled optical stimulation has demonstrated several key advantages, such as lower power requirements and contactless stimulation. Lower power requirements mean that wireless devices and diminished battery sizes are possible. As a result, devices can be further miniaturized and achieve a more non-invasive nature in order to minimally disrupt the body and sense and influence organ systems in a more natural physiological setting.

Transient gene therapy could be possible with bioresorbable devices. These types of temporary devices are composed of biologically benign materials and can self-eliminate *in vivo* via hydrolysis and natural metabolic action in a defined amount of time. Since AAV-mediated gene transfer is effected for up to one year, bioresorbable devices could deliver opsins for local expression and use bioresorbable optical stimulators to administer therapy. Once therapy is complete, both the device and viral transfection self-eliminate in tandem. Although a bioresorbable optical pacemaker for cardiac optogenetic stimulation has not yet been developed, several advancements have been made to this end. Choi et al. demonstrated a bioresorbable cardiac pacemaker that can deliver electrical pacing stimuli for several days and resorb at the end of a therapeutic or study period (Choi et al., 2021). Lu et al. have developed a bioresorbable LED (Lu et al., 2019) that can provide 0.7 mW/cm^2, which is sufficient for metronomic photodynamic cancer therapy but is not strong enough for optogenetic stimulation of intact ChR2 mouse hearts (Bruegmann et al., 2010). With further innovations in bioresorbable LEDs, a fully resorbable optical cardiac stimulator may be possible.

In considering clinical translation of optogenetics, a major barrier is the requirements for cellular changes at the genetic level so that cells endogenously respond to illumination. Adeno-associated viruses-mediated gene delivery to the heart has been attempted in clinical trials with limited success (Greenberg et al., 2016), although preclinical trials of gene delivery are still ongoing. Whether or not gene delivery to the heart, and therefore clinical optogenetics, can be realized remains to be seen in the coming years. Nevertheless, advances in photoelectric transduction alternatives to optogenetics could still allow us to take advantage of the positive aspects of optical cardiac stimulation. Polymer-silicon nanowire composite meshes (Parameswaran et al., 2018), reduced graphene oxide interfaces (Savchenko et al., 2018), and silicon radial junction stimulators (Liu et al., 2019) can enable photoelectric cardiac pacing without the need for genetic modifications.

Since its emergence nearly two decades ago, optogenetics has served as an important tool in understanding the heart in health and in disease. To further realize the advantages of optogenetic techniques, we must devise new devices and light delivery technologies. Conformal electronics that meld to the curvilinear topology of the heart enable high resolution optical stimulation. Transparent electrodes permit light to penetrate through to achieve simultaneous co-localized electrical sensing upon optical perturbation. The low energy demands of LEDs allow for device miniaturization and wireless tether-free monitoring of cell activity. Currently, the clinical use of optogenetics is fairly limited, but optogenetics and the development of optoelectronic devices has ushered in the possibility of a new optical strategy for pain-free clinical treatment of heart rhythm disorders.

AUTHOR CONTRIBUTIONS

MM contributed the abstract, sections related to overview of implantable devices, transparent technology, clinical translation, alternatives to optogenetics, and edits to all sections of the text. JB contributed the introduction and sections conformal and flexible technology sections. RY contributed the sections on wireless device technology and future directions. Each of these authors created the figures in their respective sections. HK performed literature reviews and assisted with the overall formatting and editing. IE devised the scope of the topics, supervised the writing process, and provided feedback. All authors contributed to the article and approved the submitted version.

FUNDING

This work was supported by the National Institutes of Health (NHLBI grants R01 HL141470 and R21 HL152324) and Fondation Leducq (project RHYTHM).

REFERENCES

Adamantidis, A., Arber, S., Bains, J. S., Bamberg, E., Bonci, A., Buzsáki, G., et al. (2015). Optogenetics: 10 years after ChR2 in neurons—Views from the community. *Nat. Neurosci.* 18, 1202–1212. doi: 10.1038/nn.4106

Adgey, A. A., Spence, M. S., and Walsh, S. J. (2005). Theory and practice of defibrillation: (2) defibrillation for ventricular fibrillation. *Heart* 91, 118–125. doi: 10.1136/hrt.2003.019927

Bernstein, J. G., Garrity, P. A., and Boyden, E. S. (2012). Optogenetics and thermogenetics: Technologies for controlling the activity of targeted cells within intact neural circuits. *Curr. Opin. Neurobiol.* 22, 61–71. doi: 10.1016/j.conb.2011.10.023

Boyden, E. S., Zhang, F., Bamberg, E., Nagel, G., and Deisseroth, K. (2005). Millisecond-timescale, genetically targeted optical control of neural activity. *Nat. Neurosci.* 8, 1263–1268. doi: 10.1038/nn1525

Boyle, P. M., Karathanos, T. V., and Trayanova, N. A. (2018). Cardiac Optogenetics: 2018. *JACC Clin. Electrophysiol.* 4, 155–167. doi: 10.1016/j.jacep.2017.12.006

Bruegmann, T., Malan, D., Hesse, M., Beiert, T., Fuegemann, C. J., Fleischmann, B. K., et al. (2010). Optogenetic control of heart muscle in vitro and in vivo. *Nat. Methods* 7, 897–900. doi: 10.1038/nmeth.1512

Chen, Z., Boyajian, N., Lin, Z., Yin, R. T., Obaid, S. N., Tian, J., et al. (2020). Flexible and transparent silver nanowire structures for multifunctional electrical and optical biointerfacing. *bioRxiv [Preprint]*. doi: 10.1101/2020.10.10.334755

Choi, Y. S., Yin, R. T., Pfenniger, A., Koo, J., Avila, R., Lee, K. B., et al. (2021). Fully implantable and bioresorbable cardiac pacemakers without leads or batteries. [Preprint]

Colella, P., Ronzitti, G., and Mingozzi, F. (2018). Emerging Issues in AAV-Mediated In Vivo Gene Therapy. *Mol. Therapy Methods Clin. Dev.* 8, 87–104. doi: 10.1016/j.omtm.2017.11.007

Entcheva, E. (2013). Cardiac optogenetics. *Am. J. Physiol. Heart Circulat. Physiol.* 304, H1179–H1191. doi: 10.1152/ajpheart.00432.2012

Ferenczi, E. A., Tan, X., and Huang, C. L.-H. (2019). Principles of Optogenetic Methods and Their Application to Cardiac Experimental Systems. *Front. Physiol.* 10:1096. doi: 10.3389/fphys.2019.01096

Freitag, M., Low, T., Xia, F., and Avouris, P. (2013). Photoconductivity of biased graphene. *Nat. Photonics* 7, 53–59. doi: 10.1038/nphoton.2012.314

Greenberg, B., Butler, J., Felker, G. M., Ponikowski, P., Voors, A. A., Desai, A. S., et al. (2016). Calcium upregulation by percutaneous administration of gene therapy in patients with cardiac disease (CUPID 2): a randomised, multinational, double-blind, placebo-controlled, phase 2b trial. *Lancet* 387, 1178–1186. doi: 10.1016/s0140-6736(16)00082-9

Gutruf, P., and Rogers, J. A. (2018). Implantable, wireless device platforms for neuroscience research. *Neurotechnologies* 50, 42–49. doi: 10.1016/j.conb.2017.12.007

Gutruf, P., Yin, R. T., Lee, K. B., Ausra, J., Brennan, J. A., Qiao, Y., et al. (2019). Wireless, battery-free, fully implantable multimodal and multisite pacemakers for applications in small animal models. *Nat. Communicat.* 10:5742. doi: 10.1038/s41467-019-13637-w

Han, S., and Shin, G. (2020). Biodegradable Optical Fiber in a Soft Optoelectronic Device for Wireless Optogenetic Applications. *Coatings* 10:coatings10121153. doi: 10.3390/coatings10121153

Joshi, J., Rubart, M., and Zhu, W. (2020). Optogenetics: Background, Methodological Advances and Potential Applications for Cardiovascular Research and Medicine. *Front. Bioengine. Biotechnol.* 7:466. doi: 10.3389/fbioe.2019.00466

Katz, M. G., Fargnoli, A. S., Weber, T., Hajjar, R. J., and Bridges, C. R. (2017). Use of Adeno-Associated Virus Vector for Cardiac Gene Delivery in Large-Animal Surgical Models of Heart Failure. *Hum. Gene Therapy Clin. Dev.* 28, 157–164. doi: 10.1089/humc.2017.070

Kim, C. Y., Ku, M. J., Qazi, R., Nam, H. J., Park, J. W., Nam, K. S., et al. (2021). Soft subdermal implant capable of wireless battery charging and programmable controls for applications in optogenetics. *Nat. Commun.* 12:535. doi: 10.1038/s41467-020-20803-y

Kim, D.-H., Lu, N., Ghaffari, R., Kim, Y.-S., Lee, S. P., Xu, L., et al. (2011). Materials for multifunctional balloon catheters with capabilities in cardiac electrophysiological mapping and ablation therapy. *Nat. Mater.* 10, 316–323. doi: 10.1038/nmat2971

Kim, R.-H., Kim, D.-H., Xiao, J., Kim, B. H., Park, S.-I., Panilaitis, B., et al. (2010). Waterproof AlInGaP optoelectronics on stretchable substrates with applications in biomedicine and robotics. *Nat. Mater.* 9, 929–937. doi: 10.1038/nmat2879

Klimas, A., Ortiz, G., Boggess, S. C., Miller, E. W., and Entcheva, E. (2020). Multimodal on-axis platform for all-optical electrophysiology with near-infrared probes in human stem-cell-derived cardiomyocytes. *Novel Optics Based Approac. Cardiac Electrophysiol.* 154, 62–70. doi: 10.1016/j.pbiomolbio.2019.02.004

Koopman, C. D., Zimmermann, W. H., Knöpfel, T., and de Boer, T. P. (2017). Cardiac optogenetics: Using light to monitor cardiac physiology. *Basic Res. Cardiol.* 112:56. doi: 10.1007/s00395-017-0645-y

Lee, S., Shin, S., Lee, S., Seo, J., Lee, J., Son, S., et al. (2015). Ag nanowire reinforced highly stretchable conductive fibers for wearable electronics. *Adv. Funct. Mater.* 25, 3114–3121. doi: 10.1002/adfm.201500628

Liu, Z., Wen, B., Cao, L., Zhang, S., Lei, Y., Zhao, G., et al. (2019). Photoelectric Cardiac Pacing by Flexible and Degradable Amorphous Si Radial Junction Stimulators. *Adv. Healthcare Mater.* 9:1901342. doi: 10.1002/adhm.201901342

Lu, D., Liu, T., Chang, J., Peng, D., Zhang, Y., Shin, J., et al. (2019). Transient Light-Emitting Diodes Constructed from Semiconductors and Transparent Conductors that Biodegrade Under Physiological Conditions. *Adv. Mater.* 31:1902739. doi: 10.1002/adma.201902739

Mark, D. B., Anstrom, K. J., Sun, J. L., Clapp-Channing, N. E., Tsiatis, A. A., Davidson-Ray, L., et al. (2008). Quality of Life with Defibrillator Therapy or Amiodarone in Heart Failure. *New Engl. J. Med.* 359, 999–1008. doi: 10.1056/nejmoa0706719

Mond, H. G., and Freitag, G. (2014). The Cardiac Implantable Electronic Device Power Source: Evolution and Revolution. *Pacing Clin. Electrophysiol.* 37, 1728–1745. doi: 10.1111/pace.12526

Naso, M. F., Tomkowicz, B., Perry, W. L., and Strohl, W. R. (2017). Adeno-Associated Virus (AAV) as a Vector for Gene Therapy. *BioDrugs* 31, 317–334. doi: 10.1007/s40259-017-0234-5

Nussinovitch, U., and Gepstein, L. (2015). Optogenetics for in vivo cardiac pacing and resynchronization therapies. *Nat. Biotechnol.* 33, 750–754. doi: 10.1038/nbt.3268

O'Shea, C., Holmes, A. P., Winter, J., Correia, J., Ou, X., Dong, R., et al. (2019). Cardiac Optogenetics and Optical Mapping – Overcoming Spectral Congestion in All-Optical Cardiac Electrophysiology. *Front. Physiol.* 10:182. doi: 10.3389/fphys.2019.00182

Obaid, S. N., Yin, R. T., Tian, J., Chen, Z., Chen, S. W., Lee, K. B., et al. (2020). Multifunctional Flexible Biointerfaces for Simultaneous Colocalized Optophysiology and Electrophysiology. *Adv. Funct. Mater.* 30:1910027. doi: 10.1002/adfm.201910027

Parameswaran, R., Koehler, K., Rotenberg, M. Y., Burke, M. J., Kim, J., Jeong, K.-Y., et al. (2018). Optical stimulation of cardiac cells with a polymer-supported silicon nanowire matrix. *Proc. Natl. Acad. Sci.* 116, 413–421. doi: 10.1073/pnas.1816428115

Pianca, N., Zaglia, T., and Mongillo, M. (2017). Will cardiac optogenetics find the way through the obscure angles of heart physiology? *Biochem. Biophys. Res. Communicat.* 482, 515–523. doi: 10.1016/j.bbrc.2016.11.104

Salama, G., and Morad, M. (1976). Merocyanine 540 as an optical probe of transmembrane electrical activity in the heart. *Science* 191:485. doi: 10.1126/science.191.4226.485

Savchenko, A., Cherkas, V., Liu, C., Braun, G. B., Kleschevnikov, A., Miller, Y. I., et al. (2018). Graphene biointerfaces for optical stimulation of cells. *Sci. Adv.* 4:eaat0351. doi: 10.1126/sciadv.aat0351

Seo, K. J., Qiang, Y., Bilgin, I., Kar, S., Vinegoni, C., Weissleder, R., et al. (2017). Transparent Electrophysiology Microelectrodes and Interconnects from Metal Nanomesh. *ACS Nano* 11, 4365–4372. doi: 10.1021/acsnano.7b01995

Shen, Y., Campbell, R. E., Côté, D. C., and Paquet, M. E. (2020). Challenges for therapeutic applications of opsin-based optogenetic tools in humans. *Front. Neural Circuits* 14:41. doi: 10.3389/fncir.2020.00041

Wang, Y., Xie, K., Yue, H., Chen, X., Luo, X., Liao, Q., et al. (2020). Flexible and fully implantable upconversion device for wireless optogenetic stimulation of the spinal cord in behaving animals. *Nanoscale* 12, 2406–2414. doi: 10.1039/C9NR07583F

Xu, L., Gutbrod, S. R., Bonifas, A. P., Su, Y., Sulkin, M. S., Lu, N., et al. (2014). 3D multifunctional integumentary membranes for spatiotemporal cardiac measurements and stimulation across the entire epicardium. *Nat. Communicat.* 5:ncomms4329. doi: 10.1038/ncomms4329

Yu, L., Zhou, L., Cao, G., Po, S. S., Huang, B., Zhou, X., et al. (2017). Optogenetic Modulation of Cardiac Sympathetic Nerve Activity to Prevent Ventricular Arrhythmias. *J. Am. College Cardiol.* 70, 2778–2790. doi: 10.1016/j.jacc.2017.09.1107

Zemelman, B. V., Lee, G. A., Ng, M., and Miesenböck, G. (2002). Selective Photostimulation of Genetically ChARGed Neurons. *Neuron* 33, 15–22. doi: 10.1016/S0896-6273(01)00574-8

Zgierski-Johnston, C. M., Ayub, S., Fernández, M. C., Rog-Zielinska, E. A., Barz, F., Paul, O., et al. (2020). Cardiac pacing using transmural multi-LED probes in channelrhodopsin-expressing mouse hearts. *Prog. Biophys. Mol. Biol.* 154, 51–61. doi: 10.1016/j.pbiomolbio.2019.11.004

Zhang, Y., Mickle, A. D., Gutruf, P., McIlvried, L. A., Guo, H., Wu, Y., et al. (2019). Battery-free, fully implantable optofluidic cuff system for wireless optogenetic and pharmacological neuromodulation of peripheral nerves. *Sci. Adv.* 5:eaaw5296. doi: 10.1126/sciadv.aaw5296

Zheng, W., and Wen, H. (2019). Heat activation mechanism of TRPV1: New insights from molecular dynamics simulation. *Temperature* 6, 120–131. doi: 10.1080/23328940.2019.1578634

Conflict of Interest: The authors declare that the research was conducted in the absence of any commercial or financial relationships that could be construed as a potential conflict of interest.

Publisher's Note: All claims expressed in this article are solely those of the authors and do not necessarily represent those of their affiliated organizations, or those of the publisher, the editors and the reviewers. Any product that may be evaluated in this article, or claim that may be made by its manufacturer, is not guaranteed or endorsed by the publisher.

frontiers in Physiology

REVIEW
published: 18 November 2021
doi: 10.3389/fphys.2021.769586

Novel Optics-Based Approaches for Cardiac Electrophysiology: A Review

M. Caroline Müllenbroich[1], Allen Kelly[2], Corey Acker[3], Gil Bub[4], Tobias Bruegmann[5], Anna Di Bona[6], Emilia Entcheva[7], Cecilia Ferrantini[8], Peter Kohl[9], Stephan E. Lehnart[10,11,12], Marco Mongillo[13,14], Camilla Parmeggiani[8], Claudia Richter[15], Philipp Sasse[16], Tania Zaglia[13,14], Leonardo Sacconi[8,9,17†] and Godfrey L. Smith[2†]*

[1] School of Physics and Astronomy, University of Glasgow, Glasgow, United Kingdom, [2] Institute of Cardiovascular and Medical Sciences, University of Glasgow, Glasgow, United Kingdom, [3] Center for Cell Analysis and Modeling, UConn Health, Farmington, CT, United States, [4] Department of Physiology, McGill University, Montréal, QC, Canada, [5] Institute for Cardiovascular Physiology, University Medical Center Goettingen, Goettingen, Germany, [6] Department of Cardiac, Thoracic, Vascular Sciences and Public Health, University of Padova, Padova, Italy, [7] Department of Biomedical Engineering, The George Washington University, Washington, DC, United States, [8] European Laboratory for Nonlinear Spectroscopy, Sesto Fiorentino, Italy, [9] Institute for Experimental Cardiovascular Medicine, University Heart Center and Medical Faculty, University of Freiburg, Freiburg, Germany, [10] Heart Research Center Göttingen, University Medical Center Göttingen, Göttingen, Germany, [11] Department of Cardiology and Pneumology, Georg-August University Göttingen, Göttingen, Germany, [12] Cluster of Excellence "Multiscale Bioimaging: from Molecular Machines to Networks of Excitable Cells" (MBExC), University of Göttingen, Göttingen, Germany, [13] Department of Biomedical Sciences, University of Padova, Padova, Italy, [14] Veneto Institute of Molecular Medicine, Padova, Italy, [15] German Primate Center - Leibniz Institute for Primate Research, Göttingen, Germany, [16] Institute of Physiology I, Medical Faculty, University of Bonn, Bonn, Germany, [17] National Institute of Optics, National Research Council, Florence, Italy

OPEN ACCESS

Edited by:
Ming Lei,
University of Oxford, United Kingdom

Reviewed by:
Oscar J. Abilez,
Stanford University, United States
Teun P. de Boer,
Utrecht University, Netherlands

***Correspondence:**
Godfrey L. Smith
godfrey.smith@glasgow.ac.uk

[†]These authors have contributed equally to this work

Specialty section:
This article was submitted to Cardiac Electrophysiology, a section of the journal Frontiers in Physiology

Received: *02 September 2021*
Accepted: *18 October 2021*
Published: *18 November 2021*

Citation:
Müllenbroich MC, Kelly A, Acker C, Bub G, Bruegmann T, Di Bona A, Entcheva E, Ferrantini C, Kohl P, Lehnart SE, Mongillo M, Parmeggiani C, Richter C, Sasse P, Zaglia T, Sacconi L and Smith GL (2021) Novel Optics-Based Approaches for Cardiac Electrophysiology: A Review. Front. Physiol. 12:769586. doi: 10.3389/fphys.2021.769586

Optical techniques for recording and manipulating cellular electrophysiology have advanced rapidly in just a few decades. These developments allow for the analysis of cardiac cellular dynamics at multiple scales while largely overcoming the drawbacks associated with the use of electrodes. The recent advent of optogenetics opens up new possibilities for regional and tissue-level electrophysiological control and hold promise for future novel clinical applications. This article, which emerged from the international NOTICE workshop in 2018[1], reviews the state-of-the-art optical techniques used for cardiac electrophysiological research and the underlying biophysics. The design and performance of optical reporters and optogenetic actuators are reviewed along with limitations of current probes. The physics of light interaction with cardiac tissue is detailed and associated challenges with the use of optical sensors and actuators are presented. Case studies include the use of fluorescence recovery after photobleaching and super-resolution microscopy to explore the micro-structure of cardiac cells and a review of two photon and light sheet technologies applied to cardiac tissue. The emergence of cardiac optogenetics is reviewed and the current work exploring the potential clinical use of optogenetics is also described. Approaches which combine optogenetic manipulation and optical voltage measurement are discussed, in terms of platforms that allow real-time manipulation of whole heart electrophysiology in open and closed-loop systems to study optimal ways to terminate spiral arrhythmias. The

[1] http://www.notice.cnr.it/

design and operation of optics-based approaches that allow high-throughput cardiac electrophysiological assays is presented. Finally, emerging techniques of photo-acoustic imaging and stress sensors are described along with strategies for future development and establishment of these techniques in mainstream electrophysiological research.

Keywords: electrophysiology, optogenetics, heart, arrhythmia, fluorescence

1. INTRODUCTION

1.1. Electrodes vs. Light

Our current understanding of myocardial tissue electrophysiology is derived from measurements of action potential features i.e., activation, repolarization, and conduction velocity in myocardial tissue. It has been long known that the 3-dimensional (3D) structure of the tissue and regional differences in cell type composition are key determinants of electrophysiological behavior. Therefore, tools to allow interrogation and control of the electrophysiological state at various sites within myocardial tissue have high value for both research and therapy. Electrode based approaches offer the most direct way of measuring the electrical properties of the heart. However, these techniques present significant technical limitations. The gold standard for transmembrane measurements is the sharp microelectrode that gives high-resistance access to the intracellular medium at a single point to allow transmembrane voltage recording. This is in routine use in isolated tissue preparations (Hicks and Cobbe, 1991; Sicouri and Antzelevitch, 1991; Di Diego et al., 2013) but has limitations including: (i) maintenance of the delicate high-resistance intracellular access in an actively contracting tissue; (ii) the technical challenge associated with maintaining multiple simultaneous intracellular measurements to follow propagation; (iii) the difficulty in applying this technique to record transmural electrophysiology in an intact ventricular wall that in larger mammals can reach 1–2 cm thick. Despite these limitations, this technique has done much to inform scientists and clinicians of details of cardiac physiology, with work on cardiac tissue slices allowing insight into the changes in electrophysiology deep within large animal/ human myocardium (Camelliti et al., 2011). A technically simpler alternative is to use extracellular electrodes to measure potential differences between two points either on the epicardial surface, or within a solution-filled volume containing the heart. At one level this can be in the form of an electrocardiogram (ECG) used routinely for diagnostics in medicine. The most sophisticated version of this technique is body surface mapping which consists of simultaneous recordings from 300-400 points on the human chest and back. This technology, along with significant progress in solving the mathematical "inverse problem," allows the surface body mapping to be used to create and project a 3D electrogram (Rudy, 2013) onto a 3D image of the patient's heart obtained by other clinical imaging modalities. This approach requires a very large investment in facilities and clinical expertise that currently can only be achieved in a few selected centers and cannot be easily used in experimental investigations. Furthermore, while this technique delivers 3D activation maps of the heart, a transmembrane potential signal cannot be extracted from the data. Clinically, activation mapping provides the most accurate way to diagnose conduction defects within the human heart. More routinely across clinical cardiac electrophysiology, catheter electrodes are used to detect local activation timings. These local extracellular recordings include electrode designs to provide a monophasic action potential signal using a signal from a limited depolarized region to represent the "intracellular electrode" (Franz, 1999) and needle electrodes that penetrate the myocardium to different levels to map transmural activation (Pogwizd and Corr, 1987). Cardiac stimulation in parallel with the intrinsic sinus rate activation is a necessary tool for both diagnostic and therapeutic purposes in the clinical setting and an experimental tool in research. Conventional electrodes have the same constraints as voltage measurement systems in terms of accessible surfaces of the heart chambers and the inability to stimulate discrete volumes of myocardium within the ventricle. One additional complication occurs when electrode voltage measurement and stimulation systems are used in parallel; depending on the relative positions of each, the electric fields generated by stimulating electrodes will induce transient voltages in the measurement electrodes which interfere with recording the underlying tissue response during and shortly after stimulation. As will be described in the subsequent sections of this review, many of the constraints associated with electrodes can be overcome with the use of optical probes to measure and actuate electrical signals in cardiac tissue. These optical techniques come with their own limitations, often due to the way light interacts with biological tissues. Therefore, significant sections of this review are devoted to the basic physical principles associated with light/tissue interaction.

1.2. Fluorescent Dyes as Indicators of Cardiac Activity

1.2.1. Voltage-Sensitive Dyes

Voltage-sensitive dyes (VSD) are small fluorescent molecules that incorporate into cell membranes and report changes in transmembrane potential through changes in fluorescence. Ideally, the dye molecules should not change any "normal" functional or structural properties of the cell membrane and only integrate into the plasmalemma as opposed to intracellular membranes which are not involved in electrical activity. Furthermore, the fluorophore should ideally exhibit a high dynamic range, and respond rapidly (circa 1 ms) to any membrane potential changes.

Classic electrochromic VSD such as di-4-ANEPPS (excited in the blue-green band) have been used for decades in optical mapping experiments for detailed measurements of electrical propagation across tissues or whole organs. Since then, improved VSD have been engineered which feature increased overall

brightness and voltage sensitivities through fluorination (Acker et al., 2011). Fluorination of VSD provides a tool for spectral tuning of probes, which is important for compatibility with two-photon imaging techniques (see **Box 2**) and facilitates the combination of optogenetic stimulation with optical recording (Yan et al., 2012; Crocini et al., 2016a). Another class of recently developed VSD, which relies on molecular wire photo-electron transfer (PeT), is becoming popular, thanks to their rapid response kinetics, photostability and relatively high dynamic range of fluorescence changes (20–27 %) (Miller et al., 2012). Originally developed for neuronal studies, PeT-based VSD have been used successfully in cardiac single cell and whole heart studies, proving particularly useful for deep-tissue electrophysiological measurements using two-photon imaging (Ghouri et al., 2018; Salerno et al., 2019; Klimas et al., 2020).

A common issue with dye loading is that the resulting fluorescence may display spatiotemporal variations. Uneven distribution of the probe within the tissue, heterogeneous tissue structure, non-uniform excitation light intensity, probe bleaching, motion artifacts and local changes in cell membrane structure might all contribute to time-dependent changes in detected signal. These variations then need to be removed by scaling the signal at each pixel to have the same range by calculating a $^{\Delta F}/_{F}$ transient.

These confounding signals can be reduced or eliminated using ratiometric approaches, where two separate signals with different responses are divided, canceling shared features while preserving or even amplifying the desired signal components. Ratiometry requires a VSD that undergoes a shift in the emission or excitation spectra depending on membrane voltage and can be employed to account for motion of cardiomyocytes (CM) and the beating heart. PeT-based VSD lack this property and therefore are unsuitable for ratiometric imaging. Care must therefore be taken in experimental design if confounding signals such as motion artifacts are thought to be a major issue. Successful use of a dye isobestic point to provide a ratiometric method that corrects for

BOX 1 | Light penetration in tissue

Physical Basis for Light Scattering in Tissue

Light of a given wavelength can be described as an electromagnetic wave in which the electric and magnetic components oscillate at a particular frequency. It is the vibration of the electric component of light (typically at $\approx 10^{15}$ Hz for red light) which is responsible for scattering: the wave's vibrational energy causes valence electrons in surrounding media to vibrate transiently. The energy absorbed by the electron is quickly released in its entirety again to generate a spherical wavelet of the same frequency (energy conserving elastic scattering). The repetitive absorption and re-emission of energy, typically in the order of femtoseconds for visible light, causes a cumulative delay, which is directly proportional to the number of molecules and hence of electrons the light can interact with per unit volume. The degree to which light slows while propagating through a medium is quantified by the refractive index of the media, which reports the ratio of speed of light in a vacuum (the only place where zero scattering occurs) divided by the speed of light in the medium. Apart from molecule density, the susceptibility of electrons to interact with light also affects the refractive index, which explains why lipid-rich structures such as cell membranes have a higher refractive index than surrounding water (1.45 vs. 1.33) even though they have a lower density (Richardson and Lichtman, 2015).

Scattering

Scattering occurs everywhere light enters a medium, even in transparent media like air, glass or water. In contrast to opaque media, transparent media have two important properties. Firstly, the density of scatterers is so high that many scatterers exist over distances much smaller than the wavelength of light. Secondly, the scatterers are homogeneously distributed which means that lateral scattering is effectively canceled out by destructive interference of secondary wavelets and no light propagates perpendicular to the impinging light wave. In the forward direction, scatterers are activated sequentially and their excitations sum constructively, leading to attenuation-free propagation of light. When a medium is not homogeneous but instead contains structures whose size is comparable with the wavelength of the light (300–700 nm for visible light), strong Rayleigh scattering occurs. The magnitude of Rayleigh scattering is inversely proportional to the fourth power of the wavelength which means that longer wavelengths are scattered less than shorter wavelengths. In biological tissue heterogeneous structures include cellular constituents, such as ribosomes, nuclei, nucleoli, mitochondria, lipid droplets, membranes, myelin, cytoskeletal components, and extracellular matrix constituents such as collagen and elastin. These scatterers are inhomogenously distributed and give rise to substantial lateral scattering which no longer cancels out entirely due to destructive interference. Multiple scattering over a sufficient tissue thickness leads to tissue opacity.

Light Penetration in Tissue

Light can be described as an electromagnetic wave characterized by its wavelength, its power (watts W = Joule/second) and its irradiance (intensity, W/m^2). Only in homogeneous media does light propagate along a straight line. In this case, the energy of light is mostly lost through absorption of the medium and is converted to thermal energy, fluorescence or photobiochemical reactions. In elastic scattering events, the energy of the light is not lost but the direction of light propagation changes. Consequently, irradiance decreases in the direction of propagation in the measure that scattering causes lateral spreading of the light.

The intensity of light passing through a scattering and reflecting sample is given by

$$I_\lambda(d) = (1 - R)I_0 \exp(-\epsilon_\lambda d) \quad (1)$$

where d is the distance traveled in the medium, R is the reflectance, and ϵ_λ is the extinction coefficient which is the sum of the medium's absorption and scattering coefficients (Deng et al., 2014). Using this framework, light scattering can be quantified by a single number; the penetration depth l which describes the depth at which light decays to $1/e$ (about one third) of its incident intensity I_0 and is given by the inverse of the extinction coefficient of the medium: $l = 1/\epsilon_\lambda$.

Absorption

Hemoglobin, myoglobin, and melanin are the primary molecules responsible for visible light absorption in heart tissue. The "near-infrared window" is a section of the electromagnetic spectrum in which biological tissue only weakly absorbs, usually using light with wavelengths of 650–1.350 nm for example in near-infrared (IR) fluorophore excitation or with two-photon microscopy (see **Box 2**).

movement artifact has been successfully implemented (Bachtel et al., 2011). Ratiometric imaging has been employed for optical mapping experiments during open heart surgery (Lee et al., 2012a, 2019). Recent improvements and optimization efforts, including for ratiometric imaging, were described in a recent review article (Acker et al., 2020).

Despite remaining challenges, VSD combined with appropriate imaging methods can provide easy access to high quality voltage recordings from cell culture, tissue, or whole heart preparations with high speed and spatial resolution. Constraints continue to exist in the form of light-tissue interactions (see **Box 1**) which limit the precise spatio-temporal delivery of light patterns in 3D, especially at depth. This may be overcome somewhat through invasive methods, including stimulation through intramural light delivery using optrodes or implantable micro-LEDs (Byars et al., 2003; Caldwell et al., 2005; Zgierski-Johnston et al., 2020). Red-shifting of probes additionally allows one to use longer wavelengths for excitation and emission which experience less scattering and absorption in biological tissues and therefore enable extraction of signals from deeper tissue layers. Examples of such red-shifted VSD include di-4-ANBDQPQ (electrochromic; 620–660 nm excitation) and BeRST (PeT; 630 nm excitation) (Huang et al., 2015). The latter has recently been used in all-optical cardiac electrophysiology platforms for drug screening to accommodate spectrally blue-light induced optogenetic pacing and simultaneous calcium and voltage imaging (Klimas et al., 2020). For ratiometric imaging, the additional spectral bandwidth required to perform emission or excitation ratiometry may impose constraints on multi-modal acquisition. Additionally, to detect action potential features of 1 ms duration (e.g., action potential upstroke) with a fast impulse response, the sampling rate of the optical system must exceed 1 kHz. These demands require the development of sophisticated multi-modal optical imaging systems. Common issues remain across all VSD that still limit their applicability in cardiac electrophysiology; the most prominent of these being the inability to measure absolute voltages with high precision. This combined with the lack of an option for optical measurement of transmembrane current or an easy way to inject either inward or outward current optically means that an all-optical voltage clamp is not yet feasible. However, a successful implementation of an optical dynamic clamp to boost I_{K1} in human inducible pluripotent stem cell (iPSC)-derived CM has been demonstrated (Quach et al., 2018).

1.2.2. Calcium Sensitive Dyes

Due to the fundamental importance of Ca^{2+} in the excitation contraction coupling process in CM, we briefly touch upon calcium (Ca^{2+}) imaging which optically quantifies Ca_i^{2+} transients. Still extensively used since their development in the 1980s, fluorescent probes developed in the Tsien lab combine a Ca^{2+} chelator with a fluorophore, for example fluorescein, stilbene or rhodamine, within the same molecule. A variety of probes are now available which display a range of quantum efficiencies, photobleaching stabilities, sensitivities, and selectivities for Ca^{2+}, as well as differences in excitation spectra and temporal resolution. Some probes shift in emission wavelength upon Ca^{2+} binding to enable ratiometric quantitative measurements of the intracellular free Ca^{2+} concentration (Fura-2, Grynkiewicz et al., 1985), while others are non-ratiometric (Rhod-2). A recent review on ratiometric and non-ratiometric Ca_i^{2+} probes including probes for imaging of sarcoplasmic reticulum Ca^{2+} and probes compatible with potentiometric voltage dyes for multi-modal optical mapping is provided elsewhere (Jaimes III et al., 2016). As with VSD, careful consideration must be given to Ca^{2+} probe compartmentalization and how it could be influenced by probe concentration and loading conditions, especially duration and temperature. Measuring intracellular Ca^{2+} also offers a set of considerations which strongly influence the choice of indicator. Molecule binding affinity determines the Ca^{2+} concentration range within which the indicator is useful. High affinity indicators such as Fluo-3 and Fura-2 are appropriate for cardiac cytosolic Ca^{2+} measurements. However, many intracellular compartments contain much higher concentrations (such as the sarcoplasmic reticulum where Ca^{2+} levels approach 1 mM range) and require low affinity indicators, for example Fluo-5N (Wu and Bers, 2006). It is also important to remember that indicators themselves act as Ca^{2+} ion buffers. Therefore, minimizing the influence of the indicator on physiological processes requires a trade-off between keeping intracellular dye concentration as low as possible while maintaining good signal-to-noise ratio (Paredes et al., 2008).

1.3. Optogenetics: From Genetically Expressed Indicators to Light-Sensitive Ion Channels

Optogenetics, in its broadest sense, describes a set of tools which perform complementary functions: light-driven actuators impose targeted perturbations of either electrophysiological signals (Nagel et al., 2002) or activate intracellular signaling pathways e.g., G-protein coupled receptors (Makowka et al., 2019), while light emitting reporters reveal them (Miesenböck, 2009). This powerful combination of active interrogation and passive observation affords one the ability to infer spatiotemporal dynamics of complex systems that cannot be easily elucidated from the activity of their individual components (Entcheva and Bub, 2016). The genes coding for optogenetic proteins, be they light-emitting reporters or light-driven actuators, are encoded in DNA vectors and introduced under the control of a (potentially cell type-specific) promoter into the genome of the host organism. This causes selected cells to produce the optogenetic proteins with the cell's endogenous synthesizing machinery. Using the cell itself to express the reporter (or actuator) overcomes some of the aforementioned limitations of intracellular loading associated with exogenous probes. The combination of cell-selectivity in gene expression and wavelength-specificity of protein activation, provide the outstanding scientific value of optogenetics. The possibility to spectrally combine optical actuators and reporters allows for completely contact-free all-optical interrogation and control. Recent comprehensive reviews details cardiac applications of

optogenetics over the last decade (Koopman et al., 2017; Entcheva and Kay, 2021).

Optogenetic reporters translate CM electrophysiological signals into optical signals. Virtually all genetically-encoded Ca^{2+} indicators (GECI, reviewed in Kotlikoff, 2007; Whitaker, 2010), are derivatives of the green fluorescent protein (GFP). For example, G-CaMP modulates its output signal through Ca^{2+}-dependent conformational changes that allow or restrict solvent access to the chromophore, which causes increased brightness with Ca^{2+} binding (Chen et al., 2013).

Genetically-encoded voltage indicators (GEVI) report changes in membrane potential from individual cells or populations using voltage-sensitive fluorescent proteins. Current GEVI are limited by the brightness and photostability of fluorescent proteins. The electric field decreases exponentially with distance from the cell membrane, which means the available volume for voltage indicators is restricted to the cell membrane, i.e., a very small fraction of the total cell volume. Additionally, because membrane potential changes can occur over very short timescales, only a few photons are emitted from a restricted volume over a restricted time making their detection statistically difficult. Expressing more reporter molecules bears the risk of observation interfering with the very quantity of interest, electrical excitability, because the mobile charges of voltage probes sensing the cellular membrane potential add a capacitive load to the cell membrane. Whether this increased membrane capacitance influences action potential characteristics is unclear, and seems to depend on the target system, the specific GEVI being used and its overall expression levels (Yang and St-Pierre, 2016). The most commonly used GEVI in cardiac *in vitro* applications so far is ArcLight (Jin et al., 2012), a bright GEVI with relatively slow kinetics, limiting its ability to capture detailed action potential morphology. A new chemigenetic GEVI, Voltron, combines the specificity of genetically encoded reagents with the superior photophysics of synthetic rhodamine dyes like the Janelia Fluor instead of protein-based fluorophores. In a hybrid approach, a genetically expressed scaffold, composed of a voltage-sensitive microbial rhodopsin domain with a dye-capture protein domain, irreversibly binds the synthetic dye (Abdelfattah et al., 2019). Changes in membrane potential alter the absorption spectrum of the rhodopsin domain in Voltron which in turn reversibly modulates the degree of fluorescence quenching of the dye through Förster resonance energy transfer (FRET), yielding a GEVI with increased photon output.

In addition to being used as reporters, optogenetics also includes a suite of genetically-expressed photosensitive actuators which alter the ionic flux through cellular membranes in response to light of specific wavelengths (Nagel et al., 2002). For example, upon illumination with 465 nm, Channelrhodopsin-2 (ChR2) (Nagel et al., 2003; Boyden et al., 2005) a light-sensitive cation channel opens and depolarizes the cell, which can be used to elicit action potentials in excitable cells such as neurons and CM. These channels have been extensively color-tuned (Prigge et al., 2012) and ion pumps expand the toolset to bi-directional control of transmembrane voltage. For example, light-activated potassium channels have been used to inhibit activation by hyperpolarizing the cell (Sierra et al., 2018). Optogenetic actuation allows one to conduct light stimulation or inhibition of cells that do not normally respond to light, supporting the investigation of causal relationships within networks of cells. An exciting development in optogenetics is the possibility of optically controlling exogenous gene expression itself (De Mena et al., 2018). Further manipulation of natural photo switches has expanded the toolkit from light-activated membrane channels to non-channel proteins designed to induce protein-protein interactions (Deisseroth, 2011). These new interaction tools include light-activated enzymes and transcription factors which permit expression of genes in locally defined tissue regions. An important consideration when using optical approaches is the amount of light required to either create sufficient fluorescence signal to be detected or to activate a light-driven protein function. This value is usually a balance between the need to maximize excitation/ photo-conversion and need to minimize photo-bleaching and cellular photo-damage. **Table 1** indicates the light irradiance needed at the sample/ tissue/ cell used in the study of cardiac tissue using a range of light sources and optics. For single photon applications approximately 10–100 mW μm^{-2} is commonly used, while two-photon applications require approximately 10,000 higher power but at approximately double the wavelength.

2. MULTIMODAL IMAGING OF INTRACELLULAR Ca^{2+} AND MEMBRANE POTENTIAL

Cardiac excitation-contraction coupling is governed by the complex and dynamic interplay between membrane ion fluxes and intracellular Ca^{2+} handling processes and manifested in the action potential and intracellular Ca^{2+} transient, respectively. Multimodal acquisitions, i.e., the simultaneous monitoring of calcium and voltage at high spatiotemporal resolution, are important because they provide insight into excitation contraction coupling and arrhythmia mechanism (Salama and Hwang, 2009). The prevailing technique of concurrent

TABLE 1 | Values in this table indicate the approximate irradiance required from different light sources at the sample to image Ca^{2+} or activate ChR2.

Light sources	Wavelength (typical) (nm)	Illumination optics (typical)	Irradiance
Light emitting diodes/ Xe lamps	400–700	Macro/microscope objective	10 mW mm^{-2} Funken et al., 2019, 2020
Continuous wave laser (single photon)	400–700	Microscope (1 μm × 1 μm spot)	5–10 μW μm^{-2} Centonze and White, 1998
Ultrashort pulsed laser (two photon)	700–1100	Microscope (1 μm × 1 μm spot)	5–10 mW μm^{-2} Bush et al., 2007

The wavelengths are chosen to represent common voltage/ Ca^{2+} fluorescent indicators and optogenetic applications.

tracking of fluorescent reporters of either membrane voltage or cytoplasmic Ca^{2+} is optical mapping (Jaimes III et al., 2016).

2.1. Optical Mapping

In optical mapping the most basic fluorescent microscope, a wide-field microscope (or macroscope for large field of view), is employed to flood-illuminate the sample and detect the fluorescence of indicators across the entire field of view. For the heart, in particular Langendorff setups, different geometries can be used that can be based on photodiode arrays (Efimov et al., 1994; Qu et al., 2007) or camera(s) with suitable lenses. This can be single-view (Lee et al., 2011), multiple-camera / multiple-view (Cathey et al., 2019) or single-camera/ multiple-view (Lee et al., 2012b). The wide-field illumination and detection scheme has the advantage of being fast and simple, and it can obtain both topographical and dynamic information. Usually, mercury lamps or LEDs are used for fluorescence excitation and if functional data are to be acquired, a high-speed imaging system is needed to capture and visualize small changes in fluorescence intensity. Considering the minimum sampling frequency necessary, according to the Nyquist sampling theorem, to achieve a temporal resolution suitable for tracking action potential propagation (*ms*) the camera employed in optical mapping must operate at a minimum frame rate of $\sim 2\,kHz$. Frame rate requirements for Ca^{2+} imaging, where Ca^{2+} release from the sarcoplasmic reticulum is the fastest part of the transient and time to peak is in the order of $\sim$ 10–30 ms, are more relaxed. The high costs associated with setups capable of high frame rates can be circumvented by "temporal pixel multiplexing" techniques that embed temporal information in still images to enhance the temporal resolution of imaging methods (Bub et al., 2010). Further requirements for the camera, typically a charge coupled device (CCD) or scientific complementary metal-oxide semiconductor (sCMOS) camera, are very low read-out noise, high quantum efficiency and high well depth to capture the small fluorescence variations associated with action potential or Ca^{2+} release with enough dynamic range and signal-to-noise ratio. Multimodal acquisition can be achieved in several ways. Certain combinations of Ca^{2+} indicators and VSD can be excited by a single light source due to overlapping excitation spectra but distinct emission bands, thereby minimizing signal cross talk (for example the Ca^{2+} indicator Rhod-2 and VSD RH-237, Salama and Hwang, 2009). Separation of the emitted fluorescence signal into different detectors (or different areas of the same sensor) can be achieved with dichroic mirrors and emission filters (Yan et al., 2012). Multiplexing can also occur by excitation, albeit at a reduced temporal resolution, by turning different LEDs on and off sequentially during synchronized image acquisition to excite spectrally-separable voltage and calcium probes during synchronized image acquisition (Lee et al., 2011; Klimas et al., 2020). Low-magnification cardiac optical mapping *in vitro* presents higher demands on the imaging systems compared to whole heart imaging due to the very thin layer of cells generating a signal (Entcheva and Bien, 2006). Hence the need for high-numerical aperture (NA) lenses borrowed from photography, more sensitive detectors and better fluorescent reporters to map voltage and Ca^{2+} excitation in human induced pluripotent stem-cell-derived CM, for example.

One issue that has featured in the majority of optical mapping studies is the requirement that the underlying epicardium does not move substantially during the imaging process over the contraction/relaxation cycle. In early studies, this was achieved by gently pressing the right ventricle/ left ventricle (LV/RV) surface against an optical surface during image capture (Kanai and Salama, 1995). This procedure requires care to prevent the development of ischaemic areas when physically restraining the heart. More commonly, contraction related movement is minimized by chemical electro-mechanical uncouplers such as the myosin inhibitors butanedione monoxime (Kettlewell et al., 2004) or blebbistatin (Fedorov et al., 2007). These compounds block contraction by direct inhibition of the myofilaments, thus limiting motion artifacts whilst preserving electrophysiological function. Though there is published evidence for direct effects of most of the common uncouplers on electrophysiology (Kettlewell et al., 2004; Brack et al., 2013; Kappadan et al., 2020), the magnitude and importance of this limitations is debated. Derivatives of blebbistatin, i.e., para-nitro blebbistatin (Képiró et al., 2014) and para-amino blebbistatin (Várkuti et al., 2016) have chemical features that facilitate their use as uncouplers but similarly require rigorous testing for non-specific effects on cardiac electrophysiology.

In addition to the potential direct effects of chemical uncouplers on cardiac electrophysiology there is also the physiological influence of muscle length and contraction on electrophysiology via a series of mechano-electric feedback (MEF) systems (Quinn and Kohl, 2021). This issue can be circumvented by the application of processing algorithms to the moving isolated heart to track epicardial regions during contraction, thereby minimizing movement artifact (Christoph and Luther, 2018). These approaches are not system-specific and their use is restricted to the few labs able to support the complex post-acquisition analysis. The outcome of these approaches is not just the electrical map of the imaged surface, but the mechanical behavior of the myocardium, by itself an important physiological feature and one which informs the study of phenomena associated with MEF.

Myocardial motion alone can be used to infer activation timings and patterns in the absence of probes to monitor electrical activity (Christoph et al., 2018). When applied to the whole heart during the cardiac cycle, this approach has the complication of interpretation as movement depends on a number of factors including preload and afterload. With this caveat, computationally streamlined image analysis techniques have been developed to track motion of contracting tissue (Burton et al., 2015; Sala et al., 2018). Among other advantages, dye-free imaging works at all wavelengths, which simplifies its integration with spectrally-restricted opsins used for actuation (Burton et al., 2015) and in mechanically similar muscle systems such as cultured CM monolayers these techniques can map patterns of contraction over long periods of time. Furthermore, recently developed random access parallel imaging, inspired by a Newtonian telescope-based addressing of samples without moving parts, demonstrated high-throughput dye-free

imaging in 96-well format (Ashraf et al., 2021). An important consideration when analyzing optical mapping data from thick tissue or whole heart preparations is that this technique lacks optical sectioning. Since illuminating light penetrates several millimeters into highly scattering cardiac tissue, the resultant electrophysiological signals arise from a volume below the tissue surface. As a result, signal features such as transient upstroke morphology and duration are prolonged (Girouard et al., 1996), particularly in optical action potentials. This also has implications for multimodal imaging setups utilizing distinct wavelength excitation light sources, since the longer wavelength light will penetrate deeper, exciting a larger volume of tissue. These features appear at first disadvantageous, however the fact that optical action potentials carry information about the electrophysiology of a tissue volume has been used to reveal subepicardial fiber orientation based on action potential upstroke shape (Hyatt et al., 2005). Dual excitation of spectrally separated VSD has also been used successfully to reveal unique information about transmural heterogeneities and endocardial electrophysiology in rat hearts (Walton et al., 2010). Looking to the future, with the emergence of low-cost high-speed cameras, volumetric optical mapping in small-size hearts has been shown to be possible with multi-plane multi-camera parallel imaging (Sacconi et al., 2020).

2.2. Two-Photon Microscopy for Deep Tissue Access

While optical mapping has proven to be a powerful and versatile tool, in its classic implementation, lack of depth discrimination limits the degree of information on transmural electrophysiology. The increasing need to investigate biological specimens in 3D has driven the development of optical techniques capable of volumetric imaging. As opposed to physical sectioning, these techniques, most notably confocal, two-photon (TPM) and light-sheet microscopy, use optical sectioning to obtain depth-specific information.

In confocal microscopy the sample is sequentially illuminated by a diffraction limited spot, typically employing single photon excitation, and the signal from this spot is registered using a point detector masked by a small pinhole. Similar to TPM, confocal microscopy is a serial sampling instrument which uses the same objective for excitation and detection (epi-configuration). The pinhole gives confocal microscopy its optical sectioning capability because it prevents or at least severely attenuates the detection of light emitted from areas outside of the focal volume. The pinhole is placed in an image plane and typically has a diameter of 1-2 Airy units. The image of the pinhole in the object plane restricts the volume from which photons will be collected, thereby increasing image contrast.

In confocal and wide-field microscopy, contrast is generated from light-matter interactions in which the elementary process (absorption, scattering, etc.) only involves a single photon and which therefore depends linearly on the incident light intensity. Non-linear microscopy methods, such as TPM (Denk et al., 1990) rely on higher-order light matter interactions involving two or more photons for contrast generation. This fundamental difference is the source of numerous new imaging properties. TPM is especially well-suited for deep tissue imaging as it supports imaging scattering samples non-invasively with sub-micrometer resolution in 3D. Moreover, due to the excitation process, which results from the simultaneous absorption of two photons, there are a number of unique advantages such as reduced specimen photodamage and enhanced penetration depth.

2.3. Optical Sectioning Microscopy in the Intact Heart

Optical sectioning techniques like confocal and two-photon microscopy enable one to look beneath the sample surface to resolve cellular processes and structures within discrete volumes of tissue. A wealth of information can therefore be gained from measurement of cardiac cellular electrophysiology deep beneath the epicardium of the intact heart. Cardiac TPM allows for both *in vivo* and *ex vivo* cellular and cell layer-scale electrophysiological and intracellular Ca^{2+} measurements across the myocardial wall (Rubart et al., 2003; Kelly et al., 2013, 2018; Ghouri et al., 2018). Cardiac TPM has been critical in defining the importance of structural features for transmural conduction, both in healthy tissue and in models of reduced tissue excitability (Kelly et al., 2013, 2018) including confirmation of heterocellular electrical coupling of cardiac myocytes and fibroblasts (Rubart et al., 2018), previously established by optical mapping (Quinn et al., 2016). This is aided significantly by the ability to perform simultaneous two-photon fluorescence and second harmonic generation microscopy, enabling label-free imaging and quantification of collagen in live tissue, an important marker of pathological remodeling in cardiac disease (Martin et al., 2013). For *in vivo* TPM, the motion of the heart becomes a significant technical challenge which cannot be overcome with chemical uncouplers. However, several publications have detailed methodological considerations to allow this type of imaging (Lee et al., 2012c; Vinegoni et al., 2015), which has aided in better understanding of cardiac immune cell motility and trafficking (Kreisel et al., 2010; Li et al., 2013). Here we describe several avenues of cardiac electrophysiological research which continue to benefit from developments in TPM.

2.3.1. Transmural Imaging

Electrical propagation under normal circumstances adopts a significant transmural axis, from the endocardium toward the epicardial surface. Within the intramural space, this electrical wavefront encounters an array of physical discontinuities; blood vessels, extracellular clefts and regions of heterogeneous fibrotic distribution. The laminar arrangement of CM within the ventricle shift and rotate at right angles to each other, sometimes abruptly (within 2–3 cell layers of thickness) (Hooks et al., 2007). These factors have a measurable impact on electrophysiology, even in healthy hearts. In combination with optical mapping, *ex vivo* whole heart recordings yield a wealth of information about ventricular electrophysiology across a wide region, which can then be examined at the cellular scale within the transmural wall, affording greater detail about the influence of microscopic myocardial wall tissue features (cell orientation, cell distribution,

microarchitecture, including the influence of scar tissue in disease) on electrophysiology and transmural conduction. As with optical mapping, electrophysiology can be tracked with rapid scanning TPM in conjunction with VSD such as di-4-ANEPPS, albeit over a restricted field of view using a high-NA objective. The optical sectioning power of TPM however, allows for action potential characteristics at a given transmural depth to be faithfully captured, with 2 kHz scanning rates capable of resolving action potential rise time characteristics in multiple small animal species with similar fidelity to sharp microelectrodes (Ghouri et al., 2015). Serial scanning necessitates slow volumetric rates, which requires electrical stimulation of the heart to generate a repeated sequence of activation, a common approach in isolated perfused heart experiments. This carries the added caveat however that beat-to-beat variability, an important property of whole heart electrophysiology, cannot be examined. Thus, an average profile of transmural electrical conduction can be constructed from sequential volumetric measurements using the electrical stimulus as a timing reference. This approach revealed that surface boundary conditions measurably increase action potential upstroke velocity as the wavefront approaches the epicardial surface transmurally, demonstrating the strong electrotonic load influence on CM action potential properties (Kelly et al., 2013). This technique was also key in describing conduction abnormality in a model of Brugada syndrome, an inherited arrhythmic disorder often characterized by slow conduction, right ventricular arrhythmias and higher risk of sudden death. Combining TPM with computational simulations, it was found that the less compact structural arrangement of the right ventricle made it uniquely susceptible to conduction slowing when myocyte excitability is reduced, particularly at higher heart rates (Kelly et al., 2018).

2.3.2. Electrical Coupling of Implanted iPSC-Derived CM Grafts After MI

The intrinsic regenerative capacity of the heart is limited; estimates place cell turnover in adult humans at 0.5–1 % *per annum* (Bergmann et al., 2009). As a result, ischemic insults (myocardial infarction) activate inflammation-mediated signaling cascades which replace necrotic tissue with a vascularized infarct scar, reducing the overall contractile capacity of the heart and forming a substrate for ventricular arrhythmias. One of the promising repair strategies to emerge in recent years involves implantation of engineered heart tissue (EHT) constructs, grown from iPSC-CM, directly over the infarct to restore function. This has met with some success in both small (Matsuo et al., 2015; Pecha et al., 2019) and large animal models (Gao et al., 2017), but questions remain over the extent of EHT coupling to native myocardium, as well as the long-term survival of the originally-implanted cells. Addressing these questions has generated a number of technical challenges that TPM can help overcome (Weinberger et al., 2016). Electrophysiological assessment via optical mapping of voltage sensitive dyes alone struggles to fully distinguish between electrical activity of the EHT and normal myocardium. It has been known for some time that fluorescent "bleed-through" from surviving endocardial tissue (or, if the infarct is thin enough, septal tissue) will contaminate the optical map of the infarct with implanted EHT, giving the appearance of relatively healthy looking action potentials from largely-free scar. Gene-silencing of G-CaMP indicators expressed in the EHT was also observed to occur when hearts were explanted 4 weeks post-surgery. TPM helped to overcome these setbacks by allowing delineation of EHT and infarct electrophysiology through serial optical sectioning, demonstrating that electrical coupling of EHT and native myocardium can occur, albeit with a relatively low success rate (Weinberger et al., 2016). While the above patches were developed with the aim of aiding contractile function, another exciting application of engineered tissue is to serve as electrical conduction tracts. This has been shown to efficiently bridge atrio-ventricular conduction in a murine model of atrio-ventricular node failure (Cingolani et al., 2014), and shows that electrical integration of engineered tissue constructs can indeed be achieved with potentially far-reaching consequences for translation (Kohl, 2014). In any case, the further development of EHT-based organ repair is uniquely poised to benefit from the discriminating power that TPM optical sectioning provides.

2.3.3. Origin of the Electrical Conduction Through Myocardial Infarct Scar

Questions remain over electrical interaction between the infarct scar and healthy myocardium. Surviving islands of myocardium and remnant electrical activity within the infarct are well-documented (Walker et al., 2007), with myofibroblasts implicated in permitting electrical propagation between the border zone and surviving myocardium within the scar itself (Quinn et al., 2016). Several studies using TPM have sought to elucidate the mechanism of infarct conduction. Combined optical mapping-TPM systems and dual voltage and Ca^{2+} labeling has been used to distinguish between myocyte and non-myocyte electrical propagation within the infarct zone in rat hearts, using the absence of an intracellular Ca^{2+} transient as an indicator of non-myocyte electrotonic interaction (Ghouri et al., 2018). A similar analysis of the peri-infarct zone in mice expressing CM-specific GFP, identified non-myocyte electrical activity attributed to myofibroblasts exhibiting markedly slowed action potential upstrokes (Rubart et al., 2018). Engraftment of Connexin-43 (Cx43) expressing non-myocytes (Roell et al., 2007), or over-expression of Cx43 in murine infarct tissue (Roell et al., 2018), aided trans-scar conduction, implicating heterocellular contributions to electrical propagation in the heart. A thorough investigation of myocyte-fibroblast interaction within mouse infarct using a similar CM-specific labeling approach is currently being undertaken.

2.4. Random Access Multiphoton Microscopy in the T-Tubular System

Random access multiphoton microscopy (RAMP) (Sacconi et al., 2012) based on acousto-optic deflectors (AODs) was recently used in combination with novel VSD with improved photostability (Yan et al., 2012) to measure T-tubular action potentials at multiple sites with high spatio-temporal resolution. The authors observed that a tight electrical coupling between distinct membrane domains (i.e., surface sarcolemma and

T-tubules) is guaranteed only in healthy cells. Conversely, experiments on disease models showed that action potential propagation in the structurally remodeled T-tubular system can fail and local spontaneous depolarizations can occur in the electrically disconnected T-tubules (Sacconi et al., 2012). A simultaneous recording of the action potential and local Ca^{2+} release was used to dissect the consequences of electrical defects on intracellular Ca^{2+} dynamics. Specifically, the authors implemented a double staining approach, combining a Ca^{2+} reporter (FluoForte GFP-certified) with a fluorinated VSD. Two-photon excitation features were exploited to simultaneously excite both dyes, while band-pass filters were used to select the two distinct spectral ranges of the overlapping fluorescence spectra. A spectral unmixing procedure was applied to properly uncouple voltage and Ca^{2+} signals. Employing this approach in combination with the random access modality, the authors were able to optically record action potentials in several T-tubules and, simultaneously, the corresponding local Ca^{2+} transients (Crocini et al., 2014). **Figure 1** shows an example of an optical recording of voltage and Ca^{2+} release in six different positions across the sarcolemma. The signal-to-noise ratio of the proposed method was sufficient to detect the presence of an action potential and to assess the temporal features of Ca^{2+} dynamic in single shot recordings, without averaging sequential trials. The utility of the system in detecting electrical activity and local Ca^{2+} release simultaneously in multiple sites was used to solve unanswered questions about the spatio-temporal relationship between sub-cellular alterations of Ca^{2+} release and T-tubular electrical and structural defects in several cardiac diseases including ischemic heart failure (Crocini et al., 2014), spontaneously hypertensive rats in overt heart failure (Scardigli et al., 2018a), and hypertrophic cardiomyopathy (Crocini et al., 2016b).

2.5. Enhancing the Utility of Two-Photon Optical Sectioning Microscopy for Cardiac Applications

Non-linear imaging (**Box 2**) is uniquely applicable to transmural cardiac studies and combined with several adjacent technologies, including optical mapping and emerging optogenetic tools, provides a powerful and versatile analytical tool for cardiac electrophysiology. Despite this, significant challenges remain to prevent its widespread adoption which are intrinsic both to the technology itself and cardiac muscle in particular. Understanding

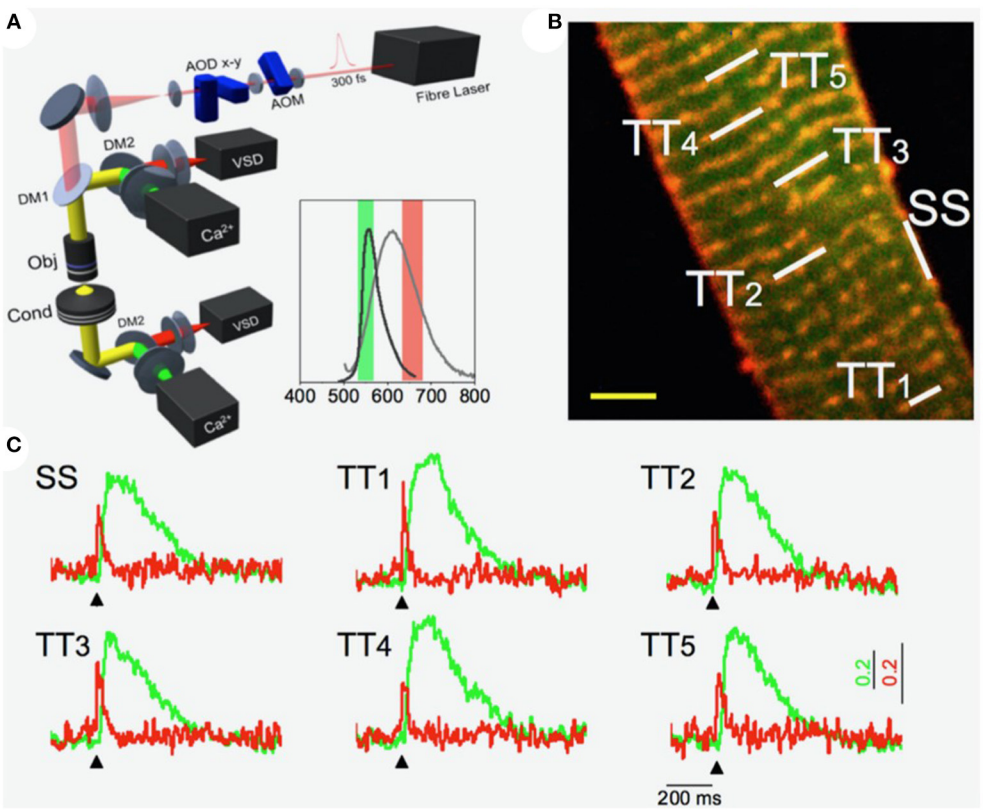

FIGURE 1 | Multi-site voltage and Ca^{2+} recording. **(A)** Scheme of the Random Access Multi-Photon (RAMP) microscope based on two orthogonally-mounted acousto-optical deflectors (AODs -x and -y) for laser scanning. Inset shows the emission spectra of the Ca^{2+} indicator (in dark gray) and voltage sensitive dye (in light gray) together with their fluorescence filter acquisition band. **(B)** Image of a stained rat ventricular cardiac cell: di-4-ANE(F)PPTEA in red and GFP-certified Fluoforte in green. Scale bar: 5 µm **(C)** Real time fluorescence traces collected from the scanned sites indicated in white in **(B)**: surface sarcolemma (SS) and five T-tubules (TTi). Membrane voltage is shown in red and Ca^{2+} in green. Reproduced and modified from Crocini et al. (2014).

BOX 2 | Two-photon microscopy

Physical Background

In conventional fluorescence spectroscopy, a fluorescent molecule is excited by absorption of one photon whose energy corresponds to the energy gap between the ground state and the excited state of the molecule. However, the same excitation is also possible by the near-simultaneous absorption, i.e., within 1e−16 s, of two photons of approximately double the wavelength via a short-lived, virtual intermediate state. The combined energy of the two long-wavelength, low-energy photons produce an excitation equivalent to the absorption of a single photon possessing twice the energy. The emitted fluorescence generated by the simultaneous absorption of two photons is indistinguishable to single photon excitation fluorescence emission. The simultaneous absorption of two photons is the origin of the quadratic dependence on the light intensity: in TPM, doubling the excitation intensity produces four times the fluorescence. This non-linear dependence of two-photon absorption is the basis for the intrinsic localization of fluorescence generation and therefore the optical sectioning capability, i.e., the imaging of specific planes within the sample without the need for physical slicing.

Requirements

Like most non-linear processes, the excitation probability in two-photon excitation fluorescence is extremely low but can be optimized to generate enough signal by concentrating the excitation light in space and time. Spatial compression is achieved by tight focusing with high-NA objective lenses. This increases the local intensity at the focal point and with it the probability for two-photon excitation. Away from the 3D focal spot the probability for simultaneous absorption drops off drastically such that virtually no fluorescence is generated outside the focal volume (Zipfel et al., 2003). Scattered excitation light is too dilute to excite by two-photon absorption and too long in wavelength to be absorbed otherwise. Owing to the low two-photon absorption cross-section inherent to non-linear processes, a useful fluorescence signal can only be achieved with ultrashort pulses which compress excitation intensity in the time domain. Ultrafast pulsed lasers concentrate photons into very short (pulse width τ), high peak intensity pulses separated by e−8 intervals (repetition rate R), keeping the average power relatively low. This increases the signal by a factor of $1/(\tau * R)^{n-1}$ compared to continuous-wave illumination, where n is the number of photons involved in the elementary process (Helmchen and Denk, 2005). At present, the most commonly used lasers in TPM setups are mode-locked titanium sapphire (Ti:Sa) which typically generate pulses with τ = 100–150 fs at τ = 80–100 MHz. They are tunable from 680 to 1, 080 nm.

Image Formation

The laser is focused onto the sample and scanned through the specimen in a raster fashion by a scanner, most commonly a pair of galvanometer mirrors (one for each image axis). The image is reconstructed from digitizing the point measurements of the fluorescence intensity at each position in the sample. Emission collection can be efficient and simple because all photons generated are signal and there is virtually no background: even multiply-scattered fluorescence photons can be assigned to their origin due to the localized nature of signal generation. To increase efficiency of fluorescence collection, non-descanned detectors are employed, most commonly large area photomultiplier tubes (PMTs) positioned close to the back aperture of the microscope objective. PMTs allow for the detection of multiply scattered fluorescence photons that may leave the objective lens at randomly divergent angles and are also favored for their high gain and low readout noise.

Advantages

A key advantage of TPM over confocal microscopy is reduced attenuation in biological specimens due to reduced scattering and absorption of near infrared light when compared to UV and visible light. Even though Rayleigh scattering is just an approximation in biological imaging, the inverse relationship ($\sim \lambda^{-4}$) between scattering and excitation wavelength remains valid. This results in deeper penetration of the pulsed laser source into scattering samples compared to conventional microscopy. Also, the "optical window," placed at 700–1.000 nm where tissue absorbance is orders of magnitude less than the absorption in the UV or visible region, falls conveniently into the spectral excitation window of TPM. Lower photon absorption in the tissue additionally means lower levels of phototoxicity and sample heating. However it should be noted that within the focal volume, the possibility of bleaching, damage and reduced viability remains.

Increasing Excitation Efficiency

Since the fluorescence signal in TPM scales with $1/(\tau^{*}R)$, an increase in signal can be achieved with a reduction in the duty cycle $\tau * R$. A reduction of the repetition rate R increases pulse energy, however, a limit is given by the repetition rate since at least one laser pulse must be delivered per image pixel. The reduction of pulse duration τ also leads to increased signal but accurate dispersion correction in the optical train becomes essential. As pulsed laser light traverses the beam path of a microscope, the optical elements slow the shorter wavelength components of the pulse relative to the longer wavelengths, consequently broadening the pulse; a phenomenon known as (positive) group velocity dispersion (GVD). Positive GVD compensation is achieved by introducing optical elements which exhibit negative GVD, introducing an equal but opposite dispersion on the pulse prior to entering the microscope, thus maintaining the shortest pulse duration at the sample plane. Dispersion compensation is often achieved using prisms (Akturk et al., 2006) or chirped mirrors where multiple layers of dielectric material with increasing layer spacing vary the distance traveled by different wavelengths of the pulse and compensate for GVD (Szipöcs et al., 1994). Importantly, GVD worsens the shorter the pulse since the spectral bandwidth of the pulse increases with decreasing pulse duration. A limit to the benefits of shorter pulses is reached when the spectral width of the laser excitation approaches or exceeds the width of the excitation spectrum of the dye ∼ 30–40 nm (full width at half maximum).

The Fundamental Depth Limit

The imaging depth in TPM cannot be increased indefinitely by increasing the excitation efficiency of the laser. A fundamentally constrained penetration depth restricts investigations in cardiac tissue to a few hundreds of micrometers in mouse left ventricle tissue (Salerno et al., 2019). In turbid media, the ballistic (unscattered) fraction of photons reaching the focal spot decays exponentially with depth. The total power of light reaching a certain depth decays more slowly, approximately as 1/depth. Due to these different decay rates, at depths depending on the scattering mean free path length and anisotropy of the tissue, the peak intensity of ballistic light will fall below that of scattered light, effectively rendering imaging impossible. Even before this depth limit is reached, background fluorescence generated partially by ballistic and mostly by scattered light near the surface will dominate the signal (Theer and Denk, 2006). The fundamental imaging depth in TPM is reached when this out-of-focus (background) fluorescence equals the fluorescence signal emanating from the focal spot; the signal-to-background ratio reaches unity. This fundamental limit to achievable tissue penetration depth is a direct consequence of light scattering by tissue and irrespective of available laser power or potential photodamage.

these limitations and available options for overcoming them is critical for informing the next generation of 3D cardiac imaging studies based on TPM.

The ubiquity of optical mapping in cardiac electrophysiological research owes its popularity not only to the high quality and throughput of the data generated, but

also the relative simplicity of the setup, particularly with regards to excitation light sources. In contrast, TPM has a relatively high cost and perceived complexity barrier which has restricted its widespread adoption in cardiac electrophysiology. Full commercial microscope systems remain expensive platforms, often bundled with tuneable Ti-sapphire lasers which do not deliver sufficient power to the sample plane for deep tissue imaging at wavelengths within the second IR imaging window ($> 1000nm$). Data throughput, particularly for whole heart imaging is also relatively low. Owing to the need for tight spatial focusing, it is technically challenging to combine the high spatial resolution of TPM with larger fields of view and/ or fast volumetric imaging rates. Axial focusing remains slow and limited to the speed of a resonant objective piezo scanner, though remote refocusing (Botcherby et al., 2008; Alfred Millett-Sikking and York, 2018) increases axial scan speed and has been used for fast measurements of sarcomere length and cell orientation in Langendorff-perfused hearts (Botcherby et al., 2013). The following sections discuss these aspects in more detail.

2.5.1. Increasing Imaging Depth

As highlighted in **Box 2**, a fundamental imaging depth limit exists for a given system, independent of the excitation efficiency of the laser. This is due primarily to tissue scattering effects and increasing background fluorescence generated near the tissue surface (assuming tissue staining is homogeneous throughout the sample thickness). Several optical techniques have been proposed to overcome the TPM depth limit, while retaining scanning rates necessary for optical electrophysiology measurements. Temporal focusing, primarily used to allow video-rate optical sectioning, images a scan line across a blazed diffraction grating to spatially separate the spectral components of the laser pulse, effectively broadening the pulse width. The grating is imaged onto the sample plane via a high-NA objective lens and scanned in one axis to form an image. In theory this should reduce surface background fluorescence because the broadened pulse entering the sample only becomes short enough to permit non-linear interactions at the objective focal plane (Tal et al., 2005). While this approach is successful for rapid-scanning, improved depth imaging is questionable. This is because while point-scanning systems can use all scattered photons to detect an image, only ballistic or weakly scattered photons are useful for image formation with temporal focusing. A direct comparison of temporal focusing microscopy and TPM estimated the latter has up to 2X the penetration depth in highly scattering biological material (Rowlands et al., 2015). Alternatively, differential aberration correction was designed specifically to reduce background fluorescence contamination by placing a deformable mirror into the beam path of a raster scanning TPM which periodically (every second line or frame) introduces an optical aberration pattern to defocus the laser pulse. This preferentially reduces focal excitation while preserving the background. Subtracting the defocused image from the original produces an enhanced contrast image (Leray and Mertz, 2006; Leray et al., 2008). Contrast at a given depth is improved by up to 6X, a potentially significant gain in TPM depth imaging. It should be noted however, that because two images must be formed, the frame rate is effectively halved. A variant of this approach using a delay line and a fixed aberration optic allows near-simultaneous acquisition of two images in separate channels (Xiao and Mertz, 2019). Differential aberration shows promise as a powerful, lightweight approach for deeper TPM imaging and a thorough quantitative evaluation of its usefulness using cardiac muscle is warranted.

2.5.2. The Red Shift

A different approach to increasing the penetration depth of non-linear microscopy techniques is to decrease the effects of scattering itself. Novel engineered fluorophores, whose absorption and emission spectra are shifted toward the IR, take advantage of the decreased scattering of longer wavelengths. However, to image deeper into highly scattering samples, 3PM, the simultaneous absorption of three photons (of 1,300 or 1.700 nm wavelength) to excite fluorescence, has emerged as a promising technique which outperforms two-photon excitation of a different fluorophore at the same wavelength. Due to the higher non-linearity of the 3-photon absorption process, its cross section is several orders of magnitude smaller compared to TPM and this leads to virtually background-free deep imaging and highly improved signal-to-background ratio. However, the extremely low 3PA cross-sections (for example resulting in absorption rates $\sim$ 20 orders of magnitude lower than 2PA), necessitate higher pulse energies, usually obtained by low repetition rate (2–4 MHz) lasers. The higher peak energy results in higher peak power and therefore an increased risk of non-linear tissue damage whereas the longer wavelength leads to higher absorption and therefore more sample heating.

3. CORRELATION OF STRUCTURE AND FUNCTION

A major current technical challenge in optical cardiac imaging is the deterministic correlation between structural features and functional performance at different hierarchical levels, from subcellular components such as individual Ryanodine receptors (RyR) using DNA-PAINT techniques (Hurley et al., 2020) to single isolated CM and intact heart tissue. Assessing the structure and the corresponding local function in a correlative manner is particularly relevant in pathological settings where structural and ultra-structural alterations occur e.g., alteration of excitation-contraction coupling machinery, myofilament disarray or extracellular fibrosis. In the subsequent two sections, two case studies are described to demonstrate the power of optical techniques to measure and assess the function of sub-resolution membrane structures within cardiac muscle cells.

3.1. Super-Resolution Techniques Applied to Cardiac Muscle Electrophysiology

The function, morphology, and proteome of atrial (ACM) vs. ventricular (VCM) CM differ significantly (Brandenburg et al., 2016a). Compared to VCM, the ACM's triangle-shaped action potential and phase-2 plateau are markedly shorter, yet followed by a more gradual phase-3 repolarization and a less negative

resting membrane potential (Fatkin et al., 2007). In contrast, intracellular Ca^{2+} release in ACM is highly heterogeneous and is frequently described as a slow inward-propagating U-shaped Ca^{2+} gradient (Thul et al., 2012; Greiser et al., 2014). However, contractile activation of atrial compared to ventricular muscle strips occurs significantly faster (Lüss et al., 1999). This results in a conceptual paradox: how is atrial excitation and contraction rapidly coupled, if cell-wide Ca^{2+} release is 1–2 orders of magnitude slower in ACM compared to VCM (Thul et al., 2012; Greiser et al., 2014)? The case study described below demonstrates the use of super-resolution techniques to investigate the details of sub-micron structures in cardiac cells.

In rodent ACM typically no or only few residual T-tubules are reported (Kirk et al., 2003). In contrast, VCM are characterized by a high density of T-tubules, where each may rapidly propagate electrical signals (see also section 2.4). To combine cell isolation with high-resolution imaging workflows for ACM, fluorescent dyes that selectively intercalate in the extracellular membrane leaflet are highly attractive to assess the local membrane structure and integrity (Wagner et al., 2014; Brandenburg et al., 2018). Surprisingly, when implementing stringent cell quality and confocal imaging workflows, 100% of ACM isolated from mouse hearts were shown to exhibit a unique cell-wide transverse-axial-tubule (TAT) membrane network (**Figure 2A**, left) (Brandenburg et al., 2016b). Importantly, analysis of the TAT components revealed that axially oriented A-tubules dominate the ACM membrane network, whereas T-tubules are far less abundant (**Figure 2A**, right).

Interestingly, confocal imaging failed to locally resolve di-8-ANEPPS stained A-tubule cross-sections, whereas STimulated Emission Depletion (STED) superresolution nanoscopy improved local contrast sufficiently to determine the width (δ)

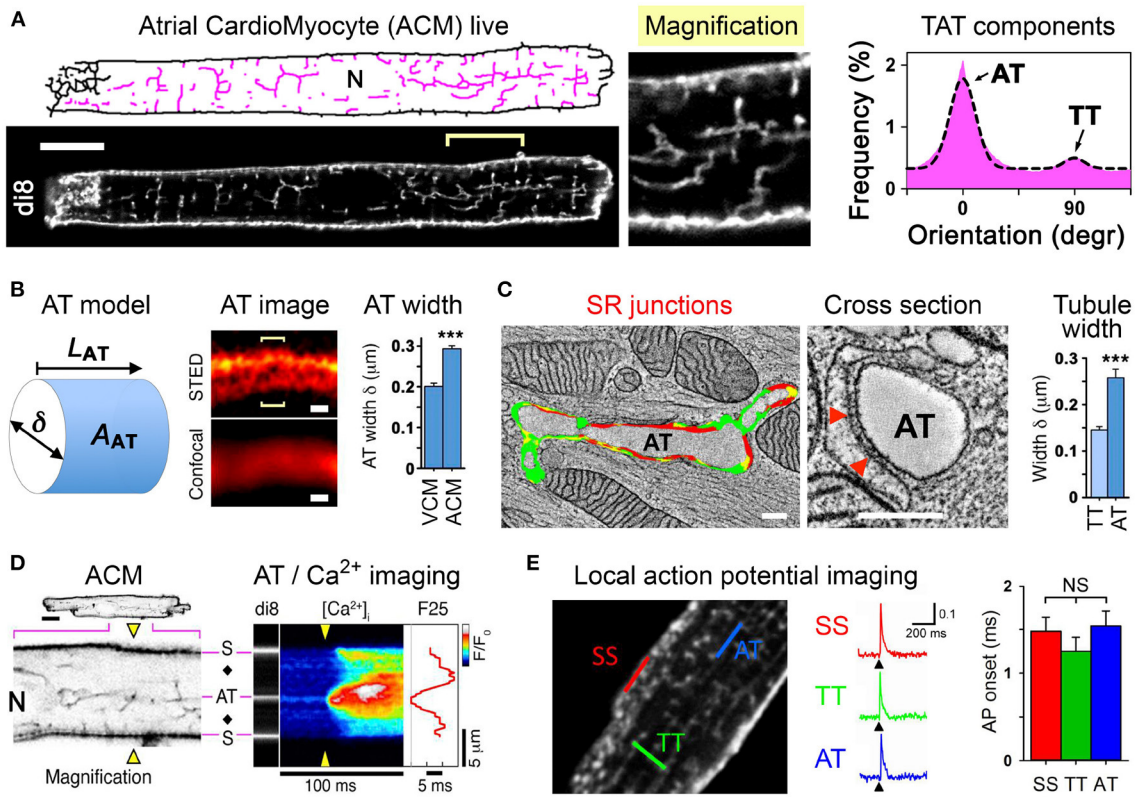

FIGURE 2 | A-tubules provide Ca^{2+} signaling super-hubs for atrial excitation-contraction coupling. **(A)** Confocal live imaging of di-8-ANEPPS stained (di8) TAT structures visualized as skeleton (pink). N, nucleus. Scale bar 10 µm. Histogram showing the TAT component orientations and Gaussian fit. Abundant AT (0°) vs. sparse TT (90°) components. **(B)** Cartoon of a cylindrical AT model. AT width (δ) measurements were used to estimate the surface area (AAT); LAT, AT component length. AT width was determined from optical cross sections (brackets) using the local STED signal distribution and compared between VCM vs. ACM as bar graph. Scales 200 nm. **(C)** Electron tomography images and segmentation of a longitudinally sectioned and a cross-sectioned AT structure. Scales 200 nm. Red color indicating AT-SR junctions $\leq$ 15 nm in gap width containing RyR2 densities. Red triangles mark two exemplary electron densities compatible with RyR2 channels. **(D)** Confocal negative contrast visualization of intracellular AT structures and transversal line scanning (yellow triangles) of intracellular Ca^{2+} imaging (fluo-4). A field potential-evoked Ca^{2+} transient is activated at AT and subsurface (S) structures; black diamonds, off-membrane cytosolic sites; F25, Ca^{2+} signal onset at 25 % signal amplitude; $^{\Delta F}/_{F_0}$, normalized fluorescence intensity ratio as indicated by look-up-table; N, nucleus. **(E)** Two-photon action potential recordings from specific TAT components labeled with the voltage-sensitive dye di-4-ANE(F)PTEA (2 µM). Normalized fluorescence traces ($^{\Delta F}/_{F_0}$) were recorded from the scan regions indicated by color. At AT, TT, and SS membranes structures the simultaneous action potential activation upon pacing (black arrowheads) is apparent. Grouped bar graph showing no significant difference for action potential onset (the time interval between the end of the stimulus and the rise of the fluorescence signal above a threshold of 4 % $^{\Delta F}/_{F_0}$. AT, A-tubule; TT, T-tubule; SS, subsurface membrane site. NS, not significant. Adapted from Brandenburg et al. (2016b).

of intact A-tubules in living ACM (**Figure 2B**). On average, the A-tubule width was significantly larger in ACM compared to VCM (**Figure 2B**) (Brandenburg et al., 2016b), suggesting that A-tubules exhibit a much larger cytosolic membrane surface area (AAT). Indeed, electron tomography of high-pressure frozen ACM showed that A-tubules exist as large cylindrical membrane structures that form extensive SR junctions densely filled with RyR2 Ca^{2+} release channels (**Figure 2C**, left) (Brandenburg et al., 2016b). Finally, quantitative analysis confirmed that A-tubules exhibit approximately 100 nm larger diameters than T-tubules in ACM (**Figure 2C**, right).

Using immunostaining of ACM, voltage-dependent L-type Ca^{2+} channels were identified in A-tubules: Cav1.2 clusters were shown to occur at a higher density in A-tubules compared to T-tubules (Brandenburg et al., 2016b), and additionally Cav1.3 clusters were localized in A-tubules (Brandenburg et al., 2018). Consistent with abundant L-type Ca^{2+} channel clusters in A-tubules, intracellular Ca^{2+} imaging combined with di-8-ANEPPS staining showed field pacing-evoked rapid Ca^{2+} release gradients around A-tubules, whereas surface membrane and particularly cytosolic sites each showed a significantly increased Ca^{2+} release latency (**Figure 2D**) (Brandenburg et al., 2016b).

Finally, RAMP was used for local *in situ* action potential recording at specific TAT sites in living ACM (**Figure 2E**, left and section 2.4). Strikingly, action potentials recorded locally at A-tubules, T-tubules, or subsurface sites showed the same rapid onset (**Figure 2E**, right), amplitude and upstroke velocity (Brandenburg et al., 2016b). Thus, despite a dramatically lower T-tubule density (**Figure 2A**, right) and a relatively large distance from the cell surface, voluminous A-tubules appear to function very effectively as electrical conduits for rapid action potential spread deep inside ACM.

While the physiological and clinical relevance of these new atria-specific A-tubule findings is still emerging, several important implications are obvious: (1) ACM express a cell-specific electrically excitable TAT network quite different from VCM; (2) the discovery of A-tubules as dominant excitable membrane conduits provides a new model of "super-hub" Ca^{2+} signaling and ACM-specific excitation-contraction coupling; (3) in addition to Cav1.3 channels thousands of proteins are differentially expressed in ACM (Brandenburg et al., 2016a), yet none of the clinically relevant ion channels and G-Protein coupled receptors have been mechanistically established in the context of A-tubule membrane organelles so far.

As functional L-type Ca^{2+} channel changes represent a disease mechanism of atrial fibrillation, major future questions are how Cav1.2 and Cav1.3 clusters are organized locally and relatively to RyR2 channel Ca^{2+} release sites, and which specific voltage-dependent roles the atrial L-type Ca^{2+} channel isoforms exert in A-tubules. Interestingly, while the Cav1.2 interacting protein junctophilin-2 is expressed five-fold less in the atria compared to the ventricles, it is highly abundant inside sarcoplasmic reticulum (SR) junctions along A-tubules (Brandenburg et al., 2019). Thus, non-invasive superresolution optical methods are not only essential for establishing differential Cav1.2 and Cav1.3 functions in ACM, but they will be instrumental for identifying early disease-causative mechanisms of atrial cardiomyopathy preceding atrial fibrillation and stroke (Goette et al., 2016).

3.2. Fluorescence Recovery After Photobleaching to Probe Structure and Function of the T-Tubular System

The optical technique of fluorescence recovery after photobleaching (FRAP) microscopy is a useful method for examining the diffusion of probes within limited structures within the cell (Bers and Shannon, 2013). In relation to examining the diffusion within the TAT structure, FRAP has been used to demonstrate marked species differences in the tortuously and therefore lumenal diffusion of solutes within these membrane structures (Kong et al., 2018). In this study the authors used FRAP microscopy to probe the diffusion properties of TAT: fluorescent dextran within the TAT system lumen was photo bleached and signal recovery by diffusion of unbleached dextran from the extracellular space was monitored. Remarkable is how an optical-based imaging approach can support or implement structural data hitherto achievable only with 3D electron tomography (Rog-Zielinska et al., 2018). More in general, combining FRAP with detailed computational modeling the authors designed a new pathway to understanding how TAT remodeling may contribute to altered cellular function. In this respect, the combination of FRAP with optical voltage measurements from TAT membranes has also offered the opportunity to study the relationship between structural alterations of the T-tubules and defects of action potential propagation found in the failing heart.

For instance, in a recent study, Scardigli et al. (2017) exploited the formal analogy between diffusion and electrical conductivity to link the latter with the diffusion properties of the TAT. The time constant of fluorescence recovery was correlated with the apparent diffusion coefficient of the fluorescent molecules and linked to electrical conductivity. These data were used to evaluate the efficiency of the passive spread of membrane depolarization along TAT system. The characteristic length constant of T-tubules was calculated as approximately 300 μm: an order of magnitude larger than the cellular radius, indicating a remarkable safety factor of the normal TAT system structure in passively conveying membrane potential changes across the cell.

Further refinement of the FRAP technique was then employed to address the role of the mechanical activity associated with contraction in the cardiac cell with the enhanced movement of solutes including ions through the tortuous TAT system driven by advection-assisted diffusion (Rog-Zielinska et al., 2021). This phenomena is thought to offset the accumulation of solutes within the TAT system as a result of changes in heart rate (Rog-Zielinska et al., 2021). This novel finding provides another potential mechanism for dysfunction, namely the reduced capacity for solute exchange that may result from a remodeled TAT system in failing hearts.

3.3. Light-Sheet Microscopy for Mesoscale Structural Imaging

Taking correlative work to another order of magnitude, extremely challenging current experiments aim to dissect

morpho-functional relationships between cellular organization and functional abnormalities at the whole organ level. At the tissue level, current studies generally associate structural alterations with the corresponding electromechanical dysfunction without showing real cause-effect relations. What is missing is a direct link between the functional study and quantification of tissue disorganization performed on the same tissue. The main limitation is the inefficacy of standard imaging methods and staining approaches in performing high resolution imaging (cellular or sub-cellular resolution) in tissue. During the past years, different methods have been developed for clearing fixed tissue. Most of them, however, present several limitations such as tissue shrinkage, structural alteration, fluorescence quenching and incompatibility with immunostaining (Silvestri et al., 2016). The challenge of producing large, transparent and fluorescently-labeled volumes has been overcome recently by applying a tissue transformation approach, CLARITY, and it's related derivatives (Chung et al., 2013; Pianca et al., 2019; Olianti et al., 2020, 2021). These methods allow high transparency, immunolabeling and structural and molecular preservation. One drawback with the current techniques is the poor penetration rates of the tissue by antibodies, to the extent that many months of incubation are sometimes required depending on tissue dimensions.

Clearing methods render biological tissue transparent by equilibrating the refractive index throughout a sample to reduce inhomogeneities in light scatterers (Richardson and Lichtman, 2015). Different approaches have been proposed based on organic solvents, high-refractive index aqueous solutions, hyperhydrating solutions and tissue transformation (Silvestri et al., 2016). Most notable amongst the latter approaches, CLARITY (Chung et al., 2013) employs hydrogel embedding of the sample by perfusing tissue with a fixative, a temperature-sensitive crosslinker and the hydrogel monomer which forms covalent links with native proteins. After fixation, the tissue of interest is warmed to induce cross-linking of the monomers into a nanoporous hydrogel mesh. Lipids are then removed from the sample with a detergent solution either passively, or actively through electrophoresis. The lipid-free samples are then incubated in refractive index matching solutions for clearing. This method in combination with advanced imaging techniques such as light-sheet or two-photon microscopy (see **Box 2**) allows 3D reconstruction of substantial heart tissues at high resolution.

Light-sheet microscopy, originally described in 1903 (Siedentopf and Zsigmondy, 1903) and re-invigorated in the early 2000s (Huisken et al., 2004), achieves optical sectioning over the entire field of view by selectively illuminating a thin slice of tissue with a sheet of light which is positioned to coincide with the focal plane of a perpendicularly placed microscope objective for fluorescence detection. In contrast to point-scanning epi-illumination methods like confocal or TPM, this uncoupled illumination—detection scheme has two major advantages. Firstly, the detection scheme is essentially that of a wide-field microscope and hence affords much faster acquisition rates through the registration of multiple points in parallel rather than sequentially. Secondly, the selective illumination greatly reduces unnecessary photoactivation and bleaching of fluorophores above and below the focal plane. However, this very same uncoupling of excitation and detection makes light-sheet microscopy particularly sensitive to tissue scattering and the technique thus requires samples that are either intrinsically transparent (e.g., Zebrafish larvae) or else an opaque tissue that has been made transparent through tissue clearing. If tissue is intrinsically transparent, it is possible to combine structural observations in live tissue, even over extended periods of time (for example to track every single cardiac cell during early ontogenetic development in the Zebrafish heart) with functional Ca^{2+} imaging (Weber et al., 2017; Taylor et al., 2019).

This mesoscopic imaging may help to elucidate the role of cellular organization in cardiac electro-mechanical (dys)function and pave the way for a unifying approach which integrates functional and structural data. Such an experimental model would enable a comprehensive investigation of the morphological changes that lead to electrical and mechanical alterations after disease-associated structural remodeling.

4. THE USE OF LIGHT TO MANIPULATE AND MEASURE CARDIAC ELECTROPHYSIOLOGY

Extending the application of optical techniques in cardiac applications, optogenetics has added the capability to manipulate cardiac function by light (see review Entcheva and Kay, 2021). Optogenetics combines targeted light stimulation and the genetic expression of light-sensitive ion channels or pumps to enable cell-specific, non-contact stimulation with sub-millisecond temporal and micrometer spatial resolution. The characterization of the non-selective cation channel Channelrhodopsin2 (ChR2) in the early 2000s (Nagel et al., 2002) initiated the explosive growth of field of optogenetics. Compared to electrical stimulation, in excitable cells expressing ChR2, pulsed illumination induces inward currents which not only trigger excitation but can also precisely modify the shape of action potentials (Park et al., 2014; Williams and Entcheva, 2015). Light responsive Cl^- and H^+ pumps, as well as K^+ and Cl^- ion channels allow light-induced hyperpolarization of cardiac tissue. Direct optogenetic hyperpolarization with patterned light has been used to provide mechanistic information about circuits involved in cardiac pacemaking (Arrenberg et al., 2010), or to affect cardiac arrhythmias by selective expression in sympathetic neurons in a canine model of post-ischemic electrophysiological remodeling (Yu et al., 2017). The ability to bi-directionally manipulate cardiac function (to excite and to inhibit) using light, and the possibility to combine these newer optical tools with optical mapping have afforded new means to address mechanistic and translational questions related to cardiac arrhythmias (Entcheva and Bub, 2016).

4.1. Optogenetic Cardioversion/Defibrillation: Progress and Challenges

Beyond optogenetic pacing demonstrated in early cardiac studies (Arrenberg et al., 2010; Bruegmann et al., 2010;

Jia et al., 2011), proof-of-concept studies for optogenetic cardioversion/defibrillation have been shown in transgenic mice and wild type mice and rats after AAV-mediated expression of ChR2 (Bruegmann et al., 2016, 2018; Crocini et al., 2016a; Nyns et al., 2016). The light parameters (light intensity, pulse duration, etc.) required for successful termination have been determined using many different approaches for illumination (optical fiber/global LED, DMD, and μLED) and computational modeling. Using this range of techniques, different excitation patterns are possible, opening the way for the investigation of a range of defibrillation approaches including: (i) targeted pacing to fill the excitable gap or (ii) continuous illumination for prolonged phases of depolarization with the aim of a complete conduction block. Interestingly, conduction block seemed to be more effective but required higher light intensities compared to targeted pacing when illumination was performed randomly without analysis of the underlying arrhythmia pattern (Bruegmann et al., 2018). However, knowing the underlying reentry wavefronts including the spatial extent of excitation gaps or global illumination of the whole ventricular surface might enable a reduction in the light intensity requirements (Crocini et al., 2016a). For targeted pacing, feedback loops between sensing electrodes or optical mapping and light stimulation have been developed which permit testing numerical hypotheses for more effective, gentle cardioversion/ defibrillation (Hussaini et al., 2021). The translation to larger animals including humans has been investigated using, *in silico* modeling. This work indicates that in principle, the optogenetic route is feasible and suggests defibrillation mechanisms distinct from that achieved by conventional chest paddles (Bruegmann et al., 2016; Hussaini et al., 2021). However, there are considerable technical issues to overcome including: (i) the need for gene transfer, (ii) the expression of non-mammalian opsins in humans and (iii) implantation of light sources. Nevertheless, the gain would be pain-free, tissue-sparing and efficient arrhythmia termination in the clinic.

4.2. Real-Time Manipulation of Cardiac Electrical Activity in a Closed-Loop System

All-optical cardiac electrophysiology is a powerful contactless interrogation and manipulation technique (Entcheva and Bub, 2016; Scardigli et al., 2018b). A recent example of the capability of optical voltage reporters combined with optogenetic actuators at the whole heart level is the development of a wide-field mesoscope to simultaneously optically map and manipulate action potential propagation in whole mouse hearts (Scardigli et al., 2018b) (**Figure 3A**). A computer-controlled digital micromirror device (DMD, see **Box 3**) capable of drawing arbitrarily-chosen illumination patterns was used to create precise spatial and temporal patterns of optogenetic stimulation on the epicardial surface of isolated hearts (**Figure 3B**). Operating in closed-loop with a feedback-control strategy, this system can react in real-time to ongoing electrophysiology as revealed by optical mapping, opening the prospect for real-time resynchronization therapy and cardiac defibrillation. These techniques can serve as a "biological stimulator" (for example by optical stimulation of ChR2), or as a "biological inhibitor" (when using optically-activated K^+ flux systems) to inform new *in vivo* strategies for controlling arrhythmias. Such a system is an ideal test-bed to investigate strategies to defibrillate or interrupt tachy-arrhythmias using the minimal power and area of illumination with a view to advancing our knowledge of the electrophysiology of arrhythmias that may be translatable to the clinics.

4.3. Wave Control to Improve Arrhythmia Management and Termination

Present-day electronic cardiac devices include cardiac pacemakers (to maintain normal rhythm) and cardioverter-defibrillators to terminate arrhythmias and restore normal rhythm. With newer optical technologies, including optogenetic modulation of cardiac function, conceptually new strategies for control have been proposed that are not possible with classic

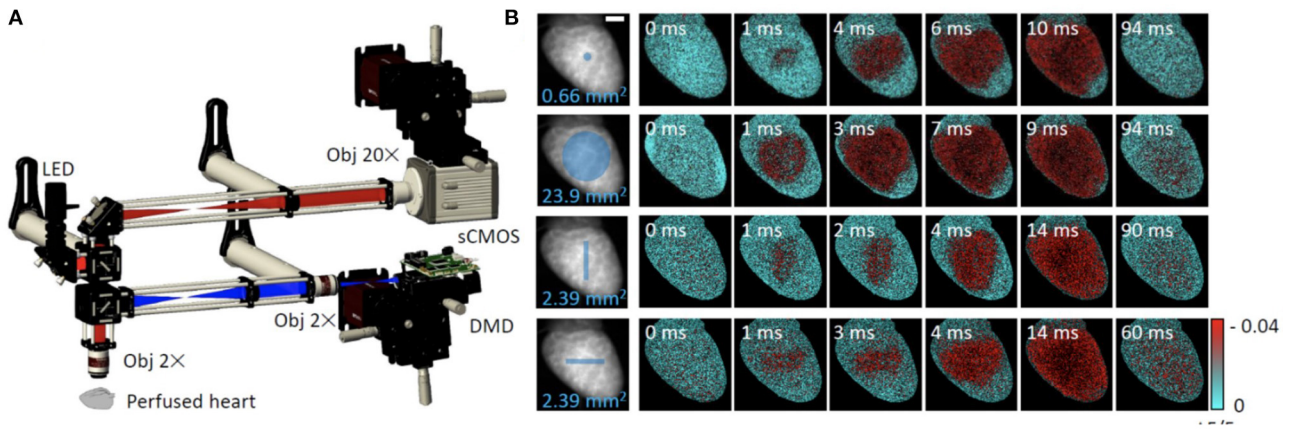

FIGURE 3 | (A) Optical setup for real-time closed-loop optogenetic stimulation with a digital micromirror device (DMD) in response to ongoing cardiac activity, simultaneously optically mapped with a sCMOS camera. **(B)** Exemplary customizable stimulation pattern and cardiac excitation wavefronts. Modified from Scardigli et al. (2018b).

BOX 3 | Digital Micromirror Devices

A digital micromirror device, or DMD, is a micro-opto-electromechanical system comprised of millions of microscopically small moving mirrors to create a video display of the type now found in digital projectors. The mirrors on the DMD are arranged on a μm diamond pixel geometry and by applying a tilt angle of ±12°, each micro-mirror can be switched on or off individually. A high numerical aperture relay system can be used to project the DMD pattern onto the sample. DMDs have been employed for controlling cardiac activity at fine spatial and temporal scales using light in cultured cardiac monolayers and whole-heart preparations. These light projectors offer sub-millisecond temporal resolution and have been used to demonstrate fine control of tissue functional properties, including wave velocity (Burton et al., 2015), or to embed high temporal resolution "small" images into larger but more slowly acquired still image sequences (temporal pixel multiplexing, Bub et al., 2010).

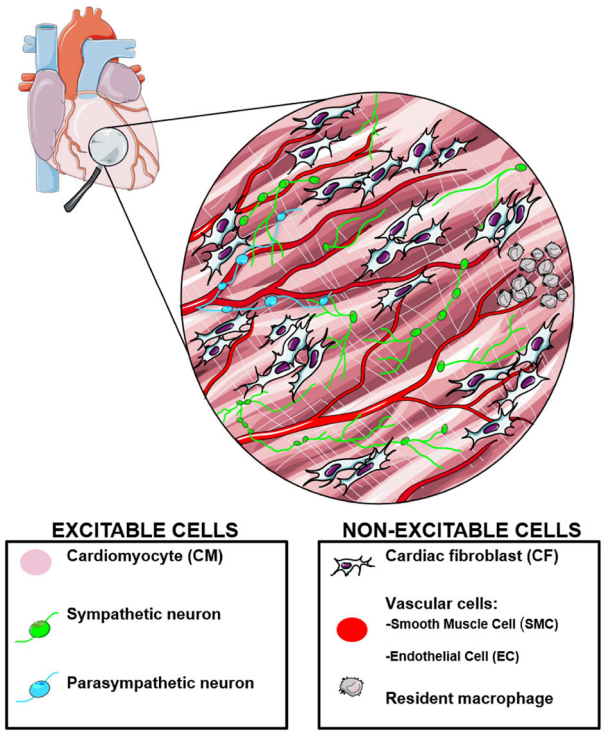

FIGURE 4 | The heart is a multicellular network of excitable and non-excitable cells, which have been targeted with various opsins for optogenetic investigation. Modified from Zaglia et al. (2019).

electrical means. Using optogenetic actuation and dye-free optical mapping, it was demonstrated that the direction, speed and chirality of cardiac excitation waves can be modulated by light (Burton et al., 2015). To achieve this, a quasi-real time feedback was applied with dynamically-modulated light patterns using a DMD. Space-time varying illumination enables "wave steering" (Entcheva and Bub, 2016) and can bring insights for finer arrhythmia control in the clinic with lower-energy approaches and devices. Until recently, the only options for wave control have been pharmacological (adding exogenous compounds that alter cardiac channel function) or electrical (using an electrode or an array of electrodes to stimulate the tissue). These approaches have limitations as they either change wave properties in the entire tissue or at a limited number of locations due to physical limits on the density and number of electrodes in an electrode array. All-optical electrophysiology offers the ability to deliver dynamic space-time patterns of light for stimulation/suppression, and the possibility for real-time feedback control of macroscopic emergent properties, i.e., cardiac waves of excitation. Wave control goes beyond the simple initiation and termination of excitation waves (pacing and defibrillation/cardioversion) and the associated frequency modulation. Instead, using all-optical means, one can focus on manipulation of the macroscopic (emergent) properties. Recent examples include termination of arrhythmias through re-entrant wave drift induced by longer low-light pulses (Hussaini et al., 2021). While high spatial and temporal resolution optogenetic manipulation in the intact heart *in vivo* is still not feasible, optogenetic tools yield, for the first time, an experimental platform to rapidly test anti-arrhythmic strategies in *ex-vivo* preparations. This offers the flexibility to manipulate the electrophysiological variables within the heart hitherto only possible in computational models.

4.4. Cell Specific Optogenetics to Interrogate the Myocardial Network

Different from conventional electrophysiological approaches, optogenetics, by its nature, is cell type specific, as sensitivity to photostimulation or optical reporting of function are achieved by transgene expression. This feature was immediately exploited in neuroscience, as it enabled the functional dissection of neuronal circuits in the multiplexed network forming the central nervous system. An emerging concept of the heart as an interconnected multicellular system is a prerequisite to formulate the appropriate physiological questions optogenetics can answer (**Figure 4**). Heart function is based on the anatomical and functional interaction between excitable (i.e., working and conducting CM), non-excitable conductive [e.g., cardiac fibroblasts (Quinn et al., 2016) and macrophages (Hulsmans et al., 2017)], and extrinsic excitable (i.e., cardiac autonomic neurons) cells, and non-excitable modulators (i.e., endothelial and smooth muscle cells) (Zaglia et al., 2019). Cell-specific optogenetic stimulation within intact heart has first been demonstrated in a proof-of-principle study by Bruegmann and colleagues (Bruegmann et al., 2010), and subsequently this approach was used to infer the contribution of working and conducting CM to arrhythmias in the normal and ischemic myocardium. While alterations in the Purkinje Fiber (PF) network, including both PF cell dysfunction and PF coupling to the working CM have been suggested in several acquired or genetic cardiovascular diseases, assessment of PF function is only indirect and

non-specific with conventional electrophysiological techniques. Cardiac optogenetics has allowed direct investigation of the source-sink relation in the conduction system vs. working myocardium, and by combining it with a 3D morphological study of the PF network, to determine that the high arrhythmogenicity of the right ventricular outflow tract depends on the peculiar displacement of the terminal PF network (Zaglia et al., 2015).

Another excitable cell population, critical for regulating cardiac function, is represented by autonomic neurons, which densely innervate the myocardium, including extracardiac sympathetic and parasympathetic neurones and a dense network of cardiac ganglia (Julian et al., 2021), influencing potentially all cardiac cell types (Franzoso et al., 2016). It is increasingly evident that neuronal remodeling (i.e., changes in distribution and function of cardiac innervation) takes place upon physiological (e.g., exercise, pregnancy, aging) and pathological (e.g., ischemic damage, heart failure) conditions. *In vivo* assessment of cardiac autonomic neuron function is technically challenging and non-selective. Several groups have used optogenetics to achieve control of cardiac sympathetic (Wengrowski et al., 2015; Yu et al., 2017; Prando et al., 2018; Burton et al., 2020) or parasympathetic (Moreno et al., 2019; Rajendran et al., 2019) neurons, to assess their effects on heart function, to study the biophysics of neuro-cardiac communication and to prevent sympathetic neurons from triggering arrhythmias in post-ischemic electrophysiological remodeling.

Furthermore, in addition to the studies of excitable cells, the method has recently been used in approaches to investigate non-myocyte cell populations. Non-CM cells in the myocardium are mostly inexcitable, and they have classically been relegated to forming the cardiac vascular bed (i.e., endothelial cells, smooth muscle cells) or regulating the extracellular compartment (e.g., fibroblasts). Rapidly accruing evidence has shown that these cell types play additional roles in paracrine and endocrine signaling, and may influence cardiac activity. In addition, some 25 years ago, it had been suggested that cardiac fibroblasts may potentially couple to CM via connexins, affecting cardiac electrophysiology (Kohl et al., 1994). This hypothesis was eventually confirmed in native tissue, using optogenetic expression of GEVI in cardiac non-myocytes (Quinn et al., 2016). Furthermore, expression of Channelrhodpsin-2 (ChR2) or Archaerhodopsin (ArchT) was achieved in primary cardiac fibroblasts, and heterocellular coupling with CM was further investigated (Yu and Entcheva, 2016; Funken et al., 2020; Simone et al., 2020; Boyle et al., 2021; Kostecki et al., 2021). ChR2 expression in smooth muscle cells of the coronary vessels has shown to be a potent tool to control vascular tone, demonstrating local and rapidly induced light-activated vasospasm (Wu et al., 2015). In parallel, selective expression of ChR2 in endothelial cells has shown that modulation of endothelial cell membrane potential can also trigger local vasospasm (Zhang et al., 2015), suggesting heterocellular coupling between the two important cellular components of the vessel wall. Optogenetics was exploited to study the biology of resident heart macrophages, which were shown to electrically communicate via connexins with atrio-ventricular node cells and to influence conduction (Hulsmans et al., 2017). Thus optogenetics revealed novel functions, especially related to heterocellular coupling, of smooth muscle cells, endothelial cells and macrophages.

Long term cardiac studies or experiments in conscious, freely moving animals are technically more demanding than in brain research, due to obvious differences in anatomical constraints. In particular, continuous movement of the heart hampers the stable implantation of light-emitting devices (for example, optrodes which have been developed for deep brain stimulation have limited use in the heart) (sta, 0000). These limitations can be overcome by progress in bioengineering aimed at the development of biocompatible and flexible light emitting tools to be positioned on the epicardial surface or around cardiac neurons (Gutruf et al., 2019). Collaboration with medical physicists would also allow simultaneous optogenetic stimulation of CM or cardiac neurons with the assessment of cardiac function by echocardiography or other imaging methods such as cardiac magnetic resonance. Another limitation, which will presumably be resolved in the next few years, is that, up to now, cardiac optogenetics has mainly been used in rodents, while very little has been performed in bigger animal models (e.g., pigs, sheep), which may be more informative for their closeness to human electrophysiology. In general terms, the clinical or experimental applicability in humans is not immediate, as it requires expression of an exogenous gene in the heart, and implantation of a light emitting source. Rapid progress in molecular biology has yielded viral vectors encoding opsins suited to the use in humans (FDA-approved, ClinicalTrials.gov NCT02556736), and opsin expression in patient hearts may thus be foreseen.

Optogenetic inhibition of autonomic sympathetic neurons is theoretically suited to ablate the adrenergic component favoring or sustaining arrhythmias. The further development of this concept will presumably be utilized to study arrhythmogenesis in genetic or acquired cardiovascular diseases in which adrenergic stress has a key role (catecholaminergic polymorphic ventricular tachycardia, arrhythmogenic cardiomyopathy, Takotsubo cardiomyopathy). While several opsin variants with specific advantages have been used in neurosciences (sta, 0000), cardiac optogenetics has thus far, exploited almost exclusively ChR2 with some exceptions (Kopton et al., 2018; Sierra et al., 2018). It is to be expected that in the next years many newly developed photoactivatable tools will be used in heart studies. In addition to channel-forming opsins, signaling opsins have been developed for spatially and temporally accurate photo-interrogation of signaling pathways in cells/ *in vivo*.

Proof of concept examples have shown light-modulation of G_q and G_s signaling pathways (Beiert et al., 2014; Makowka et al., 2019). Specifically, optogenetic stimulation of the adrenergic G_s signaling cascade using JellyFish Opsin in cultured CM and in the heart of transgenic animals was shown to have a very high light sensitivity, fast kinetics and high spatial resolution (Makowka et al., 2019). The precise time point of activation by triggered illumination allowed to identify differential downstream kinetics of cAMP/PKA effects on pacemaking (positive chronotropy), sarco/endoplasmic reticulum Ca^{2+}-ATPase activation (positive lusitropy) and Ca^{2+} induced Ca^{2+} release mechanism (positive inotropy). Furthermore, local

illumination allowed to identify regions in the heart which are more sensitive to pathological adrenergic effects such as the left atrium, in which arrhythmogenic premature contractions were induced by localized optogenetic G_s stimulation (Makowka et al., 2019). Importantly, in this special issue of Frontiers in Physiology, Cokic et al. show that long wave opsin enables control of the inhibitory G_i signaling pathway in CM using red light (625 nm), which is spectrally compatible with a blue light sensitive (450–550 nm) optogenetic actuators or reporters (Cokic et al., Optogenetic stimulation of G_i signaling enables instantaneous modulation of CM pacemaking, Cokic et al., this issue). Thus, the combination of Jellyfish Opsin with long wave cone Opsin will allow alternating activation of G_s and G_i signaling to study the effect of dysbalanced sympathetic and parasympathetic vegetative nerve input on the heart which may be involved in cardiac pathologies. Using implantable light emitting devices and optogenetic G protein-coupled receptors it will be possible to study acute and chronic effects of G_s, G_i or G_q stimulation on cardiac remodeling and electrophysiology including arrhythmia, hypertrophy or heart failure.

4.5. Immediate Translational Application of All-Optical Cardiac Electrophysiology

The pharmaceutical industry and associated regulatory authorities require that all drugs are tested for their cardiotoxic effects before being released for human testing. Early, comprehensive and inexpensive detection of pro-arrhythmic effects based on inhibition of ion channels that control excitability and action potential duration can save the industry considerable costs (Gintant et al., 2019). The CIPA (Comprehensive *In vitro* Pro-arrhythmia Assay) initiative has stimulated the development of newer testing platforms that can provide better predictive value for drug development. The features of an assay required by this sector are: (i) standardized cardiac cells/ tissue and protocols, (ii) scalability and medium-high throughput, i.e., hundreds of assays/ system/ day, and (iii) excellent predictive value relevant to human use. Over the last 10 years commercial sources of human iPSC-CM have become available as a source of standardized human myocardial material. Currently the electrophysiology of monolayer cultures human hiPSC-CM is the most common preparation with electrical activity of the monolayer assessed from an array of monopolar extracellular electrodes (micro-electrode array) embedded into the base of the culture dish. A limitation of these field potentials generated by the intrinsic spontaneous electrical activity of the coupled monolayer of cells is the poor capture of the repolarization dynamics, including action potential duration and shape, which are perceived as some of the most predictive indicators of pro-arrhythmic responses. Alternatively, ion channel responses are tested with planar automated patch clamp systems that offer scalability compared to the traditional gold standard to quantify electrophysiology. Both approaches, used by the pharmaceutical industry, have limitations stemming from the requirement for close contact between the cells and the

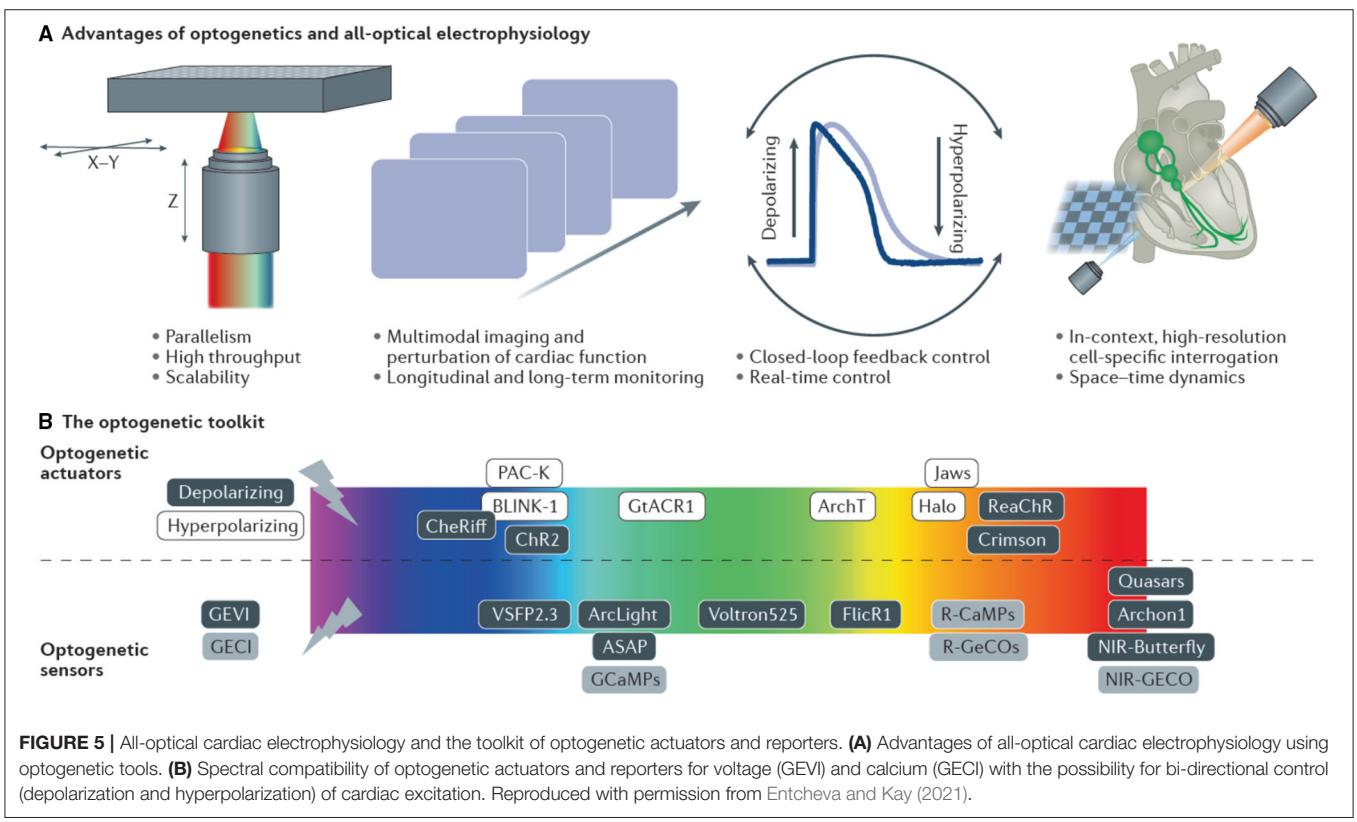

FIGURE 5 | All-optical cardiac electrophysiology and the toolkit of optogenetic actuators and reporters. **(A)** Advantages of all-optical cardiac electrophysiology using optogenetic tools. **(B)** Spectral compatibility of optogenetic actuators and reporters for voltage (GEVI) and calcium (GECI) with the possibility for bi-directional control (depolarization and hyperpolarization) of cardiac excitation. Reproduced with permission from Entcheva and Kay (2021).

electrodes for generating meaningful signals, which makes their use with iPSC-CM somewhat problematic.

Optical technologies for recording and for stimulation offer several advantages to address these challenges. As shown in **Figure 5A**, these advantages include built-in scalability and high-throughput due to: (i) contactless nature, (ii) high-content functional information through multi-modal imaging and control, (iii) longitudinal observations and (iv) the ability for closed-loop control within multicellular context. Optogenetic pacing has been combined with microelectrode array recordings for better control of the frequency (restitution) responses to drugs of human iPSC-CM (Lapp et al., 2017). Voltage-sensitive and calcium-sensitive dyes have been used in commercial pre-clinical assay platforms to quantify pro-arrhythmic responses to drugs (Hortigon-Vinagre et al., 2016; Pfeiffer-Kaushik et al., 2019).

Optogenetics-inspired developments of automated high-throughput platforms for drug testing using all-optical cardiac electrophysiology have been deployed in conjunction with human iPSC-CM (Dempsey et al., 2016; Klimas et al., 2016, 2020; Werley et al., 2017; Credi et al., 2021). These platforms incorporate spectrally-compatible optogenetic actuators with optogenetic and/or optical reporters for voltage and calcium (**Figure 5B**) to provide comprehensive characterization of electromechanical responses to drugs. Some of these systems have already found their way into the industrial setting. The immense information content from such high-throughput platforms, combined with machine learning algorithms can yield new hybrid *in vitro - in silico* methods for drug development and for better mechanistic understanding of cardiac arrhythmias. Furthermore, dye-free, completely non-invasive approaches (Ashraf et al., 2021), together with microfluidics-enabled high-throughput platforms (Wei et al., 2020) can allow the chronic longitudinal monitoring of human iPSC-CM. These techniques will facilitate studies on maturation processes, cardiac disease modeling and tissue regeneration.

5. FUNCTIONAL STUDIES IN ACTIVELY CONTRACTING CELLS AND WHOLE HEARTS

As pointed out before (e.g., section 4.3), imaging of "a moving target" poses significant challenges. In cardiac research, use of mechanical constraints that reduce tissue motion relative to the imaging system, or application of electro-mechanical uncouplers (such as blebbistatin, see section 2.1) have been employed to reduce what is often, if somewhat misleadingly, referred to as a motion artifact. Motion is an essential part of cardiac function, of course. Electrical activation, Ca^{2+}-mediated excitation-contraction coupling, contraction, relaxation and diastolic stretching, are all well-established targets for imaging. They are closely linked, over timescales from near-instantaneous beat-by-beat responses (e.g., stretch-activation of ion channels, Quinn and Kohl, 2021), over metabolic feedback to electro-mechanical function over minutes and hours (e.g., activation of K^+-channels that open in response to a reduction in ATP Van Wagoner and Lamorgese, 1994, on to tissue remodeling over years (e.g., during aging and in disease, Lyon et al., 2020). By restricting motion for the sake of functional observation, we alter the very system we wish to study (Kappadan et al., 2020).

Increasingly, therefore, attempts are being made to image cardiac structure and function while keeping the mechanical environment as close to *in vivo* conditions as possible. For cardiac cells and cultures, this involves tools to stretch single cells (Iribe et al., 2007) or cell cultures (Zhang et al., 2008). These have given rise to otherwise "hidden" physiological responses, such as the discovery of stretch-induced Ca^{2+} release from the sarcoplasmic reticulum (Iribe et al., 2009), or the mechanistic explanation of stretch-induced conduction slowing by surface membrane integration of caveolae (Pfeiffer et al., 2014). Optical voltage mapping in actively contracting Langendorff-perfused hearts, using ratiometry and software motion correction, reveals more physiologically relevant information about the electromechanical and energetic performance of the heart (Kuzmiak-Glancy et al., 2018; Kappadan et al., 2020).

It remains more difficult to take "motion" as an input parameter to ultrastructural research. Electron microscopy, for example, is conducted on fixed samples—so motion as such is excluded. Efforts have been made to control the mechanical state of cells or tissue, prior to fixation, and to use sarcomere length as a qualifier of the mechanical state of CM when exploring ultrastructural cell properties (Kohl et al., 2003). However, chemical tissue fixation is slow compared to beat-by-beat dynamics. This can be addressed by high pressure freezing, where recent commercial systems have built-in optical and electrical stimulation capacity so that CM may be preserved for electron microscopy at predefined states in their mechanical cycle. This type of approach has shown, for example, that the T-tubular system of ventricular CM (see section 2/**Figure 2**) is "squeezed" twice on every heartbeat (during diastolic stretch and during systolic contraction), and that this gives rise to an advection-mediated component of T-tubular content exchange (Rog-Zielinska et al., 2021). Over the next decade this direction of work should allow examination of the cross-talk between cardiac electrics, mechanics, metabolics, (epi-)genetics and structure in a time-resolved spatial manner as part of basic cardiac research.

All of these developments will also benefit from improved algorithms for "motion tracking"—i.e., computational post-processing that allows one to maintain the association between parameters recorded on fixed detectors (from optical mapping systems to echo and magnetic resonance imaging) with the underlying moving signal source (Inagaki et al., 2004). This can increasingly be done in a fiducial marker-free manner, using optical mapping data (Christoph and Luther, 2018), or even a combination of optical and echo data gathering (Christoph et al., 2018). The latter paper superbly illustrates the interrelation of electrical and mechanical waves, highlighting their close association in 3D myocardium.

In the clinical setting, tracking of cardiac motion not only provides important information of the ultimate function of the heart - its ability to pump blood - but it conveys insight into regional differences of activation and relaxation of ventricular myocardium. "Dys-synchrony" is problematic

for cardiac function, and mechanical mapping may provide insight into spatial heterogeneities, even of underlying electrical properties. In long QT syndrome, for example, disease diagnosis can be improved if mechanical properties are tracked (Lang et al., 2016). The benefit here is that it is comparatively straightforward to track motion non-invasively in 3D, and certainly easier to do so than to track electrical activity in 3D within the whole heart. A remaining caveat is that structural imaging to discern motion only offers direct insight into strain amplitudes and dynamics: thus far, there is no non-invasive technique to measure stress within the myocardium. In basic science, fluorescent reporters of stress are being developed (Meng et al., 2008; Grashoff et al., 2010; Meng and Sachs, 2012) which may pave the way toward—at least experimentally—tracking of both strain and stress in the heart. Metabolic optical imaging using native tissue fluorophores, e.g., NADH, is yet another clinically-translatable optical approach to quantifying cardiac function in health and disease with high spatial resolution (Wengrowski et al., 2014).

An exciting current development in dynamic cardiac 3D imaging is photoacoustic (or optoacoustic) imaging (Lin et al., 2018; Karlas et al., 2019). This uses a pulsed laser to deliver light into tissue. There, photons interact with suitable reporters, causing their transient thermoelastic expansion. The ultrasonic waves generated by this can be detected using ultrasonic transducers and analyzed to produce images of structure and function. Reporters can be native molecules, such as hemoglobin (whose photo-acoustic signature changes with oxygenation—for example allowing one to detect cancer in patients, Zalev et al., 2019), transgenically expressed probes such as GCaMP in experimental animals (Gottschalk et al., 2019), or dyes such as indocyanine green (Deán-Ben et al., 2015). The latter approach has been used for tomographic imaging of the beating, isolated mouse heart *in situ*. If this technique could be used in combination with recently developed photoacoustic voltage-sensitive dyes that allow one to "listen to voltage" (Zhang et al., 2017). This would represent a break-through for measuring transmural electro-mechanical dynamics in the heart.

6. CONCLUSIONS

This article highlights recent developments in the technical areas of optical voltage measurements and optogenetic applications to cardiac electrophysiology. While similar techniques are being developed in neuroscience, cardiac tissue presents a series of additional challenges related to the highly scattering nature of the myocardium and movement associated with contraction. In the past, progress in electrophysiology has relied on developments in physics and engineering. This article describes some of the fundamentals of physics that underlie optical techniques used to measure and manipulate the electrical activity of the heart. The prospect of translation of these research techniques to the clinic is also discussed as is their recent use in the industrial setting of toxicology screening for adverse effects on cardiac electrophysiology. In all of these situations, the use of optical tools to measure and manipulate cardiac electrophysiology is a rapidly advancing topic that promises to yield new insights and techniques to address the treatment of cardiac arrhythmias.

AUTHOR CONTRIBUTIONS

MCM, PK, LS, and GS planned the content. MCM and GS organized the writing. AK edited the initial submission. All authors contributed to the article and approved the submitted version.

ACKNOWLEDGMENTS

MCM acknowledges a Marie Sklodowska-Curie fellowship (MSCA-IF-EF-ST Grant Agreement No. 842893). AK was supported by the British Heart Foundation through project Grant PG/17/12/32847. EE acknowledges NIH Grant R01-HL144157 and NSF Grant EFMA 1830941. PK and LS are members of the German Centre of Research Excellence SFB1425 (DFG #422681845). SEL was supported by Deutsche Forschungsgemeinschaft through SFB1190 (project P03), and under Germanys Excellence Strategy 793 (EXC2067/1-390729940). SEL is an investigator of DZHK (German Centre for Cardiovascular Research). TZ acknowledges STARS-SKoOP (UNIPD). The authors would like to thank Dr. Remi Peyronnet, Dr. Eva Rog-Zielinska, Dr. Franziska Schneider-Warme, Dr. Viviane Timmermann, and Dr. Callum Zgierski-Johnston from the Institute for Experimental Cardiovascular Medicine, University of Freiburg for their critical reading of and editorial comments on a revised form of this manuscript.

REFERENCES

Optogenetics at Stanford. Available online at: https://web.stanford.edu/group/dlab/optogenetics (accessed March 11, 2020).

Abdelfattah, A. S., Kawashima, T., Singh, A., Novak, O., Liu, H., Shuai, Y., et al. (2019). Bright and photostable chemigenetic indicators for extended *in vivo* voltage imaging. *Science* 365, 699–704. doi: 10.1126/science.aav6416

Acker, C. D., Yan, P., and Loew, L. M. (2011). Single-voxel recording of voltage transients in dendritic spines. *Biophys. J.* 101, L11–L13. doi: 10.1016/j.bpj.2011.06.021

Acker, C. D., Yan, P., and Loew, L. M. (2020). Recent progress in optical voltage-sensor technology and applications to cardiac research: from single cells to whole hearts. *Prog. Biophys. Mol. Biol.* 154, 3–10. doi: 10.1016/j.pbiomolbio.2019.07.004

Akturk, S., Gu, X., Kimmel, M., and Trebino, R. (2006). Extremely simple single-prism ultrashort-pulse compressor. *Optics Express* 14, 10101–10108. doi: 10.1364/OE.14.010101

Alfred Millett-Sikking, N. H., Thayer, A. B., and York, A. G. (2018). *Remote Refocus Enables Class-Leading Spatiotemporal Resolution in 4D optical Microscopy*. Github.

Arrenberg, A., Stainier, D., Baier, H., and Huisken, J. (2010). Optogenetic control of cardiac function. *Science* 330, 971–974. doi: 10.1126/science.1195929

Ashraf, M., Mohanan, S., Sim, B., Tam, A., Rahemipour, K., Brousseau, D., et al. (2021). Random access parallel microscopy. *eLife* 10:e56426. doi: 10.7554/eLife.56426

Bachtel, A. D., Gray, R. A., Stohlman, J. M., Bourgeois, E. B., Pollard, A. E., and Rogers, J. M. (2011). A novel approach to dual excitation ratiometric optical mapping of cardiac action potentials with di-4-ANEPPS using pulsed led excitation. *IEEE Trans. Biomed. Eng.* 58, 2120–2126. doi: 10.1109/TBME.2011.2148719

Beiert, T., Bruegmann, T., and Sasse, P. (2014). Optogenetic activation of GQ signalling modulates pacemaker activity of cardiomyocytes. *Cardiovasc. Res.* 102, 507–516. doi: 10.1093/cvr/cvu046

Bergmann, O., Bhardwaj, R. D., Bernard, S., Zdunek, S., Barnabé-Heider, F., Walsh, S., et al. (2009). Evidence for cardiomyocyte renewal in humans. *Science* 324, 98–102. doi: 10.1126/science.1164680

Bers, D. M., and Shannon, T. R. (2013). Calcium movements inside the sarcoplasmic reticulum of cardiac myocytes. *J. Mol. Cell. Cardiol.* 58, 59–66. doi: 10.1016/j.yjmcc.2013.01.002

Botcherby, E. J., Corbett, A., Burton, R. A., Smith, C. W., Bollensdorff, C., Booth, M. J., et al. (2013). Fast measurement of sarcomere length and cell orientation in Langendorff-perfused hearts using remote focusing microscopy. *Circ. Res.* 113, 863–870. doi: 10.1161/CIRCRESAHA.113.301704

Botcherby, E. J., Juškaitis, R., Booth, M. J., and Wilson, T. (2008). An optical technique for remote focusing in microscopy. *Optics Commun.* 281, 880–887. doi: 10.1016/j.optcom.2007.10.007

Boyden, E. S., Zhang, F., Bamberg, E., Nagel, G., and Deisseroth, K. (2005). Millisecond-timescale, genetically targeted optical control of neural activity. *Nat. Neurosci.* 8, 1263–1268. doi: 10.1038/nn1525

Boyle, P., Yu, J., Klimas, A., Williams, J., Trayanova, N., and Entcheva, E. (2021). Optogap is an optogenetics-enabled assay for quantification of cell-cell coupling in multicellular cardiac tissue. *Sci. Rep.* 11:9310. doi: 10.1038/s41598-021-88573-1

Brack, K. E., Narang, R., Winter, J., and Ng, A. (2013). The mechanical uncoupler blebbistatin is associated with significant electrophysiological effects in the isolated heart. *Exp. Physiol.* 98, 1009–1027. doi: 10.1113/expphysiol.2012.069369

Brandenburg, S., Arakel, E. C., Schwappach, B., and Lehnart, S. E. (2016a). The molecular and functional identities of atrial cardiomyocytes in health and disease. *Biochim. Biophys. Acta Mol. Cell Res.* 1863, 1882–1893. doi: 10.1016/j.bbamcr.2015.11.025

Brandenburg, S., Kohl, T., Williams, G. S., Gusev, K., Wagner, E., Rog-Zielinska, E. A., et al. (2016b). Axial tubule junctions control rapid calcium signaling in atria. *J. Clin. Investig.* 126, 3999–4015. doi: 10.1172/JCI88241

Brandenburg, S., Pawlowitz, J., Eikenbusch, B., Peper, J., Kohl, T., Mitronova, G. Y., et al. (2019). Junctophilin-2 expression rescues atrial dysfunction through polyadic junctional membrane complex biogenesis. *JCI Insight* 4:127116. doi: 10.1172/jci.insight.127116

Brandenburg, S., Pawlowitz, J., Fakuade, F. E., Kownatzki-Danger, D., Kohl, T., Mitronova, G. Y., et al. (2018). Axial tubule junctions activate atrial Ca^{2+} release across species. *Front. Physiol.* 9:1227. doi: 10.3389/fphys.2018.01227

Bruegmann, T., Beiert, T., Vogt, C., Schrickel, J., and Sasse, P. (2018). Optogenetic termination of atrial fibrillation in mice. *Cardiovasc. Res.* 114, 713–723. doi: 10.1093/cvr/cvx250

Bruegmann, T., Boyle, P., Christoph, C., Vogt, V., Karathanos, T., Hermenegild, A., et al. (2016). Optogenetic defibrillation terminates ventricular arrhythmia in mouse hearts and human simulations. *J. Clin. Investig.* 126, 3894–3904. doi: 10.1172/JCI88950

Bruegmann, T., Malan, D., Hesse, M., Beiert, T., Fuegemann, C. J., Fleischmann, B. K., et al. (2010). Optogenetic control of heart muscle *in vitro* and *in vivo*. *Nature Methods* 7:897. doi: 10.1038/nmeth.1512

Bub, G., Tecza, M., Helmes, M., Lee, P., and Kohl, P. (2010). Temporal pixel multiplexing for simultaneous high-speed, high resolution imaging. *Nature Methods* 7, 209–211. doi: 10.1038/nmeth.1429

Burton, R., Tomek, J., Ambrosi, C., Larsen, H., Sharkey, A., Capel, R., et al. (2020). Optical interrogation of sympathetic neuronal effects on macroscopic cardiomyocyte network dynamics. *iScience* 23:101334. doi: 10.1016/j.isci.2020.101334

Burton, R. A., Klimas, A., Ambrosi, C. M., Tomek, J., Corbett, A., Entcheva, E., et al. (2015). Optical control of excitation waves in cardiac tissue. *Nat. Photon.* 9:813. doi: 10.1038/nphoton.2015.196

Bush, P. G., Wokosin, D. L., and Hall, A. C. (2007). Two-versus one photon excitation laser scanning microscopy: critical importance of excitation wavelength. *Front. Biosci.* 12:2646. doi: 10.2741/2261

Byars, J. L., Smith, W. M., Ideker, R. E., and Fast, V. G. (2003). Development of an optrode for intramural multisite optical recordings of VM in the heart. *J. Cardiovasc. Electrophysiol.* 14, 1196–1202. doi: 10.1046/j.1540-8167.2003.03203.x

Caldwell, B. J., Legrice, I. J., Hooks, D. A., Tai, D. C.-S., Pullan, A. J., and Smaill, B. H. (2005). Intramural measurement of transmembrane potential in the isolated pig heart: validation of a novel technique. *J. Cardiovasc. Electrophysiol.* 16, 1001–1010. doi: 10.1111/j.1540-8167.2005.40558.x

Camelliti, P., Abou Al-Saud, S., Smolenski, R. T., Al-Ayoubi, S., Bussek, A., Wettwer, E., et al. (2011). Adult human heart slices are a multicellular system suitable for electrophysiological and pharmacological studies. *J. Mol. Cell. Cardiol.* 51, 390–398. doi: 10.1016/j.yjmcc.2011.06.018

Cathey, B., Obaid, S., Zolotarev, A. M., Pryamonosov, R. A., Syunyaev, R. A., George, S. A., et al. (2019). Open-source multiparametric optocardiography. *Sci. Rep.* 9, 1–12. doi: 10.1038/s41598-018-36809-y

Centonze, V. E., and White, J. G. (1998). Multiphoton excitation provides optical sections from deeper within scattering specimens than confocal imaging. *Biophys. J.* 75, 2015–2024. doi: 10.1016/S0006-3495(98)77643-X

Chen, T.-W., Wardill, T. J., Sun, Y., Pulver, S. R., Renninger, S. L., Baohan, A., et al. (2013). Ultrasensitive fluorescent proteins for imaging neuronal activity. *Nature* 499, 295–300. doi: 10.1038/nature12354

Christoph, J., Chebbok, M., Richter, C., Schröder-Schetelig, J., Bittihn, P., Stein, S., et al. (2018). Electromechanical vortex filaments during cardiac fibrillation. *Nature* 555, 667–672. doi: 10.1038/nature26001

Christoph, J., and Luther, S. (2018). Marker-free tracking for motion artifact compensation and deformation measurements in optical mapping videos of contracting hearts. *Front. Physiol.* 9:1483. doi: 10.3389/fphys.2018.01483

Chung, K., Wallace, J., Kim, S.-Y., Kalyanasundaram, S., Andalman, A. S., Davidson, T. J., et al. (2013). Structural and molecular interrogation of intact biological systems. *Nature* 497, 332–337. doi: 10.1038/nature12107

Cingolani, E., Ionta, V., Cheng, K., Giacomello, A., Cho, H. C., and Marbán, E. (2014). Engineered electrical conduction tract restores conduction in complete heart block: from *in vitro* to *in vivo* proof of concept. *J. Am. Coll. Cardiol.* 64, 2575–2585. doi: 10.1016/j.jacc.2014.09.056

Credi, C., Balducci, V., Munagala, U., Cianca, C., Bigiarini, S., De Vries, A. A., et al. (2021). Fast optical investigation of cardiac electrophysiology by parallel detection in multiwell plates. *Front. Physiol.* 12:692496. doi: 10.3389/fphys.2021.692496

Crocini, C., Coppini, R., Ferrantini, C., Yan, P., Loew, L. M., Tesi, C., et al. (2014). Defects in t-tubular electrical activity underlie local alterations of calcium release in heart failure. *Proc. Natl. Acad. Sci. U.S.A.* 111, 15196–15201. doi: 10.1073/pnas.1411557111

Crocini, C., Ferrantini, C., Coppini, R., Scardigli, M., Yan, P., Loew, L. M., et al. (2016a). Optogenetics design of mechanistically-based stimulation patterns for cardiac defibrillation. *Sci. Rep.* 6:35628. doi: 10.1038/srep35628

Crocini, C., Ferrantini, C., Scardigli, M., Coppini, R., Mazzoni, L., Lazzeri, E., et al. (2016b). Novel insights on the relationship between t-tubular defects and contractile dysfunction in a mouse model of hypertrophic cardiomyopathy. *J. Mol. Cell. Cardiol.* 91, 42–51. doi: 10.1016/j.yjmcc.2015.12.013

De Mena, L., Rizk, P., and Rincon-Limas, D. E. (2018). Bringing light to transcription: the optogenetics repertoire. *Front. Genet.* 9:518. doi: 10.3389/fgene.2018.00518

Deán-Ben, X. L., Ford, S. J., and Razansky, D. (2015). High-frame rate four dimensional optoacoustic tomography enables visualization of cardiovascular dynamics and mouse heart perfusion. *Sci. Rep.* 5, 1–9. doi: 10.1038/srep13240

Deisseroth, K. (2011). Optogenetics. *Nat. Methods* 8, 26–29. doi: 10.1038/nmeth.f.324

Dempsey, G., Chaudhary, K., Atwater, N., Nguyen, C., Brown, B., McNeish, J., et al. (2016). Cardiotoxicity screening with simultaneous optogenetic pacing, voltage

imaging and calcium imaging. *J. Pharmacol. Toxicol. Methods* 81, 240–250. doi: 10.1016/j.vascn.2016.05.003

Deng, W., Goldys, E. M., Farnham, M. M., and Pilowsky, P. M. (2014). Optogenetics, the intersection between physics and neuroscience: light stimulation of neurons in physiological conditions. *Am. J. Physiol. Regul. Integr. Comp. Physiol.* 307, R1292–R1302. doi: 10.1152/ajpregu.00072.2014

Denk, W., Strickler, J. H., and Webb, W. W. (1990). Two-photon laser scanning fluorescence microscopy. *Science* 248, 73–76. doi: 10.1126/science.2321027

Di Diego, J. M., Sicouri, S., Myles, R. C., Burton, F. L., and Smith, G. L. (2013). Optical and electrical recordings from isolated coronary-perfused ventricular wedge preparations. *J. Mol. Cell. Cardiol.* 54, 53–64. doi: 10.1016/j.yjmcc.2012.10.017

Efimov, I. R., Huang, D. T., Rendt, J. M., and Salama, G. (1994). Optical mapping of repolarization and refractoriness from intact hearts. *Circulation* 90, 1469–1480. doi: 10.1161/01.CIR.90.3.1469

Entcheva, E., and Bien, H. (2006). Macroscopic optical mapping of excitation in cardiac cell networks with ultra-high spatiotemporal resolution. *Prog. Biophys. Mol. Biol.* 92, 232–257. doi: 10.1016/j.pbiomolbio.2005.10.003

Entcheva, E., and Bub, G. (2016). All-optical control of cardiac excitation: combined high-resolution optogenetic actuation and optical mapping. *J. Physiol.* 594, 2503–2510. doi: 10.1113/JP271559

Entcheva, E., and Kay, M. W. (2021). Cardiac optogenetics: a decade of enlightenment. *Nat. Rev. Cardiol.* 18, 349–367. doi: 10.1038/s41569-020-00478-0

Fatkin, D., Otway, R., and Vandenberg, J. I. (2007). Genes and atrial fibrillation: a new look at an old problem. *Circulation* 116, 782–792. doi: 10.1161/CIRCULATIONAHA.106.688889

Fedorov, V. V., Lozinsky, I. T., Sosunov, E. A., Anyukhovsky, E. P., Rosen, M. R., Balke, C. W., et al. (2007). Application of blebbistatin as an excitation-contraction uncoupler for electrophysiologic study of rat and rabbit hearts. *Heart Rhythm* 4, 619–626. doi: 10.1016/j.hrthm.2006.12.047

Franz, M. (1999). Current status of monophasic action potential recording: theories, measurements and interpretations. *Cardiovasc. Res.* 41, 25–40. doi: 10.1016/S0008-6363(98)00268-5

Franzoso, M., Zaglia, T., and Mongillo, M. (2016). Putting together the clues of the everlasting neuro-cardiac liaison. *Biochim. Biophys. Acta Mol Cell Res.* 1863, 1904–1915. doi: 10.1016/j.bbamcr.2016.01.009

Funken, M., Bruegmann, T., and Sasse, P. (2020). Selective optogenetic stimulation of fibroblasts enables quantification of hetero-cellular coupling to cardiomyocytes in a three-dimensional model of heart tissue. *Europace* 22, 1590–1599. doi: 10.1093/europace/euaa128

Funken, M., Malan, D., Sasse, P., and Bruegmann, T. (2019). Optogenetic hyperpolarization of cardiomyocytes terminates ventricular arrhythmia. *Front. Physiol.* 10:498. doi: 10.3389/fphys.2019.00498

Gao, L., Kupfer, M. E., Jung, J. P., Yang, L., Zhang, P., Da Sie, Y., et al. (2017). Myocardial tissue engineering with cells derived from human-induced pluripotent stem cells and a native-like, high-resolution, 3-dimensionally printed scaffold. *Circ. Res.* 120, 1318–1325. doi: 10.1161/CIRCRESAHA.116.310277

Ghouri, I. A., Kelly, A., Burton, F. L., Smith, G. L., and Kemi, O. J. (2015). 2-photon excitation fluorescence microscopy enables deeper high-resolution imaging of voltage and Ca^{2+} in intact mice, rat, and rabbit hearts. *J. Biophoton.* 8, 112–123. doi: 10.1002/jbio.201300109

Ghouri, I. A., Kelly, A., Salerno, S., Garten, K., Stølen, T., Kemi, O.-J., et al. (2018). Characterization of electrical activity in post-myocardial infarction scar tissue in rat hearts using multiphoton microscopy. *Front. Physiol.* 9:1454. doi: 10.3389/fphys.2019.00364

Gintant, G., Burridge, P., Gepstein, L., Harding, S., Herron, T., Hong, C., et al. (2019). Use of human induced pluripotent stem cell-derived cardiomyocytes in preclinical cancer drug cardiotoxicity testing: a scientific statement from the american heart association. *Circ. Res.* 125, e75–e92. doi: 10.1161/RES.0000000000000291

Girouard, S., Laurita, K., and Rosenbaum, D. (1996). Unique properties of cardiac action potentials recorded with voltage-sensitive dyes. *J. Cardiovasc. Electrophysiol.* 7, 1024–1038. doi: 10.1111/j.1540-8167.1996.tb00478.x

Goette, A., Kalman, J. M., Aguinaga, L., Akar, J., Cabrera, J. A., Chen, S. A., et al. (2016). EHRA/HRS/APHRS/SOLAECE expert consensus on atrial cardiomyopathies: definition, characterization, and clinical implication. *Europace* 18, 1455–1490. doi: 10.1093/europace/euw161

Gottschalk, S., Degtyaruk, O., Mc Larney, B., Rebling, J., Hutter, M. A., Deán-Ben, X. L., et al. (2019). Rapid volumetric optoacoustic imaging of neural dynamics across the mouse brain. *Nat. Biomed. Eng.* 3, 392–401. doi: 10.1038/s41551-019-0372-9

Grashoff, C., Hoffman, B. D., Brenner, M. D., Zhou, R., Parsons, M., Yang, M. T., et al. (2010). Measuring mechanical tension across vinculin reveals regulation of focal adhesion dynamics. *Nature* 466, 263–266. doi: 10.1038/nature09198

Greiser, M., Kerfant, B.-G., Williams, G. S., Voigt, N., Harks, E., Dibb, K. M., et al. (2014). Tachycardia-induced silencing of subcellular Ca^{2+} signaling in atrial myocytes. *J. Clin. Investig.* 124, 4759–4772. doi: 10.1172/JCI70102

Grynkiewicz, G., Poenie, M., and Tsien, R. Y. (1985). A new generation of Ca^{2+} indicators with greatly improved fluorescence properties. *J. Biol. Chem.* 260, 3440–3450. doi: 10.1016/S0021-9258(19)83641-4

Gutruf, P., Yin, R. T., Lee, K. B., Ausra, J., Brennan, J. A., Qiao, Y., et al. (2019). Wireless, battery-free, fully implantable multimodal and multisite pacemakers for applications in small animal models. *Nat. Commun.* 10, 1–10. doi: 10.1038/s41467-019-13637-w

Helmchen, F., and Denk, W. (2005). Deep tissue two-photon microscopy. *Nat. Methods* 2, 932–940. doi: 10.1038/nmeth818

Hicks, M., and Cobbe, S. (1991). Effect of glibenclamide on extracellular potassium accumulation and the electrophysiological changes during myocardial ischaemia in the arterially perfused interventricular septum of rabbit. *Cardiovasc. Res.* 25, 407–413. doi: 10.1093/cvr/25.5.407

Hooks, D. A., Trew, M. L., Caldwell, B. J., Sands, G. B., LeGrice, I. J., and Smaill, B. H. (2007). Laminar arrangement of ventricular myocytes influences electrical behavior of the heart. *Circ. Res.* 101, e103–e112. doi: 10.1161/CIRCRESAHA.107.161075

Hortigon-Vinagre, M., Zamora, V., Burton, F., Green, J., Gintant, G., and Smith, G. (2016). The use of ratiometric fluorescence measurements of the voltage sensitive dye Di-4-ANEPPS to examine action potential characteristics and drug effects on human induced pluripotent stem cell-derived cardiomyocytes. *Toxicol. Sci.* 154, 320–331. doi: 10.1093/toxsci/kfw171

Huang, Y., Walker, A. S., and Miller, E. W. (2015). A photostable silicon rhodamine platform for optical voltage sensing. *J. Am. Chem. Soc.* 137, 10767–10776. doi: 10.1021/jacs.5b06644

Huisken, J., Swoger, J., Del Bene, F., Wittbrodt, J., and Stelzer, E. H. (2004). Optical sectioning deep inside live embryos by selective plane illumination microscopy. *Science* 305, 1007–1009. doi: 10.1126/science.1100035

Hulsmans, M., Clauss, S., Xiao, L., Aguirre, A. D., King, K. R., Hanley, A., et al. (2017). Macrophages facilitate electrical conduction in the heart. *Cell* 169, 510–522. doi: 10.1016/j.cell.2017.03.050

Hurley, M. E., Sheard, T. M., Norman, R., Kirton, H. M., Shah, S. S., Pervolaraki, E., et al. (2020). A correlative super-resolution protocol to visualise structural underpinnings of fast second-messenger signalling in primary cell types. *Methods.* 193, 27–37. doi: 10.1016/j.ymeth.2020.10.005

Hussaini, S., Venkatesan, V., Biasci, V., Romero Sepúlveda, J. M., Quinonez Uribe, R. A., Sacconi, L., et al. (2021). Drift and termination of spiral waves in optogenetically modified cardiac tissue at sub-threshold illumination. *eLife* 10:e59954. doi: 10.7554/eLife.59954

Hyatt, C. J., Mironov, S. F., Vetter, F. J., Zemlin, C. W., and Pertsov, A. M. (2005). Optical action potential upstroke morphology reveals near-surface transmural propagation direction. *Circ. Res.* 97, 277–284. doi: 10.1161/01.RES.0000176022.74579.47

Inagaki, M., Hidaka, I., Aiba, T., Tatewaki, T., Sunagawa, K., and Sugimachi, M. (2004). "High resolution optical mapping of cardiac action potentials in freely beating rabbit hearts," in *26th Annual International Conference of the IEEE Engineering in Medicine and Biology Society* (IEEE), 3578–3580. doi: 10.1109/IEMBS.2004.1404006

Iribe, G., Helmes, M., and Kohl, P. (2007). Force-length relations in isolated intact cardiomyocytes subjected to dynamic changes in mechanical load. *Am. J. Physiol. Heart Circ. Physiol.* 292, H1487–H1497. doi: 10.1152/ajpheart.00909.2006

Iribe, G., Ward, C. W., Camelliti, P., Bollensdorff, C., Mason, F., Burton, R. A., et al. (2009). Axial stretch of rat single ventricular cardiomyocytes causes

an acute and transient increase in Ca^{2+} spark rate. *Circ. Res*. 104, 787–795. doi: 10.1161/CIRCRESAHA.108.193334

Jaimes, I. I. I., R., Walton, R. D., Pasdois, P., Bernus, O., Efimov, I. R., et al. (2016). A technical review of optical mapping of intracellular calcium within myocardial tissue. *Am. J. Physiol. Heart Circ. Physiol*. 310, H1388–H1401. doi: 10.1152/ajpheart.00665.2015

Jia, Z., Valiunas, V., Lu, Z., Bien, H., Liu, H., Wang, H., et al. (2011). Stimulating cardiac muscle by light: cardiac optogenetics by cell delivery. *Circ. Arrhythmia Electrophysiol*. 4, 753–760. doi: 10.1161/CIRCEP.111.964247

Jin, L., Han, Z., Platisa, J., Wooltorton, J. R., Cohen, L. B., and Pieribone, V. A. (2012). Single action potentials and subthreshold electrical events imaged in neurons with a fluorescent protein voltage probe. *Neuron* 75, 779–785. doi: 10.1016/j.neuron.2012.06.040

Julian, K., Prichard, B., Raco, J., Jain, R., and Jain, R. (2021). A review of cardiac autonomics: from pathophysiology to therapy. *Future Cardiol*. doi: 10.2217/fca-2021-0041. [Epub ahead of print].

Kanai, A., and Salama, G. (1995). Optical mapping reveals that repolarization spreads anisotropically and is guided by fiber orientation in guinea pig hearts. *Circ. Res*. 77, 784–802. doi: 10.1161/01.RES.77.4.784

Kappadan, V., Telele, S., Uzelac, I., Fenton, F., Parlitz, U., Luther, S., et al. (2020). High-resolution optical measurement of cardiac restitution, contraction, and fibrillation dynamics in beating vs. blebbistatin-uncoupled isolated rabbit hearts. *Front. Physiol*. 11:464. doi: 10.3389/fphys.202 0.00464

Karlas, A., Fasoula, N.-A., Paul-Yuan, K., Reber, J., Kallmayer, M., Bozhko, D., et al. (2019). Cardiovascular optoacoustics: from mice to men-a review. *Photoacoustics* 14, 19–30. doi: 10.1016/j.pacs.2019.03.001

Kelly, A., Ghouri, I. A., Kemi, O. J., Bishop, M. J., Bernus, O., Fenton, F. H., et al. (2013). Subepicardial action potential characteristics are a function of depth and activation sequence in isolated rabbit hearts. *Circ. Arrhythmia Electrophysiol*. 6, 809–817. doi: 10.1161/CIRCEP.113.000334

Kelly, A., Salerno, S., Connolly, A., Bishop, M., Charpentier, F., Stølen, T., et al. (2018). Normal interventricular differences in tissue architecture underlie right ventricular susceptibility to conduction abnormalities in a mouse model of brugada syndrome. *Cardiovasc. Res*. 114, 724–736. doi: 10.1093/cvr/cvx244

Képiró, M., Várkuti, B. H., Végner, L., Vörös, G., Hegyi, G., Varga, M., et al. (2014). para-nitroblebbistatin, the non-cytotoxic and photostable myosin ii inhibitor. *Angew. Chem. Int. Ed*. 53, 8211–8215. doi: 10.1002/anie.201403540

Kettlewell, S., Walker, N., Burton, F., and Smith, G. (2004). The electrophysiological and mechanical effects of 2,3-butanedione monoxime and cytochalasin-d in the Langendorff perfused rabbit heart. *Exp. Physiol*. 89, 163–172. doi: 10.1113/expphysiol.2003.026732

Kirk, M. M., Izu, L. T., Chen-Izu, Y., McCulle, S. L., Wier, W. G., Balke, C. W., et al. (2003). Role of the transverse-axial tubule system in generating calcium sparks and calcium transients in rat atrial myocytes. *J. Physiol*. 547, 441–451. doi: 10.1113/jphysiol.2002.034355

Klimas, A., Ambrosi, C. M., Yu, J., Williams, J. C., Bien, H., and Entcheva, E. (2016). Optodyce as an automated system for high-throughput all-optical dynamic cardiac electrophysiology. *Nat. Commun*. 7, 1–12. doi: 10.1038/ncomms11542

Klimas, A., Ortiz, G., Boggess, S., Miller, E., and Entcheva, E. (2020). Multimodal on-axis platform for all-optical electrophysiology with near-infrared probes in human stem-cell-derived cardiomyocytes. *Prog. Biophys. Mol. Biol*. 154, 62–70. doi: 10.1016/j.pbiomolbio.2019.02.004

Kohl, P. (2014). Structural and functional recoupling of atrial and ventricular myocardium. *J. Am. Coll. Cardiol*. 64, 2586–2588. doi: 10.1016/j.jacc.2014.09.055

Kohl, P., Cooper, P. J., and Holloway, H. (2003). Effects of acute ventricular volume manipulation on *in situ* cardiomyocyte cell membrane configuration. *Prog. Biophys. Mol. Biol*. 82, 221–227. doi: 10.1016/S0079-6107(03)00024-5

Kohl, P., Kamkin, A., Kiseleva, I., and Noble, D. (1994). Mechanosensitive fibroblasts in the sino-atrial node region of rat heart: interaction with cardiomyocytes and possible role. *Exp. Physiol. Transl. Integr*. 79, 943–956. doi: 10.1113/expphysiol.1994.sp003819

Kong, C. H., Rog-Zielinska, E. A., Kohl, P., Orchard, C. H., and Cannell, M. B. (2018). Solute movement in the t-tubule system of rabbit and mouse cardiomyocytes. *Proc. Natl. Acad. Sci*. 115, E7073–E7080. doi: 10.1073/pnas.1805979115

Koopman, C. D., Zimmermann, W. H., Knöpfel, T., and de Boer, T. P. (2017). Cardiac optogenetics: using light to monitor cardiac physiology. *Basic Res. Cardiol*. 112, 1–13. doi: 10.1007/s00395-017-0645-y

Kopton, R. A., Baillie, J. S., Rafferty, S. A., Moss, R., Zgierski-Johnston, C. M., Prykhozhij, S. V., et al. (2018). Cardiac electrophysiological effects of light-activated chloride channels. *Front. Physiol*. 9:1806. doi: 10.3389/fphys.2018.01806

Kostecki, G., Shi, Y., Chen, C., Reich, D., Entcheva, E., and Tung, L. (2021). Optogenetic current in myofibroblasts acutely alters electrophysiology and conduction of co-cultured cardiomyocytes. *Sci. Rep*. 11:4430. doi: 10.1038/s41598-021-83398-4

Kotlikoff, M. I. (2007). Genetically encoded Ca^{2+} indicators: using genetics and molecular design to understand complex physiology. *J. Physiol*. 578, 55–67. doi: 10.1113/jphysiol.2006.120212

Kreisel, D., Nava, R. G., Li, W., Zinselmeyer, B. H., Wang, B., Lai, J., et al. (2010). *In vivo* two-photon imaging reveals monocyte-dependent neutrophil extravasation during pulmonary inflammation. *Proc. Natl. Acad. Sci. U.S.A*. 107, 18073–18078. doi: 10.1073/pnas.1008737107

Kuzmiak-Glancy, S., Covian, R., Femnou, A., Glancy, B., Jaimes, R., Wengrowski, A. W., et al. (2018). Cardiac performance is limited by oxygen delivery to the mitochondria in the crystalloid-perfused working heart. *Am. J. Physiol. Heart Circ. Physiol*. 314, H704–H715. doi: 10.1152/ajpheart.00321.2017

Lang, C., Menza, M., Jochem, S., Franke, G., Feliz, S. P., Brunner, M., et al. (2016). Electro-mechanical dysfunction in long qt syndrome: role for arrhythmogenic risk prediction and modulation by sex and sex hormones. *Prog. Biophys. Mol. Biol*. 120, 255–269. doi: 10.1016/j.pbiomolbio.2015.12.010

Lapp, H., Bruegmann, T., Malan, D., Friedrichs, S., Kilgus, C., Heidsieck, A., et al. (2017). Frequency-dependent drug screening using optogenetic stimulation of human iPSC-derived cardiomyocytes. *Sci. Rep*. 7, 1–12. doi: 10.1038/s41598-017-09760-7

Lee, P., Bollensdorff, C., Quinn, T. A., Wuskell, J. P., Loew, L. M., and Kohl, P. (2011). Single-sensor system for spatially resolved, continuous, and multiparametric optical mapping of cardiac tissue. *Heart Rhythm* 8, 1482–1491. doi: 10.1016/j.hrthm.2011.03.061

Lee, P., Quintanilla, J. G., Alfonso-Almazan, J. M., Galán-Arriola, C., Yan, P., Sánchez-González, J., et al. (2019). *In vivo* ratiometric optical mapping enables high-resolution cardiac electrophysiology in pig models. *Cardiovasc. Res*. 115, 1659–1671. doi: 10.1093/cvr/cvz039

Lee, P., Taghavi, F., Yan, P., Ewart, P., Ashley, E. A., Loew, L. M., et al. (2012a). *In situ* optical mapping of voltage and calcium in the heart. *PLoS ONE* 7:e42562. doi: 10.1371/journal.pone.0042562

Lee, P., Yan, P., Ewart, P., Kohl, P., Loew, L. M., and Bollensdorff, C. (2012b). Simultaneous measurement and modulation of multiple physiological parameters in the isolated heart using optical techniques. *Pflügers Arch. Eur. J. Physiol*. 464, 403–414. doi: 10.1007/s00424-012-1135-6

Lee, S., Vinegoni, C., Feruglio, P. F., Fexon, L., Gorbatov, R., Pivoravov, M., et al. (2012c). Real-time *in vivo* imaging of the beating mouse heart at microscopic resolution. *Nat. Commun*.3, 1–8. doi: 10.1038/ncomms2060

Leray, A., Lillis, K., and Mertz, J. (2008). Enhanced background rejection in thick tissue with differential-aberration two-photon microscopy. *Biophys. J*. 94, 1449–1458. doi: 10.1529/biophysj.107.111476

Leray, A., and Mertz, J. (2006). Rejection of two-photon fluorescence background in thick tissue by differential aberration imaging. *Optics Express* 14, 10565–10573. doi: 10.1364/OE.14.010565

Li, W., Goldstein, D. R., and Kreisel, D. (2013). Intravital 2-photon imaging, leukocyte trafficking, and the beating heart. *Trends Cardiovasc. Med*. 23, 287–293. doi: 10.1016/j.tcm.2013.04.002

Lin, H.-C. A., Déan-Ben, X. L., Reiss, M., Schöttle, V., Wahl-Schott, C. A., Efimov, I. R., et al. (2018). Ultrafast volumetric optoacoustic imaging of whole isolated beating mouse heart. *Sci. Rep*. 8, 1–7. doi: 10.1038/s41598-018-32317-1

Lüss, I., Boknik, P., Jones, L. R., Kirchhefer, U., Knapp, J., Linck, B., et al. (1999). Expression of cardiac calcium regulatory proteins in atrium v ventricle in different species. *J. Mol. Cell. Cardiol*. 31, 1299–1314. doi: 10.1006/jmcc.1999.0962

Lyon, A., Babalis, D., Morley-Smith, A., Hedger, M., Barrientos, A. S., Foldes, G., et al. (2020). Investigation of the safety and feasibility of AAV1/SERCA2a gene transfer in patients with chronic heart failure supported with a left

ventricular assist device-the serca-lvad trial. *Gene Therapy* 27, 579–590. doi: 10.1038/s41434-020-0171-7

Makowka, P., Bruegmann, T., Dusend, V., Malan, D., Beiert, T., Hesse, M., et al. (2019). Optogenetic stimulation of G_s-signaling in the heart with high spatio-temporal precision. *Nat. Commun*. 10:1281. doi: 10.1038/s41467-019-09322-7

Martin, T. P., Norris, G., McConnell, G., and Currie, S. (2013). A novel approach for assessing cardiac fibrosis using label-free second harmonic generation. *Int. J. Cardiovasc. Imaging* 29, 1733–1740. doi: 10.1007/s10554-013-0270-2

Matsuo, T., Masumoto, H., Tajima, S., Ikuno, T., Katayama, S., Minakata, K., et al. (2015). Efficient long-term survival of cell grafts after myocardial infarction with thick viable cardiac tissue entirely from pluripotent stem cells. *Sci. Rep*. 5, 1–14. doi: 10.1038/srep16842

Meng, F., and Sachs, F. (2012). Orientation-based fret sensor for real-time imaging of cellular forces. *J. Cell Sci*. 125, 743–750. doi: 10.1242/jcs.093104

Meng, F., Suchyna, T. M., and Sachs, F. (2008). A fluorescence energy transfer-based mechanical stress sensor for specific proteins *in situ*. *FEBS J*. 275, 3072–3087. doi: 10.1111/j.1742-4658.2008.06461.x

Miesenböck, G. (2009). The optogenetic catechism. *Science* 326, 395–399. doi: 10.1126/science.1174520

Miller, E. W., Lin, J. Y., Frady, E. P., Steinbach, P. A., Kristan, W. B. J., and Tsien, R. Y. (2012). Optically monitoring voltage in neurons by photo-induced electron transfer through molecular wires. *Proc. Natl. Acad. Sci. U.S.A*. 109, 2114–2119. doi: 10.1073/pnas.1120694109

Moreno, A., Endicott, K., Skancke, M., Dwyer, M. K., Brennan, J., Efimov, I. R., et al. (2019). Sudden heart rate reduction upon optogenetic release of acetylcholine from cardiac parasympathetic neurons in perfused hearts. *Front. Physiol*. 10:16. doi: 10.3389/fphys.2019.00016

Nagel, G., Ollig, D., Fuhrmann, M., Kateriya, S., Musti, A. M., Bamberg, E., et al. (2002). Channelrhodopsin-1: a light-gated proton channel in green algae. *Science* 296, 2395–2398. doi: 10.1126/science.1072068

Nagel, G., Szellas, T., Huhn, W., Kateriya, S., Adeishvili, N., Berthold, P., et al. (2003). Channelrhodopsin-2, a directly light-gated cation-selective membrane channel. *Proc. Natl. Acad. Sci. U.S.A*. 100, 13940–13945. doi: 10.1073/pnas.1936192100

Nyns, E., Kip, A., Bart, C., Plomp, J., Zeppenfeld, K., Schalij, M., et al. (2016). Optogenetic termination of ventricular arrhythmias in the whole heart: towards biological cardiac rhythm management. *Eur. Heart J*. 38, 2132–2136. doi: 10.1093/eurheartj/ehw574

Olianti, C., Costantini, I., Giardini, F., Lazzeri, E., Crocini, C., Ferrantini, C., et al. (2020). 3d imaging and morphometry of the heart capillary system in spontaneously hypertensive rats and normotensive controls. *Sci. Rep*. 10, 1–9. doi: 10.1038/s41598-020-71174-9

Olianti, C., Giardini, F., Lazzeri, E., Costantini, I., Silvestri, L., Coppini, R., et al. (2021). Optical clearing in cardiac imaging: a comparative study. *Prog. Biophys. Mol. Biol*. doi: 10.1016/j.pbiomolbio.2021.07.012. [Epub ahead of print].

Paredes, R. M., Etzler, J. C., Watts, L. T., and Lechleiter, J. D. (2008). Chemical calcium indicators. *Methods* 46, 143–151. doi: 10.1016/j.ymeth.2008.09.025

Park, S., Lee, S., Tung, L., and Yue, D. (2014). Optical mapping of optogenetically shaped cardiac action potentials. *Sci. Rep*. 4:6125. doi: 10.1038/srep06125

Pecha, S., Yorgan, K., Röhl, M., Geertz, B., Hansen, A., Weinberger, F., et al. (2019). Human iPS cell-derived engineered heart tissue does not affect ventricular arrhythmias in a guinea pig cryo-injury model. *Sci. Rep*. 9, 1–12. doi: 10.1038/s41598-019-46409-z

Pfeiffer, E., Wright, A., Edwards, A., Stowe, J., McNall, K., Tan, J., et al. (2014). Caveolae in ventricular myocytes are required for stretch-dependent conduction slowing. *J. Mol. Cell. Cardiol*. 76, 265–274. doi: 10.1016/j.yjmcc.2014.09.014

Pfeiffer-Kaushik, E., Smith, G., Cai, B., Dempsey, G., Hortigon-Vinagre, M., Zamora, V., et al. (2019). Electrophysiological characterization of drug response in hsc-derived cardiomyocytes using voltage-sensitive optical platforms. *J. Pharmacol. Toxicol. Methods* 99:106612. doi: 10.1016/j.vascn.2019.106612

Pianca, N., Di Bona, A., Lazzeri, E., Costantini, I., Franzoso, M., Prando, V., et al. (2019). Cardiac sympathetic innervation network shapes the myocardium by locally controlling cardiomyocyte size through the cellular proteolytic machinery. *J. Physiol*. 597, 3639–3656. doi: 10.1113/JP276200

Pogwizd, S. M., and Corr, P. B. (1987). Reentrant and nonreentrant mechanisms contribute to arrhythmogenesis during early myocardial ischemia: results using three-dimensional mapping. *Circ. Res*. 61, 352–371. doi: 10.1161/01.RES.61.3.352

Prando, V., Da Broi, F., Franzoso, M., Plazzo, A. P., Pianca, N., Francolini, M., et al. (2018). Dynamics of neuroeffector coupling at cardiac sympathetic synapses. *J. Physiol*. 596, 2055–2075. doi: 10.1113/JP275693

Prigge, M., Schneider, F., Tsunoda, S. P., Shilyansky, C., Wietek, J., Deisseroth, K., et al. (2012). Color-tuned channelrhodopsins for multiwavelength optogenetics. *J. Biol. Chem*. 287, 31804–31812. doi: 10.1074/jbc.M112.391185

Qu, F., Ripplinger, C. M., Nikolski, V., Grimm, C., and Efimov, I. R. (2007). Three-dimensional panoramic imaging of cardiac arrhythmias in rabbit heart. *J. Biomed. Opt*. 12:044019. doi: 10.1117/1.2753748

Quach, B., Krogh-Madsen, T., Entcheva, E., and Christini, D. (2018). Light-activated dynamic clamp using iPSC-derived cardiomyocytes. *Biophys. J*. 115, 2206–2217. doi: 10.1016/j.bpj.2018.10.018

Quinn, T. A., Camelliti, P., Rog-Zielinska, E. A., Siedlecka, U., Poggioli, T., O'Toole, E. T., et al. (2016). Electrotonic coupling of excitable and nonexcitable cells in the heart revealed by optogenetics. *Proc. Natl. Acad. Sci*. 113, 14852–14857. doi: 10.1073/pnas.1611184114

Quinn, T. A., and Kohl, P. (2021). Cardiac mechano-electric coupling: acute effects of mechanical stimulation on heart rate and rhythm. *Physiol. Rev*. 101, 37–92. doi: 10.1152/physrev.00036.2019

Rajendran, P. S., Challis, R. C., Fowlkes, C. C., Hanna, P., Tompkins, J. D., Jordan, M. C., et al. (2019). Identification of peripheral neural circuits that regulate heart rate using optogenetic and viral vector strategies. *Nat. Commun*. 10, 1–13. doi: 10.1101/456483

Richardson, D. S., and Lichtman, J. W. (2015). Clarifying tissue clearing. *Cell* 162, 246–257. doi: 10.1016/j.cell.2015.06.067

Roell, W., Klein, A. M., Breitbach, M., Becker, T. S., Parikh, A., Lee, J., et al. (2018). Overexpression of cx43 in cells of the myocardial scar: correction of post-infarct arrhythmias through heterotypic cell-cell coupling. *Sci. Rep*. 8, 1–14. doi: 10.1038/s41598-018-25147-8

Roell, W., Lewalter, T., Sasse, P., Tallini, Y. N., Choi, B.-R., Breitbach, M., et al. (2007). Engraftment of connexin 43-expressing cells prevents post-infarct arrhythmia. *Nature* 450, 819–824. doi: 10.1038/nature06321

Rog-Zielinska, E. A., Kong, C. H. T., Zgierski-Johnston, C. M., Verkade, P., Mantell, J., Cannell, M. B., et al. (2018). Species differences in the morphology of transverse tubule openings in cardiomyocytes. *Europace* 20(Suppl_3), iii120–iii124. doi: 10.1093/europace/euy245

Rog-Zielinska, E. A., Scardigli, M., Peyronnet, R., Zgierski-Johnston, C. M., Greiner, J., Madl, J., et al. (2021). Beat-by-beat cardiomyocyte t-tubule deformation drives tubular content exchange. *Circ. Res*. 128, 203–215. doi: 10.1161/CIRCRESAHA.120.317266

Rowlands, C. J., Bruns, O. T., Bawendi, M. G., and So, P. T. (2015). Objective, comparative assessment of the penetration depth of temporal-focusing microscopy for imaging various organs. *J. Biomed. Opt*. 20:061107. doi: 10.1117/1.JBO.20.6.061107

Rubart, M., Tao, W., Lu, X.-L., Conway, S. J., Reuter, S. P., Lin, S.-F., et al. (2018). Electrical coupling between ventricular myocytes and myofibroblasts in the infarcted mouse heart. *Cardiovasc. Res*. 114, 389–400. doi: 10.1093/cvr/cvx163

Rubart, M., Wang, E., Dunn, K. W., and Field, L. J. (2003). Two-photon molecular excitation imaging of Ca^{2+} transients in Langendorff-perfused mouse hearts. *Am. J. Physiol. Cell Physiol*. 284, C1654–C1668. doi: 10.1152/ajpcell.00469.2002

Rudy, Y. (2013). Noninvasive electrocardiographic imaging of arrhythmogenic substrates in humans. *Circ. Res*. 112, 863–874. doi: 10.1161/CIRCRESAHA.112.279315

Sacconi, L., Ferrantini, C., Lotti, J., Coppini, R., Yan, P., Loew, L. M., et al. (2012). Action potential propagation in transverse-axial tubular system is impaired in heart failure. *Proc. Natl. Acad. Sci. U.S.A*. 109, 5815–5819. doi: 10.1073/pnas.1120188109

Sacconi, L., Silvestri, L., Rodriguez, E., Armstrong, G., Pavone, F., Shrier, A., et al. (2020). Khz-rate volumetric voltage imaging of the whole zebrafish heart. *bioRxiv*. doi: 10.1101/2020.07.13.196063

Sala, L., van Meer, B. J., Tertoolen, L. G., Bakkers, J., Bellin, M., Davis, R. P., et al. (2018). Musclemotion: a versatile open software tool to quantify cardiomyocyte and cardiac muscle contraction *in vitro* and *in vivo*. *Circ. Res*. 122, e5–e16. doi: 10.1101/160754

Salama, G., and Hwang, S.-,m. (2009). Simultaneous optical mapping of intracellular free calcium and action potentials from Langendorff perfused hearts. *Curr. Protoc. Cytometry* 49, 12–17. doi: 10.1002/0471142956.cy1217s49

Salerno, S., Garten, K., Smith, G. L., Stølen, T., and Kelly, A. (2019). Two-photon excitation of fluovolt allows improved interrogation of transmural electrophysiological function in the intact mouse heart. *Prog. Biophys. Mol. Biol.* 154, 11–20. doi: 10.1016/j.pbiomolbio.2019.08.007

Scardigli, M., Crocini, C., Ferrantini, C., Gabbrielli, T., Silvestri, L., Coppini, R., et al. (2017). Quantitative assessment of passive electrical properties of the cardiac t-tubular system by frap microscopy. *Proc. Natl. Acad. Sci. U.S.A.* 114, 5737–5742. doi: 10.1073/pnas.1702188114

Scardigli, M., Ferrantini, C., Crocini, C., Pavone, F. S., and Sacconi, L. (2018a). Interplay between sub-cellular alterations of calcium release and t-tubular defects in cardiac diseases. *Front. Physiol.* 9:1474. doi: 10.3389/fphys.2018.01474

Scardigli, M., Müllenbroich, C., Margoni, E., Cannazzaro, S., Crocini, C., Ferrantini, C., et al. (2018b). Real-time optical manipulation of cardiac conduction in intact hearts. *J. Physiol.* 596, 3841–3858. doi: 10.1113/JP276283

Sicouri, S., and Antzelevitch, C. (1991). A subpopulation of cells with unique electrophysiological properties in the deep subepicardium of the canine ventricle. The M cell. *Circ. Res.* 68, 1729–1741. doi: 10.1161/01.RES.68.6.1729

Siedentopf, H., and Zsigmondy, R. (1903). Visualization and size measurement of ultramicroscopic particles, with special application to gold-colored ruby glass. *Ann. Phys.* 10, 1–39.

Sierra, Y. A. B., Rost, B. R., Pofahl, M., Fernandes, A. M., Kopton, R. A., Moser, S., et al. (2018). Potassium channel-based optogenetic silencing. *Nat. Commun.* 9, 1–13. doi: 10.1038/s41467-018-07038-8

Silvestri, L., Costantini, I., Sacconi, L., and Pavone, F. S. (2016). Clearing of fixed tissue: a review from a microscopist's perspective. *J. Biomed. Opt.* 21:081205. doi: 10.1117/1.JBO.21.8.081205

Simone, S., Moyle, S., Buccarello, A., Dellenbach, C., Kucera, J., and Rohr, S. (2020). The role of membrane capacitance in cardiac impulse conduction: an optogenetic study with non-excitable cells coupled to cardiomyocytes. *Front. Physiol.* 11:194. doi: 10.3389/fphys.2020.00194

Szipöcs, R., Ferencz, K., Spielmann, C., and Krausz, F. (1994). Chirped multilayer coatings for broadband dispersion control in femtosecond lasers. *Opt. Lett.* 19, 201–203. doi: 10.1364/OL.19.000201

Tal, E., Oron, D., and Silberberg, Y. (2005). Improved depth resolution in video-rate line-scanning multiphoton microscopy using temporal focusing. *Opt. Lett.* 30, 1686–1688. doi: 10.1364/OL.30.001686

Taylor, J. M., Nelson, C. J., Bruton, F. A., Kaveh, A., Buckley, C., Tucker, C. S., et al. (2019). Adaptive prospective optical gating enables day-long 3d time-lapse imaging of the beating embryonic zebrafish heart. *Nat. Commun.* 10, 1–15. doi: 10.1038/s41467-019-13112-6

Theer, P., and Denk, W. (2006). On the fundamental imaging-depth limit in two-photon microscopy. *JOSA A* 23, 3139–3149. doi: 10.1364/JOSAA.23.003139

Thul, R., Coombes, S., Roderick, H. L., and Bootman, M. D. (2012). Subcellular calcium dynamics in a whole-cell model of an atrial myocyte. *Proc. Natl. Acad. Sci. U.S.A.* 109, 2150–2155. doi: 10.1073/pnas,.1115855109

Van Wagoner, D. R., and Lamorgese, M. (1994). Ischemia potentiates the mechanosensitive modulation of atrial atp-sensitive potassium channels A. *Ann. N. Y. Acad. Sci.* 723, 392–395. doi: 10.1111/j.1749-6632.1994.tb36755.x

Várkuti, B. H., Képiró, M., Horváth, I., Á., Végner, L., Ráti, S., et al. (2016). A highly soluble, non-phototoxic, non-fluorescent blebbistatin derivative. *Sci. Rep.* 6, 1–10. doi: 10.1038/srep26141

Vinegoni, C., Aguirre, A. D., Lee, S., and Weissleder, R. (2015). Imaging the beating heart in the mouse using intravital microscopy techniques. *Nat. Protoc.* 10:1802. doi: 10.1038/nprot.2015.119

Wagner, E., Brandenburg, S., Kohl, T., and Lehnart, S. E. (2014). Analysis of tubular membrane networks in cardiac myocytes from atria and ventricles. *J. Visual. Exp.* 92:e51823. doi: 10.3791/51823

Walker, N. L., Burton, F. L., Kettlewell, S., Smith, G. L., and Cobbe, S. M. (2007). Mapping of epicardial activation in a rabbit model of chronic myocardial infarction: response to atrial, endocardial and epicardial pacing. *J. Cardiovasc. Electrophysiol.* 18, 862–868. doi: 10.1111/j.1540-8167.2007.00858.x

Walton, R. D., Benoist, D., Hyatt, C. J., Gilbert, S. H., White, E., and Bernus, O. (2010). Dual excitation wavelength epifluorescence imaging of transmural electrophysiological properties in intact hearts. *Heart Rhythm* 7, 1843–1849. doi: 10.1016/j.hrthm.2010.08.019

Weber, M., Scherf, N., Meyer, A. M., Panakova, D., Kohl, P., and Huisken, J. (2017). Cell-accurate optical mapping across the entire developing heart. *eLife* 6:e28307. doi: 10.7554/eLife.28307

Wei, L., Li, W., Entcheva, E., and Li, Z. (2020). Microfluidics-enabled 96-well perfusion system for high-throughput tissue engineering and long-term all-optical electrophysiology. *Lab Chip* 20, 4031–4042. doi: 10.1039/D0LC00615G

Weinberger, F., Breckwoldt, K., Pecha, S., Kelly, A., Geertz, B., Starbatty, J., et al. (2016). Cardiac repair in guinea pigs with human engineered heart tissue from induced pluripotent stem cells. *Sci. Transl. Med.* 8:363ra148. doi: 10.1126/scitranslmed.aaf8781

Wengrowski, A., Kuzmiak-Glancy, S., Jaimes, R., c., and Kay, M. (2014). Nadh changes during hypoxia, ischemia, and increased work differ between isolated heart preparations. *Am. J. Physiol. Heart Circ. Physiol.* 306, H529–H537. doi: 10.1152/ajpheart.00696.2013

Wengrowski, A. M., Wang, X., Tapa, S., Posnack, N. G., Mendelowitz, D., and Kay, M. W. (2015). Optogenetic release of norepinephrine from cardiac sympathetic neurons alters mechanical and electrical function. *Cardiovasc. Res.* 105, 143–150. doi: 10.1093/cvr/cvu258

Werley, C., Chien, M., and Cohen, A. (2017). Ultrawidefield microscope for high-speed fluorescence imaging and targeted optogenetic stimulation. *Biomed. Opt. Express* 8, 5794–5813. doi: 10.1364/BOE.8.005794

Whitaker, M. (2010). "Genetically encoded probes for measurement of intracellular calcium," in *Methods in Cell Biology*, Michael Whitaker (ed), Vol. 99 (Elsevier), 153–182. doi: 10.1016/B978-0-12-374841-6.00006-2

Williams, J., and Entcheva, E. (2015). Optogenetic versus electrical stimulation of human cardiomyocytes: modelling insights. *Biophys. J.* 108, 1934–1945. doi: 10.1016/j.bpj.2015.03.032

Wu, X., and Bers, D. M. (2006). Sarcoplasmic reticulum and nuclear envelope are one highly interconnected Ca^{2+} store throughout cardiac myocyte. *Circ. Res.* 99, 283–291. doi: 10.1161/01.RES.0000233386.02708.72

Wu, Y., Li, S.-S., Jin, X., Cui, N., Zhang, S., and Jiang, C. (2015). Optogenetic approach for functional assays of the cardiovascular system by light activation of the vascular smooth muscle. *Vasc. Pharmacol.* 71, 192–200. doi: 10.1016/j.vph.2015.03.006

Xiao, S., and Mertz, J. (2019). Contrast improvement in two-photon microscopy with instantaneous differential aberration imaging. *Biomed. Opt. Express* 10, 2467–2477. doi: 10.1364/BOE.10.002467

Yan, P., Acker, C. D., Zhou, W.-L., Lee, P., Bollensdorff, C., Negrean, A., et al. (2012). Palette of fluorinated voltage-sensitive hemicyanine dyes. *Proc. Natl. Acad. Sci. U.S.A.* 109, 20443–20448. doi: 10.1073/pnas.1214850109

Yang, H. H., and St-Pierre, F. (2016). Genetically encoded voltage indicators: opportunities and challenges. *J. Neurosci.* 36, 9977–9989. doi: 10.1523/JNEUROSCI.1095-16.2016

Yu, J., and Entcheva, E. (2016). "Inscribing optical excitability to non-excitable cardiac cells: viral delivery of optogenetic tools in primary cardiac fibroblasts," *Methods Mol Biol.* 1408:303–317. doi: 10.1007/978-1-4939-3512-3_21

Yu, L., Zhou, L., Cao, G., Po, S. S., Huang, B., Zhou, X., et al. (2017). Optogenetic modulation of cardiac sympathetic nerve activity to prevent ventricular arrhythmias. *J. Am. Coll. Cardiol.* 70, 2778–2790. doi: 10.1016/j.jacc.2017.09.1107

Zaglia, T., Di Bona, A., and Mongillo, M. (2019). A light wand to untangle the myocardial cell network. *Methods Protoc.* 2:34. doi: 10.3390/mps2020034

Zaglia, T., Pianca, N., Borile, G., Da Broi, F., Richter, C., Campione, M., et al. (2015). Optogenetic determination of the myocardial requirements for extrasystoles by cell type-specific targeting of channelrhodopsin-2. *Proc. Natl. Acad. Sci. U.S.A.* 112, E4495–E4504. doi: 10.1073/pnas.1509380112

Zalev, J., Richards, L. M., Clingman, B. A., Harris, J., Cantu, E., Menezes, G. L., et al. (2019). Opto-acoustic imaging of relative blood oxygen saturation and total hemoglobin for breast cancer diagnosis. *J. Biomed. Opt.* 24:121915. doi: 10.1117/1.JBO.24.12.121915

Zgierski-Johnston, C., Ayub, S., Fernández, M., Rog-Zielinska, E., Barz, F., Paul, O., et al. (2020). Cardiac pacing using transmural multi-led probes in channelrhodopsin-expressing mouse hearts. *Prog. Biophys. Mol. Biol.* 154, 51–61. doi: 10.1016/j.pbiomolbio.2019.11.004

Zhang, H. K., Yan, P., Kang, J., Abou, D. S., Le, H. N., Jha, A. K., et al. (2017). Listening to membrane potential: photoacoustic voltage-sensitive dye recording. *J. Biomed. Opt.* 22:045006. doi: 10.1117/1.JBO.22.4.045006

Zhang, S., Cui, N., Wu, Y., Zhong, W., Johnson, C. M., and Jiang, C. (2015). Optogenetic intervention to the vascular endothelium. *Vasc. Pharmacol.* 74, 122–129. doi: 10.1016/j.vph.2015.05.009

Zhang, Y., Sekar, R. B., McCulloch, A. D., and Tung, L. (2008). Cell cultures as models of cardiac mechanoelectric feedback. *Prog. Biophys. Mol. Biol.* 97, 367–382. doi: 10.1016/j.pbiomolbio.2008.02.017

Zipfel, W. R., Williams, R. M., and Webb, W. W. (2003). Nonlinear magic: multiphoton microscopy in the biosciences. *Nat. Biotechnol.* 21, 1369–1377. doi: 10.1038/nbt899

Conflict of Interest: CA is an owner and employee of Potentiometric Probes, which develops and sells voltage-sensitive dyes. GS is a non-salaried, founder, executive and Chief Scientific Offer of Clyde Biosciences Ltd (UK).

The remaining authors declare that the research was conducted in the absence of any commercial or financial relationships that could be construed as a potential conflict of interest.

Publisher's Note: All claims expressed in this article are solely those of the authors and do not necessarily represent those of their affiliated organizations, or those of the publisher, the editors and the reviewers. Any product that may be evaluated in this article, or claim that may be made by its manufacturer, is not guaranteed or endorsed by the publisher.

frontiers in Physiology

ORIGINAL RESEARCH
published: 09 December 2021
doi: 10.3389/fphys.2021.777770

The RyR2-R2474S Mutation Sensitizes Cardiomyocytes and Hearts to Catecholaminergic Stress-Induced Oxidation of the Mitochondrial Glutathione Pool

*Jörg W. Wegener[1,2,3], Ahmed Wagdi[3,4], Eva Wagner[1], Dörthe M. Katschinski[3,4], Gerd Hasenfuss[1,3], Tobias Bruegmann[2,3,4] and Stephan E. Lehnart[1,2,3]**

[1] Department of Cardiology and Pulmonology, Heart Research Center Göttingen, University Medical Center Göttingen, Georg August University of Göttingen, Göttingen, Germany, [2] Cluster of Excellence "Multiscale Bioimaging: From Molecular Machines to Networks of Excitable Cells" (MBExC), Georg-August University of Göttingen, Göttingen, Germany, [3] DZHK (German Centre for Cardiovascular Research), Partner Site Göttingen, Göttingen, Germany, [4] Institute of Cardiovascular Physiology, University Medical Center Göttingen, Georg August University of Göttingen, Göttingen, Germany

OPEN ACCESS

Edited by:
Alexey V. Glukhov, University of Wisconsin-Madison, United States

Reviewed by:
William E. Louch, University of Oslo, Norway
Francisco J. Alvarado, University of Wisconsin-Madison, United States

***Correspondence:**
Stephan E. Lehnart
slehnart@med.uni-goettingen.edu

Specialty section:
This article was submitted to Cardiac Electrophysiology, a section of the journal Frontiers in Physiology

Received: *15 September 2021*
Accepted: *19 November 2021*
Published: *09 December 2021*

Citation:
Wegener JW, Wagdi A, Wagner E, Katschinski DM, Hasenfuss G, Bruegmann T and Lehnart SE (2021) The RyR2-R2474S Mutation Sensitizes Cardiomyocytes and Hearts to Catecholaminergic Stress-Induced Oxidation of the Mitochondrial Glutathione Pool. Front. Physiol. 12:777770. doi: 10.3389/fphys.2021.777770

Missense mutations in the cardiac ryanodine receptor type 2 (RyR2) characteristically cause catecholaminergic arrhythmias. Reminiscent of the phenotype in patients, RyR2-R2474S knockin mice develop exercise-induced ventricular tachyarrhythmias. In cardiomyocytes, increased mitochondrial matrix Ca^{2+} uptake was recently linked to non-linearly enhanced ATP synthesis with important implications for cardiac redox metabolism. We hypothesize that catecholaminergic stimulation and contractile activity amplify mitochondrial oxidation pathologically in RyR2-R2474S cardiomyocytes. To investigate this question, we generated double transgenic RyR2-R2474S mice expressing a mitochondria-restricted fluorescent biosensor to monitor the glutathione redox potential (E_{GSH}). Electrical field pacing-evoked RyR2-WT and RyR2-R2474S cardiomyocyte contractions resulted in a small but significant baseline E_{GSH} increase. Importantly, β-adrenergic stimulation resulted in excessive E_{GSH} oxidization of the mitochondrial matrix in RyR2-R2474S cardiomyocytes compared to baseline and RyR2-WT control. Physiologically β-adrenergic stimulation significantly increased mitochondrial E_{GSH} further in intact beating RyR2-R2474S but not in RyR2-WT control Langendorff perfused hearts. Finally, this catecholaminergic E_{GSH} increase was significantly attenuated following treatment with the RyR2 channel blocker dantrolene. Together, catecholaminergic stimulation and increased diastolic Ca^{2+} leak induce a strong, but dantrolene-inhibited mitochondrial E_{GSH} oxidization in RyR2-R2474S cardiomyocytes.

Keywords: ryanodine receptor, mitochondria, dantrolene, glutathione redox potential, RyR2 Ca^{2+} leak, mitochondrial oxidation, reactive oxygen species (ROS)

Abbreviations: CPVT, catecholaminergic polymorphic ventricular tachycardia; Dan Dantrolene, dTG double transgenic; DTT, dithiothreitol; EFS, electrical field stimulation; E_{GSH}, glutathione redox potential; Iso, isoproterenol; roGFP, reduction-oxidation-sensitive green fluorescent protein; ROS, reactive oxygen species; RyR2, ryanodine receptor type 2; SR, sarcoplasmatic reticulum; sTG, single transgenic.

INTRODUCTION

In the heart, where ATP consumption is highest of any tissue, Ca^{2+} homeostasis in the mitochondrial matrix and ATP synthesis in the inner mitochondrial membrane are tightly controlled and interacting in a tissue (muscle)-specific manner regulated by the mitochondrial membrane potential (Wescott et al., 2019; Boyman et al., 2020; Boyman et al., 2021). Pathologically altered intracellular Ca^{2+} signaling and impaired bioenergetics due to mitochondrial dysfunction contribute to both ventricular tachyarrhythmia (VT) and heart failure development, at least in part through increased production of reactive oxygen species (ROS) (Zhou and Tian, 2018; Santulli et al., 2021). Under physiological conditions at rest, mitochondrial oxidative phosphorylation and ATP synthesis are accompanied by a low level of cardiac ROS generation mainly through byproducts of the electron transport chain (Murphy, 2009). However, increased stress and enhanced cardiac performance strongly augment mitochondrial respiratory activity significantly increasing ROS production (Bertero and Maack, 2018). Although several enzymatic systems protect cardiomyocyte function through ROS neutralization (Munzel et al., 2017), chronically compromised mitochondrial bioenergetics in heart disease may shift the balance toward increased oxidation of the glutathione (GSH) redox potential (E_{GSH}) (Bertero and Maack, 2018), especially since an increased energy demand during sustained β-adrenergic stimulation was proposed to weaken mitochondrial antioxidant defense (Bovo et al., 2015). Notably, increased mitochondrial E_{GSH} oxidation itself is a quantitative live-cell indicator of a strongly increased ROS production, and hence may identify an early key disease process and mark the beginning of metabolic remodeling in the failing heart (Doenst et al., 2013).

Under physiological conditions of excitation-contraction (E-C) coupling, Ca^{2+} influx through voltage-gated L-type Ca^{2+} channels ($Ca_V1.2$) activates mass intracellular Ca^{2+} release via ryanodine receptor type 2 (RyR2) large-conductance channels in the sarcoplasmic reticulum (SR). This Ca^{2+}-induced Ca^{2+} release increases the intracellular Ca^{2+} concentration throughout the myofilaments activating myocardial contraction (Bers, 2002), while it accounts for up to two-thirds of cardiac ATP consumption (Suga, 1990; Meyer et al., 1998). Vice versa, for cardiac relaxation intracellular Ca^{2+} is decreased mainly via the SR Ca^{2+}-ATPase (SERCA2a) and extruded by electrogenic trans-sarcolemmal Na^+/Ca^{2+} exchange (NCX). Hence, diastolic Ca^{2+} cycling accounts for an additional ∼30% of total energy consumption at baseline in healthy cardiomyocytes and in human heart tissue (Gibbs et al., 1988; Meyer et al., 1998).

Interestingly, pathophysiological changes in cytosolic Ca^{2+} cycling are widely accepted as a central cause of arrhythmias and contractile dysfunction in atrial and ventricular tissue (Bers, 2002; Alsina et al., 2019; Brandenburg et al., 2019; Dridi et al., 2020; Berisha et al., 2021; Boyman et al., 2021; Sadredini et al., 2021; Santulli et al., 2021). In this context, increased mitochondrial ROS generation can contribute to altered Ca^{2+} handling and vice versa, which may furthermore constitute a vicious cycle in cardiomyocytes (Zhou and Tian, 2018; Santulli et al., 2021). However, the quantitative and molecular mechanisms if and how acutely increased SR Ca^{2+} leak causes excess mitochondrial Ca^{2+} uptake and ROS generation have been and continue to be controversially discussed (Mallilankaraman et al., 2012; Antony et al., 2016; Kohlhaas et al., 2017; Wescott et al., 2019; Boyman et al., 2020; Rossini and Filadi, 2020; Boyman et al., 2021; Santulli et al., 2021). Nonetheless, the largest known ion channel, RyR2, contains a relatively high number of redox-reactive cysteine residues and hence provides an important molecular substrate for increased ROS generation in cardiomyocytes (Santulli and Marks, 2015). For instance, RyR2 is oxidized in atrial tissue *in vivo* in a genetic model of catecholaminergic polymorphic ventricular tachycardia (CPVT), RyR2-R2474S$^{+/-}$ knockin mice, with increased susceptibility for pacing-induced atrial fibrillation (Shan et al., 2012).

Interestingly, while CPVT has been initially characterized solely as an arrhythmogenic cardiomyopathy (Yano et al., 2009), subsequently seizures originating in the brain (Lehnart et al., 2008; Lieve et al., 2019) and glucose intolerance in the Langerhans cells of the pancreas have been demonstrated in humans and mouse models (Santulli and Marks, 2015; Santulli et al., 2015). Although the majority of biophysically investigated RyR2 missense mutations point to a gain-of-function defect following protein kinase A phosphorylation both at the recombinant and native single-channel level (Wehrens et al., 2003; Lehnart et al., 2004; Tester et al., 2007; Lehnart et al., 2008), the role of PKA-dependent RyR2 phosphorylation remains controversial (Leenhardt et al., 2012; Wleklinski et al., 2020) since, e.g., inhibition of cardiac CaMKII by gene therapeutically applied CaMKII inhibitory peptide, but not PKA inhibitory peptide, effectively suppressed ventricular arrhythmias in a murine and an iPSC-CM model of CPTV (Bezzerides et al., 2019). However, a general consensus exists that adult cardiomyocytes and intact hearts from knockin mice expressing different gain-of-function RyR2 mutations are susceptible for significantly increased diastolic Ca^{2+} leak and Ca^{2+} waves following β-adrenergic stimulation (Lehnart et al., 2008; Fernandez-Velasco et al., 2009; Liu et al., 2009; Uchinoumi et al., 2010; Leenhardt et al., 2012; Borile et al., 2021). Strikingly, consistent with the human phenotype of a normal left-ventricular structure and function at rest, morphological and contractile changes have been excluded in a distinct independent RyR2-R2474S knockin mouse with a clear β-adrenergic driven phenotype of Ca^{2+} triggered cardiac VT (Uchinoumi et al., 2010). Given that the altered SR Ca^{2+} leak/load balance needs to be acutely compensated at the cost of increased ATP consumption during catecholaminergic stimulation (Eisner et al., 2020), CPVT-affected hearts may face a challenging metabolic state during episodes of transient intracellular Ca^{2+} overload and β-adrenergic stimulation, which may lead to increased mitochondrial Ca^{2+} load with excessive ROS generation and contribute to electrical and contractile cardiomyocyte dysfunction (Bers, 2014; Wescott et al., 2019; Boyman et al., 2021).

In the failing heart, ROS signaling has been established as a central process of the organic disease progression (Heymes et al., 2003; Yano et al., 2005; Guo et al., 2007; Akki et al., 2009). Increasing evidence suggests that excessive ROS

production can lead to chronic cardiac pathologies, such as apoptosis, fibrosis, and hypertrophy jointly promoting the maladaptive ventricular remodeling (von Harsdorf et al., 1999; Cucoranu et al., 2005; Takimoto et al., 2005; Hori and Nishida, 2009; Santulli et al., 2021). Recently, the mechanisms that temporally and spatially link excess ROS and Ca^{2+} as two principal detrimental factors have been addressed in the context of diabetic cardiomyopathy. Acute elevation of the extracellular glucose concentration induces cardiomyocyte ROS production through O-GlcNAcylation of CaMKIIδ and activation of NOX2 (NADPH oxidase type 2) resulting in increased ROS production in the cytosol but not in the mitochondria (Lu et al., 2020). On the other hand, RyR2-R2474S$^{+/-}$ knockin mice exhibiting catecholamine-induced intracellular Ca^{2+} leak subsequently revealed mitochondrial dysfunction, increased ROS production, increased atrial RyR2 channel oxidation, and arrhythmia susceptibility (Xie et al., 2015). Moreover, inhibitory pharmacological treatment selectively targeting the RyR2 Ca^{2+} leak or genetic inhibition of mitochondrial ROS production both prevented atrial fibrillation, indicating that RyR2 leakage and mitochondrial ROS generation may indeed constitute a self-enforcing subcellular cycle that can set off arrhythmias (Xie et al., 2015). However, the acute mechanism and hence direct but transient link of the catecholamine-stimulated RyR2-R2474S$^{+/-}$ Ca^{2+} leak on mitochondrial ROS production have not been investigated previously.

Novel transgenic reporter mouse lines expressing the Grx1-roGFP GSH redox biosensor in a cardiomyocyte-restricted manner targeted to either the cytoplasm or the mitochondrial matrix have been established previously (Swain et al., 2016). Thus, cardiomyocytes from Grx1-roGFP biosensor mice allow the direct live-cell monitoring of changes in compartmentalized - cytosolic vs. mitochondrial - E_{GSH} (Swain et al., 2016), as demonstrated acutely in response to high extracellular glucose concentrations recently (Lu et al., 2020).

The objective of the present study is to investigate mitochondrial and cytosolic E_{GSH} changes during pacing-controlled contractions in RyR2-R2474S cardiomyocytes and intact hearts in a knockin mouse model of CPVT. To investigate the interplay between acute catecholamine-stimulated increased SR Ca^{2+} leak and mitochondrial oxidation changes, we crossed the mitochondrial matrix-targeted Grx1-roGFP (mito-Grx1-roGFP) redox biosensor line with mitochondrial redox-competent C57BL/6N background RyR2-R2474S$^{+/-}$ knockin mouse strain by heterozygous breeding (Lehnart et al., 2008; Nickel et al., 2015; Swain et al., 2016). While double transgenic mito-Grx1-roGFP:RyR2-R2474S$^{+/-}$ (RyR2-R2474S dTG) cardiomyocytes showed a significant E_{GSH} increase during pacing-evoked contractions following β-adrenergic stimulation compared to RyR2-WT control cardiomyocytes, *ex vivo* perfusion of isoproterenol-stimulated RyR2-R2474S dTG hearts significantly extended and confirmed the cellular findings. Importantly, acute treatment of RyR2-R2474S dTG-cardiomyocytes with the RyR channel blocker dantrolene diminished this E_{GSH} increase.

MATERIALS AND METHODS

Double-Transgenic and Single-Transgenic Mouse Lines

All animal procedures were reviewed by the institutional animal care and use committee of the University Medical Center Göttingen and the veterinarian state authority (protocol T11/2; LAVES, Oldenburg, Germany) in line with Directive 2010/63/EU of the European Parliament. Isolated cardiomyocytes and hearts were harvested either from heterozygous RyR2-R2474S dTG or RyR2-WT control mice expressing the mitochondria-restricted E_{GSH} biosensor in cardiomyocytes in the C57BL/6N background (Lehnart et al., 2008; Nickel et al., 2015; Swain et al., 2016). RyR2-WT control (mito-Grx1-roGFP2$^{+/-}$:RyR2$^{+/+}$) and RyR2-R2474S dTG (mito-Grx1-roGFP2$^{+/-}$:RyR2$^{R2474S/+}$) mice of either sex were humanely euthanized between 12 and 28 weeks age for heart extraction and/or ventricular cardiomyocyte isolation. In addition, cardiomyocytes isolated from single-transgenic (sTG) mouse hearts expressing the biosensor in the cytosol [cyto-Grx1-roGFP2$^{+/-}$) were investigated following protocols reported previously (Swain et al., 2016)].

Redox Biosensor Measurements and E_{GSH} Calculation in Isolated Cardiomyocytes

Ventricular cardiomyocytes were isolated and quality controlled as described previously (Wagner et al., 2014; Peper et al., 2021). Isolated cardiomyocyte suspensions were plated onto laminin-coated glass coverslips (Imaging Dish CG 1.0, Zellkontakt, Nörten-Hardenberg, Germany) at room temperature. Only quiescent brick-shaped cardiomyocytes with cross-striations visualized at high contrast (e.g. see brightfield image below) were used if they contracted regularly in capture to electrical field stimulation (EFS; 4 ms, ± 20 V biphasic, 0.5 Hz, Myopacer, IonOptix, Westwood, MA, United States). Pacing-responsive cardiomyocytes then underwent repeated EFS-trains for 10, 30, and 60 s at 0.1, 1, or 3 Hz, respectively, for up to 20 min (see **Supplementary Figure 1**). Isolated cardiomyocytes developing sustained spontaneous contractile activity with a frequency above >0.1 Hz after EFS-pacing or during live-cell imaging were excluded from further analysis.

Cardiomyocyte redox biosensor measurements were performed on an inverted epifluorescence microscope (Axiovert Observer, Zeiss, Oberkochen, Germany) equipped with a 40x oil objective (Fluar 40x/1.3, Zeiss, Oberkochen, Germany). The roGFP2 biosensor was excited at 405 and 488 nm using a monochromator with 5 nm bandwidth (Polychrome V, Till Photonics, Gräfelfing, Germany). The emitted light was detected above >530 nm (filter set #49002, Chroma, Olching Germany) and recorded with a CMOS camera (PrimE, Photometrics, Birmingham, United Kingdom). Biosensor signal changes are represented as intensity ratio obtained at 405/488 nm excitation. Images were acquired at 1 Hz and single-cell ROIs were analyzed offline after background subtraction using proprietary software (Visiview version 3.1, Visitron Systems, Puchheim, Germany).

Cardiomyocytes with baseline intensity ratios below 0.15 were paced in series at 0.1, 1, or 3 Hz, respectively, for 10, 30, and 60 s while the redox biosensor signal changes were continuously monitored (for a schematic of the experimental protocol, please refer to **Supplementary Figure 1**). The non-paced interval between each pacing train lasted 2–3 min to establish steady-state conditions. Only after the baseline redox biosensor signal has reached a stable baseline steady-state, the subsequent EFS pacing period was executed. H_2O_2 (200 μM) was applied at the end of each experiment to confirm the maximal exogenous increase in intensity ratio (positive control) to capture the maximally oxidized state of the redox biosensor. In some experiments, dithiothreitol (DTT, 1 mM) was applied additionally after H_2O_2 treatment to obtain the maximal decrease of the redox roGFP2 biosensor signal for calculation of the glutathione redox potential (E_{GSH}). Isoproterenol (100 nM) and dantrolene (5 μM) were applied acutely for 10 min or incubated for 120 min as indicated, respectively, before the start of the biosensor imaging experiment. All experiments were performed in the HEPES-buffered bath solution (composition in mM: NaCl 140, KCl 5.4, $MgCl_2$ 1.2, $CaCl_2$ 1.2, Na_2HPO_4 0.3, HEPES 10, glucose 10; pH adjusted to 7.4 with NaOH).

E_{GSH} (glutathione redox potential) calibration was performed by protocols reported previously (Gutscher et al., 2008; Swain et al., 2016). E_{GSH} values were calculated by analysis of the fluorescence intensities at 405 and 488 nm after treatment with H_2O_2 (maximal oxidation) and DTT (maximal reduction). The redox potential $E^{0'}$ for roGFP2 was estimated to −280 mV according to protocols published previously (Dooley et al., 2004).

Whole Heart Imaging

Hearts from mito-Grx1-roGFP2$^{+/-}$:RyR2$^{+/+}$ mice (WT control) and mito-Grx1-roGFP2$^{+/-}$:RyR2$^{R2474S/+}$ mice (dTG) were quickly extracted after cervical dislocation and immediately placed in ice-cold Dulbecco's phosphate-buffered solution. Non-cardiac tissue was discarded, and the heart perfused via the aorta with Tyrode's solution (containing in mM: 1.8 $CaCl_2$, 140 NaCl, 5.4 KCl, 2 $MgCl_2$, 10 Glucose, 10 HEPES; pH adjusted to 7.4 using NaOH, bubbled with 100% O_2 at 37°C). A bipolar epicardial electrogram was obtained using a silver electrode in contact with the right atrium and a metal spoon at the heart's apex. The signal was amplified (Animal Bio Amp FE136), recorded using PowerLab 16/35, and analyzed with LabChart 8.1.18 software, all ADinstruments, Oxford, United Kingdom. Hearts were placed in the optical path of a macroscope (MVX10, MVLPAPO1x, NA: 0.25, Olympus, Hamburg, Germany) connected through a light-guide (Ø 2 mm, NA 0.5) with a LEDHub (Omicron-Laser, Rodgau, Germany). Hearts from WT control and dTG mice showed spontaneous beating rates of 286 ± 30 (n = 4) and 217 ± 32 (n = 3) bpm under untreated conditions, respectively, which increased to 382 ± 38 (n = 4) and 322 ± 50 (n = 3) bpm after β-adrenergic stimulation, respectively.

Hearts expressing the roGFP2 sensor were excited using the 385 nm LED and 460 nm LED within the LEDHub and the bandpass filters 385/26 and 475/23 nm (AHF, Tübingen, Germany), respectively. The light was sent to the epicardial surface and the emitted light was captured by the camera using the filter set F46-002XL (AHF, Tübingen, Germany) without the excitation filter. Ratiometric images were acquired at a frame rate of 0.1 Hz using a custom-made software to synchronize both LEDs with the Zyla camera (Andor, Oxford Instruments, Oxford, United Kingdom) through NI 9263 CompactDAQ (National Instruments, Austin, TX, United States). Imaging and cardiac electrogram recording were performed during stable sinus rhythm and after isoproterenol stimulation (33 nM). At the end of each experiment, H_2O_2 (200 μM) was applied followed by DTT (4 mM) to calibrate and calculate E_{GSH}.

Confocal Imaging of Cardiomyocytes

Cardiomyocyte endomembrane structures were stained using the lipophilic fluorescent dye di-8-ANEPPS (50 μM, Molecular Probes, Eugene, OR, United States) for 15 min at room temperature followed by two washing steps with buffer solution as reported previously (Wagner et al., 2014). Images were acquired with a confocal laser scanning microscope (LSM710, Carl Zeiss, Oberkochen, Germany) with a Plan-Apochromat × 63/1.4 oil Ph3 objective using 16x line averaging. For combined imaging of roGFP2 expressed in the mitochondrial matrix, the fluorescence excited at 490 nm was detected between 500 and 550 nm, and for di-8-ANEPPS, the fluorescence excited at 480 nm was detected between 550 and 650 nm. Pinhole was set to 0.8 AU.

Chemicals

All chemicals were obtained from Sigma-Aldrich (Merck KgaA, Germany) unless otherwise indicated.

Data Analysis

Data are reported as intensity ratio (I405/I488 in isolated cardiomyocytes and I385/I475 in whole hearts) or as ratio normalized to the baseline obtained at the start of each recording. Data analysis was performed with Prism 7 (GraphPad Software, San Diego, CA, United States). All data sets have passed a normality test (Kolmogorov-Smirnov). Statistical analysis between RyR2-WT control vs. RyR2-R2474S dTG cardiomyocytes was performed using paired or unpaired ANOVA with Dunnett's or Tukey's post-test as appropriate.

RESULTS

Baseline Mitochondrial Oxidation at Higher Beating Rates in sTG-Cardiomyocytes

Changes of the biosensor signal were initially characterized at increasing durations of pacing-evoked contractions in cardiomyocytes from sTG-mice expressing the redox reporter Grx1-roGFP2 targeted to either the mitochondrial matrix or the cytosol to confirm the imaging workflow as reported previously (Swain et al., 2016; Lu et al., 2020). Mito-Grx1-roGFP2 cardiomyocytes exhibited an apparent increase of the redox I405/I488 ratio after pacing when compared to non-paced

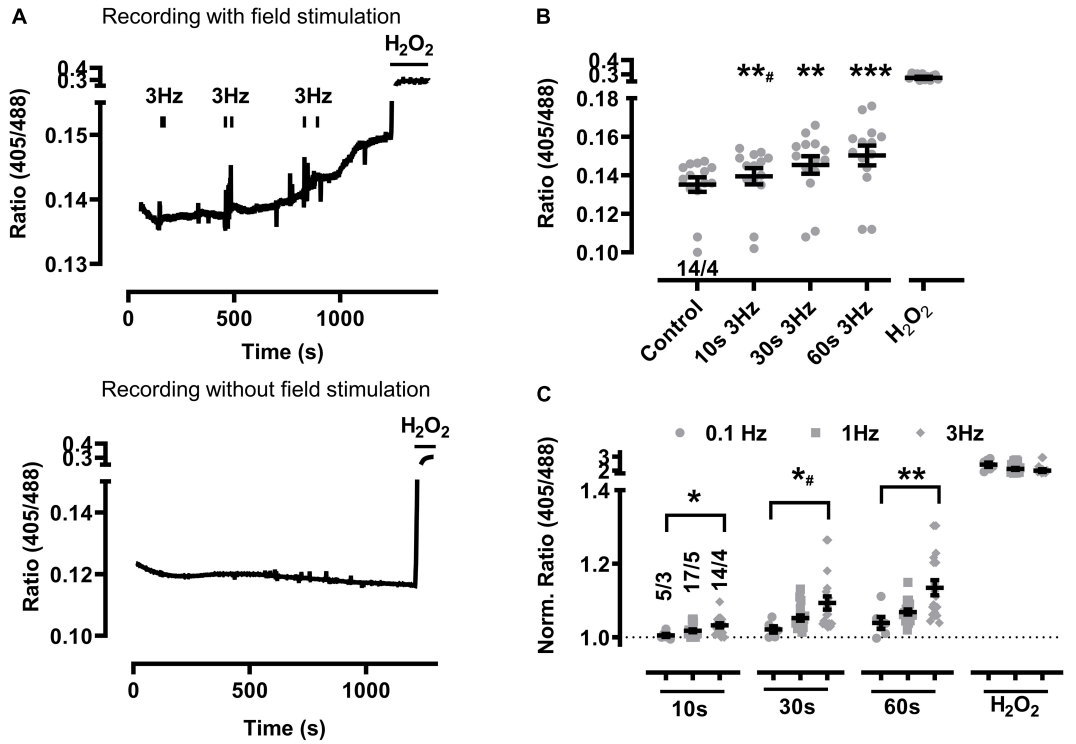

FIGURE 1 | Baseline mitochondrial oxidation at higher beating rates in sTG-cardiomyocytes. **(A)** Representative time course of the redox biosensor I405/I488 nm ratio following repeated EFS-evoked 3 Hz beating trains (*top*) compared to the absence of EFS-pacing in WT control cardiomyocytes (*bottom*). Black bars indicate the start and end of each beating interval lasting 10, 30, and 60 s as summarized by the graphical protocol in **Supplementary Figure 1**. H_2O_2 (200 μM) was added at the end of each experiment to obtain the maximal level of mitochondrial oxidation. Of note, vertical "noise" may originate from aberrant cardiomyocyte contractions. **(B)** Dot plot showing the I405/I488 nm ratio of individual cells and mean values ± SEM. Measurements were obtained under baseline conditions and following EFS-pacing at 3 Hz for the indicated beating durations. Cell/heart numbers are indicated. Paired one-way ANOVA with Dunnett's post-test. $^{**\#}P = 0.006$; $^{**}P = 0.002$; $^{***}P < 0.001$. **(C)** Dot plot summarizing individual and mean ± SEM 405/488 nm normalized ratio values recorded at the indicated beating rates and train durations. Ratio values were normalized to baseline at the start of each experiment. Cell/heart numbers are indicated. Unpaired one-way ANOVA with Tukey's post-test. $^{*}P = 0.01$; $^{*\#}P = 0.02$; $^{**}P = 0.007$.

cells which was further increased by elongating the 3 Hz EFS-trains (**Figure 1A**). On average, 10 s of 3 Hz pacing with optically confirmed contractile pacing-capture was already sufficient to significantly increase mitochondrial oxidization (**Figure 1B**). Moreover, mitochondrial oxidation was further significantly increased by longer pacing durations both 30 and 60 s, while H_2O_2 (200 μM) treatment confirmed the maximal level of the biosensor response (**Figure 1B**). Likewise, 10 s of 1 Hz pacing considerably increased mitochondrial oxidation which was further enhanced by longer pacing intervals of 30 and 60 s (**Figures 2A,B**). Of note, the original recording shows that the increase in the redox I405/I488 ratio after 30 s pacing at 1 Hz returned slowly to baseline over several minutes time indicating that the effect of pacing on the biosensor signal is reversible (**Figure 2A**). In summary, mitochondrial oxidation was significantly increased by pacing at 3 Hz compared to 0.1 Hz beating trains for 10, 30, and 60 s (**Figure 1C**).

In contrast, the cytosolic biosensor signals in cyto-Grx1-roGFP2 transgenic cardiomyocytes showed only non-significant smaller oxidation increases at 1 or 3 Hz beating, except when the 3 Hz beating rate lasted 60 s, while H_2O_2 confirmed the maximal expected response (**Figure 3**). Taken together, these data indicate that a stronger increase of the beating rate (e.g., from 0.1 to 1 and 3 Hz) leads to significantly increased oxidization of the mitochondrial GSH pool in a time-dependent manner (e.g., from 10 to 30 and 60 s), whereas a significant cytosolic oxidation increase was only observed after the longest (60 s long) 3 Hz beating rate.

Preserved Transverse Tubule and Mitochondrial Network Interface in sTG-Cardiomyocytes

Accounting for ∼30% of the cell volume of adult cardiomyocytes, it is anticipated that the regular subcellular inter-sarcomeric mitochondrial distribution is highly ordered between and along the myofilaments, as well as precisely juxtaposed by the junctional SR and transverse tubule (T-tubule) membrane invaginations at both mitochondria poles, where discontinuous T-tubule/SR contacts function as Ca^{2+} release sites containing highly concentrated $Ca_V1.2$ channels opposed to RyR2 clusters in nanometric proximity (recently reviewed in Rossini and Filadi, 2020). Whereas live-cell confocal mito-roGFP2 imaging showed the expected preserved inter-sarcomeric mitochondrial

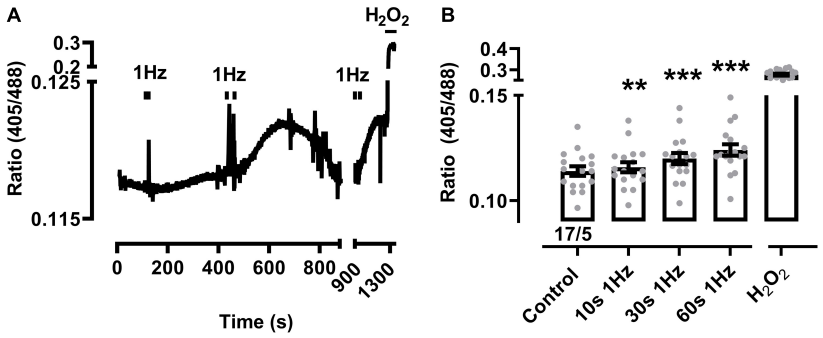

FIGURE 2 | Mitochondrial oxidation following prolonged 1 Hz beating in sTG-cardiomyocytes. **(A)** Representative time course of the redox biosensor I405/I488 nm ratio with pacing-evoked 1 Hz beating trains in a mito-Grx1-roGFP2 cardiomyocyte. Black bars indicate the start and end of each beating interval lasting 10, 30, and 60 s, respectively. H_2O_2 (200 μM) was added at the end of the experiment as indicated to confirm the maximal level of mitochondrial oxidation. The interval between 900 and 1,300 s was condensed to show the reversible signal changes after 30 s pacing. **(B)** Dot-bar plot showing the I405/I488 nm ratio of the individual cardiomyocytes and mean values ± SEM. Measurements were obtained under baseline conditions and following EFS-pacing at 1 Hz for the indicated beating durations. Cell/heart numbers are indicated. Paired one-way ANOVA with Dunnett's post-test. $^{**}P = 0.007$; $^{***}P < 0.001$.

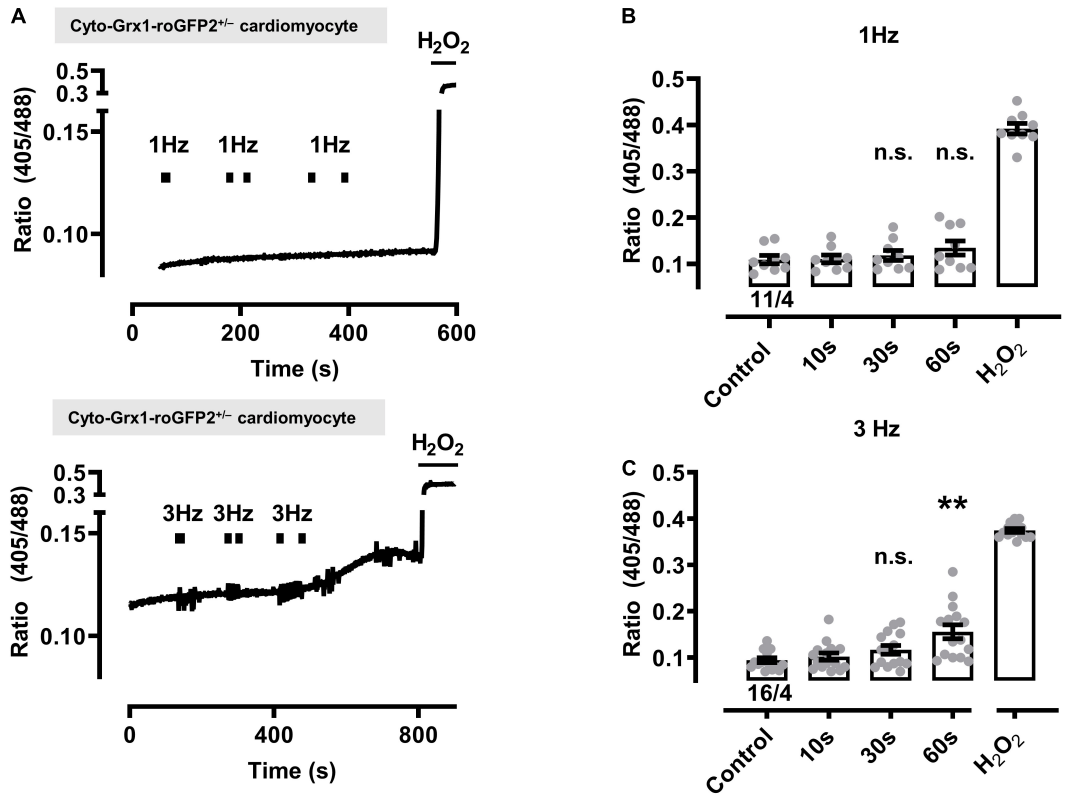

FIGURE 3 | Effect of contractile activity induced by electrical field stimulation (EFS) on the redox sensor signal in cardiomyocytes from cytosolic Grx1-roGFP2$^{+/-}$ mice. **(A)** Representative time course of the redox signal (ratio I405/I488) with contractile activity by EFS at 1 Hz (above) and 3 Hz (below). Marks indicate the start and stop of the stimulation interval which lasted 10, 30, and 60 s, respectively. H_2O_2 (200 μM) was added at the end of each experiment to obtain the maximal oxidized value. Up and down reflections of the signal represent low-frequency (<0.1 Hz) contractions of the myocyte. **(B)** Mean values ± SEM of ratio values obtained in cardiomyocytes under control conditions and after EFS at 1 Hz with a 10, 30, and 60 s duration. The signal values of each cardiomyocyte were obtained under control conditions and after the respective pacing. We used 11 cells from four mice as indicated. Statistical analysis was performed by paired one-way ANOVA with Dunnett's post-test. n.s., non-significant. **(C)** Mean values ± SEM of ratio values obtained in cardiomyocytes under control conditions and after EFS at 3 Hz with a 10, 30, and 60 s duration. We used 16 cells from four mice as indicated. Statistical analysis was performed by paired one-way ANOVA with Dunnett's post-test. $^{**}P = 0.008$; n.s., non-significant.

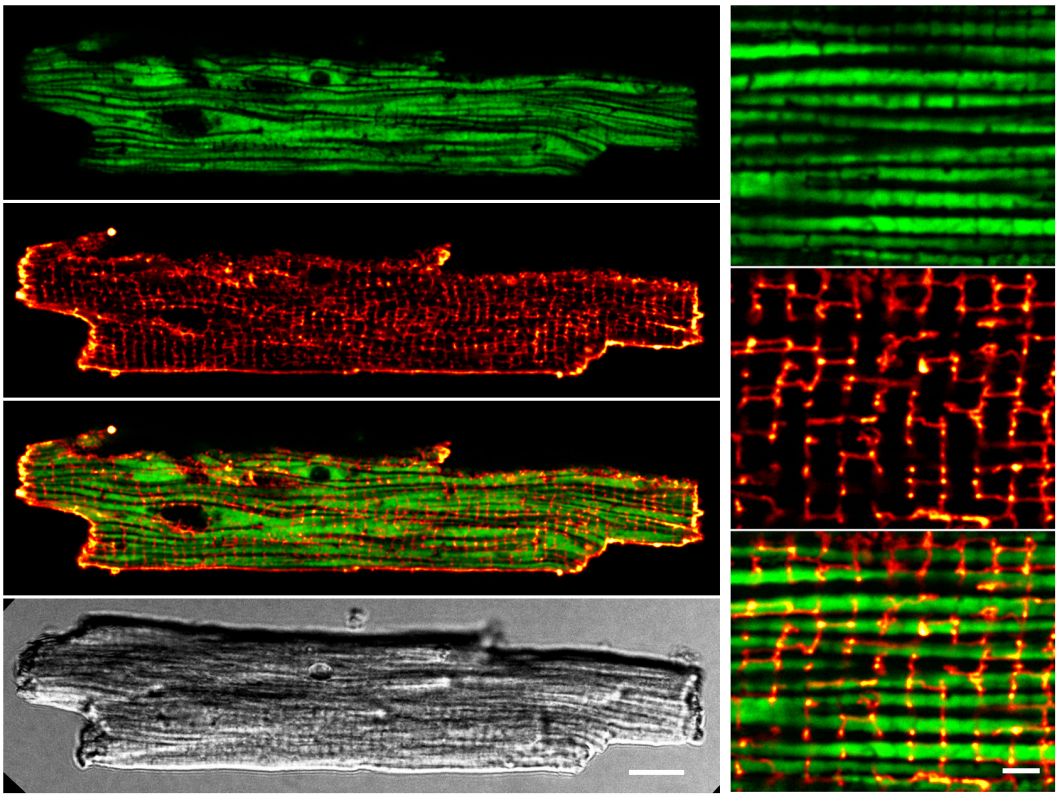

FIGURE 4 | Preserved transverse (T-)tubule and mitochondrial network interfaces in sTG-cardiomyocytes. Confocal live-cell images showing a representative ventricular cardiomyocyte expressing mitochondrial Grx1-roGFP2 after staining with the membrane dye di-8-ANEPPS. *Left* (from top to bottom): (i) roGFP2 auto-fluorescent signals (green LUT) demonstrating the longitudinal chain pattern typical for inter-sarcomeric mitochondria. (ii) di-8-ANEPPS membrane signal (red LUT) confirming a preserved, regular TAT membrane network mainly composed of T-tubule components. (iii) Overlay of the Grx1-roGFP2 and TAT membrane network signals showing a preserved gap-arrangement and confirming network interfaces of T-tubules and mitochondrial membranes. (iv) Cell quality and membrane integrity was confirmed by transmission scanning microscopy with differential interference contrast detecting regular transverse striations and sharp brick-shaped cell edges. Scale bar 10 μm. *Right* (from top to bottom): zoom-in magnifications (i–iii) visualize the distinct mitochondrial and T-tubule compartments and interfaces. Scale bar 2 μm.

density apparent as mature longitudinal chain architecture, the transverse-axial-tubule network furthermore revealed the expected invagination network components mainly composed of T-tubules (**Figure 4**) as reported previously in living mouse cardiomyocytes (Wagner et al., 2012). Apparently, the high T-tubule density regularly intersects the longitudinal mitochondria strands perpendicularly in register (**Figure 4** *overlay magnification*). These live-cell data indicate that the transgenic mito-roGFP2 expression did not affect the mechano-sensitive electrical conduction conduits in cardiomyocytes, which is an important prerequisite for a preserved excitation-bioenergetic coupling of the mitochondrial matrix reported recently (Wescott et al., 2019; Boyman et al., 2020; Boyman et al., 2021).

Increased Mitochondrial Oxidation in RyR2-R2474S dTG-Cardiomyocytes

Next we extended the post-pacing mitochondrial E_{GSH} imaging to dTG-cardiomyocytes from mouse hearts additionally expressing the heterozygous RyR2-R2474S mutated tetrameric Ca^{2+} release channels vs. RyR2-WT control cells. Apparently, relatively large changes in mitochondrial oxidation were readily evidenced in RyR2-R2474S dTG-cardiomyocytes compared to RyR2-WT control (**Figure 5A**) particularly following 30 and 60 s of 1 Hz (**Figure 5B**) and 3 Hz pacing-evoked beating (**Figure 5C**). Together these data suggest that mitochondrial oxidization is significantly increased in heterozygous RyR2-R2474S dTG-cardiomyocytes by the identical 1 and 3 Hz beating rate pacing-trains compared to RyR2-WT control cells.

β-Adrenergic Stimulation Exacerbates Mitochondrial Oxidization in RyR2-R2474S dTG-Cardiomyocytes

An increased sympathetic tone, exercise, and an increased heart rate provoke the characteristic cardiac CPVT phenotype leading to VT episodes in humans (Lehnart et al., 2004; Danielsen et al., 2018; Baltogiannis et al., 2019). Consequently, isolated cardiomyocytes were exposed to selective β-adrenergic stimulation (isoproterenol 100 nM) and pacing (**Figure 6A**). First, mitochondrial oxidation was significantly increased

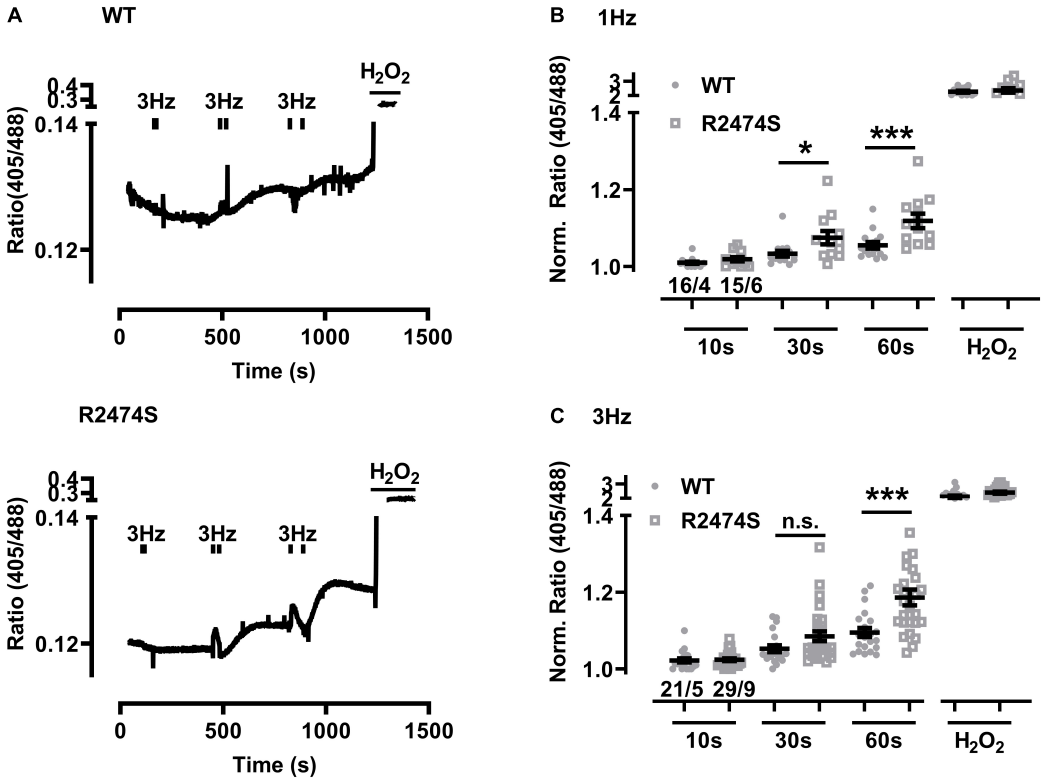

FIGURE 5 | Increased mitochondrial oxidation in RyR2-WT vs. RyR2-R2474S dTG-cardiomyocytes following different beating rates. **(A)** Representative time course of the I405/I488 nm ratio following 3 Hz beating of RyR2-WT control (*top*) and RyR2-R2474S (*bottom*) dTG-cardiomyocytes. Black bars indicate the start and end of each beating interval lasting 10, 30, and 60 s. H_2O_2 (200 μM) was added at the end of each experiment to obtain the maximal oxidized value. **(B,C)** Dot plots showing individual and mean ± SEM normalized I405/I488 nm ratio values for the indicated durations either at the 1 Hz **(B)** or 3 Hz **(C)** beating rate. The fluorescent signal values of each cardiomyocyte were obtained under baseline conditions and after the indicated beating trains each lasting 10 s, 30 s or 60 s. Cell/heart numbers are indicated. Unpaired one-way ANOVA with Tukey's post-test. ***P = 0.001; *P = 0.03; n.s., non-significant.

by isoproterenol-stimulation in WT control (**Figure 6B**) and RyR2-R2474S dTG-cardiomyocytes (**Figure 6C**) when compared to the untreated control cardiomyocytes, respectively. Notably, the isoproterenol-stimulation robustly increased mitochondrial oxidation already at post-30 s beating at 3 Hz in RyR2-R2474S dTG-cardiomyocytes compared to control (**Figure 6C**). Second, isoproterenol-treatment increased mitochondrial oxidation to a significantly larger extent in RyR2-R2474S dTG-cardiomyocytes compared to RyR2-WT control cells at the 3 Hz beating rate both after 30 and 60 s (**Figure 7A**) and even already at the lower 1 Hz beating rate after 60 s (**Figure 7B**). Third, mathematical quantification of the E_{GSH} revealed a significant depolarization/oxidation of over 10 mV following isoproterenol-treatment in RyR2-R2474S dTG-cardiomyocytes and a similarly increased oxidation at baseline and isoproterenol-stimulated between RyR2-R2474S dTG-cardiomyocytes and RyR2-WT control cells (**Figure 8**). Baseline E_{GSH} was not different between RyR2-WT control and RyR2-R2474S dTG-cardiomyocytes. Mean calculated E_{GSH} values ± SEM (in mV) were −290.9 ± 2.2 (n = 8) and −288.8 ± 3.4 (n = 9), respectively. As the level of mitochondrial oxidation was overall robustly increased after isoproterenol-stimulation when compared to non-treated control RyR2-R2474S dTG-cardiomyocytes (**Figure 7**), β-adrenergic stimulation clearly exacerbated the mitochondrial glutathione oxidization.

Isoproterenol Strongly Increases Mitochondrial Oxidation in Intact RyR2-R2474S dTG-Hearts

To monitor mitochondrial oxidation in the intact beating heart, RyR2-WT control and RyR2-R2474S dTG-hearts were Langendorff-perfused and the ventricular left and right epicardial surface imaged with simultaneous surface field-electrogram rhythm recordings. While color-coded mapping of the RyR2-WT dTG-heart apparently captured no major ventricular mitochondrial E_{GSH} change following acute β-adrenergic stimulation by isoproterenol (33 nM) in RyR2-WT control hearts (**Figure 9B**), a robust mitochondrial oxidation increase was evident in the beating RyR2-R2474S dTG-heart (**Figure 9A**). Meanwhile, both genetic heart groups showed the expected maximally increased oxidation by H_2O_2 vs. a maximally decreased oxidation after adding DTT (**Figures 9A–C**).

Comparing the isoproterenol-stimulated E_{GSH} changes confirmed a significant mitochondrial oxidation increase in

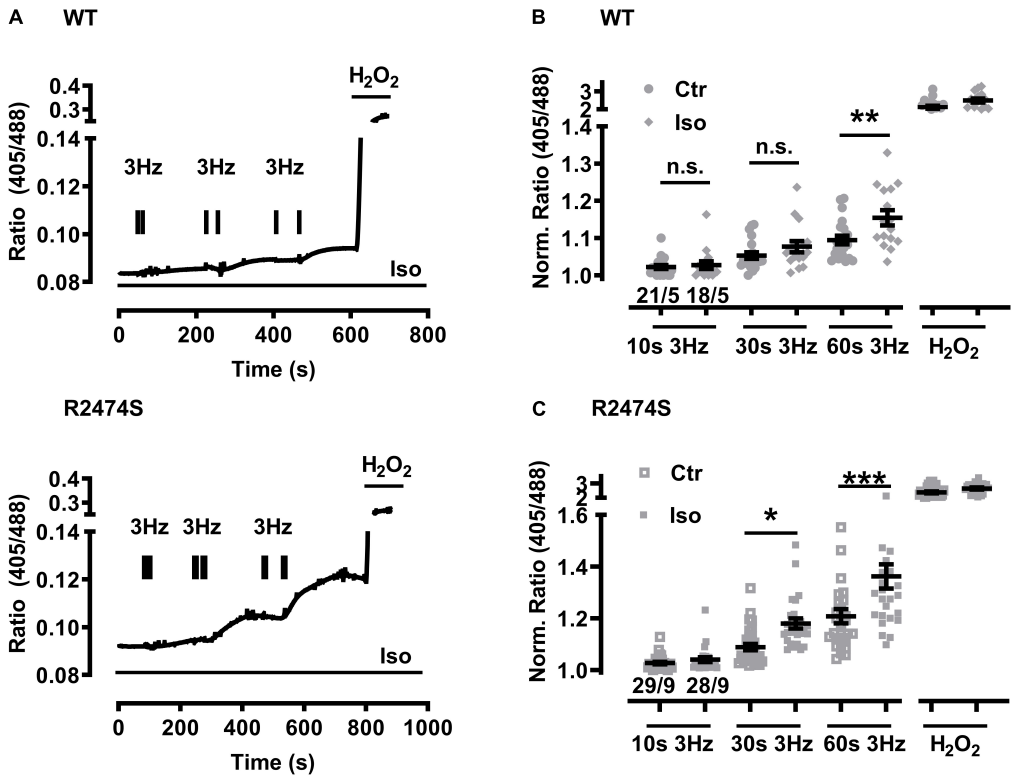

FIGURE 6 | Increased mitochondrial oxidation in WT control and RyR2-R2474S dTG-cardiomyocytes following β-adrenergic stimulation and 3 Hz beating. **(A)** Representative time course of the I405/I488 nm ratio of RyR2-WT control (*top*) and RyR2-R2474S dTG (*bottom*)-cardiomyocytes upon/during isoproterenol (100 nM) stimulation. Black bar pairs indicate the start and stop of the pacing lasting 10, 30, or 60 s. H_2O_2 (200 μM) was added at the end of each experiment to obtain the maximal oxidized value. **(B)** Dot blot showing individual and mean values ± SEM of normalized ratio values obtained after EFS at 3 Hz with a 10, 30, and 60 s duration in the absence (open squares) or presence of isoproterenol (100 nM, closed squares) in cardiomyocytes from WT control mice. Numbers indicate the number of cells/number of mice used. Statistical analysis was performed by unpaired one-way ANOVA with Tukey's post-test. $^{**}P < 0.009$; n.s., non-significant. **(C)** Dot plot summarizing the individual and mean ± SEM values of the normalized 405/488 nm ratio obtained following 3 Hz beating for 10, 30, and 60 s in the absence (open squares) and presence of isoproterenol (100 nM, closed squares) in RyR2-R2474S dTG-cardiomyocytes. Cell/heart numbers are indicated. Unpaired one-way ANOVA with Tukey's post-test. $^{***}P < 0.001$; $^{*}p = 0.03$; n.s., non-significant.

RyR2-R2474S dTG-hearts, which was, however, not observed in RyR2-WT ventricles (**Figure 9D**). Together, these results significantly extend and further confirm the findings mainly documented in isolated RyR2-R2474S dTG-cardiomyocytes, underlining a significantly more oxidized mitochondrial state in beating dTG-hearts following β-adrenergic stimulation evidenced by the pronounced changes of the redox signal I385/I475 ratio monitoring acute E_{GSH} tissue changes.

Dantrolene Prevents Mitochondrial Oxidation in RyR2-R2474S dTG-Cardiomyocytes

Dantrolene is used clinically as acute RyR1 channel blocker targeted to skeletal muscles and other tissues as emergency intervention to treat patients who develop life-threatening malignant hyperthermia episodes induced by certain anesthetic drug compounds during surgical interventions. Recent studies demonstrated that dantrolene may also cause beneficial antagonistic effects against the chronic cardiac RyR2 channel Ca^{2+} leak in human diseased cardiomyocytes isolated from failing hearts (Hartmann et al., 2017). Therefore, the acute potential of the large-conductance channel-inhibitory efficacy of dantrolene against mitochondrial oxidation was investigated in RyR2-R2474S dTG-cardiomyocytes following β-adrenergic stimulation (isoproterenol 100 nM). Strikingly, dantrolene pre-treatment (5 μM for 2 h) significantly decreased the large mitochondrial oxidation after 3 Hz 60 s-beating and non-significantly after 3 Hz 30 s-pacing (**Figure 10**). In summary, these data suggest that a pathologically increased mitochondrial oxidation in isoproterenol-stimulated RyR2-R2474S cardiomyocytes can be partly prevented by pharmacological dantrolene treatment.

DISCUSSION

This work has examined how mitochondrial E_{GSH} oxidation is increased by essential factors in cardiomyocytes with important physiological and pathophysiological consequences that converge at the dynamic interface between RyR2 channel function, sympathetic catecholaminergic stimulation, and contractile

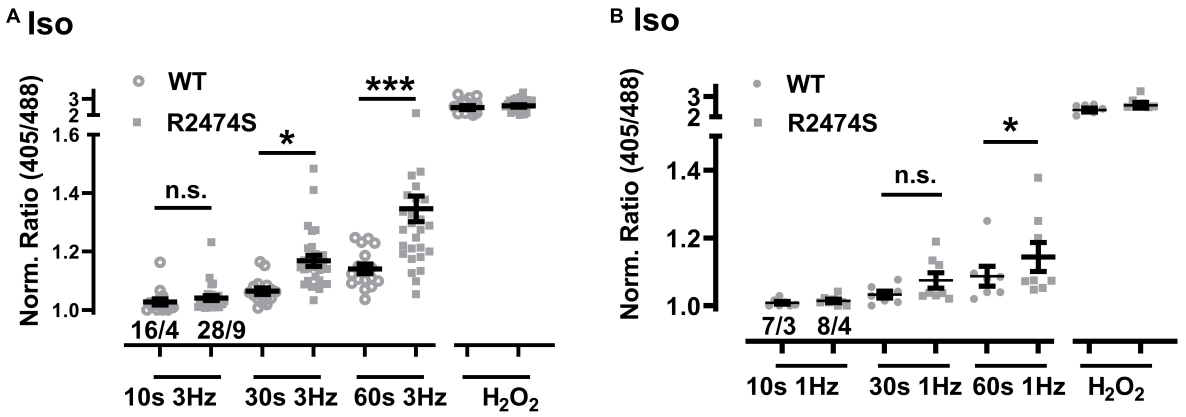

FIGURE 7 | Comparison of the increased mitochondrial oxidation in RyR2-WT control vs. RyR2-R2474S dTG-cardiomyocytes following β-adrenergic stimulation. **(A)** Dot plot showing the individual and mean values ± SEM of the normalized I405/I488 nm ratio values after 3 Hz beating for 10, 30, and 60 s in the presence of isoproterenol (100 nM). Open circles and closed squares reflect the values of the single experiments from RyR2-WT control and Ryr2-R2474S dTG mice, respectively. Cell/heart numbers are indicated. Unpaired one-way ANOVA with Tukey's post-test. ***$P < 0.001$; *$P = 0.04$; **(B)** Dot blot showing individual and mean values ± SEM of normalized ratio values obtained after EFS at 1 Hz with a 10, 30, and 60 s duration in the presence of isoproterenol (100 nM). Open circles and closed squares reflect the values of the single experiments from RyR2-WT control and Ryr2-R2474S dTG mice, respectively. Numbers indicate the number of cells/number of mice used. Statistical analysis was performed by unpaired one-way ANOVA with Tukey's post-test. *$P < 0.02$; n.s., non-significant.

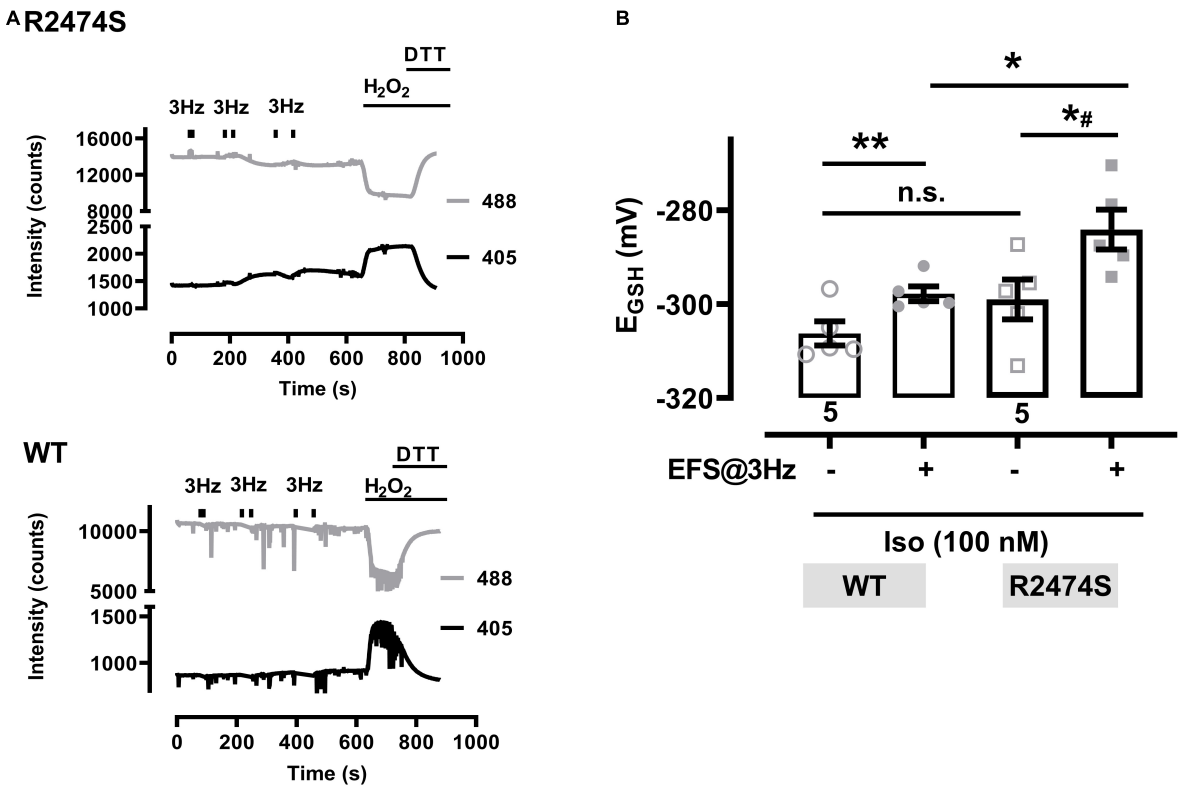

FIGURE 8 | Glutathione redox potentials (E_{GSH}) in cardiomyocytes from RyR2-WT control and RyR2-R2474S dTG mice. **(A)** Representative trace of the emitted fluorescent intensity signals at 405 and 488 nm excitation in a cardiomyocyte from a RyR2-R2474S dTG mouse (above) and a WT control mouse (below) in the presence of isoproterenol (100 nM). Bars indicate the start and stop of contractile activity induced by EFS at 3 Hz. H_2O_2 (200 μM) followed by DTT (1 mM) were applied at the end of the experiment to obtain the maximal and minimal signal values, respectively. **(B)** Calculated E_{GSH} before and after contractile activity induced by EFS-pacing (3 Hz, 60 s, time point at 600 s) in the presence of isoproterenol (100 nM) in cardiomyocytes from RyR2-WT control and RyR2-R2474S dTG mice. Numbers indicate the number of cells used (five cells from two mice, each). Statistical analysis was performed by a paired (control vs. isoproterenol) or unpaired (RyR2-WT control vs. RyR2-R2474S dTG) Student's *t*-test. **$P = 0.001$; *$P = 0.02$; *#$P = 0.01$; n.s., non-significant.

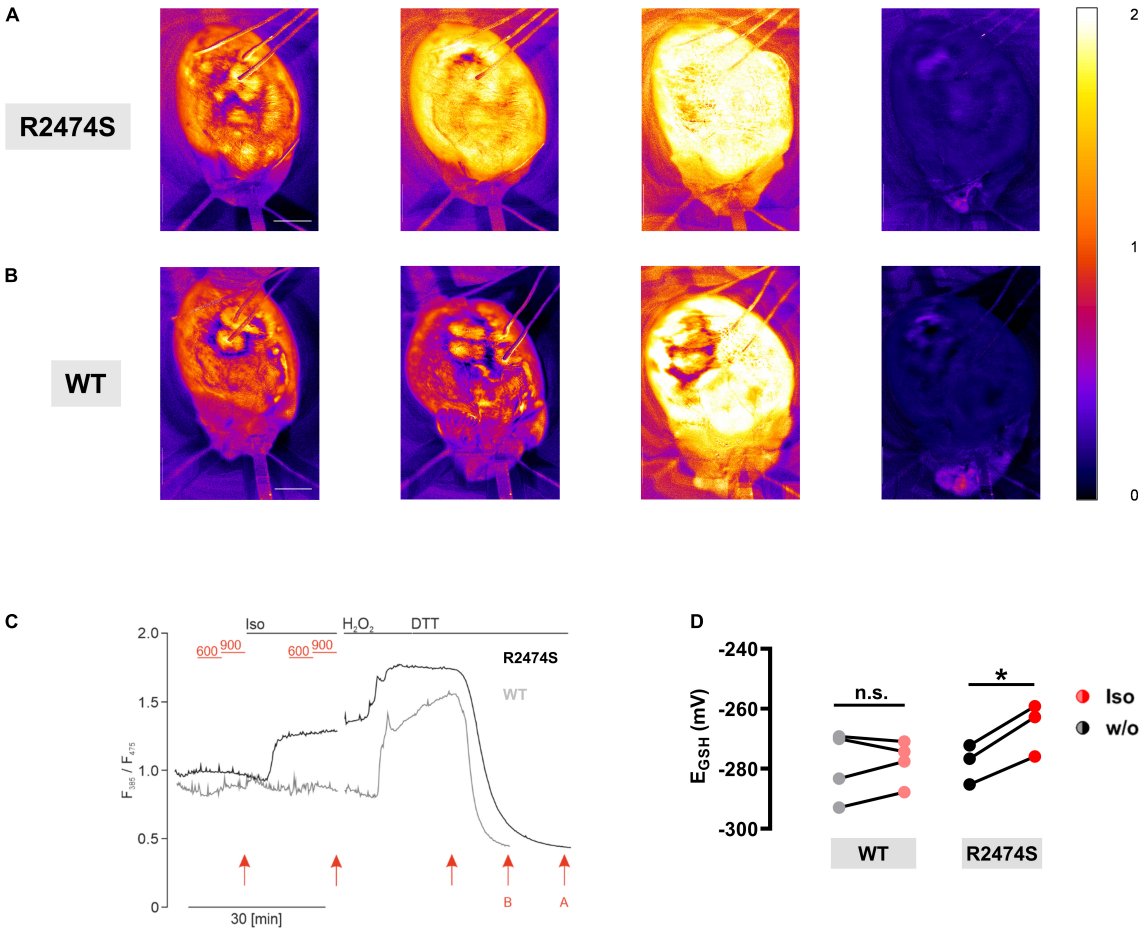

FIGURE 9 | β-adrenergic stimulation induces mitochondrial oxidation in intact RyR2-R2474S hearts. **(A,B)** Color-coded I385/I470 nm ratio comparing a representative RyR2-R2474S dTG-heart **(A)** and a RyR2-WT heart **(B)**. From left to right: (i) baseline control, (ii) following isoproterenol (33 nM) stimulation, (iii) treatment with H_2O_2 (200 μM) and iv) DTT (4 mM) (scale bar, 2.5 mm). **(C)** Representative time course of the normalized I385/I475 nm ratio comparing RyR2-WT and RyR2-R2474S dTG-hearts. Black lines indicate each perfusion with 33 nM isoproterenol, 200 μM H_2O_2, and 4 mM DTT. The baseline heart rate for RyR2-WT and RyR2-R2474S was 340 bpm and 275 bpm, respectively. In-between, we performed electrical pacing with 600 bpm and 900 bpm (red lines). Red arrows refer to time points for representative images shown in **(A,B)**. **(D)** Paired dot-line plot showing E_{GSH} calculated before and after application of isoproterenol each for RyR2-WT and RyR2-R2474S dTG-hearts. Each dot represents one heart/experiment. Paired Student's *t*-test; **P* = 0.013; n.s., non-significant.

activity. Overall, we find that a significant increase following β-adrenergic stimulation significantly changes mitochondrial E_{GSH} in dTG-cardiomyocytes and hearts, which was further dependent on both the presence of the RyR2-R2474S missense mutation and faster beating rates. Importantly, dantrolene treatment of RyR2-R2474S dTG-cardiomyocytes results in a pronounced reduction of this increased mitochondrial oxidation. We discuss our findings on these interrelated RyR2-R2474S regulatory and E_{GSH} driven mitochondrial mechanisms in the context of previously published reports.

Recent quantitative imaging studies established that an increase of mitochondrial Ca^{2+} uptake was necessary to drive inner mitochondrial membrane depolarization and enhanced ATP synthesis in a heart-specific and previously unknown voltage-dependent fashion (Wescott et al., 2019; Boyman et al., 2020; Boyman et al., 2021). This contrasts with heart disease where alterations of mitochondrial E_{GSH} may profoundly shift organelle metabolism and thus cardiac bioenergetics (Bertero and Maack, 2018). Beyond bioenergetics, increased mitochondrial E_{GSH} oxidation revealed a strongly increased ROS production, which might be of immediate relevance for heart disease progression and metabolic remodeling (Doenst et al., 2013). In analogy, increased mitochondrial oxidation and E_{GSH} depolarization in RyR2-R2474S cardiomyocytes and hearts indicate a strongly boosted ROS generation during faster beating rates concurrent with β-adrenergic stimulation.

Interestingly, increased SR Ca^{2+} leak and mitochondrial dysfunction have been demonstrated to enhance ROS production in heart disease previously (Zhou and Tian, 2018; Santulli et al., 2021). Remarkably, mitochondrial ROS scavenging attenuated the effects of augmented RyR2 activity leading to proarrhythmic Ca^{2+} waves in Calsequestrin2-null mice serving as a model for CPVT (Hamilton et al., 2020). In line with this view, ROS scavenging by mito-TEMPO was shown

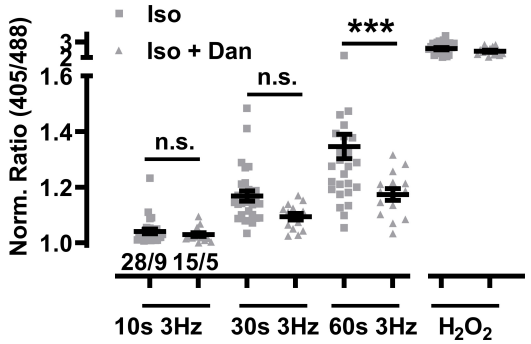

FIGURE 10 | Dantrolene diminishes mitochondrial oxidation in β-adrenergic stimulated RyR2-R2474S dTG cardiomyocytes. Dot plot showing the individual and mean ± SEM values of the normalized I405/I488 nm ratio recorded after 3 Hz beating for 10, 30, and 60 s in the presence of isoproterenol (100 nM) either with or without dantrolene pre-treatment (5 μM for 2 h). Triangles and squares represent individual experiments ± dantrolene as given by the legend. Cell/heart numbers are indicated. Unpaired one-way ANOVA with Tukey's post-test. ***$P < 0.0002$; n.s., non-significant.

to reduce the number of Ca^{2+} waves also in cardiomyocytes from rabbit hearts (Bovo et al., 2012; Cooper et al., 2013). As isoproterenol-stimulated RyR2-R2474S cardiomyocytes exhibit an over threefold increased Ca^{2+} spark frequency that additionally sustains regenerative intracellular Ca^{2+} waves, here the observed robust increase in mitochondrial oxidation will depend both on acute catecholamine stimulation and the beating rate-dependent extent and complex spatiotemporal dynamics of the cell-wide diastolic Ca^{2+} leak reported previously (Lehnart et al., 2008; Xie et al., 2015; Sadredini et al., 2021). However, even under physiological conditions, an increased mitochondrial oxidation was evidenced at higher beating rates in sTG-cardiomyocytes albeit much more pronounced in RyR2-R2474S dTG-cardiomyocytes. For the latter, the faster beating rate clearly led to mitochondrial E_{GSH} oxidation and this was most strongly increased after β-adrenergic stimulation.

Tight control of nanomolar diastolic Ca^{2+} levels is essential for normal cardiac function depending on the precise balance between cytosolic Ca^{2+} influx and efflux (Eisner et al., 2020). If the local control mechanisms become compromised, cardiomyocytes will develop arrhythmia and hypercontraction from cytosolic Ca^{2+} overload. This balance is disturbed when the diastolic Ca^{2+} spark frequency is significantly increased, a phenomenon linked molecularly to RyR2 channel gain-of-function defects (Cheng and Lederer, 2008; Bers, 2014). Interestingly, more than a dozen RyR2 mutations originally identified in CPVT patients have been shown to increase Ca^{2+} leak (Jiang et al., 2002; Wehrens et al., 2003; Lehnart et al., 2004; Kontula et al., 2005; Tester et al., 2007; Lehnart et al., 2008; Marjamaa et al., 2011; Shan et al., 2012). However, only two knockin models were confirmed to exhibit exercise-triggered VTs, RyR2-R2474S$^{+/-}$ (Lehnart et al., 2008) and RyR2-R4496C$^{+/-}$ (Priori and Napolitano, 2005; Liu et al., 2006), and are hence reminiscent of the human arrhythmia phenotype diagnosed by exercise stress testing. In line with the *in vivo* pathology, RyR2-R2474S$^{+/-}$ cardiomyocytes exhibited an overall normal diastolic Ca^{2+} spark behavior at rest, but a strong spark frequency increase occurred after isoproterenol treatment (Lehnart et al., 2008). In this context, increased diastolic Ca^{2+} extrusion mainly by SERCA2a and NCX will necessarily consume additional ATP at rest at the cost of concomitantly increased ROS generation (Bers, 2002, 2014). Thus, our data further link increased catecholaminergic RyR2 channel dysfunction in a murine CPVT model to acute mitochondrial oxidation.

In the present study, we monitored the effect of increased contractile activity on E_{GSH} in the mitochondrial matrix, while the former process has been long known to correlate with mitochondrial metabolic activity and ROS generation (Gudbjarnason et al., 1962). Since a similar extent of E_{GSH} change was excluded in the cytoplasm, NOX2 seems unlikely as ROS source here (Santos et al., 2011). In another context, high extracellular glucose concentrations increased E_{GSH} in the cytosol through NOX2 but not in the mitochondrial matrix (Lu et al., 2020). In contrast, we found that mitochondrial oxidization depended on the duration and frequency of dTG-cardiomyocyte beating. This finding is in line with reported changes of NADH in response to a stepwise increase of the beating frequency from 0.1 to 3.3 Hz in guinea-pig cardiomyocytes (Jo et al., 2006). As the increase in the mitochondrial E_{GSH} following beating was observed both in RyR2-WT and RyR2-R2474S dTG-cardiomyocytes, a relation with increased SR Ca^{2+} leak seems plausible after pacing-evoked contractile activity reported previously (Satoh et al., 1997). Finally, blocking RyR2 Ca^{2+} leak with dantrolene diminished E_{GSH} oxidation as hypothesized previously (Hartmann et al., 2017).

A recent study demonstrated that Ca^{2+} leak increased mitochondrial ROS production in cultured WT rat cardiomyocytes transfected for 48 h with the OMM-HyPer mito-ROS biosensor (Hamilton et al., 2020). An increased ROS production has also been demonstrated during increased beating in healthy cardiomyocytes with the fluorescent probe dichlorodihydrofluorescein, which is confirmed by our sTG-cardiomyocyte data (Heinzel et al., 2006). In rat trabeculae, NADH oxidation was observed at 0.25–2 Hz after 60 s with pronounced ATP hydrolysis (Brandes and Bers, 2002). A similar time frame in response to contractile activity was observed in the present study, where the maximal change of the biosensor signal occurred within 2–3 min after beating. This further agrees with the reported change of the redox signal observed in cardiomyocytes in the same biosensor cardiomyocytes after a high glucose or pH challenge (Lu et al., 2020; Kreitmeier et al., 2021). Since the observed redox changes occurred only after completion of the given beating period, it is suggested to correlate further with the aftercontraction related metabolic activity observed frequently in isoproterenol-stimulated RyR2-R2474S dTG-cardiomyocytes.

Importantly, our report provides the first evidence that E_{GSH} changes happen under quasi physiological conditions in the intact beating heart as well. Using the genetically encoded reporter targeted to mitochondria allowed to monitor the average E_{GSH} from the whole ventricular, anterior heart surface

(**Supplementary Videos 1, 2**) and to perform a ratiometric imaging excluding any major interference due to cardiac contractions. In comparison to the first description of the glutathione redox sensor mouse lines, we were able to increase the ratio differences from maximal oxidization to reduction to comparable signal-to-noise values to single-cell measurements (see **Figures 5**, **9**). This increase in signal amplitude was the key for the detection of the comparable relatively small steps in oxidization during β-adrenergic stimulation, which we could only detect in the intact hearts of dTG mice expressing the RyR2-R2474S mutated channels. However, in contrast to isolated cardiomyocytes, we could not detect a change in oxidation by additional faster pacing in the spontaneously beating Langendorff hearts. One possible explanation may be that these changes are in comparison subtle and thus still not detectable in this setting. The other is that we focused on the effects of isoproterenol and such changes would occur only after prolonged phases of pacing which we could not implement in these experiments.

In summary, we have shown that contractile activity induced by EFS-pacing in isolated cardiomyocytes increased the mitochondrial E_{GSH} to more oxidized levels in a time- and frequency-dependent manner. The increase was most pronounced after β-adrenergic stimulation and in cardiomyocytes expressing the human RyR2-R2474S mutated tetrameric channel. The catecholaminergic E_{GSH} increase, however, was significantly attenuated by the pharmacological RyR2 channel antagonist dantrolene. Likewise, we observe a larger increase in the mitochondrial E_{GSH} toward more oxidized levels in spontaneously beating hearts expressing the RyR2-R2474S mutated channels after β-adrenergic stimulation as compared to control hearts. Hence, we suggest that the RyR2-R2474S mutation induces a metabolic burden in cardiomyocytes through excess ROS generation, especially after β-adrenergic stimulation, tipping the balance from a compensated to a high energetic cost and acutely increased diastolic Ca^{2+} leak, a multifactorial process, which may acutely contribute to the development of the arrhythmogenic CPVT phenotype as proposed for calsequestrin2-null mice previously (Hamilton et al., 2020).

DATA AVAILABILITY STATEMENT

The original contributions presented in the study are included in the article/**Supplementary Material**, further inquiries can be directed to the corresponding author/s.

ETHICS STATEMENT

The animal study was reviewed and approved by the Institutional IACUC. This study has not used *in vivo* examination of mice but *ex vivo* investigations, which are not subject to an ethics protocol at our institution.

AUTHOR CONTRIBUTIONS

JW and AW performed the research and analyzed the data. JW, TB, DK, and SL wrote the manuscript. DK contributed to the biosensor mouse models and analyzed the data. JW, SL, TB, and GH designed the study. All authors approved the manuscript.

FUNDING

This work was supported by grants from Deutsche Forschungsgemeinschaft SFB1002 to SL (projects A09 and S02), TB (A14), and GH (project D01), Germany's Excellence Strategy (EXC 2067/1-390729940) to SL, and SPP1926 to TB and SL. JW and AW were supported by DZHK (German Centre for Cardiovascular Research) Partner Site GÃűttingen. SL is a principal investigator of DZHK.

ACKNOWLEDGMENTS

Excellent technical assistance by Birgit Schumann is gratefully acknowledged.

SUPPLEMENTARY MATERIAL

The Supplementary Material for this article can be found online at: https://www.frontiersin.org/articles/10.3389/fphys.2021.777770/full#supplementary-material

Supplementary Video 1 | Color coded I385/I475 nm ratio comparing representative RyR2-WT hearts. Showing the ratio images during baseline control, isoproterenol (33 nM) stimulation, treatment with H_2O_2 (200 μM), and DTT (4 mM). Scale bar = 5 mm.

Supplementary Video 2 | Color coded I385/I475 nm ratio comparing representative RyR2-R2474S dTG-hearts. Showing the ratio images during baseline control, isoproterenol (33 nM) stimulation, treatment with H_2O_2 (200 μM), and DTT (4 mM). Scale bar = 5 mm.

REFERENCES

Akki, A., Zhang, M., Murdoch, C., Brewer, A., and Shah, A. M. (2009). NADPH oxidase signaling and cardiac myocyte function. *J. Mol. Cell Cardiol.* 47, 15–22. doi: 10.1016/j.yjmcc.2009.04.004

Alsina, K. M., Hulsurkar, M., Brandenburg, S., Kownatzki-Danger, D., Lenz, C., Urlaub, H., et al. (2019). Loss of protein phosphatase 1 regulatory subunit PPP1R3A promotes atrial fibrillation. *Circulation* 140, 681–693. doi: 10.1161/CIRCULATIONAHA.119.039642

Antony, A. N., Paillard, M., Moffat, C., Juskeviciute, E., Correnti, J., Bolon, B., et al. (2016). MICU1 regulation of mitochondrial Ca(2+) uptake dictates survival and tissue regeneration. *Nat. Commun.* 7:10955. doi: 10.1038/ncomms10955

Baltogiannis, G. G., Lysitsas, D. N., Di Giovanni, G., Ciconte, G., Sieira, J., Conte, G., et al. (2019). CPVT: arrhythmogenesis, therapeutic management, and future perspectives. a brief review of the literature. *Front. Cardiovasc. Med.* 6:92. doi: 10.3389/fcvm.2019.00092

Berisha, F., Gotz, K. R., Wegener, J. W., Brandenburg, S., Subramanian, H., Molina, C. E., et al. (2021). cAMP imaging at ryanodine receptors reveals beta2-adrenoceptor driven arrhythmias. *Circ. Res.* 129, 81–94. doi: 10.1161/CIRCRESAHA.120.318234

Bers, D. M. (2002). Cardiac excitation-contraction coupling. *Nature* 415, 198–205.

Bers, D. M. (2014). Cardiac sarcoplasmic reticulum calcium leak: basis and roles in cardiac dysfunction. *Annu. Rev. Physiol.* 76, 107–127. doi: 10.1146/annurev-physiol-020911-153308

Bertero, E., and Maack, C. (2018). Calcium signaling and reactive oxygen species in mitochondria. *Circ. Res.* 122, 1460–1478.

Bezzerides, V. J., Caballero, A., Wang, S., Ai, Y., Hylind, R. J., Lu, F., et al. (2019). Gene therapy for catecholaminergic polymorphic ventricular tachycardia by inhibition of Ca(2+)/calmodulin-dependent kinase II. *Circulation* 140, 405–419. doi: 10.1161/CIRCULATIONAHA.118.038514

Borile, G., Zaglia, T., Lehnart, S. E., and Mongillo, M. (2021). Multiphoton imaging of Ca(2+) instability in acute myocardial slices from a RyR2(R2474S) murine model of catecholaminergic polymorphic ventricular tachycardia. *J. Clin. Med.* 10:2821. doi: 10.3390/jcm10132821

Bovo, E., Lipsius, S. L., and Zima, A. V. (2012). Reactive oxygen species contribute to the development of arrhythmogenic Ca(2)(+) waves during beta-adrenergic receptor stimulation in rabbit cardiomyocytes. *J. Physiol.* 590, 3291–3304. doi: 10.1113/jphysiol.2012.230748

Bovo, E., Mazurek, S. R., De Tombe, P. P., and Zima, A. V. (2015). Increased energy demand during adrenergic receptor stimulation contributes to Ca(2+) wave generation. *Biophys. J.* 109, 1583–1591. doi: 10.1016/j.bpj.2015.09.002

Boyman, L., Greiser, M., and Lederer, W. J. (2021). Calcium influx through the mitochondrial calcium uniporter holocomplex, MCUcx. *J. Mol. Cell Cardiol.* 151, 145–154. doi: 10.1016/j.yjmcc.2020.10.015

Boyman, L., Karbowski, M., and Lederer, W. J. (2020). Regulation of mitochondrial ATP production: Ca(2+) signaling and quality control. *Trends Mol. Med.* 26, 21–39. doi: 10.1016/j.molmed.2019.10.007

Brandenburg, S., Pawlowitz, J., Eikenbusch, B., Peper, J., Kohl, T., Mitronova, G. Y., et al. (2019). Junctophilin-2 expression rescues atrial dysfunction through polyadic junctional membrane complex biogenesis. *JCI Insight* 4:e127116. doi: 10.1172/jci.insight.127116

Brandes, R., and Bers, D. M. (2002). Simultaneous measurements of mitochondrial NADH and Ca(2+) during increased work in intact rat heart trabeculae. *Biophys. J.* 83, 587–604. doi: 10.1016/S0006-3495(02)75194-1

Cheng, H., and Lederer, W. J. (2008). Calcium sparks. *Physiol. Rev.* 88, 1491–1545.

Cooper, L. L., Li, W., Lu, Y., Centracchio, J., Terentyeva, R., Koren, G., et al. (2013). Redox modification of ryanodine receptors by mitochondria-derived reactive oxygen species contributes to aberrant Ca2+ handling in ageing rabbit hearts. *J. Physiol.* 591, 5895–5911. doi: 10.1113/jphysiol.2013.260521

Cucoranu, I., Clempus, R., Dikalova, A., Phelan, P. J., Ariyan, S., Dikalov, S., et al. (2005). NAD(P)H oxidase 4 mediates transforming growth factor-beta1-induced differentiation of cardiac fibroblasts into myofibroblasts. *Circ. Res.* 97, 900–907. doi: 10.1161/01.RES.0000187457.24338.3D

Danielsen, T. K., Manotheepan, R., Sadredini, M., Leren, I. S., Edwards, A. G., Vincent, K. P., et al. (2018). Arrhythmia initiation in catecholaminergic polymorphic ventricular tachycardia type 1 depends on both heart rate and sympathetic stimulation. *PLoS One* 13:e0207100. doi: 10.1371/journal.pone.0207100

Doenst, T., Nguyen, T. D., and Abel, E. D. (2013). Cardiac metabolism in heart failure: implications beyond ATP production. *Circ. Res.* 113, 709–724. doi: 10.1161/CIRCRESAHA.113.300376

Dooley, C. T., Dore, T. M., Hanson, G. T., Jackson, W. C., Remington, S. J., and Tsien, R. Y. (2004). Imaging dynamic redox changes in mammalian cells with green fluorescent protein indicators. *J. Biol. Chem.* 279, 22284–22293. doi: 10.1074/jbc.M312847200

Dridi, H., Kushnir, A., Zalk, R., Yuan, Q., Melville, Z., and Marks, A. R. (2020). Intracellular calcium leak in heart failure and atrial fibrillation: a unifying mechanism and therapeutic target. *Nat. Rev. Cardiol.* 17, 732–747. doi: 10.1038/s41569-020-0394-8

Eisner, D. A., Caldwell, J. L., Trafford, A. W., and Hutchings, D. C. (2020). The control of diastolic calcium in the heart: basic mechanisms and functional implications. *Circ. Res.* 126, 395–412. doi: 10.1161/CIRCRESAHA.119.315891

Fernandez-Velasco, M., Rueda, A., Rizzi, N., Benitah, J. P., Colombi, B., Napolitano, C., et al. (2009). Increased Ca2+ sensitivity of the ryanodine receptor mutant RyR2R4496C underlies catecholaminergic polymorphic ventricular tachycardia. *Circ. Res.* 104, 201–209. 212p following 209, doi: 10.1161/CIRCRESAHA.108.177493

Gibbs, C. L., Loiselle, D. S., and Wendt, I. R. (1988). Activation heat in rabbit cardiac muscle. *J. Physiol.* 395, 115–130. doi: 10.1113/jphysiol.1988.sp016911

Gudbjarnason, S., Hayden, R. O., Wendt, V. E., Stock, T. B., and Bing, R. J. (1962). Oxidation reduction in heart muscle. Theoretical and clinical considerations. *Circulation* 26, 937–945. doi: 10.1161/01.cir.26.5.937

Guo, Z., Xia, Z., Jiang, J., and Mcneill, J. H. (2007). Downregulation of NADPH oxidase, antioxidant enzymes, and inflammatory markers in the heart of streptozotocin-induced diabetic rats by N-acetyl-L-cysteine. *Am. J. Physiol. Heart Circ. Physiol.* 292, H1728–H1736. doi: 10.1152/ajpheart.01328.2005

Gutscher, M., Pauleau, A. L., Marty, L., Brach, T., Wabnitz, G. H., Samstag, Y., et al. (2008). Real-time imaging of the intracellular glutathione redox potential. *Nat. Methods* 5, 553–559.

Hamilton, S., Terentyeva, R., Martin, B., Perger, F., Li, J., Stepanov, A., et al. (2020). Increased RyR2 activity is exacerbated by calcium leak-induced mitochondrial ROS. *Basic Res. Cardiol.* 115:38. doi: 10.1007/s00395-020-0797-z

Hartmann, N., Pabel, S., Herting, J., Schatter, F., Renner, A., Gummert, J., et al. (2017). Antiarrhythmic effects of dantrolene in human diseased cardiomyocytes. *Heart Rhythm* 14, 412–419. doi: 10.1016/j.hrthm.2016.09.014

Heinzel, F. R., Luo, Y., Dodoni, G., Boengler, K., Petrat, F., Di Lisa, F., et al. (2006). Formation of reactive oxygen species at increased contraction frequency in rat cardiomyocytes. *Cardiovasc. Res.* 71, 374–382. doi: 10.1016/j.cardiores.2006.05.014

Heymes, C., Bendall, J. K., Ratajczak, P., Cave, A. C., Samuel, J. L., Hasenfuss, G., et al. (2003). Increased myocardial NADPH oxidase activity in human heart failure. *J. Am. Coll. Cardiol.* 41, 2164–2171. doi: 10.1016/s0735-1097(03)00471-6

Hori, M., and Nishida, K. (2009). Oxidative stress and left ventricular remodelling after myocardial infarction. *Cardiovasc. Res.* 81, 457–464. doi: 10.1093/cvr/cvn335

Jiang, D., Xiao, B., Zhang, L., and Chen, S. R. (2002). Enhanced basal activity of a cardiac Ca2+ release channel (ryanodine receptor) mutant associated with ventricular tachycardia and sudden death. *Circ. Res.* 91, 218–225. doi: 10.1161/01.res.0000028455.36940.5e

Jo, H., Noma, A., and Matsuoka, S. (2006). Calcium-mediated coupling between mitochondrial substrate dehydrogenation and cardiac workload in single guinea-pig ventricular myocytes. *J. Mol. Cell Cardiol.* 40, 394–404. doi: 10.1016/j.yjmcc.2005.12.012

Kohlhaas, M., Nickel, A. G., and Maack, C. (2017). Mitochondrial energetics and calcium coupling in the heart. *J. Physiol.* 595, 3753–3763. doi: 10.1113/JP273609

Kontula, K., Laitinen, P. J., Lehtonen, A., Toivonen, L., Viitasalo, M., and Swan, H. (2005). Catecholaminergic polymorphic ventricular tachycardia: recent mechanistic insights. *Cardiovasc. Res.* 67, 379–387. doi: 10.1016/j.cardiores.2005.04.027

Kreitmeier, K. G., Tarnowski, D., Nanadikar, M. S., Baier, M. J., Wagner, S., Katschinski, D. M., et al. (2021). CaMKIIdelta Met281/282 oxidation is not required for recovery of calcium transients during acidosis. *Am. J. Physiol. Heart Circ. Physiol.* 320, H1199–H1212. doi: 10.1152/ajpheart.00040.2020

Leenhardt, A., Denjoy, I., and Guicheney, P. (2012). Catecholaminergic polymorphic ventricular tachycardia. *Circ. Arrhythm. Electrophysiol.* 5, 1044–1052.

Lehnart, S. E., Mongillo, M., Bellinger, A., Lindegger, N., Chen, B. X., Hsueh, W., et al. (2008). Leaky Ca2+ release channel/ryanodine receptor 2 causes seizures and sudden cardiac death in mice. *J. Clin. Invest.* 118, 2230–2245. doi: 10.1172/JCI35346

Lehnart, S. E., Wehrens, X. H., Laitinen, P. J., Reiken, S. R., Deng, S. X., Cheng, Z., et al. (2004). Sudden death in familial polymorphic ventricular tachycardia associated with calcium release channel (ryanodine receptor) leak. *Circulation* 109, 3208–3214. doi: 10.1161/01.CIR.0000132472.98675.EC

Lieve, K. V. V., Verhagen, J. M. A., Wei, J., Bos, J. M., Van Der Werf, C., Roses, I. N. F., et al. (2019). Linking the heart and the brain: neurodevelopmental disorders in patients with catecholaminergic polymorphic ventricular tachycardia. *Heart Rhythm* 16, 220–228. doi: 10.1016/j.hrthm.2018.08.025

Liu, N., Colombi, B., Memmi, M., Zissimopoulos, S., Rizzi, N., Negri, S., et al. (2006). Arrhythmogenesis in catecholaminergic polymorphic ventricular tachycardia: insights from a RyR2 R4496C knock-in mouse model. *Circ. Res.* 99, 292–298. doi: 10.1161/01.RES.0000235869.50747.e1

Liu, N., Rizzi, N., Boveri, L., and Priori, S. G. (2009). Ryanodine receptor and calsequestrin in arrhythmogenesis: what we have learnt from genetic diseases

and transgenic mice. *J. Mol. Cell Cardiol.* 46, 149–159. doi: 10.1016/j.yjmcc.2008.10.012

Lu, S., Liao, Z., Lu, X., Katschinski, D. M., Mercola, M., Chen, J., et al. (2020). Hyperglycemia acutely increases cytosolic reactive oxygen species via O-linked GlcNAcylation and CaMKII activation in mouse ventricular myocytes. *Circ. Res.* 126, e80–e96. doi: 10.1161/CIRCRESAHA.119.316288

Mallilankaraman, K., Doonan, P., Cardenas, C., Chandramoorthy, H. C., Muller, M., Miller, R., et al. (2012). MICU1 is an essential gatekeeper for MCU-mediated mitochondrial Ca(2+) uptake that regulates cell survival. *Cell* 151, 630–644. doi: 10.1016/j.cell.2012.10.011

Marjamaa, A., Laitinen-Forsblom, P., Wronska, A., Toivonen, L., Kontula, K., and Swan, H. (2011). Ryanodine receptor (RyR2) mutations in sudden cardiac death: studies in extended pedigrees and phenotypic characterization in vitro. *Int. J. Cardiol.* 147, 246–252. doi: 10.1016/j.ijcard.2009.08.041

Meyer, M., Keweloh, B., Guth, K., Holmes, J. W., Pieske, B., Lehnart, S. E., et al. (1998). Frequency-dependence of myocardial energetics in failing human myocardium as quantified by a new method for the measurement of oxygen consumption in muscle strip preparations. *J. Mol. Cell Cardiol.* 30, 1459–1470. doi: 10.1006/jmcc.1998.0706

Munzel, T., Camici, G. G., Maack, C., Bonetti, N. R., Fuster, V., and Kovacic, J. C. (2017). Impact of oxidative stress on the heart and vasculature: part 2 of a 3-part series. *J. Am. Coll. Cardiol.* 70, 212–229. doi: 10.1016/j.jacc.2017.05.035

Murphy, M. P. (2009). How mitochondria produce reactive oxygen species. *Biochem. J.* 417, 1–13.

Nickel, A. G., Von Hardenberg, A., Hohl, M., Loffler, J. R., Kohlhaas, M., Becker, J., et al. (2015). Reversal of mitochondrial transhydrogenase causes oxidative stress in heart failure. *Cell Metab.* 22, 472–484. doi: 10.1016/j.cmet.2015.07.008

Peper, J., Kownatzki-Danger, D., Weninger, G., Seibertz, F., Pronto, J. R. D., Sutanto, H., et al. (2021). Caveolin3 stabilizes McT1-mediated lactate/proton transport in cardiomyocytes. *Circ. Res.* 128, e102–e120. doi: 10.1161/CIRCRESAHA.119.316547

Priori, S. G., and Napolitano, C. (2005). Intracellular calcium handling dysfunction and arrhythmogenesis: a new challenge for the electrophysiologist. *Circ. Res.* 97, 1077–1079. doi: 10.1161/01.RES.0000194556.41865.e2

Rossini, M., and Filadi, R. (2020). Sarcoplasmic reticulum-mitochondria kissing in cardiomyocytes: Ca(2+), ATP, and undisclosed secrets. *Front. Cell Dev. Biol.* 8:532. doi: 10.3389/fcell.2020.00532

Sadredini, M., Haugsten Hansen, M., Frisk, M., Louch, W. E., Lehnart, S. E., Sjaastad, I., et al. (2021). CaMKII inhibition has dual effects on spontaneous Ca(2+) release and Ca(2+) alternans in ventricular cardiomyocytes from mice with a gain-of-function RyR2 mutation. *Am. J. Physiol. Heart Circ. Physiol.* 321, H446–H460. doi: 10.1152/ajpheart.00011.2021

Santos, C. X., Anilkumar, N., Zhang, M., Brewer, A. C., and Shah, A. M. (2011). Redox signaling in cardiac myocytes. *Free Radic. Biol. Med.* 50, 777–793.

Santulli, G., and Marks, A. R. (2015). Essential roles of intracellular calcium release channels in muscle, brain, metabolism, and aging. *Curr. Mol. Pharmacol.* 8, 206–222. doi: 10.2174/1874467208666150507105105

Santulli, G., Monaco, G., Parra, V., and Morciano, G. (2021). Editorial: mitochondrial remodeling and dynamic inter-organellar contacts in cardiovascular physiopathology. *Front. Cell Dev. Biol.* 9:679725. doi: 10.3389/fcell.2021.679725

Santulli, G., Pagano, G., Sardu, C., Xie, W., Reiken, S., D'ascia, S. L., et al. (2015). Calcium release channel RyR2 regulates insulin release and glucose homeostasis. *J. Clin. Invest.* 125, 4316.

Satoh, H., Blatter, L. A., and Bers, D. M. (1997). Effects of [Ca2+]i, SR Ca2+ load, and rest on Ca2+ spark frequency in ventricular myocytes. *Am. J. Physiol.* 272, H657–H668. doi: 10.1152/ajpheart.1997.272.2.H657

Shan, J., Xie, W., Betzenhauser, M., Reiken, S., Chen, B. X., Wronska, A., et al. (2012). Calcium leak through ryanodine receptors leads to atrial fibrillation in 3 mouse models of catecholaminergic polymorphic ventricular tachycardia. *Circ. Res.* 111, 708–717. doi: 10.1161/CIRCRESAHA.112.273342

Suga, H. (1990). Ventricular energetics. *Physiol. Rev.* 70, 247–277.

Swain, L., Kesemeyer, A., Meyer-Roxlau, S., Vettel, C., Zieseniss, A., Guntsch, A., et al. (2016). Redox imaging using cardiac myocyte-specific transgenic biosensor mice. *Circ. Res.* 119, 1004–1016. doi: 10.1161/CIRCRESAHA.116.309551

Takimoto, E., Champion, H. C., Li, M., Ren, S., Rodriguez, E. R., Tavazzi, B., et al. (2005). Oxidant stress from nitric oxide synthase-3 uncoupling stimulates cardiac pathologic remodeling from chronic pressure load. *J. Clin. Invest.* 115, 1221–1231. doi: 10.1172/JCI21968

Tester, D. J., Dura, M., Carturan, E., Reiken, S., Wronska, A., Marks, A. R., et al. (2007). A mechanism for sudden infant death syndrome (SIDS): stress-induced leak via ryanodine receptors. *Heart Rhythm* 4, 733–739. doi: 10.1016/j.hrthm.2007.02.026

Uchinoumi, H., Yano, M., Suetomi, T., Ono, M., Xu, X., Tateishi, H., et al. (2010). Catecholaminergic polymorphic ventricular tachycardia is caused by mutation-linked defective conformational regulation of the ryanodine receptor. *Circ. Res.* 106, 1413–1424. doi: 10.1161/CIRCRESAHA.109.209312

von Harsdorf, R., Li, P. F., and Dietz, R. (1999). Signaling pathways in reactive oxygen species-induced cardiomyocyte apoptosis. *Circulation* 99, 2934–2941. doi: 10.1161/01.cir.99.22.2934

Wagner, E., Brandenburg, S., Kohl, T., and Lehnart, S. E. (2014). Analysis of tubular membrane networks in cardiac myocytes from atria and ventricles. *J. Vis. Exp.* 92:e51823. doi: 10.3791/51823

Wagner, E., Lauterbach, M. A., Kohl, T., Westphal, V., Williams, G. S., Steinbrecher, J. H., et al. (2012). Stimulated emission depletion live-cell super-resolution imaging shows proliferative remodeling of T-tubule membrane structures after myocardial infarction. *Circ. Res.* 111, 402–414. doi: 10.1161/CIRCRESAHA.112.274530

Wehrens, X. H., Lehnart, S. E., Huang, F., Vest, J. A., Reiken, S. R., Mohler, P. J., et al. (2003). FKBP12.6 deficiency and defective calcium release channel (ryanodine receptor) function linked to exercise-induced sudden cardiac death. *Cell* 113, 829–840. doi: 10.1016/s0092-8674(03)00434-3

Wescott, A. P., Kao, J. P. Y., Lederer, W. J., and Boyman, L. (2019). Voltage-energized calcium-sensitive ATP production by mitochondria. *Nat. Metab.* 1, 975–984.

Wleklinski, M. J., Kannankeril, P. J., and Knollmann, B. C. (2020). Molecular and tissue mechanisms of catecholaminergic polymorphic ventricular tachycardia. *J. Physiol.* 598, 2817–2834. doi: 10.1113/JP276757

Xie, W., Santulli, G., Reiken, S. R., Yuan, Q., Osborne, B. W., Chen, B. X., et al. (2015). Mitochondrial oxidative stress promotes atrial fibrillation. *Sci. Rep.* 5:11427. doi: 10.1038/srep11427

Yano, M., Okuda, S., Oda, T., Tokuhisa, T., Tateishi, H., Mochizuki, M., et al. (2005). Correction of defective interdomain interaction within ryanodine receptor by antioxidant is a new therapeutic strategy against heart failure. *Circulation* 112, 3633–3643. doi: 10.1161/CIRCULATIONAHA.105.555623

Yano, M., Yamamoto, T., Kobayashi, S., and Matsuzaki, M. (2009). Role of ryanodine receptor as a Ca(2)(+) regulatory center in normal and failing hearts. *J. Cardiol.* 53, 1–7. doi: 10.1016/j.jjcc.2008.10.008

Zhou, B., and Tian, R. (2018). Mitochondrial dysfunction in pathophysiology of heart failure. *J. Clin. Invest.* 128, 3716–3726. doi: 10.1172/JCI120849

Conflict of Interest: The authors declare that the research was conducted in the absence of any commercial or financial relationships that could be construed as a potential conflict of interest.

Publisher's Note: All claims expressed in this article are solely those of the authors and do not necessarily represent those of their affiliated organizations, or those of the publisher, the editors and the reviewers. Any product that may be evaluated in this article, or claim that may be made by its manufacturer, is not guaranteed or endorsed by the publisher.

frontiers in Physiology

BRIEF RESEARCH REPORT
published: 20 December 2021
doi: 10.3389/fphys.2021.768495

Optogenetic Stimulation of G_i Signaling Enables Instantaneous Modulation of Cardiomyocyte Pacemaking

Milan Cokić [1], Tobias Bruegmann [1,2†], Philipp Sasse [1] and Daniela Malan [1*]*

[1] Medical Faculty, Institute of Physiology I, University of Bonn, Bonn, Germany, [2] Research Training Group 1873, University of Bonn, Bonn, Germany

OPEN ACCESS

Edited by:
T. Alexander Quinn, Dalhousie University, Canada

Reviewed by:
Matthew W. Kay, George Washington University, United States
Matteo Elia Mangoni, Centre National de la Recherche Scientifique (CNRS), France

***Correspondence:**
Daniela Malan
dmalan@uni-bonn.de
Philipp Sasse
philipp.sasse@uni-bonn.de
orcid.org/0000-0002-8502-9472

†Present address:
Tobias Bruegmann, Institute for Cardiovascular Physiology, University Medical Center Goettingen, Goettingen, Germany

Specialty section:
This article was submitted to Cardiac Electrophysiology, a section of the journal Frontiers in Physiology

Received: *31 August 2021*
Accepted: *18 November 2021*
Published: *20 December 2021*

Citation:
Cokić M, Bruegmann T, Sasse P and Malan D (2021) Optogenetic Stimulation of G_i Signaling Enables Instantaneous Modulation of Cardiomyocyte Pacemaking. Front. Physiol. 12:768495. doi: 10.3389/fphys.2021.768495

G-protein signaling pathways are central in the regulation of cardiac function in physiological and pathophysiological conditions. Their functional analysis through optogenetic techniques with selective expression of opsin proteins and activation by specific wavelengths allows high spatial and temporal precision. Here, we present the application of long wavelength-sensitive cone opsin (LWO) in cardiomyocytes for activation of the G_i signaling pathway by red light. Murine embryonic stem (ES) cells expressing LWO were generated and differentiated into beating cardiomyocytes in embryoid bodies (EBs). Illumination with red light (625 nm) led to an instantaneous decrease up to complete inhibition (84–99% effectivity) of spontaneous beating, but had no effect on control EBs. By using increasing light intensities with 10 s pulses, we determined a half maximal effective light intensity of 2.4 $\mu W/mm^2$ and a maximum effect at 100 $\mu W/mm^2$. Pre-incubation of LWO EBs with pertussis toxin completely inhibited the light effect proving the specificity for G_i signaling. Frequency reduction was mainly due to the activation of GIRK channels because the specific channel blocker tertiapin reduced the light effect by ~80%. Compared with pharmacological stimulation of M_2 receptors with carbachol with slow kinetics (>30 s), illumination of LWO had an identical efficacy, but much faster kinetics (<1 s) in the activation and deactivation demonstrating the temporal advantage of optogenetic stimulation. Thus, LWO is an effective optogenetic tool for selective stimulation of the G_i signaling cascade in cardiomyocytes with red light, providing high temporal precision.

Keywords: optogenetics, cardiomyocyte, GPCR (G protein coupled receptor), G_i signaling pathway, GIRK channel, pacemaking

INTRODUCTION

G-Protein-coupled receptors (GPCR) play a pivotal role in regulating cardiac function. The counteracting effects of G_s and G_i proteins are fundamental for the heart rate regulation, contractility, neurohormonal control of circulatory system, and in pathophysiological conditions (Capote et al., 2015). As an antagonist of G_s-pathway, the G_i-pathway inhibits the adenylate cyclase, decreasing intracellular cAMP level, diminishing protein kinase A (PKA) activity, and thus, reducing L-type Ca^{2+} currents. In atrial myocytes and cells of the sinus node and AV node, acetylcholine opens a type of inwardly rectifying potassium channel ($I_{K,ACh}$/GIRK) through direct

effects of the G_i βγ subunit (Krapivinsky et al., 1995; Ivanova-Nikolova et al., 1998). This results in hyperpolarization, slowing of heart rate, prolongation of AV-node conduction, and shortening of the action potential duration in atrial cardiomyocytes (Belardinelli and Isenberg, 1983). Some G_i coupled receptors, such as adenosine-A1, are cardioprotective (Hutchinson and Scammells, 2004) and reduce the risk of cardiac arrhythmia, moreover G_i-coupled α_2 receptors exert an important sympatho-inhibitory function (Xiang and Kobilka, 2003).

Optogenetics is a photostimulation technique which selectively activates opsin proteins by specific wavelengths and the use of light has a much higher spatial and temporal precision than application and diffusion of receptor agonists (Beiert et al., 2014; Guru et al., 2015; Makowka et al., 2019). For instance, the blue light-sensitive receptor Jellyfish Opsin has been used for selective activation of G_s signaling cascade in cardiomyocytes and the heart with high spatial and temporal precision (Makowka et al., 2019), but direct control of the $G_{i/o}$ signaling cascade in cardiomyocytes with light has not been shown yet.

Short- and long-wavelength-sensitive opsins (LWO) have been used before for control of neuronal $G_{i/o}$ signaling pathways (Masseck et al., 2014) and LWO has been shown to activate rather $G_{i/t}$ than G_o signaling (Ballister et al., 2018). Thus, the aim of this study was to use the red light-activated LWO to stimulate G_i signaling pathways in cardiomyocytes.

METHODS

Vector Construction and Transfection of Embryonic Stem (ES) Cells

An LWO-enhanced yellow fluorescent protein (eYFP) plasmid was generated for the expression of LWO (human long-wavelength-sensitive opsin 1, NP_064445.1) c-terminally fused with eYFP using codon optimized synthesized DNA (GeneArt, Life Technologies, Germany) excised with SpeI und MluI and subcloned into a backbone vector with the chicken β-actin promoter (CAG) described before (Beiert et al., 2014). In this study, 40 μg of DNA was linearized with Bgl II and electroporated into 4×10^6 mouse embryonic stem (ES) cells (D3 line) with a single electrical pulse (250 V, 750 μF, 0.4 cm electrode gap, BioRad Gene Pulser, CA, USA). The electroporated cells were plated and 400 μg/ml neomycin was added for selection 24 h after transfection. The eYFP positive clones were picked and cultured separately. Two positive clones were chosen, because of their specific eYFP expression in cardiomyocytes and stable light reaction. As a control group, we used the D3 ES cells with stable expression of the enhanced green fluorescent protein (eGFP) under the control of the CAG promoter as reported before (Beiert et al., 2014).

ES Cell Culture and Differentiation

Embryonic stem cells were cultured and differentiated within embryoid bodies (EBs) using the hanging drop method as previously described (Bruegmann et al., 2010; Beiert et al., 2014). For differentiation, we used Iscove's Modified Eagle's Medium (Invitrogen, MA, USA) supplemented with 20% fetal calf serrum (FCS) (Pan-Biotech, Germany), 0.1 mM non-essential amino acids (Invitrogen), 100 U/ml penicillin (Invitrogen), 100 mg/ml streptomycin (Invitrogen), and 0.1 mmol/L β-mercaptoethanol (Sigma Aldrich, MO, USA). At day 5 of differentiation, EBs were either plated on 0.1% gelatin-coated glass cover slips for the analysis of beating frequency conducted at day 9–14 or fixated for immunohistochemical analysis. In some differentiations, the method was modified by adding Noggin (R&D System, MN, USA, 250 ng/ml) from day 4 to 6 and retinoic acid (Sigma Aldrich, 1 μM) from day 6 to 8 and Dickkopf-related protein 1 (R&D system, 200 ng/ml) from day 6 to 11.

Immunofluorescence

Embryoid bodies were fixed with 4% paraformaldehyde (Sigma Adrich) and permeabilized with 0.2% of Triton X-100 (Sigma Adrich) for 20 min, blocked with 5% of donkey serum (Jackson ImmunoResearch, UK) for 20 min and stained for 2 h at room temperature with primary antibody against α-actinin (1:400, Sigma Aldrich). Alexa Fluor 647 conjugated secondary antibody (1:400, Invitrogen) diluted in 1 μg/ml Hoechst 33342 (Sigma Aldrich) was applied for 1 h at room temperature. The pictures were taken with an Eclipse Ti2 microscope with NIS-Elements and deconvolution software (Nikon, Japan).

Frequency Analysis and Light Stimulation of EBs

Beating EBs that showed eYFP expression in beating areas were used at day 9–14 of differentiation. Then, 1–2 h before experiment, the medium was replaced with Tyrode external solution (in mM: 142 NaCl, 5.4 KCl, 1.8 $CaCl_2$, 2 $MgCl_2$, 10 glucose, and 10 HEPES; pH 7.4) containing 11-cis retinal (1 μM, Santa Cruz Biotechnology, TX, USA) or 9-cis retinal (1 μM, Sigma Aldrich). Video microscopy of beating EBs was performed while perfusing EBs with Tyrode solution without retinal at ∼35°C on an Axiovert 200 microscope with a 5× objective (Fluar, NA 0.25, Zeiss, Germany) using infrared light (760 nm, 1.8 $\mu W/mm^2$ at the focal plane) to avoid accidental LWO activation. Spontaneous contraction was recorded with a charge-coupled device (CCD) camera (piA640-210gm, Basler, Germany) at 51 fps and analyzed online using custom designed software (LabView, National Instruments, TX, USA) as described before (Bruegmann et al., 2010; Makowka et al., 2019). Optogenetic stimulation was performed with a 625 nm LED within the LedHUB (Omicron Laserage, Germany) equipped with a 10% neutral density filter and coupled to the objective with an optical fiber and a 660 nm dichroic filter (AHF Analysentechnik, Germany). Illumination was controlled by a recording system (PowerLab 4/35 and Labchart software, AD Instruments, Sydney, Australia), which was also used to record time points of individual beats to calculate the frequency. Light intensity was calibrated at the objective with a power meter (PM100 power meter, S130A sensor, Thorlabs, NJ, USA) before each experiment.

Analysis of LWO Effect and Light Sensitivity

For statistical analysis, only stable beating EBs without arrhythmical episodes over 5 min before illumination were included. The average frequency during 10 s continuous

illumination was analyzed and normalized to baseline 10 s before. To describe the effectivity of LWO, we calculated the blocking effect with 100% as complete block and 0% as no effect on beating frequency. To determine light sensitivity, the light intensity of individual light pulses was gradually increased (in $\mu W/mm^2$: 0.3; 1; 3; 10; 30; 100; and 300). In addition, 100 $\mu W/mm^2$ individual light pulses of increasing durations (0.1; 0.3; 0.5; 1; 3; 5; 10; and 30 s) were applied and the frequency was averaged 5 s after onset of illumination compared with 5 s before. Half maximal effects were analyzed by fitting the normalized frequency with a Hill function with upper level set to 100% (GraphPad Prism, CA, USA).

Pharmacology

To compare LWO effect with pharmacological activation, we used supramaximal illumination (100 $\mu W/mm^2$, 10 s) and stimulation of the muscarinergic acetylcholine receptor with carbachol (60 s, 100 µM, Sigma Aldrich). Effectiveness of the inhibition was calculated 5 s after the lowest frequency (to account for variations in perfusion kinetics) compared with 5 s before illumination/perfusion. The delay to maximum block was calculated between onset of illumination/perfusion and maximal effect and the delay to 50% recovery as end of stimulation/perfusion until frequency reached 50% of initial baseline. To block G_i proteins, pertussis-toxin (PTX, Invitrogen) was applied for 24 h in IMDM medium without FCS at a final concentration of 0.5 µg/ml. The blocker of G protein-coupled inwardly-rectifying potassium channels (GIRK) tertiapin-q (100 nM, Tocris, Bristol, UK) was incubated for 30 min after one initial measurement and kept in the solution for the second measurement (**Figure 2C**).

Statistics

Data are shown as mean ± SEM and GraphPad Prism 7.0 was used to perform the statistical analysis. For frequency experiments in **Figures 1D,E** one-way ANOVA with Tukey's multiple comparison test was used. Pertussis toxin (PTX) effect (**Figure 2B**) was analyzed with an unpaired Student's *t*-test. For the other experiments (**Figures 1G**, **2D**, **4B–D**), two-sided paired Student's *t*-tests were used. A p-value < 0.05 was considered statistically significant. The n values indicate the number of independent experiments (EBs).

RESULTS

Red Light Activation of LWO Decreases Beating Frequency of Cardiomyocytes

The human LWO in fusion with eYFP was stably expressed under the control of the CAG promoter in ES-cells (D3 line) (**Figure 1A**). For differentiation of ES cells into spontaneously beating cardiomyocytes, EBs were generated with the hanging drop method (Wobus et al., 1991; Maltsev et al., 1993; Beiert et al., 2014). Spontaneously beating areas in the EBs showed differentiation into α-actinin and eYFP positive cardiomyocytes indicating LWO expression (**Figure 1B**). An analysis of beating frequency was performed by infra-red video microscopy to avoid LWO activation. Illumination of beating areas with red light pulses ($\lambda = 625$ nm, 10 s, 100 $\mu W/mm^2$) led to an almost complete block of spontaneous beating in EBs from two separately differentiated ES cell clones (**Figures 1C,D**; clones C1 and C2). In contrast, illumination of EBs expressing only eGFP but not LWO did not reduce beating frequency (**Figures 1C,D**; Ctr). Importantly, the baseline beating frequency was similar between EBs from the two LWO clones and the control eGFP clone, suggesting that LWO expression does not negatively affect pacemaking and shows no dark activity (**Figure 1E**). Application of two identical light pulses with 90 s delay showed similar effectivity of beating block (**Figures 1F,G**) indicating that LWO can be activated repetitively without desensitization.

LWO Activates G_i-Proteins and GIRK Channels in Cardiomyocytes

To confirm the LWO specificity for G_i activation, EBs were pre-treated with PTX (0.5 µg/ml) for 24 h to block all $G_{i/o}$ proteins. Subsequent frequency measurements showed that PTX almost completely inhibited the light effect (**Figures 2A,B**) and the blocking effectivity was only 4% in contrast to an effectivity of 88% in non-treated EBs recorded in parallel. Because activation of GIRK channels by G_i-protein βγ subunits is the main mechanism for slowing the heart rate (Huang et al., 1995; Nobles et al., 2018), we compared light effects before and after application of the GIRK channel blocker tertiapin (100 nM, 30 min, **Figure 2C**, blue color) and found that tertiapin reduced the light effect significantly from 91 to 21% blocking effectivity (**Figure 2D**).

Dose-Response Relationship Shows High Light Sensitivity of LWO

To determine LWO light sensitivity, we repetitively applied light with increasing light energy by using ascending light intensities or durations (**Figure 3**). Application of 10 s long pulses with stepwise increasing light intensities from 0.3 to 300 $\mu W/mm^2$ led to a gradual decrease of beating frequency after each light pulse (**Figure 3A**) with a sigmoidal dependency of the blocking effect on the logarithm of intensity (averaged data in **Figure 3C**). The data points of each individual experiment were fitted with the Hill equation resulting in an average half maximal effective light intensity (ELi50) of 2.4 ± 0.7 $\mu W/mm^2$ ($n = 9$) and a maximum blocking effect at ∼ 100 $\mu W/mm^2$. Similarly, application of light pulses of 100 $\mu W/mm^2$ with increasing durations from 0.1 to 30 s led to gradual block of beating after each pulse (**Figure 3B**). The statistical analysis and Hill-fitting of individual experiments showed a sigmoidal dependence of blocking effect on logarithm of pulse duration with a half maximal effect at 1.2 ± 0.4 s ($n = 6$) and maximal effect at ∼ 10 s (averaged data in **Figure 3D**). To compare both gradual stimulation protocols, we calculated and overlaid the total light energy in each light pulse as s*$\mu W/mm^2$ (**Figure 3E**). Surprisingly, we found that the light intensity protocol seemed to be more effective than the pulse duration protocol (as shown in discussion).

To determine if light sensitivity and blocking efficiency is constant, we applied two brief (0.5 s) subthreshold pulses at 100 $\mu W/mm^2$ with only 20 s in-between. Because the blocking effect

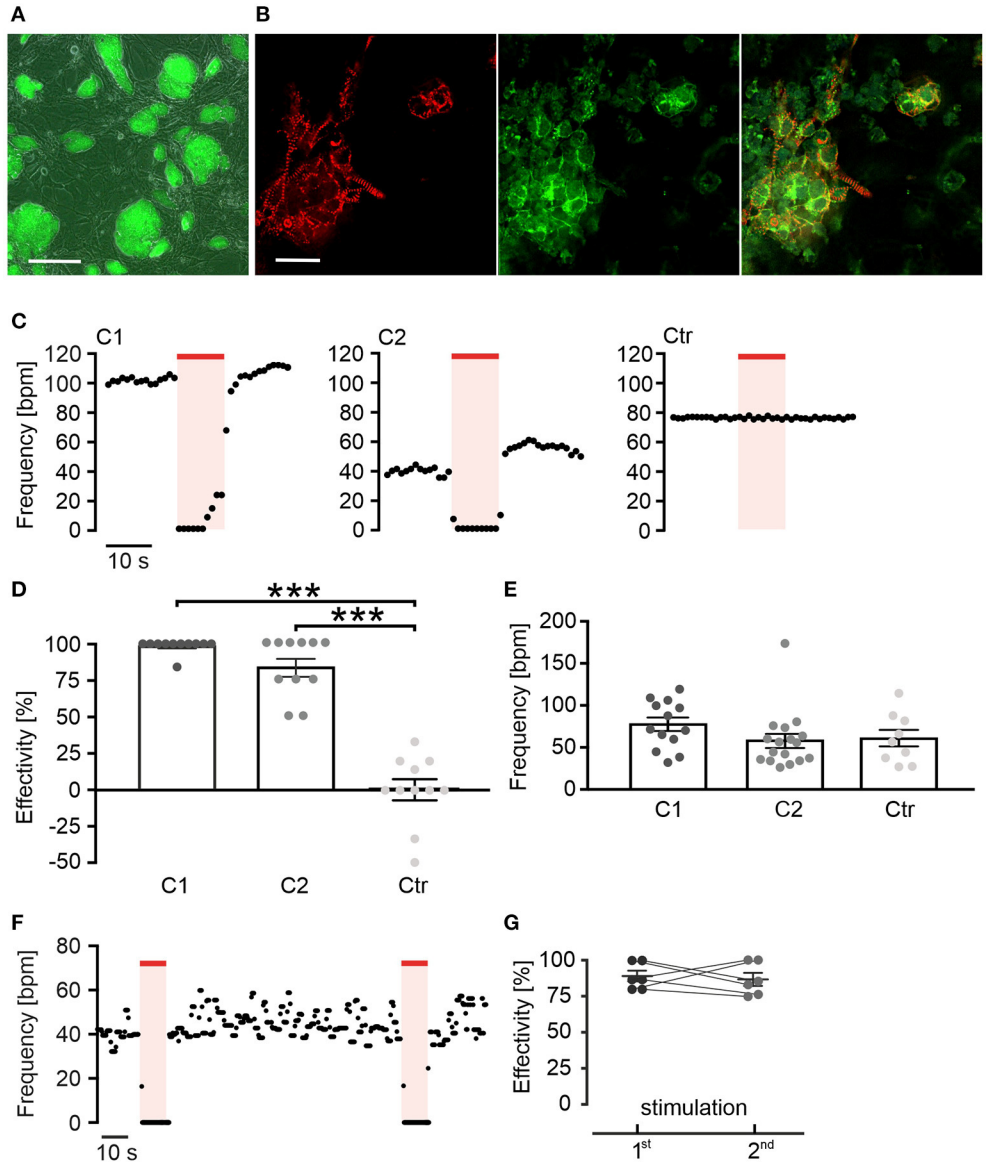

FIGURE 1 | Red light activation of long wavelength-sensitive cone opsin (LWO) decreases beating frequency of cardiomyocytes. **(A)** Embryonic stem (ES) cell colonies with LWO expression indicated by eYFP fluorescence (green, bar = 200 μm). **(B)** EYFP fluorescence (green) in α-actinin (red) positive cardiomyocytes differentiated within an embryoid body (EB), generated from LWO ES cells (bar = 25 μm). **(C)** Representative frequency traces of spontaneous beating within two EBs differentiated from ES cell LWO clones (C1 and C2) and one EB from eGFP control ES cells (Ctr) stimulated with light (625 nm, 100 μW/mm^2, red line). **(D)** Effectivity of inhibition (100% = complete block of spontaneous beating) by illumination [ANOVA Tukey's multiple comparison test: ***$p < 0.001$ (C1, C2, $n = 11$) vs. control ($n = 11$)]. **(E)** Statistical comparison of spontaneous beating frequency of EBs from two LWO clones and the wild-type ES cells [ANOVA Tukey's multiple comparison test, $p = 0.98$ (C2, $n = 17$) $p = 0.46$ (C1, $n = 13$) vs. control ($n = 9$)]. **(F)** Representative frequency trace of two supramaximal (10 s, 100 μW/mm^2) repetitive light stimuli. **(G)** Comparison of frequency reduction effectivity of the first and the second light pulse (two side paired t-test: $p = 0.73$, $n = 6$).

of the second light pulse was not different (**Figures 3F,G**, $n = 5$, $p = 0.46$), we conclude that light sensitivity was similar and the submaximal blocking effect was not compromised by LWO refractoriness at this pulse interval.

LWO Illumination Has Much Higher Temporal Precision Than Agonist Perfusion

To illustrate the temporal precision of LWO and the advantage over agonist perfusion, we compared the LWO effect with pharmacological stimulation of the G_i pathway (**Figure 4A**) by illumination (LWO, 625 nm) and perfusion of EBs with the acetylcholine-receptor agonist carbachol (CCh, 100 μM). Both stimulations led to similar blocking effectivity (**Figure 4B**, LWO 78.6 ± 8.5%, $n = 7$, CCh 72.6 ± 13.2%, $n = 7$), however, activation kinetics (delay to maximum block, **Figure 4C**: LWO 0.8 ± 0.1 s, $n = 7$: CCh 33.4 ± 7.8s, $n = 7$) and deactivation kinetics (time from end of stimulation to 50% recovery, **Figure 4D**, LWO 0.8 ± 0.3 s, $n = 7$; CCh 99.6

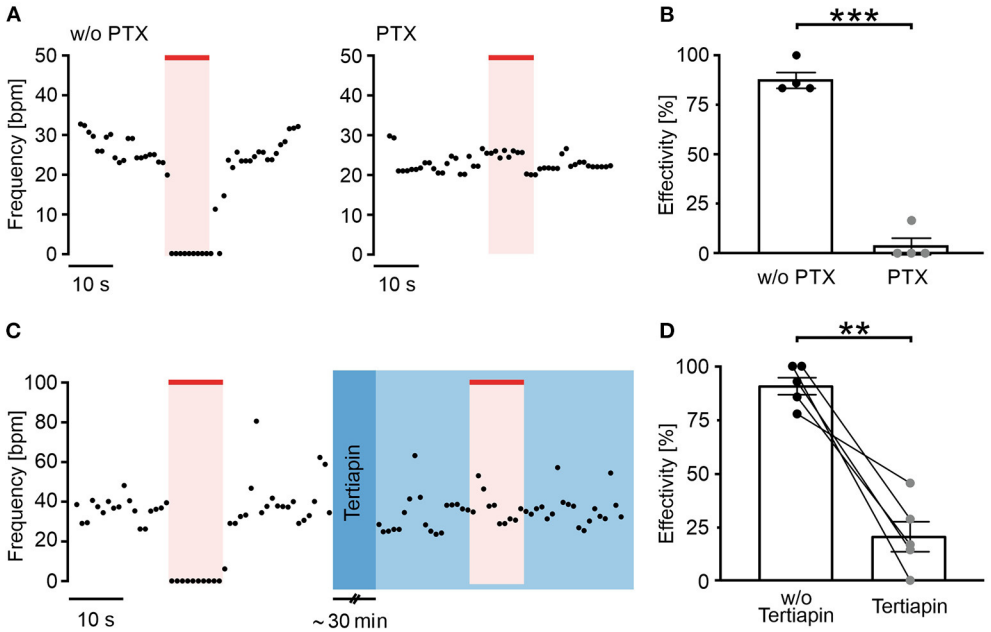

FIGURE 2 | Long wavelength-sensitive cone opsin acts through G_i proteins and GIRK channels. **(A)** Representative frequency traces of LWO-EBs without (w/o, left) and with pertussis toxin (PTX) (0.5 μg/ml, 24 h, right) treatment with illumination (625 nm, 100 μW/mm^2, red line). **(B)** Aggregated data of frequency reduction effectivity with and without PTX (unpaired *t*-test: ***$p < 0.001$, $n = 4$). **(C)** Representative frequency trace of an LWO-EB before (left) and after treatment with tertiapin (30 min incubation, right, blue) with illumination (625 nm, 100 μW/mm^2, red line). **(D)** Statistical analysis of frequency reduction effectivity with or without tertiapin treatment (two side paired *t*-test: **$p = 0.003$, $n = 5$).

± 21.9 s, $n = 7$) was significant and up to two orders of magnitude faster using LWO illumination compared with CCh perfusion.

DISCUSSION

Optogenetic methods have many advantages over pharmacological stimulation, because they allow modulation of G-protein signaling of specific cell types with high temporal and spatial precision using light instead of receptor ligands. The aim of this study was to explore the use of LWO for optogenetic activation of G_i-signaling in cardiomyocytes. For this purpose, we used stem-cell derived cardiomyocytes which resemble an early embryonic phenotype and show spontaneous beating in cell culture. Importantly, in these cells, the pacemaking mechanism is already well-controlled by G-protein signaling (Boheler et al., 2002; Touhara et al., 2016), such as G_q, G_s, and G_i proteins (Layden et al., 2010; Beiert et al., 2014; Makowka et al., 2019).

Rationale for Using LWO to Control G_i Signaling

To modulate G_i signaling in cardiomyocytes by light, we have chosen the LWO, which has been shown to activate $G_{i/o}$ proteins in HeLa cells (Karunarathne et al., 2013) as well as cultured neurons and the brain of mice (Masseck et al., 2014). Importantly, LWO is well-suited for the repetitive and long-lasting activation of G_i-dependent GIRK currents by light in HEK293 cells and neurons without desensitization (Masseck et al., 2014). This is of great advantage over vertebrate Rhodopsin, which also activates G_i signaling but the responses decline during repetitive stimulation (Masseck et al., 2014). We have chosen LWO over short-wavelength opsin (activated by 350–450 nm) because LWO can be activated by red light >600 nm, which is not absorbed by myoglobin and hemoglobin, penetrates deeper into cardiac tissue (Bruegmann et al., 2016), and has less phototoxic effects. Furthermore, red light >600 nm is spectrally compatible with blue light-activated optogenetic tools, such as Channelrhodopsin-2 for optical depolarization of cardiomyocytes (Bruegmann et al., 2010) or Jellyfish Opsin for light-induced stimulation of the G_s signaling cascade (Makowka et al., 2019) which are both not activated by red light and therefore can be combined with LWO co-expression.

LWO Is G_i Specific in Cardiomyocytes and Activates GIRK Channels

It is known that GPCR can show a promiscuous behavior and thereby activate multiple, even counteracting signaling pathways. For instance, Melanopsin, a photoreceptor of intrinsically photosensitive retinal ganglion cells, has been initially described as a G_q coupled optogenetic GPCR (Qiu et al., 2005) but it was shown later that it can signal both to G_q and G_i proteins (Bailes and Lucas, 2013) and can thus activate GIRK channels by G_i βγ subunits (Spoida et al., 2016). Our model of spontaneous beating ES-cell derived cardiomyocytes is ideal to discriminate between G_q and G_i signaling as the former will increase beating rate through PLC/IP_3/Ca^{2+}

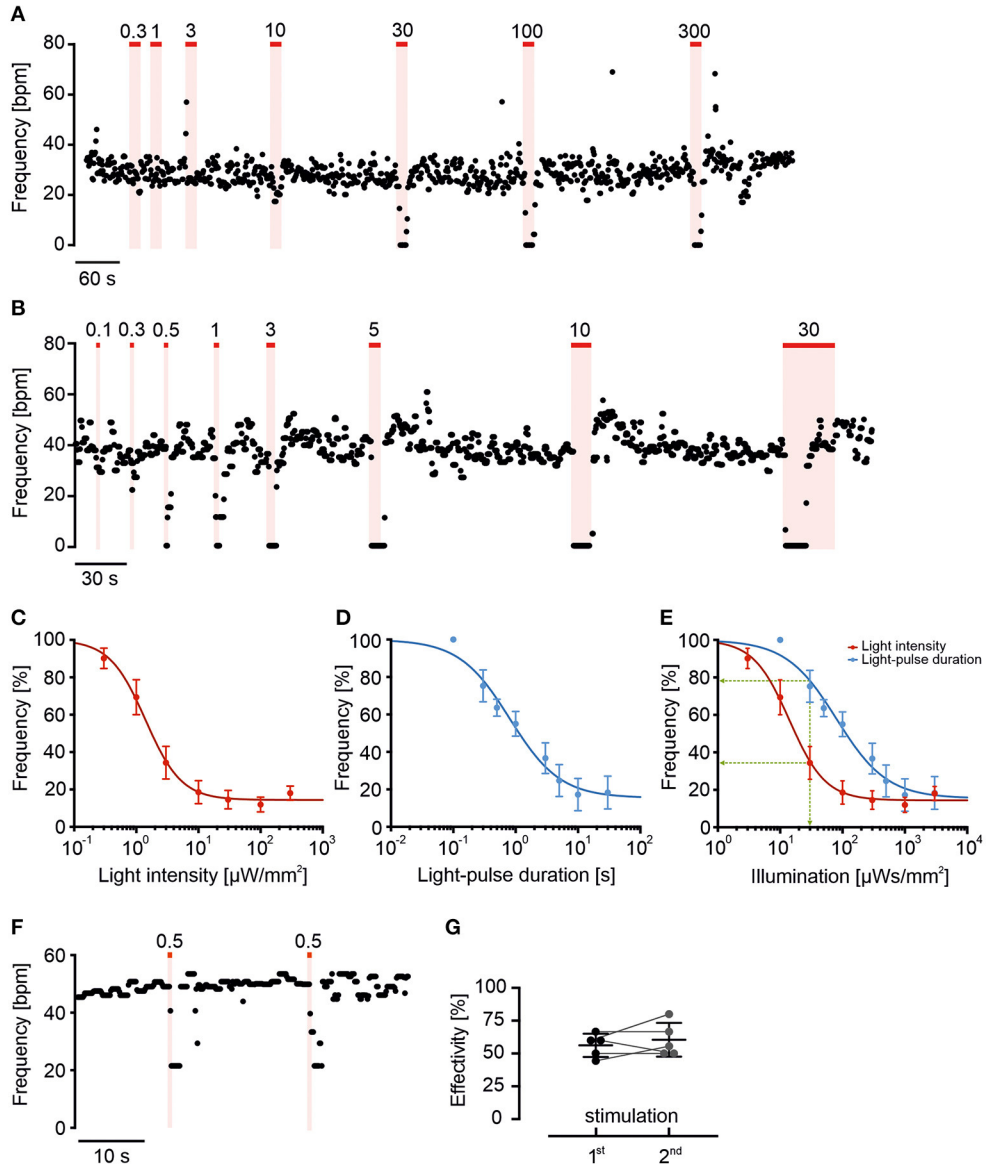

FIGURE 3 | Long wavelength-sensitive cone opsin response can be fine-tuned by light intensity and duration. **(A,B)** Representative frequency traces of LWO-EBs with light stimulation (625 nm, red line) with increasing light intensities (**A**, 10 s light, indicated values in $\mu W/mm^2$) or different durations [**(B)**, 100 $\mu W/mm^2$, indicated pulse duration in s]. **(C,D)** Relationship between change in normalized beating frequency and light intensity [**(C)**, $n = 9$] or light pulse duration [**(D)**, $n = 6$] on a logarithmic scale fitted with Hill equation. **(E)** Relationship between change in beating frequency and total light energy calculated as $s^*\mu W/mm^2$ from data in **(C)** (red) and **(D)** (blue). Note that the effect of 30 $s^*\mu W/mm^2$ light energy (green line) is stronger using 10 s at 3 $\mu W/mm^2$ (red) compared with 0.3 s at 100 $\mu W/mm^2$ (blue). **(F)** Representative frequency trace and **(G)** statistical analysis of two submaximal (0.5 s, 100 $\mu W/mm^2$) repetitive light stimuli (two side paired *t*-test: $p = 0.46$, $n = 5$).

release mechanisms enhancing the Ca^{2+} clock pacemaking machinery (Lakatta and DiFrancesco, 2009; Beiert et al., 2014), whereas the latter will reduce beating through G_i proteins (Lyashkov et al., 2009). As we have exclusively observed frequency reduction or even complete block of beating by LWO activation (**Figure 1D**), LWO signals through G_i proteins in cardiomyocytes. To confirm this, we blocked G_i proteins with PTX that completely abolished all light effects. Notably, we never observed a slightest frequency increase by light in PTX treated LWO EBs (**Figure 2B**), therefore, excluding G_q activation by LWO.

Activated G_i proteins can reduce beating rate by two mechanisms: block of adenylate cyclases by G_i α subunits with subsequent lowering of PKA-dependent phosphorylation or activation of GIRK potassium channels by G_i βγ subunits (Lyashkov et al., 2009). In our experiments, application of the specific GIRK channel inhibitor tertiapin did not affect basal beating rate but reduced the effect of LWO illumination by

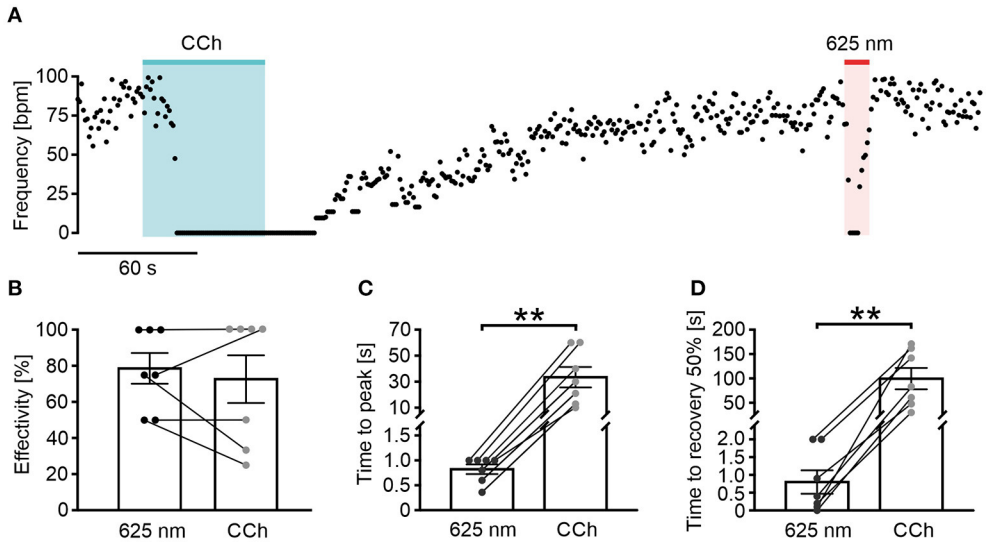

FIGURE 4 | Long wavelength-sensitive cone opsin has higher temporal precision than pharmacological G_i stimulation. **(A)** Representative frequency trace of an LWO-EB upon perfusion with carbachol (CCh, 100 μM, 60 s, blue bar) and light stimulation (625 nm, 10 s, 100 μW/mm^2, red line). **(B–D)** Statistical comparison between CCh and light application for frequency reduction effectivity [**(B)**, paired *t*-test: $p = 0.49$, $n = 7$], time to maximal frequency reduction [**(C)**, paired *t*-test: $^{**}p = 0.006$, $n = 7$], and time to 50% of beating frequency recovery [**(D)**, paired *t*-test: $^{**}p = 0.0039$, $n = 7$].

∼75% suggesting that the major G_i effect in ES-cell derived cardiomyocytes obtained by our differentiation protocol is through G_i βγ GIRK channel activation. In contrast, GIRK-based reduction of heart rate in mouse sinus nodal cells is only responsible for ∼50% of heart rate regulation (Mesirca et al., 2013) presumably reflecting the more robust pacemaking machinery in these cells or differences in GIRK expression. The remaining ∼25% of regulation we observed is most likely due to G_i α-dependent reduction of basal adenylate cyclase and PKA activity, which has been shown to reduce HCN/I_f currents (Abi-Gerges et al., 2000) and L-type-Ca^{2+} currents (Ji et al., 1999) in ES-cell derived cardiomyocytes.

LWO Overexpression Has No Negative Side-Effects

Overexpression of artificial light sensitive proteins might have negative side effects on the intracellular signaling machinery because of dark activity, G-protein binding, alteration of microdomain signaling, or other overexpression artifacts. In our experience, the spontaneous beating rate is a very sensitive parameter for such side effects. Similar to the expression of Melanopsin for optogenetic G_q stimulation (Beiert et al., 2014) and Jellyfish Opsin for optogenetic G_s stimulation (Makowka et al., 2019), we did not observe effects on basal beating rate by LWO expression. Since we did not analyze protein expression levels or performed RNA sequencing analysis in this work, we cannot fully exclude minor side effects. However, it must be admitted that the ES-cell system itself cannot exclude side effects for future *in vivo* applications and thus generation of *in vivo* models of LWO overexpression in the heart will be an important next step.

Fast Kinetics and Light Sensitivity of LWO

Parasympathetic stimulation of the intact heart can be very fast which has been shown for both electrical stimulation of the vagal nerve with ∼1.5 s delay (Ng et al., 2001) and optogenetic stimulation of parasympathetic neurons (Moreno et al., 2019) with an immediate reduction of heart rate. In contrast, diffusion-limited pharmacological activation of M2-cholinergic receptors with CCh in the three-dimensional cardiac body *in vitro* resulted in slow activation (∼30 s) and deactivation (∼100 s). In this *in vitro* setting stimulation of LWO led to 30–100 times faster effects with delays of only 0.8 s from the start of illumination to maximal effect or from end of illumination to 50% of recovery, which is similar to the *in vivo* kinetics. Thereby LWO allows the application of brief continuous light pulses with gradually increasing stimulation intensities; such a stimulation protocol would be almost impossible with slow agonist perfusion and wash out, especially in multicellular preparation, such as EB or in intact organs.

We found that gradual stimulation allows fine tuning the response of G_i-stimulation on pacemaking activity by either changing pulse duration or light intensity with a sigmoidal dependence on the logarithm of light energy (duration * intensity in s*μW/mm^2). Interestingly, the half-maximal light energy was slightly higher using variations of intensity (24 s*μW/mm^2) than pulse duration (120 s*μW/mm^2). Specifically, for a fixed total light energy at mid-sensitivity (e.g., 30 s*μW/mm^2 green line in **Figure 3E**), longer light pulses (10 s at 3 μW/mm^2, light intensity protocol) are more effective than shorter light pulses (0.3 s at 100 μW/mm^2, pulse duration protocol) indicating that temporal integration of G_i signaling is affecting the threshold blocking effect.

Compared with previous reported LWO sensitivity for GIRK activation in HEK293 cells (4 s*μW/mm^2, Eli50 at 590 nm: 0.2 s, 20 μW/mm^2, Masseck et al., 2014), we observed lower LWO sensitivity (14–80 s*μW/mm^2 at 625 nm), which could be due to difference in the wavelength used.

The calculation of total light energy allows comparison with other optogenetic GPCR, we have employed to modulate pacemaking of ES-cell derived cardiomyocytes. Using Melanopsin to accelerate pacemaking by G_q/PLC/IP_3 signaling, we determined a half maximal energy of 2.4 s*μW/mm^2 (Eli50 of 40 nW/mm^2 at 60 s pulses, Beiert et al., 2014) and using Jellyfish Opsin to stimulate G_s/cAMP/PKA signaling, we determined a half maximal energy of only 0.16 s*μW/mm^2 (Eli50 of 8 nW/mm^2 at 20 s pulses Makowka et al., 2019). Thus, LWO is less light sensitive than Melanopsin and Jellyfish Opsin, which is also advantageous in experimental handling at normal lab room light. In addition, LWO kinetics on frequency reduction (time to peak and 50% deactivation ∼0.8 s) was much faster than kinetics of frequency increase by Melanopsin or Jellyfish Opsin in EBs (activation ∼10–50 s) which underscores the involvement or fast GIRK channels in G_i signaling.

Outlook

In the future, the combination of LWO with the spectrally compatible JellyOP in transgenic mice (Makowka et al., 2019) will allow spatially confined simultaneous or alternating activation of G_i and G_s signaling in cardiomyocytes in the heart *in vivo*. This will be a valid approach to study the impact of balanced, dysbalanced, and wrong timing of parasympathetic and sympathetic input which seems to be important for the development of pathologies, such as atrial fibrillation (Ang et al., 2012). The high temporal precision of light enables to study short-term (seconds) and mid-term (minutes and hours) effects and, using implantable light emitting devices, also long-term (days and weeks) chronic G_i and G_s signaling. Furthermore, selective illumination of left and right ventricle, or of epicardial and endocardial cardiomyocytes will allow to determine regional differences of vegetative nerve input on cardiac function, arrhythmia generation of development of cardiac hypertrophy. Finally, optogenetics has the advantage of cell type-specific expression using specific promoters. Thus, using the Cre-LoxP system, expression of LWO or JellyOpsin in the different cells of the heart (cardiomyocytes, fibroblast, endothelial cells, and smooth muscle cells) will enable investigation of their G_i- and G_s-signaling *in vivo* which cannot be performed by agonists applied to the circulation or by electrical stimulation of vegetative nerves.

CONCLUSION

Long wavelength-sensitive cone opsin enables optogenetic stimulation of G_i-signaling cascade in ES-cell derived cardiomyocytes with red light, resulting in a high effective and very fast inhibition of spontaneous pacemaking, mainly through the activation of GIRK channels. Thus, LWO itself or in combination with the G_s coupled spectrally compatible optogenetic GPCR JellyOP will allow to investigate the physiological and pathological effects of balanced and dysbalanced vegetative nerve input on the heart.

DATA AVAILABILITY STATEMENT

The raw data supporting the conclusions of this article will be made available by the authors, without undue reservation.

AUTHOR CONTRIBUTIONS

MC, DM, TB, and PS designed the research. MC performed the research. MC, DM, and PS wrote the manuscript. All authors contributed to the article and approved the submitted version.

FUNDING

This work was supported by the Deutsche Forschungsgemeinschaft (DFG, German Research Foundation)—313904155/SA 1785/7-1, 380524518/SA1785/9-1, and 214362475/GRK1873/2.

ACKNOWLEDGMENTS

We thank Frank Holst for technical assistance.

REFERENCES

Abi-Gerges, N., Ji, G. J., Lu, Z. J., Fischmeister, R., Hescheler, J., and Fleischmann, B. K. (2000). Functional expression and regulation of the hyperpolarization activated non-selective cation current in embryonic stem cell-derived cardiomyocytes. *J. Physiol.* 523, 377–389. doi: 10.1111/j.1469-7793.2000.t01-2-00377.x

Ang, R., Opel, A., and Tinker, A. (2012). The role of inhibitory g proteins and regulators of G protein signaling in the *in vivo* control of heart rate and predisposition to cardiac arrhythmias. *Front. Physiol.* 3:96. doi: 10.3389/fphys.2012.00096

Bailes, H. J., and Lucas, R. J. (2013). Human melanopsin forms a pigment maximally sensitive to blue light (λmax ≈ 479 nm) supporting activation of Gq/11 and Gi/o signalling cascades. *Proc. R. Soc. B Biol. Sci.* 280:20122987. doi: 10.1098/rspb.2012.2987

Ballister, E. R., Rodgers, J., Martial, F., and Lucas, R. J. (2018). A live cell assay of GPCR coupling allows identification of optogenetic tools for controlling Go and Gi signaling. *BMC Biol.* 16:10. doi: 10.1186/s12915-017-0475-2

Beiert, T., Bruegmann, T., and Sasse, P. (2014). Optogenetic activation of Gq signalling modulates pacemaker activity of cardiomyocytes. *Cardiovasc. Res.* 102, 507–516. doi: 10.1093/cvr/cvu046

Belardinelli, L., and Isenberg, G. (1983). Isolated atrial myocytes: adenosine and acetylcholine increase potassium conductance. *Am. J. Physiol.* 244, H734–H737. doi: 10.1152/ajpheart.1983.244.5.H734

Boheler, K. R., Czyz, J., Tweedie, D., Yang, H. T., Anisimov, S. V., and Wobus, A. M. (2002). Differentiation of pluripotent embryonic stem cells into cardiomyocytes. *Circ. Res.* 91, 189–201. doi: 10.1161/01.RES.0000027865.61704.32

Bruegmann, T., Boyle, P. M., Vogt, C. C., Karathanos, T. V., Arevalo, H. J., Fleischmann, B. K., et al. (2016). Optogenetic defibrillation terminates

ventricular arrhythmia in mouse hearts and human simulations. *J. Clin. Invest.* 126, 3894–3904. doi: 10.1172/JCI88950

Bruegmann, T., Malan, D., Hesse, M., Beiert, T., Fuegemann, C. J., Fleischmann, B. K., et al. (2010). Optogenetic control of heart muscle *in vitro* and *in vivo*. *Nat. Methods* 7, 897–900. doi: 10.1038/nmeth.1512

Capote, L. A., Mendez Perez, R., and Lymperopoulos, A. (2015). GPCR signaling and cardiac function. *Eur. J. Pharmacol.* 763, 143–148. doi: 10.1016/j.ejphar.2015.05.019

Guru, A., Post, R. J., Ho, Y.-Y., and Warden, M. R. (2015). Making sense of optogenetics. *Int. J. Neuropsychopharmacol.* 18:pyv079. doi: 10.1093/ijnp/pyv079

Huang, C. L., Slesinger, P. A., Casey, P. J., Jan, Y. N., and Jan, L. Y. (1995). Evidence that direct binding of G beta gamma to the GIRK1 G protein-gated inwardly rectifying K+ channel is important for channel activation. *Neuron* 15, 1133–1143. doi: 10.1016/0896-6273(95)90101-9

Hutchinson, S. A., and Scammells, P. J. (2004). A(1) adenosine receptor agonists: medicinal chemistry and therapeutic potential. *Curr. Pharm. Des.* 10, 2021–2039. doi: 10.2174/1381612043384204

Ivanova-Nikolova, T. T., Nikolov, E. N., Hansen, C., and Robishaw, J. D. (1998). Muscarinic K+ channel in the heart. Modal regulation by G protein beta gamma subunits. *J. Gen. Physiol.* 112, 199–210. doi: 10.1085/jgp.112.2.199

Ji, G., Fleischmann, B. K., Bloch, W., Feelisch, M., Andressen, C., Addicks, K., et al. (1999). Regulation of the L-type Ca2+ channel during cardiomyogenesis: switch from NO to adenylyl cyclase-mediated inhibition. *FASEB J.* 13, 313–324. doi: 10.1096/fasebj.13.2.313

Karunarathne, W. K. A., Giri, L., Kalyanaraman, V., and Gautam, N. (2013). Optically triggering spatiotemporally confined GPCR activity in a cell and programming neurite initiation and extension. *Proc. Natl. Acad. Sci. U. S. A.* 110, E1565–E1574. doi: 10.1073/pnas.1220697110

Krapivinsky, G., Krapivinsky, L., Wickman, K., and Clapham, D. E. (1995). G beta gamma binds directly to the G protein-gated K+ channel, IKACh. *J. Biol. Chem.* 270, 29059–29062. doi: 10.1074/jbc.270.49.29059

Lakatta, E. G., and DiFrancesco, D. (2009). What keeps us ticking: a funny current, a calcium clock, or both? *J. Mol. Cell Cardiol* 47, 157–170. doi: 10.1016/j.yjmcc.2009.03.022

Layden, B. T., Newman, M., Chen, F., Fisher, A., and Lowe, W. L. (2010). G protein coupled receptors in embryonic stem cells: a role for Gs-alpha signaling. *PLoS ONE.* 5:e9105. doi: 10.1371/journal.pone.0009105

Lyashkov, A. E., Vinogradova, T. M., Zahanich, I., Li, Y., Younes, A., Nuss, H. B., et al. (2009). Cholinergic receptor signaling modulates spontaneous firing of sinoatrial nodal cells via integrated effects on PKA-dependent Ca(2+) cycling and I(KACh). *Am. J. Physiol. Heart Circ. Physiol.* 297, H949–H959. doi: 10.1152/ajpheart.01340.2008

Makowka, P., Bruegmann, T., Dusend, V., Malan, D., Beiert, T., Hesse, M., et al. (2019). Optogenetic stimulation of Gs-signaling in the heart with high spatio-temporal precision. *Nat. Commun.* 10:1281. doi: 10.1038/s41467-019-09322-7

Maltsev, V. A., Rohwedel, J., Hescheler, J., and Wobus, A. M. (1993). Embryonic stem cells differentiate *in vitro* into cardiomyocytes representing sinusnodal, atrial and ventricular cell types. *Mech. Dev.* 44, 41–50. doi: 10.1016/0925-4773(93)90015-P

Masseck, O. A., Spoida, K., Dalkara, D., Maejima, T., Rubelowski, J. M., Wallhorn, L., et al. (2014). Vertebrate cone opsins enable sustained and highly sensitive rapid control of Gi/o signaling in anxiety circuitry. *Neuron* 81, 1263–1273. doi: 10.1016/j.neuron.2014.01.041

Mesirca, P., Marger, L., Toyoda, F., Rizzetto, R., Audoubert, M., Dubel, S., et al. (2013). The G-protein–gated K+ channel, IKACh, is required for regulation of pacemaker activity and recovery of resting heart rate after sympathetic stimulation. *J. Gen. Physiol.* 142, 113–126. doi: 10.1085/jgp.201310996

Moreno, A., Endicott, K., Skancke, M., Dwyer, M. K., Brennan, J., Efimov, I. R., et al. (2019). Sudden heart rate reduction upon optogenetic release of acetylcholine from cardiac parasympathetic neurons in perfused hearts. *Front. Physiol.* 10:16. doi: 10.3389/fphys.2019.00016

Ng, G. A., Brack, K. E., and Coote, J. H. (2001). Effects of direct sympathetic and vagus nerve stimulation on the physiology of the whole heart – a novel model of isolated langendorff perfused rabbit heart with intact dual autonomic innervation. *Exp. Physiol.* 86, 319–329. doi: 10.1113/eph8602146

Nobles, M., Montaigne, D., Sebastian, S., Birnbaumer, L., and Tinker, A. (2018). Differential effects of inhibitory G protein isoforms on G protein-gated inwardly rectifying K+ currents in adult murine atria. *Am. J. Physiol. Cell. Physiol.* 314, C616–C626. doi: 10.1152/ajpcell.00271.2016

Qiu, X., Kumbalasiri, T., Carlson, S. M., Wong, K. Y., Krishna, V., Provencio, I., et al. (2005). Induction of photosensitivity by heterologous expression of melanopsin. *Nature* 433, 745–749. doi: 10.1038/nature03345

Spoida, K., Eickelbeck, D., Karapinar, R., Eckhardt, T., Mark, M. D., Jancke, D., et al. (2016). Melanopsin variants as intrinsic optogenetic on and off switches for transient versus sustained activation of G protein pathways. *Curr. Biol.* 26, 1206–1212. doi: 10.1016/j.cub.2016.03.007

Touhara, K. K., Wang, W., and MacKinnon, R. (2016). The GIRK1 subunit potentiates G protein activation of cardiac GIRK1/4 hetero-tetramers. *ELife* 5:e15750. doi: 10.7554/eLife.15750.010

Wobus, A. M., Wallukat, G., and Hescheler, J. (1991). Pluripotent mouse embryonic stem cells are able to differentiate into cardiomyocytes expressing chronotropic responses to adrenergic and cholinergic agents and Ca2+ channel blockers. *Differentiation* 48, 173–182. doi: 10.1111/j.1432-0436.1991.tb00255.x

Xiang, Y., and Kobilka, B. K. (2003). Myocyte adrenoceptor signaling pathways. *Science* 300, 1530–1532. doi: 10.1126/science.1079206

Conflict of Interest: The authors declare that the research was conducted in the absence of any commercial or financial relationships that could be construed as a potential conflict of interest.

Publisher's Note: All claims expressed in this article are solely those of the authors and do not necessarily represent those of their affiliated organizations, or those of the publisher, the editors and the reviewers. Any product that may be evaluated in this article, or claim that may be made by its manufacturer, is not guaranteed or endorsed by the publisher.

frontiers in Physiology

REVIEW
published: 23 December 2021
doi: 10.3389/fphys.2021.748570

Seeing the Light: The Use of Zebrafish for Optogenetic Studies of the Heart

Jonathan S. Baillie[1], *Matthew R. Stoyek*[1] *and T. Alexander Quinn*[1,2]*

[1] *Department of Physiology and Biophysics, Dalhousie University, Halifax, NS, Canada,* [2] *School of Biomedical Engineering, Dalhousie University, Halifax, NS, Canada*

Optogenetics, involving the optical measurement and manipulation of cellular activity with genetically encoded light-sensitive proteins ("reporters" and "actuators"), is a powerful experimental technique for probing (patho-)physiological function. Originally developed as a tool for neuroscience, it has now been utilized in cardiac research for over a decade, providing novel insight into the electrophysiology of the healthy and diseased heart. Among the pioneering cardiac applications of optogenetic actuators were studies in zebrafish, which first demonstrated their use for precise spatiotemporal control of cardiac activity. Zebrafish were also adopted early as an experimental model for the use of optogenetic reporters, including genetically encoded voltage- and calcium-sensitive indicators. Beyond optogenetic studies, zebrafish are becoming an increasingly important tool for cardiac research, as they combine many of the advantages of integrative and reduced experimental models. The zebrafish has striking genetic and functional cardiac similarities to that of mammals, its genome is fully sequenced and can be modified using standard techniques, it has been used to recapitulate a variety of cardiac diseases, and it allows for high-throughput investigations. For optogenetic studies, zebrafish provide additional advantages, as the whole zebrafish heart can be visualized and interrogated *in vivo* in the transparent, externally developing embryo, and the relatively small adult heart allows for *in situ* cell-specific observation and control not possible in mammals. With the advent of increasingly sophisticated fluorescence imaging approaches and methods for spatially-resolved light stimulation in the heart, the zebrafish represents an experimental model with unrealized potential for cardiac optogenetic studies. In this review we summarize the use of zebrafish for optogenetic investigations in the heart, highlighting their specific advantages and limitations, and their potential for future cardiac research.

Keywords: cardiac electrophysiology, opsins, membrane potential, intracellular calcium, genetically encoded voltage indicators (GEVIs), genetically encoded calcium indicators (GECIs)

OPEN ACCESS

Edited by:
Stephan E. Lehnart, University Medical Center Göttingen, Germany

Reviewed by:
Alexandra Zahradnikova, Slovak Academy of Sciences, Slovakia
Claudia Richter, Deutsches Primatenzentrum, Germany

***Correspondence:**
T. Alexander Quinn
alex.quinn@dal.ca

Specialty section:
This article was submitted to Cardiac Electrophysiology, a section of the journal Frontiers in Physiology

Received: *28 July 2021*
Accepted: *19 October 2021*
Published: *23 December 2021*

Citation:
Baillie JS, Stoyek MR and Quinn TA (2021) Seeing the Light: The Use of Zebrafish for Optogenetic Studies of the Heart. Front. Physiol. 12:748570. doi: 10.3389/fphys.2021.748570

OPTOGENETICS IN CARDIAC RESEARCH

Optogenetics involves the measurement and manipulation of cellular activity using genetically encoded light-sensitive proteins (Deisseroth et al., 2006; Miesenböck, 2009). Originally developed as a set of tools for neuroscience to activate or silence neuronal circuits and observe neuronal activity (Li et al., 2005; Nagel et al., 2005), optogenetic "reporters" (for measurement of membrane potential (Siegel and Isacoff, 1997; Sakai et al., 2001; Ataka and Pieribone, 2002) or intracellular

TABLE 1 | Advantages and limitations of the zebrafish for cardiac optogenetic studies.

Advantages	Limitations
-Relatively low cost (time, effort, money) -Fully sequenced genome -Relatively easy genetic manipulation -Large number of available transgenic lines -Majority of cardiac genes have human ortholog -Externally developing, transparent embryo -Amenable to high throughput studies -Comparable heart rate, action potential morphologies, ion channels, and calcium-handling proteins to human -Intra- and extracardiac regulatory pathways and mechanisms similar to human -Human cardiac diseases can be recapitulated	-Genome duplication (24% of genes have more than one ortholog) -Small, two-chambered heart -Relatively low-pressure system -Lack transverse tubules -Limited release of calcium from sarcoplasmic reticulum following excitation -Low sensitivity of ryanodine receptors to calcium -Dependence of calcium transient on sarcolemmal influx

calcium [Ca^{2+}] (Miyawaki et al., 1997, 1999; Baird et al., 1999)) and 'actuators' [for modulation of membrane potential (Nagel et al., 2002, 2003; Boyden et al., 2005)] have now been utilized in cardiac research for over a decade (Entcheva and Kay, 2021). Cardiac optogenetics has had a wide-range of applications, including: (i) all-optical studies of cardiac electrophysiology and high-throughput drug screening; (ii) cell-specific measurement or control to investigate cardiac sub-populations (e.g., myocytes, Purkinje cells, fibroblasts, neurons, and immune cells); (iii) manipulation of cardiac ion channels, G protein- coupled receptor signaling, and energetics; (iv) control of action potential morphology or excitation waves; and (v) cardiac pacing, cardioversion/defibrillation, or arrhythmia termination/ablation. Some of the pioneering studies that applied optogenetics to the heart were performed in zebrafish (*Danio rerio*). Here we provide an overview of the use of zebrafish for cardiac optogenetic studies, highlighting their advantages, limitations, and future potential [for a more general consideration of cardiac optogenetics, please see the recent review by Entcheva and Kay (Entcheva and Kay, 2021)].

USE OF ZEBRAFISH FOR OPTOGENETIC STUDIES OF THE HEART

The zebrafish has become an important integrative animal model for cardiac research, based on its particular advantages as an experimental tool (**Table 1**) (Gut et al., 2017; Stoyek and Quinn, 2018). The zebrafish offers a fully sequenced genome, which can be easily altered using standard genetic techniques at relatively low cost (in terms of time, effort, and money) (Rafferty and Quinn, 2018; Stoyek et al., in press), and almost every cardiac gene has a human ortholog with analogous function (Howe et al., 2013). This high degree of genetic similarity has permitted researchers to recapitulate a variety of human cardiac diseases in the zebrafish (Bowley et al., in press), which can be studied in a high throughput manner (Kithcart and MacRae, 2018). Functionally, the zebrafish heart has comparable heart rate, action potential morphologies, ion channels (Ravens, 2018), and Ca^{2+}-handling proteins (van Opbergen et al., 2018b) to human. Furthermore, it has been shown that cardiac regulatory pathways and mechanisms of both intracardiac (MacDonald et al., 2017) and extracardiac (Stoyek et al., 2016) origin are similar to human, and like the cardiac electrophysiology of the zebrafish (Nemtsas et al., 2010), are often more so than rodents.

Of course, as with any experimental model, there are also limitations to the zebrafish's use (**Table 1**). The zebrafish heart is small, has only two chambers (one atrium and one ventricle, rather than the four chambers found in human), and generates relatively low pressures (Hu et al., 2001). While over 70% of human genes have at least one zebrafish ortholog, 24% of genes have more than one ortholog (due to a duplication of the zebrafish genome), which can confer redundancy in gene function and confound results of genetic manipulations (Howe et al., 2013). Functionally, while cardiac electrophysiology appears strikingly similar to humans (Vornanen and Hassinen, 2016; Ravens, 2018), there are important differences in cellular calcium cycling (Genge et al., 2016; van Opbergen et al., 2018b). Zebrafish cardiomyocytes have a lack of transverse tubules (Brette et al., 2008), and even though sarcoplasmic reticulum Ca^{2+} levels are much higher in the zebrafish, release of Ca^{2+} from the sarcoplasmic reticulum following excitation (Ca^{2+}-induced Ca^{2+} release) appears to be limited (due in part to a low sensitivity of ryanodine receptors to Ca^{2+}) (Bovo et al., 2013). As a result, sarcolemmal Ca^{2+} influx is responsible for ∼80% of the Ca^{2+} transient in zebrafish cardiomyocytes (compared to 25% in human) (Bovo et al., 2013), although this remains somewhat controversial, as others have shown a strong dependence of contractile force on sarcoplasmic reticulum Ca^{2+} release (Haustein et al., 2015) and the existence of Ca^{2+} sparks with characteristics similar to mammals (Llach et al., 2011). Zebrafish also have a higher sodium-Ca^{2+} exchanger current than in mammals, such that its reverse-mode has been shown to trigger sarcoplasmic reticulum Ca^{2+} release (Zhang et al., 2011).

Considering its use specifically for cardiac optogenetic studies, the zebrafish has a further advantage over other animal models, in that the entire zebrafish heart can be optically accessed *in vivo* in the transparent, externally developing embryo (van Opbergen et al., 2018a) or *in situ* in the relatively small, isolated adult heart (Stoyek et al., 2018), in a manner not possible in mammals. While other non-mammalian models may have a similar advantage (e.g., *Drosophila melanogaster* [Wolf et al., 2006) and *Xenopus laevis* (Warkman and Krieg, 2007)], they are limited in other ways. For instance, while *Drosophila* have been highly utilized for studies of cardiac genetics (Wolf et al., 2006), it is an invertebrate, and differences in the morphology of its heart—which is a tube—limits its applicability for functional studies (Rotstein and Paululat, 2016). The heart of *Xenopus*, on the other hand, is in some ways more anatomically similar to humans than zebrafish—for instance, it has a pulmonary circulation—but there is a limited genetic tool box for their transgenesis (Ishibashi et al., 2008).

Ultimately, the similarities of zebrafish to human, and its particular experimental advantages, have resulted in it being a popular experimental model for optogenetic investigations, both for neuroscience [the brain and nervous system can also be optically accessed in the whole animal (Del Bene and Wyart, 2012; Simmich et al., 2012; Portugues et al., 2013)] and for cardiovascular research (**Table 2**), which is the focus of this review.

STUDIES UTILIZING OPTOGENETIC REPORTERS IN THE ZEBRAFISH HEART

The electrical activity of the heart has been optically monitored for decades, well before the emergence of modern optogenetics and the use of functional fluorescent proteins. In the 1970s, Salama and Morad published the first reports of the use of voltage sensitive fluorescent dyes to record cardiac action potentials (Salama and Morad, 1976; Morad and Salama, 1979). Since that time, optical mapping of membrane potential and intracellular Ca^{2+} in the whole heart or isolated tissue and cells has become a "standard" technique in many research labs (Herron et al., 2012; Jaimes et al., 2016; Berenfeld and Efimov, 2019), including studies using zebrafish (Sabeh et al., 2012; Lin et al., 2020). The use of optogenetic reporters (genetically encoded voltage and Ca^{2+} indicators, GEVIs and GECIs, respectively) have additional advantages as they allow for organ-, organelle-, and cell-specific measurements and for *in vitro* and *in vivo* longitudinal studies. There is now a wide array of GEVIs and GECIs available for use in the heart, with a range of excitation and emission spectra, light sensitivity and signal intensity, temporal dynamics, and other properties that dictate their specific use (**Figure 1**) (Kaestner et al., 2014, 2015; Koopman et al., 2017).

Genetically Encoded Ca^{2+} Indicators (GECIs)

The first use of an optogenetic reporter in the heart was described in the early 2000s. This involved GCaMP2, which includes a circularly permutated EGFP within an M13/Calmodulin fusion protein that fluoresces when it binds Ca^{2+}, to record Ca^{2+} waves in the isolated mouse heart and in open chest animals (Tallini et al., 2006). This was followed by a study that used GCaMP2 to demonstrate successful engraftment and electrical coupling of embryonic cardiomyocytes with surrounding myocardium in the infarcted mouse heart (Roell et al., 2007). Around the same time, the potential for using zebrafish to image intracellular Ca^{2+} in the *intact animal* was also being realized. The first published report involved the use of a transgenic zebrafish line with cardiac-specific expression of gGCaMP driven by the cardiac myosin light chain 2 (*cmlc2*) gene promoter (*Tg(cmlc2:gCaMP)*^{s878}). It was used to investigate a transgenic zebrafish model of inherited long QT syndrome in which a loss of rapid delayed-rectifier potassium current (I_{Kr}) due to a mutation in the *s290* allele of the *kcnh2* gene (*kcnh2*^{s290}) results in mechanical ventricular asystole (Arnaout et al., 2007). Using selective plane illumination microscopy (SPIM) and excitation-contraction uncoupling with a silent heart cardiac troponin (*tnnt2*) morpholino (to eliminate optical mapping motion artifact associated with contraction), Ca^{2+} transients were measured *in vivo* at various regions of the zebrafish atrium and ventricle in 2 days post-fertilization (dpf) embryos. In wild-type *tnnt2* morpholino-injected zebrafish, repetitive fluorescent waves representing an increase in cytosolic Ca^{2+} during systole were visualized, spreading from the atrium through the atrioventricular junction and into the ventricle (**Figure 2A**). In contrast, in the *kcnh2*^{s290} homozygous mutants, Ca^{2+} waves were visible in the atrium but not in the ventricle (**Figure 2A**), implying impaired ventricular Ca^{2+} cycling.

The above investigation was followed by a study using the same zebrafish line to map Ca^{2+} waves across the whole heart in intact embryos at various ages to investigate the development of the vertebrate cardiac conduction system (**Figure 2B**) (Chi et al., 2008). Four distinct stages of conduction development were identified, which corresponded to specific cellular and anatomical changes in the developing heart and were dependent on epigenetic mechanical factors such as hemodynamic flow and contraction. An *in vivo* optical mapping technique was then used as a phenotypic assay to perform a forward genetic screen, which identified 17 conduction-specific mutations (**Figure 2B**), thought to represent novel genetic regulators of the cardiac conduction system. A similar approach has been applied to other genes whose mutation is known to affect cardiac conduction, such as the Popeye domain containing (*Popdc*) gene family, with morpholino knock down of *popdc2* in 5–6 dpf embryos causing sinoatrial node conduction failure, irregular atrial and ventricular activity, and varying degrees of atrioventricular block (Kirchmaier et al., 2012).

More recently, zebrafish have been used to help in the assessment of novel GECIs for cardiac-specific applications, such as those with a ratiometric readout, which is useful for assessing absolute changes in Ca^{2+} and to help correct for the motion artifact that occurs with optical mapping in the beating heart. Four available ratiometric Förster resonance energy transfer (FRET)-based GECIs with varying Ca^{2+}-binding affinity (TN-XXL, Twitch-1, Twitch-2B, and Twitch-4) were transiently expressed in the hearts of zebrafish embryos (driven by the *cmlc2* promoter) and kinetic parameters of atrial and ventricular Ca^{2+} transients were measured at 3 dpf under various conditions. Ultimately, this revealed that Twitch-1 and Twitch-4 are the most promising for use in the heart, based on their greater sensitivity, faster kinetics, and higher affinity for Ca^{2+} (**Figure 3**) (Salgado-Almario et al., 2020).

Genetically Encoded Voltage Indicators (GEVIs)

The development of effective GEVIs has been slower than GECIs, owing to difficulties in achieving sufficiently fast kinetics and avoiding electrophysiological interference. Recently, significant progress has been made, which includes their application for cardiac research. The first reported use of GEVIs in the heart was in fact in zebrafish (Tsutsui et al., 2010), which utilized a FRET-based voltage-sensitive fluorescent protein (VSFP) called Mermaid (Tsutsui et al., 2008). The

TABLE 2 | Previous applications of cardiac optogenetics using zebrafish.

	Publication	Age of study	Optogenetic line	Application/finding
Optogenetic Reporters	Arnaout et al., 2007	2 dpf	*Tg(cmlc2:gCaMP)*^{s878}	Investigated mutant model of inherited long QT syndrome, in which loss of rapid delayed-rectifier potassium current (I_{Kr}) due to *kcnh2* mutation results in mechanical ventricular asystole. Showed lack of calcium (Ca^{2+}) waves in the ventricle, suggesting impaired Ca^{2+} cycling.
	Chi et al., 2008	1–21 dpf	*Tg(cmlc2:gCaMP)*^{s878}	Investigated development of the vertebrate cardiac conduction system and performed a forward genetic screen. Identified four stages of conduction development, which depended on epigenetic mechanical factors, and identified 17 conduction-specific mutations that may represent novel genetic regulators of the cardiac conduction system.
	Tsutsui et al., 2010	2–3 dpf	*Tg(cmlc2:Mermaid)*	Investigated the effect of the histamine H1 receptor blocker astemizole on cardiac excitation. Showed that astemizole caused retrograde propagation from the atrioventricular boundary to the atrium.
	Kirchmaier et al., 2012	5–6 dpf	*Tg(cmlc2:gCaMP)*^{s878}	Investigated effect of Popeye domain containing gene 2 knock-down. Caused sinoatrial node conduction failure, irregular atrial and ventricular activity, and varying degrees of atrioventricular block.
	Hou et al., 2014	1.5–4 dpf	*Tg(cmlc2:Arch(D95N)-GCaMP5G)* ["*CaViar*"]	Investigated the effects of L-type Ca^{2+} ($I_{Ca,L}$) or fast sodium current block. Showed that <4 dpf, cardiac excitation is initiated by Ca^{2+}, but by 4 dpf ventricular excitation it is initiated by sodium, while atrial excitation remains Ca^{2+} dependent.
	van Opbergen et al., 2018a	3, 14 dpf	*Tg(myl7:chimeric VSFP-butterfly CY)* *Tg(myl7:Gal4FF; UAS:GCaMP6f)*	Investigated effects of pharmacological modulation of the sympathetic nervous system or ion channels on cardiac electrophysiology and Ca^{2+} cycling. Showed that: (i) sympathetic stimulation or block increased or decreased diastolic Ca^{2+} and Ca^{2+} transient amplitudes; (ii) I_{Kr} block increased action potential duration; (iii) $I_{Ca,L}$ block prevented Ca^{2+} transients, increased ventricular action potential duration, and disrupted atrioventricular conduction; and (iv) differences exist in atrial and ventricular Ca^{2+} cycling during development.
	Salgado-Almario et al., 2020	3 dpf	*Tg(cmlc2:Twitch-1)* *Tg(cmlc2:Twitch-2B)* *Tg(cmlc2:Twitch-4)* *Tg(cmlc2:TN-XXL)*	Tested various novel genetically encoded ratiometric calcium indicators to determine which are the most promising for use in the heart.
Optogenetic Actuators	Arrenberg et al., 2010	1–5 dpf	*Tg(E1b:Gal4-VP16*^{s1101t}*; UAS:NpHR-mCherry*^{s1989t}*)* *Tg(E1b:Gal4*^{s1101t}*; UAS:ChR2(H134R)-eYFP*^{s1990t}*)*	Mapped cardiac pacemaker development. Showed that: (i) at 1 dpf, the pacemaker is at the venous pole; (ii) at 2 dpf, it is more confined to the sinoatrial ring; and (iii) by 3 dpf it is more defined and confined to the dorsal right quadrant of the sinoatrial ring. Further, in 4 dpf embryos, heart rate could be control by pulsed light stimulation of the sinoatrial ring.
	Kopton et al., 2018	3 mpf	*Tg(cmlc2:GtACR1-eGFP)*	Tested whether the heart could be silenced with anion-specific light-activated ion channel. Showed that stimulation applied during the resting (diastolic) phase of the action potential causes depolarization and excitation, but causes repolarization and shortening of the action potential if applied during the (systolic) plateau.

dpf, days post-fertilization. For further details on the optogenetic zebrafish lines, including the meaning of the abbreviations, see the relevant sections of the text.

Mermaid construct consists of a green-emitting fluorescent donor (mUKG; *Umi-Kinoko* from *Sarcophyton*) and an orange-emitting fluorescent acceptor (mKOκ; *Kusabira* from *Fungia concinna)* fused to a voltage sensing phosphatase from *Ciona intestinalis* (Ci-VSP) with a transmembrane domain homologous to the S1–S4 segments of voltage-gated potassium (Kv) channels (Murata et al., 2005). The Mermaid reporter was expressed specifically in the zebrafish heart under the *cmcl2* promotor [*Tg(cmlc2:Mermaid)*] and used for *in vivo* voltage mapping in 2–3 dpf embryos under normal conditions and after application of the histamine H1 receptor blocker astemizole (known to also block I_{Kr}). Measurements showed that astemizole disrupted the normal sequence of cardiac excitation, causing retrograde propagation from the atrioventricular boundary to the atrium (**Figure 4A**) (Tsutsui et al., 2010).

Since that time, a variety of new GEVIs have been developed with improved sensitivity and kinetics. In a recent study using zebrafish (van Opbergen et al., 2018a), the novel GEVI chimeric VSFP-butterfly CY (cyan-yellow, mCitrine/mCerulean) (Mishina et al., 2014) or the updated GECI GCaMP6f (Chen et al., 2013) were expressed in the heart of pigment-deficient, optically-transparent *casper* mutant zebrafish (White et al., 2008), with the myosin light chain 7 (*myl7*) promotor [*Tg(myl7:chimeric VSFP-butterfly CY)* and *Tg(myl7:Gal4FF; UAS:GCaMP6f)*]. The hearts of 3 dpf and 14 dpf zebrafish were imaged after administration of drugs targeting the sympathetic nervous system or various cardiac ion channels to assess effects on electrical activation,

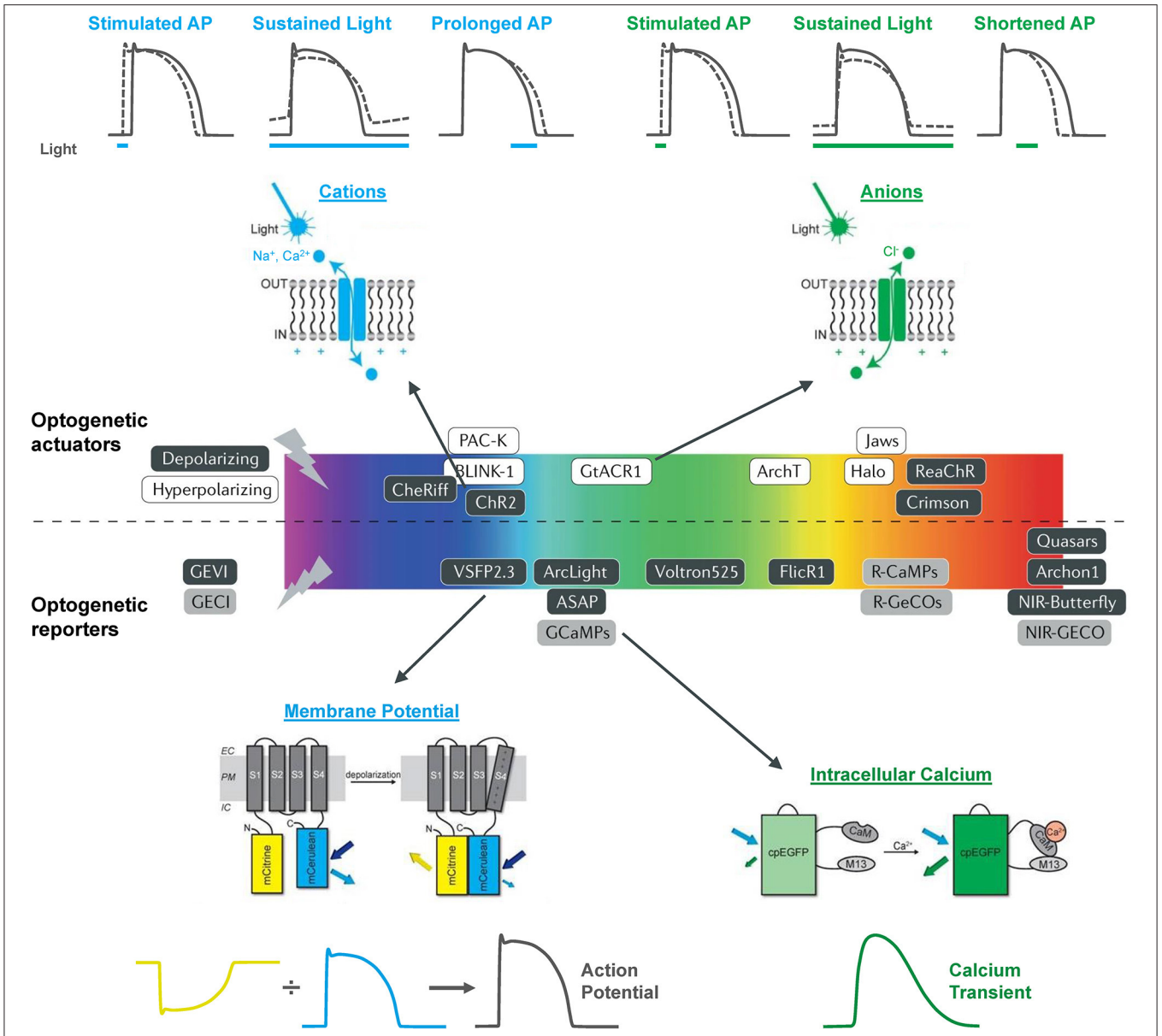

FIGURE 1 | The optogenetic toolbox for measurement and manipulation of cardiac activity. There is a large array of optogenetic actuators and reporters with a broad range of activation spectra available for use in the heart. These comprise light-activated depolarizing (excitatory) and hyperpolarizing (inhibitory) opsins that pass cations, anions, and protons and genetically encoded voltage (GEVI) and calcium (GECI) indicators that can be used to measure membrane potential and intracellular calcium. Opsin schematic from Ferenczi et al. (2019), middle panel from Entcheva and Kay (2021), and GEVI and GECI schematics from van Opbergen et al. (2018a).

action potential morphology, and intracellular Ca^{2+} dynamics (van Opbergen et al., 2018a) (**Figure 4B**). It was shown that: (i) β adrenergic receptor stimulation (with isoproterenol) or blockade (with propranolol) increased or decreased diastolic Ca^{2+} levels and Ca^{2+} transient amplitudes, respectively; (ii) I_{Kr} block (with E-4031) increased action potential duration; (iii) L-type calcium current ($I_{Ca,L}$) block (with nifedipine) prevented Ca^{2+} transients, increased ventricular action potential duration, and disrupted atrioventricular conduction; and (iv) differences exist in atrial and ventricular Ca^{2+} recovery dynamics between 3 and 14 dpf zebrafish (but not in the Ca^{2+} upstroke).

Combined Voltage-Ca^{2+} Imaging

Functional fluorescent dyes can be combined for simultaneous mapping of voltage and Ca^{2+} in the whole heart (Herron et al., 2012). There is similar interest in combining GEVIs and GECIs for dual voltage-Ca^{2+} imaging, however this is generally

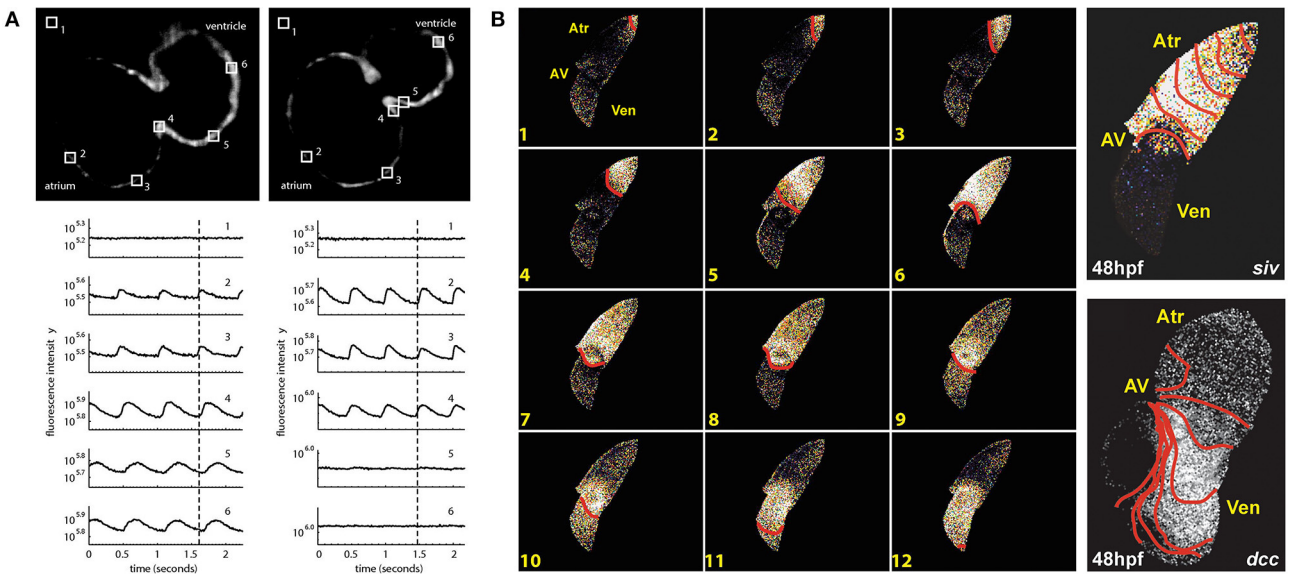

FIGURE 2 | *In vivo* imaging of intracellular calcium using genetically encoded calcium indicators (GECIs) in intact zebrafish embryos. **(A)** Hearts in 48 h post-fertilization (hpf) wild-type embryos with cardiac-specific expression of gGCaMP exhibit atrial and ventricular calcium release (left), while hearts in *kcnh2*^{s290} mutants exhibit atrial but no ventricular release (right). Each selected region in the images has a corresponding fluorescence signal plotted below. The dotted lines mark an arbitrary point in time to facilitate comparison across the different signals. From Arnaout et al. (2007). **(B)** In hearts from 48 hpf wild-type embryos, calcium activation travels from the sinus venosus across the atrium (Atr) and ventricle (Ven), with a delay at the atrioventricular (AV) junction (left), while ventricular conduction is absent in *silent ventricle* (*siv)* mutants and disorganized in *dococ*^{s215,226} (*dcc*) mutants (right). Isochronal lines represent 60 ms. From Chi et al. (2008).

prevented by spectral overlap of the relevant fluorescent proteins. The first successful study using a GEVI-GECI construct in the heart was performed in the zebrafish, using a genetically encoded dual-function voltage-Ca^{2+} reporter ("CaViar," created by fusing the GEVI Arch(D95N) with the GECI GCaMP5) under control of the heart-specific *cmlc2* promoter [*Tg(cmlc2:Arch(D95N)-GCaMP5G)*] (Hou et al., 2014). Hearts of 1.5–4.5 dpf embryos were imaged during application of the $I_{Ca,L}$ blocker nifedipine or fast sodium channel blocker quinidine, which showed that early in development the zebrafish cardiac AP is initiated by Ca^{2+}, but by 4 dpf the ventricular AP becomes driven by sodium, while the atrial AP remains Ca^{2+} dependent (**Figure 4C**).

STUDIES UTILIZING OPTOGENETIC ACTUATORS IN THE ZEBRAFISH HEART

Optogenetic actuators are light-activated proteins that generate a transmembrane ion flux. The discovery and cloning of the cation-selective ion channel channelrhodopsin-2 (ChR2) from the green alga *Chlamydomonas reinhardtii* in 2003 (Nagel et al., 2003) has led to the development of an extensive toolkit that includes depolarizing (excitatory) and hyperpolarizing (inhibitory) opsins, which are activated across a wide spectrum of wavelengths, and may be used for manipulation of cardiac membrane potential (**Figure 1**) (Schneider-Warme, 2018; Ferenczi et al., 2019; Entcheva and Kay, 2021). As for the cardiac application of GEVIs and GECIs, one of the first reports of the use of optogenetic actuators in the heart was in zebrafish (Arrenberg et al., 2010). This involved the use of both ChR2 [*Tg(E1b:Gal4*^{s1101t}*; UAS:ChR2(H134R)-eYFP*^{s1990t}*)*] and the chloride-specific ion channel halorhodopsin from *Natronomonas pharaonis* (NpHR) (Zhang et al., 2007) [*Tg(E1b:Gal4-VP16*^{s1101t}*; UAS:NpHR-mCherry*^{s1989t}*)*], to locate and control cardiac pacemaker cells in intact 1–5 dpf zebrafish embryos. In NpHR-expressing zebrafish, maps were generated at each day post-fertilization by sequentially illuminating small, overlapping regions of the heart, and measuring the heart rate response, or the incidence of cardiac arrest or arrhythmia (**Figure 5A**). It was found that: (i) at 1 dpf, the heart stopped beating when a region at the venous pole was illuminated, indicating the location of the pacemaker; (ii) at 2 dpf, the pacemaker region was more confined to the sinoatrial ring, with illumination of large adjacent areas having no effect, and atrioventricular block (of varying degree, depending on light intensity) occurred with illumination of the atrioventricular canal; and (iii) at 3 dpf, the pacemaker region was more defined, being confined to the dorsal right quadrant of the sinoatrial ring. It was further found that in 4 dpf embryos, pulsed photo-stimulation of the sinoatrial ring at a frequency of 2.7–4.7 Hz with ChR2 was able to control heart rate.

Since the time of that pioneering study, another prominent family of chloride-specific light-activated ion channels has been developed, the *Guillardia theta* anion channelrhodopsin 1 and 2 (GtACR1 and GtACR2) (Govorunova et al., 2015), which have been shown to silence neuronal AP generation (including in zebrafish) (Malyshev et al., 2017; Mauss et al.,

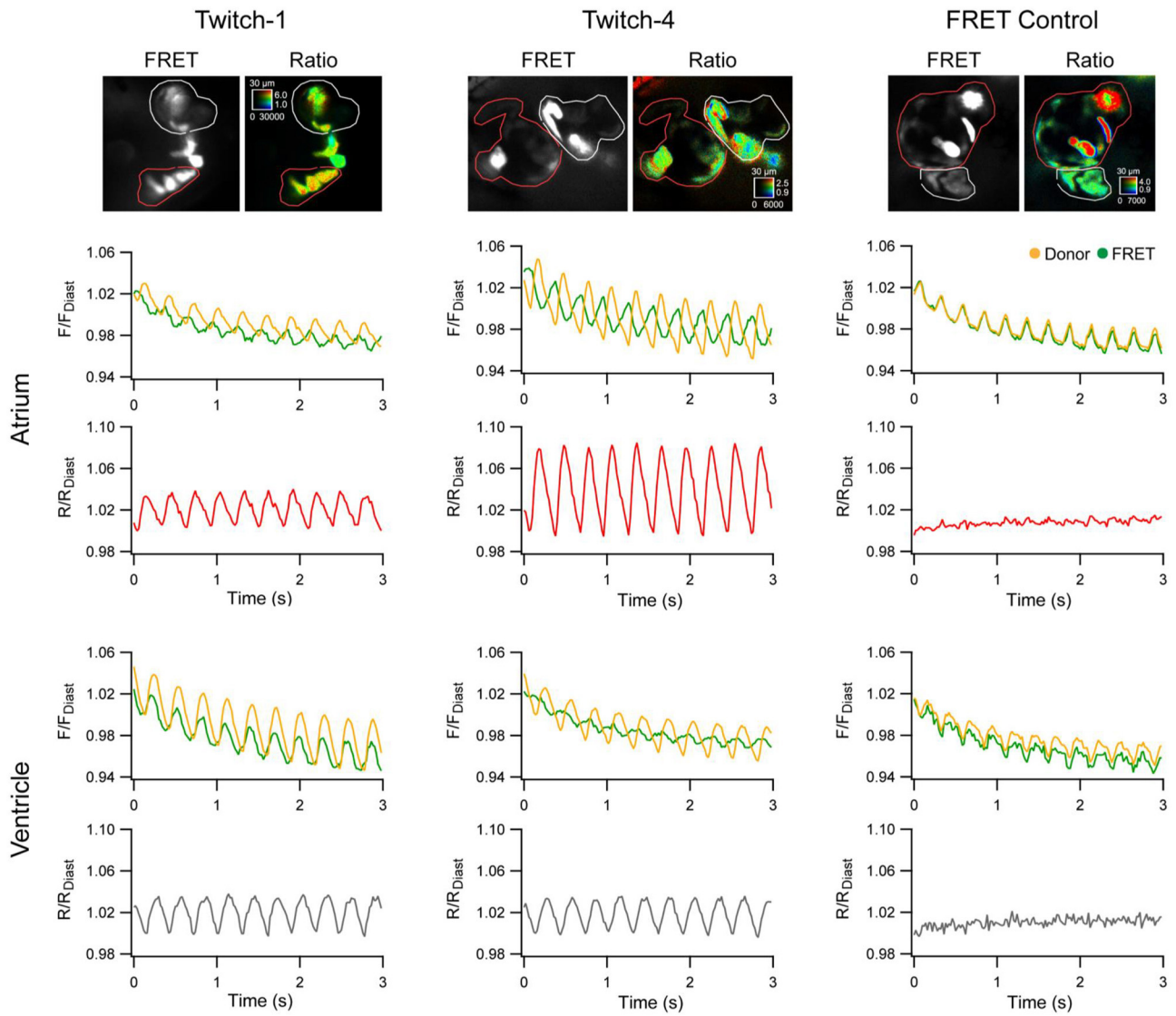

FIGURE 3 | *In vivo* ratiometric intracellular calcium measurements with a genetically encoded calcium indicator (GECI) in intact zebrafish embryos. Ratiometric intracellular calcium signals were acquired with Twitch-1, Twitch-4, or a Förster resonance energy transfer (FRET) construct insensitive to calcium (ECFP-16aa-EYFP) from the atrium (red region-of-interest) and ventricle (white region-of-interest) of 3 days post-fertilization embryos. The change in fluorescence in the donor and FRET channels normalized to the first diastolic period (F/F_{Diast}; upper graphs in atrium and ventricle) and their ratio (R/R_{Diast}; lower graphs in atrium and ventricle) are shown. From Salgado-Almario et al. (2020).

2017; Mohamed et al., 2017; Forli et al., 2018). The first cardiac application of GtACR1 involved zebrafish [using hearts isolated from 3 months post-fertilization adults with cardiac-specific GtACR1 expression, *Tg(cmlc2:GtACR1-eGFP)*], which in combination with experiments in genetically transfected single rabbit ventricular myocytes demonstrated that GtACR1 activation causes depolarization of ventricular myocytes when applied during the resting (diastolic) phase of the AP (and if suprathreshold, results in excitation), but causes repolarization when applied during the (systolic) plateau (resulting in shortening of the AP). This biphasic response relates to the reversal potential of chloride in ventricular myocytes, which is somewhere between −40 and −33 mV (Clemo et al., 1999), so that the flow of negative ions switches from outward (causing depolarization) to inward (causing repolarization) as cells are excited. As a result, pulsed illumination can be used to pace the heart, while sustained illumination can arrest the heart in a depolarized state (**Figure 5B**) (Kopton et al., 2018). This indicates that while GtACR1 does not address the need for optogenetic silencing through a physiological means (i.e., hyperpolarization), it is a potentially attractive tool for exciting cardiomyocytes by transient light-induced depolarization.

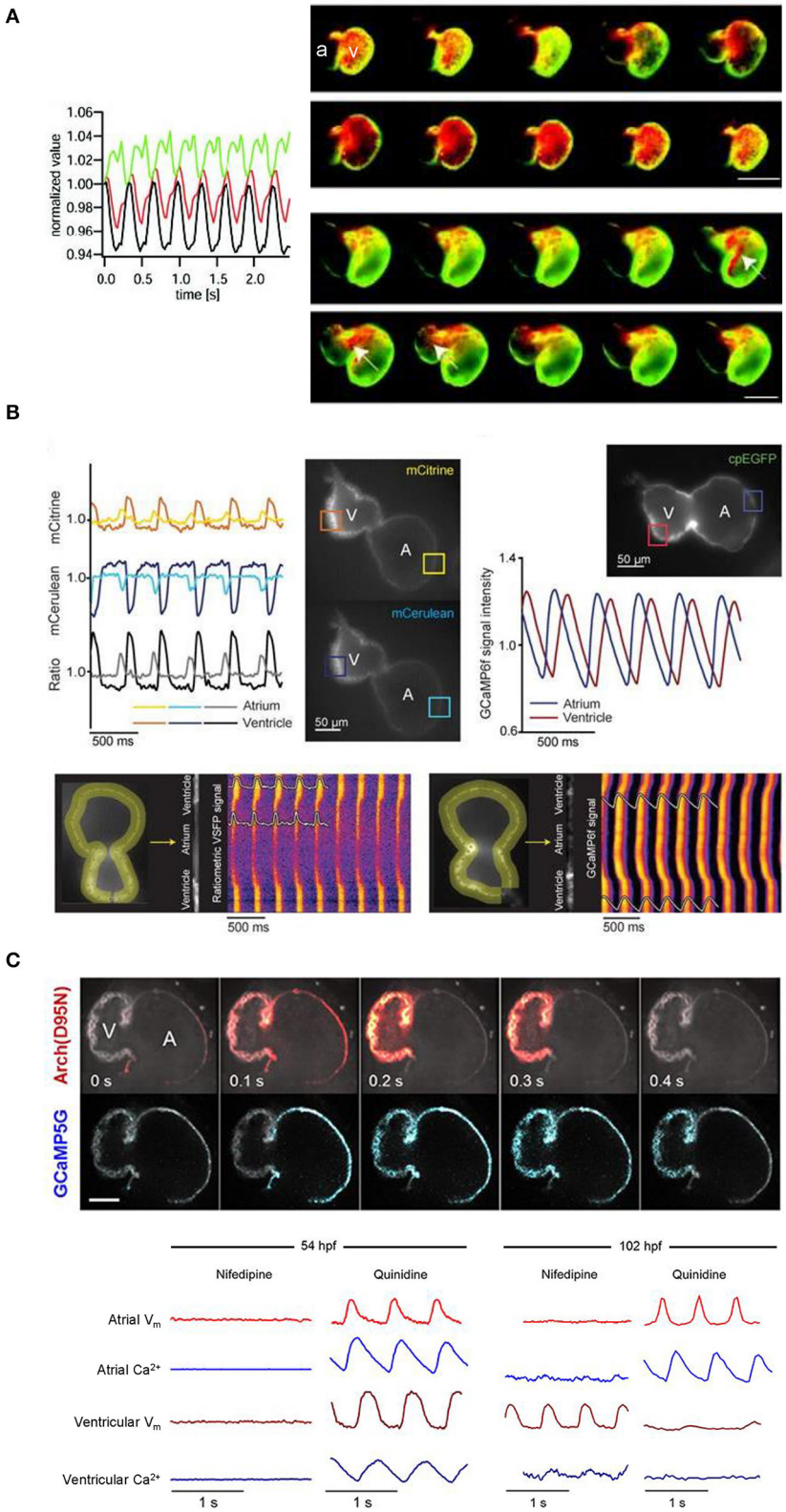

FIGURE 4 | *In vivo* imaging of membrane potential using genetically encoded voltage indicators (GEVIs), combined with genetically encoded calcium indicators (GECIs) in intact zebrafish embryos. **(A)** Signals (left) from a donor (mUKG, green) and acceptor (mKOκ, red) Förster resonance energy transfer (FRET) pair of fluorescent proteins and their ratio (mKOκ/mUKG, black) acquired from the ventricle of a 3 days post-fertilization (dpf) zebrafish embryo with cardiac-specific

(Continued)

FIGURE 4 | expression of the GEVI Mermaid. Pseudo-colored ratio images (right) representing a single cardiac cycle in wild-type, Mermaid-expressing zebrafish (upper) showing propagation of excitation from the sinus venosus in the atrium (a) to the ventricle (v), and in astemizole-treated (5 μM, 15 min) zebrafish (lower) showing retrograde propagation from the ventricle to the atrium (highlighted with arrows). Scale bar, 100 μm. From Tsutsui et al. (2010). **(B)** Signals (upper left) from a donor (mCerulean, blue) and acceptor (mCitrine, yellow) Förster resonance energy transfer (FRET) pair of fluorescent proteins and their ratio (mCitrine/mCerulean, black) acquired from the regions of interest (boxes in fluorescent images) indicated on the atrium (A) and ventricle (V) of a 3 dpf zebrafish embryo with cardiac-specific expression of GEVI VSFP-butterfly CY. Signals (upper right) acquired from the atrium (blue) and ventricle (red) of a 3 dpf zebrafish embryo with cardiac-specific expression of the GECI GCaMP6f. Line plots of chimeric VSFP-butterfly CY (lower left) and GCaMP6f (lower right) background-corrected fluorescence intensities averaged across the width of the myocardial wall superimposed on heat maps of trajectory vs. time illustrating electrical impulse and Ca^{2+} propagation throughout the heart. cpEGFP, circularly permutated enhanced green fluorescent protein. From van Opbergen et al. (2018a). **(C)** Single optical sections of a 4 dpf zebrafish heart with cardiac-specific expression of the GEVI-GECI construct CaViar showing GEVI Arch(D95N) (top) and GECI GCaMP5G (middle) fluorescence as excitation propagates from the atrium (A) to ventricle (V). Voltage (V_m, red) and calcium (Ca^{2+}, blue) signals acquired from the atrium and ventricle of 50 (upper left) and 102 (lower right) hours post-fertilization (hpf) zebrafish embryos exposed to nifedipine (L-type Ca^{2+} channel blocker) and quinidine (fast sodium channel blocker). At 52 hpf, nifedipine reversibly suppressed voltage and Ca^{2+} dynamics in both chambers, while quinidine had no effect. At 102 hpf, nifedipine largely suppressed calcium transients in both chambers but only suppressed atrial voltage, while quinidine largely suppressed voltage and calcium transients in the ventricle but did not affect either transient in the atrium. Scale bar, 50 μm. From Hou et al. (2014).

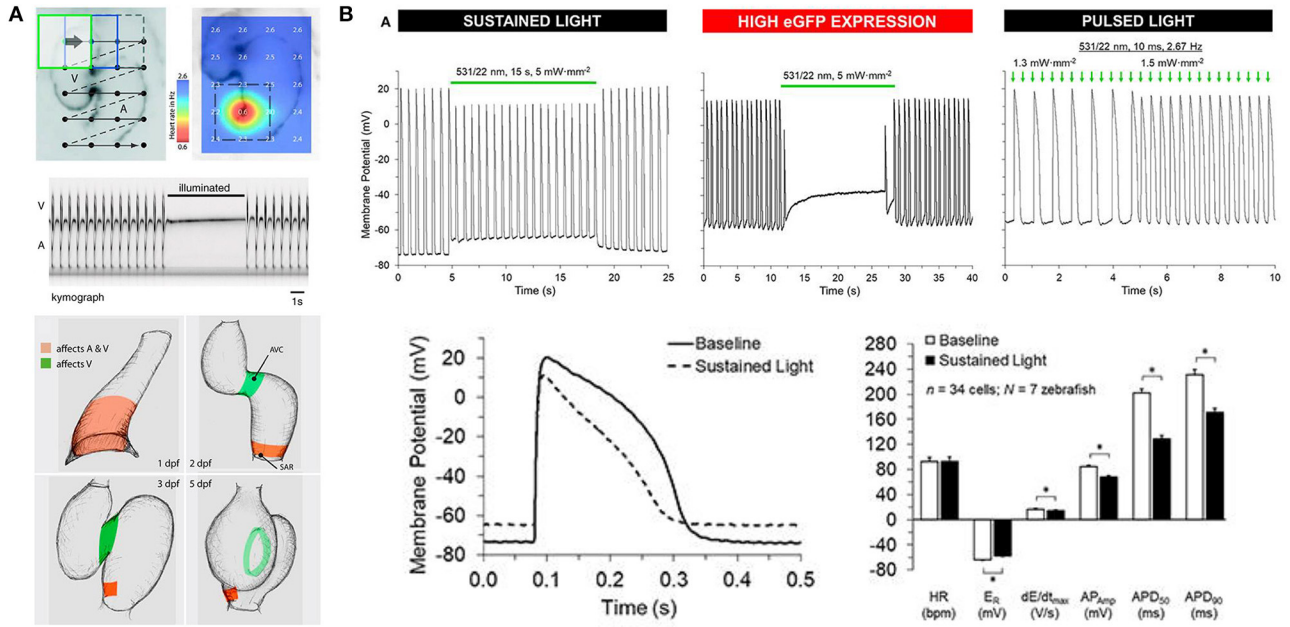

FIGURE 5 | Optogenetic manipulation of membrane potential in zebrafish hearts. **(A)** *in vivo* stimulation of halorhodopsin by patterned illumination of 3 days post-fertilization (dpf) embryonic hearts (upper left) reveals the location of the pacemaker by a reduction in heart rate (**upper right**). Illumination of the whole heart could stop atrial (A) and ventricular (V) beating (middle). Areas that control atrial and ventricular (red) or only ventricular (green) contractions were revealed throughout embryogenesis (1–5 dpf, bottom). From Arrenberg et al. (2010). **(B)** Sustained stimulation of *Guillardia theta* anion channelrhodopsins 1 (GtACR1) by spot illumination on the ventricle of 3 months post-fertilization zebrafish isolated hearts caused an immediate increase in resting membrane potential (ER) and a decrease in the maximum rate of membrane depolarization (dE/dt_{max}), AP amplitude (AP_{Amp}), and APD at 50% and 90% repolarization (APD_{50} and APD_{90}, upper left and bottom). In the case of particularly high GtACR1 expression (represented by high eGFP expression), ventricular excitation could be silenced (upper middle). Pulsed light, on the other hand, could be used to stimulate the heart (upper right). *Indicates $p < 0.0001$ by two-tailed paired Student's *t*-test. From Kopton et al. (2018).

FUTURE DIRECTIONS FOR THE USE OF CARDIAC OPTOGENETICS IN ZEBRAFISH

Unlike the prevalent use of optogenetics in zebrafish to study the nervous system (Del Bene and Wyart, 2012; Simmich et al., 2012; Portugues et al., 2013), there have been relatively few cardiac optogenetic studies performed in zebrafish (summarized in **Table 2**), yet those studies have been fundamental in progressing the application of optogenetic technologies to the heart. With the continual improvement of optogenetic techniques (Entcheva and Kay, 2021), the use of zebrafish for integrative (patho-)physiological cardiac structure-function studies holds great promise. Future research will be driven by technological advances such as high-speed, cell-accurate, three-dimensional mapping (Mickoleit et al., 2014; Weber et al., 2017; Sacconi et al., in press), more effective methods for cell-specific spatial and temporal gene expression (Reade et al., 2017; LaBelle et al., 2021), and novel optogenetic actuators and reporters with enhanced expression, fluorescence, and kinetics, combined with improved light delivery (Entcheva and Kay, 2021). As the field continues to develop, the zebrafish may be invaluable for cardiac optogenetic studies directly

related to its strengths as an experimental model (**Table 1**; i.e., development, genetic screening, drug discovery, cardiotoxicity testing, disease modeling, all-optical studies of electrophysiology and cell signaling, and anti-arrhythmic strategy development). It may also be a powerful tool for fundamental investigations of the hetero-cellular heart (e.g., structure-function interactions of myocytes, fibroblasts, intracardiac neurons, and immune and endothelial cells) and in helping to overcome hindrances related to the clinical translation of optogenetic techniques (e.g., genetic transfection, immune responses, phototoxicity) (Richter and Bruegmann, 2020). This will be enhanced by the large number of currently available transgenic lines, genetic material, and tools (easily found through online resources and central repositories), facilitated by the open zebrafish community willing to share them (Rafferty and Quinn, 2018; Stoyek et al., in press).

While a majority of cardiac optogenetic studies in the zebrafish have been performed in the early stages of development, technological advances in fluorescence imaging approaches and methods for spatially-resolved light stimulation have the promise to enable studies to be performed in the adult isolated whole heart and *in vivo*. This will be aided by the continuing development of transgenic lines that lack pigment and are thus largely transparent throughout their lifespan (i.e., "casper" [White et al., 2008) and "crystal" (Antinucci and Hindges, 2016)], and can be used as a background on which to express optogenetic reporters and actuators along with mutations of interest.

CONCLUSION

Optogenetics is a powerful and highly successful (Deisseroth, 2010) set of techniques that has been instrumental in recent developments in neuroscience research (Deisseroth, 2015; Kim et al., 2017), and more recently also for cardiac research (Entcheva and Kay, 2021). Zebrafish provide specific advantages as an experimental model for optogenetic cardiac investigations (Gut et al., 2017; Stoyek and Quinn, 2018), and have been instrumental in its early development, suggesting a bright future for this little fish. With the increasing sophistication of optogenetic methods, the zebrafish represents an experimental model with great potential for cardiac optogenetic studies. Hopefully more cardiac researchers will soon begin to see the light.

AUTHOR CONTRIBUTIONS

JB wrote the manuscript. MS and TQ revised the manuscript. All authors approved the final version.

FUNDING

This work was supported by the Natural Sciences and Engineering Research Council of Canada (RGPIN-2016-04879 to TQ), the Heart and Stroke Foundation of Canada (G-18-0022185 to TQ), and the Canadian Institutes of Health Research (MOP 342562 to TQ).

REFERENCES

Antinucci, P., and Hindges, R. (2016). A crystal-clear zebrafish for *in vivo* imaging. *Sci. Rep.* 6, 1–10. doi: 10.1038/srep29490

Arnaout, R., Ferrer, T., Huisken, J., Spitzer, K., Stainier, D. Y. R., Tristani-Firouzi, M., et al. (2007). Zebrafish model for human long QT syndrome. *Proc. Natl. Acad. Sci. U. S. A.* 104, 11316–11321. doi: 10.1073/pnas.0702724104

Arrenberg, A. B., Stainier, D. Y. R., Baier, H., and Huisken, J. (2010). Optogenetic control of cardiac function. *Science* 330, 971–974. doi: 10.1126/science.1195929

Ataka, K., and Pieribone, V. A. (2002). A genetically targetable fluorescent probe of channel gating with rapid kinetics. *Biophys. J.* 82, 509–516. doi: 10.1016/S0006-3495(02)75415-5

Baird, G. S., Zacharias, D. A., and Tsien, R. Y. (1999). Circular permutation and receptor insertion within green fluorescent proteins. *Proc. Natl. Acad. Sci. U. S. A.* 96, 11241–11246. doi: 10.1073/pnas.96.20.11241

Berenfeld, O., and Efimov, I. (2019). Optical mapping. *Card. Electrophysiol. Clin.* 11, 495–510. doi: 10.1016/j.ccep.2019.04.004

Bovo, E., Dvornikov, A. V., Mazurek, S. R., de Tombe, P. P., and Zima, A. V. (2013). Mechanisms of Ca^{2+} handling in zebrafish ventricular myocytes. *Pflügers Arch.* 465, 1775–1784. doi: 10.1007/s00424-013-1312-2

Bowley, G., Kugler, E., Wilkinson, R., Lawrie, A., Eeden, F., van, Chico, T. J. A., et al. (in press). Zebrafish as a tractable model of human cardiovascular disease. *Br. J. Pharmacol.* doi: 10.1111/bph.15473

Boyden, E. S., Zhang, F., Bamberg, E., Nagel, G., and Deisseroth, K. (2005). Millisecond-timescale, genetically targeted optical control of neural activity. *Nat. Neurosci.* 8, 1263–1268. doi: 10.1038/nn1525

Brette, F., Luxan, G., Cros, C., Dixey, H., Wilson, C., and Shiels, H. A. (2008). Characterization of isolated ventricular myocytes from adult zebrafish (*Danio rerio*). *Biochem. Biophys. Res. Commun.* 374, 143–146. doi: 10.1016/j.bbrc.2008.06.109

Chen, T.-W., Wardill, T. J., Sun, Y., Pulver, S. R., Renninger, S. L., Baohan, A., et al. (2013). Ultrasensitive fluorescent proteins for imaging neuronal activity. *Nature* 499, 295–300. doi: 10.1038/nature12354

Chi, N. C., Shaw, R. M., Jungblut, B., Huisken, J., Ferrer, T., Arnaout, R., et al. (2008). Genetic and physiologic dissection of the vertebrate cardiac conduction system. *PLoS Biol.* 6:e109. doi: 10.1371/journal.pbio.0060109

Clemo, H. F., Stambler, B. S., and Baumgarten, C. M. (1999). Swelling-activated chloride current is persistently activated in ventricular myocytes from dogs with tachycardia-induced congestive heart failure. *Circ. Res.* 84, 157–165. doi: 10.1161/01.RES.84.2.157

Deisseroth, K. (2010). Optogenetics. *Nat. Methods* 8, 26–29. doi: 10.1038/nmeth.f.324

Deisseroth, K. (2015). Optogenetics: 10 years of microbial opsins in neuroscience. *Nat. Neurosci.* 18, 1213–1225. doi: 10.1038/nn.4091

Deisseroth, K., Feng, G., Majewska, A. K., Miesenböck, G., Ting, A., and Schnitzer, M. J. (2006). Next-generation optical technologies for illuminating genetically targeted brain circuits. *J. Neurosci.* 26, 10380–10386. doi: 10.1523/JNEUROSCI.3863-06.2006

Del Bene, F., and Wyart, C. (2012). Optogenetics: a new enlightenment age for zebrafish neurobiology. *Dev. Neurobiol.* 72, 404–414. doi: 10.1002/dneu.20914

Entcheva, E., and Kay, M. W. (2021). Cardiac optogenetics: a decade of enlightenment. *Nat. Rev. Cardiol.* 18:349. doi: 10.1038/s41569-020-00478-0

Ferenczi, E. A., Tan, X., and Huang, C. L. H. (2019). Principles of optogenetic methods and their application to cardiac experimental systems. *Front. Physiol.* 10:1096. doi: 10.3389/fphys.2019.01096

Forli, A., Vecchia, D., Binini, N., Succol, F., Bovetti, S., Moretti, C., et al. (2018). Two-photon bidirectional control and imaging of neuronal excitability with high spatial resolution *in vivo*. *Cell Rep.* 22, 3087–3098. doi: 10.1016/j.celrep.2018.02.063

Genge, C. E., Lin, E., Lee, L., Sheng, X., Rayani, K., Gunawan, M., et al. (2016). The zebrafish heart as a model of mammalian cardiac function. *Rev. Physiol. Biochem. Pharmacol.* 171, 99–136. doi: 10.1007/112_2016_5

Govorunova, E. G., Sineshchekov, O. A., Janz, R., Liu, X., and Spudich, J. L. (2015). Natural light-gated anion channels: a family of microbial rhodopsins for advanced optogenetics. *Science* 349, 647–650. doi: 10.1126/science.aaa7484

Gut, P., Reischauer, S., Stainier, D. Y. R., and Arnaout, R. (2017). Little fish, big data: zebrafish as a model for cardiovascular and metabolic disease. *Physiol. Rev.* 97, 889–938. doi: 10.1152/physrev.00038.2016

Haustein, M., Hannes, T., Trieschmann, J., Verhaegh, R., Köster, A., Hescheler, J., et al. (2015). Excitation-contraction coupling in zebrafish ventricular myocardium is regulated by trans-sarcolemmal Ca^{2+} influx and sarcoplasmic reticulum Ca^{2+} release. *PLoS ONE* 10:e0125654. doi: 10.1371/journal.pone.0125654

Herron, T. J., Lee, P., and Jalife, J. (2012). Optical imaging of voltage and calcium in cardiac cells and tissues. *Circ. Res.* 110, 609–623. doi: 10.1161/CIRCRESAHA.111.247494

Hou, J. H., Kralj, J. M., Douglass, A. D., Engert, F., and Cohen, A. E. (2014). Simultaneous mapping of membrane voltage and calcium in zebrafish heart *in vivo* reveals chamber-specific developmental transitions in ionic currents. *Front. Physiol.* 5:344. doi: 10.3389/fphys.2014.00344

Howe, K., Clark, M. D., Torroja, C. F., Torrance, J., Berthelot, C., Muffato, M., et al. (2013). The zebrafish reference genome sequence and its relationship to the human genome. *Nature* 496, 498–503. doi: 10.1038/nature12111

Hu, N., Yost, H. J., and Clark, E. B. (2001). Cardiac morphology and blood pressure in the adult zebrafish. *Anat. Rec.* 264, 1–12. doi: 10.1002/ar.1111

Ishibashi, S., Kroll, K. L., and Amaya, E. (2008). A method for generating transgenic frog embryos. *Methods Mol. Biol.* 461, 447–466. doi: 10.1007/978-1-60327-483-8_31

Jaimes, R. III, Walton, R. D., Pasdois, P., Bernus, O., Efimov, I. R., et al. (2016). Arrhythmias, electrophysiology, and optical mapping: a technical review of optical mapping of intracellular calcium within myocardial tissue. *Am. J. Physiol. Heart Circ. Physiol.* 310, H1388–H401. doi: 10.1152/ajpheart.00665.2015

Kaestner, L., Scholz, A., Tian, Q., Ruppenthal, S., Tabellion, W., Wiesen, K., et al. (2014). Genetically encoded Ca^{2+} indicators in cardiac myocytes. *Circ. Res.* 114, 1623–1639. doi: 10.1161/CIRCRESAHA.114.303475

Kaestner, L., Tian, Q., Kaiser, E., Xian, W., Müller, A., Oberhofer, M., et al. (2015). Genetically encoded voltage indicators in circulation research. *Int. J. Mol. Sci.* 16, 21626–21642. doi: 10.3390/ijms160921626

Kim, C. K., Adhikari, A., and Deisseroth, K. (2017). Integration of optogenetics with complementary methodologies in systems neuroscience. *Nat. Rev. Neurosci.* 18, 222–235. doi: 10.1038/nrn.2017.15

Kirchmaier, B. C., Poon, K. L., Schwerte, T., Huisken, J., Winkler, C., Jungblut, B., et al. (2012). The Popeye domain containing 2 (popdc2) gene in zebrafish is required for heart and skeletal muscle development. *Dev. Biol.* 363, 438–450. doi: 10.1016/j.ydbio.2012.01.015

Kithcart, A. P., and MacRae, C. A. (2018). Zebrafish assay development for cardiovascular disease mechanism and drug discovery. *Prog. Biophys. Mol. Biol.* 138, 126–131. doi: 10.1016/j.pbiomolbio.2018.07.002

Koopman, C. D., Zimmermann, W. H., Knöpfel, T., and de Boer, T. P. (2017). Cardiac optogenetics: using light to monitor cardiac physiology. *Basic Res. Cardiol.* 112, 1–13. doi: 10.1007/s00395-017-0645-y

Kopton, R. A., Baillie, J. S., Rafferty, S. A., Moss, R., Zgierski-Johnston, C. M., Prykhozhij, S. V., et al. (2018). Cardiac electrophysiological effects of light-activated chloride channels. *Front. Physiol.* 9:1806. doi: 10.3389/fphys.2018.01806

LaBelle, J., Ramos-Martinez, A., Shen, K., Motta-Mena, L. B., Gardner, K. H., Materna, S. C., et al. (2021). TAEL 2.0: an improved optogenetic expression system for zebrafish. *Zebrafish* 20–28. doi: 10.1089/zeb.2020.1951

Li, X., Gutierrez, D. V., Hanson, M. G., Han, J., Mark, M. D., Chiel, H., et al. (2005). Fast noninvasive activation and inhibition of neural and network activity by vertebrate rhodopsin and green algae channelrhodopsin. *Proc. Natl. Acad. Sci. U. S. A.* 102, 17816–17821. doi: 10.1073/pnas.0509030102

Lin, E., Shafaattalab, S., Gill, J., Al-Zeer, B., Craig, C., Lamothe, M., et al. (2020). Physiological phenotyping of the adult zebrafish heart. *Mar. Genomics* 49:100701. doi: 10.1016/j.margen.2019.100701

Llach, A., Molina, C. E., Alvarez-Lacalle, E., Tort, L., Benítez, R., and Hove-Madsen, L. (2011). Detection, properties, and frequency of local calcium release from the sarcoplasmic reticulum in teleost cardiomyocytes. *PLoS ONE* 6:e23708. doi: 10.1371/journal.pone.0023708

MacDonald, E. A., Stoyek, M. R., Rose, R. A., and Quinn, T. A. (2017). Intrinsic regulation of sinoatrial node function and the zebrafish as a model of stretch effects on pacemaking. *Prog. Biophys. Mol. Biol.* 130, 198–211. doi: 10.1016/j.pbiomolbio.2017.07.012

Malyshev, A. Y., Roshchin, M. V., Smirnova, G. R., Dolgikh, D. A., Balaban, P. M., and Ostrovsky, M. A. (2017). Chloride conducting light activated channel GtACR2 can produce both cessation of firing and generation of action potentials in cortical neurons in response to light. *Neurosci. Lett.* 640, 76–80. doi: 10.1016/j.neulet.2017.01.026

Mauss, A. S., Busch, C., and Borst, A. (2017). Optogenetic neuronal silencing in drosophila during visual processing. *Sci. Rep.* 7, 1–12. doi: 10.1038/s41598-017-14076-7

Mickoleit, M., Schmid, B., Weber, M., Fahrbach, F. O., Hombach, S., Reischauer, S., et al. (2014). High-resolution reconstruction of the beating zebrafish heart. *Nat. Methods* 11, 919–922. doi: 10.1038/nmeth.3037

Miesenböck, G. (2009). The optogenetic catechism. *Science* 326, 395–399. doi: 10.1126/science.1174520

Mishina, Y., Mutoh, H., Song, C., and Knöpfel, T. (2014). Exploration of genetically encoded voltage indicators based on a chimeric voltage sensing domain. *Front. Mol. Neurosci.* 7:78. doi: 10.3389/fnmol.2014.00078

Miyawaki, A., Griesbeck, O., Heim, R., and Tsien, R. Y. (1999). Dynamic and quantitative Ca^{2+} measurements using improved cameleons. *Proc. Natl. Acad. Sci. U. S. A.* 96, 2135–2140. doi.org/10.1073/pnas.96.5.2135 doi: 10.1073/pnas.96.5.2135

Miyawaki, A., Llopis, J., Heim, R., Michael McCaffery, J., Adams, J. A., Ikura, M., et al. (1997). Fluorescent indicators for Ca^{2+} based on green fluorescent proteins and calmodulin. *Nature* 388, 882–887. doi: 10.1038/42264

Mohamed, G. A., Cheng, R.-K., Ho, J., Krishnan, S., Mohammad, F., Claridge-Chang, A., et al. (2017). Optical inhibition of larval zebrafish behaviour with anion channelrhodopsins. *BMC Biol.* 15:103. doi: 10.1186/s12915-017-0430-2

Morad, M., and Salama, G. (1979). Optical probes of membrane potential in heart muscle. *J. Physiol.* 292, 267–295. doi: 10.1113/jphysiol.1979.sp012850

Murata, Y., Iwasaki, H., Sasaki, M., Inaba, K., and Okamura, Y. (2005). Phosphoinositide phosphatase activity coupled to an intrinsic voltage sensor. *Nature* 435, 1239–1243. doi: 10.1038/nature03650

Nagel, G., Brauner, M., Liewald, J. F., Adeishvili, N., Bamberg, E., and Gottschalk, A. (2005). Light activation of channelrhodopsin-2 in excitable cells of *Caenorhabditis elegans* triggers rapid behavioral responses. *Curr. Biol.* 15, 2279–2284. doi: 10.1016/j.cub.2005.11.032

Nagel, G., Ollig, D., Fuhrmann, M., Kateriya, S., Musti, A. M., Bamberg, E., et al. (2002). Channelrhodopsin-1: a light-gated proton channel in green algae. *Science* 296, 2395–2398. doi: 10.1126/science.1072068

Nagel, G., Szellas, T., Huhn, W., Kateriya, S., Adeishvili, N., Berthold, P., et al. (2003). Channelrhodopsin-2, a directly light-gated cation-selective membrane channel. *Proc. Natl. Acad. Sci. U. S. A.* 100, 13940–13945. doi: 10.1073/pnas.1936192100

Nemtsas, P., Wettwer, E., Christ, T., Weidinger, G., and Ravens, U. (2010). Adult zebrafish heart as a model for human heart? An electrophysiological study. *J. Mol. Cell. Cardiol.* 48, 161–171. doi: 10.1016/j.yjmcc.2009.08.034

Portugues, R., Severi, K. E., Wyart, C., and Ahrens, M. B. (2013). Optogenetics in a transparent animal: circuit function in the larval zebrafish. *Curr. Opin. Neurobiol.* 23, 119–126. doi: 10.1016/j.conb.2012.11.001

Rafferty, S. A., and Quinn, T. A. (2018). A beginner's guide to understanding and implementing the genetic modification of zebrafish. *Prog. Biophys. Mol. Biol.* 138, 3–19. doi: 10.1016/j.pbiomolbio.2018.07.005

Ravens, U. (2018). Ionic basis of cardiac electrophysiology in zebrafish compared to human hearts. *Prog. Biophys. Mol. Biol.* 138, 38–44. doi: 10.1016/j.pbiomolbio.2018.06.008

Reade, A., Motta-Mena, L. B., Gardner, K. H., Stainier, D. Y., Weiner, O. D., and Woo, S. (2017). TAEL: a zebrafish-optimized optogenetic gene expression system with fine spatial and temporal control. *Development* 144, 345–355. doi: 10.1242/dev.139238

Richter, C., and Bruegmann, T. (2020). No light without the dark: perspectives and hindrances for translation of cardiac optogenetics. *Prog. Biophys. Mol. Biol.* 154, 39–50. doi: 10.1016/j.pbiomolbio.2019.08.013

Roell, W., Lewalter, T., Sasse, P., Tallini, Y. N., Choi, B.-R., Breitbach, M., et al. (2007). Engraftment of connexin 43-expressing cells prevents post-infarct arrhythmia. *Nature* 450, 819–824. doi: 10.1038/nature06321

Rotstein, B., and Paululat, A. (2016). On the morphology of the *Drosophila* heart. *J. Cardiovasc. Dev. Dis.* 3:15. doi: 10.3390/jcdd3020015

Sabeh, M. K., Kekhia, H., and MacRae, C. A. (2012). Optical mapping in the developing zebrafish heart. *Pediatr. Cardiol.* 33, 916–922. doi: 10.1007/s00246-012-0300-1

Sacconi, L., Silvestri, L., Rodríguez, E., Armstrong, G. A. B., Pavone, F., Shrier, A., et al. (in press). KHz-rate volumetric voltage imaging of the whole zebrafish heart. *Cell Rep*. doi: 10.2139/ssrn.3783403

Sakai, R., Repunte-Canonigo, V., Raj, C. D., and Knöpfel, T. (2001). Design and characterization of a DNA-encoded, voltage-sensitive fluorescent protein. *Eur. J. Neurosci.* 13, 2314–2318. doi: 10.1046/j.0953-816x.2001.01617.x

Salama, G., and Morad, M. (1976). Merocyanine 540 as an optical probe of transmembrane electrical activity in the heart. *Science* 191, 485–487. doi: 10.1126/science.191.4226.485

Salgado-Almario, J., Vicente, M., Vincent, P., Domingo, B., and Llopis, J. (2020). Mapping calcium dynamics in the heart of zebrafish embryos with ratiometric genetically encoded calcium indicators. *Int. J. Mol. Sci.* 21:6610. doi: 10.3390/ijms21186610

Schneider-Warme, F. (2018). The power of optogenetics. *Herzschrittmacherther. Elektrophysiol.* 29, 24–29. doi: 10.1007/s00399-017-0545-8

Siegel, M. S., and Isacoff, E. Y. (1997). A genetically encoded optical probe of membrane voltage. *Neuron* 19, 735–741. doi: 10.1016/S0896-6273(00)80955-1

Simmich, J., Staykov, E., and Scott, E. (2012). Zebrafish as an appealing model for optogenetic studies. *Prog. Brain Res.* 196, 145–162. doi: 10.1016/B978-0-444-59426-6.00008-2

Stoyek, M. R., and Quinn, T. A. (2018). One fish, two fish, red fish, blue fish*: zebrafish as a model for cardiac research. *Prog. Biophys. Mol. Biol.* 138, 1–2. doi: 10.1016/j.pbiomolbio.2018.11.003

Stoyek, M. R., Quinn, T. A., Croll, R. P., and Smith, F. M. (2016). Zebrafish heart as a model to study the integrative autonomic control of pacemaker function. *Am. J. Physiol. Heart Circ. Physiol.* 311, H676–H688. doi: 10.1152/ajpheart.00330.2016

Stoyek, M. R., Rafferty, S. A., and Quinn, T. A. (in press). "Genetically modified zebrafish as experimental model," in *Handbook of Molecular Biotechnology*, ed D. Liu (Boca Raton, FL: CRC Press).

Stoyek, M. R., Rog-Zielinska, E. A., and Quinn, T. A. (2018). Age-associated changes in electrical function of the zebrafish heart. *Prog. Biophys. Mol. Biol.* 138, 91–104. doi: 10.1016/j.pbiomolbio.2018.07.014

Tallini, Y. N., Ohkura, M., Choi, B.-R., Ji, G., Imoto, K., Doran, R., et al. (2006). Imaging cellular signals in the heart *in vivo*: cardiac expression of the high-signal Ca^{2+} indicator GCaMP2. *Proc. Natl. Acad. Sci. U. S. A.* 103, 4753–4758. doi: 10.1073/pnas.0509378103

Tsutsui, H., Higashijima, S., Miyawaki, A., and Okamura, Y. (2010). Visualizing voltage dynamics in zebrafish heart. *J. Physiol.* 588, 2017–2021. doi: 10.1113/jphysiol.2010.189126

Tsutsui, H., Karasawa, S., Okamura, Y., and Miyawaki, A. (2008). Improving membrane voltage measurements using FRET with new fluorescent proteins. *Nat. Methods* 5, 683–685. doi: 10.1038/nmeth.1235

van Opbergen, C. J. M., Koopman, C. D., Kok, B. J. M., Knöpfel, T., Renninger, S. L., Orger, M. B., et al. (2018a). Optogenetic sensors in the zebrafish heart: a novel *in vivo* electrophysiological tool to study cardiac arrhythmogenesis. *Theranostics* 8, 4750–4764. doi: 10.7150/thno.26108

van Opbergen, C. J. M., van der Voorn, S. M., Vos, M. A., de Boer, T. P., and van Veen, T. A. B. (2018b). Cardiac Ca^{2+} signalling in zebrafish: translation of findings to man. *Prog. Biophys. Mol. Biol.* 138, 45–58. doi: 10.1016/j.pbiomolbio.2018.05.002

Vornanen, M., and Hassinen, M. (2016). Zebrafish heart as a model for human cardiac electrophysiology. *Channels* 10, 101–110. doi: 10.1080/19336950.2015.1121335

Warkman, A. S., and Krieg, P. A. (2007). Xenopus as a model system for vertebrate heart development. *Semin. Cell Dev. Biol.* 18, 46–53. doi: 10.1016/j.semcdb.2006.11.010

Weber, M., Scherf, N., Meyer, A. M., Panáková, D., Kohl, P., and Huisken, J. (2017). Cell-accurate optical mapping across the entire developing heart. *Elife* 6:e28307. doi: 10.7554/eLife.28307.025

White, R. M., Sessa, A., Burke, C., Bowman, T., LeBlanc, J., Ceol, C., et al. (2008). Transparent adult zebrafish as a tool for *in vivo* transplantation analysis. *Cell Stem Cell* 2, 183–189. doi: 10.1016/j.stem.2007.11.002

Wolf, M. J., Amrein, H., Izatt, J. A., Choma, M. A., Reedy, M. C., and Rockman, H. A. (2006). *Drosophila* as a model for the identification of genes causing adult human heart disease. *Proc. Natl. Acad. Sci. U. S. A.* 103, 1394–1399. doi: 10.1073/pnas.0507359103

Zhang, F., Wang, L.-P., Brauner, M., Liewald, J. F., Kay, K., Watzke, N., et al. (2007). Multimodal fast optical interrogation of neural circuitry. *Nature* 446, 633–639. doi: 10.1038/nature05744

Zhang, P.-C., Llach, A., Sheng, X. Y., Hove-Madsen, L., and Tibbits, G. F. (2011). Calcium handling in zebrafish ventricular myocytes. *Am. J. Physiol. Regul. Integr. Comp. Physiol.* 300, 56–66. doi: 10.1152/ajpregu.00377.2010

Conflict of Interest: The authors declare that the research was conducted in the absence of any commercial or financial relationships that could be construed as a potential conflict of interest.

Publisher's Note: All claims expressed in this article are solely those of the authors and do not necessarily represent those of their affiliated organizations, or those of the publisher, the editors and the reviewers. Any product that may be evaluated in this article, or claim that may be made by its manufacturer, is not guaranteed or endorsed by the publisher.

frontiers in Physiology

ORIGINAL RESEARCH
published: 11 January 2022
doi: 10.3389/fphys.2021.750535

Patterned Illumination Techniques in Optogenetics: An Insight Into Decelerating Murine Hearts

Laura Diaz-Maue[1,2,3*†], *Janna Steinebach*[2†] *and Claudia Richter*[3,4*]

[1] Department of Research Electronics, Max-Planck-Institute for Dynamics and Self-Organization, Göttingen, Germany, [2] Biomedical Physics Research Group, Max-Planck-Institute for Dynamics and Self-Organization, Göttingen, Germany, [3] German Center for Cardiovascular Research (DZHK e., V.), Göttingen, Germany, [4] Laboratory Animal Science Unit, German Primate Center, Leibniz-Institute for Primate Research, Göttingen, Germany

OPEN ACCESS

Edited by:
Ruben Coronel,
University of Amsterdam, Netherlands

Reviewed by:
Robert Kass,
Columbia University, United States
Matthew W. Kay,
George Washington University, United States
Thomas Beiert,
Universität Bonn, Germany

***Correspondence:**
Laura Diaz-Maue
laura.diaz@ds.mpg.de
Claudia Richter
CRichter@dpz.eu

[†]These authors share first authorship

Specialty section:
This article was submitted to Cardiac Electrophysiology, a section of the journal Frontiers in Physiology

Received: 30 July 2021
Accepted: 02 December 2021
Published: 11 January 2022

Citation:
Diaz-Maue L, Steinebach J and Richter C (2022) Patterned Illumination Techniques in Optogenetics: An Insight Into Decelerating Murine Hearts. Front. Physiol. 12:750535. doi: 10.3389/fphys.2021.750535

Much has been reported about optogenetic based cardiac arrhythmia treatment and the corresponding characterization of photostimulation parameters, but still, our capacity to interact with the underlying spatiotemporal excitation patterns relies mainly on electrical and/or pharmacological approaches. However, these well-established treatments have always been an object of somehow heated discussions. Though being acutely life-saving, they often come with potential side-effects leading to a decreased functionality of the complex cardiac system. Recent optogenetic studies showed the feasibility of the usage of photostimulation as a defibrillation method with comparatively high success rates. Although, these studies mainly concentrated on the description as well as on the comparison of single photodefibrillation approaches, such as locally focused light application and global illumination, less effort was spent on the description of excitation patterns during actual photostimulation. In this study, the authors implemented a multi-site photodefibrillation technique in combination with Multi-Lead electrocardiograms (ECGs). The technical connection of real-time heart rhythm measurements and the arrhythmia counteracting light control provides a further step toward automated arrhythmia classification, which can lead to adaptive photodefibrillation methods. In order to show the power effectiveness of the new approach, transgenic murine hearts expressing channelrhodopsin-2 *ex vivo* were investigated using circumferential micro-LED and ECG arrays. Thus, combining the best of two methods by giving the possibility to illuminate either locally or globally with differing pulse parameters. The optical technique presented here addresses a number of challenges of technical cardiac optogenetics and is discussed in the context of arrhythmic development during photostimulation.

Keywords: cardiac optogenetics, channelrhodopsin-2, arrhythmia, photostimulation, feedback techniques, arrhythmia classification, deceleration

1. INTRODUCTION

Ventricular arrhythmias are not only complex in clinical practice but also pose a challenge in the exploration and optimization of new, gentler termination approaches. In particular, the bar is set high for exploratory, experimental studies in characterizing the underlying modes of function and the resulting translational approaches.

It seems that the best known clinical approach is the global termination of ventricular tachyarrhythmia by delivery of high-energy electrical shocks, either externally or internally, which have been shown to be very effective and, most importantly, fast-acting. However, especially in cases of frequently necessary or incorrect application, considerable side effects, such as electroporation and traumatic tissue damages (Moss et al., 1996; Tokano et al., 1998), make it necessary to optimize this method. In the course of this, termination protocols with more than one shock or more specific electrical pulses have come into focus. The application of multiple less energetic pulses can counteract the arrhythmia in its origin as a circularly propagating cardiac excitation (Efimov et al., 2000; Exner, 2005), as e.g., already applied as anti-tachycardia pacing (ATP) in patients (see e.g., Wathen et al., 2004). Furthermore, there are also experimental, pre-clinical multi-pulse protocols since such protocols have a significant influence on synchronization of excitation patterns (Exner, 2005), which try to reach the minimum necessary energy for a successful termination in different approaches, on the one hand with changing pacing frequency or on the other hand with changing amplitude level (Pumir et al., 2007; Luther et al., 2011; Janardhan et al., 2012).

Though, the majority of experimental studies face the hurdle that during the administration of electrical pulses, the measurement systems, such as the electrocardiogram (ECG), get "blinded," due to the artifacts caused by either the defibrillation or pacing pulses applied. To circumvent this, optical mapping is frequently used, which itself sometimes exerts strong influences on the cardiac system, e.g., through the use of chemicals such as fluorescent dyes or corresponding mechanical uncouplers (see e.g., Kolega, 2004; Swift et al., 2012; Zaglia et al., 2015). In this context, cardiac optogenetics and photostimulation exhibit great advantages. Its modus operandi is not based on electrical pulses, but on light pulses, so that there are no negative influences on the ECG to be expected. When using transgenic animal models, the genetic expression distribution of the optogenetic sensors/channels is homogeneous or locally specified. In addition, the application of non-electrical pulses is also less susceptible to short-term side effects such as electroporation. Lastly, since the light pulses can be delivered in a locally specific manner, cardiac regional success differences in termination can be further investigated with globally acting protocols.

In this study, the authors intend to show that cardiac optogenetics is a valid experimental tool for the investigation of arrhythmia behavior during pacing, which can provide information about the termination probability of the arrhythmia. To characterize and visualize this, a new multi-ECG setup was developed, making possible to observe different multi-pulse protocols with respect to their termination success and effects on the arrhythmia. Finally, the possibility of such a system for heart-specific arrhythmia termination will be discussed.

2. MATERIALS AND METHODS

Experiments involving lab animals were performed in accordance with the current version of the German animal welfare law and reported to our animal welfare representatives. Application for approval has been approved by the responsible animal welfare authority (Lower Saxony State Office for Consumer Protection and Food Safety). Moreover, humane welfare-oriented procedures were carried out in accordance with the Guide for the Care and Use of Laboratory Animals and were performed after recommendations of the Federation of Laboratory Animal Science Associations (FELASA).

2.1. Langendorff Perfusion

This study was accomplished using a constitutive transgenic mouse model, α-MHC-ChR2, at the age of 17 weeks and older, whereby ChR2 expression was proven by biomolecular protocols and restricted exclusively to cardiac tissue. In the experiment, a retrograde *ex vivo* perfusion after Langendorff was used. For this method, as described elsewhere (Richter et al., 2016), the murine heart was explanted, afterwards cannulated *via* the aorta and perfused with Tyrode's solution (130 mM NaCl, 4 mM KCl, 1 mM $MgCl_2$, 24 mM $NaHCO_3$, 1.8 mM $CaCl_2$, 1.2 mM $KH2PO_4$, 5.6 mM glucose, and 1% albumin/BSA; aerated with carbogen (5% CO_2 and 95% O_2)). A constant flow rate of (2.63 ± 0.58) ml/min was applied, whereby normal heart rate varied from 4 to 6 Hz and arrhythmic frequencies were observed between 15 and 30 Hz.

For experimental induction of arrhythmic patterns, normal perfusion was switched to low-K^+ Tyrode's solution (130 mM NaCl, 2 mM KCl, 1 mM $MgCl_2$, 24 mM $NaHCO_3$, 1.8 mM $CaCl_2$, 1.2 mM KH_2PO_4, 5.6 mM glucose, and 1 % albumin/BSA were aerated with carbogen (95 % oxygen and 5 % CO_2)) with 100 µM Pinacidil as described by Bruegmann et al. (2016). In contrast to other publications, Richter et al. (2016), Quiñonez Uribe et al. (2018), and Sasse et al. (2019) the initiation of arrhythmia in this work was induced with rapid optical pacing as also shown in Diaz-Maue et al. (2021). Sustained arrhythmias were achieved when remaining for $t_{term} = 5$ s, control experiments which confirm this criterion are further detailed in section 3.2. Should the induced arrhythmia terminate within t_{term}, it was classified as self-terminated. In addition, if an arrhythmia failed to be terminated at the fifth photostimulation attempt, then backup was used. The backup consisted of activating all μLED arrays at the same time at the highest experimentally used light intensity resulting in global illumination.

2.2. Multi-Lead ECG and μLED Arrays

A custom-built Multi-Lead ECG device was designed to simultaneously record cardiac activity from different regions of the heart. Based on the Wilson Hypothesis by Wilson et al. (1934, 1946), a Wilson Central Terminal (WCT) was built by connecting three surface Ag/AgCl electrodes V1, V2, and V3 to a common point. The potential difference between these three

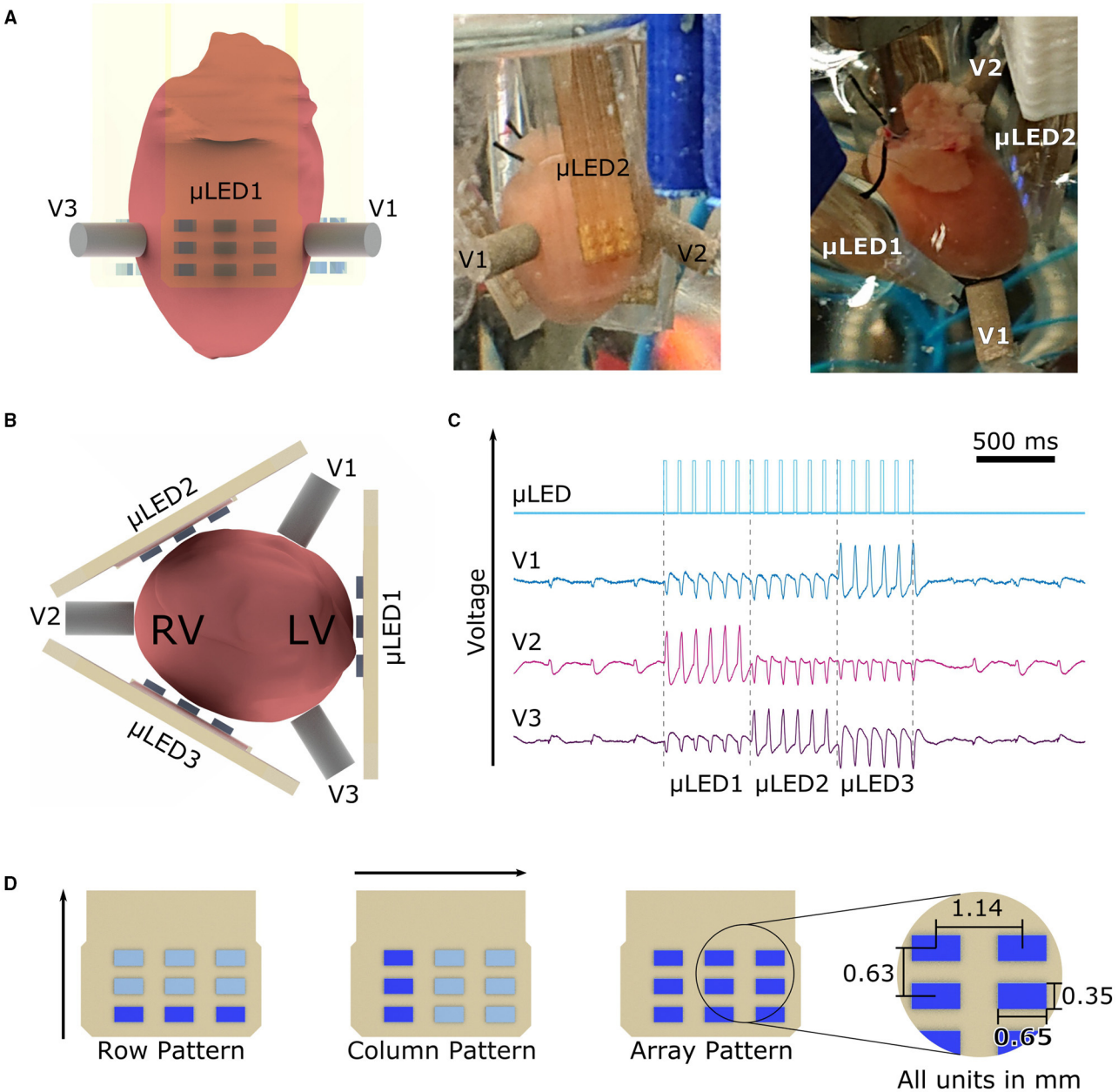

FIGURE 1 | Experimental setup with three lead ECGs, three μLED arrays, and illumination patterns used. **(A)** The murine heart was encompassed by three μLED arrays and three ECG Electrodes as shown in all panels from different angles. **(B)** μLED1 was always positioned onto the left ventricle of the heart, following μLED arrays were positioned with a 120° angle with respect to each other. In a similar way, the ECG electrodes V1, V2, and V3 are positioned in the space between μLED arrays. **(C)** ECG recording showing the photostimulation given by the μLED array and the corresponding responses measured by V1, V2, and V3 electrodes. The change of polarity, as well as the change in amplitude, demonstrate that the chosen measuring electrode registers the highest potential when the opposite μLED array is activated **(D)** Applied illumination patterns. The row pattern initiates illumination in the lower row of every array at the given frequency and pulse width, the column pattern starts with the left column and rotates around the heart with the parameters set. The array pattern activated the nine μLEDs at the same time in μLED1 then turned off after the given pulse width, similarly, μLED2 was then activated, and finally μLED3 irradiated the heart at last. The spacing of the μLED in x-direction is 1.14 mm and in y-direction is 0.63 mm.

electrodes and the WCT are referred to in this work as unipolar lead measurements. During the experiments, the three electrodes were positioned at an angle of 120° as shown in **Figures 1A,B**. The signals acquired were digitally converted and afterward analyzed.

Motivated by the work of Schwaerzle et al. (2014) and Diaz-Maue et al. (2018, 2021), a set of custom-built micro-LED (μLED) arrays were designed. Briefly, blue LEDs (XZBBR155W5MAV, SunLED, USA) with a central wavelength $\lambda_{blue} = 470$ nm were reflow soldered onto a printed circuit board

(PCB). The material used for the PCB was a prepreg laminate (104 ML, LPKF, Garbsen, Germany) with a thickness of 200 µm. The blue LEDs were arranged in a 3 × 3 array with a horizontal distance of 1.14 mm as shown in **Figure 1D**, yielding to an active illumination area of 4.76 mm^2. The conductive tracks on the PCB were isolated embedding the complete array into a layer of Polydimethylsiloxane (PDMS, Sylgard 184, Dow Corning, USA). PDMS was chosen because of its excellent biocompatibility, long-term stability, and electrical isolation properties (Hamelink, 1992). The optical characterization of the μLED arrays was performed with a PM100D optical power meter (Thorlabs, Germany) and the S120VC photodiode power sensor (Thorlabs, Germany). In this study, three μLED arrays (μLED1, μLED2, and μLED3) were positioned as well as the ECG electrodes in a 120° angle encircling the heart (cf. **Figure 1B**). The current flowing through the resulting 27 μLEDs was controlled *via* the lab computer using a custom-made μLED-Driver. Control and analysis were realized with a custom-software written in Python (Python Software Foundation, USA).

The proof-of-working of the system was achieved by conducting an experiment measuring pacing thresholds (refer to **Supplementary Figure 1**). As it can be seen in **Figure 1C**, no electrical artifacts were induced in any uni-polar lead during photostimulation. This confirms that the PDMS layer provided adequate isolation for the electrical tracks on the PCB. **Figure 1C** shows as well, that the pacing signal of every μLED array is measured in the opposite electrode, i.e., when μLED1 illuminates the heart, the electrical activity is recorded in V2. In this scenario, since all three electrodes are forming the WCT terminal (zero voltage point), the change of potential that is caused by the expanding electrical wave initiated by μLED1 is measured by V1 and V3, these two contribute to the WCT equally due to their proximity, as a consequence, the maximum change of potential is then recorded by electrode V2.

2.3. Illumination Patterns

Inspired by the theory of excitable media, three different illumination patterns, namely row, column, and array protocols, were designed to explore the most effective way of breaking or blocking the arrhythmia-generating spiral waves. The motivation for the row protocol was to drive the spiral wave(s) upward toward the atria, so that the uncoordinated electrical activity collides with non-excitable tissue, getting thereby terminated. As for the column and array protocol, it was intended to evoke a conduction block to terminate the arrhythmia by first exciting a defined area of tissue, consequently leading to a refractory period and therefore causing the spiral wave to be absorbed or blocked at the boundary. The column protocol illuminates only a small area of the heart at once, thus putting several successive segments into the non-excitable state. On the contrary, the array protocol illuminates larger areas at once thereby limiting the number of non-excitable segments to three. In this study, these three approaches were compared to determine which is more effective in terminating arrhythmia.

Accordingly, these three experimental protocols were applied in order to determine illumination patterns that optimize defibrillation success in terms of defibrillation energy and frequency of illumination. Furthermore, it was investigated whether the applied protocols were especially suitable for certain arrhythmia types or arrhythmia frequencies.

In the row protocol, the bottom three μLEDs of all three arrays were activated simultaneously, so that the illumination formed a ring around the heart. Afterwards, the two rows above followed one after the other with one pulse each. In this study, five repetitions of the mentioned sequence were used to deliver a total of $k = 15$ pulses per attempt. During the column protocol, first the very left column of μLED1 emitted one pulse. Subsequently, the middle and right column of μLED1 followed, afterwards μLED2 and μLED3 continued with the same pattern, respectively. In this case, the protocol was repeated only two times, consequently the light pulses circulated two times around the surface of the heart in a counterclockwise direction resulting in $k = 18$ pulses. The last protocol tested was the array protocol. Hereby, the entire μLED1 was activated to deliver five pulses to the heart. μLED2 and μLED3 followed, emitting five pulses each as well. In this way, the heart was circled only one time with a total number of $k = 15$ pulses. All illumination patterns are illustrated in **Figure 1D.**

In order to investigate the effect of light intensity, three different radiant fluxes, $\Phi = (1.7 \pm 0.1)$ mW, (2.4 ± 0.1) mW and (3.3 ± 0.1) mW, were chosen for all three illumination patterns. Furthermore, five different pulse frequencies $f_{stim} = 18$, 20, 22, 24, and 26 Hz were tested to assess whether the chosen stimulation frequency f_{stim} influences the success of termination. The pulse duration of each pulse was kept constant at $d_{stim} = 20$ ms since this value proved to be particularly successful in earlier experiments (Diaz-Maue et al., 2021). The energy applied for every arrhythmia termination attempt Q was calculated as the product of the number of pulses k, the radiant flux Φ, and the pulse duration d_{stim}, yielding values between $Q_{min} = (0.51 \pm 0.03)$ mJ and $Q_{max} = (1.19 \pm 0.03)$ mJ (cf. **Supplementary Figure 2**).

Finally, a positive control group was introduced with $N_m = 4$ mice. Defibrillation attempts were performed with global illumination using three high-power LEDs arranged as described in Quiñonez Uribe et al. (2018). Here, the light intensity was $LI = 1\,mW/mm^2$ which corresponds to a radiant flux of $\Phi = (58 \pm 5)$ mW. Similarly to the three proposed protocols, photostimulation was performed with $k = 15$ pulses, pulse width $d_{stim} = 20$ ms, and frequencies of $f_{stim} = 18$, 20, 22, 24, and 26 Hz. This resulted in an energy of photostimulation of $Q = (52.2 \pm 4.5)$ mJ.

2.4. Arrhythmia Classification

In cardiac tissue, ventricular tachyarrhythmia is subdivided into tachycardia (VT) and fibrillation (VF). In order to correctly assess the successes or failures of photodefibrillation attempts, it is necessary to classify the individual arrhythmia into different categories depending on their complexity.

The obtained ECG recordings were post-processed after the experimental series to classify the arrhythmia type. For this purpose, a segment of every uni-polar lead measurement was extracted 1 s before every photostimulation attempt. Three different procedures were applied to determine the complexity

of an arrhythmia. First, the evaluation of the morphology of the ECG signal according to the updated Lambeth convention (Curtis et al., 2013) was considered. Second, a sine fit was applied to the ECG recordings to identify the dominant frequency of the arrhythmia. The sine fit was implemented in the mathematical language Python by means of a curve fit that uses non-linear least squares to fit a sine function to the data. Amplitude, frequency, and phase were thereby fitted simultaneously. The sine fit represents an automated version of the periodicity analysis, as similarly performed by Skanes et al. (1998) in Langendorff perfused sheep hearts. Third, the Fast Fourier Transform (FFT) in combination with a Lorentzian fit was employed. The resulting spectrum of the FFT was used to estimate the dominant frequency of the arrhythmia as well as to investigate the variety of frequencies involved, as also described by Skanes et al. (1998). Based on the results of these methods, all arrhythmia were classified into three categories, namely monomorphic ventricular tachycardia (mVT), polymorphic ventricular tachycardia (pVT), and ventricular fibrillation (VF), with spatiotemporal complexity increasing from mVT to pVT and VF (Curtis et al., 2013).

Figure 2 shows illustrative examples of the three types of arrhythmia. The ECG representative recordings shown here were all acquired by electrode V3. Clearly, it is shown that the ECG turns into a more irregular pattern the more complex the arrhythmia becomes.

Accordingly, the sine fit for the rather regular mVT is almost in perfect agreement with the ECG signal, apart from slight variations in the amplitude (cf. **Figure 2A**). Furthermore, the increasing complexity of the arrhythmia leads to the occurrence of moderate deviations of the fit to the ECG signal in pVT (cf. **Figure 2B**) and to major deviations in VF (cf. **Figure 2C**). In order to quantify the observed deviations, the sine fit algorithm computes the normalized difference between the fitted signal and the original signal, in addition to the optimal parameters for amplitude and frequency. This value is then subtracted from 1 and the self-defined indicator "goodness of fit" (*gof*) is obtained. When *gof* is close to 1, the fit is more precise. Thereupon, the following intervals were defined, $gof > 0.6$ for mVT, $0.2 \leq gof \leq 0.6$ for pVT, and finally, $gof < 0.2$ for VF.

Moreover, an FFT was performed to evaluate the ECG signal in the frequency domain. Since the FFT returns a spectrum of frequencies that can be detected in the original signal, a Lorentzian fit was applied to quantify the relevance of the different frequencies. The values for the center of the fit and the full width half max (*fwhm*) gave information about the dominant frequency and the width of the fit indicating if there was only one dominant frequency or if several frequencies contributed substantially. Accordingly, if $1 < fwhm < 10$, the arrhythmia was classified as pVT, as mVT if $fwhm \leq 1$, and as VF if $fwhm \geq 10$.

In the case of the mVT in **Figure 2A**, the Lorentzian curves fitted to the FFT of the ECG signals of V1, V2, and V3 were very narrow and coincide for all three ECG signals. **Figure 2B** corresponds to a pVT, in this example, the Lorentzian curves were broader and slightly different for each electrode. Furthermore, components of different frequencies could be observed alongside the main peak. Notably, the Lorentzian fits varied substantially for the VF shown in **Figure 2C**. It is therefore clear that the three electrodes V1, V2, and V3 recorded ECG signals that contain distinct frequency information, which is reflected in the large width of the curves.

The described analysis was performed for all three uni-polar lead recordings. Should one of the three mentioned methods suggest different arrhythmia types, the whole arrhythmia was classified according to the most complex type.

2.5. Time-Frequency Analysis

Obtaining information about the frequency content of a signal is a usual task of the FFT (Chorro et al., 2006; Nash et al., 2006; Masse et al., 2007; Umapathy et al., 2010; Caldwell et al., 2012) or of the Short-Time Fourier Transform STFT (Tseng and Tseng, 2020; Coult et al., 2021). However, both require stationary signals (Clayton and Murray, 1993; Mansier et al., 1996; Seely and Macklem, 2004) and are therefore only suited for providing information about a signal as a whole. In the case of cardiac arrhythmia, the obtained signals contain short-term transients which cannot be completely described in the frequency domain alone and also require temporal resolution. Accordingly, to do a comprehensive evaluation of the transitory events in the ECG recordings, especially during photodefibrillation, the continuous wavelet transform (CWT) was chosen to deliver information in the combined time-frequency domain as also described by Torrence and Compo (1998), Abbate et al. (2002). The CWT signal processing was done using MATLAB (Mathworks, USA). First, all photodefibrillation attempts were localized and the recorded signal was shortened to 3 s before and 3 s after photostimulation, where the points t_o and t_f were defined, respectively, as the time for the first and last light pulse given. Afterwards, the CWT was calculated using a Morse wavelet as mother wavelet and the corresponding magnitude scalograms were plotted. Second, in order to obtain the frequencies which correspond to the largest scales present in the CWT, the maximum scale $a_{max}(t_s(i))$ for every sampling point $t_s(i)$ was computed, then all scales in the scalogram matrix a which were larger than $0.8 \cdot a_{max}(t_s(i))$ were extracted. Following this criteria, the frequencies corresponding to $a > 0.8 \cdot a_{max}$ were obtained yielding an array with several values for every $t_s(i)$. The mean value of every array was then calculated yielding to $\overline{fc}(t_s(i))$ which represents now the instantaneous frequency for every point at time t_s. Furthermore, the dominant frequencies for every time range of interest, namely, before fc_{bef}, during fc_{dur}, and after fc_{aft} photodefibrillation were calculated as the mean value of $\overline{fc}(t_s(i))$ during the required intervals, defined as *before* $t_0 - 3 \leq t_{s_{bef}} \leq t_0$, *during* $t_0 < t_{s_{dur}} \leq t_f$, and *after* $t_f < t_{s_{aft}} \leq t_f + 3$. The same method was applied for every ECG recording acquired, generating the values $fc_{bef(1-3)}$, $fc_{dur(1-3)}$, and $fc_{aft(1-3)}$.

3. RESULTS

3.1. Arrhythmia Distribution and Characteristics

Performing the arrhythmia classification as mentioned in section 2.4 for the total number of recorded arrhythmia $N_{arr} = 458$ from $N_m = 11$ mice, it was found that the majority of events, namely

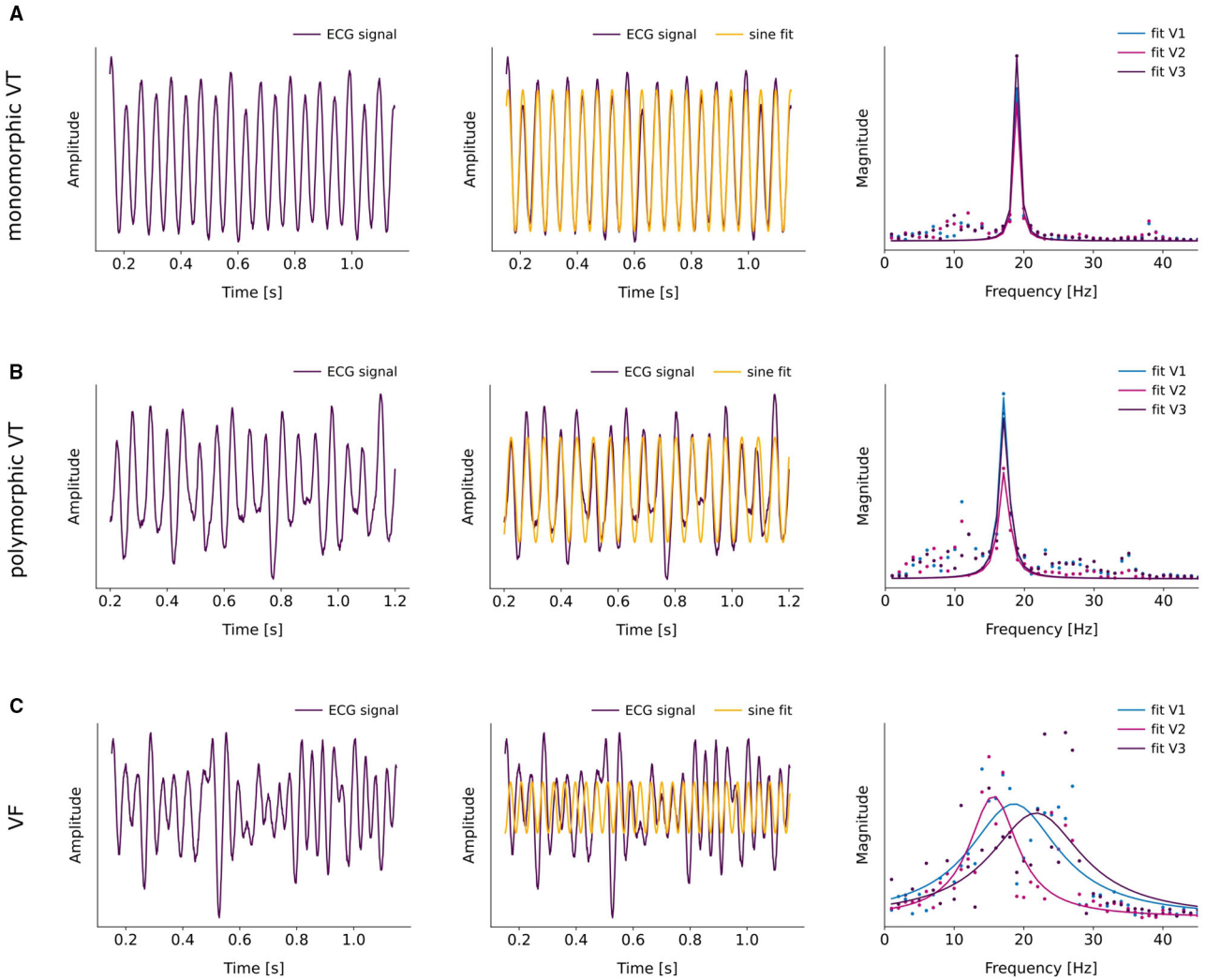

FIGURE 2 | Representative examples of the classification of the three arrhythmia types mVT **(A)**, pVT **(B)** and VF **(C)**. The left column shows the ECG recording acquired by electrode V3, the middle column displays the applied sine fit to the corresponding ECG signal and the right column illustrates the fitting of a Lorentzian function to the FFT of the ECG signal. **(A)** Example of a monomorphic VT. The sine fit results in a dominant frequency of $f_{dom} = (19.2 \pm 0.5)$ ($gof = 0.8$). The FFTs and Lorentzian fits of the three ECG signals of V1, V2 and V3 agree to a large extent. They yield the dominant frequencies $f_{dom,V1} = (19.0 \pm 0.1)$ Hz and $fwhm = (0.9 \pm 0.1)$. **(B)** Example of a polymorphic VT. According to the sine fit, the dominant frequency of the arrhythmia lies at $f_{dom} = (17.3 \pm 0.4)$ Hz with $gof = 0.6$. The Lorentzian fits to the FFT spectra result in $f_{dom} = (17.1 \pm 0.1)$ Hz for all three ECG signals with slightly varying widths $fwhm_{V1} = (1.5 \pm 0.2)$, $fwhm_{V2} = (1.8 \pm 0.3)$ and $fwhm_{V3} = (1.6 \pm 0.3)$. **(C)** Example of a VF. Sine fitting the ECG signal of V3 gives a dominant frequency of $f_{dom} = (26.4 \pm 0.3)$ Hz at $gof = 0.1$. The Lorentzian fit to the FFT of the the ECG signals of V1, V2 and V3 provides rather distinct peaks with variable widths, resulting in $f_{dom,V1} = (18.6 \pm 0.7)$ Hz, $f_{dom,V2} = (15.6 \pm 0.5)$ Hz, $f_{dom} = (21.8 \pm 1.1)$ Hz and $fwhm_{V1} = (15.7 \pm 2.2)$, $fwhm_{V2} = (8.4 \pm 1.4)$, $fwhm_{V3} = (16.2 \pm 3.2)$.

55 % were classified as pVTs. mVT and VF events made up 24% and 21%, respectively. Regarding the three illumination patterns, $\bar{N}_{arr} = 143 \pm 16$ arrhythmias were acquired per pattern.

In order to define successful termination, it was examined whether an arrhythmia terminated simultaneously with the end of illumination or whether it continued beyond the point t_f. In case of the latter, the time until the ECG signal returned to the base line was denoted as transient time. About half of all recorded arrhythmia exhibited transient times ranging between 50 and 2200 ms. Since 90 % of all arrhythmia with transients were terminated within 1300 ms after the end of illumination, it was defined that transient times which were less than or equal to 1300 ms correspond to successful termination whereas transient times larger than 1300 ms were classified as non-successful.

3.2. Termination Success

When considering the success rates of photodefibrillation regarding the three different illumination patterns without further distinguishing the parameters frequency of stimulation f_{stim} or applied radiant flux Φ, it became apparent that for mVTs,

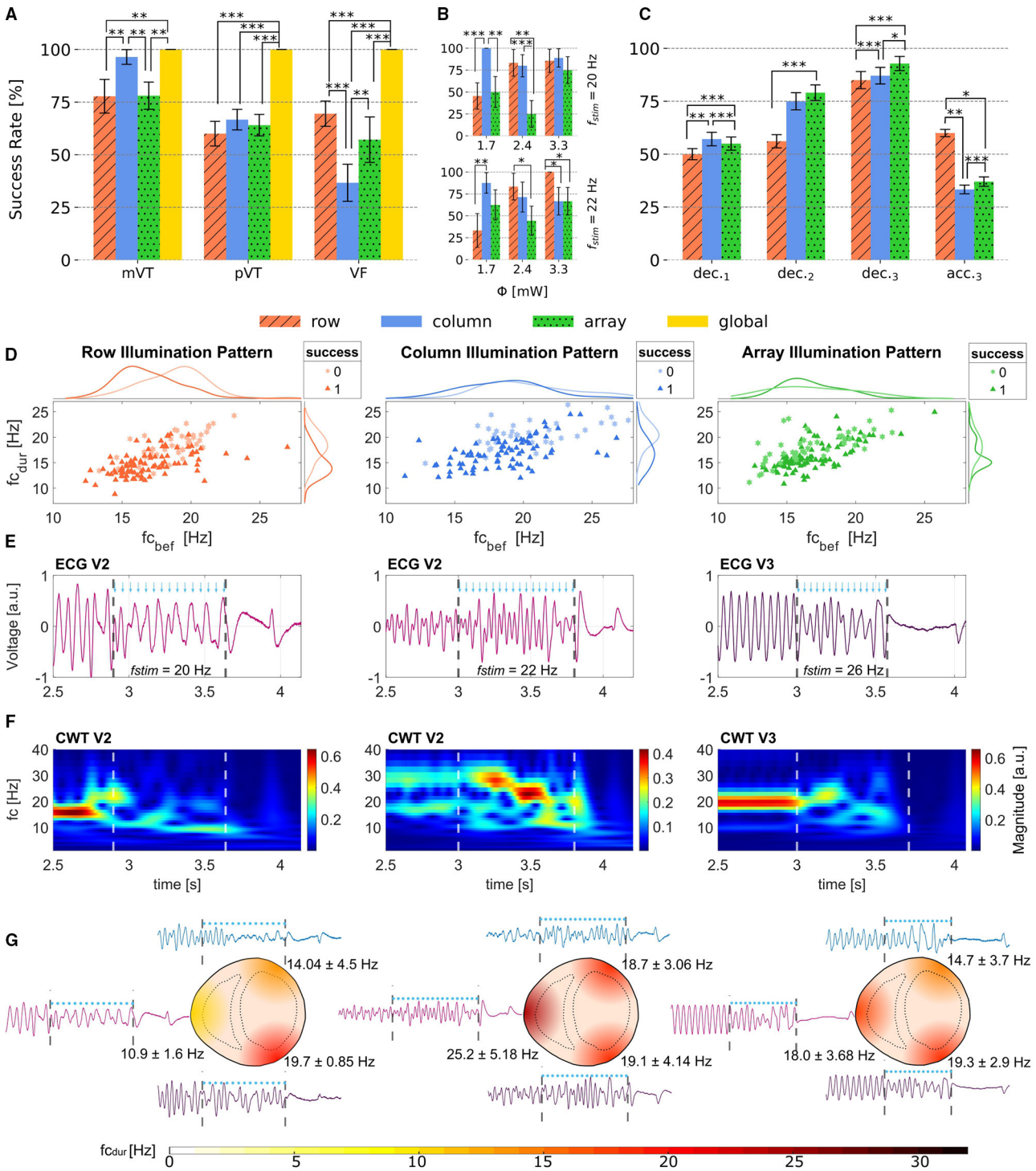

FIGURE 3 | Obtained Success Rates and effects of illumination during arrhythmia. **(A)** Success rates for mVT, pVT and VF depending on the illumination pattern. **(B)** Success rates for the photostimulation frequencies f_{stim} = 20 and 22 Hz and the three different radiant fluxes applied. While the array protocol has the lowest termination rate for this two selected f_{stim}, the row pattern terminates better with f_{stim} = 20 Hz and the lowest radiant flux applied, and the column pattern reaches a success rate of 100% when applying 3.3 mW radiant flux and f_{stim} = 22 Hz. **(C)** Termination rates shown with the deceleration observed in 1,2 and 3 Leads or acceleration measured in 3 leads. The data shown in **(A–C)** is reported with Error bars calculated with Standard Error of Mean (SEM). **(D)** Scatter plots showing the relation between fc_{bef} and fc_{dur} for row, column and array patterns. In addition the marginal histograms show the occurrence of success and failed attempts. **(E)** ECG recordings from different electrodes for one successful event using the three illumination patterns. The blue arrows show the timing of the light pulses and the dashed lines show the interval during illumination. **(F)** Magnitude Scalograms from the ECG leads shown in **(E)**. It can be observed that all three protocols are able to change both frequency and amplitude of the arrhythmia. **(G)** Representation of the heart for row (left), column (center) and array (right) protocols illustrating the extracted frequencies fc_{dur} from V1, V2, and V3. Statistical significance illustrated as $^{*}p$ <0.1, $^{**}p$ <0.05 and $^{***}p$ <0.01.

the column protocol worked most efficiently, since it was able to terminate (96.4 ± 1.7) % of all mVT independently of the selected parameters (see **Figure 3A**). The row and array protocol both showed a lower success rate around 78 % for mVT. In comparison, no such clear trend emerged for the pVT events. All protocols showed similar success rates for this arrhythmia type, on average (63.6 ± 4.5) %. Moreover, the column illumination pattern offered the lowest success rate of (37 ± 9) % for VF events. Regarding the row protocol, it is remarkable that it terminated VF events more reliably than pVT even though VF represent the more complex arrhythmia type.

In summary, these results indicate that different illumination patterns could be suited for different arrhythmia types. **Figure 3A** shows that the row protocol is overall most efficient for VF, whereas the column protocol should be chosen when attempting to terminate mVT. During pVT, all illumination patterns worked comparably well. In contrast, the control group employing global illumination terminated 100 % of $N_{arr} = 75$ independently of their type. In order to confirm the significance of the presented results, statistical tests were made using a one-tailed z-test for proportions as shown in **Figure 3A**.

Unfortunately, the sample size for VF events proved to be too limited to provide meaningful results once a further distinction according to the stimulation parameters was to be made. This is a consequence of the circumstance that it was not possible to determine the arrhythmia type during the experiments, leading to a randomized distribution of mVT, pVT, and VF. For further evaluation, mVT and pVT were combined into the group of VT, because this supports a sufficient sample size of arrhythmia when analyzing the success of termination based on different parameters. Considering the individual illumination patterns, the mean number of VT for evaluation per protocol type lies at $\bar{N}_{VT} = 116 \pm 14$.

In order to analyze the dependence on the applied radiant flux Φ, the termination success was investigated for two fixed stimulation frequencies $f_{stim} = 20$ Hz as well as $f_{stim} = 22$ Hz and varying radiant flux considering only VT events. **Figure 3B** top and bottom display the success rates of the row and column protocol exceeding those of the array protocol. It is important to notice that the column illumination pattern obtained the highest success rates with the lowest applied radiant flux $\Phi = (1.7 \pm 0.1)$ mW and therefore the lowest energy of stimulation $Q = (0.61 \pm 0.04)$ mJ for $f_{stim} = 20$ Hz. Conversely, the row illumination pattern delivered better results with increasing radiant flux and stimulation energy in both cases. Both the column and the row protocol reached a 100 % success rate for a certain parameter combination thereby providing a reliable mechanism for arrhythmia termination.

Supplementary Figure 3 displays the success rates for each illumination pattern in dependence on the dominant frequency of the arrhythmia f_{arr} 1 s before illumination considering all VT events. In this case, the dominant frequency f_{arr} was determined as the weighted average of the results of the sine fit, the FFT, and the Lorentz fit to the FFT spectrum. Moreover the distribution of f_{arr} can be found in **Supplementary Figure 4**. The presented results show that the success rate of the row protocol declined with increasing f_{arr}. Conversely, the column and array protocol showed no such trend. Overall, the array protocol reached the highest success rate only in one case, namely for $f_{arr} = 21$ Hz. In all the other cases, the success rates of either the row or column protocol exceeded that of the array illumination pattern.

Additionally, experimental validation regarding the possibility of self-termination was performed by inducing arrhythmia with the μLED arrays in place, but without applying photostimulation. Given that the arrhythmia was sustained for at least 5 s, it persisted for (30.97 ± 2.50) s for all arrhythmia $N_{arr} = 53$ evaluated. Subsequently, the arrhythmia was terminated using global illumination to prevent permanent damage to the heart due to the ongoing chaotic behavior. Thus, it can be concluded that the induced arrhythmia have a self-termination time above (30.97 ± 2.50) s once they have persisted for more than $t_{term} = 5$ s. Since the stimulation protocols take a maximum of 15 s upon completion, the termination of the chaotic cardiac rhythm can clearly be attributed to the stimulation by the μLED arrays.

3.3. Effect of Illumination Patterns During Cardiac Arrhythmia

Optical based stimulation does not induce electrical artifacts due to saturation of the amplifier in the ECG recordings, therefore it was possible to analyze time series of the three acquired uni-polar leads before, during, and immediately after all photodefibrillation attempts. Since the dynamic transients of complex arrhythmia could be better characterized with the CWT, the results in this section always use the frequencies fc calculated with the method described in section 2.5. Additionally, all types of arrhythmia were included without distinguishing between them during evaluation. In particular, it could be observed that the local dominant frequencies fc_{dur} notably changed during photodefibrillation independently of the frequency used for photostimulation f_{stim}. Trials in which fc_{bef} remained constant could not be found, refer to **Supplementary Figure 5**.

Table 1 shows that during illumination all three tested patterns provoked a change of the mean frequency $\overline{\Delta fc}$ calculated for the three recorded ECG, where $\Delta fc = fc_{dur} - fc_{bef}$. This effect is more prominent in the row illumination pattern where 76 % of all arrhythmia displayed a decrease in dominant frequency during photostimulation. Moreover, all three illumination patterns showed to perform better when Δfc was decreased. In other words, when fc_{dur} decelerates compared to fc_{bef}, the probability of termination success increases, as it is presented in columns 5 and 6 of **Table 1**. To support this result, the success rates for deceleration and acceleration measured in different uni-polar leads around the heart were extracted and are shown in **Figure 3C**. The success rates here were organized in four groups, where the first group $dec._1$ contains the attempts in which deceleration could be observed only in one lead, whereas acceleration was detected in the other two leads. In a similar way, the second group $dec._2$ contains the tries in which two leads got decelerated, thus one was accelerated. Finally, the last two groups $dec._3$ and $acc._3$ show the termination rates when all three uni-polar leads measured deceleration, respectively, acceleration. The most efficient approach for terminating arrhythmia is given when the deceleration of fc_{dur} is achieved in all three monitored areas of

TABLE 1 | Change of average frequency from the CWT during photostimulation where $\Delta fc = fc_{dur} - fc_{bef}$.

Protocol	N_{tot}	$N_{\Delta fc>0}$ [%]	$N_{\Delta fc<0}$ [%]	$S_{\Delta fc>0}$ [%]	$S_{\Delta fc<0}$ [%]	$\overline{\Delta}fc > 0$ [Hz]	$\overline{\Delta}fc < 0$ [Hz]
Row	141	34	76	17	83	1.3 ± 1.1	-2.6 ± 1.9
Column	117	37	63	27	72	1.7 ± 1.6	-2.7 ± 2.1
Array	138	47	53	36	64	1.8 ± 1.9	-1.5 ± 1.2

Shown is the average frequency Δfc resulting from the three uni-polar leads. Columns 3 and 4 display the percentage of arrhythmias that increased or decreased their frequency during photostimulation, respectively. Columns 5 and 6 present the obtained success rates for accelerating and decelerating the heart frequency. In Columns 7 and 8, the amount of change of the average frequency can be seen. It can also be noted that in comparison, the change of frequency $\overline{\Delta}fc$ is higher using row and column pattern than using the array protocol.

the heart, here the array pattern reached the best efficiency. With exception of the row protocol, the termination rate of the group $acc._3$ exhibits rather low values.

To further analyze this behavior, **Figure 3D** shows the scatter plots with marginal smoothed histograms of the conducted experiments. The smoothed histograms on the right show that there is an accumulation of successful cases when the frequency of the arrhythmia during photostimulation fc_{dur} drops below 20 Hz approximately. Directly comparing the three tested patterns, it can be observed that the distribution of terminated arrhythmia in the column protocol is broader than for row and array patterns, demonstrating that the column protocol is more robust against the arrhythmia measured in this work. Furthermore, the right side histograms suggest that the row protocol is more successful when it is able to reduce fc_{dur} to around 15 Hz, the same claim holds for the array protocol. Considering the upper histograms, it can be observed that column and array protocol perform better for slow arrhythmias.

In order to illustrate the evolution of arrhythmia during photostimulation **Figures 3E–G** show an example of a termination event for each row, column, and array patterns with corresponding representative uni-polar lead recording, calculated CWT, and the representation of the local change of frequency on the heart fc_{dur}. In **Figure 3E**, it is shown that the frequency and morphology changes of the measured ECG are clearly noticeable during photodefibrillation. Dashed lines indicate the beginning and end of the light pulses. The frequency and amplitude changes can be seen more pronounced in **Figure 3F**. These magnitude scalograms show that all three row (left), column (center) and array (right) protocol, modify the initial frequency fc_{bef} to some extent. **Figure 3G** emphasizes that uni-polar lead recordings were able to register different cardiac dynamics in the different locations. Moreover, it could also be observed that the change of dominant frequency did not necessarily appear in all regions of the heart during photostimulation. This fact might indicate that the electrical activity of some cardiac tissue was not altered in a significant way. For instance, setting a change of frequency threshold to $\Delta fcT = \pm 0.5$ Hz for every uni-polar lead, it was found that the employed illumination patterns induced a variation in frequency below ΔfcT in only one ECG recording in 19.9 % of the cases for the row protocol, 23.1 % of the total cases in the column protocol, and 29.7 % in the array protocol.

The presented results also point out that the Multi-Lead recording of cardiac activity delivers more spatial information about the dynamics and temporal evolution of an arrhythmia, e.g., during transient events such as during photodefibrillation, than single lead recordings as commonly used.

4. DISCUSSION

The motivation for the present study was to demonstrate the great potential of cardiac optogenetics as an investigative tool for elucidating the underlying mechanisms of defibrillation. So far, this question could not be clarified unambiguously, because especially in studies with electrical pulses the ECG is briefly "blind," i.e., due to the high electrical pulse voltage, the actual cardiac signal is masked. However, with the help of optogenetic channelrhodopsins, here specifically channelrhodopsin-2, no electrical voltage is used for defibrillation, but light pulses, which are suitable in appropriate light intensity to initiate new excitation signals (Bruegmann et al., 2011; Deisseroth, 2011).

In the application of cardiac optogenetics itself, various termination mechanisms are currently being discussed. First and foremost are the physiological processes induced by the applied light intensity, as well as the change of light intensity along the penetration depth into the myocardium (Lubart et al., 2007; Bruegmann et al., 2010; Hussaini et al., 2021). Though, the analysis of the development of the arrhythmia frequency is often limited to the required termination time, so that conclusions can be drawn about the minimum required pulse duration or stimulation duration, but not about the underlying termination process. To try to understand the defibrillation mechanisms, the authors tested three different multi-pulse protocols and analyzed them with respect to arrhythmic behavior during photostimulation. It was shown that the probability of successful arrhythmia termination is strongly dependent on the frequency evolution. With decreased arrhythmia frequency (deceleration), the probability of success is significantly increased compared with increasing frequency (acceleration). Such frequency dependence of defibrillation has also been shown in other pre-clinical or clinical studies with electrical stimulation (Everett et al., 2001; Panfilov et al., 2013). Similarly, the dependence of the probability of success on the pacing frequency used has been demonstrated in other works. For example, Weinberg et al. (2013) tested high-frequency stimulation protocols (50–500 Hz) and identified conduction block as a putative mechanism (Tandri et al., 2011). That is, cardiomyocytes are globally maintained in the refractory phase until the arrhythmia is

terminated. Such type of experimental studies could possibly be equated with long-time global photostimulation, such as it can be applied in the array protocol presented here or by Quiñonez Uribe et al. (2018). Nevertheless, such a mechanism is apparently not ostensible for the other two protocols, row and column. Here, the local influence of light-induced depolarization on excitation propagation and thus on the complexity of arrhythmia propagation seems to play a crucial role. These two protocols are a very good example of the use of optogenetic photodefibrillation. The idea hereby is simple, through the targeted local application of light pulses, the arrhythmic excitation pattern is counteracted by a new motion pattern.

As shown in **Figure 3A**, the different pulse protocols can be used for different arrhythmia types. With regard to automated feedback pacing, this means that different pulse protocols could be applied based on the frequency analysis and arrhythmia classification preceding the termination pacing, thus increasing the termination probability. This was also confirmed for conventional defibrillation by Povoas et al. (2002) by analyzing pre-clinical data for CPR. It is important to mention that, in order to exclude effects in the success rate analysis due to spontaneous self-termination, experiments were performed with the same setup except for the activation of the μLED arrays. The experiments have shown that the probability of self-termination decreases with the duration of the induced arrhythmia (see section 3.2). Based on this, the authors assume that the terminations shown here occurred mainly because of photostimulation. Bruegmann et al. (2016) have shown that both ChR2 expression by itself and pure illumination of wild-type hearts have no effect on termination rates. Taking this into account, the authors decided not to use such a control group in the present work. Although this study provides the proof of principle that different illumination patterns do influence the termination success of an arrhythmia depending on its complexity (mVT, pVT, or VF), the necessity for further testing remains. Based on this, there is plenty of potential for optimization with the aim of establishing specific termination parameters based on arrhythmia characteristics and applying these dynamically during the experiment so that each event can be treated in a customized manner. More precise defibrillation mechanisms cannot yet be represented by the data generated in this study and are therefore object of ongoing research.

In addition, it could be successfully proven that the integration of simultaneous Multi-Lead ECG measurements in combination with frequency and time-frequency analyzes allows a better spatial characterization of arrhythmia compared to conventional one lead ECG, without the need of using optical mapping. Consequently, the design and development of targeted termination pulses with patterned illumination were made possible. It is also important to mention that the use of a triangular constellation of measuring electrodes as shown here gives a better understanding of the arrhythmia distribution, but for the precise spatial classification of the arrhythmia only rather large-scale statements can be made (see **Figure 3G**). To refine this, further studies in the group are looking at the use of new ECG arrays with higher spatial resolution. Further examples from the literature comply with the intended way to follow (Uzelac and Fenton, 2020).

4.1. Limitations and Outlook

The present study describes a possible dependence of the termination success on the development of the arrhythmia frequency during pacing. Though, at the present time, no conclusions can be drawn about the underlying excitation patterns. The complexity of arrhythmia and, consequently, the arrhythmia frequency may change spatially due to meandering spirals. To investigate this, the number of ECG electrodes used is not sufficient. For this, the electrode density needs to be increased in relation to the heart surface. Another method to overcome this challenge would be the usage of optical mapping, however, while it is true that it is widely accepted as the standard technique for the electrical spatial characterization of arrhythmia, it can also produce non-desired electrophysiological changes as shown by Kappadan et al. (2020). Other methods like combined optical mapping with motion tracking (Christoph et al., 2017, 2018) could also be helpful, but the motion compensation can only be done after the experiments during post-processing. Therefore, and with the motivation of opening the possibility to translate the presented results into *in vivo* trials or also bigger animal models, the authors decided to introduce the Multi-Lead ECG measurement as a local monitor of cardiac electrical activity. Further efforts are being invested in the real-time processing of the acquired ECG measurements. While optical mapping data requires much more computational power, ECG measurements can be directly analyzed during trials with lower processing resources such as microcontrollers or digital signal processors, facilitating the near to instantaneous analysis of measured data.

A somehow obvious limiting factor of the present study is the currently difficult translation of the described technique into clinically relevant *in vivo* applications. For this purpose, in addition to the above mentioned optimizations of the electrical measurement methods, anatomically adapted measurement and stimulation arrays are needed, the detailed study of which is the subject of current investigations.

Further limitations arise from the optical characteristics of the μLED used, such as the beam angle. This affects the distribution of the emitted light intensity on the cardiac surface and thus the propagation mode of the initiated excitation. Characterization of the propagation parameters would be highly important for understanding the termination processes and for establishing a feedback system based on them. Therefore, increasing ECG resolution and the study of μLED light distribution patterns in combination with optical visualization as a validation method is part of ongoing research.

With the intention of finding parameters that might predict the termination of an arrhythmia even before the photodefibrillation attempt is finished, the CWT processing method was introduced in this work as an alternative method to the FFT for determining the dominant frequency. It could successfully be shown that the CWT facilitates the characterization of arrhythmia frequency during short events

of light stimulation. Further looking for prediction parameters, Yang et al. (2019) investigated whether the amplitude spectrum area (AMSA) and spectral energy could be considered indicative for the success of subsequent attempts at arrhythmia termination. As a result, they found that both parameters significantly increased in cases that lead to successful defibrillation. In contrast, if defibrillation did not succeed, no increase in AMSA or spectral energy could be observed. Likewise, in the present study, a change in the amplitude of the ECG recording of arrhythmia was noticed in some cases. Based on these two approaches (frequency and amplitude analysis) and the presented arrhythmia classification method, the design of a new feedback protocol is being pursued, with the goal of improving the photodefibrillation outcome by evaluating the mentioned parameters in real-time.

5. CONCLUSION

In conclusion, the presented experimental setup and the analyses obtained from it so far are the first step toward the description of arrhythmic development during multi-pulse photostimulation, which contributes to the successful termination due to the better resolution in spatial and temporal information, as well as better classification of the occurring arrhythmia. Further protocol flexibility is given by the fact that the proposed setup is able to individually control single μLEDs rather than only follow rigid illumination patterns, providing a fast theory-to-proof to experimental-implementation time. The authors are convinced that for the elucidation of defibrillation mechanisms, cardiac optogenetics is a well-suited experimental tool. Even so, there are still a few hurdles along the way, such as linking the arrhythmia frequency to the light intensity used and the associated change in amplitude or integrating flexible pacing frequencies.

DATA AVAILABILITY STATEMENT

The original contributions presented in the study are included in the article/**Supplementary Material**, further inquiries can be directed to the corresponding authors.

ETHICS STATEMENT

The animal study was reviewed and approved by Lower Saxony State Office for Consumer Protection and Food Safety (LAVES) Dezernat 33-Tierschutzdienst Postfach 3949 26029 Oldenburg.

AUTHOR CONTRIBUTIONS

LD-M and JS performed and analyzed the experiments. LD-M and CR designed research and experiments. LD-M, JS, and CR conceptualized, wrote, and edited the manuscript. All authors agree to be accountable for the content of the work.

FUNDING

The support was provided by the DZHK e.V., the German Federal Ministry of Education and Research (BMBF, project FKZ 031A147, Go-Bio), the German Research Foundation (DFG, Collaborative Research Centers SFB 1002, Projects B05 and C03), and the Max Planck Society.

ACKNOWLEDGMENTS

The authors want to thank Marion Kunze for her excellent technical assistance during experimental setup and experiment conduction, and Andreas Barthel and Sven Franz for their exceptional support during the electronic design and preparation of the printed circuit boards. Many thanks to Baltasar Ruechardt, Aidai Mamyraiym kyzy, and Stefan Luther for fruitful discussions and thought-provoking impulses. Thanks as well to Annette Witt for providing the initial template for the sine fit algorithm and the counseling during the statistical evaluation of the data.

SUPPLEMENTARY MATERIAL

The Supplementary Material for this article can be found online at: https://www.frontiersin.org/articles/10.3389/fphys.2021.750535/full#supplementary-material

REFERENCES

Abbate, A., DeCusatis, C., and Pankaj, K. (2002). *Wavelets and Subbands Fundamentals and Applications*. New York, NY: Springer Science+Business Media.

Bruegmann, T., Boyle, P. M., Vogt, C. C., Karathanos, T. V., Arevalo, H. J., Fleischmann, B. K., et al. (2016). Optogenetic defibrillation terminates ventricular arrhythmia in mouse hearts and human simulations. *J. Clin. Invest.* 126, 3894–3904. doi: 10.1172/JCI88950

Bruegmann, T., Malan, D., Hesse, M., Beiert, T., Fuegemann, C., Fleischmann, B., et al. (2011). Channelrhodopsin2 expression in cardiomyocytes: a new tool for light-induced depolarization with high spatio-temporal resolution *in vitro* and *in vivo*. Thorac. *Cardiovasc. Surg.* 59:MO19. doi: 10.1055/s-0030-1269109

Bruegmann, T., Malan, D., Hesse, M., Beiert, T., Fuegemann, C. J., Fleischmann, B. K., et al. (2010). Optogenetic control of heart muscle *in vitro* and *in vivo*. *Nat. Methods* 7, 897–900. doi: 10.1038/nmeth.1512

Caldwell, J., Burton, F., Cobbe, S., and Smith, G. (2012). Amplitude changes during ventricular fibrillation: a mechanistic insight. *Front. Physiol.* 3:147. doi: 10.3389/fphys.2012.00147

Chorro, J., Guerrero, J., Trapero, I., Such-Miquel, L., Mainar, L., Cnoves, J., et al. (2006). Time-frequency analysis of ventricular fibrillation. an experimental study. *Revista Espaola de Cardiologa (English Edition)* 59, 869–878. doi: 10.1157/13092794

Christoph, J., Chebbok, M., Richter, C., Schrder-Schetelig, J., Bittihn, P., Stein, S., et al. (2018). Electromechanical vortex filaments during cardiac fibrillation. *Nature* 555:667 EP. doi: 10.1038/nature 26001

Christoph, J., Schröder-Schetelig, J., and Luther, S. (2017). Electromechanical optical mapping. *Prog. Biophys. Mol. Biol.* 130, 150–169. doi: 10.1016/j.pbiomolbio.2017.09.015

Clayton, R., and Murray, A. (1993). "Estimation of the ecg signal spectrum during ventricular fibrillation using the fast fourier transform and maximum entropy methods," in *Proceedings of Computers in Cardiology Conference* (London), 867–870.

Coult, J., Rea, T. D., Blackwood, J., Kudenchuk, P. J., Liu, C., and Kwok, H. (2021). A method to predict ventricular fibrillation shock outcome during chest compressions. *Comput. Biol. Med.* 129:104136. doi: 10.1016/j.compbiomed.2020.104136

Curtis, M. J., Hancox, J. C., Farkas, A., Wainwright, C. L., Stables, C. L., Saint, D. A., et al. (2013). The lambeth conventions (ii): Guidelines for the study of animal and human ventricular and supraventricular arrhythmias. *Pharmacol. Therapeutics* 139, 213–248. doi: 10.1016/j.pharmthera.2013.04.008

Deisseroth, K. (2011). Optogenetics. *Nat. Methods* 8, 26–29. doi: 10.1038/nmeth.f.324

Diaz-Maue, L., Luther, S., and Richter, C. (2018). "Towards optogenetic control of spatiotemporal cardiac dynamics," in *Proceedings SPIE-Optogenetics and Optical Manipulation 2018* (SPIE), 1482G.

Diaz-Maue, L., Steinebach, J., Schwaerzle, M., Luther, S., Ruther, P., and Richter, C. (2021). Advanced cardiac rhythm management by applying optogenetic multi-site photostimulation in murine hearts. *J. Vis. Exp*. 174:e62335. doi: 10.3791/62335

Efimov, I., F., A., Cheng, Y., Wollenzier, B., and Trayanova, N. (2000). Virtual electrode polarization in the far field: implications for external defibrillation. *Am. J. Physiol. Heart Circ*. 279, H1055–H1070. doi: 10.1152/ajpheart.2000.279.3.H1055

Everett, T., Kok, L.-C., Vaughn, R., Moorman, R., and Haines, D. (2001). Frequency domain algorithm for quantifying atrial fibrillation organization to increase defibrillation efficacy. *IEEE Trans. Biomed. Eng*. 48, 969–978. doi: 10.1109/10.942586

Exner, D. (2005). Is antitachycardia pacing a safe and efficacious alternative to shocks for fast ventricular tachyarrhythmia treatment? *Nat. Cl. Pract. Card. Med*. 2:68. doi: 10.1038/ncpcardio0116

Hamelink, J. L. (1992). *Silicones*. Berlin; Heidelberg: Springer Berlin Heidelberg.

Hussaini, S., Venkatesan, V., Biasci, V., Romero Seplveda, J. M., Quiñonez Uribe, R. A., Sacconi, L., et al. (2021). Drift and termination of spiral waves in optogenetically modified cardiac tissue at sub-threshold illumination. *Elife* 10:e59954. doi: 10.7554/eLife.59954

Janardhan, A., Li, W., Fedorov, V., Yeung, M., Wallendorf, M., Schuessler, R., et al. (2012). A novel low-energy electrotherapy that terminates ventricular tachycardia with lower energy than a biphasic shock when antitachycardia pacing fails. *JACC* 60, 2393–2398. doi: 10.1016/j.jacc.2012.08.1001

Kappadan, V., Telele, S., Uzelac, I., Fenton, F., Parlitz, U., Luther, S., et al. (2020). High-resolution optical measurement of cardiac restitution, contraction, and fibrillation dynamics in beating vs. blebbistatin-uncoupled isolated rabbit hearts. *Front. Physiol*. 11:464. doi: 10.3389/fphys.2020.00464

Kolega, J. (2004). Phototoxicity and photoinactivation of blebbistatin in UV and visible light. *Biochem. Biophys. Res. Commun*. 320, 1020–1025. doi: 10.1016/j.bbrc.2004.06.045

Lubart, R., Lavi, R., Friedmann, H., and Rochkind, S. (2007). Photochemistry and photobiology of light absorption by living cells. *Photomed. Laser Surg*. 24, 179–185. doi: 10.1089/pho.2006.24.179

Luther, S., Fenton, F. H., Kornreich, B. G., Squires, A., Bittihn, P., Hornung, D., et al. (2011). Low-energy control of electrical turbulence in the heart. *Nature* 475, 235–239. doi: 10.1038/nature10216

Mansier, P., Clairambault, J., Charlotte, N., Mdigue, C., Vermeiren, C., LePape, G., et al. (1996). Linear and non-linear analyses of heart rate variability: a minireview. *Cardiovasc. Res*. 31, 371–379. doi: 10.1016/S0008-6363(96)00009-0

Masse, S., Downar, E., Chauhan, V., Sevaptsidis, E., and Nanthakumar, K. (2007). Ventricular fibrillation in myopathic human hearts: mechanistic insights from *in vivo* global endocardial and epicardial mapping. *Am. J. Physiol. Heart Circ. Physiol*. 292, H2589–H2597. doi: 10.1152/ajpheart.01336.2006

Moss, A. J., Hall, W. J., Cannom, D. S., Daubert, J. P., Higgins, S. L., Klein, H., et al. (1996). Improved survival with an implanted defibrillator in patients with coronary disease at high risk for ventricular arrhythmia. *New Engl. J. Med*. 335, 1933–1940. doi: 10.1056/NEJM199612263352601

Nash, M. P., Mourad, A., Clayton, R. H., Sutton, P. M., Bradley, C. P., Hayward, M., et al. (2006). Evidence for multiple mechanisms in human ventricular fibrillation. *Circulation* 114, 536–542. doi: 10.1161/CIRCULATIONAHA.105.602870

Panfilov, I., Lever, N. A., Smaill, B. H., and Larsen, P. D. (2013). Ventricular fibrillation frequency from implanted cardioverter defibrillator devices. *EP Europace* 11, 1052–1056. doi: 10.1093/europace/eup159

Povoas, H. P., Weil, M. H., Tang, W., Bisera, J., Klouche, K., and Barbatsis, A. (2002). Predicting the success of defibrillation by electrocardiographic analysis. *Resuscitation* 53, 77–82. doi: 10.1016/S0300-9572(01)00488-9

Pumir, A., Nikolsky, V., Hoerning, M., Isomura, A., Agladze, K., Yoshikawa, K., et al. (2007). Wave emission from heterogeneities opens a way to controlling chaos in the heart. *Phys. Rev. Lett*. 99:208101. doi: 10.1103/PhysRevLett.99.208101

Quiñonez Uribe, R. A., Luther, S., Diaz-Maue, L., and Richter, C. (2018). Energy-reduced arrhythmia termination using global photostimulation in optogenetic murine hearts. *Front. Physiol*. 9:1651. doi: 10.3389/fphys.2018.01651

Richter, C., Christoph, J., Lehnart, S. E., and Luther, S. (2016). "Optogenetic light crafting tools for the control of cardiac arrhythmias," in *Optogenetics-Methods and Protocols, Vol. 1408*, ed A. Kianianmomeni (New York, NY: Springer Science+Business Media), 293–302.

Sasse, P., Funken, M., Beiert, T., and Bruegmann, T. (2019). Optogenetic termination of cardiac arrhythmia: Mechanistic enlightenment and therapeutic application? *Front. Physiol*. 10:675. doi: 10.3389/fphys.2019.00675

Schwaerzle, M., Elmlinger, P., Paul, O., and Ruther, P. (2014). Miniaturized tool for optogenetics based on an led and an optical fiber interfaced by a silicon housing. *Ann. Int. Conf. IEEE Eng. Med. Biol. Soc*. 2014, 5252–5255. doi: 10.1109/EMBC.2014.6944810

Seely, A., and Macklem, P. (2004). Complex systems and the technology of variability analysis. *Crit. Care* 8, 367–384. doi: 10.1186/cc2948

Skanes, A. C., Mandapati, R., Berenfeld, O., Davidenko, J. M., and Jalife, J. (1998). Spatiotemporal periodicity during atrial fibrillation in the isolated sheep heart. *Circulation* 98, 1236–1248. doi: 10.1161/01.CIR.98.12.1236

Swift, L., Asfour, H., Posnack, N., Arutunyan, A., Kay, M., and Sarvazyan, N. (2012). Properties of blebbistatin for cardiac optical mapping and other imaging applications. *Pflugers Arch. Eur. J. Physlol*. 464, 503–512. doi: 10.1007/s00424-012-1147-2

Tandri, H., Weinberg, S. H., Chang, K. C., Zhu, R., Trayanova, N. A., Tung, L., et al. (2011). Reversible cardiac conduction block and defibrillation with high-frequency electric field. *Sci. Transl. Med*. 102, 102ra96. doi: 10.1126/scitranslmed.3002445

Tokano, T., Bach, D., Chang, J., Davis, J., Souza, J., Zivin, A., et al. (1998). Effect of ventricular shock strength on cardiac hemodynamics. *J. Cardiovasc. Electrophysiol*. 9, 791–797. doi: 10.1111/j.1540-8167.1998.tb00118.x

Torrence, C., and Compo, G. P. (1998). A practical guide to wavelet analysis. *Bull. Metereol. Soc*. 79, 61–78. doi: 10.1175/1520-0477(1998)079<0061:APGTWA>2.0.CO;2

Tseng, L.-M., and Tseng, V. S. (2020). Predicting ventricular fibrillation through deep learning. *IEEE Access* 8, 221886–221896. doi: 10.1109/ACCESS.2020.3042782

Umapathy, K., Nair, K., Masse, S., Krishnan, S., Rogers, J., Nash, M. P., et al. (2010). Phase mapping of cardiac fibrillation. *Circ. Arrhythm. Electrophysiol*. 3, 105–114. doi: 10.1161/CIRCEP.110.853804

Uzelac, I., and Fenton, F. H. (2020). Personalized low-energy defibrillation through feedback based resynchronization therapy. *Comput. Cardiol*. doi: 10.22489/CinC.2020.471

Wathen, M. S., DeGroot, P. J., Sweeney, M. O., Stark, A. J., Otterness, M. F., Adkisson, W. O., et al. (2004). Prospective randomized multicenter trial of empirical antitachycardia pacing versus shocks for spontaneous rapid ventricular tachycardia in patients with implantable cardioverter-defibrillators: pacing fast ventricular tachycardia reduces shock therapies. *Circulation* 110, 2591–2596. doi: 10.1161/01.CIR.0000145610.64014.E4

Weinberg, S. H., Chang, K. C., Zhu, R., Tandri, H., Berger, R. D., Trayanova, N. A., et al. (2013). Defibrillation success with high frequency electric fields is related to degree and location of conduction block. *Heart Rhythm* 10, 740–748. doi: 10.1016/j.hrthm.2013.01.016

Wilson, F. N., Johnston, F. D., Macleod, A., and Barker, P. S. (1934). Electrocardiograms that represent the potential variations of a single electrode. *Am. Heart J*. 9, 447–458. doi: 10.1016/S0002-8703(34)90093-4

Wilson, F. N., Johnston, F. D., Rosenbaum, F. F., and Barker, P. S. (1946). On einthoven's triangle, the theory of unipolar electrocardiographic leads, and the interpretation of the precordial electrocardiogram. *Am. Heart J*. 32, 277–310. doi: 10.1016/0002-8703(46)90791-0

Yang, Q., Li, M., Huang, Z., Xie, Z., Wang, Y., Ling, Q., et al. (2019). Validation of spectral energy for the quantitative analysis of ventricular fibrillation waveform to guide defibrillation in a porcine model of cardiac arrest and resuscitation. *J. Thorac. Dis*. 11, 3853–3863. doi: 10.21037/jtd.2019.09.18

Zaglia, T., Pianca, N., Borile, G., Da Broi, F., Richter, C., Campione, M., et al. (2015). Optogenetic determination of the myocardial requirements for extrasystoles by cell type-specific targeting of ChannelRhodopsin-2. *Proc. Natl. Acad. Sci. U.S.A.* 112:1509380112. doi: 10.1073/pnas.1509380112

Conflict of Interest: The authors declare that the research was conducted in the absence of any commercial or financial relationships that could be construed as a potential conflict of interest.

Publisher's Note: All claims expressed in this article are solely those of the authors and do not necessarily represent those of their affiliated organizations, or those of the publisher, the editors and the reviewers. Any product that may be evaluated in this article, or claim that may be made by its manufacturer, is not guaranteed or endorsed by the publisher.

frontiers in Physiology

ORIGINAL RESEARCH
published: 25 March 2022
doi: 10.3389/fphys.2022.691829

An Optogenetic Arrhythmia Model—Insertion of Several Catecholaminergic Polymorphic Ventricular Tachycardia Mutations Into *Caenorhabditis elegans* UNC-68 Disturbs Calstabin-Mediated Stabilization of the Ryanodine Receptor Homolog

Marcial Alexander Engel[1,2], Yves René Wörmann[1,2], Hanna Kaestner[1,2] and Christina Schüler[1,2]*

[1] Buchmann Institute for Molecular Life Sciences, Goethe University Frankfurt, Frankfurt, Germany, [2] Institute of Biophysical Chemistry, Goethe University Frankfurt, Frankfurt, Germany

OPEN ACCESS

Edited by:
Tobias Bruegmann, University Medical Center Göttingen, Germany

Reviewed by:
Olga Kopach, University College London, United Kingdom
Shimrit Oz, Technion Israel Institute of Technology, Israel
Manu Ben-Johny, Columbia University, United States
Ivy Dick, University of Maryland, Rockville, United States

***Correspondence:**
Christina Schüler
c.schueler@em.uni-frankfurt.de

Specialty section:
This article was submitted to Membrane Physiology and Membrane Biophysics, a section of the journal Frontiers in Physiology

Received: *08 April 2021*
Accepted: *15 February 2022*
Published: *25 March 2022*

Citation:
Engel MA, Wörmann YR, Kaestner H and Schüler C (2022) An Optogenetic Arrhythmia Model—Insertion of Several Catecholaminergic Polymorphic Ventricular Tachycardia Mutations Into Caenorhabditis elegans UNC-68 Disturbs Calstabin-Mediated Stabilization of the Ryanodine Receptor Homolog. Front. Physiol. 13:691829. doi: 10.3389/fphys.2022.691829

Catecholaminergic polymorphic ventricular tachycardia (CPVT) is an inherited disturbance of the heart rhythm (arrhythmia) that is induced by stress or that occurs during exercise. Most mutations that have been linked to CPVT are found in two genes, i.e., ryanodine receptor 2 (RyR2) and calsequestrin 2 (CASQ2), two proteins fundamentally involved in the regulation of intracellular Ca^{2+} in cardiac myocytes. We inserted six CPVT-causing mutations *via* clustered regularly interspaced short palindromic repeats (CRISPR)-Cas9 into *unc-68* and *csq-1*, the *Caenorhabditis elegans* homologs of RyR and CASQ, respectively. We characterized those mutations *via* video-microscopy, electrophysiology, and calcium imaging in our previously established optogenetic arrhythmia model. In this study, we additionally enabled high(er) throughput recordings of intact animals by combining optogenetic stimulation with a microfluidic chip system. Whereas only minor/no pump deficiency of the pharynx was observed at baseline, three mutations of UNC-68 (S2378L, P2460S, Q4623R; RyR2-S2246L, -P2328S, -Q4201R) reduced the ability of the organ to follow 4 Hz optogenetic stimulation. One mutation (Q4623R) was accompanied by a strong reduction of maximal pump rate. In addition, S2378L and Q4623R evoked an altered calcium handling during optogenetic stimulation. The 1,4-benzothiazepine S107, which is suggested to stabilize RyR2 channels by enhancing the binding of calstabin2, reversed the reduction of pumping ability in a mutation-specific fashion. However, this depends on the presence of FKB-2, a *C. elegans* calstabin2 homolog, indicating the involvement of calstabin2 in the disease-causing mechanisms of the respective mutations. In conclusion, we showed for three CPVT-like mutations in *C. elegans* RyR a reduced pumping ability upon light stimulation, i.e., an arrhythmia-like phenotype, that can be reversed in two

cases by the benzothiazepine S107 and that depends on stabilization *via* FKB-2. The genetically amenable nematode in combination with optogenetics and high(er) throughput recordings is a promising straightforward system for the investigation of RyR mutations and the selection of mutation-specific drugs.

Keywords: CPVT, RyR2, calsequestrin, arrhythmia model, optogenetics, S107, Calstabin2/FKBP12.6, *C. elegans*

INTRODUCTION

Catecholaminergic polymorphic ventricular tachycardia (CPVT) is a condition of abnormal heart rhythm (arrhythmia), induced by stress or physical activity. If untreated, CPVT is highly lethal. It often remains unnoticed due to normal baseline electrocardiograms and structurally normal hearts. The exact prevalence of CPVT is not known but is estimated to be around 1:10,000 (Liu et al., 2008). The mean age of symptom onset is between 7 and 8 years (Leenhardt et al., 1995). Most mutations that have been linked to CPVT are found in two genes, i.e., ryanodine receptor 2 (RyR2) and calsequestrin 2 (CASQ2), two proteins fundamentally involved in the regulation of intracellular Ca^{2+} in cardiac myocytes (Priori et al., 2002; Faggioni and Knollmann, 2012). The cardiac RyR2 is a Ca^{2+} release channel located in the sarcoplasmic reticulum (SR). In vertebrates, three RyR isoforms are present, whereas *Caenorhabditis elegans* has a single RyR gene encoded by the *unc-68* locus (Maryon et al., 1998). Therefore, our model may recapitulate general ryanodinopathy, even when CPVT-related RyR2 mutations are chosen. The UNC-68 protein shares about 45% sequence identity and 63% homology with the human RyR2. The expression of UNC-68 was shown by immunostaining in several muscle cell types, including pharyngeal muscles, where it was detected in the terminal bulb and posterior isthmus (Maryon et al., 1998; Hamada et al., 2002). The expression of a GFP reporter gene construct was also observed in head neurons (Maryon et al., 1998). Two EF-hand motifs and the C-terminus of UNC-68 were demonstrated to be Ca^{2+} binding regions, and based on these results, a proposed model for the functional domains of UNC-68 was found to agree well with a model of mammalian skeletal RyR (Hamada et al., 2002). Null mutants of *unc-68* are not lethal, but they move slowly and exhibit a languid, incomplete flaccid paralysis, and pharyngeal pumping is weaker than in wild type (Maryon et al., 1996). This suggests that UNC-68 is not essential for excitation-contraction coupling in nematodes but acts to amplify a calcium signal that is sufficient for contraction (Maryon et al., 1996). Calsequestrin is the major Ca^{2+} binding protein in the SR, where it forms linear chains. Only one isoform is present in *C. elegans*, CSQ-1, which shows about 31% sequence identity and 55% homology to the human CASQ2. Reporter gene analysis revealed CSQ-1 expression in body-wall muscles (BWM), vulval muscles, and in the isthmus and terminal bulb regions of the pharynx (Cho et al., 2000). A *csq-1* null-mutant showed no obvious defects in *C. elegans* muscle function or development but is highly sensitive to perturbation of Ca^{2+} homeostasis (Cho et al., 2007). Polymerization *via* back-to-back and front-to-front interaction, as well as the relevant residues, are conserved in *C. elegans* (Cho et al., 2007). While junctin and triadin are implicated in anchoring CASQ2 to RyR2 (Guo and Campbell, 1995; Jones et al., 1995), there are, based on the genome sequence, no obvious homologs of junctin and triadin in *C. elegans*. Therefore, a direct interaction of the positively charged CSQ-1 C-terminus with the negatively charged luminal loops of UNC-68 is postulated (Cho et al., 2007).

Many different (>170) CPVT mutations and polymorphisms are known (Medeiros-Domingo et al., 2009). These mutations result in a Ca^{2+} leakage from the SR, which leads to cytosolic Ca^{2+} overload, generating delayed afterdepolarizations (DADs), triggered activity, and ventricular arrhythmias, in particular, under adrenergic conditions (Leenhardt et al., 2012). There are different hypotheses about how mutations in RyR2 lead to CPVT. One possibility is that mutations in RyR2 affect the ability of calstabin2 [a.k.a. FK506-binding protein 12.6 (FKBP12.6)] to bind and stabilize RyR2 in its closed state (Wehrens et al., 2003, 2004). Recent cryo-EM of rabbit RyR2 shows that FKBP12.6 is bound to a hollow formed by the handle, Spore lysis A (SplA) kinase and Ryanodine Receptor (SPRY)1 and SPRY3 domains (Dhindwal et al., 2017). In addition, crystal structures, as well as FKBP binding and docking studies, implicate a hydrophobic cluster within a SPRY1 loop as a major FKBP binding determinant (Yuchi et al., 2015). Those areas are widely conserved in *unc-68*. A second hypothesis suggests instability *via* defective interdomain interactions, evoking so-called "unzipping" of the domains, which results in a calcium leak (George et al., 2006). However, either in combination with one of the proposed mechanisms or on its own, a sensitization of RyR2 channels to SR luminal calcium, leading to store overload-induced calcium release (SOICR), is also discussed (Jiang et al., 2004).

In this study, we aimed to investigate the effects of CPVT-related mutations on pharyngeal pumping after insertion of known mutations *via* clustered regularly interspaced short palindromic repeats (CRISPR)-Cas9 into the *C. elegans csq-1* and *unc-68* loci. Using the *C. elegans* pharynx, a rhythmically active muscular pump acting as the feeding organ of the nematode, enabled us to study their effects on contraction and intracellular Ca^{2+} concentration in an entire organ of a living animal. Obvious similarities exist between the heart and the pharynx, i.e., both are tubes that pump materials along their lumina, both possess gap junctions to synchronize their contractions that can continue without neuronal input and the fact that the pharynx expresses orthologs of most of the proteins involved in human cardiac muscle physiology. These similarities suggest that the pharynx and the myocardium may represent convergent evolution between two muscular pumps faced with similar biological roles (Mango, 2007). The pharynx itself consists of six sections which are, from anterior to posterior, the buccal

cavity, procorpus, metacorpus, the isthmus, the terminal bulb, and the pharyngeal-intestinal valve (Albertson and Thomson, 1976; Mango, 2007). *C. elegans* is a filter feeder, a complex sequence of contractions and relaxations transports food particles in two successive trap stages before passage into the terminal bulb and the intestine (Fang-Yen et al., 2009). The grinder, located in the terminal bulb, crushes bacteria before passage to the intestine. The pump activity is maintained by action potentials, which qualitatively bear a resemblance to vertebrate cardiac action potentials (Franks et al., 2002). *C. elegans* lacks a voltage-gated sodium channel that initiates the action potential in the heart. In the pharyngeal muscle instead, its role is played by CCA-1, a T-type calcium channel (Shtonda and Avery, 2005). EGL-19, the *C. elegans* L-type voltage-dependent Ca^{2+}channel α1-subunit, maintains depolarization during the plateau phase (∼200 ms) and activates muscle contraction. EGL-19 slowly inactivates, and EXP-2, a voltage-gated K^{+}-channel, causes membrane repolarization and action potential termination (Shtonda and Avery, 2005). Though homology is low, EXP-2 is functionally similar to the human ether-a-go-go-related gene (hERG) channel (Davis et al., 1999).

We previously established the pharynx as an optogenetically controlled arrhythmia test system (Schuler et al., 2015; Fischer et al., 2017). Since spontaneous pharynx pumping is too irregular to allow the detection of arrhythmic events, we optically paced the pharynx using channelrhodopsin-2 (ChR2) to yield millisecond-precise and stable rhythmicity (Schuler et al., 2015). Blue light stimulation of pumping was achieved with a gain-of-function variant of ChR2, ChR2(H134R), that was directed to the plasma membrane of the pharyngeal muscle cells (PMCs) by the specific promoter *pmyo-2*. Importantly, we were able to show previously that the optogenetically paced pharynx, in contrast to spontaneous pumping on food, is not appreciably affected by neuronal input (Schuler et al., 2015). Furthermore, we were able to demonstrate the conservation of function between human RyR and *C. elegans* UNC-68. Incubation with caffeine (1 mM), a well-known activator of RyR, increased the spontaneous pump rate in EPG recordings of wild-type animals, while no effect of caffeine was observed in two different mutants lacking UNC-68 (Fischer et al., 2017). A deletion of *unc-68* (allele *r1162*) led to severe effects on optogenetically 4 Hz paced pumping in our pharynx model and was reversed by an expression of wild type UNC-68 in the deletion background (Fischer et al., 2017). In addition, UNC-68 was recently established to study human myopathic mutations of the skeletal muscle channel RyR1 (Graham et al., 2020). The conservation of functionality between RyR1 and UNC-68 is emphasized by an increased sensitivity to the inhalational anesthetic halothane of all tested RyR1 equivalent variants and an increased caffeine sensitivity for variants corresponding to malignant hyperthermia and central core disease (Nicoll Baines et al., 2017; Graham et al., 2020).

Caenorhabditis elegans is highly suited to study the effects of disease-causing mutations, not only because it is a genetically amenable experimental system but also because it enables, straightforward mass cultivation, with a 3-day life cycle. Therefore, the effects of mutations that cause human diseases can be investigated in *C. elegans* to the point that high-throughput screening becomes possible, which cannot be easily achieved in other *in vivo* models. Certainly, there are limitations: the small nematode is due to the lack of a heart and a vascular system not suitable for studying several aspects of human cardiac function and diseases including chamber development, fibrosis, hypertrophy, remodeling, and hemodynamics (Benian and Epstein, 2011). Further limitations of the pharynx regarding the analysis of CPVT mutations are that no adrenergic receptor is expressed in its muscle cells (Sanyal et al., 2004) and that the possible involvement of regulatory mechanisms by NCX or SERCA in the optogenetic arrhythmia model is not yet investigated.

We have chosen one *csq-1* mutation and five *unc-68* mutations. All chosen CPVT mutations occur in homologous regions of the respective proteins (see RyR alignment: **Supplementary Information**) and have been found in human patients (**Table 1**). Furthermore, their mechanism has been described by other groups in animal models or cell cultures (**Table 1**). In the case of CSQ-1, we selected a mutation bearing a putative mechanism other than triadin/junction interaction. For RyR2 mutations, we selected mutations with different putative mechanisms. In addition, the selected RyR2-mutations are distributed over the three hotspot regions known to bear CPVT-mutations: the N-terminal (aa 62–466), the central (aa 2113–2534), and the C-terminal region (aa 3778–4959), including the channel domain (Leenhardt et al., 2012). Many proteins, for example, protein kinase A or calmodulin, are associated with the N-terminal region of RyR2, whereas calsequestrin, junctin, and triadin are linked to the C-terminus (see also Leenhardt et al., 2012). We inserted the mutations into *C. elegans via* different CRISPR-Cas9 approaches (Ward, 2015; Prior et al., 2017) and crossed them with our strain expressing ChR2 in PMCs. In contrast to extrachromosomal arrays, genome-editing should most closely resemble an expression level and protein distribution reflecting the wild-type condition.

We recorded conventional electropharyngeograms (EPGs), extracellular measurements of electrical events in the pharynx. The excitation phase consists of two positive peaks, the first one smaller than the second, that correlate with muscle contraction. The relaxation phase consists of two negative peaks, the second one smaller than the first, that correlate with muscle relaxation. A plateau phase is between the two phases (Raizen and Avery, 1994). In addition, we have established EPG recordings of intact nematodes with optogenetic stimulation by combining an Arduino-controlled high-power LED with a microfluidic system (ScreenChip^{TM}, *InVivo* Biosystems) that enables higher throughput than conventional electrophysiological approaches. This method allows a precise light stimulation during recordings while registering pharyngeal potentials, similar to an electrocardiogram. Several mutations of UNC-68 led to a reduced ability to follow light stimulation. This effect was reversed in a mutation-specific way by the 1,4-benzothiazepine S107, which is suggested to stabilize RyR channels by enhancing the binding of calstabin (Bellinger et al., 2008; Lehnart et al., 2008; Kushnir et al., 2020). In addition, we explored the effects of the CPVT mutations on intracellular Ca^{2+} concentration *in vivo* by using RCaMP1h, a genetically encoded Ca^{2+}

TABLE 1 | Catecholaminergic polymorphic ventricular tachycardia (CPVT) mutations found in human characterized in this study with their homologous sites in *Caenorhabditis elegans unc-68* and their suggested mechanism.

Human	*C. elegans*	Suggested mechanism
RyR2-R420Q (Medeiros-Domingo et al., 2009; van der Werf et al., 2011; Arad et al., 2012)	*unc-68(R414Q)*	Reorients the first two N-terminal domains relative to the third domain, destabilizing intersubunit interactions (Kimlicka et al., 2013)
RyR2-S2246L (Priori et al., 2001; Tester et al., 2004; Medeiros-Domingo et al., 2009)	*unc-68(S2378L)*	Abnormally tight local sub-domain interaction, defective interaction between N-terminal and central domains (Suetomi et al., 2011) Decreased affinity for calstabin2 (Wehrens et al., 2003)
RyR2-P2328S (Lehnart et al., 2004; Medeiros-Domingo et al., 2009)	*unc-68(P2460S)*	Decreased binding of calstabin2 (Lehnart et al., 2004)
RyR2-Q4201R (Lehnart et al., 2004; Medeiros-Domingo et al., 2009)	*unc-68(Q4623R)*	Decreased binding of calstabin2 (Lehnart et al., 2004)
RyR2-I4867M (Priori et al., 2002)	*unc-68(I5231M)*	Increases channel sensitivity to activation by luminal Ca^{2+} (Jiang et al., 2005)
CASQ2-K206N (Kirchhefer et al., 2010)	*csq-1(K214N)*	Hyperglycosylation, altered cellular calcium handling (Kirchhefer et al., 2010)

indicator in the pharynx. The red-shifted RCaMP1h can be used in combination with ChR2 under optogenetic stimulation (Akerboom et al., 2013).

Since no homologs of triadin and junctin are present in *C. elegans*, we were also interested in the mode of interaction between CSQ-1 and UNC-68. This is especially because mutations of triadin are as well known to cause CPVT (Roux-Buisson et al., 2012; Rooryck et al., 2015). Thus, we disturbed the proposed electrostatic interaction by a replacement *via* CRISPR-Cas9 of negatively charged amino acids of a UNC-68 luminal loop with neutral ones.

In conclusion, we showed for several of the inserted CPVT mutations a reduction in the ability of pharyngeal pumping under optogenetic pacing and an altered Ca^{2+} handling, which can be designated here as an arrhythmia-like phenotype. The benzothiazepine S107 reversed the pumping ability of those strains in a mutation-specific manner and therefore we suggest the involvement of a FKB-2 dependent stabilization mechanism.

MATERIALS AND METHODS

Caenorhabditis elegans Cultivation and Transgenic Strains

Worms were cultivated on nematode growth medium (NGM) plates (55 mm, 8 ml NGM), seeded with an *E. coli* OP50-1 strain. We used the following strains: N2 (wild type), **ZX1423:** *zxEx795 [pmyo-2::RCaMP1h; pmyo-3::CFP]*, **ZX1662:** *zxIs20 [pmyo-2::ChR2(H134R)::mCherry; pges-1::nls::GFP]*, **GE24:** *pha-1(e2123) III*, and **RB2222:** *fkb-2(ok3007) I*. Strains generated by SunyBiotech, China (SunyBiotech nomenclature in brackets): **ZX2655:** *csq-1(zx7[K214N])* [**PHX2058:** *csq-1(syb2058)*], **ZX2745:** *unc-68(zx9[neutral luminal loop])* [**PHX2420:** *unc-68(syb2420)*], **ZX2747:** *unc-68(zx10[I5231M])* [**PHX2421:** *unc-68(syb2421)*], and **ZX2749:** *unc-68(zx11[S2378L])* [**PHX2494:** *unc-68(syb2494)*].

We generated the following strains: **ZX2255:** *fkb-2(ok3007) I; zxIs20 [pmyo-2::ChR2(H134R)::mCherry; pges-1::nls::GFP],* **ZX2256:** *pha-1(zx2); unc-68(zx4[Q4623R]),* **ZX2257:** *pha-1(zx2); unc-68(zx4[Q4623R]); zxIs20 [pmyo2::ChR2(H134R)::mCherry; pges1::nls::GFP],* **ZX2258:** *pha-1(zx2),* **ZX2259:** *pha-1(zx2); zxIs20 [pmyo2::ChR2(H134R)::mCherry; pges1::nls::GFP],* **ZX2260:** *pha-1(zx2); zxIs20 [pmyo-2::ChR2(H134R)::mCherry; pges1::nls::GFP]; zxIs124[pmyo-2::RCaMP1h; pmyo-3::CFP],* **ZX2261:** *zxEx795 [pmyo-2::RCaMP1h; pmyo-3::CFP]; zxIs20 [pmyo2::ChR2(H134R)::mCherry; pges1::nls::GFP],* **ZX2264:** *zxIs124[pmyo-2::RCaMP1h; pmyo-3::CFP],* **ZX2266:** *pha-1(zx2); unc-68(zx5[R414Q]),* **ZX2267:** *pha-1(zx2); unc-68(zx5[R414Q]); zxIs20 [pmyo-2::ChR2(H134R)::mCherry; pges-1::nls::GFP],* **ZX2269:** *pha-1(zx2); unc-68(zx4[Q4623R]); zxIs20 [pmyo-2::ChR2(H134R)::mCherry; pges-1::nls::GFP]; zxIs20 [pmyo-2::ChR2(H134R)::mCherry; pges-1::nls::GFP]; zxIs124[pmyo-2::RCaMP1h; pmyo-3::CFP],* **ZX2270:** *fkb-2(ok3007) I; unc-68(zx4[Q4623R]); zxIs20 [pmyo2::ChR2(H134R)::mCherry; pges1::nls::GFP],* **ZX2567:** *csq-1(ok2672); zxIs20[pmyo-2::ChR2(H134R)::mCherry; pges-1::nls::GFP]; zxIs124[pmyo-2::RCaMP1h; pmyo-3::CFP],* **ZX2568:** *unc-68(r1162)V; zxIs20[pmyo-2::ChR2(H134R)::mCherry; pges-1::nls::GFP]; zxIs124[pmyo-2::RCaMP1h; pmyo-3::CFP],* **ZX2707:** *csq-1(zx7[K214N]); zxIs20 [pmyo-2::ChR2(H134R)::mCherry; pges-1::nls::GFP],* **ZX2708:** *unc-68(zx8[P2460S]),* **ZX2718:** *unc-68(zx8[P2460S]); zxIs20 [pmyo-2::ChR2(H134R)::mCherry; pges-1::nls::GFP],* **ZX2743:** *fkb-2(ok3007) I; unc-68(zx8[P2460S]); zxIs20 [pmyo-2::ChR2(H134R)::mCherry; pges-1::nls::GFP],* **ZX2744:** *unc-68(zx8[P2460S]); zxIs20 [pmyo-2::ChR2(H134R)::mCherry; pges-1::nls::GFP]; zxIs124[pmyo-2::RCaMP1h; pmyo-3::CFP],* **ZX2746:** *unc-68(zx9[neutral luminal loop]); zxIs20 [pmyo-2::ChR2(H134R)::mCherry; pges-1::nls::GFP],* **ZX2748:** *unc-68(zx10[I5231M]); zxIs20 [pmyo-2::ChR2(H134R)::mCherry; pges-1::nls::GFP],* **ZX2750:** *unc-68(zx11[S2378L]); zxIs20 [pmyo-2::ChR2(H134R)::mCherry; pges-1::nls::GFP],* **ZX2775:** *unc-68(zx9[neutral luminal loop]); zxIs20 [pmyo-2::ChR2(H134R)::mCherry; pges-1::nls::GFP]; zxIs124[pmyo-2::RCaMP1h; pmyo-3::CFP],* **ZX2777:** *unc-68(zx11[S2378L]); zxIs20 [pmyo-2::ChR2(H134R)::mCherry; pges-1::nls::GFP]; zxIs124[pmyo-2::RCaMP1h; pmyo-3::CFP],*

ZX2778: *fkb-2(ok3007) I; unc-68(zx11[S2378L]); zxIs20 [pmyo-2::ChR2(H134R)::mCherry; pges-1::nls::GFP].*

Generation of Point Mutation Alleles

Using a temperature-sensitive embryonic lethal mutation *pha-1(e2123)* co-conversion approach, ZX2256, ZX2258, and ZX2266 were generated (Ward, 2015). Several sgRNA templates were tested for one mutation site. Primers for the generation of these linear PCR-derived sgRNA templates can be found in **Supplementary Information**. Injection mixes consisted of pJW1285 (60 ng/μl), *pha-1(e2123)* repair template RT01 (50 ng/μl), fusion PCR derived sgRNA template targeting the desired locus (25 ng/μl), and a linear oligo as a repair template carrying the desired mutation (50 ng/μl). Animals that were not embryonic lethal at 25°C were PCR genotyped for successful CRISPR events.

Through mainly following the protocol described by Prior et al. (2017), ZX2708 was generated. sgRNA was generated by annealing TrueGuide^{TM} tracrRNA with crRNA (both Invitrogen, United States), targeting the region of interest (AGAGCAACACCAAGGCAUUC) according to the manufacturer's manual. The injection mix consisted of sgRNA (5 μM), Cas9 nuclease (5 μM) (TrueCut Cas9 v2, Invitrogen, United States), linear oligo as a repair template (50 ng/μl), *pmyo-3::CFP* (50 ng/μl) as an injection marker, KCl (300 mM), and HEPES (20 mM). Fluorescent progeny was picked and PCR genotyped for successful CRISPR events. For both methods, sgRNA target sites were predicted with the online tool CRISPOR (Concordet and Haeussler, 2018), taking the distance to the point mutation site (< 20 bp), the specificity score, and as few off-targets as possible into account. As repair templates synthesized oligos (Eurofins Genomics, Germany) carrying the desired point mutation as well as 40 bp homology arms were used. The PAM site was deactivated by introducing a silent mutation or, if not possible, by introducing several silent mutations in the sgRNA recognition site. Allele identity was verified by sequencing. Every strain derived from CRISPR needed to be outcrossed with N2 animals before subsequent crossing with ZX1662, ZX2255, ZX2260, and ZX2261. For detailed information on plasmids and repair templates for CRISPR and oligos for sgRNA template generation and genotyping (see **Supplementary Information**).

Generation of Transgenic Strains

By integrating the extrachromosomal array of ZX1423 *via* UV radiation (two pulses of 33.3 mJ each) and subsequent backcrossing (4x) with N2 strain, ZX2261 was obtained.

Determination of Spontaneous Pump Rate on Food and Swimming Cycles in Liquid

One day before experiments, L4 larvae were picked on NGM dishes seeded with OP50-1 culture. Spontaneous pumping of animals on food was video recorded (Powershot G9, Canon, Tokyo, Japan). The NGM dish was manually directed to allow a continuous video recording of a freely moving animal. The grinder movements (pumps) were visually counted for 20 s, to gain a representative number of pumps per animal (about 80–100 pumps for wild type). Loss of focal plane, e.g., due to animals crossing borders of the bacterial lawn, and concomitant impossibility to count pumping, led to exclusion of single animals from the analysis. For the recording of swimming cycles, a 96-well plate was filled with 100 μl NGM and 200 μl M9 buffer. Up to ten young adult animals were picked into one well. Swimming cycles were video recorded (Powershot G9, Canon, Japan) for 60 s and visually counted.

Optical Paced Electropharyngeogram-Recording With the ScreenChip^{TM} System

One day before experiments, L4 larvae were transferred onto NGM plates seeded with OP50-1 from bacterial suspensions supplemented with ATR (Sigma-Aldrich, United States) with a final concentration of 0.3 mM. Prior to recording, young adult animals were collected in M9 buffer and washed three times. S107 (MedChemExpress, United States) was added in a final concentration of 50 μM (0.1% DMSO) and incubated for 30 min. EPGs were recorded with the ScreenChip^{TM} System (*InVivo* Biosystems (formerly Nemametrix), United States) according to the manufacturer's manual. Worms were sucked into ScreenChips^{TM} 30 or 40, with respect to their size. Pharyngeal pumping was induced by applying 1.5 mW/mm^2 of 470 nm light in 50 ms pulses through an inverse microscope (Leica DM IL LED) equipped with a 470 nm LED (KSL 70, Rapp OptoElectronic, Germany), 10x objective (Leica HI Plan I 10x/0.22 ∞/- Ph1), as well as a GFP filter set (450–490 nm excitation, dichroic mirror 510 nm, 515 nm long pass emission, Leica, Germany). Worms in the reservoir of the ScreenChip^{TM} were protected from blue light with red foil (color filter, foil, primary red, Frederiksen, Denmark). Stimulation was performed with 4 Hz pulses for 60 s. Recordings were performed with the software NemAcquire and analyzed with NemAnalysis (both open source from *InVivo* Biosystems). Further analysis was performed in OriginPro (OriginLab, United States).

Conventional Electropharyngeogram-Recording With Optical Pacing

As for the ScreenChip^{TM} recordings, L4 larvae were transferred 1 day before experiments onto NGM plates seeded with OP50-1 supplemented with 0.3 mM ATR. We performed EPG recordings on cut head preparations; therefore, the head of an animal was cut away from the body with a scalpel (Braun Aesculap, Germany) directly posterior to the terminal bulb. Electrophysiology was performed as described in the study of Schuler et al. (2015). The tip of the worm head was sucked into an EPG-suction electrode. For optical pacing with a 470 nm LED (KSL-70, Rapp Optoelectronics, Germany), the pharynx was positioned below a 60x water immersion objective (LUMIplan FI/IR, 0.9 NA) and an EGFP-ET filter set (AHF Analysentechnik AG, Germany) was used. Recording of EPGs and triggering of light pulses were synchronized by the PatchMaster software (Heka, Germany).

The pharynx was stimulated with 470 nm light pulses (1.5–2 mW/mm^2) in a stress test. The stimulation frequency was increasing stepwise: 1–7 Hz; pulse duration: 35 ms, over a period of 5 s each. The initial stimulation frequency of 1 Hz was held for 15 s to allow a stable rhythm without additional spontaneous pumps. The Review software (Bruxton Corporation, Seattle, WA, United States) was used to translate PatchMaster files. The pump rate was analyzed by AutoEPG (Dillon et al., 2009) (kindly provided by Dr. Christopher James, Embody Biosignals Ltd., United Kingdom), afterward every recording was checked for possible misdetected EPGs. Every EPG showing a clear E (contraction) and R (relaxation) peak was marked and added for subsequent analysis. The highest stimulation frequency (1, 2, 3, 4, 5, 6, or 7 Hz), where every light pulse was followed by each one EPG/pump (for the complete 5 s), was selected as the maximal pump rate per animal.

Optically Paced Calcium Imaging

We have chosen a genetically encoded calcium indicator (GECI) to specifically target PMCs. Additionally, the nematodes cuticle would prevent uptake of bath-applied dyes. RCaMP1h is a red-shifted GECI that allows a parallel blue-light stimulation of ChR2 (Akerboom et al., 2013).

A day before experiments, L4 larvae were transferred onto NGM plates seeded with OP50-1 from bacterial suspensions supplemented with ATR with a final concentration of 0.3 mM. For imaging of RCaMP1h in *C. elegans* pharynx, young adult animals were placed onto 10% agarose pads (M9 buffer) mounted on microscope slides and were immobilized with polystyrene beads (0.1 μm diameter, at 2.5% w/v, Sigma-Aldrich, United States). Imaging was performed on an inverted microscope (Zeiss Axio Observer Z1), equipped with 40x oil immersion objective (Zeiss EC Plan-NEOFLUAR 40x/N.A. 1.3, Oil DIC ∞/0.17), a 470 nm LED for ChR2 excitation (light pulses of 50 ms, 1.5 mW/mm^2, 4 Hz), and a 590 nm LED for RCaMP1h excitation (∼0.3 mW/mm^2) (both KSL-70, Rapp OptoElectronic, Hamburg, Germany), a 80R/20T beam splitter (F21-002, AHF Analysentechnik, Germany), and an EMCCD Camera (Evolve 512 Delta, Photometrics; EM-gain: 25), as well as the following filters: GFP/mCherry (479/585 nm) Dualband ET Filter was combined with a 647/57 nm emission filter and a 605 nm beamsplitter (F56-019, F37-647, and F38-605, respectively, all AHF Analysentechnik, Germany). The terminal bulb of one pharynx was focused. Movies were acquired at 2 ms exposure (ca. 156 fps) and a binning of 4 × 4. The blue-light stimulation started 3 s after the onset of the video-recording and lasted for 10 s to enable the achievement of a plateau phase. Raw image sequences were analyzed *via* ROI selection of signal (terminal bulb of the pharynx) and background, a multi-measure function in ImageJ (National Institutes of Health, United States). Changes in fluorescence were calculated as $\Delta F/F_0$. The amplitude of $\Delta F/F_0$ was analyzed during the plateau phase (10–13 s). Importantly, only worms that were able to follow light stimulation have been included for analysis. Experiments were performed in the dark and illumination protocols were applied as short as possible to avoid degradation of photosensitive proteins or substances.

Statistics

Mean values, SEM, and further statistics (two-sample *t*-test or 1-way ANOVA with the Bonferroni *post-hoc* test) were calculated with OriginPro (OriginLab, United States). Based on experimental settings, every animal was tested only once.

RESULTS

Effects of the Insertion of Homologous Catecholaminergic Polymorphic Ventricular Tachycardia Mutations on Spontaneous Pumping and Swimming

After working with extrachromosomal arrays in a previous study (Fischer et al., 2017), we now inserted six different CPVT mutations into *C. elegans unc-68* or *csq-1* (**Table 1**) *via* different CRISPR-Cas9 approaches (Ward, 2015; Prior et al., 2017) and introduced them into our optogenetic arrhythmia model, a *C. elegans* strain expressing ChR2 in PMCs (Schuler et al., 2015; Fischer et al., 2017).

We characterized those genome-edited strains regarding their spontaneous pump rate on food to assess their effect on pharyngeal muscles under normal, non-stressed conditions (**Figure 1A**). The usual pump rate of young adult wild-type animals is about 4.5 Hz (**Figure 1B**). One allele, S2378L, showed a significant reduction of the spontaneous pump rate in comparison to wild-type allele (**Supplementary Videos 1, 2**). Analysis of swimming cycles, reflecting the influence of UNC-68 on the function of BWM and the nervous system, revealed a reduction of the swimming ability in R414Q and Q4623R (**Figure 1C**). Either the need for movement in the fluid substrate (stress) or the different type of muscle cells, as well as the influence of the nervous system present for BWM, may play a role in these diverse effects. Importantly, we have shown previously that the pharyngeal nervous system does not influence EPG parameters during optogenetically paced pumping (Schuler et al., 2015).

For several CPVT mutations, a disturbance of calstabin2 binding is suggested (Wehrens et al., 2003; Lehnart et al., 2004; Meli et al., 2011). For one of those mutations, R4497C, we observed in a previous study effects in *C. elegans* (Fischer et al., 2017). Thus, we now investigated the effect of calstabin in our model. Calstabin2 stabilizes the closed conformation of RyR (Brillantes et al., 1994). A clear calstabin2 homolog is yet to be identified in *C. elegans*, which contains 8 members of the *fkb* gene class. We tested the presumably best homolog FKB-2 (Fischer et al., 2017) and found, as for the majority of our tested CPVT mutations, minor/no reduction of spontaneous pump rate on food and swimming (**Figures 1B,D**), indicating no severe effects on BWM or under basal pumping conditions.

Three Mutations of UNC-68 Cause an Arrhythmic Phenotype

We performed electrophysiological measurements with a microfluidic ScreenChip^{TM} system (*InVivo* Biosystems, United States) that enables higher throughput EPG recordings of

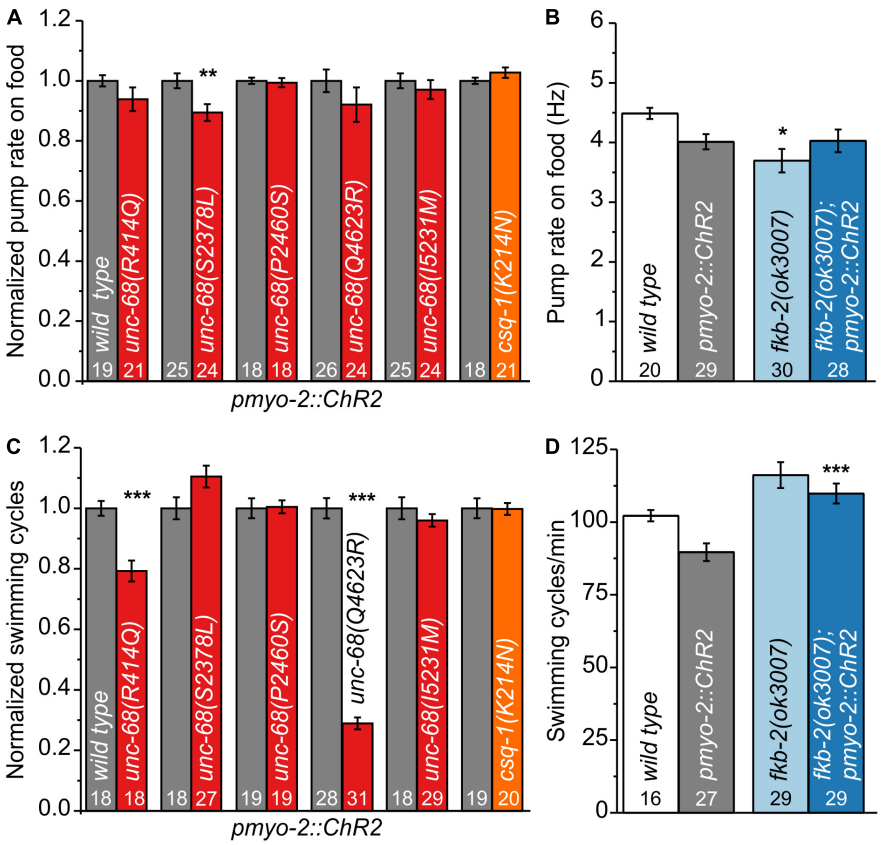

FIGURE 1 | Effect of catecholaminergic polymorphic ventricular tachycardia (CPVT) alleles and *fkb-2* deletion on pharyngeal muscle cells (PMCs) and body-wall muscles (BWMs). **(A)** *Unc-68(S2378L)* shows a reduced normalized pump rate compared to the respective wild type (wt) control strain (young adult animals). **(B)** Deletion of *fkb-2* [*fkb-2(ok3007)*] has no/minor effect on spontaneous pump rate on food. **(C)** Alleles R414Q and Q4623R show a reduction of normalized swimming cycles. **(D)** No significant effect of *fkb-2* deletion on numbers of swimming cycles in comparison to the respective wild-type control. Whereas *fkb-2* deletion in the *pmyo-2::ChR2* background shows an increased number of swimming cycles in comparison to *pmyo-2::ChR2*. Bar graphs display mean values ± SEM. One-way ANOVA with the Bonferroni *post-hoc* test **(B,D)** or two-sample *t*-test for the comparison of only two mean values **(A,C)**: $^{*}p \leq 0.05$, $^{**}p \leq 0.01$, and $^{***}p \leq 0.001$.

intact nematodes in combination with optogenetic stimulation. We observed a significantly reduced ability to follow 4 Hz pacing over a period of 60 s for three of the CPVT alleles *unc-68(S2378L)*, *(P2460S),* and *(Q4623R)* (**Figure 2** and **Supplementary Figure 1**). This was indicated either by an inability to follow more than about every second stimulus with a pump movement or by a complete stop of pumping. In addition, the maximal pump rate of the different alleles was determined in a stress test with conventional EPG recordings on single cut-head preparations (Raizen and Avery, 1994; Cook et al., 2006). The frequency of light pulses was increased here stepwise from 1 to 7 Hz (**Figure 3**). Wild-type animals and most of the mutants are able to follow 5 Hz pacing, while *unc-68(Q4623R)*, similar as already shown for *unc-68(R4743C)* (Fischer et al., 2017), follows only about every second pump or stops pumping altogether.

The electrophysiological findings of ScreenChip^{TM} and stress test recordings manifest a "worm arrhythmia" phenotype of several CPVT-related mutations in our optogenetic arrhythmia model. For all alleles showing reduced ability to follow the optogenetic stimulation, a decreased binding of calstabin2 was detected by another group (Wehrens et al., 2003; Lehnart et al., 2004). Nevertheless, a reduced calstabin2 binding of those mutations could not be verified by different groups and is still discussed controversially (Jiang et al., 2005; George et al., 2006).

Stabilization *via* FKB-2 Is Involved in the Disease-Causing Mechanism of Q4623R and P2460S

To shed light on the disease-causing mechanism of the three CPVT mutations that show effects on pharyngeal pump ability in *C. elegans,* we decided to use a 1,4-benzothiazepine known to enhance calstabin binding and to reduce leakiness of RyR. The 1,4-benzothiazepine derivative JTV519 (a.k.a. K201) is a non-specific blocker of sodium, potassium, and calcium channels (Kaneko et al., 2009), and there are "mixed" results for JTV519, with side-effects outweighing benefits (Driessen et al., 2014). Thus, we decided to test a RyR2-specific compound (S107, CAS 927871-76-9) (Bellinger et al., 2008). A more specific 1,4-benzothiazepine derivative, which in the rodent model enhanced the binding of calstabin2 to the mutant RyR2-R2474S channel,

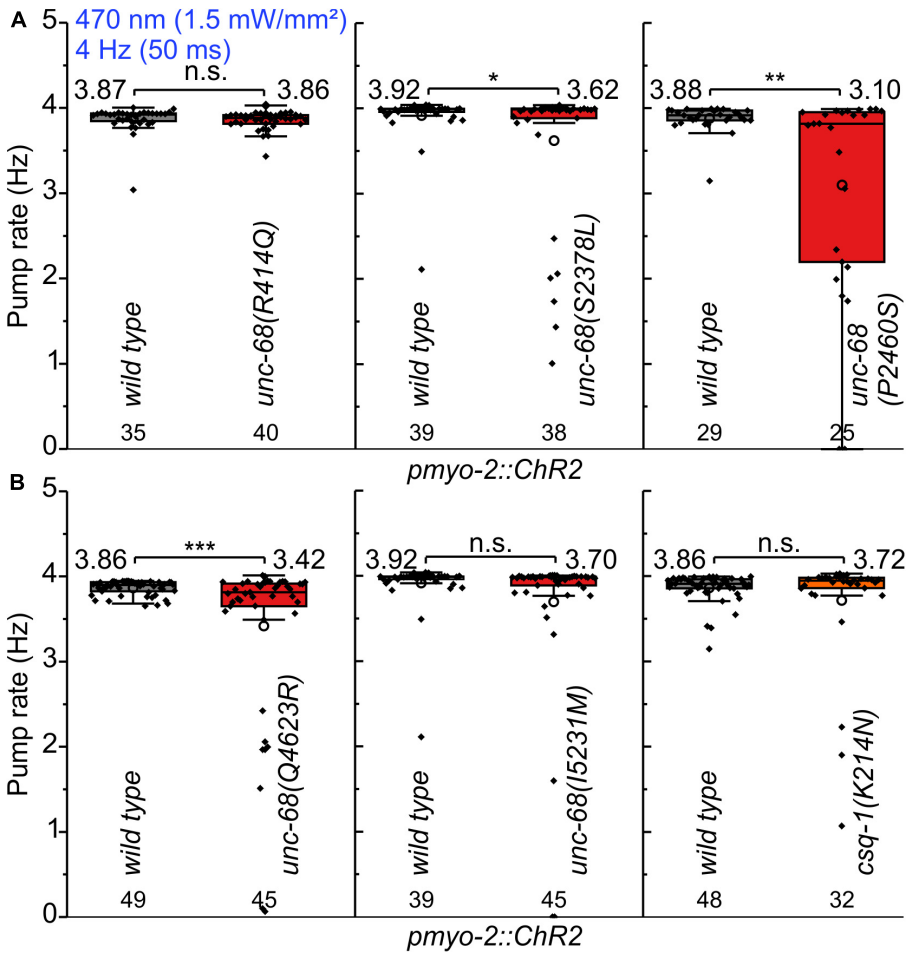

FIGURE 2 | Pumping ability of CPVT mutation bearing strains upon 4 Hz stimulation. **(A,B)** In ScreenChip^{TM} recordings, S2378L, P2460S, and Q4623R show a reduced pump rate compared to wild type in *pmyo-2::ChR2* background. Box plot (25%, 75%; whisker: 1.5 IQR) includes every data point (rhomb), mean (circle), and median (line). Mean values, N-numbers, and significance levels (asterisks) are next to the corresponding box. Two-sample *t*-test: n.s., not significant, $^{*}P \leq 0.05$, $^{**}P \leq 0.01$, and $^{***}P \leq 0.001$.

inhibited the channel leak and prevented cardiac arrhythmias (Lehnart et al., 2008). In a previous study, we found, after a 30 min incubation in S107 (50 μM), a complete rescue of the pumping ability of extrachromosomal R4743C mutation bearing nematodes (Fischer et al., 2017). In addition, there was no rescue of pumping ability in the deletion mutant, indicating an *unc-68* (RyR) specific effect of S107, that was not elicited *via* other, unknown channels (Fischer et al., 2017). In ScreenChip^{TM} recordings, during 4 Hz blue light stimulation, we detected a significant rescue of the pumping ability after S107 treatment in two of the three CPVT variants tested (P2460S and Q4623R) (**Figure 4**). Importantly, this rescue was absent for P2460S in the *fkb-2* deletion background (**Figure 4B**), indicating that the drug requires the presence of calstabin/FKB-2 to exert beneficial effects on the RyR. While in the case of Q4623R, no significant loss of pumping ability was observed in the *fkb-2* deletion background at all (**Figure 4C**), as well indicating the involvement of calstabin2 in the disease-causing mechanism. Variant S2378L did not show a rescue upon S107 incubation (**Figure 4A**), and no effects of S107 appeared in variant I5231M (**Supplementary Figure 2**). A mutant that *per se* showed no reduction of pump ability in the arrhythmia model (**Figure 2**).

In line with our results showing the FKB-RyR stabilizing effect of the 1,4-benzothiazepine derivative S107 in UNC-68 variants R4743C (Fischer et al., 2017), P2460S, and Q4623R (homologous to RyR2-R4497C, P2328S, and Q4201R), a decreased binding affinity for calstabin2 is discussed by another group for the respective RyR2 mutations (Wehrens et al., 2003; Lehnart et al., 2004). Whereas other groups could not confirm an alteration of the calstabin2-RyR2 interaction for RyR2-R4497C, -S2246L, -R2474S, -Q4201R, and -I4867M (Jiang et al., 2005; George et al., 2006). In the case of RyR2-I4867M (**Figure 2**) and -R2474S (Fischer et al., 2017), we observed no "worm arrhythmia" phenotype in EPG recordings of the related nematode allele. Possibly, this could be based on the evocation of not only mild Ca^{2+} handling alterations in those two mutant alleles but also differences between the structure of UNC-68 and RyR2, as well as FKB-2 and calstabin2, might be possible reasons. Nevertheless,

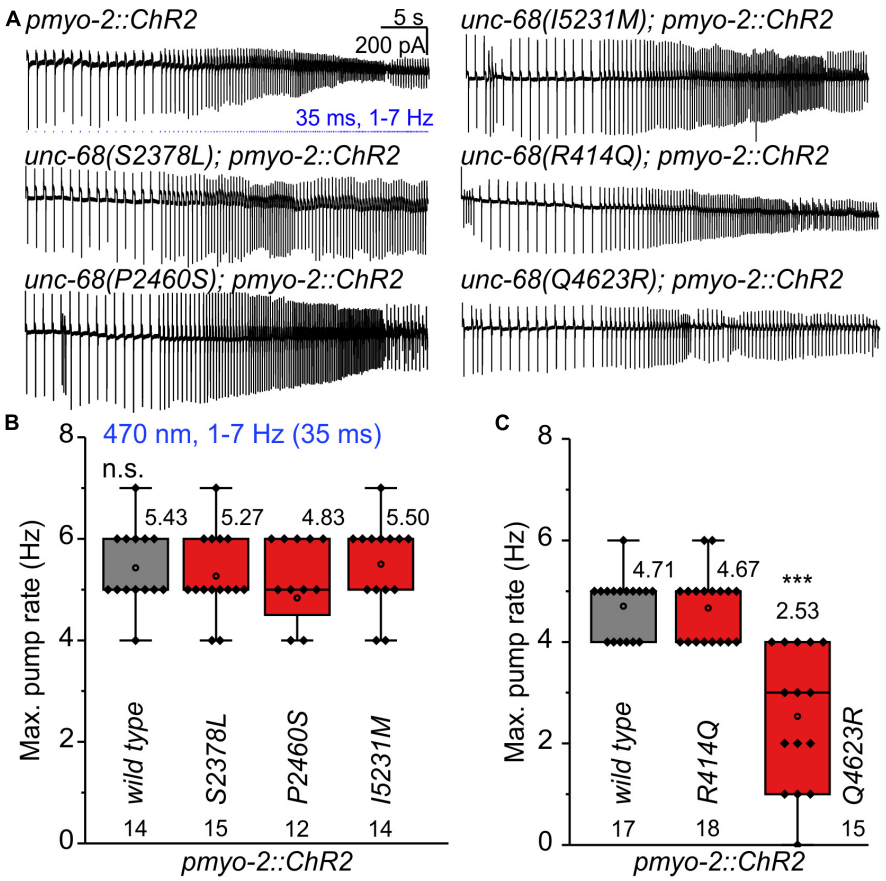

FIGURE 3 | Stress test (1–7 Hz) to determine the maximal pump rate of CPVT mutation-bearing strains. **(A)** Original recordings of electropharyngeograms (EPGs) obtained by electrophysiological characterization of cut-head preparations. Application of 1 Hz blue light pulses (1.5 mW/mm^2, 35 ms) for 15 s followed by a stepwise increase (every 5 s) from 2 to 7 Hz. **(B,C)** *unc-68(Q4623R)* shows a reduced maximal pump rate in comparison to wt. Since pharyngeal pump ability sometimes varies among different experimental days, likely due to experimental conditions (room temperature, light-sensitivity of ATR), mutant alleles were always compared to the control animals recorded in the same batch of experiments. Box plots include every data point (rhomb), mean (open circle), and median (line). N-numbers, mean values, and significance levels (asterisks), referring to respective wt controls, are located either below or above the corresponding boxes. One-way ANOVA with the Bonferroni *post-hoc* test was performed: n.s., not significant, and ***$P \leq 0.001$.

in this study, we were able to shed light on the mechanism of UNC-68-P2460S and -Q4623R and proved the controversially discussed involvement of FKB-2/calstabin2 in functional assays in an intact organ of a living animal.

Several Mutations of *unc-68* Cause Alterations in Ca^{2+} Handling

We used Ca^{2+} imaging with genetically encoded indicators that we have established earlier (Akerboom et al., 2013) and that can be used in combination with optogenetics to examine intracellular calcium alterations evoked by CPVT mutations. In the present study, we used the Ca^{2+} indicator RCaMP1h, expressed in PMCs of respective CPVT-related alleles, together with ChR2. We stimulated the pharynxes with 50 ms blue light pulses at 4 Hz for a period of 10 s (**Figures 5**, **6**). This allows the generation of a comparable number of pumps (and pump frequency) that can be easily compared within the different alleles and control animals. The light stimulation induced a significant increase of the change (Δ) of F/F_0 RCamP1h fluorescence, but only when all-trans-retinal (ATR, the cofactor of ChR2) was present (**Figures 5A–C**). This demonstrates the ability to measure the cytosolic entry of Ca^{2+} during ChR2 stimulation.

Upon blue light stimulation, the *unc-68* null allele *r1162* shows a strong rise of fluorescence ($\Delta F/F_0$) (**Figures 5D–F**). Since UNC-68 is not present, this increase likely depends on other proteins, e.g., the voltage-gated Ca^{2+} channel, and demonstrates the disturbance of cytosolic Ca^{2+} concentration and its regulation by compensatory effects in this allele. Indeed, an application of Nemadipine-A, a specific inhibitor of the *C. elegans* voltage-gated Ca^{2+} channel EGL-19 (Kwok et al., 2006; Schuler et al., 2015), reversed the strong Ca^{2+} rise in the *unc-68* null allele (20 μM, **Supplementary Figures 3A,C,D**). We did not expect a major effect of EGL-19 in CPVT-related mutations since the variants express UNC-68 protein with only one point-mutation, in contrast to the "channel null" allele r1162 that lacks a 3.7 kb area including all transmembrane domains. The null allele exhibits strong effects on swimming and pumping

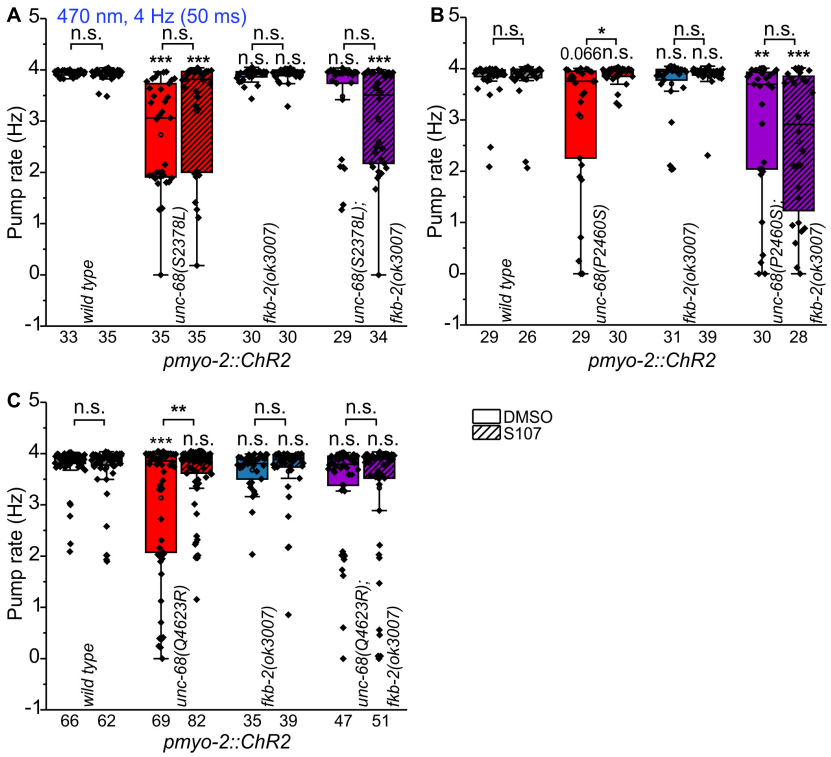

FIGURE 4 | Effect of the benzothiazepine S107. In ScreenChip™ recordings of EPGs under blue light stimulation (4 Hz, 50 ms), the effect of S107 (50 μM, 30 min pre-incubation, shaded boxes) in comparison to the vehicle DMSO (0.1% in M9 buffer) on pump rate of UNC-68 mutants S2378L **(A)**, P2460S **(B)** and Q4623R **(C)** was determined. Alleles have been crossed with a *fkb-2* deletion [*fkb-2(ok3007)*, violet boxes] to check for drug-induced UNC-68 stabilization *via* FKB-2. S107 rescues UNC-68 function of Q4623R and P2460S only in FKB-2 wt background. Box plots include mean (open circle) and median (line). Significance levels (asterisks), referring to respective controls (wild type, either with or without S107), are located above the corresponding boxes. Comparison of each strain with and without S107 treatment is indicated above the line pointing on the respective boxes. N-numbers as indicated. One-way ANOVA with the Bonferroni *post-hoc* test was performed: n.s., not significant, $^{*}P \leq 0.05$, $^{**}P \leq 0.01$, and $^{***}P \leq 0.001$.

on food (Fischer et al., 2017), while the three CPVT-related mutations show either no or less effect on swimming cycles and no or up to only ∼10% reduction of spontaneous pumping (**Figure 1**). Thus, their effects, especially in pharynx muscle, are weaker and thus implicating only a minor need for compensatory effects. Consistently, the application of Nemadipine-A (20 μM) does not reverse the strong Ca^{2+} rise of the Q4623R allele (**Supplementary Figures 3B–D**).

No significant difference of the amplitude of $\Delta F/F_0$ in comparison to wild type was observed for the *csq-1* deletion, while reduced spontaneous pumping on food and reduced ability to follow optogenetic pacing have previously been shown for this allele. Nevertheless, one has to take into account that the effect of *csq-1(ok2672)* on pumping ability during light stimulation is about 3-fold smaller in comparison to *unc-68(r1162)* (Fischer et al., 2017).

Alleles S2378L and Q4623R exhibit a significant increase of the amplitude of $\Delta F/F_0$ (**Figures 6A–C,G–I**), presumably based on UNC-68 leakiness during light stimulated pumping. In the case of allele Q4623R, this increase is reversed by the 1,4-benzothiazepine derivative S107 (**Supplementary Figure 4**).

In contrast, the amplitude of $\Delta F/F_0$ of allele P2460S is not increased compared with wild type (**Figures 6D–F**). Allele P2460S showed the strongest arrhythmic phenotype during 4 Hz stimulation (**Figure 2**), thus the reduced changes of absolute fluorescence might result from impaired or weaker pumping during stimulation. Also, the deletion of *fkb-2* leads to the reduced amplitude of $\Delta F/F_0$ (**Supplementary Figure 5**), suggesting either involvement of a possible second FKB protein or, as discussed for the P2460S allele, due to impaired pumping. We observed no change in the amplitude of $\Delta F/F_0$ for CPVT-related alleles without an arrhythmic phenotype (**Supplementary Figure 6**).

Possible Electrostatic Interaction of UNC-68 and CSQ-1 Plays No Role in Pharyngeal Muscle Cells

We were also interested in the interaction of UNC-68 and CSQ-1 in *C. elegans* pharynx, as differences in the interaction between the two proteins are known for human and *C. elegans*. In mammals, CASQ2 is linked to the RyR through interactions with triadin (Guo and Campbell, 1995) and junctin (Jones et al., 1995). Whereas for junctin no CPVT-causing mutations exist so far, several mutations of triadin have been identified that lead to decreased levels of the protein itself and cause

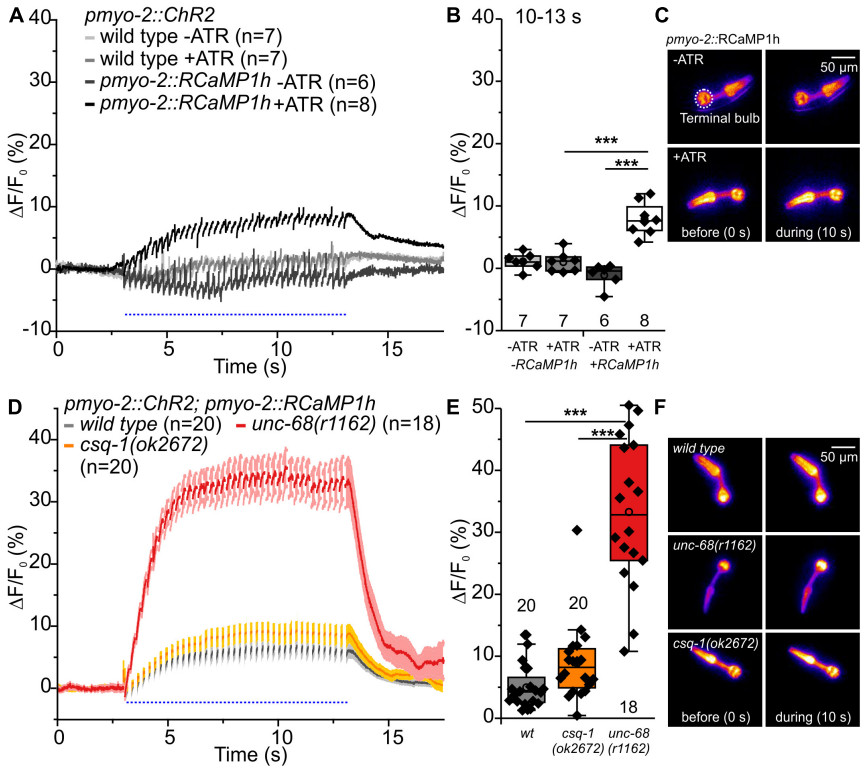

FIGURE 5 | RCaMP1h Ca^{2+} imaging in PMC of *unc-68* and *csq-1* alleles. **(A)** Increase of $\Delta F/F_0$ during stimulation (4 Hz, 50 ms, 470 nm) and **(B)** amplitude of $\Delta F/F_0$ during plateau phase (time period: 10-13 s). An increase of $\Delta F/F_0$ (%) upon light stimulation is only present in ChR2 and RcaMP1h co-expressing pharynxes and in the presence of the ChR2 cofactor ATR. **(C)** False-color representations of fluorescence intensity of ChR2 and RcaMP1h co-expressing pharynxes raised with and without ATR before blue light stimulation (0 s) and during stimulation (∼10 s). The terminal bulb of the pharynx, which is used for analysis, is labeled with a circle. **(D,E)** The null allele of *unc-68*, but not of *csq-1*, leads to an increase of cytosolic Ca^{2+} concentration. **(F)** Exemplary false-color representation of fluorescence intensity. Only worms that were able to follow 4 Hz stimulation have been included for analysis. Depicted is the mean of $\Delta F/F_0$ (%) without **(A)** or with SEM **(D)**, time periods (∼50 ms), including unspecific peaks induced by blue light stimulation are not displayed here for a better outline. Box plots include every data point (rhomb), mean (open circle), and median (line). N-numbers and significance levels (asterisks) are located either below or above the corresponding boxes. One-way ANOVA with the Bonferroni *post-hoc* test was performed for comparisons of the mean values during the plateau phase of the fluorescence rise (10–13 s): $^{***}P \leq 0.001$.

the disease (Roux-Buisson et al., 2012; Rooryck et al., 2015). For the skeletal RyR1, three negatively charged residues of the luminal loop appear to be critical for the association with triadin (Lee et al., 2004). Based on the genomic sequence, there are no obvious homologs of junctin and triadin in *C. elegans*. Therefore, Cho et al. (2007) suggested a physical interaction between UNC-68 and CSQ-1, which might be due to positively charged residues at the C-terminal end of CSQ-1, interacting with negatively charged residues of two luminal UNC-68 loops. In an *in vitro* binding assay, they could show with GST-RyR1 loop 1 and 2 fusion proteins an interaction with CSQ-1. Because of the new insights into RyR structure (Yan et al., 2015; Zalk et al., 2015), there seems only one large luminal loop between S5 and S6 (RyR2: aa 4792-4808), which is also shorter than the formerly suggested loop 2. We replaced *via* CRISPR-Cas9 genome editing negatively charged residues of the proposed S5-S6 luminal loop, which is conserved in *C. elegans unc-68* (aa5156-YVQ**E**G**EE**G**EE**P**D**RKC-5170), with the neutral residue alanine (YVQ**A**G**AA**G**AA**P**A**RKC) to prevent an electrostatic interaction with the positively charged residues of CSQ-1.

In functional assays, we then investigated the effect of UNC-68 mutated in the putative CSQ direct interaction site. No effect of mutated UNC-68 was observed on spontaneous pumping on food (**Figure 7A**), whereas swimming was significantly impaired (**Figure 7B**). Through ScreenChip^{TM} EPG recordings of arrhythmic events, no reduced ability to follow a 4 Hz long-term light stimulation in the optogenetic arrhythmia model was observed (**Figure 7C**). In addition, the maximal pump rate of cut-head preparations obtained in EPG recordings was not affected (**Figure 7D**). Ca^{2+} imaging of the UNC-68 neutral luminal loop mutant reveals, as for the *csq-1* deletion (**Figures 5D–F**), no significant change of intracellular Ca^{2+} concentration ($p = 0.06$) based on RCaMP1h fluorescence ($\Delta F/F_0$) upon light stimulation (**Figures 7E–G**). Since the proposed interaction of positively charged residues at the C-terminal end of CSQ-1 and negatively charged residues of UNC-68 luminal loop should be eliminated after an exchange with neutral luminal loop residues, a decreased amount of Ca^{2+} near the channel pore for transport *via* UNC-68 would be expected, subsequently resulting in a decrease of the cytosolic Ca^{2+} concentration. Combined with a lack of obvious differences in the distribution of CSQ-1::CFP

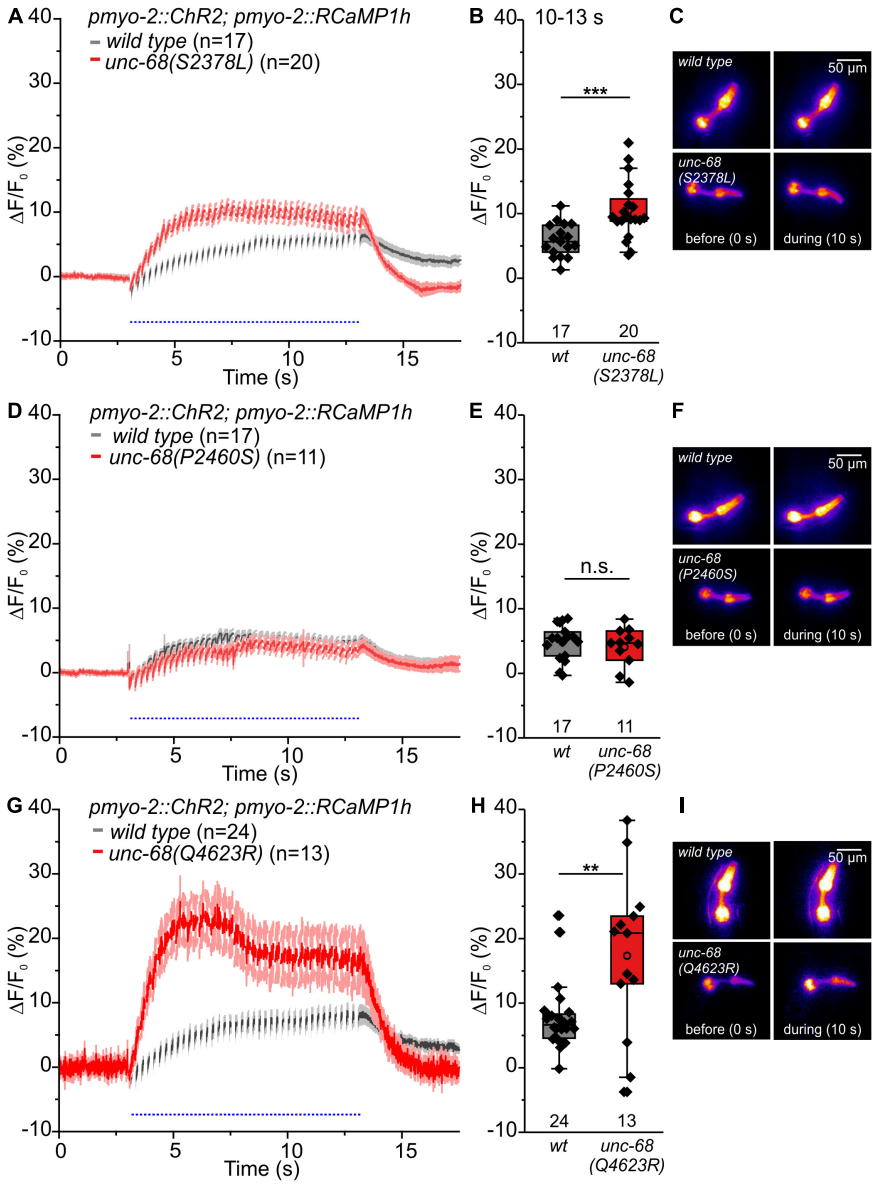

FIGURE 6 | RCaMP1h Ca^{2+} imaging in PMC reveals effects of CPVT mutations inserted into *unc-68* on cytosolic Ca^{2+} concentration. **(A,B,G,H)** Alleles Q4623R and S2378L show an increase of $\Delta F/F_0$ in comparison to wt animals upon light stimulation (10–13 s). **(D,E)** Whereas allele P2460S does not exhibit a significant change (10–13 s). **(C,F,I)** Exemplary false-color representation of fluorescence intensity. Only worms that were able to follow 4-Hz stimulation have been included for analysis. Depicted is the mean of $\Delta F/F_0$ (%) with SEM, time periods (~50 ms), including unspecific peaks induced by blue light stimulation, are not displayed here for better outline **(A,D,G)**. Box plots include every data point (rhomb), mean (open circle), and median (line). N-numbers and significance levels (asterisks) are located either below or above the corresponding boxes. *T*-test was performed for comparisons of the mean values during the plateau phase of the fluorescence rise (10–13 s): n.s., not significant, $^{**}P \leq 0.01$, and $^{***}P \leq 0.001$.

in PMCs and BWMs (**Supplementary Figure 7**), there is likely no influence on CSQ-1 interaction in PMCs by the exchange of luminal loop residues.

DISCUSSION

We have previously established the *C. elegans* pharynx for the analysis of arrhythmogenic CPVT-mutations, but also of Long QT-8 mutations affecting the $Ca_V1.2$ voltage-gated calcium channel (Schuler et al., 2015; Fischer et al., 2017). An optogenetic stimulation of the pharynx *via* ChR2(H134R) enables pacing up to 6 Hz for periods of > 1 min. In the present study, we established the insertion of CPVT mutations *via* CRISPR-Cas9 genome-editing into the optogenetic arrhythmia model. In contrast to extrachromosomal expression, genome-editing allows a stable expression level and a protein distribution that reflects the wild-type condition. In addition,

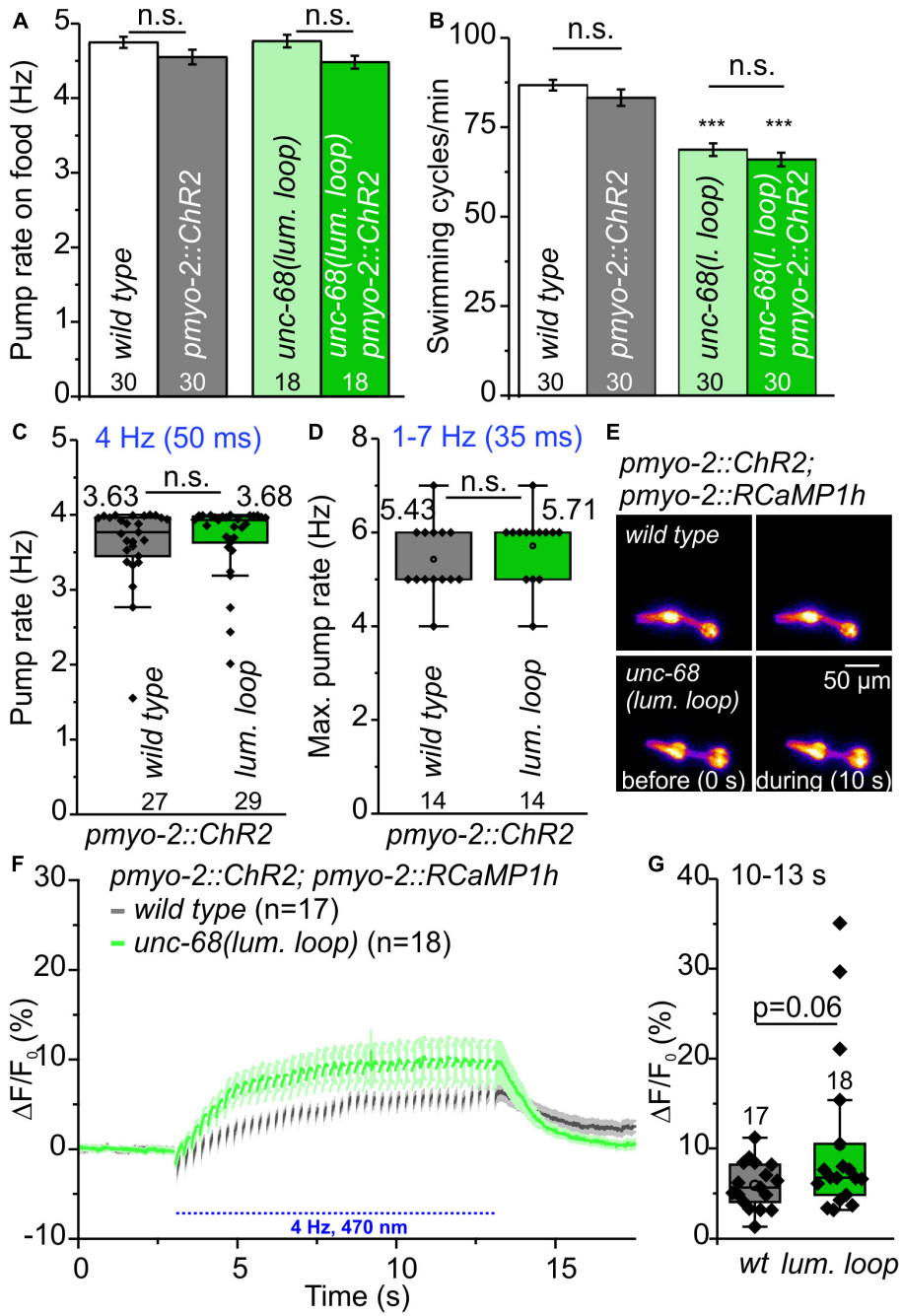

FIGURE 7 | Characterization of neutral amino acid insertion into UNC-68 luminal loop (lum. loop). **(A,B)** No effect on spontaneous pumping on food and reduced number of swimming cycles/min evoked by neutral luminal loop insertion. **(C)** Pumping ability is not reduced in the ScreenChip^{TM} system (4 Hz stimulation, 60 s). **(D)** No effect on maximal pump rate of cut-head preparations in the stress test. **(E)** Exemplary false-color representation of fluorescence intensity. **(F)** Mean ± SEM of the $\Delta F/F_0$ of RCaMP1h fluorescence before and during light stimulation. **(G)** The amplitudes of $\Delta F/F_0$ (mean: 10–13 s) show no significant difference between wild-type and neutral luminal loop-expressing animals. Bar graphs represent mean ± SEM, box plots include data points (rhomb), mean (circle), and median (line). N-numbers and significance levels (asterisks) are displayed. One-way ANOVA with the Bonferroni test **(A,B)** or a two-sample *t*-test **(C,D,G)**: n.s., not significant, and $^{***}P \leq 0.001$.

there is no requirement of a manual preselection of transgenic animals, which facilitates higher throughput experiments. For the first time, we implemented here higher throughput electrophysiological recordings of *C. elegans* with optogenetic stimulation by combining a microfluidic ScreenChip^{TM} system (*InVivo* Biosystems) with an Arduino controlled high power LED. This allows precise light stimulation in combination with EPG recordings, succeeded by an automated analysis of

the recordings. In sum, it is an excellent option for patient-specific drug testing.

In this study, three of the CPVT alleles *unc-68(S2378L)*, *(P2460S),* and *(Q4623R)* show an arrhythmic phenotype characterized by a significantly reduced ability to follow 4 Hz pacing in EPG recordings (**Figure 2**). In addition, alleles S2378L and Q4623R exhibit a significant increase of the amplitude of $\Delta F/F_0$ in RCaMP1h Ca^{2+} imaging (**Figure 6**). Corresponding results have been observed in induced pluripotent stem cell-derived cardiomyocytes (iPSC-CM), expressing two different CPVT mutations. Analysis of local Ca^{2+} release events in iPSC-CM loaded with the Ca^{2+} indicator Fluo-4 showed that CPVT cardiomyocytes bearing a mutation in a proposed calstabin binding site (RyR2-F2483I, not conserved in *unc-68*) exhibit higher amplitudes and longer durations of spontaneous local Ca^{2+} release events already at a basal state (Fatima et al., 2011). Also, arrhythmias in iPSC-CM carrying RyR2-R420Q and CASQ2-D307H, evoked by isoproterenol, a synthetic catechol compound, or even sometimes pacing alone, were associated with an elevation in the resting level, probably resulting from a prominent diastolic intracellular Ca^{2+} rise (Novak et al., 2012, 2015).

Up to now, β-blockers are the first therapeutic option for patients with CPVT. Although these substances, which block the binding sites for adrenaline and noradrenaline on β-adrenergic receptors, reduce the occurrence of ventricular tachycardia, 30% of patients still experience cardiac arrhythmias and eventually require cardioverter-defibrillator implantation to prevent cardiac arrest (Priori et al., 2002; Liu et al., 2008). *C. elegans* itself lacks (nor)adrenalin as well as the respective receptors (Sanyal et al., 2004). Tyramine receptor 3 (*tyra-3*), a G-protein-coupled catecholamine receptor for the invertebrate noradrenaline-like neurotransmitters tyramine and octopamine, acts in sensory neurons but is not expressed in PMCs (Bendesky et al., 2011). Nevertheless, since there is a strong motivation to identify more specific drugs to treat CPVT arrhythmias that act directly on the RyR2, particularly to enable treatment with respect to the various mutations affecting the different domains of RyR2 or CASQ2, and their interactions with other proteins, *C. elegans* is a valid model in this respect.

The rycal S107, a 1,4-benzothiazepine derivative, is such a RyR-specific compound (Bellinger et al., 2008). S107 enhances the binding of calstabins to the RyRs. In the rodent model, it inhibited the channel leak and prevented cardiac arrhythmias by enhancing the binding of calstabin2 to mutant RyR2-R2474S channels (Lehnart et al., 2008). Also, in iPSCs carrying the CPVT mutation I4587V, the development of DADs in the presence of isoproterenol was significantly suppressed by S107 (Sasaki et al., 2016). Furthermore, there are observations that fixing RyR2-mediated ER Ca^{2+} leak with the S107 improves cognitive and locomotor function in a murine model of Huntington's disease (Dridi et al., 2020). In the treatment of RYR1-related myopathies, S107 normalizes an increased calcium leak and activity of calcium-activated proteases (Kushnir et al., 2020). S107 fixes Ca^{2+} leak *via* RyR1 and improves exercise capacity in aging (Andersson et al., 2011) and may represent a new therapeutic approach for Duchenne muscular dystrophy (Bellinger et al., 2009). In a previous study, we found that S107 rescues the pharyngeal pumping ability of CPVT-mutation R4497C [UNC-68(R4743C)] carrying nematodes (Fischer et al., 2017). This is a specific effect of S107 on RyR since no rescue of pumping ability was observed in an *unc-68* deletion mutant (Fischer et al., 2017). For the R4497C mutation, a disturbance of calstabin2 binding is suggested (Wehrens et al., 2003) but is controversially discussed (Liu et al., 2006; Fernández-Velasco et al., 2009). In the present study, three out of five chosen and tested RyR2 mutations are suggested to cause a disturbance of calstabin2 mediated RyR stabilization. In contrast to the two other CPVT mutations included in this study, we observed only for those suggested to bear disturbed calstabin binding an arrhythmia-like phenotype, characterized by a reduced ability to continuously follow light stimulated 4 Hz pacing with a pharyngeal pump movement. The CPVT alleles *unc-68(S2378L)*, *(P2460S)*, and *(Q4623R)* (RyR2-S2246L, -P2328S and -Q4201R, respectively) had a significantly reduced ability to follow 4 Hz pacing over a period of 60 s, indicated by either following about every second stimulus with a pump or a complete stop of pumping (**Figure 2**). In addition, Q4623R showed a 46% reduced maximal pump rate in comparison to wild type (**Figure 3**). S107 treatment completely rescued the pumping ability of alleles P2460S and Q4623R (**Figure 4**). In the case of P2460S, only if FKB-2 was present, which strongly suggests an involvement of calstabin2-mediated stabilization in the disease-causing mechanism of this CPVT-mutation. Interestingly, the allele Q4623R showed no significant reduction of pump rate in the *fkb-2* deletion background, which may hint at different strengths or modes of FKB-2 stabilization involved in the tested alleles. We observed no rescue in nematodes bearing RyR2 mutation S2246L (*unc-68(S2378L)*) after S107 treatment. This is consistent with results obtained in a murine knock-in model of RyR2-S2246L, where treatment with JTV519 (a.k.a. K201), a more unspecific 1,4-benzothiazepine derivative, was without effect on the inducible VT, presumably owing to the fact that the interaction between the 2246 domain (2234–2750 region) and the K201 binding domain (2114–2149 region) was so tight that the drug-binding domain was inaccessible (Suetomi et al., 2011). The respective group could not observe changes in calstabin2 binding but suggests that introduction of CPVT mutation S2246L into the mouse RyR2 induces an aberrant activation of channel gating by forming abnormally tight domain-domain interaction between the two sub-domains located in the central domain, which produces a defective domain unzipping between the N-terminal and the central domain (Suetomi et al., 2011). For RyR2-P2328S and -Q4201R, beneficial effects of a JTV519 treatment have been shown in cell culture (Lehnart et al., 2004; Zhang et al., 2021). Accordingly, mutation-specific drugs may be identified in our optogenetic arrhythmia model that could prevent cardiac arrhythmias based on different mechanisms. Modified 1,4-benzothiazepine derivatives should be tested to access the drug-binding domain of S2246L or possible further mutations and clarify the involvement of a calstabin-mediated stabilization also in those variants.

Interestingly, the deletion of FKB-2 itself had no effect on light stimulated paced pumping (**Figure 4**) and had only

minor effects on spontaneous pumping on food in young adult animals (**Figure 1B**). Murine knockout models exist for calstabin2 and display different phenotypes. Some calstabin2-deficient mice show no structural cardiac abnormalities and no electrocardiogram abnormalities or arrhythmias at rest but consistently exhibited exercise-induced ventricular arrhythmias that are similar to those observed in patients with CPVT (Wehrens et al., 2003). Another calstabin2-null mouse line showed mild, sex-dependent cardiac hypertrophy but exhibited no stress-induced ventricular tachycardia (Xin et al., 2002; Xiao et al., 2007; Liu et al., 2011). Possibly, differences in the genetic background may account here for the different phenotypes. For *C. elegans*, no clear calstabin2 homolog is known yet and little is known about pharyngeal FKB protein expression. Only for FKB-6, a weak expression in PMCs was shown so far (Richardson et al., 2007). Both, calstabin1 (FKBP12) and calstabin2 (FKBP12.6), bind RyR2 in the heart at a stoichiometry of 4 FKBP per homotetramer (Timerman et al., 1993, 1996). Calstabin1 binds RyR2 with lower affinity but has a higher expression level (Jeyakumar et al., 2001). This suggests that, although calstabin1's affinity for RyR2 is lower than that of calstabin2, the greater abundance may result in more calstabin1 bound to RyR2 and could explain why RyR2 is not strongly affected in calstabin2 deficient mice in one of the studies (see review Gonano and Jones, 2017). Possibly, as for RyR2, there might be more than one FKB protein interacting with UNC-68 in PMCs which would explain our results for the FKB-2 deletion.

There must be differences in the interaction of RyR and calsequestrin between *C. elegans* and human, as obvious homologs of junctin and triadin are missing in the *C. elegans* genome. We were not able to prove with functional assays a suggested electrostatic interaction between negatively charged residues of UNC-68 luminal loop and positively charged residues at the C-terminus of CSQ-1 (Cho et al., 2007) in PMCs. Another group observed for a nearby mutation, *unc-68(R5153H),* strong effects on swimming (Graham et al., 2020). This allele, homologous to a known RyR1-mutation, behaved in liquid as a null mutant but is clearly not a null (Graham et al., 2020). It lies within the transmembrane, pore-forming domain of RyR (Yan et al., 2015) and might be critical to channel function. Thus, possible effects on channel function itself, as seen in swimming assays (**Figure 7B**), by the exchange of several close-by residues of the luminal loop cannot be excluded here. There is also the possibility that effects might occur in other muscle cells or neurons of the nematode, e.g., due to alternative splicing (Marques et al., 2020), whereas PMCs are not affected. Nevertheless, as demonstrated by a *csq-1* deletion allele, calsequestrin itself influences the pumping and the ability to follow pacing in the optogenetic arrhythmia model (Fischer et al., 2017). Instead of a postulated regulation of the RyR *via* the complex of CASQ, triadin, and/or junctin (Györke and Terentyev, 2008; Qin et al., 2008), only the loss of Ca^{2+} binding and buffering capacity in the *csq-1* deletion might be involved in *C. elegans* PMCs. Based on the differences in the interaction of RyR and calsequestrin between human and *C. elegans*, results obtained for CPVT-related calsequestrin mutations in the pharynx should be carefully considered.

CONCLUSION

In conclusion, we were able to shed some light on the mechanism of those CPVT mutations showing effects in *C. elegans* and, hence, to prove the involvement of FKB-2-mediated stabilization of UNC-68 in PMCs. The stabilizing mechanism of calstabin is suggested to be involved here because the specific calstabin-RyR stabilizing drug S107 rescues the pumping ability of P2460S and Q4623R mutations in the nematode, its involvement is already described (or discussed) for the homologous human mutations. Nevertheless, a combination of the calstabin mechanism with one of the other discussed CPVT mechanisms cannot be excluded. Furthermore, the selective effect of S107 on the different CPVT-mutations emphasizes the importance of the development of patient-specific drugs that could be tested in the *C. elegans* optogenetic arrhythmia model with high(er) throughput.

DATA AVAILABILITY STATEMENT

The raw data supporting the conclusions of this article will be made available by the authors, without undue reservation.

AUTHOR CONTRIBUTIONS

CS designed and directed the project. ME, YW, HK, and CS performed the experiments and analyzed the data. ME and CS wrote the article. All authors contributed to the article and approved the submitted version.

FUNDING

This research was funded by the Deutsche Forschungsgemeinschaft (DFG) grant SCHU3177/1-1/2 to CS. Publication was funded by Goethe University.

ACKNOWLEDGMENTS

Some strains were provided by the CGC, which is funded by the NIH Office of Research Infrastructure Programs (P40 OD010440). Plasmids pJW1285, pJW1310, and pJW1311were a gift from Jordan Ward (Addgene plasmids #61252-4). We are indebted to H. Fettermann, R. Wagner, and F. Baumbach for expert technical assistance. We thank A. Gottschalk for helpful discussions and advice as well as for the possibility to conduct this study in his lab at Goethe University.

SUPPLEMENTARY MATERIAL

The Supplementary Material for this article can be found online at: https://www.frontiersin.org/articles/10.3389/fphys.2022.691829/full#supplementary-material

REFERENCES

Akerboom, J., Carreras Calderón, N., Tian, L., Wabnig, S., Prigge, M., Tolö, J., et al. (2013). Genetically encoded calcium indicators for multi-color neural activity imaging and combination with optogenetics. *Front. Mol. Neurosci.* 6:2. doi: 10.3389/fnmol.2013.00002

Albertson, D. G., and Thomson, J. N. (1976). The pharynx of *Caenorhabditis elegans*. *Philos. Trans. R. Soc. Lond. B Biol. Sci.* 275, 299–325. doi: 10.1098/rstb.1976.0085

Andersson, D. C., Betzenhauser, M. J., Reiken, S., Meli, A. C., Umanskaya, A., Xie, W., et al. (2011). Ryanodine receptor oxidation causes intracellular calcium leak and muscle weakness in aging. *Cell Metab.* 14, 196–207. doi: 10.1016/j.cmet.2011.05.014

Arad, M., Glikson, M., El-Ani, D., and Monserrat-Inglesias, L. (2012). A family with recurrent sudden death and no clinical clue. *Ann. Noninvasive Electrocardiol.* 17, 387–393. doi: 10.1111/anec.12024

Bellinger, A. M., Reiken, S., Carlson, C., Mongillo, M., Liu, X., Rothman, L., et al. (2009). Hypernitrosylated ryanodine receptor calcium release channels are leaky in dystrophic muscle. *Nat. Med.* 15, 325–330. doi: 10.1038/nm.1916

Bellinger, A. M., Reiken, S., Dura, M., Murphy, P. W., Deng, S. X., Landry, D. W., et al. (2008). Remodeling of ryanodine receptor complex causes "leaky" channels: a molecular mechanism for decreased exercise capacity. *Proc. Natl. Acad. Sci. U.S.A.* 105, 2198–2202. doi: 10.1073/pnas.0711074105

Bendesky, A., Tsunozaki, M., Rockman, M. V., Kruglyak, L., and Bargmann, C. I. (2011). Catecholamine receptor polymorphisms affect decision-making in C. elegans. *Nature* 472, 313–318. doi: 10.1038/nature09821

Benian, G. M., and Epstein, H. F. (2011). Caenorhabditis elegans muscle: a genetic and molecular model for protein interactions in the heart. *Circ. Res.* 109, 1082–1095. doi: 10.1161/CIRCRESAHA.110.237685

Brillantes, A. B., Ondrias, K., Scott, A., Kobrinsky, E., Ondriasová, E., Moschella, M. C., et al. (1994). Stabilization of calcium release channel (ryanodine receptor) function by FK506-binding protein. *Cell* 77, 513–523. doi: 10.1016/0092-8674(94)90214-3

Cho, J. H., Ko, K. M., Singaruvelu, G., Lee, W., Kang, G. B., Rho, S. H., et al. (2007). Functional importance of polymerization and localization of calsequestrin in C. elegans. *J. Cell Sci.* 120, 1551–1558. doi: 10.1242/jcs.001016

Cho, J. H., Oh, Y. S., Park, K. W., Yu, J., Choi, K. Y., Shin, J. Y., et al. (2000). Calsequestrin, a calcium sequestering protein localized at the sarcoplasmic reticulum, is not essential for body-wall muscle function in *Caenorhabditis elegans*. *J. Cell Sci.* 113, 3947–3958.

Concordet, J. P., and Haeussler, M. (2018). CRISPOR: intuitive guide selection for CRISPR/Cas9 genome editing experiments and screens. *Nucleic Acids Res.* 46, W242–W245. doi: 10.1093/nar/gky354

Cook, A., Franks, C. J., and Holden-Dye, L. (2006). "Electrophysiological recordings from the pharynx," in *The C. elegans Research Community*, ed. WormBook (WormBook). Available online at: http://www.wormbook.org

Davis, M. W., Fleischhauer, R., Dent, J. A., Joho, R. H., and Avery, L. (1999). A mutation in the C. elegans EXP-2 potassium channel that alters feeding behavior. *Science* 286, 2501–2504. doi: 10.1126/science.286.5449.2501

Dhindwal, S., Lobo, J., Cabra, V., Santiago, D. J., Nayak, A. R., Dryden, K., et al. (2017). A cryo-EM-based model of phosphorylation- and FKBP12.6-mediated allosterism of the cardiac ryanodine receptor. *Sci. Signal.* 10:eaai8842. doi: 10.1126/scisignal.aai8842

Dillon, J., Andrianakis, I., Bull, K., Glautier, S., O'Connor, V., Holden-Dye, L., et al. (2009). AutoEPG: software for the analysis of electrical activity in the microcircuit underpinning feeding behaviour of *Caenorhabditis elegans*. *PLoS One* 4:e8482. doi: 10.1371/journal.pone.0008482

Dridi, H., Liu, X., Yuan, Q., Reiken, S., Yehia, M., Sittenfeld, L., et al. (2020). Role of defective calcium regulation in cardiorespiratory dysfunction in Huntington's disease. *JCI Insight* 5:e140614. doi: 10.1172/jci.insight.140614

Driessen, H. E., Bourgonje, V. J., van Veen, T. A., and Vos, M. A. (2014). New antiarrhythmic targets to control intracellular calcium handling. *Neth. Heart J.* 22, 198–213. doi: 10.1007/s12471-014-0549-5

Faggioni, M., and Knollmann, B. C. (2012). Calsequestrin 2 and arrhythmias. *Am. J. Physiol. Heart Circ. Physiol.* 302, H1250–H1260. doi: 10.1152/ajpheart.00779.2011

Fang-Yen, C., Avery, L., and Samuel, A. D. (2009). Two size-selective mechanisms specifically trap bacteria-sized food particles in *Caenorhabditis elegans*. *Proc. Natl. Acad. Sci. U.S.A.* 106, 20093–20096. doi: 10.1073/pnas.0904036106

Fatima, A., Xu, G., Shao, K., Papadopoulos, S., Lehmann, M., Arnáiz-Cot, J. J., et al. (2011). In vitro modeling of ryanodine receptor 2 dysfunction using human induced pluripotent stem cells. *Cell Physiol. Biochem.* 28, 579–592. doi: 10.1159/000335753

Fernández-Velasco, M., Rueda, A., Rizzi, N., Benitah, J. P., Colombi, B., Napolitano, C., et al. (2009). Increased Ca^{2+} sensitivity of the ryanodine receptor mutant $RyR2^{R4496C}$ underlies catecholaminergic polymorphic ventricular tachycardia. *Circ. Res.* 104, 201–209. doi: 10.1161/CIRCRESAHA.108.177493

Fischer, E., Gottschalk, A., and Schuler, C. (2017). An optogenetic arrhythmia model to study catecholaminergic polymorphic ventricular tachycardia mutations. *Sci. Rep.* 7, 17514. doi: 10.1038/s41598-017-17819-8

Franks, C. J., Pemberton, D., Vinogradova, I., Cook, A., Walker, R. J., and Holden-Dye, L. (2002). Ionic basis of the resting membrane potential and action potential in the pharyngeal muscle of *Caenorhabditis elegans*. *J. Neurophysiol.* 87, 954–961. doi: 10.1152/jn.00233.2001

George, C. H., Jundi, H., Walters, N., Thomas, N. L., West, R. R., and Lai, F. A. (2006). Arrhythmogenic mutation-linked defects in ryanodine receptor autoregulation reveal a novel mechanism of Ca^{2+} release channel dysfunction. *Circ. Res.* 98, 88–97. doi: 10.1161/01.RES.0000199296.70534.7c

Gonano, L. A., and Jones, P. P. (2017). FK506-binding proteins 12 and 12.6 (FKBPs) as regulators of cardiac ryanodine receptors: insights from new functional and structural knowledge. *Channels (Austin)* 11, 415–425. doi: 10.1080/19336950.2017.1344799

Graham, B., Shaw, M. A., and Hope, I. A. (2020). Single amino acid changes in the ryanodine receptor in the human population have effects. *Front. Genet.* 11:37. doi: 10.3389/fgene.2020.00037

Guo, W., and Campbell, K. P. (1995). Association of triadin with the ryanodine receptor and calsequestrin in the lumen of the sarcoplasmic reticulum. *J. Biol. Chem.* 270, 9027–9030. doi: 10.1074/jbc.270.16.9027

Györke, S., and Terentyev, D. (2008). Modulation of ryanodine receptor by luminal calcium and accessory proteins in health and cardiac disease. *Cardiovasc. Res.* 77, 245–255. doi: 10.1093/cvr/cvm038

Hamada, T., Sakube, Y., Ahnn, J., Kim, D. H., and Kagawa, H. (2002). Molecular dissection, tissue localization and Ca^{2+} binding of the ryanodine receptor of *Caenorhabditis elegans*. *J. Mol. Biol.* 324, 123–135. doi: 10.1016/s0022-2836(02)01032-x

Jeyakumar, L. H., Ballester, L., Cheng, D. S., McIntyre, J. O., Chang, P., Olivey, H. E., et al. (2001). FKBP binding characteristics of cardiac microsomes from diverse vertebrates. *Biochem. Biophys. Res. Commun.* 281, 979–986. doi: 10.1006/bbrc.2001.4444

Jiang, D., Wang, R., Xiao, B., Kong, H., Hunt, D. J., Choi, P., et al. (2005). Enhanced store overload-induced Ca^{2+} release and channel sensitivity to luminal Ca^{2+} activation are common defects of RyR2 mutations linked to ventricular tachycardia and sudden death. *Circ. Res.* 97, 1173–1181. doi: 10.1161/01.RES.0000192146.85173.4b

Jiang, D., Xiao, B., Yang, D., Wang, R., Choi, P., Zhang, L., et al. (2004). RyR2 mutations linked to ventricular tachycardia and sudden death reduce the threshold for store-overload-induced Ca^{2+} release (SOICR). *Proc. Natl. Acad. Sci. U.S.A.* 101, 13062–13067. doi: 10.1073/pnas.0402388101

Jones, L. R., Zhang, L., Sanborn, K., Jorgensen, A. O., and Kelley, J. (1995). Purification, primary structure, and immunological characterization of the 26-kDa calsequestrin binding protein (junctin) from cardiac junctional sarcoplasmic reticulum. *J. Biol. Chem.* 270, 30787–30796. doi: 10.1074/jbc.270.51.30787

Kaneko, N., Matsuda, R., Hata, Y., and Shimamoto, K. (2009). Pharmacological characteristics and clinical applications of K201. *Curr. Clin. Pharmacol.* 4, 126–131. doi: 10.2174/157488409788184972

Kimlicka, L., Tung, C. C., Carlsson, A. C., Lobo, P. A., Yuchi, Z., and Van Petegem, F. (2013). The cardiac ryanodine receptor N-terminal region contains an anion binding site that is targeted by disease mutations. *Structure* 21, 1440–1449. doi: 10.1016/j.str.2013.06.012

Kirchhefer, U., Wehrmeister, D., Postma, A. V., Pohlentz, G., Mormann, M., Kucerova, D., et al. (2010). The human CASQ2 mutation K206N is associated with hyperglycosylation and altered cellular calcium handling. *J. Mol. Cell Cardiol.* 49, 95–105. doi: 10.1016/j.yjmcc.2010.03.006

Kushnir, A., Todd, J. J., Witherspoon, J. W., Yuan, Q., Reiken, S., Lin, H., et al. (2020). Intracellular calcium leak as a therapeutic target for RYR1-related myopathies. *Acta Neuropathol.* 139, 1089–1104. doi: 10.1007/s00401-020-02150-w

Kwok, T. C., Ricker, N., Fraser, R., Chan, A. W., Burns, A., Stanley, E. F., et al. (2006). A small-molecule screen in C. elegans yields a new calcium channel antagonist. *Nature* 441, 91–95. doi: 10.1038/nature04657

Lee, J. M., Rho, S. H., Shin, D. W., Cho, C., Park, W. J., Eom, S. H., et al. (2004). Negatively charged amino acids within the intraluminal loop of ryanodine receptor are involved in the interaction with triadin. *J. Biol. Chem.* 279, 6994–7000. doi: 10.1074/jbc.M312446200

Leenhardt, A., Denjoy, I., and Guicheney, P. (2012). Catecholaminergic polymorphic ventricular tachycardia. *Circ. Arrhythm. Electrophysiol.* 5, 1044–1052. doi: 10.1161/CIRCEP.111.962027

Leenhardt, A., Lucet, V., Denjoy, I., Grau, F., Ngoc, D. D., and Coumel, P. (1995). Catecholaminergic polymorphic ventricular tachycardia in children. A 7-year follow-up of 21 patients. *Circulation* 91, 1512–1519. doi: 10.1161/01.cir.91.5.1512

Lehnart, S. E., Mongillo, M., Bellinger, A., Lindegger, N., Chen, B. X., Hsueh, W., et al. (2008). Leaky Ca^{2+} release channel/ryanodine receptor 2 causes seizures and sudden cardiac death in mice. *J. Clin. Invest.* 118, 2230–2245. doi: 10.1172/JCI35346

Lehnart, S. E., Wehrens, X. H., Laitinen, P. J., Reiken, S. R., Deng, S. X., Cheng, Z., et al. (2004). Sudden death in familial polymorphic ventricular tachycardia associated with calcium release channel (ryanodine receptor) leak. *Circulation* 109, 3208–3214. doi: 10.1161/01.CIR.0000132472.98675.EC

Liu, N., Colombi, B., Memmi, M., Zissimopoulos, S., Rizzi, N., Negri, S., et al. (2006). Arrhythmogenesis in catecholaminergic polymorphic ventricular tachycardia: insights from a RyR2 R4496C knock-in mouse model. *Circ. Res.* 99, 292–298. doi: 10.1161/01.RES.0000235869.50747.e1

Liu, N., Ruan, Y., and Priori, S. G. (2008). Catecholaminergic polymorphic ventricular tachycardia. *Prog. Cardiovasc. Dis.* 51, 23–30. doi: 10.1016/j.pcad.2007.10.005

Liu, Y., Chen, H., Ji, G., Li, B., Mohler, P. J., Zhu, Z., et al. (2011). Transgenic analysis of the role of FKBP12.6 in cardiac function and intracellular calcium release. *Assay Drug Dev. Technol.* 9, 620–627. doi: 10.1089/adt.2011.0411

Mango, S. E. (2007). "The C. elegans pharynx: a model for organogenesis," in *The C. elegans Research Community*, ed. WormBook (WormBook). Available online at: http://www.wormbook.org

Marques, F., Thapliyal, S., Javer, A., Shrestha, P., Brown, A. E. X., and Glauser, D. A. (2020). Tissue-specific isoforms of the single C. elegans Ryanodine receptor gene unc-68 control specific functions. *PLoS Genet.* 16:e1009102. doi: 10.1371/journal.pgen.1009102

Maryon, E. B., Coronado, R., and Anderson, P. (1996). unc-68 encodes a ryanodine receptor involved in regulating C. elegans body-wall muscle contraction. *J. Cell Biol.* 134, 885–893. doi: 10.1083/jcb.134.4.885

Maryon, E. B., Saari, B., and Anderson, P. (1998). Muscle-specific functions of ryanodine receptor channels in *Caenorhabditis elegans*. *J. Cell Sci.* 111, 2885–2895. doi: 10.1242/jcs.111.19.2885

Medeiros-Domingo, A., Bhuiyan, Z. A., Tester, D. J., Hofman, N., Bikker, H., van Tintelen, J. P., et al. (2009). The RYR2-encoded ryanodine receptor/calcium release channel in patients diagnosed previously with either catecholaminergic polymorphic ventricular tachycardia or genotype negative, exercise-induced long QT syndrome: a comprehensive open reading frame mutational analysis. *J. Am. Coll. Cardiol.* 54, 2065–2074. doi: 10.1016/j.jacc.2009.08.022

Meli, A. C., Refaat, M. M., Dura, M., Reiken, S., Wronska, A., Wojciak, J., et al. (2011). A novel ryanodine receptor mutation linked to sudden death increases sensitivity to cytosolic calcium. *Circ. Res.* 109, 281–290. doi: 10.1161/CIRCRESAHA.111.244970

Nicoll Baines, K., Ferreira, C., Hopkins, P. M., Shaw, M. A., and Hope, I. A. (2017). Aging Effects of *Caenorhabditis elegans* ryanodine receptor variants corresponding to human myopathic mutations. *G3 (Bethesda)* 7, 1451–1461. doi: 10.1534/g3.117.040535

Novak, A., Barad, L., Lorber, A., Gherghiceanu, M., Reiter, I., Eisen, B., et al. (2015). Functional abnormalities in iPSC-derived cardiomyocytes generated from CPVT1 and CPVT2 patients carrying ryanodine or calsequestrin mutations. *J. Cell Mol. Med.* 19, 2006–2018. doi: 10.1111/jcmm.12581

Novak, A., Barad, L., Zeevi-Levin, N., Shick, R., Shtrichman, R., Lorber, A., et al. (2012). Cardiomyocytes generated from CPVTD307H patients are arrhythmogenic in response to β-adrenergic stimulation. *J. Cell Mol. Med.* 16, 468–482. doi: 10.1111/j.1582-4934.2011.01476.x

Prior, H., Jawad, A. K., MacConnachie, L., and Beg, A. A. (2017). Highly efficient, rapid and Co-CRISPR-independent genome editing in.*Caenorhabditis elegans*. *G3 (Bethesda)* 7, 3693–3698. doi: 10.1534/g3.117.300216

Priori, S. G., Napolitano, C., Memmi, M., Colombi, B., Drago, F., Gasparini, M., et al. (2002). Clinical and molecular characterization of patients with catecholaminergic polymorphic ventricular tachycardia. *Circulation* 106, 69–74. doi: 10.1161/01.cir.0000020013.73106.d8

Priori, S. G., Napolitano, C., Tiso, N., Memmi, M., Vignati, G., Bloise, R., et al. (2001). Mutations in the cardiac ryanodine receptor gene (hRyR2) underlie catecholaminergic polymorphic ventricular tachycardia. *Circulation* 103, 196–200. doi: 10.1161/01.cir.103.2.196

Qin, J., Valle, G., Nani, A., Nori, A., Rizzi, N., Priori, S. G., et al. (2008). Luminal Ca^{2+} regulation of single cardiac ryanodine receptors: insights provided by calsequestrin and its mutants. *J. Gen. Physiol.* 131, 325–334. doi: 10.1085/jgp.200709907

Raizen, D. M., and Avery, L. (1994). Electrical activity and behavior in the pharynx of *Caenorhabditis elegans*. *Neuron* 12, 483–495.

Richardson, J. M., Dornan, J., Opamawutthikul, M., Bruce, S., Page, A. P., and Walkinshaw, M. D. (2007). Cloning, expression and characterisation of FKB-6, the sole large TPR-containing immunophilin from C. elegans. *Biochem. Biophys. Res. Commun.* 360, 566–572. doi: 10.1016/j.bbrc.2007.06.080

Rooryck, C., Kyndt, F., Bozon, D., Roux-Buisson, N., Sacher, F., Probst, V., et al. (2015). New Family With catecholaminergic polymorphic ventricular tachycardia linked to the triadin gene. *J. Cardiovasc. Electrophysiol.* 26, 1146–1150. doi: 10.1111/jce.12763

Roux-Buisson, N., Cacheux, M., Fourest-Lieuvin, A., Fauconnier, J., Brocard, J., Denjoy, I., et al. (2012). Absence of triadin, a protein of the calcium release complex, is responsible for cardiac arrhythmia with sudden death in human. *Hum. Mol. Genet.* 21, 2759–2767. doi: 10.1093/hmg/dds104

Sanyal, S., Wintle, R. F., Kindt, K. S., Nuttley, W. M., Arvan, R., Fitzmaurice, P., et al. (2004). Dopamine modulates the plasticity of mechanosensory responses in *Caenorhabditis elegans*. *EMBO J.* 23, 473–482. doi: 10.1038/sj.emboj.7600057

Sasaki, K., Makiyama, T., Yoshida, Y., Wuriyanghai, Y., Kamakura, T., Nishiuchi, S., et al. (2016). Patient-Specific human induced pluripotent stem cell model assessed with electrical pacing validates S107 as a potential therapeutic agent for catecholaminergic polymorphic ventricular tachycardia. *PLoS One* 11:e0164795. doi: 10.1371/journal.pone.0164795

Schuler, C., Fischer, E., Shaltiel, L., Steuer Costa, W., and Gottschalk, A. (2015). Arrhythmogenic effects of mutated L-type Ca $^{2+}$-channels on an optogenetically paced muscular pump in *Caenorhabditis elegans*. *Sci. Rep.* 5, 14427. doi: 10.1038/srep14427

Shtonda, B., and Avery, L. (2005). CCA-1, EGL-19 and EXP-2 currents shape action potentials in the *Caenorhabditis elegans* pharynx. *J. Exp. Biol.* 208, 2177–2190. doi: 10.1242/jeb.01615

Suetomi, T., Yano, M., Uchinoumi, H., Fukuda, M., Hino, A., Ono, M., et al. (2011). Mutation-linked defective interdomain interactions within ryanodine receptor cause aberrant Ca^{2+}release leading to catecholaminergic polymorphic ventricular tachycardia. *Circulation* 124, 682–694. doi: 10.1161/CIRCULATIONAHA.111.023259

Tester, D. J., Spoon, D. B., Valdivia, H. H., Makielski, J. C., and Ackerman, M. J. (2004). Targeted mutational analysis of the RyR2-encoded cardiac ryanodine receptor in sudden unexplained death: a molecular autopsy of 49 medical examiner/coroner's cases. *Mayo. Clin. Proc.* 79, 1380–1384. doi: 10.4065/79.11.1380

Timerman, A. P., Ogunbumni, E., Freund, E., Wiederrecht, G., Marks, A. R., and Fleischer, S. (1993). The calcium release channel of sarcoplasmic reticulum is modulated by FK-506-binding protein. *J. Biol. Chem.* 268, 22992–22999. doi: 10.1016/s0021-9258(19)49416-7

Timerman, A. P., Onoue, H., Xin, H. B., Barg, S., Copello, J., Wiederrecht, G., et al. (1996). Selective binding of FKBP12.6 by the cardiac ryanodine receptor. *J. Biol. Chem.* 271, 20385–20391. doi: 10.1074/jbc.271.34.20385

van der Werf, C., Kannankeril, P. J., Sacher, F., Krahn, A. D., Viskin, S., Leenhardt, A., et al. (2011). Flecainide therapy reduces exercise-induced ventricular arrhythmias in patients with catecholaminergic polymorphic ventricular tachycardia. *J. Am. Coll. Cardiol.* 57, 2244–2254. doi: 10.1016/j.jacc.2011.01.026

Ward, J. D. (2015). Rapid and precise engineering of the *Caenorhabditis elegans* genome with lethal mutation co-conversion and inactivation of NHEJ repair. *Genetics* 199, 363–377. doi: 10.1534/genetics.114.172361

Wehrens, X. H., Lehnart, S. E., Huang, F., Vest, J. A., Reiken, S. R., Mohler, P. J., et al. (2003). FKBP12.6 deficiency and defective calcium release channel (ryanodine receptor) function linked to exercise-induced sudden cardiac death. *Cell* 113, 829–840. doi: 10.1016/s0092-8674(03)00434-3

Wehrens, X. H., Lehnart, S. E., Reiken, S. R., Deng, S. X., Vest, J. A., Cervantes, D., et al. (2004). Protection from cardiac arrhythmia through ryanodine receptor-stabilizing protein calstabin2. *Science* 304, 292–296. doi: 10.1126/science.1094301

Xiao, J., Tian, X., Jones, P. P., Bolstad, J., Kong, H., Wang, R., et al. (2007). Removal of FKBP12.6 does not alter the conductance and activation of the cardiac ryanodine receptor or the susceptibility to stress-induced ventricular arrhythmias. *J. Biol. Chem.* 282, 34828–34838. doi: 10.1074/jbc.M707423200

Xin, H. B., Senbonmatsu, T., Cheng, D. S., Wang, Y. X., Copello, J. A., Ji, G. J., et al. (2002). Oestrogen protects FKBP12.6 null mice from cardiac hypertrophy. *Nature* 416, 334–338. doi: 10.1038/416334a

Yan, Z., Bai, X., Yan, C., Wu, J., Li, Z., Xie, T., et al. (2015). Structure of the rabbit ryanodine receptor RyR1 at near-atomic resolution. *Nature* 517, 50–55. doi: 10.1038/nature14063

Yuchi, Z., Yuen, S. M., Lau, K., Underhill, A. Q., Cornea, R. L., Fessenden, J. D., et al. (2015). Crystal structures of ryanodine receptor SPRY1 and tandem-repeat domains reveal a critical FKBP12 binding determinant. *Nat. Commun.* 6, 7947. doi: 10.1038/ncomms8947

Zalk, R., Clarke, O. B., des Georges, A., Grassucci, R. A., Reiken, S., Mancia, F., et al. (2015). Structure of a mammalian ryanodine receptor. *Nature* 517, 44–49. doi: 10.1038/nature13950

Zhang, X. H., Wei, H., Xia, Y., and Morad, M. (2021). Calcium signaling consequences of RyR2 mutations associated with CPVT1 introduced via CRISPR/Cas9 gene editing in human-induced pluripotent stem cell-derived cardiomyocytes: Comparison of RyR2-R420Q, F2483I, and Q4201R. *Heart Rhythm* 18, 250–260. doi: 10.1016/j.hrthm.2020.09.007

Conflict of Interest: The authors declare that the research was conducted in the absence of any commercial or financial relationships that could be construed as a potential conflict of interest.

Publisher's Note: All claims expressed in this article are solely those of the authors and do not necessarily represent those of their affiliated organizations, or those of the publisher, the editors and the reviewers. Any product that may be evaluated in this article, or claim that may be made by its manufacturer, is not guaranteed or endorsed by the publisher.

frontiers | Frontiers in Physiology

TECHNOLOGY AND CODE
published: 18 May 2022
doi: 10.3389/fphys.2022.779514

High-Resolution 3D Heart Models of Cardiomyocyte Subpopulations in Cleared Murine Heart

Huiying Ren[1,2†], Zhaoli Pu[1,2†], Tianyi Sun[3†], Tangting Chen[1], Leiying Liu[1], Zhu Liu[1], Christopher O'Shea[4], Davor Pavlovic[4], Xiaoqiu Tan[1,2*] and Ming Lei[1,3*]*

[1]Laboratory of Medical Electrophysiology, Ministry of Education, Collaborative Innovation Center for Prevention and Treatment of Cardiovascular Disease/Institute of Cardiovascular Research, Luzhou Medical College, Luzhou, China, [2]Department of Cardiology, The Affiliated Hospital of Southwest Medical University, Luzhou, China, [3]Department of Pharmacology, University of Oxford, Oxford, United Kingdom, [4]Institute of Cardiovascular Sciences, College of Medicine and Dental Sciences, University of Birmingham, Birmingham, United Kingdom

OPEN ACCESS

Edited by:
Tobias Bruegmann,
University Medical Center Göttingen,
Germany

Reviewed by:
David Sedmera,
Charles University, Czechia
Leonardo Sacconi,
University of Florence, Italy

***Correspondence:**
Tianyi Sun
tianyi.sun@pharm.ox.ac.uk
Xiaoqiu Tan
tanxiaoqiu@swmu.edu.cn
Ming Lei
ming.lei@pharm.ox.ac.uk

†These authors have contributed equally to this work and share first authorship

Specialty section:
This article was submitted to Cardiac Electrophysiology, a section of the journal Frontiers in Physiology

Received: 18 September 2021
Accepted: 31 March 2022
Published: 18 May 2022

Citation:
Ren H, Pu Z, Sun T, Chen T, Liu L, Liu Z, O'Shea C, Pavlovic D, Tan X and Lei M (2022) High-Resolution 3D Heart Models of Cardiomyocyte Subpopulations in Cleared Murine Heart. Front. Physiol. 13:779514. doi: 10.3389/fphys.2022.779514

Biological tissues are naturally three-dimensional (3D) opaque structures, which poses a major challenge for the deep imaging of spatial distribution and localization of specific cell types in organs in biomedical research. Here we present a 3D heart imaging reconstruction approach by combining an improved heart tissue-clearing technique with high-resolution light-sheet fluorescence microscopy (LSFM). We have conducted a three-dimensional and multi-scale volumetric imaging of the ultra-thin planes of murine hearts for up to 2,000 images per heart in x-, y-, and z three directions. High-resolution 3D volume heart models were constructed in real-time by the Zeiss Zen program. By using such an approach, we investigated detailed three-dimensional spatial distributions of two specific cardiomyocyte populations including HCN4 expressing pacemaker cells and $Pnmt^{+}$ cell-derived cardiomyocytes by using reporter mouse lines $Hcn4^{DreER/tdTomato}$ and $Pnmt^{Cre/ChR2-tdTomato}$. HCN4 is distributed throughout right atrial nodal regions (i.e., sinoatrial and atrioventricular nodes) and the superior-inferior vena cava axis, while $Pnmt^{+}$ cell-derived cardiomyocytes show distinct ventral, left heart, and dorsal side distribution pattern. Our further electrophysiological analysis indicates that Pnmt + cell-derived cardiomyocytes rich left ventricular (LV) base is more susceptible to ventricular arrhythmia under adrenergic stress than left ventricular apex or right ventricle regions. Thus, our 3D heart imaging reconstruction approach provides a new solution for studying the geometrical, topological, and physiological characteristics of specific cell types in organs.

Keywords: HCN4 expression (HCN4+) pacemaker cells, Pnmt+ cell-derived cardiomyocytes (PdCMs), heart tissue-clearing, light-sheet fluorescence microscopy, 3D volume heart models, optogenetics

INTRODUCTION

Biological tissues are naturally three-dimensional (3D) structures and are usually opaque. This causes a major problem in deep imaging for defining the spatial distribution and positioning of specific cell types in intact organs, especially in highly complex tissues such as the heart and the brain. While modern fluorescent microscopic platforms, such as wide-field fluorescent microscopy or confocal scanning microscopy, have a high spatial resolution for imaging cellular structures, they

suffer from insufficient axial resolution, as well as phototoxic damage if prolonged imaging is required (Sanderson et al., 2014). An alternative approach is to combine the traditional histological sectioning approach to produce thin-sliced tissue specimens (e.g., immunohistological staining on sectioned tissue samples) with post-imaging 3D reconstruction through computation. Histological sectioning also has significant limitations including tissue structure distortion and displacement, destruction of cell connections, and low spatial resolution when slicing samples.

The recently emerged tissue-clearing approach provides an exciting opportunity to solve such problems by allowing efficient fluorescent labeling and rapid 3D volumetric imaging of intact tissues, organs, and even entire organisms (Susaki and Ueda, 2016; Ueda et al., 2020). After the clearance, the tissue becomes transparent, so the imaging depth possible is less attenuated by the tissue sample. Such deep tissue visibility enables the interrogation of whole organs and even whole organisms without the need for sectioning the target tissue (Ueda et al., 2020). Clearing also removes strongly light-scattering and light-absorbing components of tissue and equalizes the refractive index of the imaging medium to that of the tissue (Verveer et al., 2007). Currently, three major tissue-clearing methods are being used: hydrophobic- ('solvent'), hydrophilic- ('aqueous'), and hydrogel-based methods (Susaki et al., 2015; Susaki and Ueda, 2016; Tainaka et al., 2016; Ueda et al., 2020). The hydrophobic clearing approach uses organic solvents and results in quick transparency of the tissue (Vigouroux et al., 2017). The 3D imaging of solvent-cleared organs (3DISCO) is a good example developed by Ertürk and colleagues (Ertürk et al., 2011; Ertürk et al., 2012). It is able to clear a complete adult mouse brain within 2 days (Ertürk et al., 2011; Ertürk et al., 2012). The protocol is simple and straightforward, which only involves a series of incubation of the samples. 3DISCO is now widely applied in neuronal research, stem and cancer cells in rodent and human specimens (Ertürk et al., 2011; Ertürk et al., 2012; Acar et al., 2015; Garofalo et al., 2015; Oshimori et al., 2015; Tanaka et al., 2017; von Neubeck et al., 2018). The disadvantage of this method is that the pretreatment solution contains H_2O_2 and methanol, which damage and even remove most of the epitopes for antibodies staining. Thus, immunohistochemistry remains a challenge in using such an approach (Renier et al., 2016).

Compared to the hydrophobic clearing method, hydrophilic tissue clearing has the advantages of high biocompatibility, biosafety, and the integrity of protein function although the transparency is not as good as the hydrophobic clearing method (Ueda et al., 2020). During the clearing process, hydrogen bonds are formed to link the clearing reagents and tissue components as well as proteins and water molecules (Ueda et al., 2020). Therefore, it greatly protects the structure of specimens and fluorescent proteins. CUBIC is a typical representative. CUBIC is composed of a series of imaging cocktails including CUBIC-L (use for delipidation) and CUBIC-R (RI match). It is reported that the clearing performance of CUBIC is even better than the hydrophobic clearing methods. Together with the advantages of hydrophilic clearing methods, CUBIC has been applied and illustrates the 3D structures with immunohistochemistry with antibodies for the adult mouse brain, heart, lung, stomach, and intestine (Susaki et al., 2014; Tainaka et al., 2014; Susaki et al., 2015; Kubota et al., 2017; Tainaka et al., 2018).

The third method is the hydrogel-based tissue clearing method, its typical application is 'cleared lipid-extracted acryl-hybridized rigid immunostaining/*in situ* hybridization-compatible tissue hydrogel' (CLARITY) (Chung et al., 2013). Unlike the hydrophilic clearing method, it forms hydrogels by covalent links to uniformly remove the lipid with fewer structure damages and bimolecular losses (Chung et al., 2013). The clearing force is driven by electrophoresis and simple passive, which improves the clearing performance but is time-consuming compared to the other two methods (Ueda et al., 2020).

Despite a plethora of advanced cleaning methods, most of them are designated for brain and nervous tissues and lack the consideration of the nature of the heart (Kolesová et al., 2021). Unlike the brain, the heart is enriched in connective tissues and autofluorescence (Sands et al., 2022). The heart consists of clustered cardiomyocytes arrayed into ventricular transmural layers from subepicardial to subendocardial tissues (Matryba et al., 2019). Packed cardiomyocytes are surrounded by thicker connective tissue (perimysium) (Ho, 2009). The heme a precursor to hemoglobin within the myocardium is pigmented, leading to autofluorescence, which in turn impedes the penetration of light when visualization (Matryba et al., 2019). Researchers compared and optimized the protocols for clearing experiments on heart and vasculature tissue. DISCO is a successful trial in heart clearing. By combining 3DISCO and immunostaining, the vasculature development of the human heart was illustrated by showing the smooth muscle-specific alpha-actin (SMA) (Belle et al., 2017; Epah et al., 2018). The conduction system of the mouse heart was also reconstructed by applying iDISCO + tissue clearing method (Goodyer et al., 2019). However, the drawback of DISCO is the poor preservation of GFP fluorescence (Pan et al., 2016). CUBIC is commonly used for heart clearing research because it can effectively remove the autofluorescence and allow observation of the detailed structure of the whole heart (Susaki et al., 2015; Susaki and Ueda, 2016). Kolwsová and colleagues tested different clearing protocols for imaging whole embryos, embryonic, and adult hearts with GFP genetic fluorescence. The results pointed out that DBE (dibenzylether) did not preserve the GFP signals and triggers the shrinking of tissue; CLARITY improved the clearing effect but compromise the GFP signals; SCALE clearing led to good clearing until E12.5 but failed to function well in large-scaled samples in later stages; CUBIC showed better performance of clearing with imaging although adult hearts took a longer time (7–14 days) (Kolesová et al., 2021).

Recently, CUBIC clearing of rat hearts by perfusing CUBIC solutions through the coronary circulation system was also described by Sands et al. (2022). When tissue clearing combines with light-sheet fluorescence microscopy (LSFM), 3D imaging of biological samples with high speed and low photo-bleaching can be achieved. Hence, this approach has emerged as a powerful tool for biological research. LSFM itself

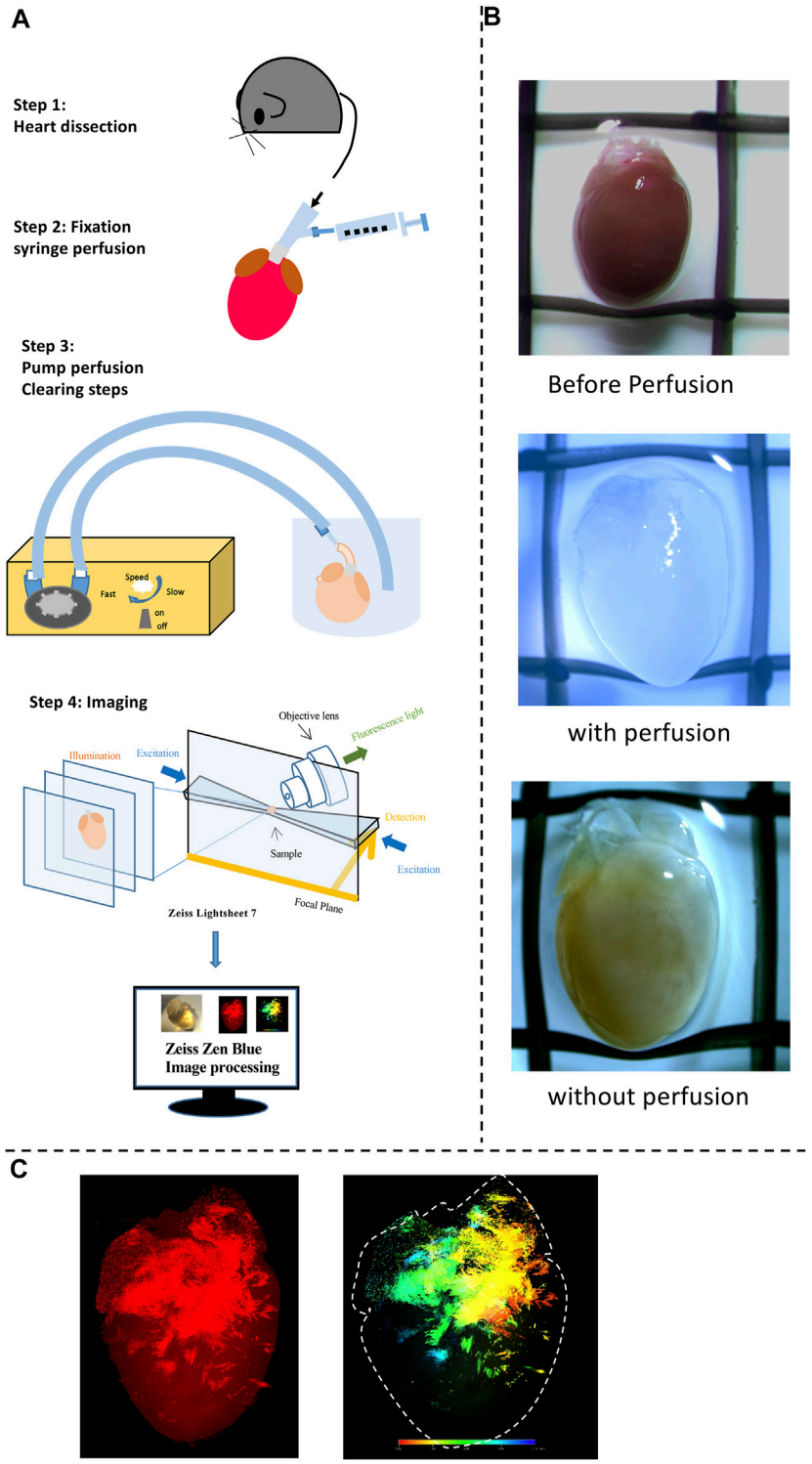

FIGURE 1 | A workflow for tissue clearing and examples of 3D reconstruction. **(A)** A schematic overview of the workflow of the study and the process of the experimental procedures. Heart dissection was conducted. Afterward tissue fixation and clearing were done to obtain transparent hearts. Finally, Fluorescence images for detecting fluorescent positive cells were obtained using Zeiss Fluorescent microscopy (provide the model details here) in transparent hearts; Diagram illustrating the procedure for the 3D reconstruction achieved using the ZEISS ZEN software to present both Tdtomato fluorescence and depth color code models. 3D volume data (Videos 1–4) was visualized in Paraview following Gaussian smoothing and down-sampling. **(B)** Images of Heart samples showing the appearance before, with, and without the perfusion. **(C)** Examples of fluorescence and depth code images for final products.

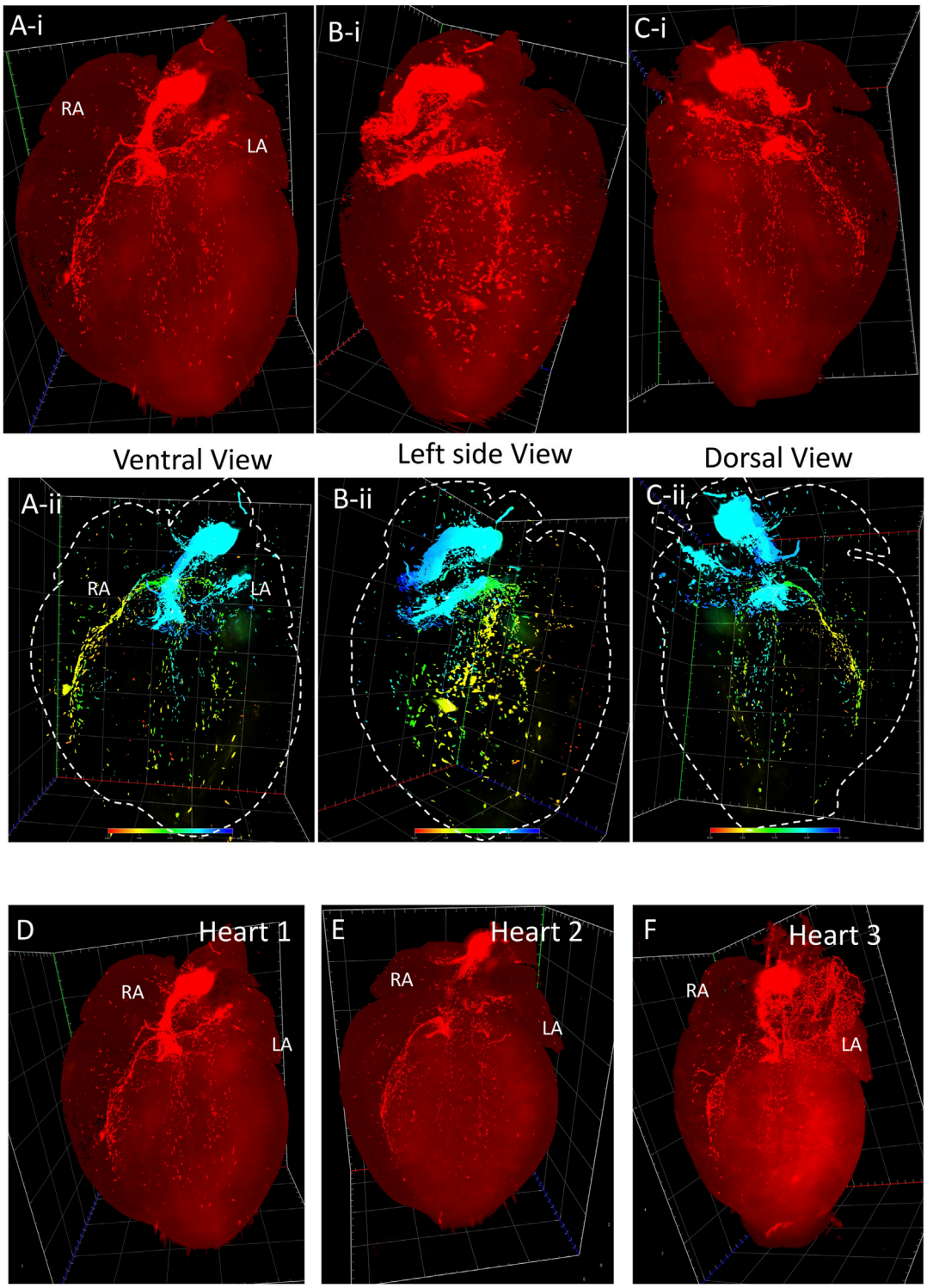

FIGURE 2 | 3D volume reconstruction of the spatial distribution of HCN4+ pacemaker cells in adult $Hcn4^{DreER/tdTomato}$ mouse heart. **(Ai–Ci)** The tdTomato fluorescence images show the distribution of HCN4+ cells from the ventral, left side, and dorsal view respectively (also see online video 1, heart size: 10.05 mm × 12.01 mm x 7.565 mm). **(Aii–Cii)** The depth code image showing the distribution of HCN4+ cells from the ventral, left side, and dorsal view respectively, corresponding to **(Ai–Ci)** (also see online video 2). **(D–F)** Three representatives of tdTomato fluorescence image showing the consistent signal pattern in adult $Hcn4^{DreER/tdTomato}$ mouse hearts. (n number = 3). LA: left atrium; RA: right atrium.

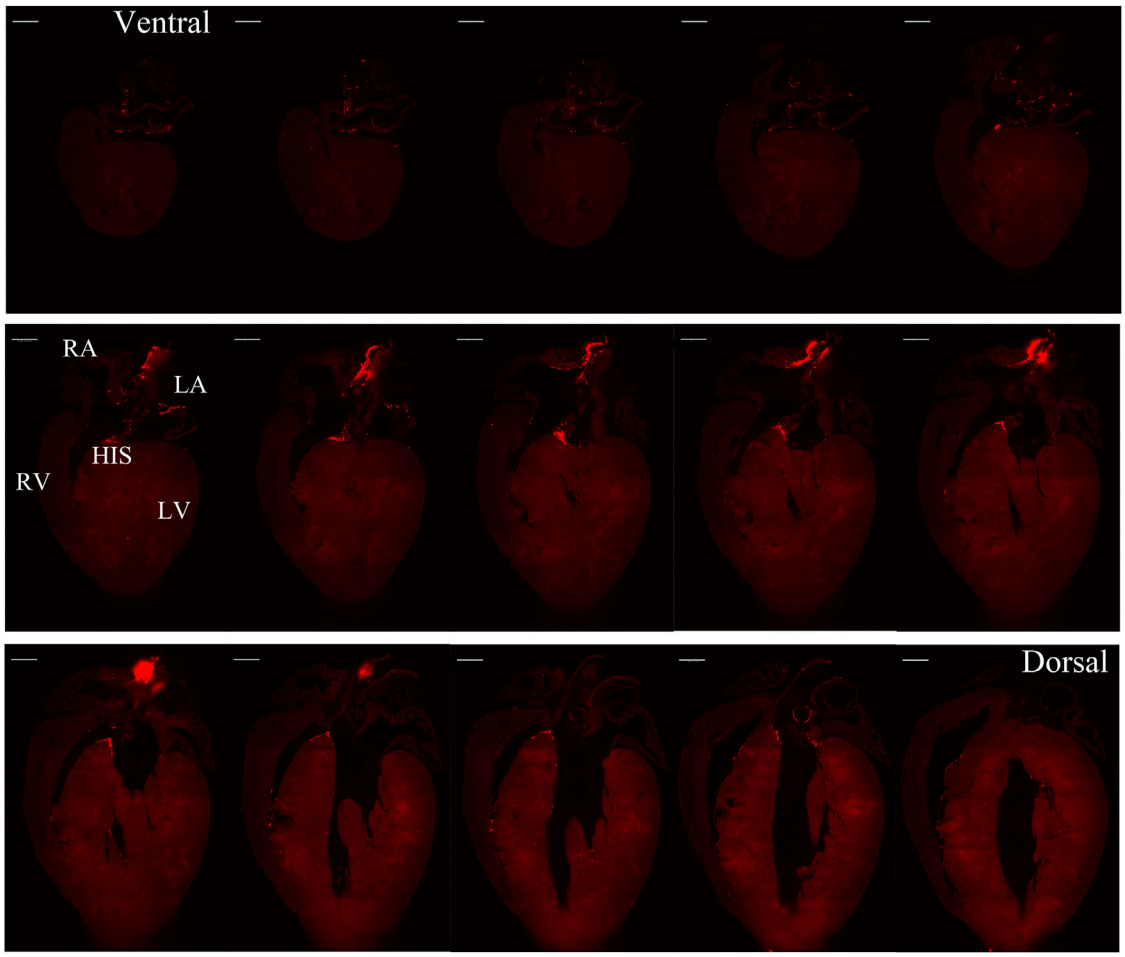

FIGURE 3 | Selected representative coronal sections of $Hcn4^{DreER/tdTomato}$ showing the distribution of HCN4+ cells from ventral side to dorsal side in adult mouse heart. Scale bar: 1,000 μm.

provides higher speed, better signal-to-noise ratio, lower level of photo-bleaching, and improved optical penetration depth than conventional wide-field fluorescent microscopy or confocal microscopy (Tomer et al., 2013). Furthermore, it has the ability to selectively illuminate an ultra-thin plane of the sample via the application of a sheet of light orthogonal to the detection path (Tomer et al., 2013).

Recent work has identified a previously unknown subpopulation of cardiomyocytes (CMs): $Pnmt^{+}$ cell-derived cardiomyocytes (PdCMs) and their unique left-side preferential distribution (Wang et al., 2017). We developed a novel optogenetic mouse strain by crossing Pnmt-Cre mice with Ai27D mice that expressed an improved channelrhodopsin-2(ChR2)/tdTomato fusion protein, following excision of a STOP sequence that was flanked with -loxp sequences. The fluorescence signal from tdTomato provided an excellent endogenous marker to identify PdCMs. Coronal sections of hearts agreed with earlier work that shows the left atrium, left ventricle, and interventricular septum were particularly rich in PdCMs (Wang et al., 2017). In remarkable proximity to earlier quantitative approaches, an average of 86% of ChR2/tdTomato + cells were on the left side of the heart. Moreover, this study now quantitatively reported the contribution of PdCMs to the overall number of CMs; PdCMs estimates suggest that approximately 50% of the left atrium, and 21% of the left ventricle CMs are PdCMs—in agreement with the extensive distribution of Pnmt-derived cardiomyocytes in the left atrium in previous studies (Ebert et al., 1996). These estimates provide concrete quantitative evidence of the significance of PdCMs in terms of development heterogeneity in the heart (Wang et al., 2017). Moreover, in agreement with previous studies, we reported a great deal of co-localization of HCN4+ cells with tdTomato + cells in the AVN, but with less so in the SAN—suggesting that the AVN has a richer population of PdCMs than the SAN (Wang et al., 2017; Ni et al., 2017).

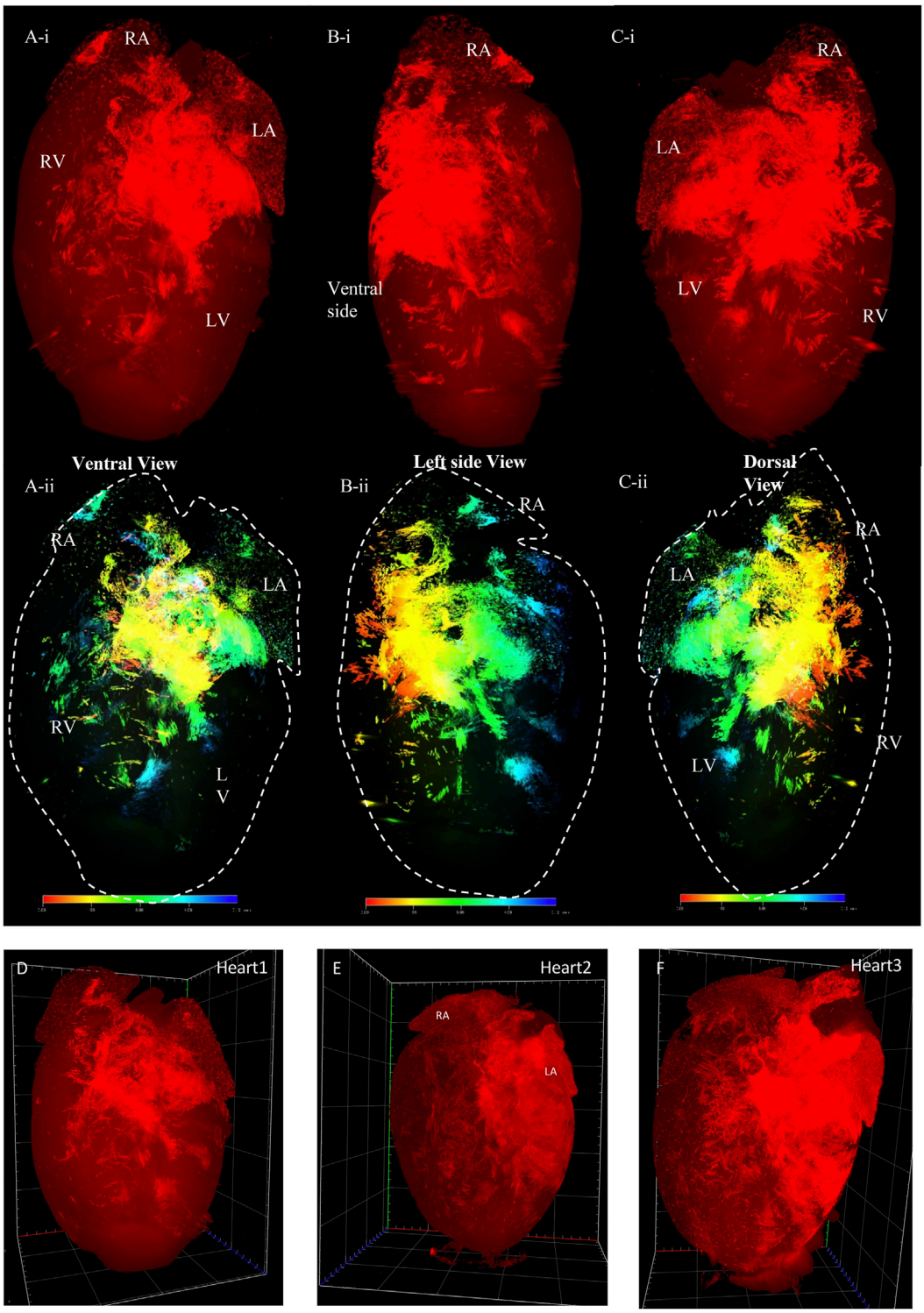

FIGURE 4 | 3D volume reconstruction of the spatial distribution of Pnmt + cell-derived cardiomyocytes (PdCMs) in adult $Pnmt^{Cre/ChR2-tdTomato}$ heart. **(Ai–Ci)** The tdTomato fluorescence images show the distribution of PdCMs from the ventral, left side, and dorsal view respectively (also see online video 3, heart size: 7.86 mm × 11.26 mm x 6.113 mm). **(Aii–Cii)** The depth code image showing the distribution of PdCMs from the ventral, left side, and dorsal view respectively, corresponding to **(Ai–Ci)** (also see online video 4). **(D–F)** Three representatives of tdTomato fluorescence image showing the consistent signal pattern in adult $Pnmt^{Cre/ChR2-tdTomato}$ mouse hearts. (n number = 3). LA: left atrium; RA: right atrium. LV: left ventricular; RV: right ventricular.

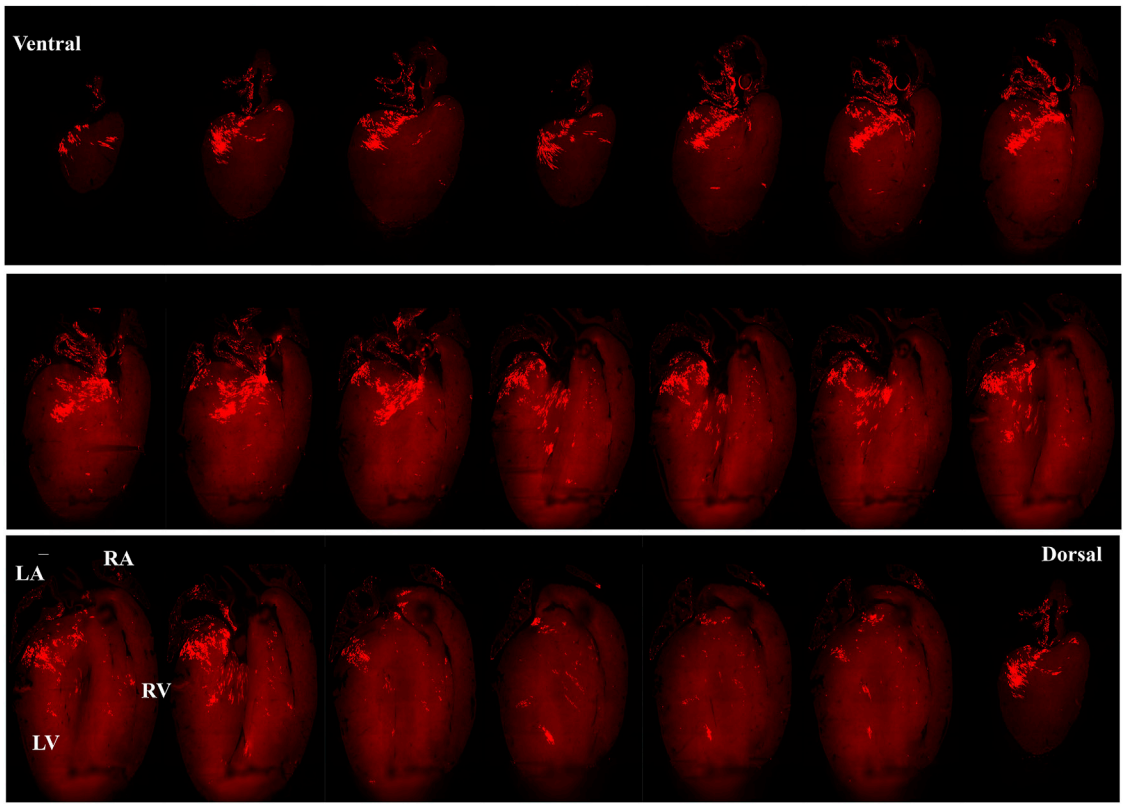

FIGURE 5 | Selected representative coronal sections from an adult $Pnmt^{Cre/ChR2-tdTomato}$ mouse heart showing the distribution of PdCMs from ventral side to dorsal side. Scale bar: 1,000 μm.

In this study, we present a new 3D heart imaging reconstruction approach to generate murine heart volume models of spatial distribution of specific cell types (e.g., Pnmt-Derived Cardiomyocytes) obtained by combining an improved heart tissue clearing method with high-resolution LSFM. The experiment has three major steps. First, the heart sample is perfused by physiological solution in the Langendorff perfusion system allowing the effective clearance of blood and tissue clearing. Such a step is critical for reducing cardiac tissue autofluorescence background. Second, the heart then undergoes a number of methodological interventions enabling efficient tissue clearing. Crucially, we found a slow perfusion rate for clearing solution for 24–48 h *via* coronary circulation system provides the best clearing protocol for obtaining a transparent heart. Third, a high-resolution LSFM is used for imaging transparent hearts. Finally, high-resolution 3D volume heart models are constructed in real-time by the Zeiss Zen program.

Therefore, we successfully developed a series of 3D volume models to define the spatial distributions of specific cardiomyocyte populations, which is comparable to the computational 3D models based on the histological images. Our approach is efficient, not necessitating tissue sectioning, maintaining optimal tissue structure and organization, and has a much higher axial and spatial resolution.

TECHNOLOGY DEVELOPMENT

Animal Models

The $Pnmt^{Cre/ChR2-tdTomato}$ mouse line was generated by crossing Pnmt-Cre mice with B6. Cg-*Gt(ROSA)26Sor*$^{tm27.1(CAG-COP4H134R/tdTomato)Hze}$/J strain (Stock No. 012567, Jackson Labs) as we described previously (Wang et al., 2017).

The second mouse line $HCN4^{Dre/tdTomato}$ was generated by crossing C57BL/6-$Hcn4^{em1(kozak-DreER-WPRE-A)/Smoc}$ mice with C57BL/6-$Igs2^{em1(CAG-RSR-tdTomato)/Smoc}$ mice from Shanghai Model Organisms Center, Inc. (Shanghai, China). The model generation was performed with the approval of the Animal Care and Use Committee of the Southwest Medical University (Sichuan, China) (No: 20160930) in conformity with the NIH Guide for the Care and Use of Laboratory Animals.

SAMPLE PREPARATION AND TISSUE CLEARING

Step 1. Heart preparation

The general procedure has been demonstrated in **Figure 1A**. All mice were killed via cervical dislocation in accordance with the Animals Scientific Procedures Act (1986). Before killing, the mice

were heparinized by intraperitoneal injection of heparin sodium physiological salt solution (Sigma-Aldrich, 500 U/mL) 0.2 ml. The heart was excised, cannulated, and mounted onto a Langendorff system, then perfused (flow rate: 3 ml/min; Watson-Marlow Bredel Peristaltic pumps, model 505S, Falmouth, Cornwall, UK) with Krebs' Ringer (KR) (mM) (NaCl: 119, $NaHCO_3$: 25, Glucose: 10, Na Pyruvate: 2, KCl: 4, $MgCl_2$: 1, KH_2PO4: 1.2, and $CaCl_2$: 1.8) warmed solution (37°C) for 5–10 min. The heart was removed from the Langendorff system and then flushed with phosphate-buffered saline (PBS) briefly. Afterwards, the heart was continued prepared by steps 2 and 3 (**Figure 1A**).

Step 2. Fixation

Followed by 4% paraformaldehyde (PFA) in phosphate buffer solution for fixation for 2 h at 4 °C. After a 15 ml PBS wash, the whole heart was then immediately perfused with CUBIC-P for 30 min, which is a chemical allowing efficient perfusion-fixation compatibility with downstream steps. This CUBIC-P is specially designed for organs with cavity structures such as hearts.

Step 3. Perfused Clearing

After washing out the remaining PFA and CUBIC-P with PBS, the heart was treated with a lipid-removal chemical named CUBIC-L for delipidation. This process was conducted at 37°C for 5°days. Perfusion is crucial at this stage to convey the reagent, enabling a better clearing. Because the mouse models we used have genetically-encoded fluorescence labeling of the cells of interest, no staining is required. Followed by washing, the heart was then treated with 50% CUBIC-R diluted by distilled water 1 day and then 100% CUBIC-R reagent to adjust the refractive index of the organs for at least 5days.

Step 4. Light-sheet Imaging

The transparent heart was illuminated by Zeiss 7 LSFM. The adult murine heart (8 weeks old) is approximately 1.3°cm × 0.7cm x 0.7 cm in height, width, and thickness. This LSFM with dedicated optics, enhanced sample chambers, and designated sample holders enables high-quality whole field imaging of the murine heart. LSFM separates the fluorescence of excitation and detection into two solo light paths. In this case, the axis of illumination is perpendicular to the detection axis as shown in **Figure 1A**, allowing the illumination of a single thin section of the heart at one point and thus generating inherent sections from the focus plane by merely exciting the fluorescence (Matsumoto et al., 2019). As a result, no pinhole or image processing procedures are needed. Unlike normal confocal fluorescent microscopes, LSFM is able to collect the light from the focus plane on the pixels rather than pixel by pixel, infinitely improving the resolution for the subsequent 3D reconstruction. After imaging, the features and details of the heart were captured and reconstructed for the 3D model by using Zeiss Zen Blue software. The stitching program was processed to combine multiple images with overlapped fields of view to generate high-resolution images. Fluorescent mode and depth code mode was selected to demonstrate the distribution of cell subpopulations of interest at three-dimensional presentation. A series of image galleries were collected at certain intervals of layers to show the distribution at a two-dimensional presentation. The raw video was recorded directly after the illumination without using other processing software. The thickness for PdCM and HCN4 hearts are 6.113 and 8.352 mm respectively. The total magnification was 4.22. The emission filter bandpass was 575–615 nm. High-resolution 3D volume heart models are constructed in real-time by the Zeiss Zen program. 3D iterative deconvolution was applied. By applying the maximum intensity, the reconstruction of the whole cardiac architecture was achieved to present clearly Tdtomato fluorescence by contrast with the background area in the transparent heart. The depth color code was employed to detect the depth of the signals which provided the accurate location of fluorescence in both epicardium and endocardium indicated by the color spectrum.

3D DATA CONSTRUCTION

The genetic fluorescence of the mouse models was captured by the Zeiss Light Sheet fluorescence microscope Lightsheet 7. After stitching from raw files, 3D movies were recorded and further processed in Zen Blue software. On the 3D View module, the maximum intensity was adjusted to reduce the background and illuminate the fluorescent positive cells throughout the whole heart (online Video 1, 3). The depth color code was applied to show the specific location of the signals (online Video 2, 4). Visualizations were created by rotating the 3D volume and adding keyframes to the record module.

ELECTROCARDIOGRAPHY (ECG) RECORDING WITH PROGRAMMED LIGHT STIMULATION (PLS) AND PROGRAMMED ELECTRICAL STIMULATION (PES)

Optical stimulation of ChR2 light-sensitive channel. Whole hearts, tissues, or single cells were paced through the activation of ChR2 light-sensitive channels. This was achieved by the delivery of 470 nm blue light pulses (10 ms pulse width) generated by OptoFlash (Cairn Research, UK). Pulses were triggered by a 1,401 digitizer and Spike 2 software (Cambridge Electronic Design, UK). Approximate blue light intensity was measured with an 818-ST2 Wand Detector connected to an 843 R Power meter (both Newport Corporation, CA, United States) and expressed normalized for the area being illuminated through simulating the average light intensity reached to the surface of the tissue by mimicking the distance of fiber-heart.

Langendorff-perfused *ex vivo* hearts from $Pnmt^{Cre/ChR2}$ mice were subjected to PLS or PES while ECG was being measured from an electrode placed on the left ventricle of the heart. Two protocols were carried out as follows: 1) continuous pacing protocol: Stimuli were delivered continuously with a constant frequency. 2) S1S2 pacing protocol: a pacing train of eight stimuli (S1) was delivered at a basic cycle length of 100 ms, with a single (S2) premature extra stimulus introduced at progressively shorter intervals until arrhythmia was induced or the ventricular refractory period was reached. (C) burst pacing protocol: multiple burst stimuli with progressively reduced stimulus

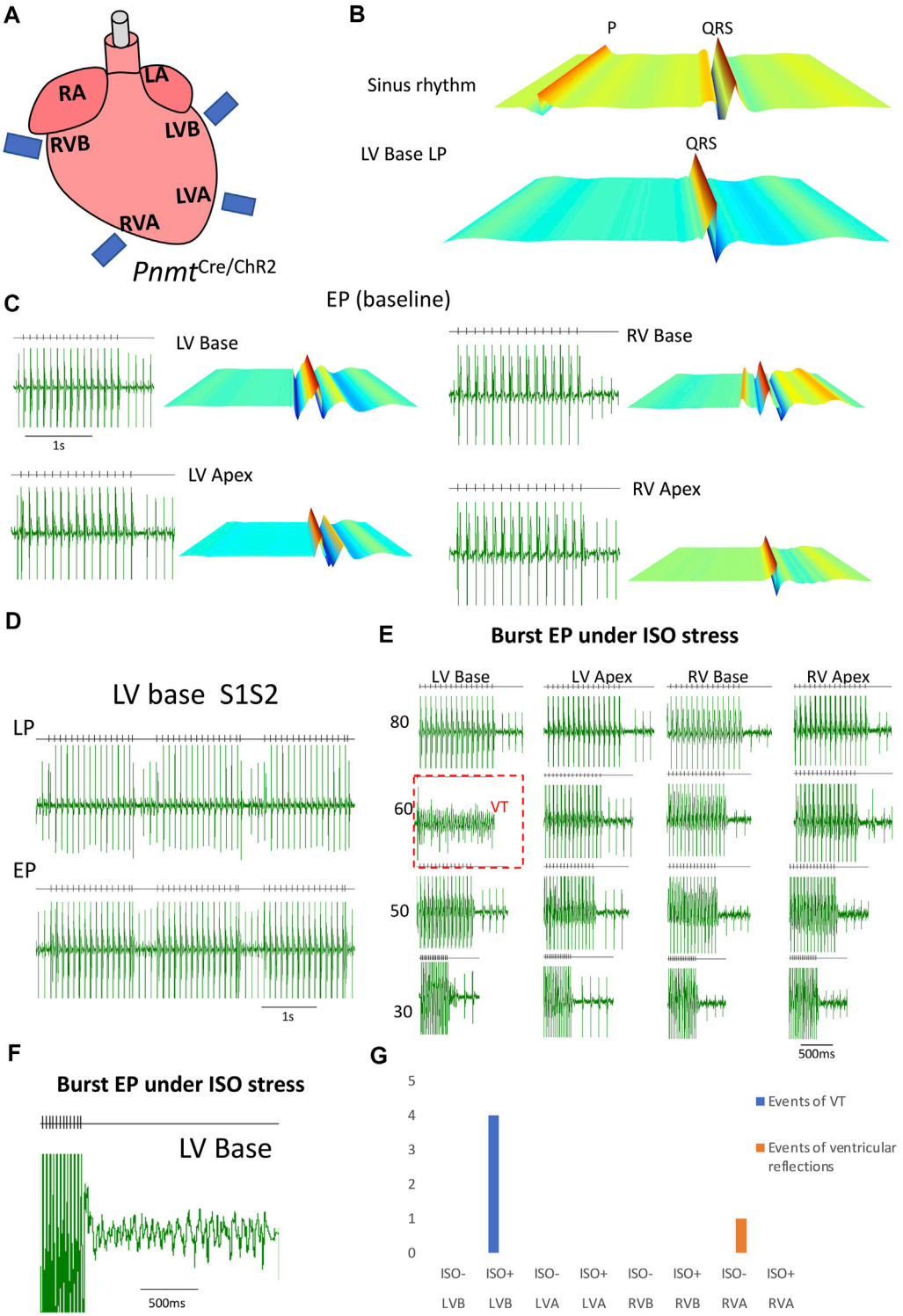

FIGURE 6 | Controlling heart rhythm with selective optogenetic stimulation and electrical pacing under β-adrenergic stress conditions induced by administration of isoprenaline (ISO) compared with a baseline condition in an adult Pnmt$^{Cre/ChR2m}$ mouse model. **(A)**. Localized light pacing and electrical pacing in different regions of the heart. **(B)**. The upper panel shows a representative ECG recording of a Pnmt$^{Cre/ChR2}$ heart in intrinsic sinus rhythm. The bottom panels show representative ECG recordings of this heart paced by targeting blue light pulses to LV base regions respectively. "P" in representative ECG recordings stands for "P wave". **(C)**. Examples of ECG recordings in the four different regions of Pnmt$^{Cre/ChR2}$ mouse hearts under baseline conditions. **(D)**. ECG was recorded in the LV base of a Pnmt$^{Cre/ChR2}$ heart by programmed light stimulation (PLS) and electrical pacing with the S1S2 protocol. **(E)**. ECG of Pnmt$^{Cre/ChR2}$ in four different regions with frequency-

(*Continued*)

FIGURE 6 | dependent pacing under β-adrenergic (ISO) stress conditions. **(F)**. A typical example of VT occurred by burst electrical pacing under β-adrenergic stress conditions. **(G)**. Summary of the occurrence of VT in four different regions with frequency-dependent pacing under baseline and β-adrenergic stress conditions. The left ventricular base of hearts showed higher occurrences of VT under β-adrenergic stress. (n number = 5). LA: left atrium; RA: right atrium. LV: left ventricular; RV: right ventricular; LVB: left ventricular base; LVA: left ventricular apex; RVB: right ventricular base; RVA: right ventricular apex.

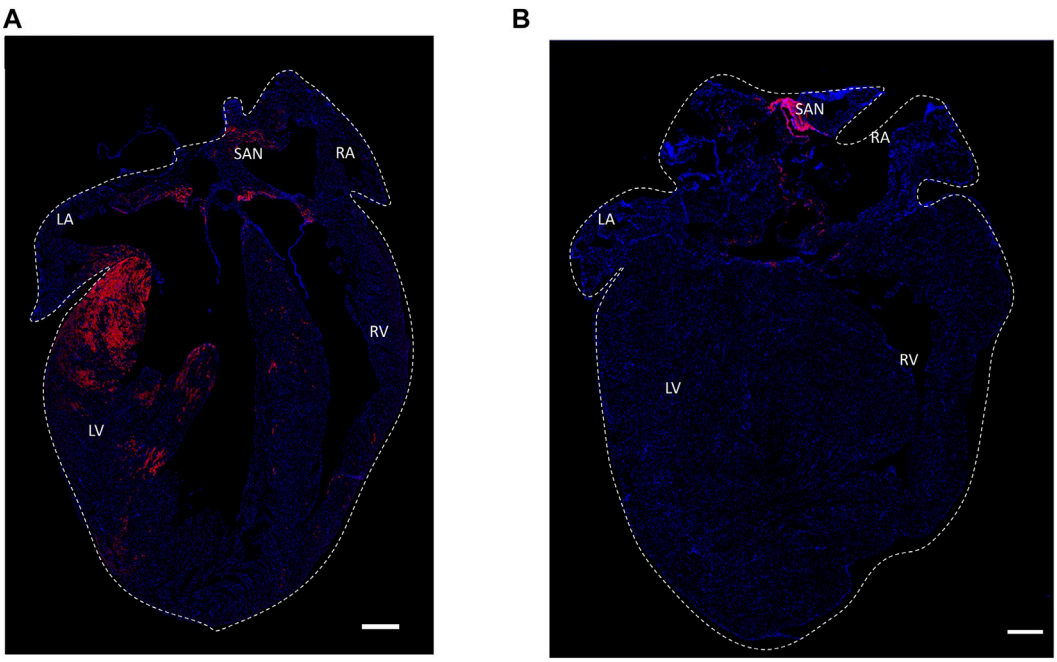

FIGURE 7 | Histological section confocal microscopic images of expression of distribution patterns of the HCN4^{+} cells in Hcn4$^{DreER/tdTomato}$ heart **(A)** and Pnmt^{+}/Tdtomato positive cells in Pnmt$^{Cre/ChR2-tdTomato}$ heart **(B)**. Tdtomato fluorescence signal indicating PdCMs was observed on the left side of the heart and SAN region. **(B)** Tdtomato fluorescence signal was mainly observed in the SAN and AVN regions in Hcn4$^{DreER/tdTomato}$ heart. Blue: nuclear staining by DAPI. Scale bar: 500 μm. Online video 1: The video was generated to show the HCN4+ cells (tdTomato) in an adult mouse heart. The video can be found in the following link: https://figshare.com/s/26bbc6c38ae7a01c7778heart size: 10.05 mm × 12.01 mm x 7.565 mm. Online video 2: The video was generated to show the depth details of HCN4+ cells in the adult mouse heart. The video can be found in the following link: https://figshare.com/s/21c472847c46f0936dddheart size: 10.05 mm × 12.01 mm x 7.565 mm. Online video 3: The video was processed to show the PdCMs (tdTomato) in the adult mouse heart. The video can be found in the following link: https://figshare.com/s/01471ea1c3eda4f6bc43.heart size: 7.86 mm × 11.26 mm x 6.113 mm. Online video 4: The video was processed to show the depth details of PdCMs in the adult mouse heart. The video can be found in the following link: https://figshare.com/s/4d9bb0b180cb58c3082f heart size: 7.86 mm × 11.26 mm x 6.113 mm.

intervals (from 80 to 30 ms) were delivered. Ventricular tachycardia was defined as six or more consecutive premature ventricular waveforms; tachycardia with regular waveforms defined as VT and VF was characterized by irregular fibrillating waveforms.

RESULTS AND DISCUSSION

Figure 1 illustrates a schematic overview of the study design and experimental procedure. We first determined the spatial distribution of cardiac pacemaker cells by using potassium/sodium hyperpolarization-activated cyclic nucleotide-gated channel 4 (HCN4) as a marker. **Figure 2** presents the 3D volume reconstruction of the spatial distribution of HCN4 positive pacemaker cells in the heart (also shown in online videos 1 and 2). HCN4 is distributed throughout the right atrium with heavy staining localized in the right atrial nodal regions (i.e., sinoatrial and atrioventricular nodes). The distribution of the HCN4 along the superior-inferior vena cava axis is in line with recent observations by Brennan et al. (2020) and supports the wandering pacemaker hypothesis with two competing right atrial pacemakers localized near the superior vena cava and the inferior vena cava. Selected images captured using LSFM imaging representing coronal sections from an adult tdTomato mouse heart show the distribution of HCN4^{+} pacemaker cells in adult HCN4$^{Dre/tdTomato}$ mice from ventral to dorsal, allowing visualizing the regional distribution of HCN4 positive pacemaker cells in two dimensions (**Figure 3**). High-resolution images are available in online videos 1 and 2. The concurrent use of a programmed high-resolution LSFM imaging allowed for the capture of ~2,000 ultra-thin plane images from a single murine heart with a spatial resolution of 1.54 μm ×

1.54 μm × 4.01 μm per pixel respectively in the x-, y- and *z*-direction, in corresponding to 5,113 × 7,325 × 1,254 pixels in scaled image size.

In the second series of models, we determined the spatial distribution of $Pnmt^{+}$ cell-derived cardiomyocytes (PdCMs) that we discovered recently (Wang et al., 2017). **Figure 4** presents examples of two 3D volume reconstruction models of the spatial distribution of $Pnmt^{+}$ cell-derived cardiomyocytes (PdCMs) in adult $Pnmt^{Cre/ChR2-tdTomato}$ hearts (also shown in the online videos 3 and 4). The use of the same programmed high-resolution LSFM imaging for the capture of ~2,000 ultra-thin plane images from a single murine heart with similar spatial resolution in the x-, y-, and *z*-direction as obtained in $HCN4^{Dre/tdTomato}$ hearts. The 3D volume model illustrates the reconstruction of the spatial distribution of $Pnmt^{+}$ cell-derived cardiomyocytes (PdCMs) in adult $Pnmt^{Cre/ChR2-tdTomato}$ heart. The tdTomato fluorescence is present from ventral, left, and dorsal views, respectively (**Figures 4A–C**). We also use depth code showing the localization of PdCMs in the heart from the ventral, left side, and dorsal side, respectively (**Figures 4D–F**). The localization of PdCMs has not been shown previously in a computational 3D representation with such a high spatial resolution. In **Figure 4**, the multiple views are given and detailed structure and localization, and depth of the PdCMs are shown.

Figure 5 presents images captured by LSFM imaging representing coronal sections from an adult ChR2/tdTomato mouse heart. This shows the distribution of PdCMs from the ventral side to the dorsal side, allowing visualizing of the regional distribution of PdCMs in a two-dimensional manner.

Figure 6 describes controlling heart rhythm with regional selective stimulation by electrical pacing under β-adrenergic stress conditions. First, by applying localized light pacing, we determined the light pacing responding region corresponding to the localization of Pnmt-derived cardiomyocytes (**Figure 6A**). In the ventricle, among four divided regions tested, only the left ventricular base responded (**Figure 6B**). We further conducted electrophysiological analysis compared ECG of PnmtCre/ChR2 in four different regions with frequency-dependent pacing under β-adrenergic (ISO) stress conditions. As shown in **Figures 6E–G**, the left ventricular base of hearts showed higher occurrences of VT under β-adrenergic stress.

Figure 7 shows an identical expression of distribution patterns of the $HCN4^{+}$ cells in $Hcn4^{DreER/tdTomato}$ heart (A) and $Pnmt^{+}$/Tdtomato positive cells in $Pnmt^{Cre/ChR2-tdTomato}$ heart (B).

The results presented here have several advantages and features. First, we used mouse models with conditional cell-type-specific overexpression of fluorescent protein allowing cell-type-specific visualization. These models provide the unique advantage of using tissue clearing for studying specific cell types without the requirement of using immunostaining with antibodies. Second, our modified clearing approach achieves high-quality transparent heart tissue with reduced auto-fluorescent background for optical imaging. Third, imaging by a high-resolution light-sheet system allows global heart view and cellular visualization achieved by rapid changes in optical lens and is integrated with 3D reconstruction without the requirement of additional mathematic modeling. Finally, the 3D reconstruction allows for detailed geometrical and topological analysis. The datasets presented here thus offer a means for reuse and a basis for further development of functional models of the heart by incorporating physiological data in the future.

DATA AVAILABILITY STATEMENT

The raw data supporting the conclusion of this article will be made available by the authors, without undue reservation.

ETHICS STATEMENT

The animal study was reviewed and approved by the Animal Care and Use Committee of the Southwest Medical University (Sichuan, China) (No: 20160930).

AUTHOR CONTRIBUTIONS

TS, HR, ZP, TC, and LL carried out the experiments. TS, HR, ZP, LL, CO'S, and DP carried out the data process and data analysis. ML and XT designed the experiments. ML, TS, and HR drafted the manuscript. CO'S, DP, XT, and ML revised and edited the. manuscript.

FUNDING

This study was supported by MRC (G10002647, G1002082, ML), BHF (PG/14/80/31106, PG/16/67/32340, PG/12/21/29473, PG/11/59/29004ML), BHF CRE at Oxford (ML) grants, the Chinese Nature Science Foundation Grant (31871181: ML, 81670310: XT), 221650/Z/20/Z Sir Henry Wellcome Trust Fellowship, The Wellcome Trust (CO'S, DP) and Collaborative Innovation Center for Prevention and Treatment of Cardiovascular Disease Grant (XT, ML).

ACKNOWLEDGMENTS

We thank Dennis Zhang and Nan Zheng from Carl Zeiss (Shanghai) Co., Ltd., and Carl Zeiss Microscopy Customer Centre Shanghai for the assistance with the imaging work on Lightsheet 7 microscopy.

REFERENCES

Acar, M., Kocherlakota, K. S., Murphy, M. M., Peyer, J. G., Oguro, H., Inra, C. N., et al. (2015). Deep Imaging of Bone Marrow Shows Non-dividing Stem Cells Are Mainly Perisinusoidal. *Nature* 526, 126–130. doi:10.1038/nature15250

Belle, M., Godefroy, D., Couly, G., Malone, S. A., Collier, F., Giacobini, P., et al. (2017). Tridimensional Visualization and Analysis of Early Human Development. *Cell* 169, 161–173. doi:10.1016/j.cell.2017.03.008

Brennan, J. A., Chen, Q., Gams, A., Dyavanapalli, J., Mendelowitz, D., Peng, W., et al. (2020). Evidence of Superior and Inferior Sinoatrial Nodes in the Mammalian Heart. *JACC: Clin. Electrophysiol.* 6, 1827–1840. doi:10.1016/j.jacep.2020.09.012

Chung, K., Wallace, J., Kim, S.-Y., Kalyanasundaram, S., Andalman, A. S., Davidson, T. J., et al. (2013). Structural and Molecular Interrogation of Intact Biological Systems. *Nature* 497, 332–337. doi:10.1038/nature12107

Ebert, S., Baden, J. M., Mathers, L. H., Siddall, B. J., and Wong, D. L. (1996). Expression of Phenylethanolamine N-Methyltransferase in the Embryonic Rat Heart. *J. Mol. Cell Cardiol.* 28, 1653–1658. doi:10.1006/jmcc.1996.0155

Epah, J., Pálfi, K., Dienst, F. L., Malacarne, P. F., Bremer, R., Salamon, M., et al. (2018). 3D Imaging and Quantitative Analysis of Vascular Networks: A Comparison of Ultramicroscopy and Micro-computed Tomography. *Theranostics* 8, 2117–2133. doi:10.7150/thno.22610

Ertürk, A., Becker, K., Jährling, N., Mauch, C. P., Hojer, C. D., Egen, J. G., et al. (2012). Three-dimensional Imaging of Solvent-Cleared Organs Using 3DISCO. *Nat. Protoc.* 7, 1983–1995. doi:10.1038/nprot.2012.119

Ertürk, A., Mauch, C. P., Hellal, F., Förstner, F., Keck, T., Becker, K., et al. (2011). Three-dimensional Imaging of the Unsectioned Adult Spinal Cord to Assess Axon Regeneration and Glial Responses after Injury. *Nat. Med.* 18, 166–171. doi:10.1038/nm.2600

Garofalo, S., D'Alessandro, G., Chece, G., Brau, F., Maggi, L., Rosa, A., et al. (2015). Enriched Environment Reduces Glioma Growth through Immune and Non-immune Mechanisms in Mice. *Nat. Commun.* 6, 6623. doi:10.1038/ncomms7623

Goodyer, W. R., Beyersdorf, B. M., Paik, D. T., Tian, L., Li, G., Buikema, J. W., et al. (2019). Transcriptomic Profiling of the Developing Cardiac Conduction System at Single-Cell Resolution. *Circ. Res.* 125, 379–397. doi:10.1161/circresaha.118.314578

Ho, S. Y. (2009). Structure and Anatomy of the Aortic Root. *Eur. J. Echocardiogr* 10, i3–10. doi:10.1093/ejechocard/jen243

Kolesová, H., Olejníčková, V., Kvasilová, A., Gregorovičová, M., and Sedmera, D. (2021). Tissue Clearing and Imaging Methods for Cardiovascular Development. *iScience* 24, 102387. doi:10.1016/j.isci.2021.102387

Kubota, S. I., Takahashi, K., Nishida, J., Morishita, Y., Ehata, S., Tainaka, K., et al. (2017). Whole-Body Profiling of Cancer Metastasis with Single-Cell Resolution. *Cel Rep.* 20, 236–250. doi:10.1016/j.celrep.2017.06.010

Matryba, P., Kaczmarek, L., and Gołąb, J. (2019). *Advances in* Ex Situ *Tissue Optical Clearing, Laser and Photonics Reviews*. Wiley-VCH Verlag.

Matsumoto, K., Mitani, T. T., Horiguchi, S. A., Kaneshiro, J., Murakami, T. C., Mano, T., et al. (2019). Advanced CUBIC Tissue Clearing for Whole-Organ Cell Profiling. *Nat. Protoc.* 14, 3506–3537. doi:10.1038/s41596-019-0240-9

Ni, H., Wang, Y., Crawford, W., Zhang, S., Cheng, L., Zhang, H., et al. (2017). Three-dimensional Image Reconstruction of Distribution of Pnmt+ Cell-Derived Cells in Murine Heart. *Sci. Data* 4, 170134. doi:10.1038/sdata.2017.134

Oshimori, N., Oristian, D., and Fuchs, E. (2015). TGF-β Promotes Heterogeneity and Drug Resistance in Squamous Cell Carcinoma. *Cell* 160, 963–976. doi:10.1016/j.cell.2015.01.043

Pan, C., Cai, R., Quacquarelli, F. P., Ghasemigharagoz, A., Lourbopoulos, A., Matryba, P., et al. (2016). Shrinkage-mediated Imaging of Entire Organs and Organisms Using uDISCO. *Nat. Methods* 13, 859–867. doi:10.1038/nmeth.3964

Renier, N., Adams, E. L., Kirst, C., Wu, Z., Azevedo, R., Kohl, J., et al. (2016). Mapping of Brain Activity by Automated Volume Analysis of Immediate Early Genes. *Cell* 165, 1789–1802. doi:10.1016/j.cell.2016.05.007

Sanderson, M. J., Smith, I., Parker, I., and Bootman, M. D. (2014). Fluorescence Microscopy. *Cold Spring Harbor Protoc.* 2014, pdb.top071795-pdb. doi:10.1101/pdb.top071795

Sands, G. B., Ashton, J. L., Trew, M. L., Baddeley, D., Walton, R. D., Benoist, D., et al. (2022). It's Clearly the Heart! Optical Transparency, Cardiac Tissue Imaging, and Computer Modelling. *Prog. Biophys. Mol. Biol.* 168, 18–32. doi:10.1016/j.pbiomolbio.2021.06.005

Susaki, E. A., Tainaka, K., Perrin, D., Kishino, F., Tawara, T., Watanabe, T. M., et al. (2014). Whole-Brain Imaging with Single-Cell Resolution Using Chemical Cocktails and Computational Analysis. *Cell* 157, 726–739. doi:10.1016/j.cell.2014.03.042

Susaki, E. A., Tainaka, K., Perrin, D., Yukinaga, H., Kuno, A., and Ueda, H. R. (2015). Advanced CUBIC Protocols for Whole-Brain and Whole-Body Clearing and Imaging. *Nat. Protoc.* 10, 1709–1727. doi:10.1038/nprot.2015.085

Susaki, E. A., and Ueda, H. R. (2016). Whole-body and Whole-Organ Clearing and Imaging Techniques with Single-Cell Resolution: Toward Organism-Level Systems Biology in Mammals. *Cel Chem. Biol.* 23, 137–157. doi:10.1016/j.chembiol.2015.11.009

Tainaka, K., Kubota, S. I., Suyama, T. Q., Susaki, E. A., Perrin, D., Ukai-Tadenuma, M., et al. (2014). Whole-body Imaging with Single-Cell Resolution by Tissue Decolorization. *Cell* 159, 911–924. doi:10.1016/j.cell.2014.10.034

Tainaka, K., Kuno, A., Kubota, S. I., Murakami, T., and Ueda, H. R. (2016). Chemical Principles in Tissue Clearing and Staining Protocols for Whole-Body Cell Profiling. *Annu. Rev. Cel Dev. Biol.* 32, 713–741. doi:10.1146/annurev-cellbio-111315-125001

Tainaka, K., Murakami, T. C., Susaki, E. A., Shimizu, C., Saito, R., Takahashi, K., et al. (2018). Chemical Landscape for Tissue Clearing Based on Hydrophilic Reagents. *Cel Rep.* 24, 2196–2210. doi:10.1016/j.celrep.2018.07.056

Tanaka, N., Kanatani, S., Tomer, R., Sahlgren, C., Kronqvist, P., Kaczynska, D., et al. (2017). Whole-tissue Biopsy Phenotyping of Three-Dimensional Tumours Reveals Patterns of Cancer Heterogeneity. *Nat. Biomed. Eng.* 1, 796–806. doi:10.1038/s41551-017-0139-0

Tomer, R., Khairy, K., and Keller, P. J. (2013). Light Sheet Microscopy in Cell Biology. *Methods Mol. Biol.* 931, 123–137. doi:10.1007/978-1-62703-056-4_7

Ueda, H. R., Ertürk, A., Chung, K., Gradinaru, V., Chédotal, A., Tomancak, P., et al. (2020). Tissue Clearing and its Applications in Neuroscience. *Nat. Rev. Neurosci.* 21, 61–79. doi:10.1038/s41583-019-0250-1

Verveer, P. J., Swoger, J., Pampaloni, F., Greger, K., Marcello, M., and Stelzer, E. H. K. (2007). High-resolution Three-Dimensional Imaging of Large Specimens with Light Sheet-Based Microscopy. *Nat. Methods* 4, 311–313. doi:10.1038/nmeth1017

Vigouroux, R. J., Belle, M., and Chédotal, A. (2017). Neuroscience in the Third Dimension: Shedding New Light on the Brain with Tissue Clearing. *Mol. Brain* 10, 33–10. doi:10.1186/s13041-017-0314-y

von Neubeck, B., Gondi, G., Riganti, C., Pan, C., Parra Damas, A., Scherb, H., et al. (2018). An Inhibitory Antibody Targeting Carbonic Anhydrase XII Abrogates Chemoresistance and Significantly Reduces Lung Metastases in an Orthotopic Breast Cancer Model *In Vivo*. *Int. J. Cancer* 143, 2065–2075. doi:10.1002/ijc.31607

Wang, Y., Lin, W. K., Crawford, W., Ni, H., Bolton, E. L., Khan, H., et al. (2017). Optogenetic Control of Heart Rhythm by Selective Stimulation of Cardiomyocytes Derived from Pnmt+ Cells in Murine Heart. *Sci. Rep.* 7, 40687. doi:10.1038/srep40687

Conflict of Interest: The authors declare that the research was conducted in the absence of any commercial or financial relationships that could be construed as a potential conflict of interest.

Advantages of publishing in Frontiers

OPEN ACCESS
Articles are free to read for greatest visibility and readership

FAST PUBLICATION
Around 90 days from submission to decision

HIGH QUALITY PEER-REVIEW
Rigorous, collaborative, and constructive peer-review

TRANSPARENT PEER-REVIEW
Editors and reviewers acknowledged by name on published articles

Frontiers
Avenue du Tribunal-Fédéral 34
1005 Lausanne | Switzerland

Visit us: www.frontiersin.org
Contact us: frontiersin.org/about/contact

REPRODUCIBILITY OF RESEARCH
Support open data and methods to enhance research reproducibility

DIGITAL PUBLISHING
Articles designed for optimal readership across devices

FOLLOW US
@frontiersin

IMPACT METRICS
Advanced article metrics track visibility across digital media

EXTENSIVE PROMOTION
Marketing and promotion of impactful research

LOOP RESEARCH NETWORK
Our network increases your article's readership